



Metallo drugs as inducers and inhibitors of chemical nuclease activity

Andreea Prisecaru B.Sc.

Thesis submitted in partial fulfilment of the
requirements for the degree of

Doctor of Philosophy

Research supervisor: Dr. Andrew Kellett, DCU

External co-supervisor: Dr. Nicholas Gathergood, TUT Estonia

School of Chemical Sciences

Dublin City University

September 2015

I hereby certify that this material, which I now submit for assessment on the programme of study leading to the award of Doctor of Philosophy (PhD) is entirely my own work, that I have exercised reasonable care to ensure that the work is original, and does not to the best of my knowledge breach any law of copyright, and has not been taken from the work of others save and to the extent that such work has been cited and acknowledged within the text of my work.

Signed: _____ (Candidate) ID No.: 11212747 Date: _____

Dedicated to my parents

ACKNOWLEDGEMENTS

I would like to express my sincere gratitude to my supervisor Dr. Andrew Kellett for believing in my abilities and giving me the opportunity to work in his group. This work would have not been possible without his patience, motivation, enthusiasm, and extended knowledge. I do not have words to describe my feelings about his dedication, hard work and quest for the research. His guidance helped me in all of my research and writing of this thesis. I could not have imagined having a better mentor for my Ph.D. study. Thanks Andrew.

A very special thanks goes out to Dr. Niall Barron in NICB. He provided me with direction, support and advice with all of the biological work.

I would like to thank my co-supervisor Dr. Nick Gathergood for his assistance along the way.

I would like to express my gratitude to my PhD colleagues, Zara and Creina. They were always supporting me and encourage me with their best wishes. Also, my daily work I have been blessed with a friendly and cheerful group of fellow postgrads and postdocs Deepak, Tadgh, Natasha, Adam, and Paul.

I would also like to thank NICB staff (Carol, Gillian, and Mairead) and technical staff in the Chemical Sciences (Veronica, Catherine, Ambrose, Damien, Vinny, John) for all their help and support.

Research Career Start Programme at Dublin City University, and Irish Research Council (IRC) grant GOIPG/2013/937 is gratefully acknowledged.

Finally, I would like to thank my family, Mariel and Kevin. They were always there cheering me up and stood by me through the good times and bad.

PUBLICATIONS

Prisecaru A., Molphy Z., Kipping R.G., Peterson E.J., Qu Y., Kellett A., and Farrell N.P. 2014. The phosphate clamp: sequence selective nucleic acid binding profiles and conformational induction of endonuclease inhibition by cationic Triplatin complexes. *Nucleic Acids Research*, **42**, 22, pp13474-13487

Prisecaru A., Molphy Z., Slator C., Barron, N., McCann M., Colleran J., Chandran D., Gathergood N. and Kellett A. 2014. Copper Phenanthrene Oxidative Chemical Nucleases. *Inorganic Chemistry*, **53**, 10, pp5392-5404.

Prisecaru A., McKee V., Howe O., Rochford G., McCann M, Colleran J., Barron N., Pour M., Gathergood N. and Kellett A. 2013. Regulating Bioactivity of Cu²⁺ Bis-1,10-Phenanthroline Artificial Metallonucleases with Sterically Functionalised Pendant Carboxylates. *Journal Of Medicinal Chemistry*, **56**, 21, pp8599-8615.

McCann M., McGinley J., Ni K., O'Connor M., Kavanagh K., McKee V., Colleran J., Devereux M., Gathergood N., Barron N., Prisecaru A. and Kellett A. 2013. A new phenanthroline-oxazine ligand: synthesis, coordination chemistry and atypical DNA binding interaction. *Chemical Communications* **49**, pp2341-2343

Kellett A., Prisecaru A., Slator C., Molphy Z., McCann M. 2013. Metal-Based Antimicrobial Protease Inhibitors. *Current Medicinal Chemistry*, **20**, 25, pp3134-3151. (review)

Prisecaru A., Devereux M., Barron N., McCann M., Colleran J., Casey A., McKee V. and Kellett A. 2012. Potent oxidative DNA cleavage by the di-copper cytotoxin: [Cu₂(terephthalate)(1,10-phen)₄]²⁺. *Chemical Communications*, **48**, 55, pp6906-6908

POSTER AND SCIENTIFIC TALKS

Poster title:

Prisecaru A., Molphy Z., Kipping R.G., Peterson E.J., Qu Y., Kellett A., and Farrell N.P. 2014. The phosphate clamp: sequence selective nucleic acid binding profiles and conformational induction of endonuclease inhibition by cationic Triplatin complexes, *Inorganic Ireland, Royal College of Surgeons in Ireland, 11-December 2014.*

Potent Oxidative DNA Cleavage by the Di-Copper Cytotoxin:

$[\text{Cu}_2(\mu\text{-terephthalate})(1,10\text{-phen})_4]^{2+}$ Andreea Prisecaru, Michael Devereux, Niall Barron, Malachy McCann, John Colleran, Alan Casey, Vickie McKee and Andrew Kellett, *2012 Symposium on Inorganic Chemistry in Ireland, 07-DEC-12 – National University of Ireland, Galway*

Scientific talks:

Prisecaru A., Molphy Z., Kipping R.G., Peterson E.J., Qu Y., Kellett A., and Farrell N.P. 2014. The phosphate clamp: sequence selective nucleic acid binding profiles and conformational induction of endonuclease inhibition by cationic Triplatin complexes, *13th International Symposium on Applied Bioinorganic Chemistry - ISABC13, June 12-15, 2015 NUI Galway, Galway, Ireland*

Prisecaru, A., Molphy, Z., McCann, M. and Kellett, A. Molecular Methods at the Metallodrug-DNA Interface, *66th Irish Universities Chemistry Research Colloquium, 19-20th June 2014, National University of Ireland, Galway*

Andreea Prisecaru, Potent Oxidative DNA Cleavage by the Di-Copper Cytotoxin: $[\text{Cu}_2(\mu\text{-terephthalate})(1,10\text{-phen})_4]^{2+}$, *6th European Young Investigator Conference 26 – 30 June, 2013, Shubice, Poland, COST Action CM1201*

AWARDS:

Awarded the winner of the best poster presentation at the *2012 Symposium on Inorganic Chemistry in Ireland, National University of Ireland Galway (NUIG)*

Awarded by Irish Research Council (IRC) scholar GOIPG/2013/937, with the project title: *Metallo-Phenoxazine Agents as Chiral DNA-Targeting Therapeutics*

AIMS OF THE RESEARCH

The aim of this research is to develop a wide range of biophysical assays in order to investigate the biological activity of metallodrugs. In particular, this thesis focuses on:

A detail analysis of DNA cleavage profiles using plasmid dsDNA by copper-phenanthroline derivatised complexes.

A unique experimental design in order to identify the site-specific oxidative cleavage of dsDNA by inorganic materials using type II endonucleases.

Synthesis and characterisation of Cu^{2+} -Phen complexes containing sterically functionalized pendant carboxylates along with detailed DNA binding analysis.

The oxidative chemical nuclease examination of copper complexes containing oxazine and/or diimine N,N' - ligands.

The design of a microfluidic “on chip” method employed to quantify and visualise double stranded DNA damage.

The study of site-specific trinuclear platinum (II) (Triplatin) complexes on binding affinity, and the condensation effect on both DNA and tRNA, along with endonuclease enzyme recognition.

CONTRIBUTION TO PEER-REVIEWED PUBLICATIONS

This thesis includes five original papers published in peer-reviewed journals. All of the work was done in collaboration with colleagues from my group and through collaborations with other universities.

My contribution to each paper presented in this thesis is outlined in the table below:

Thesis Chapter	Publication Title	Publication Status	Nature and Extent of Candidates Contribution
II	Potent Oxidative DNA Cleavage by the Di-Copper Cytotoxin $[\text{Cu}_2(\mu\text{-terephthalate})(1,10\text{-phen})_4]^{2+}$	Published in <i>Chem. Commun.</i> , 2012, 48 , 6906-6908	Manuscript 1 st author, DNA cleavage experiments, site-selective cleavage using type II endonucleases and identification of mode of DNA cleavage using T4 ligase.
III	A new phenanthroline-oxazine ligand: synthesis, coordination chemistry and atypical DNA binding interaction	Published in <i>Chem. Commun.</i> , 2013., 49 , 2341-2343	Manuscript co-author, designing and conducting the DNA binding experiments, DNA cleavage reactions and viscosity experiments.
IV	Regulating Bioactivity of Cu^{2+} Bis-1,10-Phenanthroline Artificial Metallonucleases with Sterically Functionalised Pendant Carboxylates	Published in <i>J. Med. Chem.</i> , 2013, 56 , 21, 8599-8615.	Manuscript 1 st author, synthesis and characterization of the complexes. DNA cleavage, binding and viscosity analyses, UV- vis stabilities studies and the quantification of H_2O_2 with Amplex Red.
V	Copper Phenanthrene Oxidative Chemical Nucleases	Published in <i>Inorg. Chem.</i> , 2014, 53 , 10, 5392-5404	Manuscript 1 st author with Zara Molphy, chemical nuclease activity using the “on chip” microfluidic analysis and the comparison study of different DNA plasmids cleavage activity. Helped with DNA quenching and T_M of poly[d(G-C) ₂] and poly[d(A-T) ₂] synthetic nucleotides.
VI	The phosphate clamp: sequence selective nucleic acid binding profiles and conformational induction of endonuclease inhibition by cationic Triplatin complexes.	Published in <i>Nucleic Acids Res.</i> , 2014, 42 , 22, 13474-13487	Manuscript 1 st author, DNA binding on different types of DNA, nuclease inhibition using the “on chip” microfluidic analysis.

Signed: _____
Andreea Prisecaru

Date: _____

Signed: _____
Dr. Andrew Kellett

Date: _____

THESIS OUTLINE

A detailed overview of each chapter is given below:

Chapter I

This chapter gives an overview of the topics common to most of the chapters in the context of literature review. Important topics include: biological importance of copper, DNA as molecular target, oxidative damage of DNA and the mechanism of oxidative DNA damage are discussed in order to introduce concepts that will be further used in the experimental chapters (Chapters II to VI).

Chapter II

This chapter describes in detail the oxidative DNA damage of $[\text{Cu}(\mu\text{-terephthalate})(\text{Phen})_4]^{2+}$ (phen = 1,10-phenanthroline) that was previously shown to damage DNA in the absence of oxidant and reductant. This chapter highlights a unique experimental design employed to detect site-specific damage on plasmid DNA, and that the “self-cleavage” DNA damage is oxidatively linked is also described.

Chapter III

This chapter introduces a novel series of copper-oxazine (Cu-PDT) complexes, where PDT is a ligand formed between amino acid *L*-tyrosine methyl ester and 1,10-phenanthroline-5,6-dione. In order to establish how these complexes interact with DNA, a high-throughput fluorescence DNA binding assay was developed using 96 well plates. In this chapter, the viscosity and DNA cleavage experiments are also described.

Chapter IV

This chapter describes the synthesis and characterisation of a novel class of small-molecules containing a carboxylate group coordinate to the copper(II)-bis-1,10-phenanthroline molecule. The interaction of this new class of inorganic molecule with macromolecules (DNA and bovine serum albumin) is described in detail. The artificial metallonuclease activity of these compounds is detected using plasmid DNA; the *in vitro* cytotoxicity is examined on a wide range of cancerous cell line along with the detection of double strand breaks on ovarian cancer cell line using the immunodetection of γ -H2AX foci is also described in detail.

Chapter V

This chapter describes the synthesis and characterisation of a new class of copper-phenanthroline complexes containing fused diimine *N,N'*-ligands along with their interaction with a variety of synthetic and natural dsDNA. Also, this chapter describes a novel assay using microfluidic on-chip method employed to quantify and visualize double strand breaks in linear plasmid DNA. Furthermore, the *in vitro* cytotoxicity studies on ovarian cancer cell line are also shown.

Chapter VI

This chapter describes the effect of trinuclear platinum(II) complexes on dsDNA and tRNA binding affinity, and also detailed analysis - using microfluidic chip assay used to describe type II endonuclease enzyme recognition. Base-specific interaction studies using 2D NMR spectra on adenine-thymine rich and guanine-cytosine rich duplexes are reported

TABLE OF CONTENTS

ACKNOWLEDGEMENTS.....	i
PUBLICATIONS.....	ii
POSTER AND SCIENTIFIC TALKS.....	iii
Poster title:.....	iii
Scientific talks:.....	iii
AWARDS:	iv
AIMS OF THE RESEARCH	v
CONTRIBUTION TO PEER-REVIEWED PUBLICATIONS.....	vi
Chapter I.....	viii
Chapter II.....	viii
Chapter III.....	viii
Chapter IV.....	ix
Chapter V	ix
Chapter VI.....	ix
TABLE OF CONTENTS	x
TABLE OF FIGURE	xiv
TABLE OF TABLES.....	xxi
TABLE OF SCHEMES	xxiii
ABBREVIATIONS	xxiv
ABSTRACT	xxvi
Metallodrugs as Inducers And Inhibitors of Chemical Nuclease Activity	xxvi
By Andreea Prisecaru.....	xxvi
CHAPTER I.....	1
I.1 Copper in biological systems	2
I.1.1 Biological importance of copper	2
I.1.2 An overview of copper proteins	2
I.1.3 Entry of copper into mammalian cells.....	4
I.1.4 Copper diseases	6
I.2 DNA as a molecular target.....	8
I.2.1 DNA: structure and function	8
I.2.2 Metal binding sites on DNA	10
I.2.3 Copper functionalised groove binders	17
I.3 Oxidative cleavage of DNA	22
I.3.1 Reactive oxygen Species (ROS)	22
I.3.2 Oxidative damaged to nucleobases	23
I.3.3 Copper-binding (ATCUN) motif.....	27
I.4 Mechanisms of oxidative DNA damage.....	28
I.4.1 [Cu(1,10-phenanthroline) ₂] ²⁺	28
I.4.2 Bleomycin.....	31
References.....	35
CHAPTER II	50
II.1 Abstract	51
II.2 Introduction	51
II.3 Results and discussion	53
II.4 Conclusion	58

II.5 Materials and methods	59
II.5.1 Preparation of the Complexes	59
II.5.2 DNA cleavage experiments	59
II.5.3 Cytotoxicity experiments	60
II.5.5 Electrochemical experiments	62
References	68
Chapter III	70
III.2. Introduction	71
III.3 Conclusion	77
III.4 Material and Methods	78
III.4.2 Preparation of the complexes	78
III.4.3 X-ray crystallography	79
III.4.4 DNA binding experiments	80
III.4.5 DNA cleavage experiments	83
III.5.6 Viscosity experiments	84
III.4.7 Electrochemistry	85
References	88
CHAPTER IV	90
IV.1 Abstract	91
IV.2 Introduction	92
IV.3 Results And Discussion	94
IV.3.1 Synthesis and characterisation	94
IV.3.2 Binding affinity toward bovine serum albumin and calf thymus DNA	97
IV.3.3 <i>In vitro</i> cytotoxicity	103
IV.3.4 Artificial metallonuclease activity	110
IV.3.5 Interactions with H ₂ O ₂	111
IV.3.6 Induction of dsDNA breaks in SK-OV-3 cells	113
IV.4 Conclusion	116
IV.5 Experimental	118
IV.5.1 Synthesis	118
IV.5.2 Electrochemistry	119
IV.5.3 X-Ray Crystallography	120
IV.5.4 Bovine Serum Albumin Binding	122
IV.5.6 <i>In Vitro</i> Cytotoxicity with Human-Derived Cancer Cell Lines	122
IV.5.7 Antibacterial Activity ⁵⁸	123
IV.5.9 DNA Cleavage Studies	125
IV.5.10 Quantitation of Hydrogen Peroxide with Amplex Red	125
IV.5.11 Detection of double-strand DNA breaks (DSBs) within SK-OV-3 Cancer cells	125
IV.6 Methods	126
IV.6.1 Crystallography	126
IV.6.2 Electrospray ionisation mass spectra (ESI-MS)	127
IV.6.3 Linearisation of pBR322	127
IV.6.4 Electrochemical Stability of Complexes	127
IV.6.5 UV-vis stability studies	128
References	131
Chapter V	138
V.1. Abstract	139
V.2. Introduction	139
V.3. Results	141
V.3.8 <i>In vitro</i> cytotoxicity toward SKOV3 cancer cells	154
V.4 Discussion	158
V.5 Materials And Methods	161

V.5.2 DNA binding studies.....	164
V.5.4 Artificial metallonuclease activity	165
V.5.9 Optimization of thermal melting on poly[d(A-T) ₂] and poly[d(G-C) ₂]..	169
References.....	171
Chapter VI.....	174
VI. 1 Abstract	175
VI.2 Introduction.....	175
VI. 3 Materials and Methods.....	179
VI.3.1. Preparation of Triplatin complexes [{ <i>trans</i> -Pt(NH ₃) ₂ (NH ₂ (CH ₂) _n NH ₃)} ₂ - μ- <i>trans</i> -Pt(NH ₃) ₂ (NH ₂ (CH ₂) _n NH ₂) ₂] (NO ₃) ₈	180
VI.3.2. DNA binding experiments	180
VI.3.2. NMR Analysis of TriplatinNC Modified DNA Oligomers.....	184
VI.3.3. Endonuclease enzyme inhibition	185
VI.3.4. tRNA binding.....	186
VI.4. Results And Discussion	187
VI.4.1. Binding to calf thymus and salmon testes DNA.....	187
VI.4.2 Base-specific nucleic acid interactions	192
VI.4.8 Binding to yeast tRNA	199
VI.4.9 Interactions with superhelical pUC19 and endonuclease inhibition ...	201
VI.4.10 On-chip identification of endonuclease inhibition	204
VI.5 Conclusions	207
References.....	209
Appendix A.....	A-1
A.A.1 X-ray crystallography of methyl 2-(4-hydroxyphenyl)-4a,12b- dihydro-2H-[1,4]oxazino[2,3-f][1,10]phenanthroline-3-carboxylate (PDT)	A-2
Appendix B.....	B-1
A.B.1 Infrared spectroscopy of [Cu(R-COO)(1,10-Phen) ₂] ⁺	B-2
A.B.2 Crystallography	B-5
A.B.2.1 [Cu(For)(1,10-Phen) ₂](NO ₃)·6H ₂ O, (Cu-For-Phen)	B-5
A.B.2.2 [Cu(Ace)(1,10-Phen) ₂](NO ₃)·2H ₂ O, (Cu-Ace-Phen).....	B-9
A.B.2.3 [Cu(Pro)(1,10-Phen)]·½(CO ₃)·4½H ₂ O, (Cu-Pro-Phen)	B-14
A.B.2.4 [Cu(Iso)(1,10-Phen) ₂] ₂ ·2(NO ₃)·4H ₂ O, (Cu-Iso-Phen)	B-19
A.B.2.5 [Cu(Piv)(1,10-Phen) ₂] ₂ (piv) ₂ ·(Hpiv)·9H ₂ O, (Cu-Piv-Phen)	B-25
A.B.3 Electrospray ionisation mass spectra (ESI-MS).....	B-33
Appendix C	C-1
A.C.1 Electrogram data generated by the Bioanalyzer 2100.....	C-2
A.C.2 ctDNA thermal melting analysis.....	C-6
A.C.3 Circular dichroism experiments	C-6
A.C.4 ITC of polynuclear DNA titrated with TriplatinNC.....	C-7
A.C.5 NMR Analysis of TriplatinNC Modified DNA Oligomers	C-7
A.C.6 Binding affinity of ethidium bromide to ctDNA and tRNA	C-9
A.C.8 tRNA thermal melting analysis.....	C-10
Appendix D	D-1
“Metal-Based Antimicrobial Protease Inhibitors”	D-1
A.D.2 Introduction	D-2
A.D.3 HIV-1 Protease Inhibitors.....	D-4
A.D.3.1 Introduction.....	D-4
A.D.3.2 Metallacarboranes	D-6
A.D.3.3 Polyoxometalates	D-13
A.D.3.3 Gold Complexes.....	D-16

A.D.3.4 Copper Complexes	D-18
A.D.4 Parasitic Protease Inhibitors.....	D-20
A.D.4.1 Introduction.....	D-21
A.D 4.2 Gold(I) and gold(III) complexes.....	D-24
A.D 4.3 Palladium(II) and Oxorhenium(V) complexes	D-29
A.D.5. Conclusion.....	D-32
References.....	D-35

TABLE OF FIGURE

Figure I.1 Copper delivering proteins (Protein Data Bank, PDB, codes indicated) a. First transmembrane domain from human copper transporter 1 CTR1 (PDB, 2LS2), b. COX17 (PDB, 2RNB) delivers copper to mitochondrial cytochrome <i>c</i> oxidase c. Copper chaperons, Sco1 (PDB, 2GQM) play a fundamental role in delivery of copper to the mitochondria, d. ATOX1 (PDB, 1TL4) mediates copper transport to the Golgi apparatus, and e. 1 st domain of copper chaperons for superoxide dismutase, CCS (PDB, 2RSQ) play a fundamental role in delivering copper to the pro-form of SOD.	5
Figure I.2 Simplified scheme showing intracellular distribution of copper into the human cell. Copper enters into the human cell through high affinity copper uptake protein (CTR1). Once inside the cell, copper is passed onto the specific enzymes, ATOX1, CCS, COX, which escort copper ions to its specific destination (Golgi apparatus, SOD1 and mitochondria, respectively). Upon reaching its destination, copper is either incorporated into Golgi network and released using a P-type ATPase (cP), inserted into apo-SOD1 or incorporated into cytochrome <i>c</i> oxidase located in mitochondria.	6
Figure I.3 Simplified scheme of the disruption of copper transport in Wilson's and Menkes's disease. ⁵⁰	7
Figure I.4 a. The 5'-phosphate nucleotide of DNA. Each nucleotide contains a phosphate group, a deoxyribose sugar molecule and a nitrogen base. DNA contains four types of nitrogen bases, adenine (A), cytosine (C), guanine (G), and thymine (T). b. Connectivity in a strand of DNA. The 3'-ATCG-5' sequence is shown.	8
Figure I.5 The building blocks of DNA. DNA is made up of molecules called nucleotides. Each nucleotide contains a phosphate group, a sugar group, and a base that are linked covalently into a polynucleotide chain. Nucleotides are attached together to form strands that spiral around one another to create a structure called a double helix. The two strands are held together by hydrogen bonds, two hydrogen bonds formed between A and T, and three hydrogen bonds formed between G and C.	9
Figure I.6 Schematic of chelator containing nucleotides i. Cu ²⁺ phenylenediamine β-C-nucleoside and ii. H-Cu-H nucleotide, iii. Cu-salen complex, and iv pyrazole-Cu-pyrazole self base pair system.	11
Figure I.7 Non-covalent binding. A. Minor groove binding. B. Binding through intercalation. i. Netropsin structure and 3'-AATT dsDNA sequence. B. Ethidium bromide (EtBr) structure and DNA 3'-TAGC dsDNA sequence.	13
Figure I.8 Selection of the clinically use minor groove binders. These crescent shaped molecules alters DNA conformation by binding to A-T-rich domains in DNA. ...	16
Figure I.9 Chemical structure of several DNA intercalators. Classical intercalators: ethidium bromide and diaminoacridine; threading intercalators: DAPI; non-classical intercalators: naphthalene diimide.	17
Figure I.10 Structure of minor-groove binder-intercalator. Cu(II)-tripeptide glycylhistidyllysine (colour green), oligopyrrolicarboxamide part of netropsin (coloured blue) which is covalently linked to an intercalating 9-(4-glycylanilino)-acridine derivative (coloured purple).	18
Figure I.11 Potential diagram for O ₂ at pH 7. Successive one-electron reduction yields the O ₂ ^{•-} . H ₂ O ₂ produce the [•] OH and H ₂ O.	24
Figure I.12 Structure of diastereoisomers: A. (5'R) and (5'S) of 5'8-cyclo-2'-deoxyadenosine and B. (5'R) and (5'S) of 5'8-cyclo-2'-deoxyguanosine.	27
Figure I.13 Structure of the copper – GGH complex. GGH mimics the specific copper transport site of albumin and has the required planar geometry needed to bind copper. ¹³⁷	28
Figure I.14 Proposed formation of reactive copper-oxo species <i>via</i> Fenton chemistry ^{90,145}	29

- Figure I.15** **A.** Structure of Sigman's reagent $[\text{Cu}(1,10\text{-phenanthroline})_2]^{2+}$ ($[\text{Cu}(\text{phen})_2]^{2+}$) **B.** Proposed mechanism for scission of DNA by $[\text{Cu}(\text{phen})_2]^+$. Cu-oxo species are formed by the oxidation of DNA bound to $[\text{Cu}(\text{phen})_2]^+$ in the presence of H_2O_2 **a.** C1' radical formation by hydrogen atom abstraction followed by carbocation (**b.**) stabilized by partial double bond to furanose oxygen, species **c.** is formed by deprotonation at C2' followed by elimination of 3'-phosphate resulting in strand scission (**d.**). Attack by H_2O on species **d.** leads to elimination of purine/pyrimidine base resulting in species **e.** followed by the formation of abasic site 5-methylenefuranone (5-MF) and 3'-and 5'-phosphorylated ends.^{90,148} 30
- Figure I.16** **a.** Structure of bleomycin and functional domains. The metal binding region is colored in blue and the nitrogenous atoms that coordinates metal are colored in black. The linker region is in purple and the bithiazole tail is colored in green. The disaccharide (R) is colored in brown and the positively charged tail from the bithiazole tail (R') is colored in red. **b.** Crystal structure of Co(III)-Bleomycin A(2) bound to d(GGAAGCTTCC)₂ (PDB, 1MXK) C – green, H – black, O – red, N – blue S – yellow, and Co(III) in pink. 33
- Figure I.17** Formation of activated bleomycin and cleavage of DNA. The activated bleomycin is formed in the presence of O_2 and reductant. The initial step in DNA damages is the removal of hydrogen atom from C-4' from deoxyribose sugar. In the presence of O_2 , 4'-peroxy radical is formed which is further reduced to 4'-hydroperoxyde. The later undergoes a series of chemical transformations with the formation of base propenals and oligonucleotide 3'-phosphoroglycolates (pathway to right).^{177,182} When O_2 is limited, oxidant is added and alkali liable lesion occurs at C-4' known as C-4' hydroxylated apurinic acids (pathway to the left).¹⁷⁷ 34
- Figure II.18** **a.** Two perspective, space-filling views of the cation in **S1**, the copper ions are bridged by the terephthalate group. Colour scheme: copper, green; oxygen, red; nitrogen, blue, carbon, grey. **b.** X-Ray structure of the cation in $[\{\text{Cu}(\text{phen})_2\}_2(\text{terph})](\text{terph})$ ¹⁸³ 52
- Figure II.19** DNA cleavage reactions using 400 ng of pBR322 plasmid DNA were carried out at 37 °C using $[\text{Cu}_2(\mu\text{-terph})(1,10\text{-phen})_4](\text{terph})$ (**S1**) and the positive control agent $\text{Cu}(1,10\text{-phen})_2\text{Cl}_2$ (**S2**) in 80 mM HEPES at pH 7.2 with 25 mM NaCl then analysed using agarose gel electrophoresis.† **A.** Time-dependant study using 30 μM of **S1**, **S2** and CuCl_2 exposed to the plasmid for 0.5, 1.0, 2.5, 5.0 and 10 h, **B.** 0.5 h incubation using 20 μM of **S1**, **S2** and CuCl_2 in the presence of 1 mM added oxidant or reductant, **C.** Cleavage reactions, after 0.5 h incubation, using 0.5, 1.0 and 10.0 μM of **S1** in the presence of 1 mM added oxidant and/or reductant. 53
- Figure II.20** Experimental design for identifying sequence-specific DNA cleavage. **A.** The unknown double-stranded scission mode, specific (■) or random (■), of plasmid DNA occurs by **S1**, **B.** Introduction of a site-specific restriction enzyme (■) (e.g. *EcoRI* or *EcoRV*) hydrolyses the **S1** linearized DNA exactly once, **C.** Gel electrophoresis of the resulting cleavage reaction reveals either random cutting (laddering) or site-specific cutting (precise fragmentation). 54
- Figure II.21** **A.** Cleavage reactions of pBR322 by the restriction enzyme *EcoRV* (lane 2), **S1** (lane 3), **S1** followed by exposure of *EcoRV* or *EcoRI* (lanes 4 and 5).† **B.** Reaction of pBR322 by the restriction enzyme *EcoRV* (lane 1), cleaved plasmid DNA by **S1** and *EcoRI* extracted and purified from gel **A** (using a Qiagen QIAquick gel extraction kit) were subsequently incubated with T4 ligase (lanes 2 and 3), control DNA and a 1 kb ladder (lanes 5 and 6).† (Note all reactions performed without exogenous agents) 55
- Figure II.22** **A.** *In vitro* cytotoxicity of **S1** and mitoxantrone against cisplatin-resistant ovarian cancer SK-OV-3 and non-tumorigenic ovarian HS-832 cell lines,† **B.** Generation of endogenous ROS within epithelial lung cancer cells (A549) following exposure to **S1**.† 56

- Figure II.23** Typical cyclic voltammograms describing the redox behaviour of 1 mM **S1** in the absence (black trace) and presence (red trace) of 2 mM ascorbate, in 0.1 M KCl aqueous solution. Experimental details in section 2.5.5.† 58
- Figure II.24** Enlargement of Figure 6 from manuscript; Typical cyclic voltammograms detailing the electrochemical behaviour of **S1** in the absence (black trace) and presence (red trace) of 2 mM ascorbate in 0.1 M KCl aqueous solution. The A_1/C_1 peaks describe the coupled 1-electron $\text{Cu}^{2+}/\text{Cu}^+$ redox behaviour of **S1** in the absence of ascorbate. On addition of reductant the peak C_1 describes two 1-electron processes. Peak A_2 is the 2-electron, 2-proton oxidation of L-ascorbate. Glassy Carbon working electrode, platinum counter electrode, SCE reference electrode, and scan rate 100 mV s^{-1} . The diminished solubility of **S1**, in aqueous solution, results in lower peak current values when compared to the **S1** current values returned in pure DMF (II.5.5.5). 63
- Figure II.25** Typical cyclic voltammograms detailing the stability of 1 mM **S1**, with potential cycling, in a 0.1 M KCl aqueous solution. Little activity is lost after 30 potential cycles. Glassy Carbon working electrode, platinum counter electrode, SCE reference electrode, and scan rate 100 mV s^{-1} 63
- Figure II.26** Typical cyclic voltammograms detailing the redox behaviour of 1 mM $[\text{Cu}(\text{phen})_2]^{2+}$ (**S2**) in the absence (black trace) and presence (red trace) of 2 mM ascorbate in 0.1 M TBAPF₆/DMF. The peaks correspond to the following processes; A_1/C_1 - $\text{Cu}^{2+}/\text{Cu}^+$ couple, A_2 - ascorbate oxidation, A_3/C_3 - uncomplexed $\text{Cu}^{2+}/\text{Cu}^+$. Glassy Carbon working electrode, platinum counter electrode, Ag^+/Ag non-aqueous reference electrode, and scan rate of 100 mV s^{-1} 64
- Figure II.27** Typical cyclic voltammograms detailing the redox behaviour of 1 mM **S1** in the absence (black trace) and presence (red trace) of 2 mM ascorbate, in 0.1 M TBAPF₆/DMF. Peak A_2 describes the irreversible oxidation of unreacted ascorbate. Glassy Carbon working electrode, platinum counter electrode, Ag^+/Ag non-aqueous reference electrode, and scan rate of 100 mV s^{-1} . Note: No electrochemical redox activity is observed for uncomplexed $\text{Cu}^{2+}/\text{Cu}^+$, as is evident with the $\text{Cu}^{2+}/\text{Cu}^+$ couple in $[\text{Cu}(\text{phen})_2]^{2+}$ (**S2**). 64
- Figure III.28** A. Space-fill view of pdtme in **PDT**·MeOH (MeOH shown in stick view), B. A view of **PDT**·MeOH with atoms depicted with displacement ellipsoids at their 50% probability level. 73
- Figure III.29** A. Competitive ethidium bromide displacement for netropsin, pentamidine, metal salts, free ligands and complexes with CT-DNA, and B. DNA cleavage reactions with 400 ng of pBR322 plasmid DNA carried out for 30 min at 37°C in 80 mM HEPES at pH 7.2 with 25 mM NaCl and 1 mM Na-L-ascorbate then analysed using agarose gel electrophoresis. Lane 1: DNA control; lane 2: $[\text{Cu}(\text{OAc})_2]$; lane 3: AgNO_3 ; lane 4: **PDT**; lane 5: **CuPhen**; lane 6: **AgPhen**; lane 7: **CuPDT**; lane 8: **AgPDT** 75
- Figure III.30** A. Relative viscosity changes in salmon testes dsDNA (1 mM in DNAP in 80 mM HEPES) upon exposure to EtBr, netropsin, **CuPhen** and **CuPDT**, and B. typical cyclic voltammograms describing the redox behaviour of 1 mM **CuPhen** (left) and **CuPDT** (right), at a scan rate of 100 mV s^{-1} , in the absence (solid black trace) and presence (dashed black trace) of 2 mM ascorbate.† 76
- Figure III.31** Competitive ethidium bromide displacement for netropsin, pentamidine, metal salts, free ligands and complexes with CT-DNA. 81
- Figure III.32** Fluorescence quenching (Q) of EtBr-DNA and Hoechst 33258-DNA as a function of added test compound. 83
- Figure III.33** Cleavage reactions using $\text{Cu}(\text{phen})_2(\text{ClO}_4)_2$ with 1 mM Na-L-ascorbate with phenol (5 – 100 μM) in the presence of 1 mM added reductant. Lane 1: pUC19 control; lane 2: **CuPhen**; lane 3: **CuPhen** + 5 μM phenol; lane 4: **CuPhen** + 10 μM phenol; lane 5: **CuPhen** + 20 μM phenol; lane 6: **CuPhen** + 40 μM phenol; lane 7: **CuPhen** + 100 μM phenol 84

Figure III.34 Typical cyclic voltammograms detailing the redox behaviour of 1 mM CuPhen in the presence of 2 mM ascorbate, over a range of scan rates, in 0.1 M TBAPF ₆ /DMF. Glassy Carbon working electrode, platinum counter electrode, Ag ⁺ /Ag non-aqueous reference electrode.	85
Figure III.35 Typical cyclic voltammograms detailing the redox behaviour of 1 mM CuPDT in the presence of 2 mM ascorbate, over a range of scan rates, in 0.1 M TBAPF ₆ /DMF. Glassy Carbon working electrode, platinum counter electrode, Ag ⁺ /Ag non-aqueous reference electrode.	85
Figure III.36 Typical cyclic voltammograms detailing the redox behaviour of 1 mM CuPhen over a range of scan rates, in 0.1 M TBAPF ₆ /DMF. Glassy Carbon working electrode, platinum counter electrode, Ag ⁺ /Ag non-aqueous reference electrode.	86
Figure III.37 Corresponding Randles-Sevcik Plot, 1 mM CuPhen , the peak currents exhibit a linear dependence with the square root of the scan rate. Thus the redox behaviour of CuPhen is under diffusion control.	86
Figure III.38 Typical cyclic voltammograms detailing the redox behaviour of 1 mM CuPDT over a range of scan rates, in 0.1 M TBAPF ₆ /DMF. Glassy Carbon working electrode, platinum counter electrode, Ag ⁺ /Ag non-aqueous reference electrode.	87
Figure III.39 Randles-Sevcik behaviour of CuPDT , indicating a diffusion controlled redox regime.	87
Figure IV.40 Molecular structures of the [Cu(RCOO)(1,10-phen) ₂] ⁺ cations (top), single X-ray crystal structures of the complexes (centre), and perspective space-filled views of the five cations (bottom).	96
Figure IV.41 Electronic spectra of selected metal complexes recorded in 100% methanol at 5 mM complex or metal salt concentrations with λ_{d-d} maxima indicated; Cu(NO ₃) ₂ (····), Cu-Phen (— —) and Cu-Piv-Phen (—).	97
Figure IV.42 BSA tryptophan fluorescence quenching for Cu ²⁺ ions, 1,10-phen along with the carboxylate complexes. Cu ²⁺ complexes display non-linear quenching (solid circles) and are modeled using a quenching ‘Sphere-of-Action’ (open circles) with data points being displayed as an average of triplicate measurement.	98
Figure IV.43 Competitive fluorescence quenching of ethidium bromide (12.6 μ M) bound to ctDNA (10 μ M in DNAP) by DNA binding drugs, Cu ²⁺ and metal complexes. Data points displayed as an average of triplicate measurement.	101
Figure IV.44 Fluorescence quenching of bound intercalator (ethidium) or minor groove binder (Hoechst 33258) to ctDNA by minor groove binding drugs, pentamidine and netropsin along and metal complexes. Data points are displayed as an average of triplicate measurement.	102
Figure IV.45 Viscosity data from the complexes, standard DNA binding agents and the partial intercalator [Cu(1,10-phen)] ²⁺	102
Figure IV.46 IC ₅₀ data (at the 95% confidence interval) of metal complexes, 1,10-phen and cisplatin toward human cancer cells of the prostate (PC3), ovaries (SK-OV-3), non-cancerous prostate (PNT1A) post 24 h and 96 h exposure.	105
Figure IV.47 MIC ₉₅ data of metal complexes and 1,10-phen toward a range of gram positive and negative bacteria post 24 h or 48 h exposure (note: both 24 h and 48 h activities were identical). SA, <i>Staphylococcus aureus</i> ; MRSA, methicillin resistant <i>Staphylococcus aureus</i> ; SE, <i>Staphylococcus epidermidis</i> ; EF, <i>Enterococcus sp.</i> ; EC, <i>Escherichia coli</i> ; KP, <i>Klebsiella pneumonia</i> ; KP-E, <i>Klebsiella pneumonia</i> ; PA, <i>Pseudomonas aeruginosa</i>	106
Figure IV.48 MIC data of metal complexes and 1,10-phen toward a range of pathogenic fungi post 24 h or 48 h exposure to non-filamentous fungi and post 72 h or 120 h exposure to filamentous fungi (note: both 24 h / 48 h and 72 h / 120 h activities were identical). CA1, <i>Candida albicans</i> ATCC 44859; CA2, <i>Candida albicans</i> ATCC 90028; CA3, <i>Candida parapsilosis</i> ATCC 22019; CK1, <i>Candida krusei</i>	

ATCC 6258, clinical yeast isolates CK2, <i>Candida krusei</i> E28; CT, <i>Candida tropicalis</i> 156; CG, <i>Candida glabrata</i> 20/I; CL, <i>Candida lusitanae</i> 2446/I; TA, <i>Trichosporon asahii</i> 1188, and filamentous fungi AF, <i>Aspergillus fumigatus</i> 231; AC, <i>Absidia corymbifera</i> 272; TM, <i>Trichophyton mentagrophytes</i> 445.	107
Figure IV.49 Degradation of superhelical pBR322 with Cu ²⁺ complexes, using 2.5, 5.0, 10.0 and 20.0 µM of tested agent (from left to right), in the presence of A. 1 mM Na-L-ascorbate and B. 1 mM H ₂ O ₂ . Reactions were carried out using 400 ng of pBR322 plasmid DNA for 30 min at 37 °C in 80 mM HEPES at pH 7.2 with 25 mM NaCl before being quenched and analysed using agarose gel electrophoresis. Degradation of linearized pBR322 (by EcoRI) in C. with 5 µM of 1. CuPhen , 2. Cu-For-Phen , 3. Cu-Ace-Phen , 4. Cu-Pro-Phen , 5. Cu-Iso-Phen and 6. Cu-Piv-Phen ; D. + 1000 Units of Catalase; E. + 1000 Units of SOD; F. + 10% v/v DMSO, and; G. + 100 µM neocuproine.	111
Figure IV.50 A. Standard fluorescence response curve from H ₂ O ₂ detected using the Amplex Red assay (Invitrogen) using 530 nm excitation and 590 nm emission; B. Fenton breakdown of H ₂ O ₂ (5 µM) over a period of 120 min in the presence of Cu ²⁺ complexes (5 µM in EtOH) and 100 µM of Na-L-ascorbate.	113
Figure IV.51 Confocal microscopy images of γ-H2AX foci (green) within propidium iodide stained SK-OV-3 nuclei (red) after 24 h of drug treatment at the IC ₂₅ level (indicated in µM).	115
Figure IV.52 Mean intensity fluorescence ± SD, in arbitrary units, of γ-H2AX fluorescence in SK-OV-3 cells (left) and percentage of overall γ-H2AX positive SK-OV-3 cells (± SD) (right).	115
Figure IV.53 Typical cyclic voltammogram traces, recorded at a scan rate of 100 mV s ⁻¹ , for (a) 1 mM solution of Cu-For-Phen, after 1 hour (solid black trace), 4 hours (solid blue trace), and 13 hours (dashed trace); (b) 1 mM solutions of Cu(bis-phen), (solid trace), and Cu(mono-phen), (dashed trace). Experimental conditions; glassy carbon working electrode, platinum counter electrode, non-aqueous Ag /Ag ⁺ reference electrode, 0.1M TBAPF ₆ in 10% v/v DMF.	128
Figure IV.54 Absorption spectra of i. 5 mM [Cu(1,10-phen)(R-COO)] ²⁺ in 80 mM HEPES with 3.5% v/v methanol between 0- 168 h, recorded every 24 h, ii. Absorption spectra of 5 mM Cu-bis-phen (a.) and Cu-mono-phen (b.) in 80 mM HEPES.	130
Figure V.55 Binding of Cu ²⁺ complexes 1-4 to ethidium-saturated solutions of dsDNA (ctDNA), fluorescence quenching of limited ethidium bromide or Hoechst 33258 bound dsDNA (ctDNA) upon titration of complex and viscosity properties of complex treated salmon testes dsDNA. (data points presented as an average of triplicate fluorescence measurement, ± S.D.).	144
Figure V.56 Fluorescence quenching of limited bound intercalator (ethidium bromide) to poly[d(G-C) ₂] and poly[d(A-T) ₂] upon titration of netropsin, actinomycin D and Cu ²⁺ complexes. (data points presented as an average of duplicate fluorescence measurement, ± S.D.).	147
Figure V.57 ‘On-Chip’ protocol for examining artificial metallonuclease activity using the Bioanalyzer 2100.	150
Figure V.58 [A] Electrograms of linearized pUC19 (400 ng) exposed to metal complex (500 nM) between 0 – 12.5 min on the Bioanalyzer 2100 with DNA 7500 microfluidic chips, [B] %DNA degradation (from peak height analysis of triplicate experiments, error bars ± S.D.) of pUC19 exposed to Cu ²⁺ complexes between 0-30 min, [C] %DNA degradation (from peak area analysis of triplicate experiments, error bars ± S.D.) of pUC19 exposed to Cu ²⁺ complexes between 0-30 min, and, [D] typical electropherograms generated by the Bioanalyzer 2100, L = ladder, lane 1 = pUC19 control, lanes 2-12 = pUC19 + complex exposed between 1-15 min for bis-phen (i.) and DPQ (ii.) samples and between 1-30 min for DPPZ (iii.) and DPPN (iv.) samples.	151

- Figure V.59** Agarose gel electrophoresis of purified (EDTA free) supercoiled pUC19 (400 ng) with 1 mM Na-L-ascorbate incubated for 30 min with 500 nM of metal complexes (**A**), and in the presence of 1000 units of bovine liver catalase (**B**), 100 μ M neocuproine (**C**), 1000 units of bovine SOD (**D**) and 10% v/v DMSO (**E**). Ctrl = pUC19 complex untreated control, Lanes 1-4 = 500 nM **Cu-Phen**, **Cu-DPQ-Phen**, **Cu-DPPZ-Phen** and **Cu-DPPN-Phen**, respectively. 152
- Figure V.60** Degradation of 400 ng of linearised plasmid pBC4 (**A**.) and pUC19 (**B**.) DNA with 2.5, 5.0, and 10.0 μ M of tested metal complex in the presence of 1 mM of added reductant for 30 min at 37 °C; **A**. pBC4 (59% G-C); **B**. pUC19 (51% G-C). 153
- Figure V.61** DNA cleavage reactions with 10 μ M of **Cu-Phen**, **Cu-DPQ-Phen**, **Cu-DPPZ-Phen**, and **Cu-DPPN-Phen** (lanes 1 – 4, respectively) with 400 ng of commercial (EDTA buffered) superhelical pUC19. Reactions were carried out with 1 mM of added Na-L-ascorbate over 30 min at 37 °C. 153
- Figure V.62** Dose response inhibition and IC₅₀ values (at the 95% confidence interval) of Cu²⁺ complexes and the clinical agent, doxorubicin, within SKOV3 human cancer cells over 24 h of drug exposure. 154
- Figure V.63** Cyclic voltammograms describing the redox behavior of 1 mM of complex, at a scan rate of 100 mV s⁻¹, (solid black trace), and in the presence of 2 mM Na-L-ascorbate (dashed black trace), and 2 mM H₂O₂ (solid blue trace), [**a**] **Cu-Phen**, [**b**] **Cu-DPQ-Phen**, [**c**] **Cu-DPPZ-Phen** and, [**d**] **Cu-DPPN-Phen**, and, electrochemical parameters (V) for complexes, and in the presence of added Na-L-ascorbate, and H₂O₂ (bottom). Analysis conducted in 10% v/v DMF; [**i**] complex without exogenous treatment (V) [**ii**] complex with added Na-L-ascorbate (V) [**iii**] complex with added H₂O₂ (V). 156
- Figure V.64** [**A**] Fenton-like degradation of hydrogen peroxide (5 μ M) in the presence of 5 μ M of metal complex and 100 μ M Na-L-ascorbate determined using the Amplex Red hydrogen peroxide assay kit (Invitrogen) (replicate experiments conducted on four separate occasions), a calibration curve is also shown which details the linear ($r^2 > 0.99$) fluorescent response achieved from hydrogen peroxide detection in the assay, [**B**] superoxide dismutase mimetic (SODm) activity determined by the xanthine/xanthine-oxidase system, metal complexes were examined between 0.98 – 0.33 μ M at 25 °C under constant enzymatic production of superoxide (~1 μ M / min) using the detector molecule, nitrobluetetrazolium chloride and this data was plotted as a function of V₀/V_c (catalytic rate in the absence / presence of catalyst) as a function of [complex] to yield the catalytic rate K_{cat} in units, M⁻¹ s⁻¹. 157
- Figure VI.65** Perspective views of the double-stranded B-DNA Dickerson-Drew dodecamer bound to TriplatinNC via backbone tracking (**A**) and groove-spanning (**B**) modes (1, NDB entry 2DYW). DNA backbone (connecting P positions), orange; carbon, grey80; oxygen, red; nitrogen, slate (all in cartoon mode). Triplatin complex (space-filling mode) atoms coloured as DNA; platinum, grey30. Platinum(II) amine nitrogen atoms, and selected phosphate coordinated oxygen atoms, engaged in phosphate clamping shown with dotted surface. Figures generated by PyMOL Molecular Graphics System, Version 1.5.0.4 Schrödinger, LLC. 179
- Figure VI.66** **A**. Competitive fluorescence binding of TriplatinNC (AH78), pentamidine, and netropsin to ethidium bromide (12.6 μ M) saturated solutions of calf thymus DNA (10 μ M) (data points generated from triplicate measurement, error bars \pm S.D.). **B**. Relative viscosity changes in salmon testes dsDNA (1 mM) upon treatment with tested agents. **C**. Kinetic competitive fluorescence binding of ethidium bromide (12.6 μ M) bound calf thymus DNA(ctDNA) (10.0 μ M) upon titration of Triplatin complex at $r = 0.10$ (data points generated from triplicate measurement, error bars \pm S.D., note that AH78 and AH78H produced identical, overlapping, quenching profiles). 181

Figure VI.67 .Relative viscosity changes in salmon testes dsDNA (1 mM) upon treatment with AH78P using both sheared and non-sheared stDNA.	182
Figure A.D.68 Top-down views of HIV-1 protease, a. unbound (PDB 1HHP) and, b. bound to the organic antiviral agent saquinavir (PDB 1HXB). A rear view of saquinavir bound in the active site is show in c.	D-5
Figure A.D.69 Molecular structures of octahedral (a.), dodecahedral (b.) and icosahedral (c.) borane cages; <i>ortho</i> -, <i>meta</i> - and <i>para</i> -icosahedral carboranes are represented in structures d. to f. respectively; formation of <i>nido</i> -carboranes results through modification of <i>o</i> -, <i>m</i> - and <i>p</i> -cages in g. to i., respectively; metallacarboranes such as the <i>commo</i> -metallabisdicarbollide (j.) are generated from metal coordinated <i>nido</i> -clusters. (• = boron; • = carbon).....	D-7
Figure A.D.70 HIV-1 protease ligated by two cobaltabis(1,2-dicarbollide) molecules (PDB 1ZTZ).	D-10
Figure A.D.71 Perspective views of a. the dual cage metallacarbollide compound 7 , bound to HIV-1 PR (PDB 3I8W) and, b. two individual cobaltabis(1,2-dicarbollide) molecules from compound 1 bound to HIV-1 PR (PDB 1ZTZ)....	D-11
Figure A.D.72 Crystal structure of a synthetic HIV-1 protease (PDB 3HVP) with lysine residues 55, 43 and 41 shown (spacefill, coloured teal) along the hinge region behind the hair-pin flaps.	D-15
Figure A.D.73 Molecular structures of the HIV-1 PR active Au(I) phosphine complexes, 25 to 29 , the Au(III) tetrachloride anion in complex 5 and auranofin. D-16	
Figure A.D.74 Molecular structures and HIV-1P inhibitory properties of a range of copper(I) and copper(II) complexes.	D-20
Figure A.D.75 Crystal structures of, a. <i>Plasmodium falciparum</i> cysteine protease, Falcipain-2 (coloured cream) bound to a cystatin inhibitor (coloured white) (PDB 1YVB),[74] and b. of Falcipain-2 with the small molecule cysteine protease inhibitor, epoxysuccinate E64 (coloured teal) (PDB 3BPF).[72]	D-23
Figure A.D.76 Molecular structures for the antimalarial drugs chloroquine (CQ), {[RuCl ₂ (CQ) ₂]} ₂ (RQ), ferroquine (FQ), [Au(PPh ₃)(CQ)]PF ₆ and the antileishmaniasis Sb(V) complexes, Glucantime® and Pentosam®.	D-23
Figure A.D.77 Molecular structures and cathepsin B inhibitory properties of a range of gold(I) and oxo-rhenium(V) complexes.	D-30
Figure A.D.78 Molecular structures of dinuclear (67 and 68) mononuclear (69) cyctometallated Pd(II) phosphine complexes.	D-32

TABLE OF TABLES

Table I.1 Selected copper containing enzymes and their function	4
Table I.2 Chemical structure of dipyrrophenazine ligands	19
Table I.3 Selected Cu-complexes containing <i>N,N'</i> -donor heterocyclic bases such as bpy, phen, tmp, DPQ, DPPZ, and dmdppz ligands with potential intercalative properties on B-DNA.....	20
Table II.1 (a): Summary of the parameters calculated for S1 in the absence and presence of 2 mM ascorbate in aqueous solution. In this table voltage values (V) are quoted versus the SCE calomel electrode. ¹⁹	65
Table II.2 (b): Comparison of the redox behaviour of S1 and S2 in DMF.....	66
Table III.1 A. Apparent DNA binding constants (K_{app}) of the test compounds, and B. Fluorescence quenching (Q) values obtained against Hoechst 33258 (groove binder) and ethidium bromide (intercalator).	75
Table III.2 Summary of electrochemical parameters for CuPhen and CuPDT in the absence and presence of ascorbate. The redox behaviour of CuPhen is near reversible in the presence of ascorbate, $\Delta E_p = 0.065$ V. CuPDT remains quasi-reversible in the presence of ascorbate, $\Delta E_p = 0.119$ V.	86
Table IV.1 Electrochemical parameters (V) for complexes in the absence and presence of added reductant (2 mM Na-L-ascorbate). Analysis conducted in 10% v/v DMF.	96
Table IV.2 BSA tryptophan fluorescence quenching by Cu^{2+} ions, 1,10-phen and complexes.	99
Table IV.3 A. Apparent ctDNA binding constants (K_{app}) determined using competitive ethidium bromide competitive quenching, B. fluorescence quenching (Q) values obtained against ctDNA bound with Hoechst 33258 (groove binder) or ethidium bromide (intercalator), and C. relative viscosity at $r = 0.20$ using dsDNA from salmon testes.....	103
Table IV.4 <i>In vitro</i> cytotoxicity data for complexes, Cu^{2+} ions, 1,10-phen and cisplatin toward human derived cancer and non-cancers cells.....	108
Table IV.5 <i>In vitro</i> cytotoxicity data for complexes, Cu^{2+} ions and 1,10-phen toward gram positive and negative bacteria.....	108
Table IV.6 <i>In vitro</i> cytotoxicity data for complexes, Cu^{2+} ions and 1,10-phen toward filamentous and non-filamentous pathogenic fungi.....	109
Table IV.7 Crystallographic data for the five carboxylate complexes generated.....	121
Table V.1 DNA binding properties of netropsin, actinomycin D, $[Co(NH_3)_6]Cl_3$ and the copper(II) complex series.	145
Table V.2 Fluorescence quenching (Q) of limited ethidium bromide (5 μ M) bound poly[d(G-C) ₂] and poly[d(A-T) ₂] (25 μ M) by standard agents netropsin, actinomycin D and Cu^{2+} complexes.....	148
Table V.3 Influence of standard agents (netropsin, actinomycin D) and copper phenazine complexes on the thermal denaturation of poly[d(G-C) ₂] and poly[d(A-T) ₂] alternating co-polymers.....	148
Table V.4 Kinetic properties of the complex series under Fenton-like and SODm conditions and catalytic cycle of Cu^+/Cu^{2+} ions with molecular oxygen, superoxide and hydrogen peroxide.	158
Table V.5 Thermal melting analysis of poly[d(G-C) ₂] under alternating buffer, pH and ionic strength.	170
Table A.D.1 Structures and activities of metallacarborane HIV-1 protease inhibitors. (• = boron; • = carbon; • = cobalt).....	D-9
Table A.D.2 Structures and activities of dual cage metallacarborane HIV-1 protease inhibitors. (• = boron; • = carbon; • = cobalt).....	D-12
Table A.D.3 Selected polyoxometalate families, formulae and structures.	D-14

Table A.D.4 HIV-1 protease inhibition, antiviral and cytotoxicity data for a range of Nb-POMs.....	D-15
Table A.D.5 Effect of metal cations on wild-type protease activity.[57].....	D-19
Table A.D.6 Molecular structures and cathepsin B inhibitory effects of cyctometallated Au(III) complexes.[79].....	D-25
Table A.D.7 Inhibition of Fp2 and antiplasmodial activity of gold(I) and gold(III) complexes.[91]	D-26
Table A.D.8 FP-2 inhibition and antiplasmodial activity of gold(I) TSC complexes.[69]	D-28
Table A.D.9 Comparative IC ₅₀ inhibitory values for selected complexes against parasite cysteine proteases and chymotrypsin.....	D-31

TABLE OF SCHEMES

Scheme I.1 A. The physiological balance between the ROS production and antioxidative defences prevents the accumulation of ROS. ¹⁰⁸ B. Oxidative stress due to severe disturbance between ROS formation and antioxidative defences C. Potential toxicity associated with ROS.....	23
Scheme I.2 Schematic showing the oxidative damage of DNA.	23
Scheme I.3 Reaction of $\cdot\text{OH}$ with guanine. ¹²⁸	25
Scheme I.4 Reaction of $\cdot\text{OH}$ with adenine. ¹²⁶	26
Scheme III.1 Proposed reaction mechanism of phendio with L-tyrosine methyl ester leading to the formation of PDT	72
Scheme IV.1 Molecular structures of cytotoxic Cu^{2+} complexes incorporating N,N'-O,O' or N,N'-O,N'' chelators.	93
Scheme V.1 Molecular structures of cytotoxic platinum(II) complexes cisplatin and phenanthriplatin, the ruthenium(II) DNA light switch complex, Δ -[Ru(DPPZ)(Phen) ₂] ²⁺ , and the copper(II) chemical nuclease, [Cu(Phen) ₂] ²⁺	140
Scheme V.2 Molecular structures of the Cu^{2+} coordination complexes 1-4	142
Scheme VI.1 Molecular structures of [$\{\text{Pt}(\text{NH}_3)_3\}_2$ - μ -{ <i>trans</i> -Pt(NH ₃) ₂ (NH ₂ (CH ₂) ₆ NH ₂) ₂ }]} ⁶⁺ (AH44, TriplatinNC-A) and [$\{\text{trans}$ -Pt(NH ₃) ₂ (NH ₂ (CH ₂) _n NH ₃) ₂ }\}_2- μ -(<i>trans</i> Pt(NH ₃) ₂ (NH ₂ (CH ₂) _n NH ₂) ₂)}]} ⁸⁺ cations where <i>n</i> = 5 (AH78P), 6 (AH78H, TriplatinNC) and 7 (AH78H).	178

ABBREVIATIONS

1,10-phen	1,10-phenanthroline
A	adenine
ATCUN	amino terminal Cu- and Ni-binding protein
C	cytosine
cP	cytosolic copper protein
CpG	cytosine-phosphate-guanine
ctDNA	calf thymus double stranded DNA
CTR1	copper uptake transport proteins
Cu/Zn-SOD	copper and zinc superoxide dismutase
DBSs	double-stranded breaks
DCFH-DA	2',7'-dichlorodihydrofluorescein diacetate
DDD	Dickerson–Drew dodecamer
DNA	deoxyribonucleic acid
DPQ	dipyrido[3,2- <i>f</i> :2',3'- <i>h</i>]quinoxaline
DPPZ	dipyrido[3,2- <i>a</i> :2',3'- <i>c</i>]phenazine
DPPN	benzo[<i>i</i>]dipyrido[3,2- <i>a</i> :2',3'- <i>c</i>]phenazine)
dsDNA	double stranded DNA
EC-SOD	extracellular superoxide dismutase
EtBr	ethidium bromide
Et ⁺	ethidium cation
FCS	fetal calf serum
FITC	fluorescein isothiocyanate
FBS	fetal bovine serum
G	guanine
Gly	glycine
H	hydrogen
His	histidine
HP	human protamine
HS-832	non-tumorigenic human ovarian cell line
ICL	interstrand cross-linking
K_{app}	apparent DNA binding constant
L-PheH	L-phenylalanine
MIF	mean intensity fluorescence
MT	Metallothionein
MTT	methylthiazolyldiphenyl-tetrazolium bromide
NanoSIMS	nano-scale secondary ion mass spectrometry
NBT	nitro blue tetrazolium
OC	open circular
$\cdot\text{OH}$	hydroxyl radical
$\text{O}_2^{\cdot-}$	superoxide anion radical
PAM	peptidylglycine α -hydroxylase monooxygenase
PDT	2-(4-hydroxyphenyl)-4 <i>a</i> ,12 <i>b</i> -dihydro-2H-[1,4]oxazino[2,3- <i>f</i>][1,10]phenanthroline-3-carboxylate
PI	propidium iodide
PC-3	prostate epithelial human-derived cancer cells
phendio	1,10-phenanthroline-5,6-dione
PNT1A	prostate epithelial human-derived non-cancerous cells
ROS	reactive oxygen species
RNA	ribonucleic acid

RNS	reactive nitrogen species
rpm	rotation per minute
T	thymine
TBA ⁺ PF ₆ ⁻	tetrabutylammonium hexafluorophosphate
T _m	thermal melting
TerphH ₂	terphthalic acid
tRNA	transfer RNA
SK-OV-3	ovarian epithelial human-derived cancer cells
SOD	superoxide dismutase
SODm	superoxide dismutase mimetic
stDNA	salmon testes DNA

Units

bp	base pair
Å	Angstrom
cm	centimeter
°C	degree Celsius
cP	centipoise
kDa	kiloDalton
µg	micrograms
µl	microliter
µM	micromolar
F	Faraday
g	grams
h	hour
Hz	Hertz
J	J-coupling (indirect dipole-dipole coupling)
°K	degree Kelvin
<i>K</i> _{cat}	apparent catalytic rate constant
L	liter
λ _{<i>d-d</i>}	Lambda max (<i>d</i> → <i>d</i> transition)
M	molar
MHz	megahertz
mol	mole
mm	millimetre
mmol	milimole
mg	milligram
min	minutes
mL	milliliters
mM	millimolar
Mp	melting point
ng	nanograms
ppm	parts per million
r	[drug] / [DNA] ratio
s	seconds
U	enzyme units
v/v	volume/volume
ε _{max}	molar absorption coefficient
δ	Delta (NMR chemical shift)

ABSTRACT

Metallo drugs as Inducers And Inhibitors of Chemical Nuclease Activity

By Andreea Prisecaru

Manipulation of DNA is both an intrinsic and essential component of molecular biology and biotechnology. Reagents capable of cutting DNA are applied within these fields as probes for DNA structure and function, with the ultimate aim being the design of target-specific—customised endonucleases—capable of modifying genomic DNA. Thus, DNA cleaving reagents are essential tools for both sequence analysis and genome engineering. Furthermore, the discovery of new molecular mechanisms by which small molecules modify DNA structure, reactivity, and biological repair contributes significantly to potential drug development.

The chemical nuclease of $[\text{Cu}(\text{Phen})_2]^{2+}$ (where Phen = 1,10-phenanthroline), is a well studied reagent which randomly cleaves nucleic acids in the presence of molecular oxygen (or hydrogen peroxide) upon reduction to Cu^+ . In addition, compounds based on this chemotype have found application in the biological field as antimicrobial and anticancer agents, DNA intercalators, and as nucleoside constituents for incorporation into the DNA backbone. $[\text{Cu}(\text{Phen})_2]^+$ oxidises duplex DNA without specificity, predominately at the minor groove with C-H bonds at C1', C4', and C5' being the main targets of hydrogen atom abstraction.

The aim of this research was to extend structure-activity relationships of Cu^{2+} -Phen complexes containing sterically functionalized pendant carboxylates and to investigate how synthetic extension of the ligated phenazine ligand within this complex model influences DNA recognition and oxidative degradation. These compounds have shown an enhanced DNA recognition relative to the well-studied chemical nuclease, $[\text{Cu}(\text{Phen})_2]^+$. Furthermore, the effects of nuclearity on DNA oxidation were elucidated using the $[\text{Cu}(\mu\text{-terephthalate})(\text{Phen})_4]^{2+}$ cation with results showing potent DNA oxidation in the absence of exogenous reductant. Many compounds developed in this work constitute a series of novel

anticancer leads capable of intracellular DNA oxidation leading to genomic double strand breaks. In addition to the application of developmental metallodrugs as inducers of chemical nuclease activity, the effects of cytotoxic trinuclear platinum(II) complexes as high-affinity DNA binders that inhibit—or block—endonuclease enzyme recognition and excision are reported through a wide variety of biophysical and molecular biological methods.

CHAPTER I

DNA oxidation by copper 1,10- phenanthroline complexes

I.1 Copper in biological systems

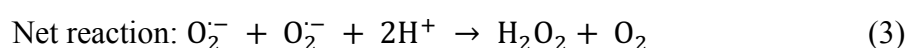
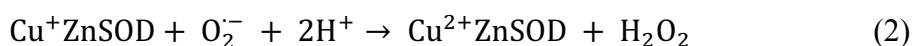
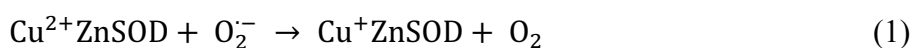
I.1.1 Biological importance of copper

Copper (Cu) plays a fundamental role in biological systems, and its essentiality in mammals was first remarked in 1928 when rats exposed to a copper-deficient diet developed anemia.¹ Copper is an essential transition metal found in most human organs and tissues, in concentrations varying from few ppm to several hundred ppm, with the liver representing the main storage organ.^{2–4} As a transition metal, copper is biologically converted between facile redox states, namely oxidized cupric (Cu(II)) and reduced cuprous (Cu(I)) forms.⁴ With this attractive attribute, copper has been exploited for catalysis by a plethora of enzymes whose activities are critical to a broad range of cellular biochemical and regulatory functions.⁵

I.1.2 An overview of copper proteins

Copper is absorbed in the body from the stomach and once in the intestinal epithelial cells, it is incorporated into Cu-dependent proteins and transported across the basolateral membrane into the peripheral circulation, where binds strongly to serum albumin. Once in the liver, copper is distributed to metabolically active sites by ceruloplasmin which accounts for about 90-95% of the total plasma copper, by albumin and other less quantitatively important copper binders.^{5–7} Free copper is a potent oxidant, and in order to avoid cellular toxicity, it is incorporated into chaperons and proteins.⁷ These cupro-proteins are needed for diverse metabolic processes, such as mitochondrial respiration, melanin biosynthesis, dopamine metabolism, iron homeostasis, antioxidants defence, connective tissue formation and peptide amidation.⁸ Copper also forms a vital part of a number of oxidase enzymes, sometimes in combination with other metal ions (Table I.1). Cytochrome *c* oxidase—a large protein found in the mitochondrial inner membrane—contains both copper and haem-iron and its specific function is to activate oxygen, the terminal electron acceptor of the mitochondrial respiratory chain.^{9,10} CuZn-superoxide dismutase (CuZnSOD) is a prototypical dinuclear metalloprotein containing one copper and one zinc subunit. The imidazole ring of His61, which bridged Cu and Zn together, coordinates both metals. Copper is coordinated by four histidines residues and a

water molecule in a distorted square pyramidal geometry and zinc is coordinated by three histidines residues and an aspartate molecule in a distorted tetrahedral geometry.¹¹ CuZnSOD is considered the defence system against the cytotoxic superoxide free radical ($O_2^{\bullet-}$), catalysing the disproportion of superoxide, which involves the cyclic reduction (Eq. 1) and oxidation (Eq. 2) of copper to generate hydrogen peroxide and oxygen (Eq. 3).¹²⁻¹⁷



Tyrosinase contains a binuclear copper active site and is the key enzyme in melanin synthesis.^{18,19} Ceruloplasmin, copper containing glycoprotein produced in the liver, is responsible for binding 95% of the copper found in plasma.²⁰ The enzyme is a multicopper oxidase protein that utilizes copper to couple substrate oxidation with the four-electron reduction of oxygen to water.^{5,21,22} Another copper containing enzyme essential for stabilisation of extracellular matrix is lysyl oxidase, involved in the maturation tissue, especially the enzymatic crosslinking of collagen and elastin.^{23,24} Dopamine β -hydroxylase is an oxygenase enzyme critically involved in the biosynthesis of catecholamine and consequently plays an important role in the regulation of noradrenergic and adrenergic neurotransmission.^{25,26} Finally, peptidylglycine α -amidating monooxygenase (PAM) is a copper dependent enzyme that catalyses the carboxyl-terminal amidation of glycine-extended peptide precursors, a modification essential for the bioactivity of numerous hormones and neuropeptides.^{27,28}

Table I.1 Selected copper containing enzymes and their function

Enzymes	Function
Cytochrome <i>c</i> oxidase	Mitochondrial respiration, electron transport chain
CuZn-SOD	Antioxidant, free radical defence
Tyrosinase	Formation of melanin
Lysyl oxidase	Maturation of connective tissue (collagen and elastin)
Ceruloplasmin	Copper and iron transport
Dopamine β -monooxygenase	Biosynthesis of catecholamine
Peptidylglycine α -amidating mono-oxygenase (PAM)	Neuropeptide processing

I.1.3 Entry of copper into mammalian cells

As described in Fig. I.2, copper is transported into the human cell through the high-affinity copper uptake transport protein (CTR1) (Fig. I.1a.). CTR1 is a 32 kDa membrane protein consisting of 190 amino acids and is encoded by the SLC31A1 human gene.^{29–31} After crossing the plasma membrane, copper binds to cytosolic copper chaperons, which direct subcellular copper delivery to specific proteins, overcoming a high copper chelation capacity of the cytoplasm. Copper is mediated to the Golgi apparatus via the ATOX1 protein (Fig. I.1d.). The ATOX1 gene encodes a copper chaperone that plays a role in copper homeostasis by binding and transporting cytosolic copper to the ATPase protein (cP) in the trans-Golgi apparatus for incorporation with ceruloplasmin. Recently, ATOX1 was also identified as a copper-dependent suppressor of oxidative damage in yeast lacking of superoxide dismutase.^{32,33} Once inside the Golgi, copper is released and then binds to target proteins, ATP7A and ATP7B which normally reside in the trans-Golgi membrane, and form part of the secretory pathway including extracellular SOD (EC-SOD). COX17 (Fig. I.1b.) found in cytoplasm and also in the mitochondrial intermembrane space, delivers copper to mitochondrial cytochrome *c* oxidase via the chaperons COX11, Sco1 (Fig. I.1c.) and Sco2.^{34–37} Indeed, copper chaperons for superoxide dismutase (CCS) (Fig. I.1e.), play a fundamental role in delivering copper to pro-form of SOD (apo-SOD) with CCS containing three binding domains; domain I contains Cu-binding sites, domain II is homologous to SOD, and domain III contains cysteine residues essential to the transfer of Cu to apo-SOD.^{38,39}

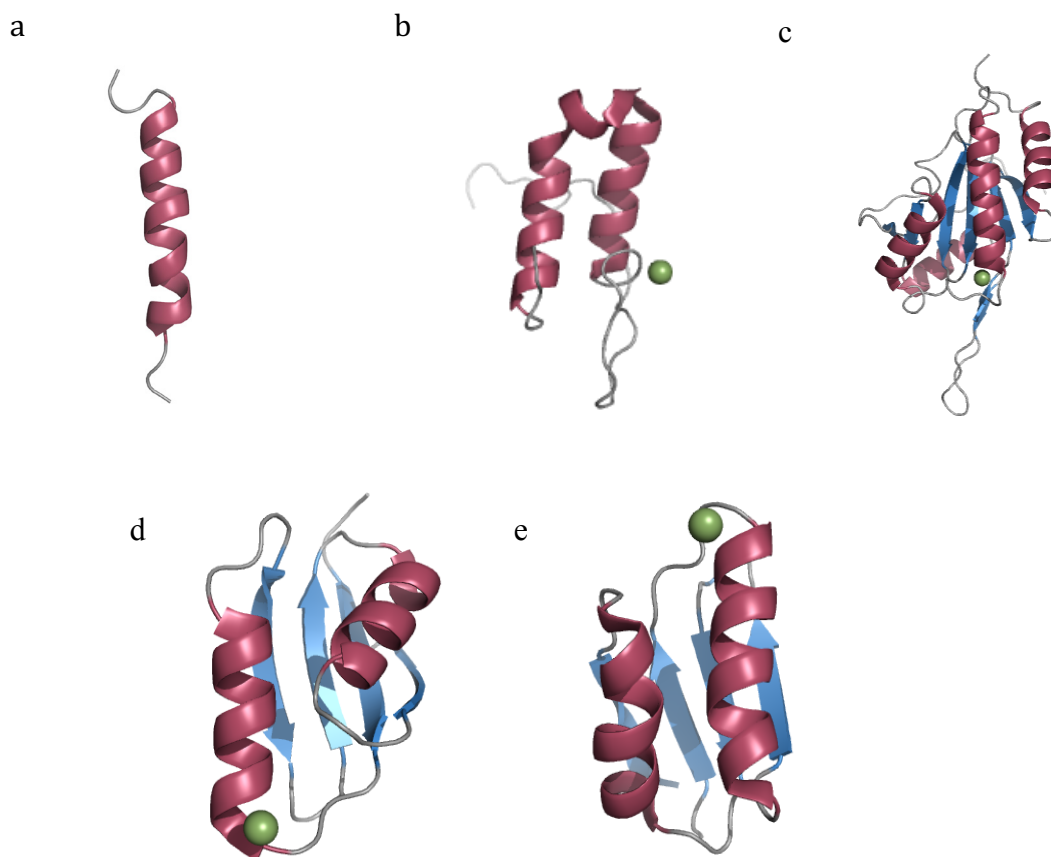


Figure I.1 Copper delivering proteins (Protein Data Bank, PDB, codes indicated) a. First transmembrane domain from human copper transporter 1 CTR1 (PDB, 2LS2), b. COX17 (PDB, 2RNB) delivers copper to mitochondrial cytochrome *c* oxidase c. Copper chaperons, Sco1 (PDB, 2GQM) play a fundamental role in delivery of copper to the mitochondria, d. ATOX1 (PDB, 1TL4) mediates copper transport to the Golgi apparatus, and e. 1st domain of copper chaperons for superoxide dismutase, CCS (PDB, 2RSQ) play a fundamental role in delivering copper to the pro-form of SOD.

Metallothioneins (MT) are small molecular weight—cysteine-rich thiol containing proteins—important in the transport and storage of copper ions. Since copper is reactive, well known to produce reactive oxygen species (ROS), copper binding is an important detoxification mechanism for Cu-associated toxicities. Thus, metallothioneins have a critical role to protect the intracellular proteins from copper toxicity.^{38,40,41}

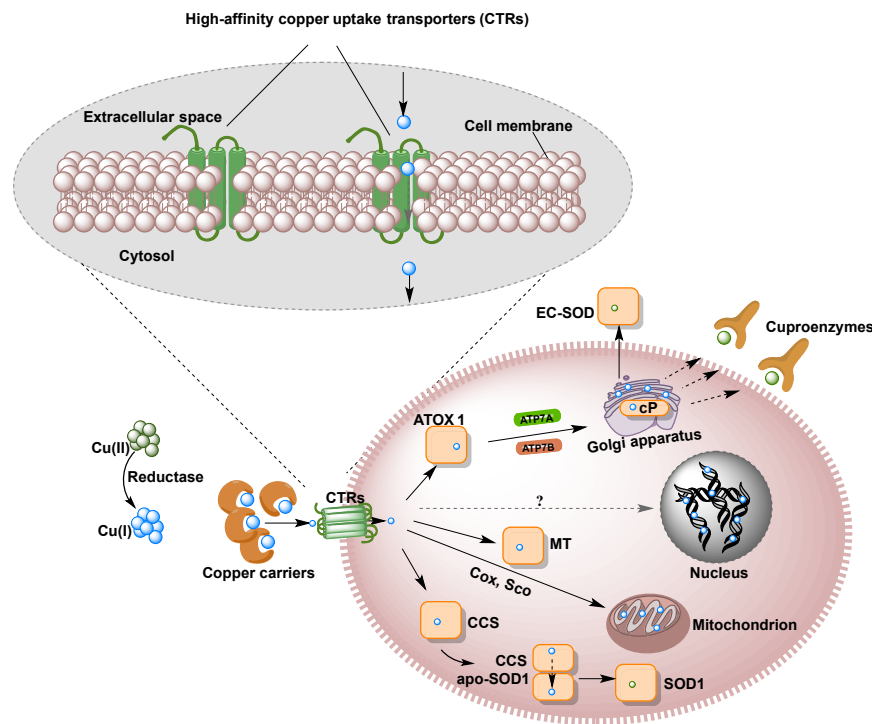


Figure I.2 Simplified scheme showing intracellular distribution of copper into the human cell. Copper enters into the human cell through high affinity copper uptake protein (CTR1). Once inside the cell, copper is passed onto the specific enzymes, ATOX1, CCS, COX, which escort copper ions to its specific destination (Golgi apparatus, SOD1 and mitochondria, respectively). Upon reaching its destination, copper is either incorporated into Golgi network and released using a P-type ATPase (cP), inserted into apo-SOD1 or incorporated into cytochrome c oxidase located in mitochondria.

I.1.4 Copper diseases

Although copper is an essential metal ion, it can become toxic to cells when at elevated concentrations. The disruption of copper transport can cause both accumulation of excess copper (Wilson's disease) or copper deficiency (Menkes' syndrome) (Fig. I.3). However, these two diseases affect different tissues.⁴²

Wilson's disease, firstly described in 1912 by Samuel Wilson, is a autosomal recessive disorder characterised by toxic accumulation of copper in liver and brain resulting in cirrhosis and neuronal deterioration.⁴³ In patients with Wilson's disease more than 190 mutations have been located in the ATP7B gene, which results in abnormal function of the ATP-dependent P-type copper transporting ATPase.⁴⁴ The function of ATP7B gene is to encode a copper-transport proteins located at the trans-Golgi network and to transfer copper into the secretory

pathway into ceruloplasmin and excretion into the bile.²⁰ Hence, disruption of protein function reduces or prevents the incorporation of copper into ceruloplasmin and in the transport of copper out of the cell.^{44,45}

Menkes' syndrome is an X-linked recessive disorder caused by mutation in ATP7A gene, which is expressed in most tissues except the liver. ATP7A is an ATP-dependent P-type copper transporting ATPase, localised in the trans-Golgi network.^{46–48} ATP7A contains several domains required for ATPase function and copper binding. In Menkes's syndrome, mutations in the ATP7A gene result in poor distribution of copper throughout the human body; copper accumulates in some tissues, such as the small intestine and kidneys, while the brain and other tissues have unusually low levels. The decrease supply of copper can reduce the activity of numerous copper-containing enzymes that are necessary for the structure and function of bone, skin, blood vessels and the nervous system.^{20,49}

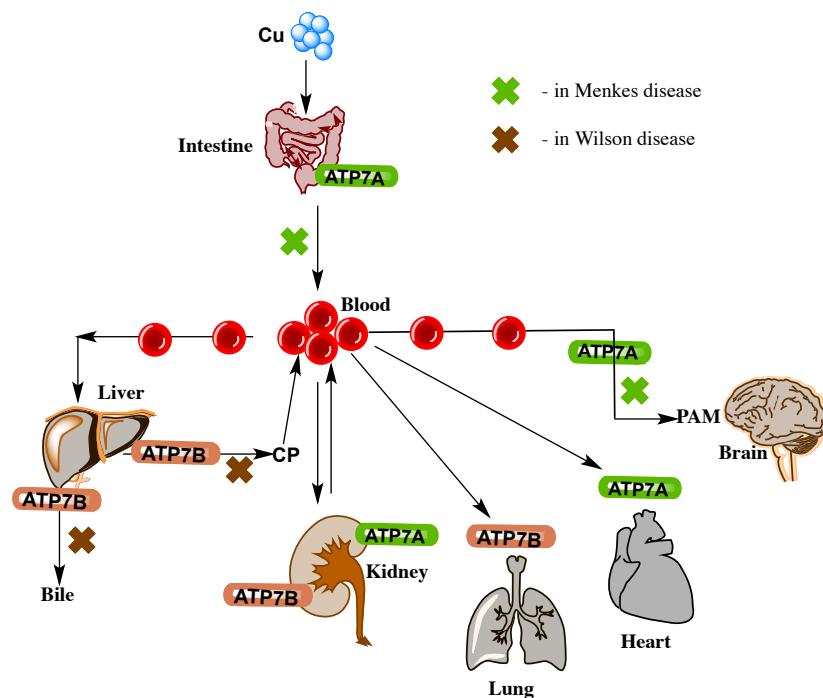


Figure I.3 Simplified scheme of the disruption of copper transport in Wilson's and Menkes's disease.⁵⁰

I.2 DNA as a molecular target

I.2.1 DNA: structure and function

Deoxyribonucleic acid (DNA) is an important biomolecule that can be targeted by metal complexes. DNA is a nucleic acid polymer that contains all the genetic material of all living cells that make up the body, and along side proteins and carbohydrates forms the three macromolecules essential for all known forms of life. DNA consists of two polynucleotide chains held together by hydrogen bonds. Each nucleotide is composed of a purine or pyrimidine base (adenine (A), thiamine (T), cysteine (C) and guanine (G)), and a deoxyribose sugar attached to a single phosphate group (Fig. I.4a.).

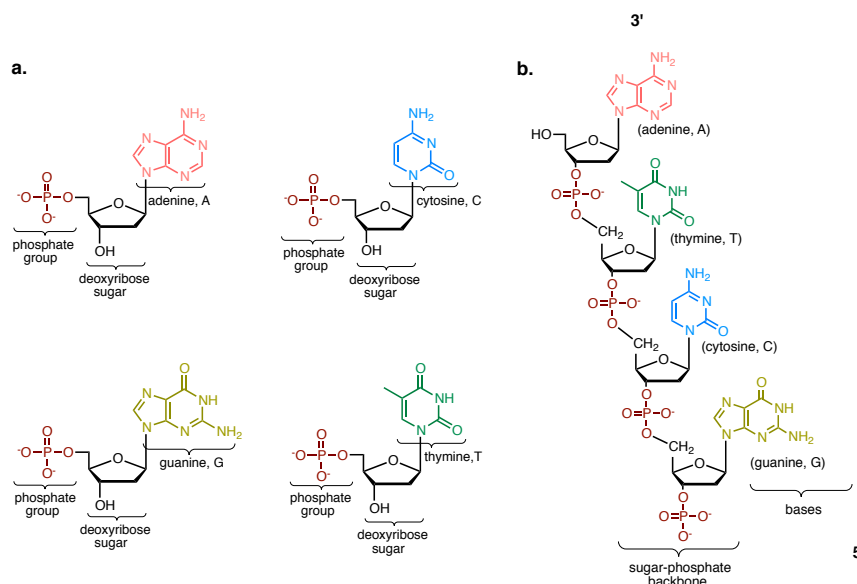


Figure I.4 a. The 5'-phosphate nucleotide of DNA. Each nucleotide contains a phosphate group, a deoxyribose sugar molecule and a nitrogen base. DNA contains four types of nitrogen bases, adenine (A), cytosine (C), guanine (G), and thymine (T). **b.** Connectivity in a strand of DNA. The 3'-ATCG-5' sequence is shown.

Nucleotides are held together by covalent bonds in a chain, which form the “back bone” of alternating sugar-phosphate-sugar-phosphate (Fig. I.4b.). The way in which nucleotides are linked together gives the DNA double helix chemical polarity. The two ends of chain are easily distinguishable; the 5' end having a terminal phosphate group with the 3' end having a terminal hydroxyl group. Because both strands are held together by hydrogen bonding between complementary bases, the sugar-phosphate backbones lie on the outside with

bases residing at the interior (Fig. I.5). In canonical DNA, the two-ring heterocyclic base purine is paired with a single-ring heterocyclic base pyrimidine; A is always paired with T and G is always paired with C and this is known as complementary base pairing.⁵¹

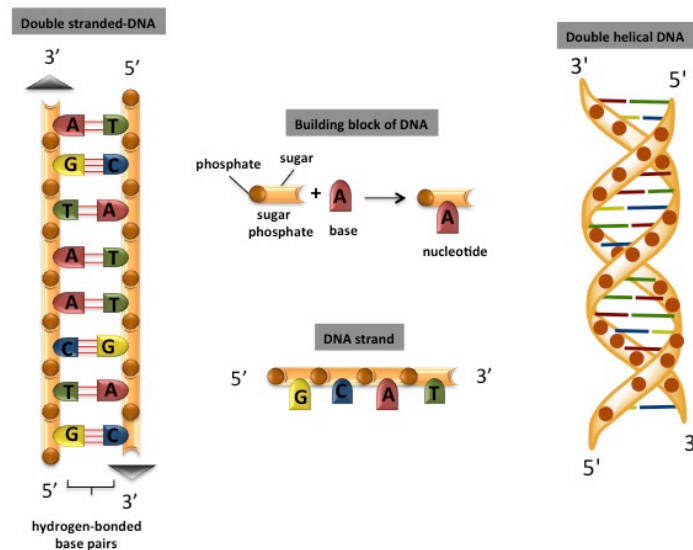


Figure I.5 The building blocks of DNA. DNA is made up of molecules called nucleotides. Each nucleotide contains a phosphate group, a sugar group, and a base that are linked covalently into a polynucleotide chain. Nucleotides are attached together to form strands that spiral around one another to create a structure called a double helix. The two strands are held together by hydrogen bonds, two hydrogen bonds formed between A and T, and three hydrogen bonds formed between G and C.

To maximize the efficiency of base pair packing, the two sugar-phosphate backbones wind around each other to form a double helix, with one complete turn every ten base pairs in B-DNA. A more detailed analysis of DNA structure reveals that the junction of the two strands coiling around each other creates two grooves, each with a different width. The wider groove is called the major groove with the smaller being called the minor groove.

The B-DNA double helix is held together by two main forces: Watson-Crick hydrogen bonds between purine and complementary pyrimidine base pairs inside the helix, and Van der Waals base-stacking interactions between parallel nucleotides.⁵² It is important to note that three hydrogen bonds form between G and C complementary bases and only two hydrogen bonds are found between A and T complementary base pairs. For this reason DNA strands containing high G-C content are more stable and more difficult to separate, thermodynamically,

than DNA strands that contain A-T base pairs.^{53,54} H-bonds between the two complementary bases facilitate interstrand stabilization and allow base recognition due to the enhanced structure directionality property from their pronounced electrostatic nature. Base stacking interactions between parallel bases A//T and G//C are primarily electrostatic in nature being coordinated by London dispersion forces followed by π - π -electrostatic interactions. Depending on the type of nucleotide involved in base pairing, the energetic contribution of H-bond between complementary base pairs can vary between 15.4 - 28.8 kcal mol⁻¹ while the energetic contribution to the parallel base stacking interaction are 11.6 - 16.9 kcal mol⁻¹.⁵⁵ However, studies performed by Kamenetski *et al.* showed that thermal stability of DNA is mainly determined by base-stacking interactions. Additionally, stacking effects are probably the major influence of base pair stability and are the major forces holding the double helix together. It is interestingly to note that canonical DNA bases, overall, stack weakly to moderately, and researchers have demonstrated many artificial bases that stack more strongly than natural ones.⁵⁴

1.2.2 Metal binding sites on DNA

The interaction of DNA with copper complexes has stimulated interest in relation to the function of nucleic acids, DNA replication, transcription of genetic codes, and various other enzyme reactions with DNA. This macromolecules targets for therapeutic interventions and the development of diagnostic probes of nucleic acid structure.⁵⁶ DNA has two sites for accommodating direct metal ion binding; at the phosphate group—through the negatively charged oxygen atoms of the phosphodiester linkage—and at the nitrogenous bases (*e.g.* N7 of guanine).⁵⁷ Copper complexes, however, interact with DNA in two primarily modes of binding: metallo-DNA binding and non-covalent binding (groove binding and intercalation).

1.2.2.1 Nucleobase modification of duplex DNA

Chemical modification of nucleic acid constituents has become an important tool in medicinal chemistry and in biological investigation. The incorporating of copper complexes into oligonucleotides is a key design target for the

functionalization of DNA with novel catalytic and electronic properties by alternating bases that are biologically important. Shionoya *et al.* used a pioneering approach whereby a metal complex was incorporated into oligonucleotide by changing the DNA base itself into a chelator-containing base. A hydrogen-bonded base-pairing was replaced with a metal-assisted base-pairing creating a novel binding motif in duplex DNA (Fig. I.6i.).⁵⁸

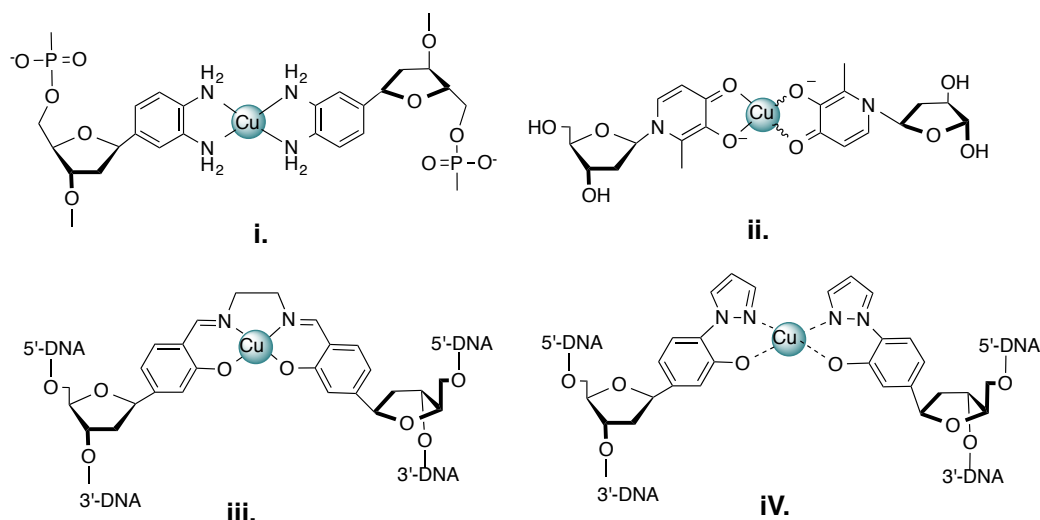


Figure I.6 Schematic of chelator containing nucleotides **i.** Cu^{2+} phenylenediamine β -C-nucleoside and **ii.** H-Cu-H nucleotide, **iii.** Cu-salen complex, and **iv** pyrazole-Cu-pyrazole self base pair system.

Based on this principle the same group designed and synthesized a novel hydroxypyridone nucleobase (**H**)^{59–63} (Fig. I.6ii.) as a planar bidentate ligand containing the Cu^{2+} metal ion. The base pair (**H-H**) was introduced into a 15-nucleosides natural type DNA duplex, between two hydrogen-bonded base pairs d(5'-CACATTA**H**TGTTGTA-3')•d(3'-GTGTAAT**H**ACAACAT-5'). In the presence of equimolar Cu^{2+} ions duplex containing **H-H** base pairs had a high thermal stabilization of 13 °C in comparison with duplex containing **A-T** bases in place of **H-H** pair.^{59,64}

Carell *et al.* then reported a copper-salen-base-pair complex in DNA with a high duplex thermal stabilization. This salen complex (Fig. I.6iii.) contains a covalent cross-link of both DNA single strands through metal complexation. Here, the diamine molecule is necessary to form the ligand and the coordinated metal prevents hydrolysis of the formed imines.^{65–67} In a more recent study, same group designed a pyrazole (Pz) base pairs having copper as a metal coordination

geometry (ligandosides) (Fig. I.6iV). They showed that, this system stabilize double helix structure in a cooperative manner through the combination of Pz and the Cu^{2+} salen ligandosides.⁶⁸

Overall, these modified oligonucleotides readily bind to their respective complementary nucleotide and can potentially find use as probes in genetic testing, research and forensics providing powerful tools for programming molecular arrays in a pre-designed manner.

I.2.2.2 Non-covalent DNA binding

The specific, non-covalent interaction of molecules with duplex DNA is the molecular basis of many antitumor, antiprotozoal, antiviral, and antibacterial drugs. Compounds that bind to DNA with high specificity can influence gene expression and hence effect cell proliferation and differentiation.⁶⁹ Most of the research into the non-covalent DNA binding complexes focuses on the development of anti-cancer agents. Copper complexes can interact with DNA non-covalently (Fig. I.7) by binding at either groove (Fig. I.7A.) (both minor and major groove) or through intercalation (Fig. I.7B.).⁷⁰

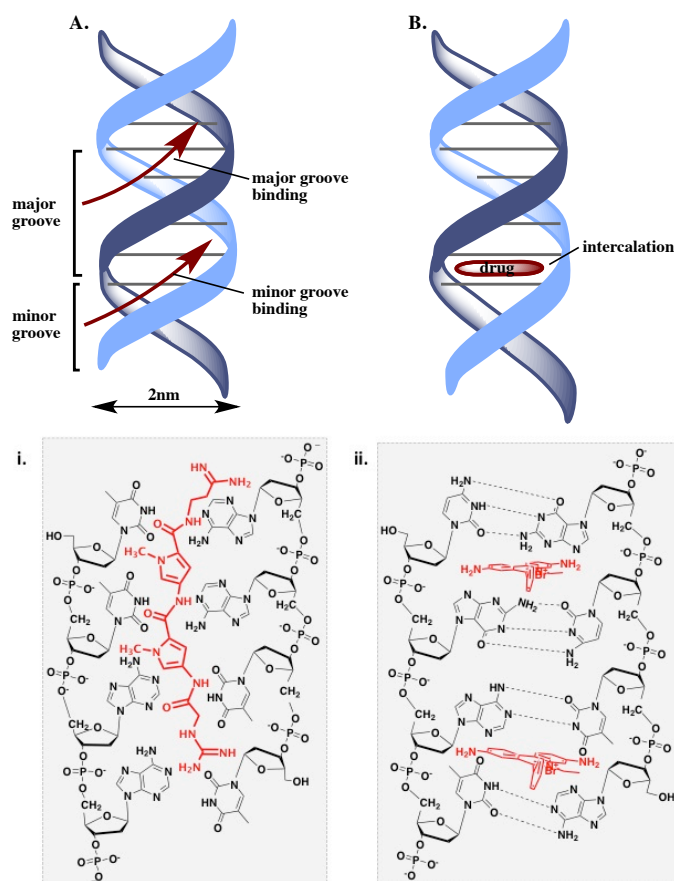


Figure I.7 Non-covalent binding. **A.** Minor groove binding. **B.** Binding through intercalation. **i.** Netropsin structure and 3'-AATT dsDNA sequence. **B.** Ethidium bromide (EtBr) structure and DNA 3'-TAGC dsDNA sequence.

Groove binding. Each turn in the B-DNA helix is made up of 10.4 nucleotide pairs, and the centre-to-centre distance between adjacent nucleotides is 3.4 nm. The coiling of the strands around each other creates two grooves; a wider groove of 22 Å called the major groove, and a smaller groove of 12 Å called the minor groove. These grooves are formed due to hydrogen bonding between complementary bases of DNA that cause sugar groups to project at 120° angle from each other.⁶⁹ Most proteins that are essential to the normal function of the cell, bind to specific sequences in double-stranded DNA (dsDNA) usually through the amino-acid side chain and hydrogen bond donor and acceptor interactions of individual bases at the major groove. This binding is due to the unique binding-signature present in the major groove, but absent in the minor groove.^{71–73} However, most ligands smaller than 1000 Da are known to bind DNA at the minor groove.⁷⁰ Minor groove binding agents can be divided into two functional classes: *a)* those that can induce permanent damage through the covalent interactions with

nucleophilic minor groove component such as N3 of adenine or the 2-amino group of guanine, **b**) compounds that reversibly inhibit DNA function, via non-covalent interaction (electrostatic, hydrogen bonding, and Van der Waals forces).^{69,74} Structurally, minor groove binding agents have certain characteristics that distinguish them from other DNA binding agents. Their shape is rather annular, containing aromatic rings, which matches the curvature of the minor of DNA (Fig. I.7i.). As a rule, members of this group are cations, providing affinity for the tunnel of negative potential in the groove and in addition many ligands possess H-bonds atoms. These agents tend to bind in minor groove with relatively no distortion of the phosphate backbone, stabilizing the regular B-DNA structure.⁷⁴ Several organic and synthetic compounds, many used clinically as anticancer agents, have been reported to bind DNA at the minor groove, mostly at the A-T rich regions (Fig. I.8).

Distamycin and *Netropsin* interact with A-T-rich regions of DNA in the minor groove by forming hydrogen bonding and hydrophobic interactions. The crescent shape and the presence of amide group facing towards the base of the minor groove along with the positively charged amidine group enables the molecule to bind non-covalently in the minor groove for interactions with A-T-rich sequence.⁷⁵

Tallimustine is an A-T specific alkylating antitumor derivative of distamycin. The distamycin portion can form hydrogen bonds with the bases in the minor groove conferring A-T specific sequence recognition, and the nitrogen mustard can alkylate DNA bases. Because of the binding through minor groove, tallimustine alkylates N3 position of adenine residues, unlike conventional nitrogen mustards which, alkylates N7 positions of guanine residues in the minor groove.^{75,76} An interesting group of minor groove binding agents is represented by the synthetic bis(benzimidazole) derivatives - *Hoechst 33258* - which becomes fluorescent upon binding to dsDNA. The dye binds strongly in the minor groove of DNA sequences that are rich in A-T. The molecule is crescent shape and consists of flat hydrophobic aromatic ring creating a fit in the minor groove. Hoechst 33258 is positively charged molecule, which match the strongly electronegative potential at the minor groove of A-T rich, which is more negative than region with high G-C content. Hoechst 33258 has shown to display antitumor and antibiotic properties,

but due to the fluorescent properties it is used as chromosomal stain and DNA quantification.⁷⁷

1-methyl-4-[4-[4-[4-(1-methylquinolinium)aminobenzamide]aniline]-pyridinium dichloride (SN6999) is a synthetic compound that belongs to a family of quinolone-containing DNA binders, which have been shown to possess potent antitumor and antiviral properties. SN6999 has a curved shaped that fits in the minor groove and it forms hydrogen bonds with the bases of DNA sequence, as well as possible electrostatic interactions with the phosphate backbone in an intercalation complex; however, binding in the minor groove is much favourable energetically than intercalation.⁷⁸

Brostallicin, a bromoacrylamido tetra-pyrrole structurally related to distamycin, showed potent *in vivo* cytotoxic activity against tumour cells with an IC₅₀ present in low nanomolar range. Brostallicin, interacts reversibly with the DNA minor groove AT-rich sequence, but appears unreactive in classical *in vitro* DNA alkylating assays.⁷⁹

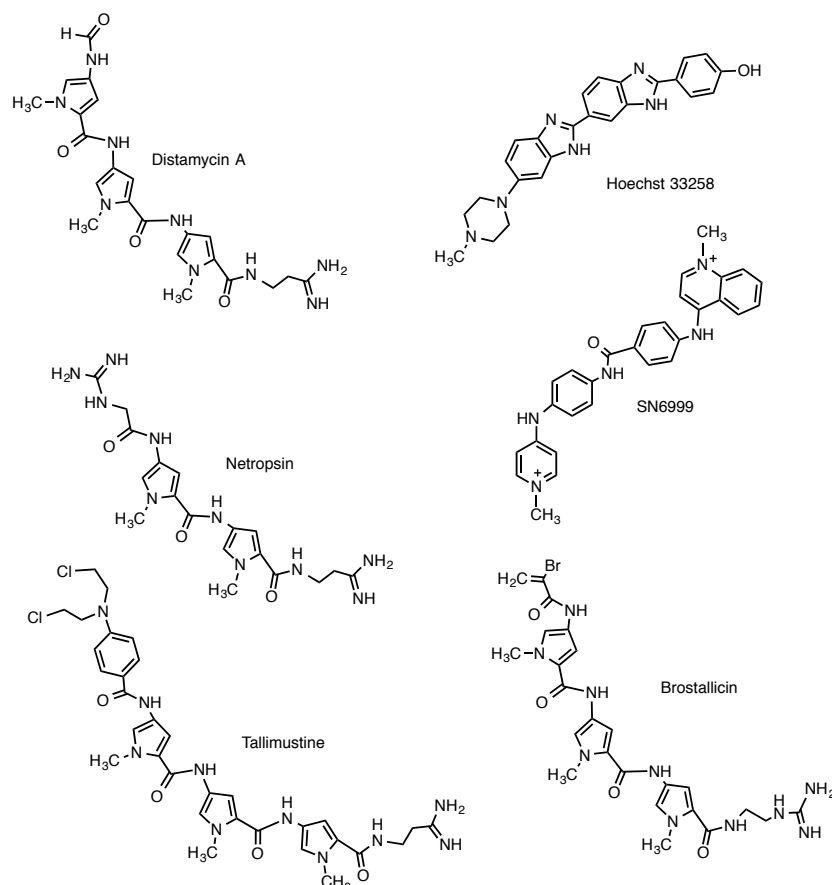


Figure I.8 Selection of the clinically use minor groove binders. These crescent shaped molecules alters DNA conformation by binding to A-T-rich domains in DNA.

Intercalation. This binding mode involves the insertion of a planar aromatic molecule (Fig. I.9) between two successive DNA base pairs (Fig. I.7ii.) with concomitant winding and lengthening of the DNA.⁸⁰ The degree of unwinding varies depending on the ligand used, for example, ethidium bromide unwinds DNA by about 26° ^{81,82} while proflavine (diaminoacridine) unwinds DNA by about 17° . This unwinding causes the base pairs to separate creating an opening by about 3.4 \AA , hence inducing local structural changes to the DNA strand such as lengthening of the DNA or twisting of the base pairs.⁸³ These structural changes can lead to functional changes of the DNA, such as inhibition of transcription and replication and DNA repair mechanism. Thus, intercalators are potent mutagens.⁸⁴ Classical intercalators such as ethidium bromide⁸¹ and proflavin are fused aromatic molecules with positive charge on an attached side chain or ring system itself that interact with DNA without interfering with hydrogen bonding of the base pairs. In threading intercalation, however, the aromatic system is inserted between the base pairs, while one cationic substituent

interacts with the minor groove. Naphthalene diimide interacts with DNA duplex in this way.^{84,85} Another example is provided by 4',6-diamidino-2-phenylindole (DAPI), which is a non-classical intercalator. The binding of DAPI is dependent of DNA sequence. In this regard DAPI binds very strongly to three to four consecutive A-T base pairs in a minor groove complex. However, when fewer consecutive A-T base pairs are present, DAPI binds in the G-C-rich region by intercalation.^{86,87}

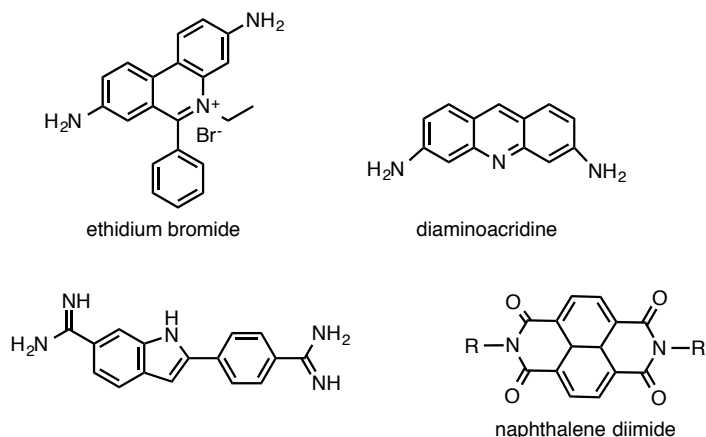


Figure I.9 Chemical structure of several DNA intercalators. Classical intercalators: ethidium bromide and diaminoacridine; threading intercalators: DAPI; non-classical intercalators: naphthalene diimide.

I.2.3 Copper functionalised groove binders

Henichart *et al.* investigated the DNA binding properties of a minor groove binder–intercalator compound that in the presence of copper ions, and reductant, showed sequence specificity and high affinities towards dsDNA binding. This molecule (Fig. I.10) consists of an intercalating acridine derivatives an oligopyrrolecarboxamide moiety of netropsin, and Cu-tripeptide molecule. This Cu-tripeptide molecule was first reported by Dervan *et al.* and was shown that, the natural occurring tripeptide, H-gly-gly-his-OH which, when bound to Cu(II) in the presence of ascorbate has chemical-nuclease like activity.⁸⁸ The attachment of two well known anticancer agents, (netropsin a well known minor groove binder, and acridine an intercalating fluorescent DNA probe), in the presence of a reduced copper-tripeptide molecule, are capable of inducing dsDNA damage at a specific recognised position in the minor groove.⁸⁹

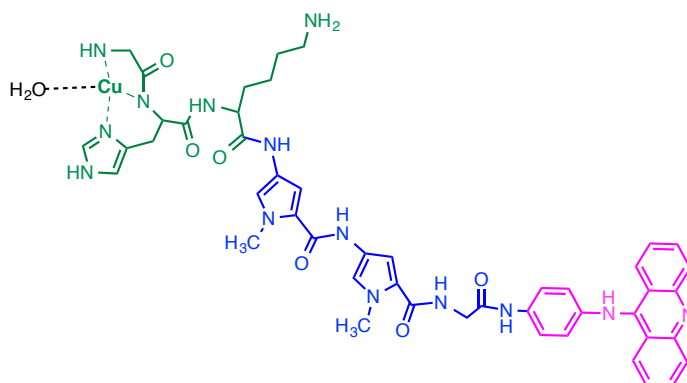


Figure I.10 Structure of minor-groove binder-intercalator. Cu(II)-tripeptide glycylhistidyllysine (colour green), oligopyrrolecarboxamide part of netropsin (coloured blue) which is covalently linked to an intercalating 9-(4-glycyanilino)-acridine derivative (coloured purple).

1.2.3.1 Copper complexes with intercalative properties on B-DNA

The binding activity of Cu-bis-phen (phen = 1,10-phenanthroline, table. I.2b.) on B-DNA is known to be via intercalation in the minor groove by one of the phen molecules, while the other phen ligand makes favourable secondary non-covalent contact within the groove.⁹⁰ Cu-bis-phen cleaves B-DNA in the presence of both oxidant and reductant *via* one electron oxidation reaction at the sugar moiety of DNA through a Fenton-type reaction⁹¹ (Section 1.4.1), however, binds dsDNA with moderate affinity with a binding constant (K_b) on calf thymus DNA (ctDNA) of $2.7 \times 10^3 \text{ M}^{-1}$.⁹² Copper complexes, containing modified diimine N,N' ligands, are known to modulate binding and cleaving dsDNA under oxidative conditions (Table I.2). The extension of aromatic ring of phen ligand in the Cu-bis-phenanthroline species was shown to enhance the intercalative binding properties in comparison to bis-phen analogues with a K_b value of $4.5 \times 10^4 \text{ M}^{-1}$ for Cu-bis-dpq (dpq = dipyrido[3,2-*d*:2',3'-*f*]quinoxaline, Table I.2d.) and $2.0 \times 10^4 \text{ M}^{-1}$ for Cu-bis-dppz (dppz = dipyrido[3,2-*a*:2',3'-*c*]phenazine, Table I.2e.) under similar experimental conditions.⁹² Studies by Chakravarty, Yan, Hadadzadeh, and Palaniandavar *et al.* on copper complexes containing at least one diimine N,N' -ligand (Table I.3, except complex 9), revealed that complexes containing 2,2'-bipyridine (bpy, Table I.2a.), phen, 3,4,7,8-tetramethyl-1,10-phenanthroline (tmp, Table I.3c.) and dipyrido[3,2-*d*:2',3'-*f*]quinoxaline (dpq) ligands prefer intercalation through the minor groove, while complexes containing dipyrido[3,2-*a*:2',3'-*c*]phenazine (dppz) and 11,12-

dimethyldipyrido[3,2-*a*:2',3'-*c*]phenazine (dmdppz, table. I.2f.) ligands bind B-DNA predominantly through the major groove.^{92–104}

In contrast to previously described copper complexes containing *N,N'*-ligands with intercalative binding properties, complex **9** (Table I.3) shows preferential binding towards A-T rich region with a K_b of $1.8 \times 10^6 \text{ M}^{-1}$ on poly (dA)•(dT) , in comparison to ctDNA and pol(dG)•(dC) with a K_b $7.0 \times 10^5 \text{ M}^{-1}$ and $3.4 \times 10^5 \text{ M}^{-1}$, respectively. This preferential binding might be due to the crescent-shape like structure and also the presence of guanidinium end group similar to that of netropsin.¹⁰⁰

Table I.2 Chemical structure of dipyridophenazine ligands

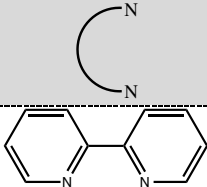
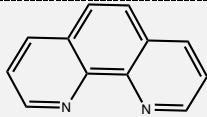
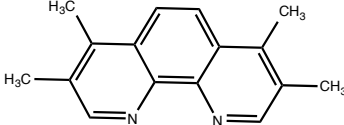
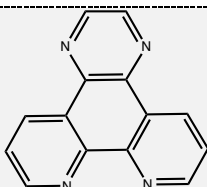
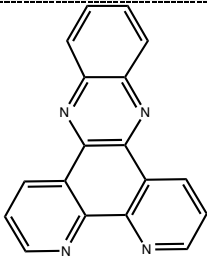
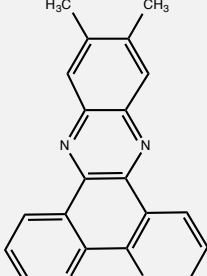
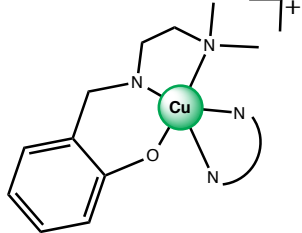
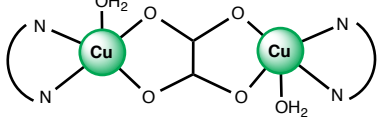
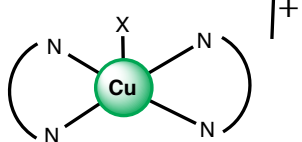
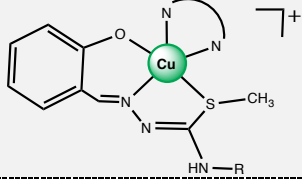
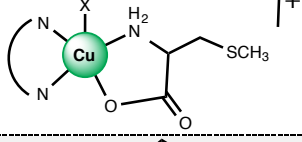
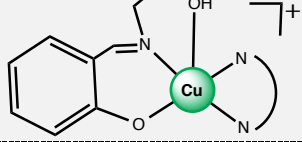
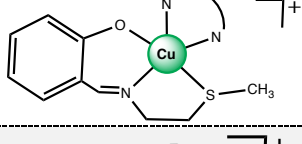
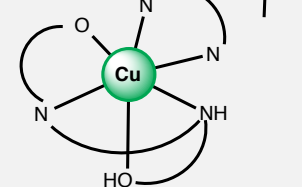
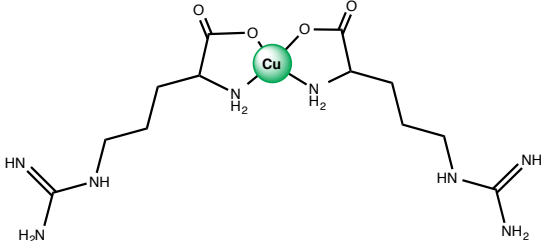
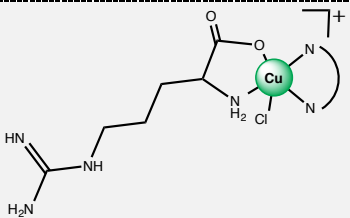
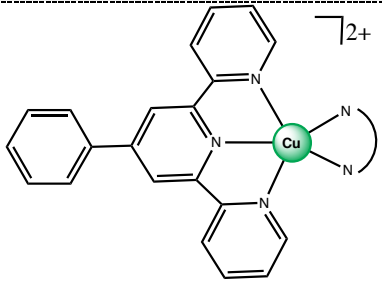
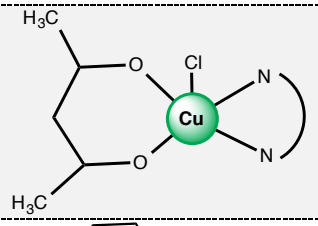
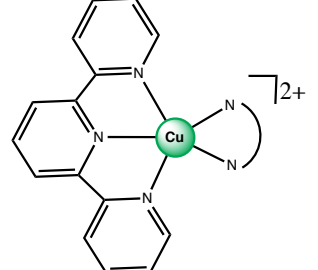
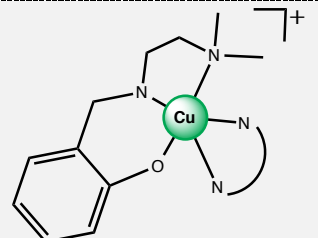
	Diimine <i>N-N</i> ligand	Chemical name and abbreviation
a.		2,2'-bipyridine (bpy)
b.		1,10-phenanthroline (phen)
c.		3,4,7,8-tetramethyl-1,10-phenanthroline (tmp)
d.		dipyrdo[3,2- <i>a</i> :2',3'- <i>f</i>]quinoxaline (dpq)
e.		dipyrdo[3,2- <i>a</i> :2',3'- <i>c</i>]phenazine (dppz)
f.		11,12-dimethyldipyrido[3,2- <i>a</i> :2',3'- <i>c</i>]phenazine (dmdppz)

Table I.3 Selected Cu-complexes containing *N,N'*-donor heterocyclic bases such as bpy, phen, tmp, DPQ, DPPZ, and dmdppz ligands with potential intercalative properties on B-DNA.

Complex no.	Chemical structure	Diimine <i>N-N</i> ligand	Reference
1.		bpy, phen, dpq, dppz	⁹³
2.		bpy, phen, dpq, dppz	⁹³
3.		dpq, dppz X= Cl (dppz only), (NO ₃) ₂ (dpq, dppz)	^{92, 94}
4.		phen, dpq, dppz R = ph, MeOH (phen only)	⁹⁵
5.		bpy, phen, dpq, dppz X = H ₂ O, MeOH (phen only)	^{97, 105}
6.		dpq, dppz	⁹⁸
7.		dpq, dppz	⁹⁸
8.		bpy, phen, tmp, dppz	⁹⁹
9.			¹⁰⁰

8.		bpy, phen, dpq, dppz	100
10.		phen, dpq, dppz	101
11.		dpq, dppz	102
12.		dppz	103
13.		bpy, phen, dpq, dppz, dmdppz	104

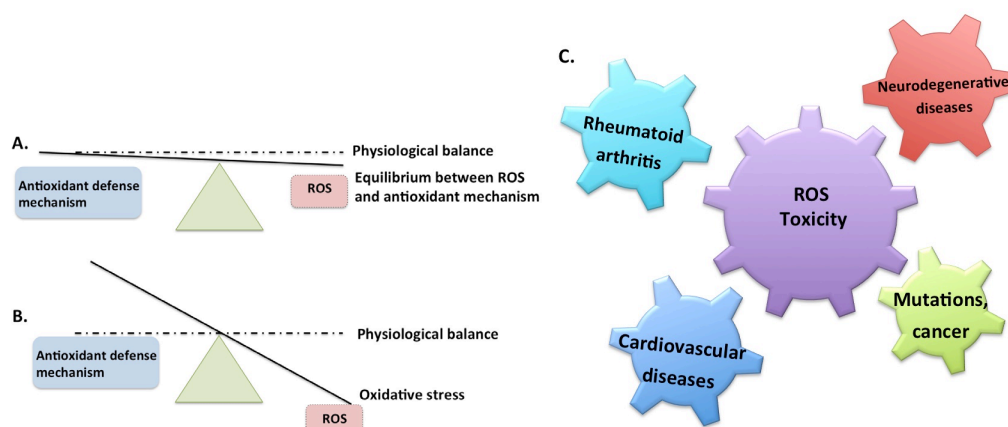
I.3 Oxidative cleavage of DNA

I.3.1 Reactive oxygen Species (ROS)

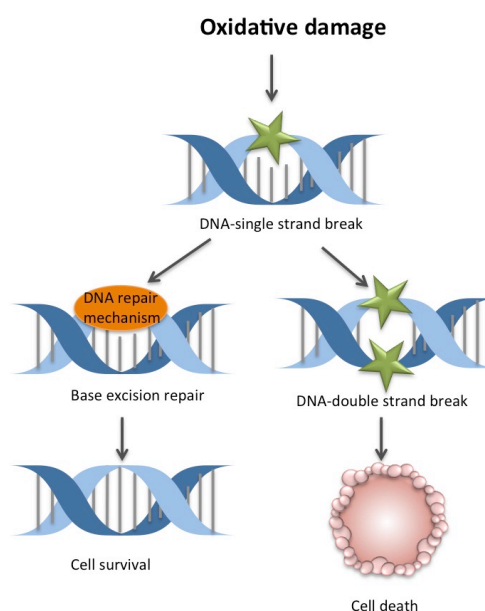
In eukaryotic cells reactive oxygen species (ROS) are generated as a by-product of normal aerobic metabolism or during metabolism of xenobiotics. During times of environmental stress such as exposure to high variation in temperature or radiation, ROS levels can elevate dramatically. The generations of ROS involves the transport of hydrogen ions across the inner mitochondrial membrane in form of electron transport chain. Free radical damage is linked to formation of many degenerative diseases as outlined in scheme I.1.C. Usually there is a equilibrium between free radical formation and antioxidant defence mechanisms (Scheme I.1 A.), hence an imbalance between the body's natural oxidant defence mechanism and the production of ROS leads to oxidative stress (Scheme I.1 B.)—and therefore to cell damage and ultimately cellular death.^{106–108}

Cleavage of DNA (Scheme I.2) is an important process of normal functionalization of living cell. Many enzymes such as topoisomerase solve problems associated with DNA replication, transcription, recombination and chromatin remodelling by introducing temporarily single or double stranded breaks in DNA.¹⁰⁹ Other enzymes such as restriction endonucleases protect the cell against foreign DNA (viral infections) by cleaving the affected DNA sequence.¹¹⁰ The activities of many anticancer drugs rely on the ability to introduce extended damage to the DNA structure, which can trigger apoptosis¹¹¹ leading to cell death.^{112,113} In general, three types of DNA cleavage can be distinguished: oxidative damage, DNA hydrolysis and photochemical damage, however, only oxidative damage will be described in detail here.

Reactive oxygen species (ROS) such as hydroxyl radicals ($\cdot\text{OH}$), the superoxide anion radical ($\text{O}_2^{\cdot-}$), and hydrogen peroxide (H_2O_2) can damage either directly or indirectly, most of cell components, including DNA. Further, disruption of essential enzyme pathways and structural proteins and also can provoke uncontrolled chain reactions such as lipid peroxidation or autoxidation reactions.^{106,114,115}



Scheme I.1 A. The physiological balance between the ROS production and antioxidative defences prevents the accumulation of ROS.¹⁰⁸ B. Oxidative stress due to severe disturbance between ROS formation and antioxidative defences C. Potential toxicity associated with ROS.



Scheme I.2 Schematic showing the oxidative damage of DNA.

I.3.2 Oxidative damaged to nucleobases

The $\cdot\text{OH}$ radical, produced through the Fenton¹¹⁶ reaction, has a redox potential of 2.32 V¹¹⁷ (Fig. I.11) and is a highly diffusible oxidant properties, capable of inducing DNA damage either at the base or sugar moiety.¹¹⁸ $\cdot\text{OH}$ generation can be driven by the reduction of Cu^{2+} by superoxide (Eq. 4) under oxidative stress conditions (*e.g.* in the presence of H_2O_2) that promotes the Fenton reaction (Eq.5). Overall these reactions couple to produce the copper (or iron) – catalysed Haber-Weiss processes (Eq. 6) and are known promoters of oxygen radicals under aerobic conditions. The damage at the sugar molecule of the nucleoside is initiated in two ways: *a.*) by hydrogen atom abstraction from one of the

deoxyribose carbons resulting in strand breakage, base release, and cyclonucleoside formation or, **b.**) β to α inversion at the C-1' position that disrupts B-DNA strand conformation. Radical attack at the nucleobase is characterized by the addition of an -OH group to the electron-rich double bond to give adduct radicals and bases, particularly the purine N-7-C-8. An abstraction of the H atom by $\cdot\text{OH}$ from the methyl-group of thymine is also known to occur.¹¹⁹ In general, radical attack on the DNA base does not give rise to chemically altered sugar moieties or strand breaks, except when base modifications labialise the N-glycosyl bond, allowing the formation of abasic sites that are subject to β -elimination.^{107,114,120–122} Among all DNA bases, purine bases – guanine and adenine – has the lowest redox potential with the best electron donor which makes these bases particularly vulnerable to ROS and leads to a plethora of oxidised products.¹²³ In the case of guanine, the hydroxyl radical adds to C4, C5 and C8-position and also to C2 but to a lesser extent. C4-OH radical adducts and C8-OH radical adducts are formed with high yields up to 70%, whereas C5-OH radical adducts appear to be less than 10%. In the presence of O_2 , the C8-OH radical adducts undergoes one-electron oxidation mechanism with the formation of 7,8-dihydro-8-oxoguanine (8-oxo-dG). In contrast, in the absence of O_2 , C8-OH radical adducts undergoes one-electron reduction step and 2,6-diamino-4-hydroxy-5-formaminopyrimidine (Fapy-G) is formed (Scheme I.3).^{122,124–128} The introduction of an “oxo” group on the C8 position and an hydrogen atom on the nitrogen at position N7, facilitate the ability to mimic thymine functionally in *syn* conformation forming a stable 8-oxo-G(*syn*)•A(*anti*) base pair. If this mutation is not recognised and restored by DNA repair enzymes, DNA subsequently replicated will contain a point mutation.¹²⁹

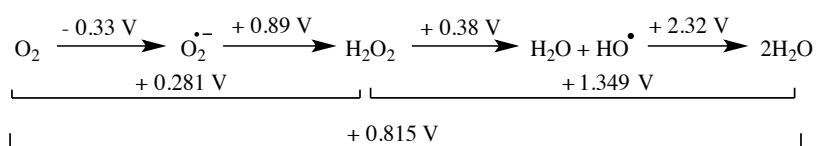
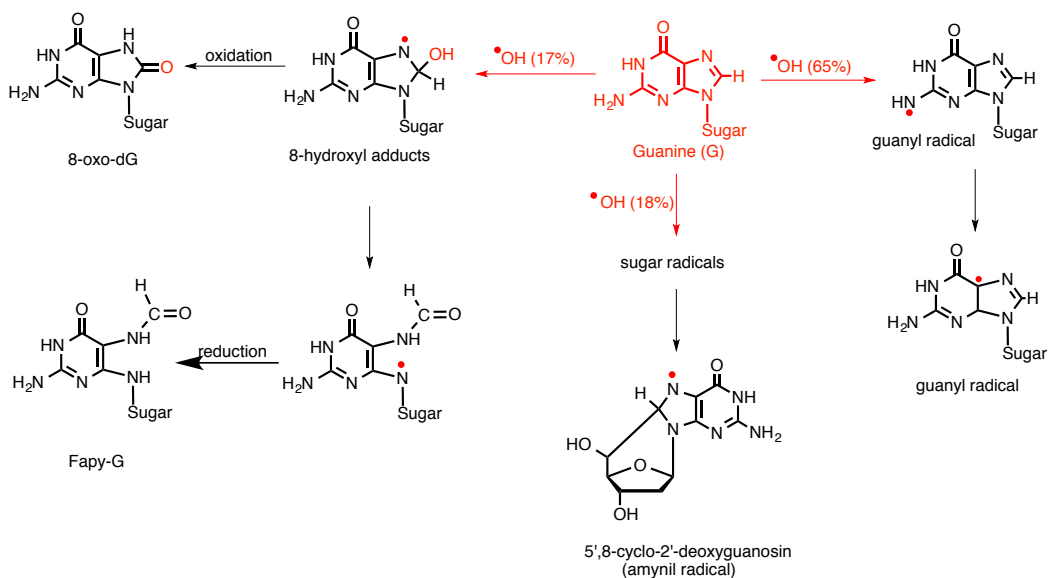
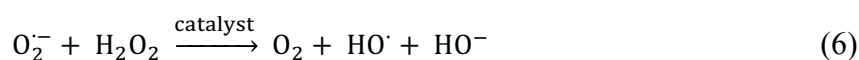
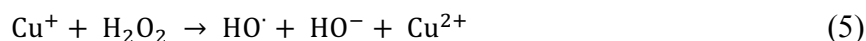
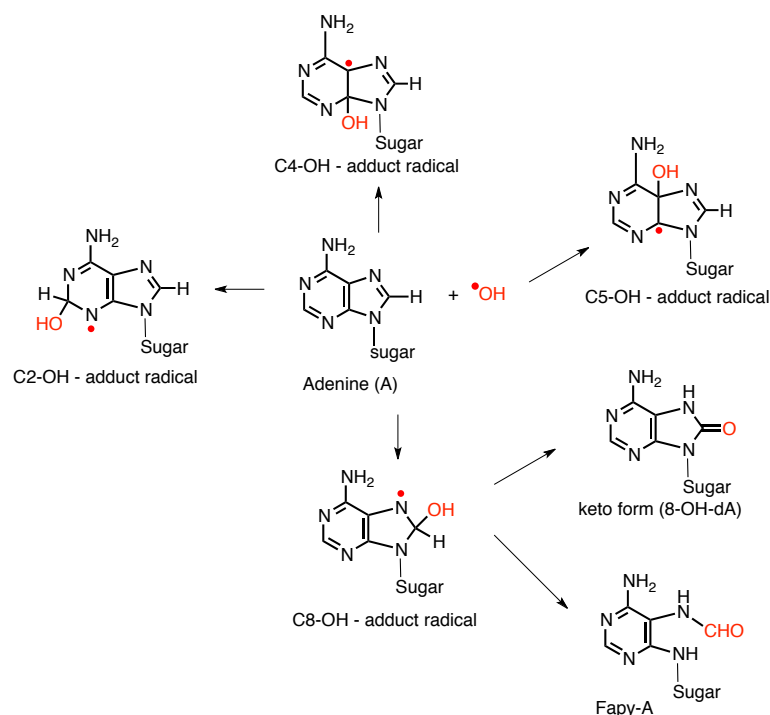


Figure I.11 Potential diagram for O_2 at pH 7. Successive one-electron reduction yields the $\text{O}_2^{\cdot-}$. H_2O_2 produce the $\cdot\text{OH}$ and H_2O



Scheme I.3 Reaction of $\cdot\text{OH}$ with guanine.¹²⁸

The redox potential of adenine is slightly higher than that of guanine, hence is not as easily oxidisable. Similar to guanine, $\cdot\text{OH}$ reacts with adenine at C4 and C8 forming C4-OH, C8-OH radical adducts up to 50% yields and to a lesser extent at C5 and C2 forming C5-OH and C2-OH radical adducts up to 5% yields. A one-electron oxidation reaction in the presence of oxygen undergoes at C8-OH-radical adducts with the formation of the keto form of adenine, 8-hydroxyadenine (8-OH-dA), however, in the absence of O_2 adenine undergoes ring opening in one-electron reduction reaction with the formation of 4,6-diamino-5-formamidopyrimidine (Fapy-A) (Scheme I.4). Other oxidation products can form at adenine base, with a much lesser extend.^{122,126}



Scheme I.4 Reaction of $\bullet\text{OH}$ with adenine.¹²⁶

Purine bases, exposed to reactive oxygen species ($\bullet\text{OH}$) generated from γ -radiation, under hypoxic conditions form an internal cyclization between C5' of deoxyribose and C8-position of purine with formation of cyclopurine deoxynucleoside. A covalent bond is formed between the C8-position of the purine with the C-5' residue of the adjacent deoxyribose, with cyclodeoxyadenosine being formed slightly more frequently than cyclodeoxyguanosine. The proposed mechanism for the cyclization of purine nucleosides is by free radical abstraction of hydrogen from the carbohydrate moiety, leading to (5'*R*) and (5'*S*) diastereoisomers of 5'8-cyclo-2'-deoxyadenosine (Fig. I.12. A) and 5'8-cyclo-2'-deoxyguanosine (Fig. I.12. B).^{126,130–132}

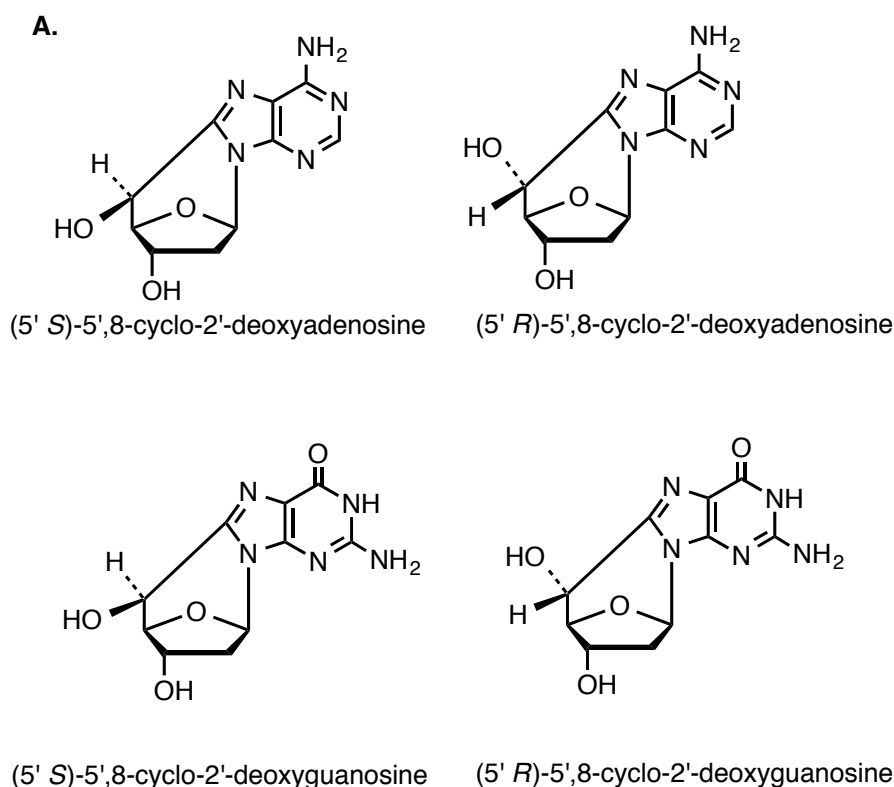


Figure I.12 Structure of diastereoisomers: A. (5'*R*) and (5'*S*) of 5'8-cyclo-2'-deoxyadenosine and B. (5'*R*) and (5'*S*) of 5'8-cyclo-2'-deoxyguanosine.

I.3.3 Copper-binding (ATCUN) motif

Most copper complexes *in vivo* are not able to generate $\cdot\text{OH}$ in free solution, however, when copper ions bound to specific targets such as DNA, RNA, enzymes, cause damage by generating $\cdot\text{OH}$ inducing site-specific damage.¹³³ Studies performed by Kasprak *et al.* showed that Cu(II) and Ni(II) form a stable complex with the *N*-terminal amino-acid sequence motifs of human protamine (HP2). This group showed that Cu(II) and Ni(II) binds with high affinity the *N*-terminal peptide model,¹³⁴ and in the presence of H_2O_2 , Cu(II)/Ni(II)-HP2 complex can mediate single and double strand oxidative DNA damage.^{135,136} Pauling *et al.* then synthesised a tripeptide glycyl-glycyl-histidine complex (Gly-Gly-His) designed to mimic the specific Cu(II) transport site of the albumin molecule (Fig. I.13). This group showed that Cu(II) bound to the Gly-Gly-His sequence had antitumor activity.¹³⁷ The chemical structure of this tripeptide motif shows an NH_2 -terminus, a histidine residue in the third position and two intervening nitrogens. This structural feature is defined as the amino terminal Cu(II)-and Ni(II)-binding (ATCUN).¹³⁸ The ATCUN motif occurs naturally in human serum albumin and other proteins, but synthetic ATCUN and can bind

Cu(II) and Ni(II) with high affinity inducing oxidative DNA damage, cross-link-proteins, and damage cancer cells in the presence of H_2O_2 .^{139–141} In a recent study, Cowan *et al.* designed a novel class of copper-acridine-ATCUN (CuGGHK-Acr) complex in K^+ solution, that targets G-guadruplex telomeric DNA.¹⁴² G-guadruplex DNA are guanine-rich sequences of nucleic acids capable of forming a four-stranded helix. G-guadruplex DNA – stabilised by monovalent cations (Na^+ , K^+), are formed by the coplanar arrangement of four-guanine bases and held together by Hoogsten bonds – are involved in telomere replication.¹⁴³ In this study, Cu-GGHK-Acr selectively binds to G-guadruplex telomeric DNA, inducing irreversible damage, with moderate anticancer activity.¹⁴²

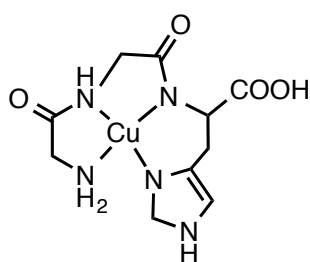


Figure I.13 Structure of the copper – GGH complex. GGH mimics the specific copper transport site of albumin and has the required planar geometry needed to bind copper.¹³⁷

I.4 Mechanisms of oxidative DNA damage

I.4.1 $[\text{Cu}(1,10\text{-phenanthroline})_2]^{2+}$

Metal ions such as Fe^{2+} and Cu^{2+} can react with H_2O_2 via Fenton chemistry to produce ROS, resulting in DNA damage. The first chemical nuclease was reported by Sigman *et al.* and is the $[\text{Cu}(1,10\text{-phenanthroline})_2]^{2+}$ ($[\text{Cu}(\text{phen})_2]^{2+}$, Fig. I.15A.) complex. This species was discovered in 1979 during investigations into the inhibition by 1,10-phenanthroline –cuprous complex on poly(dA-dT) direct polymerization catalysed by *E. coli*-DNA polymerase I in an oxygen-dependent reaction.¹⁴⁴ The proposed mechanism of DNA cleavage reaction by copper(II) bis-1,10-phenanthroline, in the presence of H_2O_2 , consists of one electron transfer reaction from $[\text{Cu}(\text{phen})_2]^+$ with the formation of reactive oxygen species and copper-oxo-species (Fig. I.14), which are directly responsible for DNA strand breaks.^{119,144}

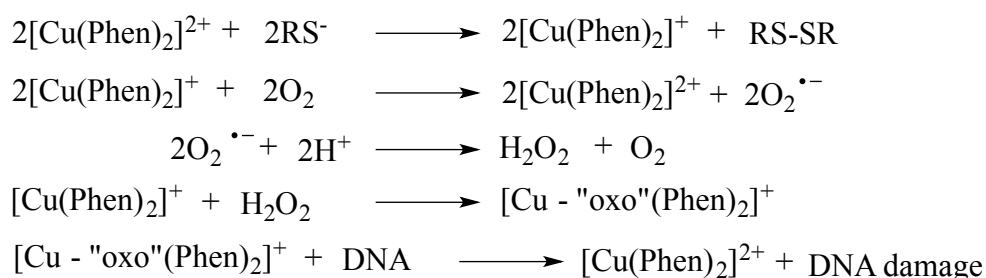


Figure I.14 Proposed formation of reactive copper-oxo species *via* Fenton chemistry^{90,145}

The actual DNA scission is initiated by hydrogen atom abstraction from deoxyribose residue and the reaction requires exogenous agents along with Cu^+ . $[\text{Cu}(\text{phen})_2]^+$ binds to the surface of DNA within the minor groove, since the hydrogen atom abstraction occurs at the C1' along with varying amounts of oxidation at the C4' and or C5'-positions of the sugar (Fig I.15B.).^{145–147} A novel aspect of copper-phenanthroline chemistry is C1'–oxidation, a process that gives rise to the alkali-labile 2'-deoxyribonolactone lesion, which was then proposed as a mediator of direct strand scission.⁹⁰

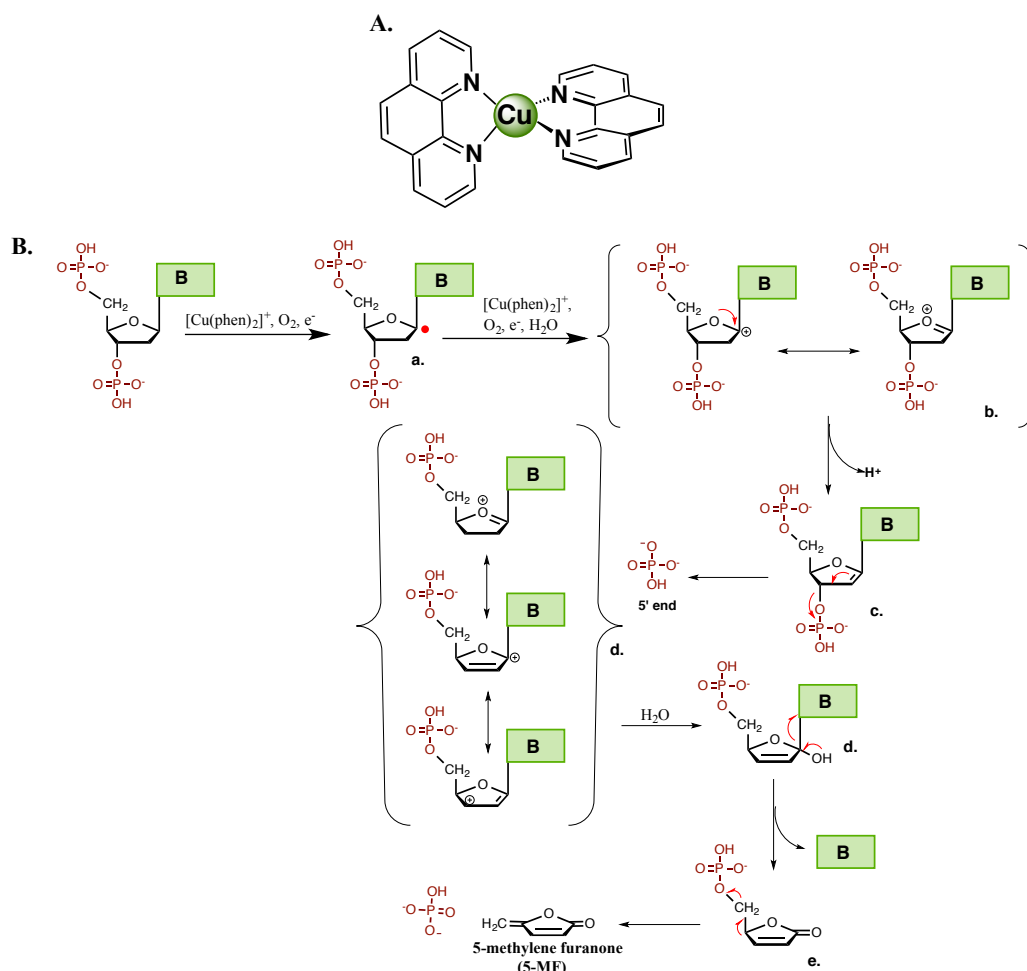


Figure I.15 **A.** Structure of Sigman's reagent $[\text{Cu}(1,10\text{-phenanthroline})_2]^{2+}$ ($[\text{Cu}(\text{phen})_2]^{2+}$) **B.** Proposed mechanism for scission of DNA by $[\text{Cu}(\text{phen})_2]^+$. Cu-oxo species are formed by the oxidation of DNA bound to $[\text{Cu}(\text{phen})_2]^+$ in the presence of H_2O_2 **a.** C1' radical formation by hydrogen atom abstraction followed by carbocation (**b.**) stabilized by partial double bond to furanose oxygen, species **c.** is formed by deprotonation at C2' followed by elimination of 3'-phosphate resulting in strand scission (**d.**). Attack by H_2O on species **d.** leads to elimination of purine/pyrimidine base resulting in species **e.** followed by the formation of abasic site 5-methylenefuranone (5-MF) and 3'- and 5'-phosphorylated ends.^{90,148}

In order to improve the binding specificity of Cu-1,10-phenanthroline reagent and its conjugates, a variety of molecules that damage duplex DNA via oxidative mechanism have since been analysed as artificial nucleases.^{149–166} $[\text{Cu}(1,10\text{-phenanthroline})_2]^{2+}$ cleaves DNA only in the presence of added oxidant or reductant, in order to generate DNA-reactive cupric species. Kellett *et al.* have developed a series of 'self-activating' copper bis-phenanthroline complexes containing phthalates isomers¹⁶⁷ or an octanedioate¹⁶⁸ ligand that oxidatively cleave DNA in the absence of added exogenous reductant. These compounds

showed significant *in vitro* cytotoxicity against a wide range of human-derived cancer cell lines.^{167,168} The self-cleaving mechanism by which these Cu^{2+} complexes damage DNA is thought to be *via* the formation of π carboxylate radicals, which leads to the formation of the reduced Cu^+ species.¹⁶⁸

I.4.2 Bleomycin

Bleomycines, firstly isolated from *Streptomyces verticillus* in 1966, belongs to a family of glycopeptides antitumor antibiotic. As a chemotherapeutic agent, Bleomycin is now routinely used in testicular cancer and certain types of lymphomas as Bleonaxane (Bristol Myer Squibb) and it is composed of two forms of Bleomycin A₂ and B₂ (Fig I.16a.).¹⁶⁹ Bleomycin induces sequence specific single and double strand breaks through multiple binding modes with the latter being responsible for its antitumor effect.¹⁷⁰ In the presence of several metal ions (Fe(II), Co(III) and Cu(I)) and oxygen, ROS are being generated, and through a one-electron reductant mechanism, highly reactive Metal-Bleomycin complex is generated.^{171–173} The chemical structure of Bleomycin can be divided into several functional domains. The metal-binding region, where transition metal form an octahedral complex with the nitrogen atoms of the ligands, the peptide linker region, which, together with the metal binding domain bind within minor groove of DNA and defined the basis for its specificity of DNA cleavage.^{174,175} The highly charged bithiazole tail, are involved in the DNA binding either by intercalation or intercalation at minor group (Fig I.16b.).¹⁷⁶ The role of disaccharide region remains unknown, however DNA cleavage studies done in the absence of the sugar ligand showed a reduce affinity of bleomycin towards DNA binding and also is less effective producing dsDNA breaks.¹⁷⁷ The DNA cleavage sequence specificity of bleomycin is mediated by the binding of N2- and N3- of guanine in the 5' direction (G-5') to the pyrimidine (Py) cleavage site. One single molecule of metal - bleomycin complex in the presence of oxygen or reductant is sufficient to mediate dsDNA breaks. The flexibility of bithiazole tail allows intercalation of the bleomycin molecule at the site directly 3' to the 5'-GT and GC recognition site^{172,178} and therefore cleavage of the second strand of DNA at higher concentration.¹⁷⁹ The bases facing opposite direction TG and CG are not being cleaved.¹⁷² The ratio of single-strand DNA to dsDNA damage is 6:1,¹⁸⁰ but sometimes up to 20:1 depending on the DNA

sequence.¹⁷⁷ The mechanism of DNA cleavage by an “activated” bleomycin, outline in Fig I.17, involves in a primary step, a H[•] atom abstraction of C-4' from the DNA deoxyribose resulting a C-4' deoxyribose radical. In presence of O₂ C-4' hydroperoxy complex occur followed by rapid scission of the C-3'-C-4' bond of the sugar with the formation of base propenals and oligonucleotide 3'-phosphoroglycolates. When oxygen is limited an alkali liable lesion occur at C-4' known as C-4' hydroxylated apurinic acids.^{176,181}

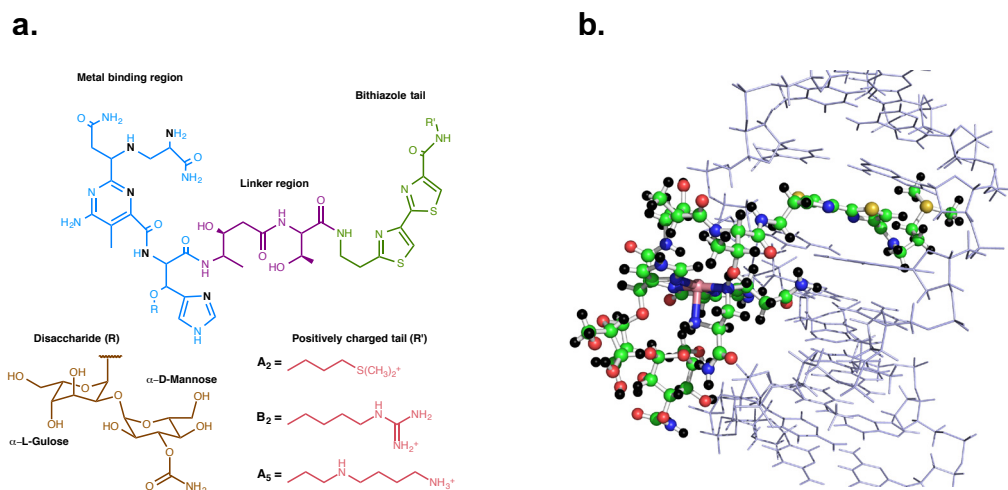


Figure I.16 a. Structure of bleomycin and functional domains. The metal binding region is colored in blue and the nitrogenous atoms that coordinates metal are colored in black. The linker region is in purple and the bithiazole tail is colored in green. The disaccharide (R) is colored in brown and the positively charged tail from the bithiazole tail (R') is colored in red. **b.** Crystal structure of Co(III)-Bleomycin A(2) bound to d(GGAAGCTTCC)₂ (PDB, 1MXK) C – green, H – black, O – red, N – blue S – yellow, and Co(III) in pink.

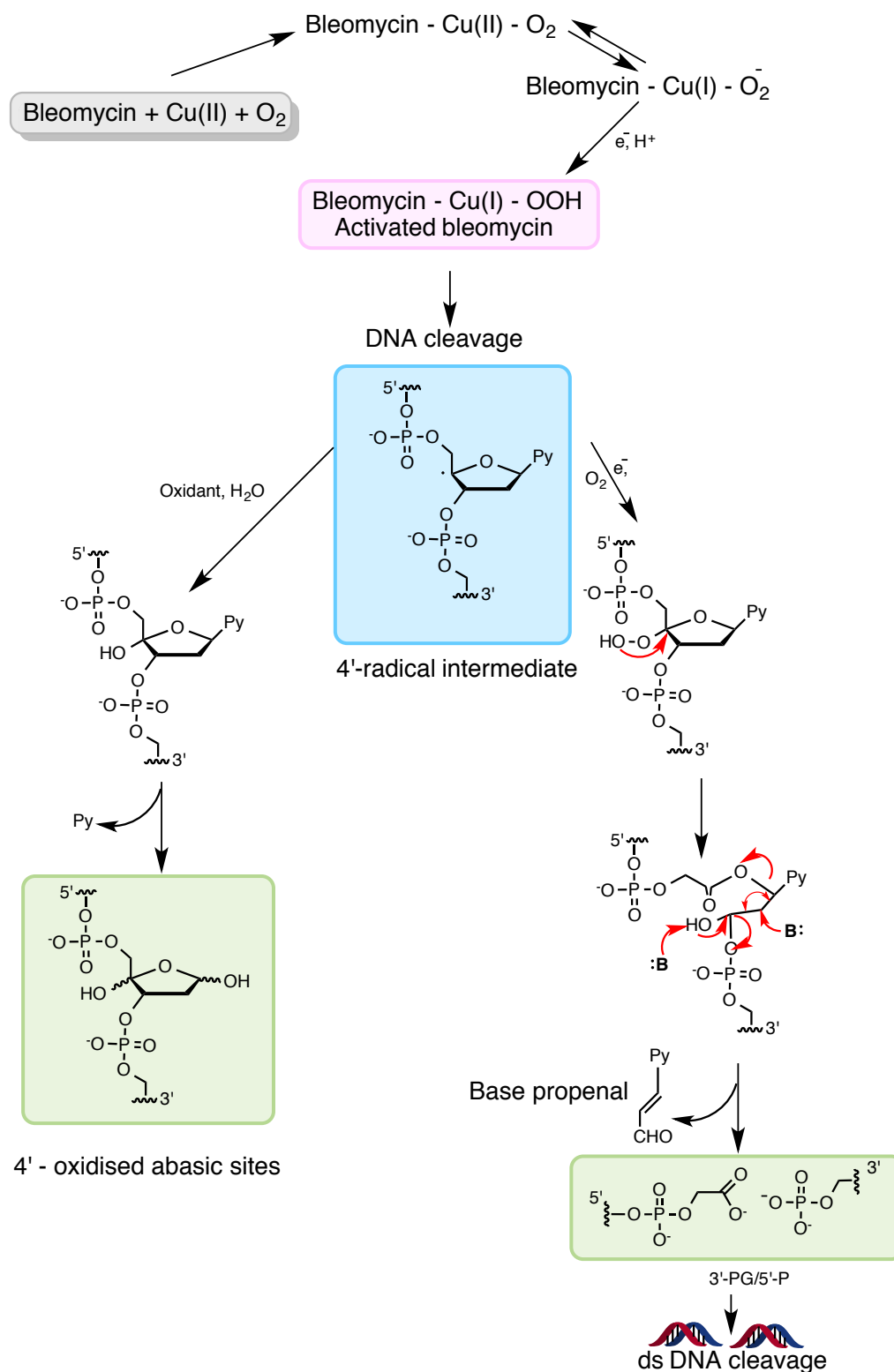


Figure I.17 Formation of activated bleomycin and cleavage of DNA. The activated bleomycin is formed in the presence of O_2 and reductant. The initial step in DNA damages is the removal of hydrogen atom from C-4' from deoxyribose sugar. In the presence of O_2 , 4'-peroxy radical is formed which is further reduced to 4'-hydroperoxyde. The later undergoes a series of chemical transformations with the formation of base propenals and oligonucleotide 3'-phosphoroglycolates (pathway to right).^{177,182} When O_2 is limited, oxidant is added and alkali liable lesion occurs at C-4' known as C-4' hydroxylated apurinic acids (pathway to the left).¹⁷⁷

References

1. Hart E.B., Steenbock H., W. C. A. Iron in nutrition: VII. Copper as a supplement to iron for hemoglobin building in the rat. *J. Biol. Chem* **77**, 797–833 (1928).
2. Shorrocks V M. Copper Development Association. *Copp. Hum. Heal.* **34**, 1–16 (1984).
3. Theophanides T. and Anastassopoulou J. Copper and carcinogenesis. *Crit. Rev. Oncol. Hematol.* **42**, 57–64 (2002).
4. Shim Hoon and Leah Z. Harris. Regulation of Intracellular Trace Element Metabolism. *Am. Soc. Nutr. Sci.* **1**, 1527–1531 (2003).
5. Kim, B. E. & Nevitt, Tracy Thiele, D. J. Mechanisms for copper acquisition, distribution and regulation. *Nat. Chem. Biol.* **4**, 176–185 (2008).
6. Tardito, Saverio and Marchiò, L. Copper compounds in anticancer strategies. *Curr. Med. Chem.* **16**, 1325–1348 (2009).
7. Goodman, V L Brewer, G J and Merajver, S. D. Copper deficiency as an anti-cancer strategy. *Endocr. Relat. Cancer* **11**, 255–263 (2004).
8. Kitzberger, Reinhard and Madl, Christian and Ferenci, P. Wilson disease. *Metab. Brain Dis.* **20**, 295–302 (2005).
9. Yoshikawa, S. Redox-Coupled Crystal Structural Changes in Bovine Heart Cytochrome c Oxidase. *Science (80-.)*. **280**, 1723–1729 (1998).
10. Brunory M., Antonini G., Malatesta F., S. P. and W. T. M. Cytochrome-c oxidase Subunit structure and proton pumping. *Eur. J. Biochem.* **196**, 1–8 (1987).
11. Hough, M. a & Hasnain, S. S. Crystallographic structures of bovine copper-zinc superoxide dismutase reveal asymmetry in two subunits: functionally important three and five coordinate copper sites captured in the same crystal. *J. Mol. Biol.* **287**, 579–592 (1999).
12. Valentine, J. S. and Hart, P. J. Misfolded CuZnSOD and amyotrophic lateral sclerosis. *Proc. Natl. Acad. Sci.* **100**, 3617–3622 (2003).
13. Oberley, L.W. and Buettner, G. R. Role of Superoxide Dismutase in Cancer: A Review. *Cancer Res.* **39**, 1141–1149 (1979).
14. Mao, G.D., Thomas, P.D., Lopaschuks, G.D. and Poznanskyq, M. J. Superoxide Dismutase (SOD) -Catalase Conjugates. *J. Biol. Chem.* **268**, 416–420 (1993).

15. Li, H.T., Jiao, M., Chen, J., and Liang, Y. Roles of zinc and copper in modulating the oxidative refolding of bovine copper, zinc superoxide dismutase. *Acta Biochim Biophys Sin* **42**, 183–194 (2010).
16. Ellerby, L.M., Cabelli, D.E., Graden, J.A and Valentine, J. S. Copper - Zinc Superoxide Dismutase : Why Not pH-Dependent ? *J. Am. Chem. Soc.* **118**, 6556–6561 (1996).
17. Lyons, T J, Gralla, E B and Valentine, J. S. Biological chemistry of copper-zinc superoxide dismutase and its link to amyotrophic lateral sclerosis. *Met. Ions Biol. Syst.* **36**, 125–177 (1999).
18. Müller, G., Ruppert, S., Schmid, E and Schütz, G. Functional analysis of alternatively spliced tyrosinase gene transcripts. *EMBO J.* **7**, 2723–2730 (1988).
19. Hearing, V.J., and Tsukamoto, K. Enzymatic control of pigmentation in mammals. *FASEB J.* **5**, 2902–2909 (1991).
20. Iakovidis, Isidoros, Delimaris, Ioannis and Piperakis, S. M. Copper and its complexes in medicine: a biochemical approach. *Mol. Biol. Int.* **2011**, 594529 (2011).
21. Hellman, Nathan E and Gitlin, J. D. Ceruloplasmin metabolism and function. *Annu. Rev. Nutr.* **22**, 439–58 (2002).
22. Bielli, P and Calabrese, L. Structure to function relationships in ceruloplasmin : a ‘ moonlighting ’ protein. *Cell. Mol. Life. Sci.* **59**, 1413–1427 (2002).
23. Rucker, R. B., Kosonen, T., Michael S.C., Mitchell, A. E Rucker, B. R., Uriu-Hare, J., and Keen, C. L. Copper, lysyl oxidase, and extracellular matrix protein. *Am J Clin Nutr* **67**, 996–1002 (1998).
24. Reiser, K., McCormick, R. J., and Rucker, R. B. Enzymatic and nonenzymatic cross-linking of collagen and elastin. *FASEB J.* **6**, 2439–2449 (1992).
25. Hess, C., Reif, A., Strobel, A., Boreatti-Hümmer, A., Heine, M., Lesch, K-P., and Jacob, C. P. A functional dopamine-beta-hydroxylase gene promoter polymorphism is associated with impulsive personality styles, but not with affective disorders. *J. Neural Transm.* **116**, 121–130 (2009).
26. Molinoff, P. B., Weinshilboum, R., and Axelrod, J. A sensitive enzymatic assay for dopamine- β -hydroxylase. *J. Pharmacol. Exp. Ther.* **178**, 425–431 (1971).
27. Eipper, B. A., Milgram, S L., Husten, E. J. Yun, H Y and Mains, R. E. Peptidylglycine alpha-amidating monooxygenase: a multifunctional protein with catalytic, processing, and routing domains. *Protein Sci.* **2**, 489–497 (1993).

28. El Meskini, Rajaâ Culotta, Valeria Cizewski Mains, Richard E. and Eipper, B. A. Supplying copper to the cuproenzyme peptidylglycine alpha-amidating monooxygenase. *J. Biol. Chem.* **278**, 12278–12284 (2003).
29. De Feo, Christopher J Aller, Stephen G Siluvai, Gnana S Blackburn, Ninian J., and Unger, V. M. Three-dimensional structure of the human copper transporter hCTR1. *Proc. Natl. Acad. Sci. U. S. A.* **106**, 4237–4242 (2009).
30. Kuo, Yien-ming, Zhou, B., Cosco, D. and Gitschier, J. The copper transporter CTR1 provides an essential function in mammalian embryonic development. *PNAS* **98**, 6836–6841 (2001).
31. Maryon, E. B. Molloy, Shannon A, Ivy, K., Yu, H. and Kaplan, J. H. Rate and regulation of copper transport by human copper transporter 1 (hCTR1). *J. Biol. Chem.* **288**, 18035–18046 (2013).
32. Kelner, G. S., Lee, M.H., Clark, M.E., Maciejewski D., Mcgrath D., Rabizadeh S., Lyons T., Bredesen D., Jenner, P., and Maki, R. A. The Copper Transport Protein Atox1 Promotes Neuronal Survival. *J. Biol. Chem.* **275**, 580–584 (2000).
33. Lin, S. J., and Culotta, V. C. Suppression of oxidative damage by *Saccharomyces cerevisiae* ATX2, which encodes a manganese-trafficking protein that localizes to Golgi-like vesicles. *Mol. Cell. Biol.* **16**, 6303–6312 (1996).
34. Zimmnicka, A. M., Maryon, E. B and Kaplan, J. H. Human copper transporter hCTR1 mediates basolateral uptake of copper into enterocytes: implications for copper homeostasis. *J. Biol. Chem.* **282**, 26471–26480 (2007).
35. Robinson, N. J. and Winge, D. R. Copper metallochaperones. *Annu. Rev. Biochem.* **79**, 537–562 (2010).
36. Ba, L. A., Doering, M., Burkholz, T. and Jacob, C. Metal trafficking: from maintaining the metal homeostasis to future drug design. *Metallomics* **1**, 292–311 (2009).
37. Field, L. S., Luk, E., and Culotta, V. C. Copper chaperones: personal escorts for metal ions. *J. Bioenerg. Biomembr.* **34**, 373–379 (2002).
38. Lyons, T. J., and Eide, D. J. *Transport and Storage of Metal Ions in Biology*. **2006**, (2006).
39. Chu, C.C., Lee, W. C., Guo, W. Y. Pan, S. M., Chen, L. J., and Li, H. M. A Copper Chaperone for Superoxide Dismutase That Confers Three Types of Copper / Zinc Superoxide Dismutase Activity in Arabidopsis 1. *Am. Soc. Plant Biol.* **139**, 425–436 (2005).

40. Kuo, M. T., Chen, H. H. W., Song, I.S. Savaraj, N., and Ishikawa, T. The roles of copper transporters in cisplatin resistance. *Cancer Metastasis Rev.* **26**, 71–83 (2007).
41. Kelly, E.J., and Palmiter, R. D. A murine model of Menkes disease reveals a physiological function of metallothionein. *Nat. Genet.* **13**, 219–222 (1996).
42. Tanzi, R.E., Petrunikhin, K., Chernov, I., Pellequer, J.L., wasco, W., Boss, B., Romano, D.M., parano, E., pavone, L., Brzustowicz L.M., devotoM., Peppercorn, J., Bush, A.I., Sternlieb, I., Pirastu, M., Gusella, J.F., Evgrafov, O., Penchaszadeh, G.K., Honi, T. C. The wilson disease gene is a copper transporting ATPase with homology to the Menkes disease gene. *Nat. Genet.* **5**, 344–350 (1993).
43. Roberts, Eve A., and Schilsky, M. L. Diagnosis and treatment of Wilson disease: an update. *Hepatology* **47**, 2089–2111 (2008).
44. Gu, M., Cooper, J.M., Butler, P., Walker, A.P., Mistry, P.K., Dooley, J.S., and Schapira, A. H. V. Oxidative-phosphorylation defects in liver of patients with Wilson’s disease. *Lancet* **356**, 469–474 (2000).
45. Festa, R. A., and Thiele, D. J. Copper: an essential metal in biology. *Curr. Biol.* **21**, 877–883 (2011).
46. Petris, M.J. and Mercer, J. F. The Menkes protein (ATP7A; MNK) cycles via the plasma membrane both in basal and elevated extracellular copper using a C-terminal di-leucine endocytic signal. *Hum. Mol. Genet.* **8**, 2107–2115 (1999).
47. Petris, M. J., Mercer, J. F., Culvenor, J. G., Lockhart, P., Gleeson, P. A. and Camakaris, J. Ligand-regulated transport of the Menkes copper P-type ATPase efflux pump from the Golgi apparatus to the plasma membrane: a novel mechanism of regulated trafficking. *EMBO J.* **15**, 6084–6095 (1996).
48. Dierick, H.A., Adam, A.N., Escara-Wilke, J. F., and Glover, T. W. Immunocytochemical localization of the Menkes copper transport protein (ATP7A) to the trans-Golgi network. *Hum. Mol. Genet.* **6**, 409–416 (1997).
49. Cobbold, C. The Menkes disease ATPase (ATP7A) is internalized via a Rac1-regulated, clathrin- and caveolae-independent pathway. *Hum. Mol. Genet.* **12**, 1523–1533 (2003).
50. Lutsenko, S., Barnes, N. L., Bartee, M. Y. & Dmitriev, O. Y. Function and regulation of human copper-transporting ATPases. *Physiol. Rev.* **87**, 1011–1046 (2007).
51. Bruce A., Alexander J., Julian L., Martin R., Keith R., and P. W. in *Mol. Biol. Cell* 263–329 (Garland Science, 2007).

52. Karabiyik, H., Sevinçek, R. & Karabiyik, H. π -Cooperativity effect on the base stacking interactions in DNA: is there a novel stabilization factor coupled with base pairing H-bonds? *Phys. Chem. Chem. Phys.* **16**, 15527–38 (2014).
53. Sponer, J., Leszczynski, J. & Hobza, P. Electronic properties, hydrogen bonding, stacking, and cation binding of DNA and RNA bases. *Biopolym. (Nucleic Acid Sci.)* **61**, 3–31 (2002).
54. Yakovchuk, P., Protozanova, E. & Frank-Kamenetskii, M. D. Base-stacking and base-pairing contributions into thermal stability of the DNA double helix. *Nucleic Acids Res.* **34**, 564–574 (2006).
55. Subirana, J. a. Hydrogen Bonding, Base Stacking, and Steric Effects in DNA Replication. *Annu. Rev. Biomol. Struct.* **30**, 27–45 (2003).
56. Boerner, Leigh J.K. and Zaleski, J. M. Metal complex-DNA interactions: from transcription inhibition to photoactivated cleavage. *Curr. Opin. Chem. Biol.* **9**, 135–144 (2005).
57. Shirai, H., Itoh, Y., kurose, A., hanabusa, K., Abe, K., and Hojo, N. Formation of Complexes of Deoxyribonucleic Acid (DNA) with Copper(II) and Other Bivalent Metal Ions. *Polym. J.* **16**, 207–215 (1984).
58. Tanaka, K. and Shionoya, M. Synthesis of a Novel Nucleoside for Alternative DNA Base Pairing through Metal Complexation Chemical modification of nucleic acid constituents has gained more and more attention from the viewpoints of medicinal chemistry as well as material sciences . *J.Org.Chem.* **64**, 5002–5003 (1999).
59. Tanaka, K., Tengeiji, A., Kato, T., Toyama, N., Shiro, M., and Shionoya, M. Efficient incorporation of a copper hydroxypyridone base pair in DNA. *J. Am. Chem. Soc.* **124**, 12494–12498 (2002).
60. Tanaka, K., Yamada, Y., Tengeiji, A. Kato, T., Toyama, N. Takezawa, Y., Yori, M., Shiro, M., and Shionoya, M. Artificial metallo-DNA: structural control and discrete metal assembly. *Nucleic acids Res. Suppl.* **3**, 121–122 (2003).
61. Tanaka, K., Tengeiji, A., Kato, T., Toyama, N., and Shionoya, M. A discrete self-assembled metal array in artificial DNA. *Science* **299**, 1212–1213 (2003).
62. Tanaka, K., Clever, G.H., Takezawa, Y., Yamada, Y., Kaul, C., Shionoya, M., and Carell, T. Programmable self-assembly of metal ions inside artificial DNA duplexes. *Nat. Nanotechnol.* **1**, 190–194 (2006).
63. Liu, S., Clever, G.H., Takezawa, Y., Kaneko, M., Tanaka, K., Guo, X., Shionoya, M. Direct conductance measurement of individual metallo-DNA duplexes within single-molecule break junctions. *Angew. Chem. Int. Ed. Engl.* **50**, 8886–8890 (2011).

64. Shionoya, M. and Tanaka, K. Artificial metallo-DNA: a bio-inspired approach to metal array programming. *Curr. Opin. Chem. Biol.* **8**, 592–597 (2004).
65. Clever, G.H., Sörtl, Y., Burks, H., Spahl, W., and Carell, T. Metal-salen-base-pair complexes inside DNA: complexation overrides sequence information. *Chemistry* **12**, 8708–8718 (2006).
66. Clever, G.H., Polborn, K., and Carell, T. A highly DNA-duplex-stabilizing metal-salen base pair. *Angew. Chem. Int. Ed. Engl.* **44**, 7204–7208 (2005).
67. Clever, G.H., and Carell, T. Controlled stacking of 10 transition-metal ions inside a DNA duplex. *Angew. Chem. Int. Ed. Engl.* **46**, 250–253 (2007).
68. Su, M., Tomás-Gamasa, M. & Carell, T. DNA based multi-copper ions assembly using combined pyrazole and salen ligandosides. *Chem. Sci.* **6**, 632–638 (2015).
69. Cai, X., Gray, P.J., and Von Hoff, D. D. DNA minor groove binders: back in the groove. *Cancer Treat. Rev.* **35**, 437–450 (2009).
70. Wan, K.X., Shibue, T., and Gross, L. M. Non-covalent complexes between DNA-binding drugs and double-stranded deoxyoligonucleotides: a study by ionspray mass spectrometry. *J. Mass Spectrom.* **32**, 1186–1194 (1997).
71. Seeman, N.C., Rosenberg, J.M. and Rich, A. Sequence-specific recognition of double helical nucleic acids by proteins. *Proc. Natl. Acad. Sci. U. S. A.* **73**, 804–808 (1976).
72. Rohs, R., West, S.M., Sosinsky, A., Liu, P., Mann, R.S., and Honig, B. The role of DNA shape in protein-DNA recognition. *Nature* **461**, 1248–1253 (2009).
73. Pabo, C.O. and Sauer, T. Protein-DNA recognition. *Ann. Rev. Biochem.* **53**, 293–321 (1984).
74. Turner, P.R., and Denny, W. A. The mutagenic properties of DNA minor-groove binding ligands. *Mutat. Res.* **355**, 141–169 (1996).
75. Khan, G. S., Shah, A., Zia-ur-Rehman & Barker, D. Chemistry of DNA minor groove binding agents. *J. Photochem. Photobiol. B.* **115**, 105–18 (2012).
76. Herzig, M. C. S., Trevino, A. V., Arnett, B. & Woynarowski, J. M. Tallimustine lesions in cellular DNA are AT sequence-specific but not region-specific. *Biochemistry* **38**, 14045–14055 (1999).

77. Fornander, L. H., Wu, L., Billeter, M., Lincoln, P. & Nordén, B. Minor-groove binding drugs: Where is the second hoechst 33258 molecule? *J. Phys. Chem. B* **117**, 5820–5830 (2013).
78. Gao, Y. G., Sriram, M., Denny, W. a & Wang, a H. Minor groove binding of SN6999 to an alkylated DNA: molecular structure of d(CGC[e6G]AATTCGCG)-SN6999 complex. *Biochemistry* **32**, 9639–9648 (1993).
79. Lorusso, D. *et al.* Brostallicin (PNU-166196), a new minor groove DNA binder: preclinical and clinical activity. *Expert Opin. Investig. Drugs* **18**, 1939–1946 (2009).
80. Palchaudhuri, R., and Hergenrother, P. J. DNA as a target for anticancer compounds: methods to determine the mode of binding and the mechanism of action. *Curr. Opin. Biotechnol.* **18**, 497–503 (2007).
81. Deniss, I.S., and Morgan, A. R. Studies on the mechanism of DNA cleavage by ethidium. *Nucleic Acid Res.* **3**, 315–323 (1976).
82. Depew, R.E., and Wang, J. C. Conformational fluctuations of DNA helix. *Proc. Nat. Acad. Sci. USA* **72**, 4275–4279 (1975).
83. Williams, L.D., Egli, M., Gao, Q., and Rich, A. DNA Intercalation: Helix Unwinding and Neighbor-Exclusion. *Struct. Funct.* **1**, 107–125 (1992).
84. Strekowski, L., and Wilson, B. Noncovalent interactions with DNA: An overview. *Mutat. Res.* **623**, 3–13 (2007).
85. Mcknight, R. E. in *Appl. Calorim. a Wide Context. Scanning calorimetry, Isothermal Titration Calorim. Microcalorim.* 129–152 (2013).
86. Wilson, W.D., Tanious, F.A., Barton, H.J., Jones, R.L., Fox, K., and Wydra, R. L. DNA Sequence Dependent Binding Modes. *Biochemistry* **29**, 8452–8461 (1990).
87. Wilson, W.D., Tanious, F.A., Barton, H. J., Jones, R.L., Strekowski, L., and Boykin, D. W. Binding of 4',6-diamidino-2-phenylindole (DAPI) to GC and mixed sequences in DNA: intercalation of a classical groove-binding molecule. *J. Am. Chem. Soc.* **111**, 5008–5010 (1989).
88. Mack, D. P. *et al.* Design and chemical synthesis of a sequence-specific DNA-cleaving protein. *J. Am. Chem. Soc.* **110**, 7572–7574 (1988).
89. Bailly, C. *et al.* Design of a sequence-specific DNA-cleaving molecule which conjugates a copper-chelating peptide, a netropsin residue, and an acridine chromophore. *Bioconjug. Chem.* **3**, 100–103 (1992).
90. Bales, B. C. *et al.* Mechanistic studies on DNA damage by minor groove binding copper-phenanthroline conjugates. *Nucleic Acids Res.* **33**, 5371–5379 (2005).

91. Theodore B. Thederahn, Michio D. Kuwabara, Teresa A. Larsen, and D. S. S. Nuclease Activity of 1,10-Phenanthroline-Copper: Kinetic Mechanism. *J. Am. Chem. Soc.* **111**, 4941–4946 (1989).
92. Gupta, Tarkeshwar Dhar, Shanta Nethaji, Munirathinam Chakravarty, A. R. Bis(dipyridophenazine)copper(II) complex as major groove directing synthetic hydrolase. *Dalt. Trans.* 1896–1900 (2004).
93. Chakravarty, A. R., Anreddy, P. a. N., Santra, B. K. & Thomas, A. M. Copper complexes as chemical nucleases. *J. Chem. Sci.* **114**, 391–401 (2002).
94. Navarro, M. *et al.* Design of copper DNA intercalators with leishmanicidal activity. *J. Biol. Inorg. Chem.* **8**, 401–408 (2003).
95. Thomas, A. M., Naik, A. D., Nethaji, M. & Chakravarty, A. R. Synthesis, crystal structure and photo-induced DNA cleavage activity of ternary copper(II)-thiosemicarbazone complexes having heterocyclic bases. *Inorganica Chim. Acta* **357**, 2315–2323 (2004).
96. Patra, A. K., Nethaji, M. & Chakravarty, A. R. Red-light photosensitized cleavage of DNA by (l-lysine)(phenanthroline base)copper(II) complexes. *Dalton Trans.* 2798–2804 (2005). doi:10.1039/b506310h
97. Patra, A. K., Nethaji, M. & Chakravarty, A. R. Synthesis, crystal structure, DNA binding and photo-induced DNA cleavage activity of (S-methyl-l-cysteine)copper(II) complexes of heterocyclic bases. *J. Inorg. Biochem.* **101**, 233–244 (2007).
98. Dhar, S., Nethaji, M. & Chakravarty, A. R. DNA cleavage on photoexposure at the d-d band in ternary copper(II) complexes using red-light laser. *Inorg. Chem.* **45**, 11043–11050 (2006).
99. Rajendiran, V. *et al.* Mixed-ligand copper (II)-phenolate complexes: effect of coligand on enhanced DNA and protein binding, DNA cleavage, and anticancer activity. *Inorg. Chem.* **46**, 8208–8221 (2007).
100. Patra, A. K., Bhowmick, T., Roy, S., Ramakumar, S. & Chakravarty, A. R. Copper(II) complexes of L-arginine as netropsin mimics showing DNA cleavage activity in red light. *Inorg. Chem.* **48**, 2932–2943 (2009).
101. Roy, S., Saha, S., Majumdar, R., Dighe, R. R. & Chakravarty, A. R. DNA photocleavage and anticancer activity of terpyridine copper(II) complexes having phenanthroline bases. *Polyhedron* **29**, 2787–2794 (2010).
102. Chen, G. J. *et al.* Synthesis, DNA binding, photo-induced DNA cleavage, cytotoxicity and apoptosis studies of copper(II) complexes. *J. Inorg. Biochem.* **105**, 119–126 (2011).
103. Abdi, K., Hadadzadeh, H., Weil, M. & Salimi, M. Mononuclear copper(II) complex with terpyridine and an extended phenanthroline base,

- [Cu(tpy)(dppz)]²⁺: Synthesis, crystal structure, DNA binding and cytotoxicity activity. *Polyhedron* **31**, 638–648 (2012).
104. Jaividhya, P., Dhivya, R., Akbarsha, M. A. & Palaniandavar, M. Efficient DNA cleavage mediated by mononuclear mixed ligand copper(II) phenolate complexes: The role of co-ligand planarity on DNA binding and cleavage and anticancer activity. *J. Inorg. Biochem.* **114**, 94–105 (2012).
 105. Patra, A. K., Dhar, S., Nethaji, M. & Chakravarty, A. R. Metal-assisted red light-induced DNA cleavage by ternary L-methionine copper(II) complexes of planar heterocyclic bases. *Dalton Trans.* **2**, 896–902 (2005).
 106. De Bont, R. & van Larebeke, N. Endogenous DNA damage in humans: A review of quantitative data. *Mutagenesis* **19**, 169–185 (2004).
 107. Hemnani, T., and Parihar, M. S. Reactive Oxygen Species and Oxidative DNA Damage. *Indian J Physiol Pharmacol* **42**, 440–452 (1998).
 108. Poljsak, B., Šuput, D. & Milisav, I. Achieving the balance between ROS and antioxidants: When to use the synthetic antioxidants. *Oxid. Med. Cell. Longev.* **2013**, (2013).
 109. Champoux, J. J. DNA Topoisomerases: Structure, Function, and Mechanism. *Annu. Rev. Biochem.* **70**, 369–413 (2001).
 110. Pingoud, A., and Jeltsch, A. Structure and function of type II restriction endonucleases. *Nucleic Acid Res.* **29**, 3705–3727 (2001).
 111. Hengartner, M. O. The biochemistry of apoptosis. *Nature* **407**, 770–776 (2000).
 112. Rich, T., Allen, R.L., and Wyllie, A. H. Defying death after DNA damage. *Nature* **407**, 777–783 (2000).
 113. Dabrowiak, C. J. in *Met. Med.* 58–62 (John Wiley and Sons, 2009).
 114. Breen, A.P., and Murphy, J. A. Reactions of oxyl radicals with DNA. *Free Radic. Biol. Med.* **18**, 1033–1077 (1995).
 115. Kanti Das, T., Wati, M. R. & Fatima-Shad, K. Oxidative Stress Gated by Fenton and Haber Weiss Reactions and Its Association With Alzheimer's Disease. *Arch. Neurosci.* **2**, 1–8 (2014).
 116. Fenton, H. J. H., M. A. Oxidation of Tartaric in Presence of Iron. *J. Chem. Soc. Trans* **65**, 899–910 (1894).
 117. Wood, P. M. The potential diagram for oxygen at pH 7. *Biochem. J.* **253**, 287–289 (1988).
 118. Imlay, J. a. Pathways of oxidative damage. *Annu. Rev. Microbiol.* **57**, 395–418 (2003).

119. Pitié, M., and Pratviel, G. Activation of DNA carbon-hydrogen bonds by metal complexes. *Chem. Rev.* **110**, 1018–1059 (2010).
120. Ueda, J., Takai, M., Shimazu, Y., and Ozawa, T. Reactive oxygen species generated from the reaction of copper(II) complexes with biological reductants cause DNA strand scission. *Arch. Biochem. Biophys.* **357**, 231–239 (1998).
121. Balasubramanian, B., Pogozielski, W.K., and Tullius, T. D. DNA strand breaking by the hydroxyl radical is governed by the accessible surface areas of the hydrogen atoms of the DNA backbone. *Proc. Natl. Acad. Sci. U. S. A.* **95**, 9738–9743 (1998).
122. Cooke, M.S., Evans, M.D., Dizdaroglu, M., and Lunec, J. Oxidative DNA damage: mechanisms, mutation, and disease. *FASEB J.* **17**, 1195–1214 (2003).
123. David, S. S., O'Shea, V. L. & Kundu, S. Base-excision repair of oxidative DNA damage. *Nature* **447**, 941–950 (2007).
124. Cadet, J. *et al.* Hydroxyl radicals and DNA base damage. *Mutat. Res. - Fundam. Mol. Mech. Mutagen.* **424**, 9–21 (1999).
125. Chatgililoglu, C., D'Angelantonio, M., Guerra, M., Kaloudis, P. & Mulazzani, Q. G. A reevaluation of the ambident reactivity of the guanine moiety towards hydroxyl radicals. *Angew. Chemie - Int. Ed.* **48**, 2214–2217 (2009).
126. Dizdaroglu, M. & Jaruga, P. Mechanisms of free radical-induced damage to DNA. *Free Radic. Res.* **46**, 382–419 (2012).
127. Martinez, G. R. *et al.* Oxidative and alkylating damage in DNA. *Mutat. Res. - Rev. Mutat. Res.* **544**, 115–127 (2003).
128. Chatgililoglu, Chrysostomos D'Angelantonio, Mila Kciuk, Gabriel Bobrowski, K. New insights into the reaction paths of hydroxyl radicals with 2'-deoxyguanosine. *Chem. Res. Toxicol.* **24**, 2200–2206 (2011).
129. Burrows, C. J. *et al.* Structure and potential mutagenicity of new hydantoin products from guanosine and 8-oxo-7,8-dihydroguanine oxidation by transition metals. *Environ. Health Perspect.* **110**, 713–717 (2002).
130. Chatgililoglu, C., Bazzanini, R., Jimenez, L. B. & Miranda, M. a. (5'S)- and (5'R)-5',8-cyclo-2'-deoxyguanosine: Mechanistic insights on the 2'-deoxyguanosin-5'-yl radical cyclization. *Chem. Res. Toxicol.* **20**, 1820–1824 (2007).
131. Chatgililoglu, C., Guerra, M. & Mulazzani, Q. G. Model studies of DNA C5' radicals. Selective generation and reactivity of 2'-deoxyadenosin-5'-yl radical. *J. Am. Chem. Soc.* **125**, 3839–3848 (2003).

132. Navacchia, M. L., Chatgililoglu, C. & Montevecchi, P. C. C5'-Adenosinyl Radical Cyclization. A Stereochemical Investigation. *J. Org. Chem.* **71**, 4445–4452 (2006).
133. Valko, M., Morris, H. & Cronin, M. T. D. Metals, toxicity and oxidative stress. *Curr. Med. Chem.* **12**, 1161–1208 (2005).
134. Bal, W., Jezowska-Bojczuk, M. & Kasprzak, K. S. Binding of nickel(II) and copper(II) to the N-terminal sequence of human protamine HP2. *Chem. Res. Toxicol.* **10**, 906–914 (1997).
135. Bal, W., Lukszo, J. & Kasprzak, K. S. Mediation of oxidative DNA damage by nickel(II) and copper(II) complexes with the N-terminal sequence of human protamine HP2. *Chem. Res. Toxicol.* **10**, 915–921 (1997).
136. Liang, R. *et al.* Effects of Ni(II) and Cu(II) on DNA interaction with the N-terminal sequence of human protamine P2: enhancement of binding and mediation of oxidative DNA strand scission and base damage. *Carcinogenesis* **20**, 893–898 (1999).
137. Pauling, L., Hospital, T. & Alto, P. Enhancement of Antitumor Activity of Ascorbate against Ehrlich Ascites Tumor Cells by the Copper : Glycylglycylhistidine Complex 1 CuN₄ X Cp-I. *Cancer Res.* **43**, 824–828 (1983).
138. Harford, C. & Sarkar, B. Amino Terminal Cu(II)-and Ni(II)-Binding (ATCUN) Motif of Proteins and Peptides: Metal Binding, DNA Cleavage, and Other Properties. *Acc. Chem. Res.* **30**, 123–130 (1997).
139. Neupane, K. P., Aldous, A. R. & Kritzer, J. a. Metal-binding and redox properties of substituted linear and cyclic ATCUN motifs. *J. Inorg. Biochem.* **139**, 65–76 (2014).
140. Sankararamakrishnan, R., Verma, S. & Kumar, S. ATCUN-like metal-binding motifs in proteins: identification and characterization by crystal structure and sequence analysis. *Proteins* **58**, 211–221 (2005).
141. Libardo, M. D. J., Nagella, S., Lugo, A., Pierce, S. & Angeles-Boza, A. M. Copper-binding tripeptide motif increases potency of the antimicrobial peptide Anoplin via Reactive Oxygen Species generation. *Biochem. Biophys. Res. Commun.* **456**, 446–451 (2015).
142. Yu, Z., Han, M. & Cowan, J. a. Toward the Design of a Catalytic Metallodrug: Selective Cleavage of G-Quadruplex Telomeric DNA by an Anticancer Copper-Acridine-ATCUN Complex. *Angew. Chemie Int. Ed.* **54**, 1901–1905 (2015).
143. Murat, P. & Balasubramanian, S. Existence and consequences of G-quadruplex structures in DNA. *Curr. Opin. Genet. Dev.* **25**, 22–29 (2014).

144. Sigman, D.S., Graham, D.R., Aurora, V.D., and Stern, M. Oxygen-dependent cleavage of DNA by the 1,10-phenanthroline cuprous complex. Inhibition of Escherichia coli DNA polymerase I. *J. Biol. Chem.* **254**, 12269–12272 (1979).
145. Sigman, S. D. Nuclease Activity of 1,10-Phenanthroline-Copper Ion. *Acc. Chem. Res* **19**, 180–186 (1986).
146. Sigman, D. S. Chemical nucleases. *Biochemistry* **29**, 9097–9105 (1990).
147. Goyne T., and Sigman, D. S. Nuclease activity of 1,10-phenanthroline-copper ion. Chemistry of deoxyribose oxidation. *J.Am.Chem.Soc* **109**, 2846–2848 (1987).
148. Meijler, Michael M Zelenko, Otilie Sigman, D. S. Chemical Mechanism of DNA Scission by (1,10-Phenanthroline)copper. Carbonyl Oxygen of 5-Methylenefuranone Is Derived from Water. *J.Am.Chem.Soc* **119**, 2935–2936 (1997).
149. Xiao, G., Cole, D.L., Gunsalus, R.P., Sigman, D.S., and Chen, C.-H. B. Site-specific DNA cleavage of synthetic NarL sites by an engineered Escherichia coli NarL protein – 1, 10-phenanthroline cleaving agent. *Protein Sci.* **11**, 2427–2436 (2002).
150. Pan, C.Q., Johnson, R.C. and Sigman, D. S. Identification of New Fis Binding Sites by DNA Scission with. *Biochemistry* **35**, 4326–4333 (1996).
151. Pan, C.Q., Landgraf, R., and Sigman, D. S. MicroReview DNA-binding proteins as site-specific nucleases. *Mol. Microbiol.* **12**, 335–342 (1994).
152. Sigman, D.S., Bruice, T.W., Mazumder, A., and Sutton, C. L. Targeted chemical nucleases. *Acc. Chem. Res.* **26**, 98–104 (1993).
153. Lu, L. P., Zhu, M.L., and Yang, P. Crystal structure and nuclease activity of mono(1,10-phenanthroline) copper complex. *J. Inorg. Biochem.* **95**, 31–36 (2003).
154. Boldron, C., Ross, S.A., Pitié, M., Meunier, B. Acridine conjugates of 3-clip-phen: influence of the linker on the synthesis and the DNA cleavage activity of their copper complexes. *Bioconjug. Chem.* **13**, 1013–1020 (2002).
155. Pitié, M., Van Horn, J.D., Brion, D., Burrows, C.J. and Meunier, B. Targeting the DNA cleavage activity of copper phenanthroline and clip-phen to A.T tracts via linkage to a poly-N-methylpyrrole. *Bioconjug. Chem.* **11**, 892–900 (2000).
156. Li, L., Karlin, K.D. and Rokita, S. E. Changing selectivity of DNA oxidation from deoxyribose to Guanine by ligand design and a new binuclear copper complex. *J. Am. Chem. Soc.* **127**, 520–521 (2005).

157. Bales, B.C., Kodama, T., Weledji, Y.N., Pitié, M., Meunier, B., and Greenberg, M. M. Mechanistic studies on DNA damage by minor groove binding copper-phenanthroline conjugates. *Nucleic Acids Res.* **33**, 5371–5379 (2005).
158. Alemón-Medina, R., Breña-Valle, M. & Muñoz-Sánchez, J.L., Gracia-Mora, M.I., and Ruiz-Azuara, L. Induction of oxidative damage by copper-based antineoplastic drugs (Casiopeínas). *Cancer Chemother. Pharmacol.* **60**, 219–228 (2007).
159. Bales, B.C., Pitié, M., Meunier, B., and Greenberg, M. M. A minor groove binding copper-phenanthroline conjugate produces direct strand breaks via beta-elimination of 2-deoxyribonolactone. *J. Am. Chem. Soc.* **124**, 9062–9063 (2002).
160. De Avellar, I.G.J., Magalhães, M.M.M., Silva, André B., Souza, L.L., Leitão, A.C., and Hermes-Lima, M. Reevaluating the role of 1,10-phenanthroline in oxidative reactions involving ferrous ions and DNA damage. *Biochim. Biophys. Acta* **1675**, 46–53 (2004).
161. Gallagher, J., Chen, C.H., Pan, C.Q., Perrin, D.M., Cho, Y.M., and Sigman, D. S. Optimizing the targeted chemical nuclease activity of 1,10-phenanthroline-copper by ligand modification. *Bioconjug. Chem.* **7**, 413–420 (1996).
162. García-Giménez, J.L., Hernández-Gil, J., Martínez-Ruiz, A., Castiñeiras, A., Liu-González, M., Pallardó, F.V., Borrás, J., and Alzuet Piña, G. DNA binding, nuclease activity, DNA photocleavage and cytotoxic properties of Cu(II) complexes of N-substituted sulfonamides. *J. Inorg. Biochem.* **121**, 167–178 (2013).
163. Geraghty, M., Cronin, J.F., Devereux, M., and McCann, M. Synthesis and antimicrobial activity of copper(II) and manganese(II) alpha,omega-dicarboxylate complexes. *BioMetals* **13**, 1–8 (2000).
164. Metcalfe, C., and Thomas, J. A. Kinetically inert transition metal complexes that reversibly bind to DNA. *Chem. Soc. Rev.* **32**, 215–224 (2003).
165. Kellett, A., Howe, O., O'Connor, M., McCann, M., Creaven, B.S., McClean, S., Foltyn-Arfa Kia, A., Casey, A., and Devereux, M. Radical-induced DNA damage by cytotoxic square-planar copper(II) complexes incorporating o-phthalate and 1,10-phenanthroline or 2,2'-dipyridyl. *Free Radic. Biol. Med.* **53**, 564–576 (2012).
166. Reddy, P.R. and Shilpa, A. Oxidative and hydrolytic DNA cleavage by Cu(II) complexes of salicylidene tyrosine schiff base and 1,10 phenanthroline/bipyridine. *Polyhedron* **30**, 565–572 (2011).
167. Kellett, A., O'Connor, M., McCann, M., McNamara, M., Lynch, P., Rosair, G., McKee, V., Creaven, B., Walsh, M., McClean, S., Foltyn, A.,

- O'Shea, D., Howe, O., and Devereux, M. Bis-phenanthroline copper(II) phthalate complexes are potent in vitro antitumour agents with 'self-activating' metallo-nuclease and DNA binding properties. *Dalton Trans.* **40**, 1024–1027 (2011).
168. Kellett, A., O'Connor, M., McCann, M., Howe, O., Casey, A., McCarron, P., Kavanagh, K., McNamara, M., Kennedy, S., May, D.D., Skell, P.S., O'Shea, D., Devereux, D. Water-soluble bis(1,10-phenanthroline) octanedioate Cu²⁺ and Mn²⁺ complexes with unprecedented nano and picomolar in vitro cytotoxicity: promising leads for chemotherapeutic drug development. *Med. Chem. Comm* **2**, 579–584 (2011).
 169. Einhorn, L. H. Curing metastatic testicular cancer. *Proc. Natl. Acad. Sci. U. S. A.* **99**, 4592–4595 (2002).
 170. Sugiyama, H., Ehrenfeld, G. U. Y. M., Shipley, J. B., Kilkuskie, R. E. & Hecht, M. DNA strand scission by Bleomycin group antibiotics. *J. Nat. Prod.* **48**, 869–877 (1985).
 171. Hoehn, S. T., Junker, H. D., Bunt, R. C., Turner, C. J. & Stubbe, J. Solution structure of Co(III)-bleomycin-OOH bound to a phosphoglycolate lesion containing oligonucleotide: Implications for bleomycin-induced double-strand DNA cleavage. *Biochemistry* **40**, 5894–5905 (2001).
 172. Takeshita, M., Grollman, a P., Ohtsubo, E. & Ohtsubo, H. Interaction of bleomycin with DNA. *Proc. Natl. Acad. Sci. U. S. A.* **75**, 5983–5987 (1978).
 173. Sugiyama, H., Kilkuskie, R. E., Chang, L., Ma, L. & Hecht, S. M. DNA Strand Scission. 3852–3854 (1986).
 174. Wu, W., Vanderwall, D. E., Turner, C. J., Kozarich, J. W. & Stubbe, J. Solution Structure of Co³⁺, Bleomycin A2 Green Complexed with d (CCAGGCCTGG). **49**, 1281–1294 (1996).
 175. Zhao, C. *et al.* Structures of HO₂-Co(III)bleomycin A2 bound to d(GAGCTC)₂ and d(GGAAGCTTCC)₂: Structure-reactivity relationships of Co and Fe bleomycins. *J. Inorg. Biochem.* **91**, 259–268 (2002).
 176. Chen, J., Ghorai, M. K., Kenney, G. & Stubbe, J. Mechanistic studies on bleomycin-mediated DNA damage: Multiple binding modes can result in double-stranded DNA cleavage. *Nucleic Acids Res.* **36**, 3781–3790 (2008).
 177. Chen, J. & Stubbe, J. Bleomycins: towards better therapeutics. *Nat. Rev. Cancer* **5**, 102–112 (2005).
 178. Goodwin, K. D., Lewis, M. a, Long, E. C. & Georgiadis, M. M. Crystal structure of DNA-bound Co(III) bleomycin B2: Insights on intercalation

and minor groove binding. *Proc. Natl. Acad. Sci. U. S. A.* **105**, 5052–5056 (2008).

179. Povirk, L. F., Han, Y. H. & Steighner, R. J. Structure of bleomycin-induced DNA double-strand breaks: predominance of blunt ends and single-base 5' extensions. *Biochemistry* **28**, 5808–5814 (1989).
180. Tounekti, O., Kenani, a, Foray, N., Orłowski, S. & Mir, L. M. The ratio of single- to double-strand DNA breaks and their absolute values determine cell death pathway. *Br. J. Cancer* **84**, 1272–1279 (2001).
181. Burger, R. M., Peisach, J. & Horwitz, S. B. Stoichiometry of DNA strand scission and aldehyde formation by bleomycin. *J. Biol. Chem.* **257**, 8612–8614 (1982).
182. John C.Wu, John W. Kozarich and Stubbeqll, J. The Mechanism of Free Base Formation from DNA by Bleomycin. *J. Biol. Chem.* **258**, 4694–4697 (1983).
183. Kellett, A., O'Connor, M., McCann, M., McNamara, M., Lynch, P., Rosair, G., McKee, V., Creaven, B., Walsh, M., McClean, S., Foltyn, A., O'Shea, D., Howe, O., and Devereux, M. Bis-phenanthroline copper(II) phthalate complexes are potent in vitro antitumour agents with 'self-activating' metallo-nuclease and DNA binding properties. *Dalton Trans.* **40**, 1024–1027 (2011).

CHAPTER II

Potent Oxidative DNA Cleavage by the Di-Copper Cytotoxin: $[\text{Cu}_2(\mu\text{-terephthalate})(1,10\text{-phen})_4]^{2+}$

This work was published in *Chemical Communications*, 2012, **48**, 55, pp6906-6908

Prisecaru A., Devereux M., Barron N., McCann M., Colleran J., Casey A., McKee V. and Kellett A.

My contribution to this paper is: Manuscript 1st author, DNA cleavage experiments, site-selective cleavage using type II endonucleases and identification of mode of DNA cleavage using T4 ligase.

II.1 Abstract

The di-copper(II) cation, $[\text{Cu}_2(\mu\text{-terephthalate})(1,10\text{-phen})_4]^{2+}$, is a powerful, non-sequence-specific, minor-groove oxidizer of duplex DNA which, unlike copper(II) bis-1,10-phenanthroline chloride, operates independently of exogenous reagents. The agent displays excellent *in vitro* cytotoxicity towards cisplatin-resistant ovarian cancer cells, producing intracellular reactive oxygen species upon nano-molar exposure.

II.2 Introduction

Manipulation of DNA is both an intrinsic and essential component of molecular biology and biotechnology. Reagents capable of cutting DNA are applied within these fields as probes for DNA structure and function, with the ultimate aim being the design of target-specific, customized endonucleases, capable of modifying genomic DNA.¹ Thus, DNA cleaving reagents are essential tools for both sequence analysis and genome engineering.² Additionally, through these manipulations, tremendous therapeutic potential has been offered in the treatment of gene-specific disease and malfunction.³

DNA cleavage reagents operate using one of two distinct mechanisms; (i) oxidative scission of deoxyribose residues through redox chemistry,⁴ and (ii) hydrolysis of the phosphodiester sugar backbone.⁵ Since the discovery of the first synthetic, oxidative chemical nuclease, $[\text{Cu}(1,10\text{-phen})_2]^{2+}$ (1,10-phen = 1,10-phenanthroline),⁶ metal complexes which facilitate catalytic transformations of DNA have been intensively investigated.⁷ In addition to their application within site-specific gene-manipulation, oxidative DNA cutters have found clinical application in cancer chemotherapy, as demonstrated by the natural antitumor antibiotic, bleomycin (Blenoxane®).⁸ The cleaving limitations of $[\text{Cu}(\text{phen})_2]^{2+}$ include a reliance on exogenous reductant (e.g. ascorbate) or oxidant (e.g. H_2O_2) which are essentially required to generate DNA-reactive cupric or metal-oxo species.^{4a} The design of “self-active” Cu(II) 1,10-phen chemical nucleases represents an important goal, as both the *in vitro* and *in vivo* application of such

agents should not be limited by the establishment of a local oxidizing or reducing environment.

Recently, we have shown that the di-copper(II), bis-1,10-phen complex, $[\text{Cu}_2(\mu\text{-terph})(1,10\text{-phen})_2](\text{terph})$ (**S1**) [terephthalic acid = terphH_2], containing the active cation, $[\text{Cu}_2(\mu\text{-terph})(1,10\text{-phen})_2]^{2+}$, (Fig. II.1), is capable of inducing single-stranded DNA scission in the absence of exogenous reductant or oxidant.⁹ This agent, along with a di-copper(II), μ -octanedioate derivative,¹⁰ have shown significant potential toward DNA manipulation and offer promise as cytotoxic agents. Herein, we present a detailed analysis of the DNA cleavage profile of **S1** using pBR322 plasmid DNA. Direct comparisons are made with the activity of Sigman's reagent, $\text{Cu}(1,10\text{-phen})_2\text{Cl}_2$ (**S2**).[†] Additionally, we employ unique experimental design to identify site-specific cleavage of **S1** along with evidence showing that the "self-active" cleavage mechanism by **S1** is oxidatively linked. Finally, *in vitro* cytotoxicities of **S1** against the platinum-resistant, human-derived ovarian cancer, SK-OV-3, and non-tumorigenic human-derived ovarian cells, HS-832, is presented, with activity being compared to the clinical, type II topoisomerase inhibitor, mitoxantrone. Direct evidence of intracellular ROS generation, within human cancer cells, by **S1** is also revealed.

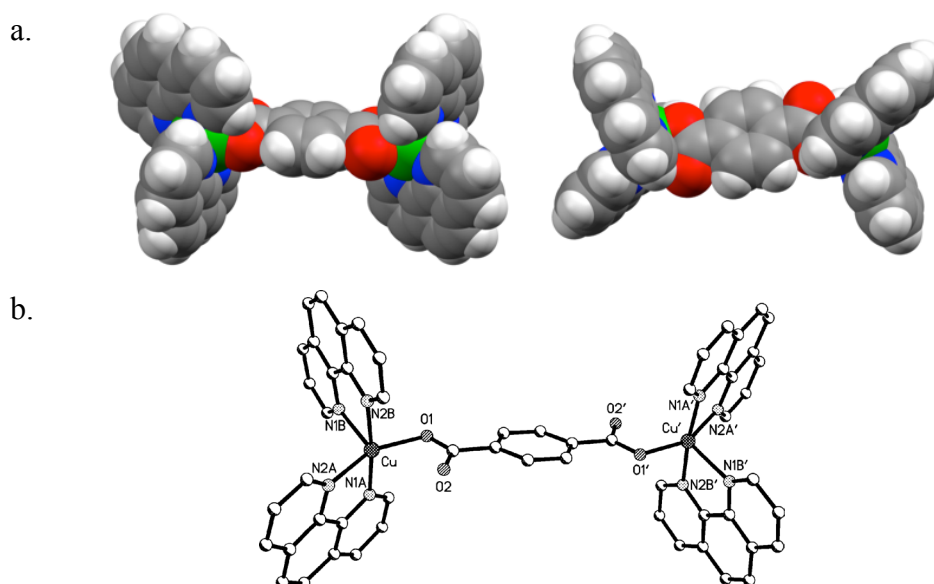


Figure II.18 a. Two perspective, space-filling views of the cation in **S1**, the copper ions are bridged by the terephthalate group. Colour scheme: copper, green; oxygen, red; nitrogen, blue, carbon, grey. b. X-Ray structure of the cation in $[\{\text{Cu}(\text{phen})_2\}_2(\text{terph})](\text{terph})$ ¹⁸³

II.3 Results and discussion

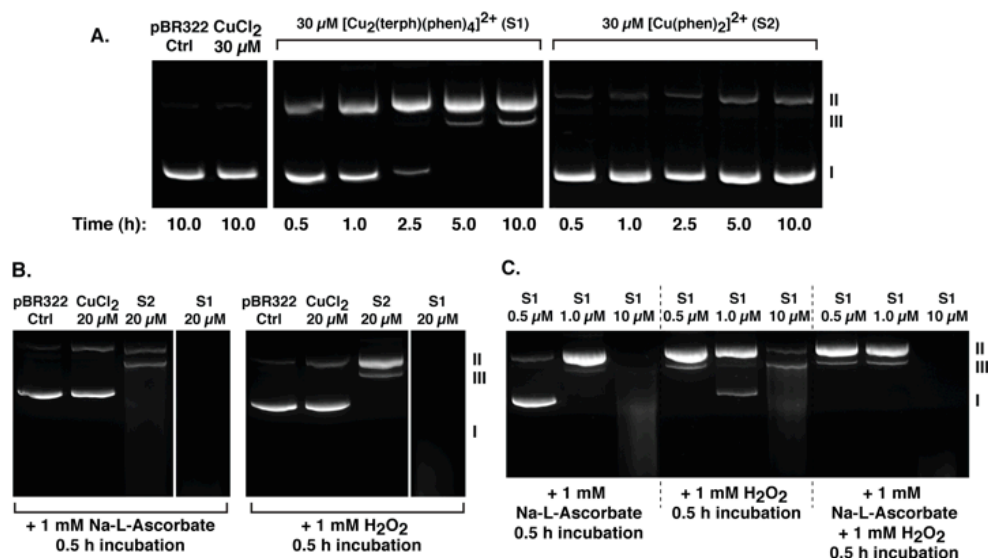


Figure II.19 DNA cleavage reactions using 400 ng of pBR322 plasmid DNA were carried out at 37 °C using [Cu₂(μ -terph)(1,10-phen)₄](terph) (**S1**) and the positive control agent Cu(1,10-phen)₂Cl₂ (**S2**) in 80 mM HEPES at pH 7.2 with 25 mM NaCl then analysed using agarose gel electrophoresis.† **A.** Time-dependant study using 30 μ M of **S1**, **S2** and CuCl₂ exposed to the plasmid for 0.5, 1.0, 2.5, 5.0 and 10 h, **B.** 0.5 h incubation using 20 μ M of **S1**, **S2** and CuCl₂ in the presence of 1 mM added oxidant or reductant, **C.** Cleavage reactions, after 0.5 h incubation, using 0.5, 1.0 and 10.0 μ M of **S1** in the presence of 1 mM added oxidant and/or reductant.

The ability of **S1** and **S2** (see section II.5.1.1 for preparation†) to cleave DNA was studied using agarose gel electrophoresis with supercoiled pBR322 plasmid DNA (Form I) and is shown in Fig. II.2.† Efficient, time-dependent DNA scission, in the absence of exogenous reagents occurred using 30 μ M of **S1** with complete conversion to nicked (Form II) in 2.5 h being followed by partial linearization (Form III) across the 10 h period (Fig. II.2 A). In comparison, **S2** and CuCl₂ did not cleave DNA to any significant extent under identical conditions. Following 30 min of incubation at 37 °C in the presence of either 1 mM of exogenous oxidant (H₂O₂) or reductant (Na-*L*-ascorbate), 20 μ M of **S1** was found to completely digest the plasmid, as evidenced by the absence of a detectable band in Fig. II.2 B. In the cleavage reaction using 1 mM of added reductant, **S2**, as anticipated, was found to be active with a large proportion of plasmid being digested. In the presence of oxidant, however, **S2** was found only to predominantly nick super helical DNA (FI→FII). Additionally, the simple

CuCl₂ salt was found not to affect any change on the plasmid under these same conditions. In order to probe further the activity of **S1**, reactions were preformed using 0.5, 1.0 and 10.0 μ M concentrations under conditions of added reductant, oxidant and with an admixture of both (Fig. II.2 C). At the lowest **S1** tested concentration (0.5 μ M), the presence of H₂O₂ was found to induce complete relaxation of the plasmid to FII while no similar relaxation with Na-L-ascorbate was witnessed. Reactions with 1.0 μ M of **S1** resulted in an overall cleavage enhancement with complete relaxation to Form II in the reductant reaction, and linearization beginning (FII→FIII) in the peroxide reaction. A further increase in concentration of **S1** to 10.0 μ M afforded almost complete digestion of the plasmid with each exogenous reagent or the admixture of both. Overall, it appears that the presence of H₂O₂ is more important in the DNA cleavage reaction at lower **S1** concentrations, while at higher concentrations the presence of reductant becomes more significant.

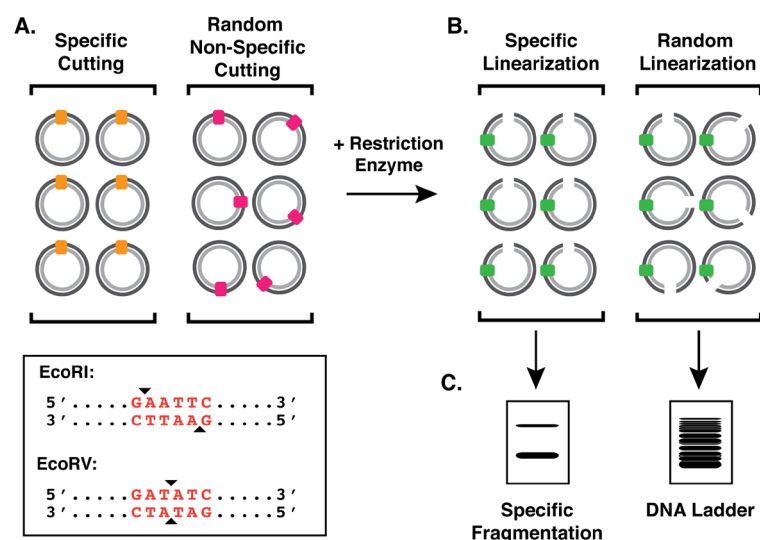


Figure II.20 Experimental design for identifying sequence-specific DNA cleavage. **A.** The unknown double-stranded scission mode, specific (■) or random (■), of plasmid DNA occurs by **S1**, **B.** Introduction of a site-specific restriction enzyme (■) (e.g. *EcoRI* or *EcoRV*) hydrolyses the **S1** linearized DNA exactly once, **C.** Gel electrophoresis of the resulting cleavage reaction reveals either random cutting (laddering) or site-specific cutting (precise fragmentation).

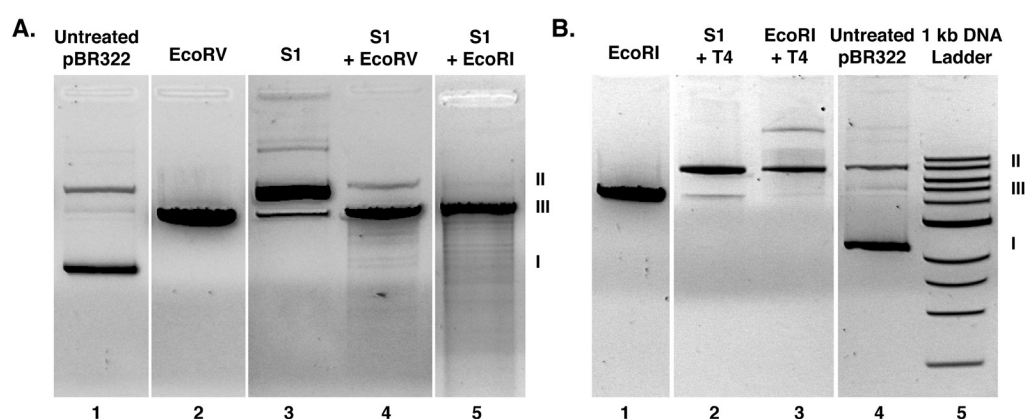


Figure II.21 A. Cleavage reactions of pBR322 by the restriction enzyme *EcoRV* (lane 2), **S1** (lane 3), **S1** followed by exposure of *EcoRV* or *EcoRI* (lanes 4 and 5).† B. Reaction of pBR322 by the restriction enzyme *EcoRV* (lane 1), cleaved plasmid DNA by **S1** and *EcoRI* extracted and purified from gel A (using a Qiagen QIAquick gel extraction kit) were subsequently incubated with T4 ligase (lanes 2 and 3), control DNA and a 1 kb ladder (lanes 5 and 6).† (Note all reactions performed without exogenous agents)

A novel experimental strategy to identify site-selective DNA cleaving capability for **S1** was devised and is described in detail within Fig II.3. The use of two type II endonuclease restriction enzymes, *EcoRI*, which cuts pBR322 exclusively once at the major groove producing a 5' overhang (sticky end) cleavage fragment,¹¹ and *EcoRV*, which also cuts pBR322 exclusively once requiring a conformational DNA change, or kinking, at the minor-groove prior to producing a “blunt end” cleavage fragment,¹² were utilized in this experiment. Control cleavage reactions with pBR322 using *EcoRI* and *EcoRV* produced complete linearization (FI→FIII) corresponding to site-specific, double-stranded hydrolysis (lanes A2 and B1, Fig. II.4) while **S1** exposed to the plasmid produced a mixture of FII (majority) and FIII scission products (lane A3, Fig. II.4). Cleavage reaction products induced by **S1** were then subsequently exposed to *EcoRI* or *EcoRV* (lanes A4 and A5, Fig. II.4). Double-stranded DNA cleavage by **S1** does not appear to occur with sequence-specificity as evidenced by the laddering pattern in the **S1** + *EcoRV* and **S1** + *EcoRI* lanes. Additionally, **S1** appears to favour the minor groove as DNA nicked by this agent and subsequently treated with the endonuclease (*EcoRV*), is not completely relaxed to FIII. Thus, the remaining or protected FII in the **S1** + *EcoRV* lane must arise from **S1** nicking either the *EcoRV* recognition sequence (GATATC, Fig. II.4) or the minor groove sequence required for conformational modification prior to its cutting. Conversely, no protection of nicked FII DNA is observed in the **S1** +

*Eco*RI lane, indicating that DNA cleavage by **S1** does not occur on the exclusive *Eco*RI major groove recognition site (GAATTC. Fig II.4) within pBR322.

In order to identify the mode of DNA cleavage (oxidative or hydrolytic), DNA from the agarose gel in Fig II.4 A was isolated and purified using the Qiagen QIAquick Gel Extraction method, and then incubated with T4 ligase. Plasmid cleaved by *Eco*RI was utilized as “sticky end” religation is generally more successful with ligases such as T4. Plasmid treated with T4, post *Eco*RI exposure, was successfully religated to the open circular form (FII), with a typical banding pattern corresponding to successful ligation of larger linear concatamers also being evident (lane B3, Fig. II.4). Isolated plasmid DNA treated with T4, post exposure to **S1**, produced an identical FII and FIII banding pattern as **S1** alone (lanes B2 and A3, Fig. II.4) indicating non-occurrence of religation. Such behaviour is typical of oxidatively damaged DNA.

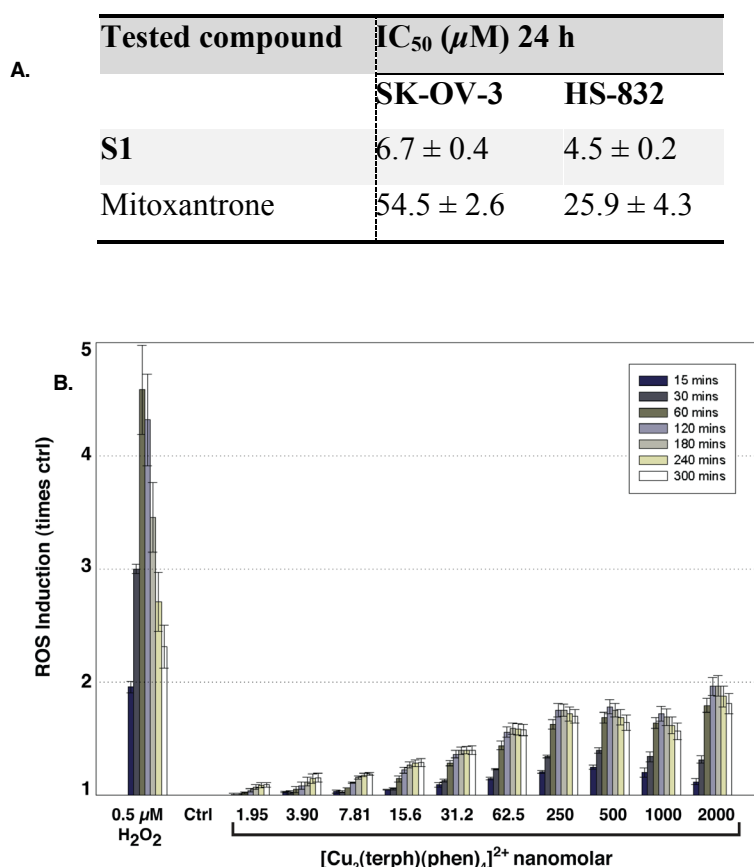


Figure II.22 A. *In vitro* cytotoxicity of **S1** and mitoxantrone against cisplatin-resistant ovarian cancer SK-OV-3 and non-tumorigenic ovarian HS-832 cell lines,† **B.** Generation of endogenous ROS within epithelial lung cancer cells (A549) following exposure to **S1**.†

The *in vitro* chemotherapeutic potential of **S1** was assessed, over 24 h, using a platinum-resistant, human-derived ovarian cancer cell line (SK-OV-3) and a non-tumorigenic human ovarian cell line (HS-832).[†] Results were compared with the clinical type II topoisomerase inhibitor, mitoxantrone, which is also known to function as a DNA intercalator. **S1** is a potent cytotoxin toward both platinum-resistant and non-tumorigenic ovarian cells and was found to be approximately 8 times more active, under these conditions, than mitoxantrone against SK-OV-3 cancer cells, with the clinical agent also being poorly cytoselectivity toward the non-tumorigenic cell line. Of course the potential utility of this agent as a therapeutic will require extensive toxicity profiling in various cell culture and animal models. In order to identify the role of oxidative stress in the cytotoxic mechanism, **S1** was added, between 2000 to 2.0 nM, to human-derived lung cancer cells (A549) pre-treated with the intracellular ROS indicator, 2',7'-dichlorodihydrofluorescein diacetate (DCFH-DA).^{13†} In the presence of endogenously generated ROS, DCFH-DA gets oxidised and releases the fluorophore, DCFH, which becomes trapped in the cytosol. The presence of endogenously generated ROS and reactive nitrogen species (RNS) trigger the formation of the fluorescent probe, 2',7'-dichlorofluorescein (DFC). Results are shown as increases in cellular ROS levels after **S1** exposure and are expressed in comparison to the ROS level of the unexposed control (Ctrl). A positive control of 0.5 μM H₂O₂ was utilised as it is considered a potent ROS generator. Fluorescence measurements were recorded at intervals between 15 and 300 min (Fig. II.4 B) with results showing a concentration-dependent propensity by **S1** to generate intracellular ROS within this cancer cell line.

Electrochemical measurements (Section II.5.5 †) were employed to elucidate the redox properties of **S1** in aqueous solution (DMF, 10%), and typical voltammograms are presented in Fig. II.6 **S1** exhibits good stability with well-defined redox waves, centred about -0.062 and +0.097 V, describing the one-electron quasi-reversible ($\Delta E_p = 0.159$ V) reduction (peak C₁) and oxidation (peak A₁) processes of **S1**, respectively. Addition of 2 mM ascorbate promotes more facile oxidation of **S1**, and complex reversibility is enhanced ($\Delta E_p = 0.041$ V, 3-electron overall). These data indicate that one Cu²⁺ centre is reduced by ascorbate, the remaining Cu²⁺ is reduced electrochemically (1e⁻) and both are re-

oxidised to Cu^{2+} ($2 \times 1e^-$). Comparison in pure DMF reveals added reductant has a marked enhancement on **S1** reversibility and activity but has little effect on **S2**. The phthalate-bridge may confer structural stability on **S1** resulting in redox potentials which are accessible within biological systems.¹⁴

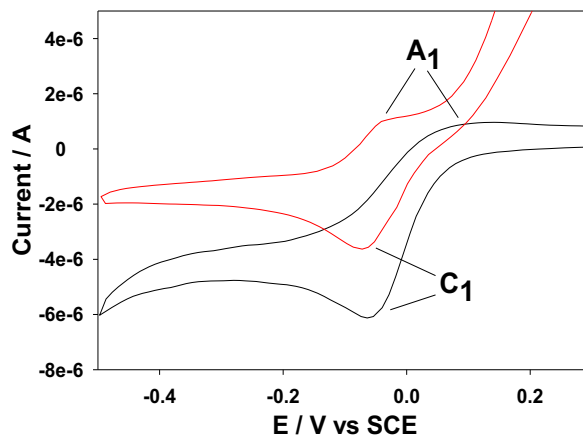


Figure II.23 Typical cyclic voltammograms describing the redox behaviour of 1 mM **S1** in the absence (black trace) and presence (red trace) of 2 mM ascorbate, in 0.1 M KCl aqueous solution. Experimental details in section 2.5.5.†

II.4 Conclusion

In conclusion, we have demonstrated that $[\text{Cu}_2(\mu\text{-terph})(1,10\text{-phen})_4](\text{terph})$ is a potent oxidizer of duplex DNA which operates independently of exogenous reagents and with enhanced activity in their presence. To our knowledge, this is the first “self-active” oxidative copper(II)-bis-1,10-phen system to be reported. We have shown, using innovative experimental design, that this di-copper(II) reagent cleaves DNA in a non-sequence-specific fashion, potentially at the minor-groove. The agent displays excellent *in vitro* chemotherapeutic activity toward cisplatin-resistant ovarian cancer and there is evidence of intracellular ROS production, at nano-molar exposure levels, within human-derived lung cancer cells. A major focus within our laboratory is to now develop probes suitable of inducing specific DNA cleavage, with high efficiency, at a predetermined locus. The innovative work by Barton *et al.* on the conjugation of sequence-specific proteins to DNA-targeting metal complexes may inform this effort.^{7b, 7d} While other Cu^{2+} “self-active” oxidative DNA cleavers known,^{7f, 15} none of these agents can be considered structurally similar to **S1**. Furthermore, it

is our belief that the development of cleaving agents from readily available commercial ligands (1,10-phen and terephthalic acid in this case) is of broad chemical interest.

II.5 Materials and methods

Materials: Chemicals and reagents of analytical grade were purchased from Sigma-Aldrich Ireland and used without further purification.

II.5.1 Preparation of the Complexes.

II.5.1.1 Synthesis of $[\text{Cu}_2(\mu\text{-terphthalate})(1,10\text{-phen})_4](\mu\text{-terphthalate})$ (S1):

The complex was prepared and characterized according to the method reported by Kellett et al.⁹ Prior to biological analysis the complex was finely ground and suspended in DMF with the resultant suspension being heated on a water bath at 70 °C for 2 hours. The suspension was then vortexed prior to buffer dilution.

II.5.1.2 Synthesis of $\text{Cu}(\text{phen})_2\text{Cl}_2 \cdot 3.5\text{H}_2\text{O}$ (S2): An ethanolic solution of copper(II) chloride dihydrate (0.50 g, 2.9 mmol) was treated with 1,10-phenanthroline monohydrate (1.2 g, 6.0 mmol) and refluxed under constant stirring at 90 °C for 2 hours. The green suspension was cooled on ice then filtrated with the resulting green powder being washed with a minimum amount of cold ethanol before being air-dried. Yield: 1.09 g (68.5 %), Elemental analysis: **T%:** C, 51.67; H, 4.16; N, 10.04, **F%:** C, 51.59; H, 4.56; N, 10.01, IR (KBr): 3392, 1624, 1517, 1427, 851, 722 cm^{-1} . Solubility: methanol, ethanol.

II.5.2 DNA cleavage experiments.

II.5.2.1 General procedure: Reactions were carried out according to the literature procedure reported by Melvin *et al.*¹⁶ with slight modifications; in a total volume of 20 μL using 80 mM HEPES buffer (Fisher) at pH = 7.2 with 25 mM NaCl, an aliquot of the stock complex (S1 initially prepared in DMF and S2 and $\text{CuCl}_2 \cdot 2\text{H}_2\text{O}$ in MeOH) was mixed with 400 ng of pBR322 (Roche). Samples were incubated at 37 °C before being quenched with 6x loading dye (Fermentas), containing 10 mM Tris-HCl (pH 7.6), 0.03% bromophenol blue, 0.03% xylene

cyanol, 60% glycerol and 60 mM EDTA, then loaded onto agarose gel (1%) containing 2.0 μL of GelRedTM (10,000X). Electrophoresis was completed at 80 V for 1.5 h using a wide mini-sub cell (BioRad) in 1XTAE buffer (Millipore). Experiments with exogenous reagents were conducted using 1 μL of 20 mM Na-L-ascorbate and/or 1 μL of 20 mM H_2O_2 .

II.5.2.2 Experiments with restriction enzymes. General procedure: In a total volume of 20 μL using 2 μL of 100 mM HEPES buffer (pH = 7.2), 2 μL of 10x NEBuffer 3 (New England BioLabs), 0.2 μL 100x BSA (New England BioLabs), 2 μL 10x NEBuffer *EcoRI* (New England BioLabs) [used where appropriate], 1 μL of 20,000 U/mL *EcoRV* or 20,000 U/mL *EcoRI* (New England BioLabs) and 30 μM of the complex (from stock DMF) were mixed with 400 ng of pBR322 (Roche), and deionized H_2O . Samples containing the complex were incubated at 50 °C for 5 h then ice cooled prior to the restriction enzyme (*EcoRI* or *EcoRV*) being added. This mixture was further incubated at 37 °C for 1.5 h. 6x loading dye (Fermentas) was then added and samples were loaded onto agarose gel (1%) containing 2.0 μL of GelRedTM (10,000X). Electrophoresis was completed at 70 V for 2.0 h using a wide mini-sub cell (BioRad) in 1XTAE buffer (Millipore).

II.5.2.3 Religation experiments. In a total volume of 36 μL containing 30 μL of purified DNA (Qiagen QIAquick gel extraction kit as per manual protocol), 5 μL of 10x T4 ligation buffer (New England BioLabs) and 1 μL of T4 ligase (400,000 U/mL) (New England BioLabs) were incubated in a slush ice bath which was slowly allowed to reach room temperature overnight. 6x loading dye (Fermentas) was added and samples were loaded onto agarose gel (1%) containing 2.0 μL of GelRedTM (10,000X). Electrophoresis was completed at 70 V for 2.0 h using a wide mini-sub cell (BioRad) in 1XTAE buffer (Millipore).

II.5.3 Cytotoxicity experiments.

II.5.3.1 Human Ovarian non-malignant cell line, HS-832 (passage 4 and 5, ATCC, USA), was grown in Dulbecco's modified eagle's medium supplemented with 2 mM L-glutamine and 10% fetal bovine serum (FBS) containing penicillin-streptomycin (100 U/mL and 100 $\mu\text{g/mL}$) at 37 °C in a humidified atmosphere with 5% CO_2 .

II.5.3.2 Human Ovarian Cancer cell line, SK-OV-3 (passage 51 to 64, ATCC, USA), was grown in McCoy's 5a Medium supplemented with 2 mM L-glutamine and 10% fetal bovine serum (FBS) containing penicillin-streptomycin (100 U/mL and 100 µg/mL) at 37 °C in a humidified atmosphere with 5% CO₂. Compounds were tested by the MTT assay following 24 h exposure of cells to **S1** and mitoxantrone (both prepared in DMSO). Each value represents the mean IC₅₀ of three independent experiments +/- STD error.

II.5.3.3 MTT Assay. This method is based on the reduction of the tetrazolium salt, methylthiazolyldiphenyl-tetrazolium bromide (MTT), into a crystalline blue formazan product by the cellular oxidoreductases of viable cells.¹⁷ The resultant formazan crystal formation is proportional to the number of viable cells. Cells were seeded at 4x 10⁵ cells/mL in 96-well plates and incubated at 37 °C in 5% CO₂ for 24 hours. Cells were treated with a four log range of concentration of the test compounds in triplicate from 0.1 to 500 µM or with a solvent control (0.5% DMSO) in complete medium. Following 24 h incubation, cells were incubated with 20 µL of MTT (5 mg/mL) in 0.1 M PBS, pH 7.4 at 37 °C in a humid atmosphere with 5% CO₂ for 4 h. Media was then gently aspirated from test cultures and 100 µL of dimethyl sulphoxide (DMSO) was added to all wells. The plates were then shaken for 2 min and the absorbance was read at 550 nm in a Varioscan plate reader. The IC₅₀ was defined as the concentration of test compound required to reduce the absorbance of the MTT-formazan crystals by 50%, indicating 50% cell deactivation.

II.5.3.4 Cellular reactive oxygen species (ROS) experiments.

Intracellular oxidative stress.

Intracellular oxidative stress was quantified using 2',7'-Dichlorofluorescein diacetate (DCFH-DA).¹⁸ Briefly, healthy confluent A549 cells were harvested and seeded (1000 cells/well) into black bottomed 96 well plates (Nunc, Denmark) and allowed to attach for a period of 24 h prior to exposure. For ROS quantification, three independent experiments were performed. In each independent experiment, eight replicate wells were used for control, eight replicate wells were employed for the positive control and eight replicate wells

were used for each test compound per micro-plate. A working stock of 20 μM DCFH-DA in PBS was prepared and all test compounds, unexposed controls and positive controls were prepared and exposed to the cells in this working stock. The first control consisted of the working stock solely, namely a 20 μM DCFH-DA solution in PBS, the positive control consisted of a 0.5 μM hydrogen peroxide (H_2O_2) prepared in the 20 μM DCFH-DA/PBS working stock solution and finally a concentration range (2000 – 2.0 nM) of the tested complex (**S1**) were prepared in the working stock of 20 μM DCFH-DA/PBS solution. After the initial 24 h attachment period, the media was removed, the cells were subsequently washed with 100 μL of PBS and treated with 100 μL of the control, positive control and the test compounds and then incubated. The rate of intracellular oxidative stress was then monitored by the emission at 529 nm (after 504 nm excitation) of the DCFH-DA dye at time intervals of 15 to 300 minutes (the exposure plates were re-incubated for the remaining time after each measurement had been recorded). Fluorescence measurements were conducted using a microplate reader (TECAN GENios, Grödig, Austria).

II.5.5 Electrochemical experiments

II.5.5.1 Experimental Set-up: A glassy carbon working electrode (3 mm diam.) and a platinum counter electrode were used to determine electrochemical parameters on a Solartron potentiostat, model 1875. Compounds were analysed in 1 mM concentrations and (in a 1:2 ratio with added ascorbate) at a scan rate of 100 mV s^{-1} . Aqueous solutions were made up by dissolving **S1** in 1 ml DMF and 9 ml of H_2O added. Aqueous (DMF, 10%) experiments were performed in 0.1 M KCl using saturated calomel reference electrode (SCE). Voltammetry was performed in DMF with 0.1 M tetrabutylammonium hexafluorophosphate ($\text{TBA}^+\text{PF}_6^-$). Prior to electrochemical measurements all solutions were purged with N_2 for 15 minutes. Experiments performed in DMF required the use of a Ag^+/Ag non-aqueous reference electrode [$E_{1/2} = 0.078\text{V}$ vs $\text{Fe}(\text{Cp})^+/\text{Fe}(\text{Cp})$] and potentials were corrected and are presented here *versus* SCE.¹⁹ Electrodes were polished using 0.05 micron aluminium oxide paste on microcloth (both Buehler) and sonicated for ten minutes in ethanol

II.5.5.2 Electrochemical behaviour of S1 in aqueous solution (DMF, 10%) in the absence and presence of ascorbate.

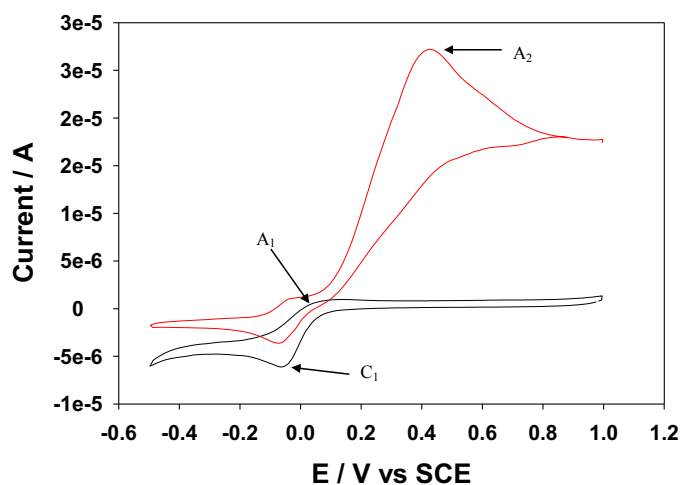


Figure II.24 Enlargement of Figure 6 from manuscript; Typical cyclic voltammograms detailing the electrochemical behaviour of **S1** in the absence (black trace) and presence (red trace) of 2 mM ascorbate in 0.1 M KCl aqueous solution. The A_1/C_1 peaks describe the coupled 1-electron $\text{Cu}^{2+}/\text{Cu}^+$ redox behaviour of **S1** in the absence of ascorbate. On addition of reductant the peak C_1 describes two 1-electron processes. Peak A_2 is the 2-electron, 2-proton oxidation of L-ascorbate. Glassy Carbon working electrode, platinum counter electrode, SCE reference electrode, and scan rate 100 mV s^{-1} . The diminished solubility of **S1**, in aqueous solution, results in lower peak current values when compared to the **S1** current values returned in pure DMF (II.5.5.5).

II.5.5.3 Electrochemical stability of S1 with potential cycling in aqueous solution

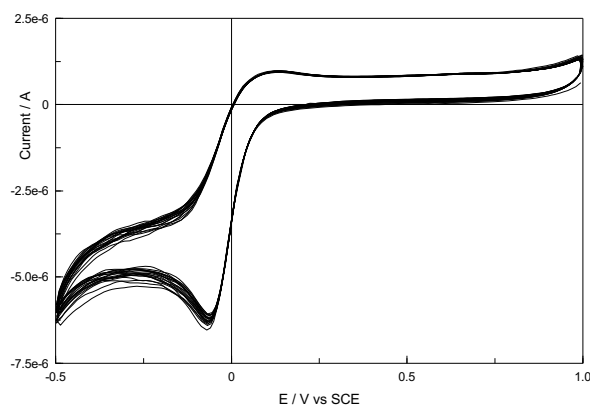


Figure II.25 Typical cyclic voltammograms detailing the stability of 1 mM **S1**, with potential cycling, in a 0.1 M KCl aqueous solution. Little activity is lost after 30 potential cycles. Glassy Carbon working electrode, platinum counter electrode, SCE reference electrode, and scan rate 100 mV s^{-1} .

II.5.5.4 Redox profile of $[\text{Cu}(\text{phen})_2]^{2+}$ in DMF in the absence and presence of ascorbate

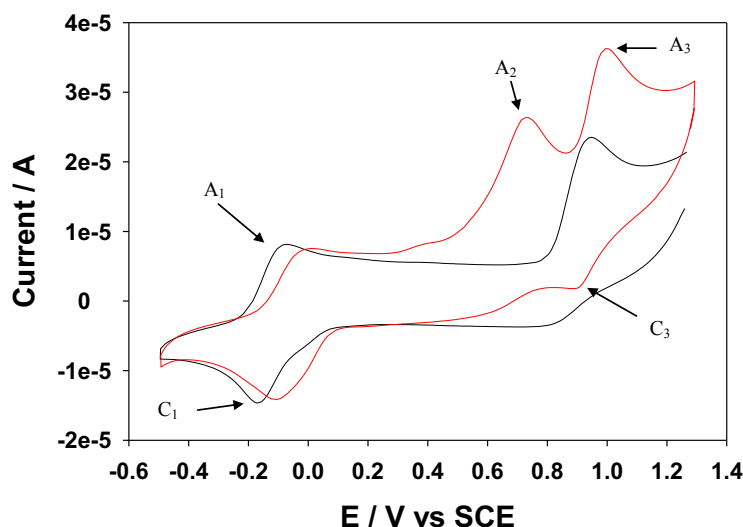


Figure II.26 Typical cyclic voltammograms detailing the redox behaviour of 1 mM $[\text{Cu}(\text{phen})_2]^{2+}$ (S2) in the absence (black trace) and presence (red trace) of 2 mM ascorbate in 0.1 M TBAPF₆/DMF. The peaks correspond to the following processes; A₁/C₁ - $\text{Cu}^{2+}/\text{Cu}^+$ couple, A₂ - ascorbate oxidation, A₃/C₃ - uncomplexed $\text{Cu}^{2+}/\text{Cu}^+$. Glassy Carbon working electrode, platinum counter electrode, Ag⁺/Ag non-aqueous reference electrode, and scan rate of 100 mV s⁻¹.

II.5.5.5 Redox profile of S1 in DMF in the absence and presence of ascorbate

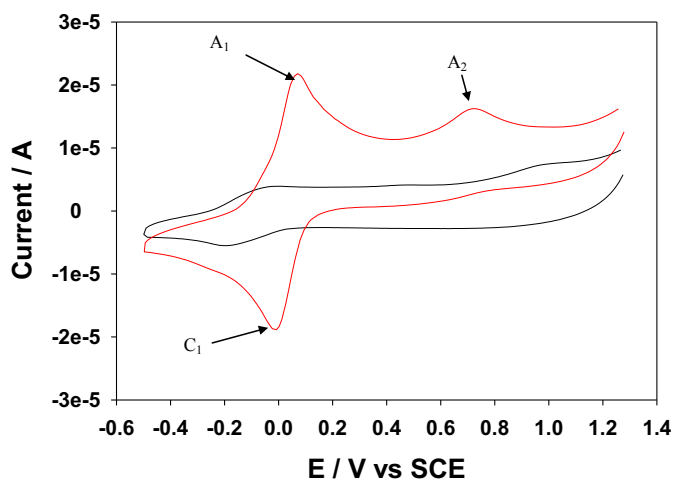


Figure II.27 Typical cyclic voltammograms detailing the redox behaviour of 1 mM S1 in the absence (black trace) and presence (red trace) of 2 mM ascorbate, in 0.1 M TBAPF₆/DMF. Peak A2 describes the irreversible oxidation of unreacted ascorbate. Glassy Carbon working electrode, platinum counter electrode, Ag⁺/Ag non-aqueous reference electrode, and scan rate of 100 mV s⁻¹. Note: No electrochemical redox activity is observed for uncomplexed $\text{Cu}^{2+}/\text{Cu}^+$, as is evident with the $\text{Cu}^{2+}/\text{Cu}^+$ couple in $[\text{Cu}(\text{phen})_2]^{2+}$ (S2).

Tables II.1 (a) and (b) summarise the electrochemical parameters and all potentials are quoted *versus* SCE.¹⁹:

Table II.1 (a): Summary of the parameters calculated for **S1** in the absence and presence of 2 mM ascorbate in aqueous solution. In this table voltage values (V) are quoted versus the SCE calomel electrode.¹⁹

	E_P (V)	ΔE_P (V)	$E_P - E_{P/2}$ (V)	n^*	α value
Reduction, C₁	-0.062	-	0.066	1	0.71
Oxidation, A₁	0.097	0.159	0.138	1	0.66
With 2 mM AA, C₁	-0.072	-	0.052	1	-
With 2 mM AA, A₁	-0.031	0.041	0.029	2	-

Summary of the calculated parameters for the redox behaviour of **S1** in aqueous solution.

Table II.2 (b): Comparison of the redox behaviour of **S1** and **S2** in DMF

S1 (DMF)	E_p (V)	ΔE_p (V)	E_p-E_{p/2} (V)	n*	α*	k^{0†} (x 10⁻³) cm s⁻¹
Redn, C₁	-0.196	-	0.132	1	0.38	-
Oxidn, A₁	-0.007	0.189	0.133	1	0.65	1.6
With 2 mM AA, C₁	-0.008	-	0.062	2	0.33	-
With 2 mM AA, A₁	+0.071	0.079	0.074	2	0.68	16.9

S2 (DMF)	E_p (V)	ΔE_p (V)	E_p-E_{p/2} (V)	n*	α*	k^{0†} (x 10⁻³) cm s⁻¹
Redn, C₁	-0.171	-	0.092	1	0.51	-
Oxidn, A₁	-0.076	0.095	0.071	1	0.32	8.6
With 2 mM AA, C₁	-0.105	-	0.114	1	0.41	-
With 2 mM AA, A₁	+0.012	0.117	0.084	1	0.44	10.3

Summary of the calculated parameters for the redox behaviour, at $\nu = 100 \text{ mV s}^{-1}$, of **S1** and **[Cu(phen)₂]²⁺ (S2)**, in the absence and presence of 2 mM ascorbate. In the absence of ascorbate **S1** exhibits a 1-electron redox process. Addition of ascorbate promotes reversibility in **S1**, allowing the 2-electron reduction and oxidation of both Cu centres. Experiments performed in 0.1 M TBAPF₆ in DMF and potentials corrected to the SCE reference electrode.¹⁹

† Standard heterogeneous rate constant values, (k^0), were estimated from the magnitude of peak separation, ΔE_p , according to Nicholson.²⁰

$$\Psi = \frac{k^0}{\left[\pi D \frac{nF\nu}{RT} \right]^{1/2}}$$

The dimensionless kinetic parameter, Ψ , is obtained using ΔE_p according to Nicholson;⁶ E_p is the peak potential in (V), D is the diffusion coefficient of the compound ($\text{cm}^2 \text{s}^{-1}$), ν is the scan rate (V s^{-1}), R is the gas constant = $8.314 \text{ J mol}^{-1} \text{ K}^{-1}$, T is temperature = 295 K, n is the number of electrons involved in the process, and F is the Faraday constant = $96,485 \text{ C mol}^{-1}$. Assumptions 1) Diffusion coefficient taken as $10^{-5} \text{ cm}^2 \text{s}^{-1}$ and 2) $D_O/D_R = 1$.

* To determine the electrochemical parameters (**n** and **α**) summarised in **Table II.1 (a), (b)**, the following equations can be used:²¹

For an reversible redox process

$$|E_P - E_{P/2}| = \frac{2.2 RT}{nF}$$

2) For an irreversible reduction process

$$|E_P - E_{P/2}| = \frac{1.857 RT}{\alpha nF}$$

and

3) For an irreversible oxidation process.

$$|E_P - E_{P/2}| = \frac{1.857 RT}{(1 - \alpha)nF}$$

E_P is the peak potential in volts, $E_{P/2}$ is the potential at $I_{P/2}$, R is the gas constant, $8.314 \text{ J mol}^{-1} \text{ K}^{-1}$, T is temperature = 295 K , n is the number of electrons involved in the process, F is the Faraday constant = $96,485 \text{ C mol}^{-1}$, and α is the transfer coefficient.

For an irreversible process we expect to observe peak potential a shift of *ca.* $1.15RT/(1-\alpha)nF$ over a 10 fold increase in scan rate - this is the case here; $E_{P, A1} = -0.098 \text{ V}$ at 10 mV s^{-1} , and $E_{P, A1} = -0.007 \text{ V}$ at 100 mV s^{-1} . Theoretical shift = 0.086 V , Experimental shift = 0.0

References

- (a.) M. A. McMahon, M. Rahdar and M. Porteus, *Nat. Methods*, 2012, **9**, 27-31; (b.) J. A. Cowan, *Curr. Opin. Chem. Bio.*, 2001, **5**, 634-642.
- (a.) M. Komiyama, Y. Aiba, Y. Yamamoto and J. Sumaoka, *Nat. Protoc.*, 2008, **3**, 655-662; (b.) Y. Aiba, J. Sumaoka and M. Komiyama, *Chem. Soc. Rev.*, 2011, **40**, 5657-5668.
- (a.) J. San Filippo, P. Sung and H. Klein, *Annu. Rev. Biochem.*, 2008, **77**, 229-257; (b.) D. J. Segal, *Nat. Methods*, 2011, **8**, 53-55.
- (a.) M. Pitie and G. Pratviel, *Chem Rev*, 2010, **110**, 1018-1059; (b.) Q. Jiang, N. Xiao, P. Shi, Y. Zhu and Z. Guo, *Coord. Chem. Rev.*, 2007, **251**, 1951-1972.
- F. Mancin, P. Scrimin, P. Tecilla and U. Tonellato, *Chem. Comm.*, 2005, 2540-2548.
- (a.) D. S. Sigman, D. R. Graham, V. D'Aurora and A. M. Stern, *J. Biol. Chem.*, 1979, **254**, 12269-12272; (b.) D. S. Sigman, *Biochem.*, 1990, **29**, 9097-9105.
- (a.) B. C. Chu and L. E. Orgel, *Proc. Natl. Acad. Sci. U.S.A*, 1985, **82**, 963-967; (b.) K. D. Copeland, A. M. Lueras, E. D. Stemp and J. K. Barton, *Biochem.*, 2002, **41**, 12785-12797; (c.) J. C. Francois, T. Saison-Behmoaras, C. Barbier, M. Chassignol, N. T. Thuong and C. Helene, *Proc. Natl. Acad. Sci. U.S.A*, 1989, **86**, 9702-9706; (d.) M. P. Fitzsimons and J. K. Barton, *J. Am. Chem. Soc.*, 1997, **119**, 3379-3380; (e.) B. C. Bales, T. Kodama, Y. N. Weledji, M. Pitie, B. Meunier and M. M. Greenberg, *Nucl. Acids Res.*, 2005, **33**, 5371-5379; (f.) M. S. Melvin, J. T. Tomlinson, G. R. Saluta, G. L. Kucera, N. Lindquist and R. A. Manderville, *J. Am. Chem. Soc.*, 2000, **122**, 6333-6334.
- J. Stubbe, J. W. Kozarich, W. Wu and D. E. Vanderwall, *Acc. Chem. Res.*, 1996, **29**, 322-330.
- A. Kellett, M. O'Connor, M. McCann, M. McNamara, P. Lynch, G. Rosair, V. McKee, B. Creaven, M. Walsh, S. McClean, A. Foltyn, D. O'Shea, O. Howe and M. Devereux, *Dalton Trans.*, 2011, **40**, 1024-1027.

A. Kellett, M. O'Connor, M. McCann, O. Howe, A. Casey, P. McCarron, K. Kavanagh, M. McNamara, S. Kennedy, D. D. May, P. S. Skell, D. O'Shea and M. Devereux, *Med. Chem. Comm.*, 2011, **2**, 569-676.

C. A. Frederick, J. Grable, M. Melia, C. Samudzi, L. Jen-Jacobson, B. C. Wang, P. Greene, H. W. Boyer and J. M. Rosenberg, *Nat.*, 1984, **309**, 327-331.

N. C. Horton, C. Otey, S. Lusetti, M. D. Sam, J. Kohn, A. M. Martin, V. Ananthnarayan and J. J. Perona, *Biochem.*, 2002, **41**, 10754-10763.

B. Halliwell and M. Whiteman, *Br. J. Pharmacol.*, 2004, **142**, 231-255.

O. Iranzo, *Bioorg. Chem.*, 2011, **39**, 73-87.

(a.) S. Borah, M. S. Melvin, N. Lindquist and R. A. Manderville, *J. Am. Chem. Soc.*, 1998, **120**, 4557-4562; (b.) P. U. Maheswari, S. Roy, H. den Dulk, S. Barends, G. van Wezel, B. Kozlevcar, P. Gamez and J. Reedijk, *J. Am. Chem. Soc.*, 2006, **128**, 710-711; (c.) P. U. Maheswari, M. v. d. Ster, S. Smulders, S. Barends, G. P. v. Wezel, C. Massera, S. Roy, H. d. Dulk, P. Gamez and J. Reedijk, *Inorg. Chem.*, 2008, **47**, 3719-3727.

M. S. Melvin, J. T. Tomlinson, G. R. Saluta, G. L. Kucera, N. Lindquist and R. A. Manderville, *J. Am. Chem. Soc.* 2000, **122**, 6333-6334

T. Mosmann, *J. Immunol. Meth.*, 1983; **65**, 55-63

B. Halliwell and M. Whiteman, *Br. J. Pharmacol.*, 2004, **142**, 231-255

V. V. Pavlishchuk, A. W. Addison, *Inorg. Chim. Acta*, 2000, **298**, 97-102.

R. S. Nicholson, *Anal. Chem.*, 1965, **37**, 1351-1355.

A. J. Bard, L. R. Faulkner, "Electrochemical Methods: Fundamentals and Applications", 2nd Edition, Wiley, New York, 2001, p. 236.

Chapter III

A New Phenanthroline-Oxazine Ligand: Synthesis, Coordination Chemistry and Atypical DNA Binding Interaction

This work was published in: *Chemical Communications*, 2013, **49**, pp2341-2343

McCann M., McGinley J., Ni K., O'Connor M., Kavanagh K., McKee V., Colleran J., Devereux M., Gathergood N., Barron N., Prisecaru A. and Kellett A.

My contribution to this paper is: Manuscript co-author, designing and conducting DNA binding experiments, DNA cleavage reactions and viscosity experiments.

III.1. Abstract

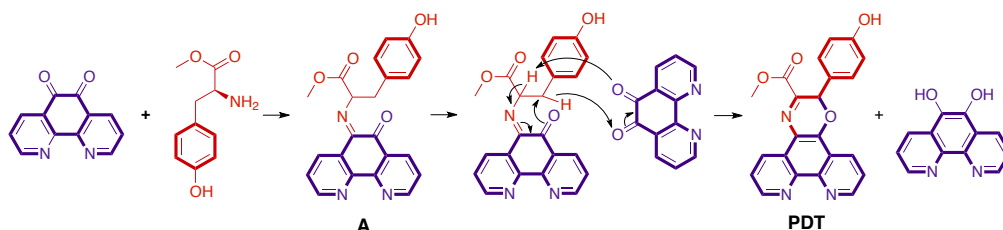
1,10-Phenanthroline-5,6-dione and L-tyrosine methyl ester react to form phenanthroline-oxazine (PDT) and from which $[\text{Cu}(\text{PDT})_2](\text{ClO}_4)_2$ and $[\text{Ag}(\text{PDT})_2]\text{ClO}_4 \cdot 2\text{MeOH}$ are obtained. Binding to calf-thymus DNA by Ag(I) and Cu(II) PDT complexes exceed bis-1,10-phenanthroline analogues and the minor groove binding drugs, pentamidine and netropsin. Furthermore, unlike the artificial metallonuclease, $[\text{Cu}(\text{phen})_2]^{2+}$, the $[\text{Cu}(\text{PDT})_2]^{2+}$ complex does not cleave DNA in the presence of added reductant indicating unique interaction with DNA.

III.2. Introduction

1,10-Phenanthroline (phen), its organic derivatives and the plethora of metal complexes containing these *N,N'*-chelating heterocycles, find use as optical devices,^{1,2} catalysts³ and as integral components of supramolecular structures.⁴ In addition, these compounds have found application in the biological field as antimicrobial and anticancer agents,⁵ DNA intercalators,⁶ and as nucleoside constituents for incorporation into the DNA backbone.⁷

The quest to make new and tailored phenanthrolines is ongoing, and methods include synthesising the bases from elementary building blocks^{1,8} and extending existing, functionalised phenanthrolines.¹ In the latter context, the quinone, 1,10-phenanthroline-5,6-dione (phendio), has been used as the starting material for grafting appendages onto the phenanthroline framework, via simple Schiff base condensation reactions with primary amines.^{7,9-14} All of these diimines were produced by the straightforward Schiff base condensation reaction of phendio with the appropriate diamine. However, not all reactions of phendio with primary amines have resulted in the expected Schiff base product. For example, combining phendio with urea¹⁵ and *N,N'*-bis(2-aminophenyl)ethylenediamine¹⁶ unexpectedly produced a glycoluril and a gem-*cis*-bis(aminal), respectively. Generally, phendio and its Ag(I) and Cu(II) complexes are considerably more biologically active than phen and its corresponding metal complexes.^{5a,5b} With this in mind, we sought to improve biological activity, selectivity and compatibility by attempting to prepare a double Schiff base, phen-type ligand by reacting phendio with two equivalents of (*S*)-methyl 2-amino-3-(4-

hydroxyphenyl)propanoate (L-tyrosine methyl ester). Herein, we report the synthesis of an unusual and unexpected phen derivative, the preparation of its Ag(I) and Cu(II) complexes, and also the DNA binding and cleavage properties of the three new compounds. Phendio was initially treated with L-tyrosine methyl ester (1:2 mol ratio) in anticipation of forming a double Schiff base condensation product (Scheme III.1). Unexpectedly, this combination produced 1,10-phenanthroline-5,6-diol and a relatively low yield of the new orange-yellow tetracyclic oxazine, **PDT**. The structure of **PDT**·MeOH (Figs. III.1A and B) showed that chirality within the compound is retained, with C13 being the stereogeniccentre (originally it was C20). The molecule crystallises in the centrosymmetric space group, P2(1)/c, and so is a racemic mixture. Interestingly, the phenol ring is almost orthogonal to the oxazine ring (bond angle 89.12(2)°) forming a ‘chair’ profile. The pdtme molecules are linked into zig-zag chains via hydrogen bonding through the methanol solvate; the phenol group makes a H-bond to the oxygen of the methanol (2.6288(18)Å), and the methanol OH makes an unsymmetric, bifurcated H-bond to the phenanthroline nitrogen atoms of a second molecule (3.028(2) and 2.907(2)Å to N1 and N2, respectively, under symmetry operation $-x+2, y-1/2, -z+3/2$).



Scheme III.1 Proposed reaction mechanism of phendio with L-tyrosine methyl ester leading to the formation of **PDT**.

What is the mechanism of the cyclization reaction that leads to the formation of the oxazine ring in pdtme? In their paper on the oxidation of α -amino acids by quinones, Lourak and co-workers¹⁷ obtained cyclic derivatives containing oxazine rings. These researchers proposed a mechanism for their reaction in which a second quinine molecule acted as a dehydrogenating agent to give the cyclic product. In the present work, the isolation of 1,10-phenanthroline-5,6-diol as a by-product of the reaction suggested that reduction of some phendio was occurring as part of the reaction mechanism. It is thought that the first step of the

mechanism is the formation of a Schiff base (molecule **A** in Scheme III.1). A plausible, concerted mechanism for formation of the oxazine ring is offered in Scheme 1 and involves the participation of a second phendio molecule as a dehydrogenating agent. Due to steric restraints, resulting from both **A** and phendio, this reaction is expected to be slow, which indeed is what was observed.

Interestingly, in the preparation of the phendio-amino acid ternary complexes, $[\text{Cu}(\text{phendio})(\text{L-Phe})(\text{H}_2\text{O})]\text{ClO}_4 \cdot \text{H}_2\text{O}$ and $[\text{Ni}(\text{phendio})(\text{Gly})(\text{H}_2\text{O})]\text{ClO}_4 \cdot \text{H}_2\text{O}$ (L-PheH = L-phenylalanine, GlyH = glycine), no interaction between the phendio carbonyl functions and the amine group of the amino acid was reported.¹⁸ Reaction of **PDT** with AgClO_4 in a *ca.* 2:1 molar ratio gave the green solid, $[\text{Ag}(\text{PDT})_2]\text{ClO}_4 \cdot 2\text{MeOH}$ (**AgPDT**), in good yield. The complex cation, $[\text{Ag}(\text{PDT})_2]^+$, is thought to be essentially isostructural with the cation in the structurally characterised complex, $[\text{Ag}(\text{phendio})_2]\text{ClO}_4$,¹⁹ where the metal has approximately tetrahedral geometry. In comparison to the ^1H NMR spectrum of metal-free **PDT**, the spectrum of **AgPDT** showed shifts in the signals associated with the phen part of the pdtme molecule rather than the ester part of the molecule, indicating that the Ag^+ ion is chelated by the two nitrogen atoms. In a similar reaction using $\text{Cu}(\text{ClO}_4)_2 \cdot 6\text{H}_2\text{O}$, the green solid, $[\text{Cu}(\text{PDT})_2](\text{ClO}_4)_2$ (**CuPDT**), was obtained in moderate yield. Again, it is believed that $[\text{Cu}(\text{PDT})_2]^{2+}$ is structurally similar to the known tetrahedral cation in $[\text{Cu}(\text{phen})_2](\text{ClO}_4)_2$ (**CuPhen**).²⁰

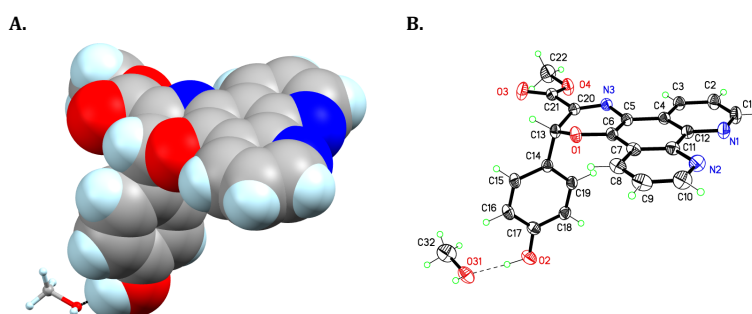


Figure III.28 A. Space-fill view of pdtme in **PDT**·MeOH (MeOH shown in stick view), B. A view of **PDT**·MeOH with atoms depicted with displacement ellipsoids at their 50% probability level.

In an effort to establish how the metal-free **PDT** ligand and its Cu(II) and Ag(I) complexes interact with DNA four distinct assays were conducted. To establish

an apparent DNA binding constant (K_{app}) a sample of high-purity calf thymus (CT) DNA is firstly treated with an excess of EtBr and then this highly fluorescent, Et⁺-saturated DNA sample is exposed to a range of concentrations of the competitor test compound. A reduction in fluorescence indicates ejection of the bound Et⁺ from the DNA backbone and replacement by the test species. Samples are compared based on their K_{app} values, which are calculated from the concentration of sample required to accomplish a 50% reduction of the initial fluorescence (Fig. III.2A, Table III.1A). Metal-free **PDT**, phen and the simple metal salts all showed considerably less DNA binding affinities than **AgPDT** and **CuPDT**, which have almost identical K_{app} values (*ca.* 7.60×10^6). The Ag(I) and Cu(II) **PDT** complexes also showed a higher binding capacity than the known groove-binding drugs, pentamidine and netropsin (K_{app} 1.09×10^6 and 4.77×10^6 , respectively). The binding of metal-free **PDT** to DNA is significantly stronger than that of metal-free phen, suggesting that the additional functionalities on the backbone provide secondary binding interactions with the nucleic acid. The contribution of these extra interactions is also apparent when the binding constants of **PDT** and phen metal complexes are compared (K_{app} for **AgPDT** is *ca.* 3 times larger than that for [Ag(phen)₂]ClO₄ (**AgPhen**), and **CuPDT** is *ca.* 11 times greater than for **CuPhen**). Competitive displacement of DNA-bound Hoechst 33258 (minor groove binder) and ethidium cations (Et⁺, intercalator) was assessed using fluorescence quenching, which utilises an unsaturated dye-DNA combination in which a limited number of binding spaces on the DNA polymer are occupied at any one time by the interacting dye, which strongly fluoresces once bound with a relatively high number of unoccupied sites remaining for test compound interaction. The introduction of a new compound to the DNA may then displace Hoechst or Et⁺ either directly or indirectly (i.e. through a conformational change which results in dye ejection) and can give valuable information regarding a binding interaction mode,²¹ although, caution must be exercised here considering the binding constant and binding stoichiometry of ethidium bromide and Hoechst to CT-DNA. The minor groove binders, pentamidine and netropsin, displayed high quenching affinity (Q) for Hoechst 33258 bound DNA and were, as expected, an order of magnitude less effective in their quenching of ethidium (Table III.1B). Both **AgPhen** and **CuPhen** displayed higher Q values toward Et⁺ than compared with Hoechst.

Interestingly, both **AgPDT** and **CuPDT** displayed higher Q values, along with different profiles,[†] and were almost identical in their ejection of bound Hoechst and Et⁺. From these quenching data it is evident that the **PDT** complexes have significantly higher binding affinities (K_{app}) and an alternate binding mode compared with their bis-phen analogues.

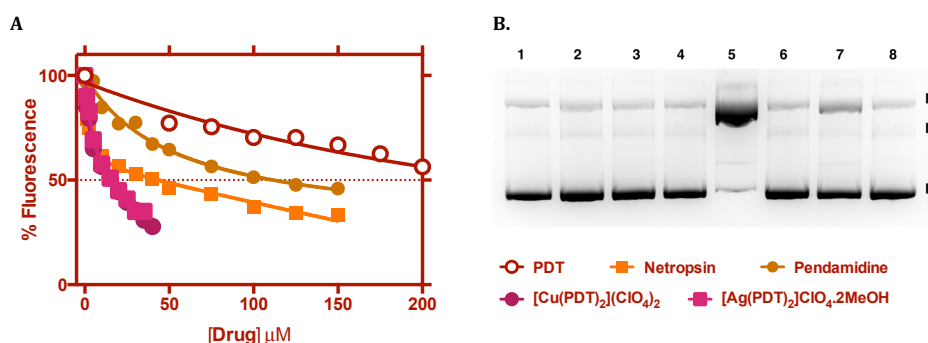


Figure III.29 A. Competitive ethidium bromide displacement for netropsin, pentamidine, metal salts, free ligands and complexes with CT-DNA, and B. DNA cleavage reactions with 400 ng of pBR322 plasmid DNA carried out for 30 min at 37°C in 80 mM HEPES at pH 7.2 with 25 mM NaCl and 1 mM Na-L-ascorbate then analysed using agarose gel electrophoresis. Lane 1: DNA control; lane 2: [Cu(OAc)₂]; lane 3: AgNO₃; lane 4: **PDT**; lane 5: **CuPhen**; lane 6: **AgPhen**; lane 7: **CuPDT**; lane 8: **AgPDT**

Table III.1 A. Apparent DNA binding constants (K_{app}) of the test compounds, and B. Fluorescence quenching (Q) values obtained against Hoechst 33258 (groove binder) and ethidium bromide (intercalator).

Compound	A.		B.	
	$C_{50}^*(\mu M)$	K_{app}^{**}	Q^\dagger Hoechst 33258(μM)	Q^\dagger Ethidium Bromide (μM)
pentamidine	109.41	1.09×10^6	35.86	>150
netropsin	39.99	4.77×10^6	3.50	35.98
AgPDT	15.75	7.60×10^6	24.65	18.18
CuPDT	15.70	7.62×10^6	18.00	18.59
AgPhen	45.01	2.65×10^6	45.54	27.90
CuPhen	179.21	6.67×10^5	34.96	20.38
1,10-phen	>300	N/A	-	-
PDT	247.21	4.80×10^5	-	-
AgClO ₄	>300	N/A	-	-
[Cu(OAc) ₂]	>300	N/A	-	-

* C_{50} = concentration required to reduce fluorescence by 50%;

** $K_{app} = K_e \times 12.6/C_{50}$ where $K_e = 9.5 \times 10^6(\text{bp})^{-1}$; N/A = not available;

[†] Q = reduction of 50% initial fluorescence from DNA-bound dye

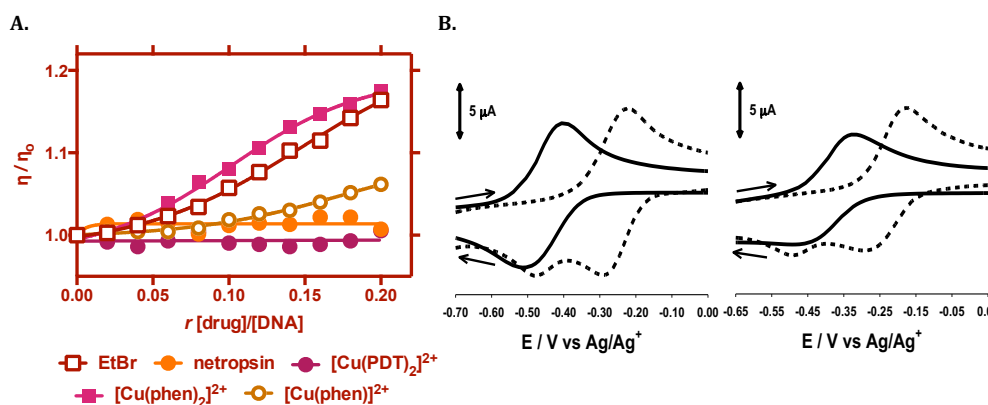


Figure III.30 A. Relative viscosity changes in salmon testes dsDNA (1 mM in DNAP in 80 mM HEPES) upon exposure to EtBr, netropsin, **CuPhen** and **CuPDT**, and B. typical cyclic voltammograms describing the redox behaviour of 1 mM **CuPhen** (left) and **CuPDT** (right), at a scan rate of 100 mV s^{-1} , in the absence (solid black trace) and presence (dashed black trace) of 2 mM ascorbate.†

To further explore the DNA binding properties of **PDT**, viscosity experiments were conducted using salmon testes dsDNA (1 mM in DNAP) (Fig. III.3A).† Intercalating agents (e.g. ethidium) are known to increase viscosity which results from a conformational change induced after accommodation between DNA bases, while surface binding species (e.g. netropsin) can typically have only a moderate or diminished effect on viscosity. This expected pattern emerged during our analysis of both these standard agents (Fig. III.3). It was also evident that **CuPhen**, containing the $[\text{Cu}(\text{phen})_2]^{2+}$ cation, produced an intercalative profile while, significantly, **CuPDT** did not appear to intercalate DNA but had a profile similar to the surface binding drugs, netropsin and pentamide. Furthermore, the viscosity profile for **CuPDT** was distinctive from that of the partial intercalating mono-phen complex, $[\text{Cu}(\text{phen})]^{2+}$. Relaxation of supercoiled pBR322 (Form I) into open circular (Form II) and linear (Form III) conformations was used to quantify the relative DNA cleavage efficiency (nuclease activity) of the test complexes. DNA cleavage by $[\text{Cu}(\text{phen})_2]^{2+}$ is known to be dependent on the presence of added oxidant and/or reductant, and in the case of the present compounds the assay was conducted in an aerobic environment (O_2 oxidant) along with the addition of a 1 mM solution of the reductant, sodium L-ascorbate. Samples (5 μM) were incubated for 30 min at 37°C before being quenched and analysed using gel electrophoreses. The only complex found to be active (Fig. III.2B) was the

known chemical nuclease, $[\text{Cu}(\text{phen})_2]^{2+}$.²² This dication renders almost complete degradation of Form I to linear Form III by interacting at the surface of the minor groove of DNA and in the presence of a reductant, which can gain access to the Cu(II) centre in the complex, DNA oxidation occurs predominantly in this region. It was somewhat surprising that **CuPDT** was almost inactive compared with $[\text{Cu}(\text{phen})_2]^{2+}$. Furthermore, any role that the phenol moiety in **PDT** may play in scavenging free radicals to prevent DNA damage looks quite unlikely as **CuPhen**, incubated with up to 100 μM of phenol, produced only a marginal inhibition of pBR322 cleavage (Fig. III.6†). The redox behaviour of **CuPhen** and **CuPDT** was investigated, using cyclic voltammetry, to shed light on the observed differences in their efficacy as DNA nuclease agents (Fig. III.3B and Fig. III.7 – Fig. III.12).† The Cu(II)/Cu(I) redox couple was centred around -0.46 and -0.39 V for **CuPhen** and **CuPDT**, respectively. Addition of 2 mM ascorbate results in a significant anodic shift in the Cu(II)/Cu(I) redox couple of both complexes, indicative of a more facile electron transfer regime. The original Cu(II) reduction peak for **CuPhen** is observed at -0.47 V but, interestingly, is not evident at scan rates $\leq 40 \text{ mV s}^{-1}$, which suggests a transient species. While **CuPhen** tends toward reversibility in the presence of ascorbate ($\Delta E_p = 65 \text{ mV}$), **CuPDT** remains quasi-reversible ($\Delta E_p = 119 \text{ mV}$, Table III.2). Thus, the reversibility of the $\text{Cu}^{2+}/\text{Cu}^+$ couple may justify the greater DNA cleavage ability of **CuPhen**.

III.3 Conclusion

In conclusion, the new oxazine, **PDT**, can be made in moderate yield from phendio and L-tyrosine methyl ester, and this *N,N'*-chelating base readily coordinates to Cu(II) and Ag(I) centres forming the respective bis-chelates, $[\text{Cu}(\text{PDT})_2](\text{ClO}_4)_2$ and $[\text{Ag}(\text{PDT})_2]\text{ClO}_4 \cdot 2\text{MeOH}$. There is a clear enhancement in the DNA binding properties of the Ag(I) and Cu(II) bis-**PDT** complexes compared with their bis-phen analogues. The binding constants for the two **PDT** complexes, at neutral pH, surpass those of the known minor groove binding agents, pentamidine and netropsin, and it appears they coordinate in quite an alternative manner compared with their bis-phen analogues. Though $[\text{Cu}(\text{PDT})_2](\text{ClO}_4)_2$ and $[\text{Ag}(\text{PDT})_2]\text{ClO}_4 \cdot 2\text{MeOH}$ bind strongly to DNA they do not degrade the polymer. This may be rationalised in terms of non-constructive

binding orientation, by the Cu²⁺ **PDT** complex, that does not promote facile cleavage with its quasi-reversible nature when compared with [Cu(phen)₂]²⁺ upon the addition of reductant.

III.4 Material and Methods

III.4.1 Materials: Chemicals and reagents of analytical grade were purchased from Sigma-Aldrich Ireland and used without further purification.

III.4.2 Preparation of the complexes

III.4.2.1 Preparation of methyl 2-(4-hydroxyphenyl)-4a,12b-dihydro-2H-[1,4]oxazino[2,3-f][1,10]phenanthroline-3-carboxylate (**PDT**)

1,10-Phenanthroline-5,6-dione (0.80 g, 3.81 mmol) was dissolved in dry, refluxing methanol (95 cm³) and L-tyrosine methyl ester (0.74 g, 3.81 mmol) was added. The resulting orange solution was refluxed for 20 h and some yellow 1,10-phenanthroline-5,6-diol precipitated. The solid diol was filtered off, washed with MeOH and air dried. Yield: 0.17 g (21%). The original filtrate was then concentrated and allowed to stand. After 1 week, orange-yellow crystals of **PDT**·MeOH formed. A few of these crystals in the mother liquor were forwarded for X-ray crystallographic studies. The remaining crystals were filtered off, washed with cold methanol and then air-dried. Yield: 0.30 g (19%). Using a similar experimental procedure, but with a 2:1 L-tyrosine methyl ester:phendiol reactant ratio, the **pdtme** yield decreased to 11%. The compound was soluble in hot DMSO and sparingly soluble in hot MeOH and EtOH. Mp: decomposed at >250 °C. Anal. Calc. for C₂₃H₁₉N₃O₅ (**PDT**·MeOH): C, 66.18; H, 4.59; N, 10.07. Found: C, 66.43; H, 4.21; N, 9.80. ¹H NMR (d₆-DMSO): 3.90 (s, 3H ?OMe), 6.58 (s, 1H), 6.67 (d, J = 8.7 Hz, 2H), 7.20 (d, J = 8.7 Hz, 2H), 7.79(dd, J₁ = 4.2 Hz, J₂ = 8.1 Hz, 1H), 7.84 (dd, J₁ = 4.2 Hz, J₂ = 8.1 Hz, 1H), 8.59 (dd, J₁ = 1.8 Hz, J₂ = 8.4 Hz, 1H), 8.88 (dd, J₁ = 1.8 Hz, J₂ = 8.1 Hz, 1H), 9.03 (dd, J₁ = 1.8 Hz, J₂ = 4.2 Hz, 1H), 9.12 (dd, J₁ = 1.8 Hz, J₂ = 4.5 Hz, 1H), 9.71 (s, b, 1H) ppm. ¹³C NMR (d₆-DMSO): 48.6, 52.9, 72.0, 115.8, 121.2, 121.7, 123.7, 124.1, 124.8, 126.0, 128.9, 129.8, 130.9, 138.4, 142.2, 146.4, 148.6, 149.7, 151.5, 158.7, 162.6 ppm. IR: 3426, 1742, 1712, 1608, 1587, 1515, 1504, 1434, 1345, 1325, 1287, 1259, 1173, 1132, 1112, 1020, 973, 808, 741, 679, 632 cm⁻¹. Mass spec: M+1 = 386.3, found *m/z* = 386.1.

III.4.2.2 Preparation of [Ag(PDT)₂](ClO₄)₂·2MeOH (AgPDT)

To a yellow suspension of **PDT** (0.12 g, 0.29 mmol) in refluxing dry methanol (36 cm³) was added, drop-wise, a solution of AgClO₄ (0.03 g, 0.14 mmol) in dry methanol (1 cm³). The resulting green suspension was refluxed for 0.5 h and then stirred for 2 h at room temperature. The green solid was filtered off, washed with methanol and then air-dried. Yield: 0.116 g (79%). The complex was only soluble in hot DMSO. Anal. Calc. for C₄₆H₃₈ClN₆O₁₄Ag ([Ag(**PDT**)₂](ClO₄)₂·2MeOH): C, 53.12; H, 3.48; N, 8.08. Found: C, 52.85; H, 3.43; N, 7.92. ¹H NMR (d₆-DMSO): 3.92 (s, 3H), 6.66 (d, J = 3.6 Hz, 2H), 6.70 (s, 1H), 7.24 (d, J = 8.7 Hz, 2H), 7.97 (dd, J₁ = 5.1 Hz, J₂ = 8.7 Hz, 1H), 8.02 (t, J = 5.4 Hz, 1H), 8.79 (dd, J₁ = 1.5 Hz, J₂ = 8.4 Hz, 1H), 9.04 (d, J = 1.8 Hz, 1H), 9.06 (s, 1H), 9.12 (t, J = 3.0 Hz, 1H), 9.78 (s, 1H). IR: 3431, 1715, 1611, 1509, 1436, 1347, 1260, 1098, 812, 735, 623 cm⁻¹. Mass spec: [Ag(**PDT**)₂]⁺: M = 879.5, found *m/z* = 879.1.

III.4.2.3 Preparation of [Cu(PDT)₂](ClO₄)₂ (CuPDT)

To a yellow suspension of **PDT** (0.10 g, 0.25 mmol) in dry, refluxing methanol (45 cm³) was added, drop-wise, a solution of Cu(ClO₄)₂·6H₂O (0.04 g, 0.12 mmol) in dry methanol (2 cm³). Gradually, a green solution formed and this was then refluxed for 2 h. The solution was then concentrated to *ca.* 5 cm³ and the green product precipitated. The mixture was centrifuged for 10 min at 5000 rpm and the supernatant then carefully removed. The remaining green solid was washed with cold methanol and then air-dried. Yield: 0.04 g (32%). The complex was soluble in MeOH, EtOH and DMSO. Anal. Calc. for C₄₄H₃₀Cl₂N₆O₁₆Cu ([Cu(**PDT**)₂](ClO₄)₂): C, 51.15; H, 2.93; N, 8.13. Found: C, 50.57, H, 3.12, N, 8.78. IR: 3430, 1720, 1611, 1516, 1437, 1353, 1267, 1174, 1107, 814, 731, 624 cm⁻¹. Mass spec: [Cu(**PDT**)₂]⁺: M = 833.5, found *m/z* = 833.1. μ_{eff} = 1.67 B.M.

III.4.3 X-ray crystallography

Data for **PDT**·MeOH were collected at 150K on a Bruker APEX II CCD diffractometer and the structure was solved by direct methods and refined by full-matrix least-squares on F² using all the data.¹ All non-hydrogen atoms were refined with anisotropic atomic displacement parameters and the hydrogen atoms

bonded to carbon were inserted at calculated positions using a riding model. The hydrogen atoms bonded to oxygen were located from difference maps and refined with a fixed isotropic thermal parameter. Data collection and refinement parameters are summarized in Appendix A.A.1.

III.4.4 DNA binding experiments.

III.4.4.1 Competitive ethidium displacement This protocol was designed as a high-throughput version of the previously reported method.² A working solution of 20.0 μM UltraPure calf thymus DNA (CT-DNA, Invitrogen 15633-019, $\epsilon_{260} = 12,824 \text{ M (bp)}^{-1} \text{ cm}^{-1}$) along with 25.2 μM ethidium bromide (EtBr) in HEPES buffer (80 mM, pH = 7.2) and NaCl (40 mM) was prepared. Stock solutions of metal complexes, metal salts, free ligands and groove binding drugs were prepared at $\sim 4.0 \text{ mM}$ in DMSO and diluted further with ultra-pure water. 50 μL of DNA-Et working solution were placed each well of a 96 well microplate with the exception of the blanks which contained 100 μL HEPES buffer. Serial aliquots of the tested compound were added to the working solutions and the volume was adjusted to 100 μL in each well such that the final concentration of CT-DNA and EtBr were 10.0 μM and 12.6 μM , respectively. The plate was allowed to incubate at room temperature for 1 h before being analysed using a Bio-Tek synergy HT multi-mode microplate reader with excitation and emission wavelengths being set to 530 and 590 nm, respectively. Concentrations of the tested compounds were optimized such that fluorescence was 30-40% of the initial control (i.e. 50 μL working solution + 50 μL HEPES buffer) at their highest reading. Each drug concentration was measured in triplicate, on at least two separate occasions, and the apparent binding constants were calculated using $K_{\text{app}} = K_e \times 12.6/C_{50}$ where $K_e = 9.5 \times 10^6 \text{ M (bp)}^{-1}$.

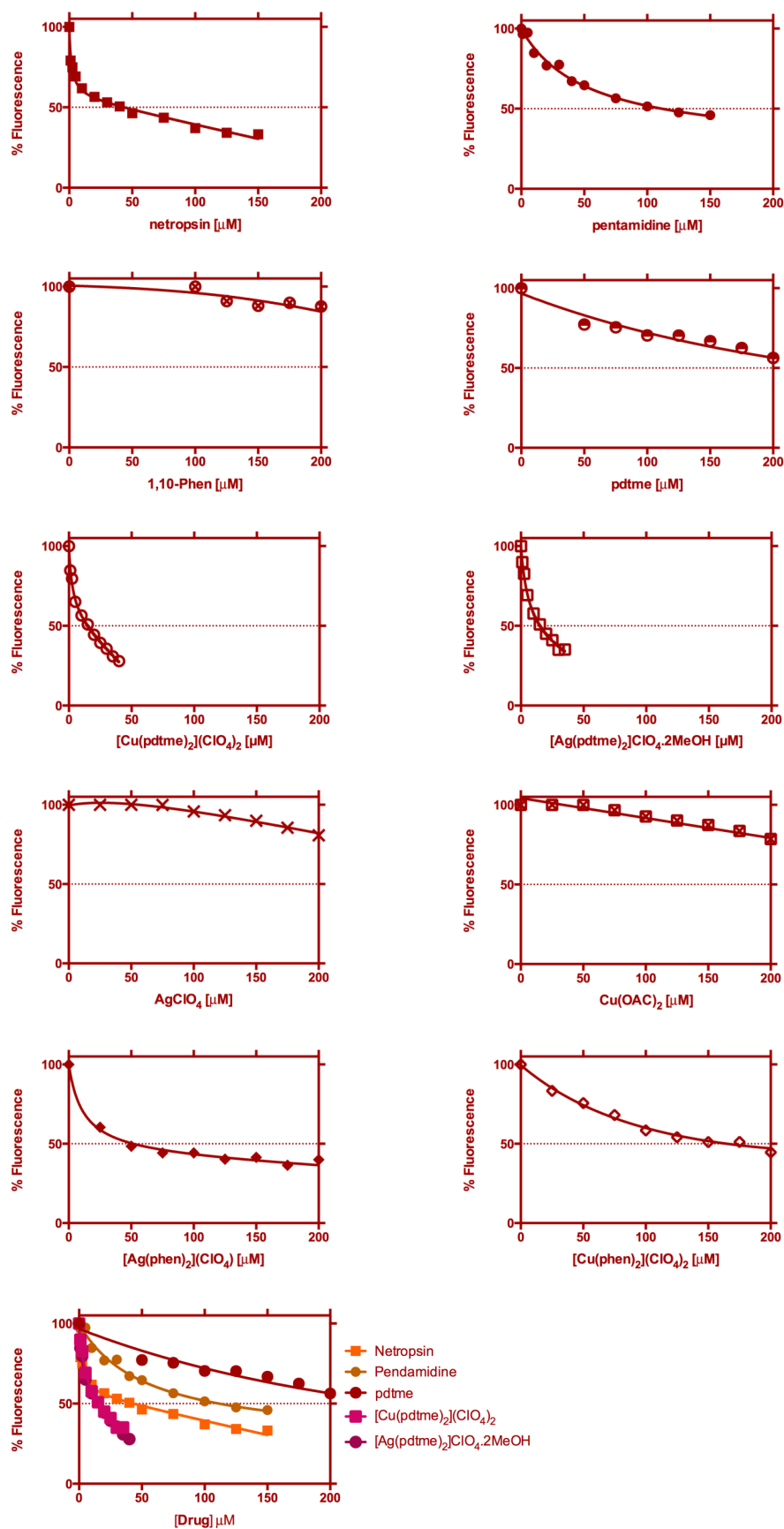


Figure III.31 Competitive ethidium bromide displacement for netropsin, pentamidine, metal salts, free ligands and complexes with CT-DNA.

III.4.4.2 DNA–ethidium fluorescence quenching This protocol was also designed as a high-throughput version of the previously reported method.² A working solution of 50.0 μM UltraPure calf thymus DNA (CT-DNA, Invitrogen 15633-019, $\epsilon_{260} = 12,824 \text{ M (bp)}^{-1} \text{ cm}^{-1}$) along with either 10.0 μM ethidium bromide (EtBr) or Hoechst 33258 (Sigma) in HEPES buffer (80 mM , $\text{pH} = 7.2$) and NaCl (40 mM) was prepared. Stock solutions of metal complexes, metal salts, free ligands and groove binding drugs were prepared at $\sim 4.0 \text{ mM}$ in DMSO and diluted further with ultra-pure water. 50 μL of DNA-Et or DNA-Hoechst working solution were placed each well of a 96 well microplate with the exception of the blanks which contained 100 μL HEPES buffer and 5 μM of either Hoechst or EtBr. Serial aliquots of the tested compound were added to the working solutions and the volume was adjusted to 100 μL in each well such that the final concentration of CT-DNA and EtBr/Hoechst were 25.0 μM and 5 μM , respectively. The plate was allowed to incubate at room temperature for 5 min before being analysed using a Bio-Tek synergy HT multi-mode microplate reader with excitation and emission wavelengths being set to 530 and 590 nm for Et detection or 360 nm and 460 nm for Hoechst 33258 detection. Concentrations of the tested compounds were optimized such that fluorescence was 30-40% of the initial control at their highest reading. Each drug concentration was measured in triplicate, on at least two separate occasions. From a plot of fluorescence versus added drug concentration, the Q value is given by the concentration required to effect 50% removal of the initial fluorescence of bound dye.

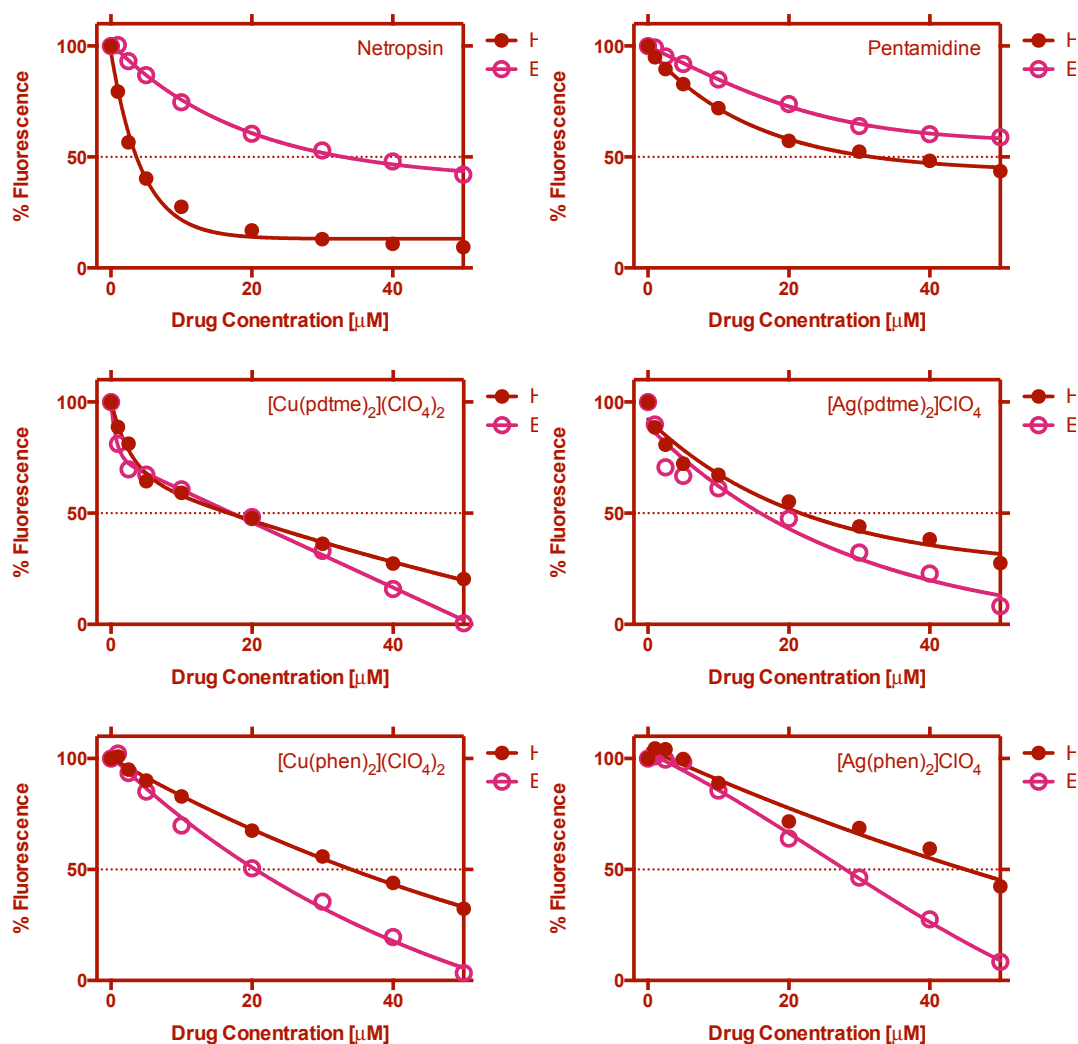


Figure III.32 Fluorescence quenching (Q) of EtBr-DNA and Hoechst 33258-DNA as a function of added test compound.

III.4.5 DNA cleavage experiments

III.4.5.1 Nuclease activity Reactions were carried out according to the literature procedure.³ Briefly, in a total volume of 20 μL using 80 mM HEPES buffer (Fisher) at pH 7.2 with 25 mM NaCl, an aliquot of the stock complex (prepared in DMSO) was mixed with 400 ng of pBR322 (Roche) and 1 μL of 20 mM Na-L-ascorbate. Samples were incubated at 37 $^{\circ}\text{C}$ before being quenched with 6x loading dye (Fermentas), containing 10 mM Tris-HCl (pH 7.6), 0.03% bromophenol blue, 0.03% xylene cyanol, 60% glycerol and 60 mM EDTA, then loaded onto agarose gel (1%) containing 2.0 μL of GelRedTM (10,000X). Electrophoresis was completed at 80 V for 1.5 h using a wide mini-sub cell (BioRad) in 1XTAE buffer (Millipore).

III.4.5.2 Phenol inhibition studies In order to determine the effect of phenol on the cleavage properties of $[\text{Cu}(\text{phen})_2]^{2+}$, 5 μM of $\text{Cu}(\text{phen})_2(\text{ClO}_4)_2$ (**CuPhen**) was incubated with 1 mM Na-L-Ascorbate in presence of 5 – 100 μM phenol (Fig. III.6) as follow: in a total volume of 20 μL using 80 mM HEPES buffer (Fisher) at pH 7.2 with 25 mM NaCl, an aliquot of the phenol (prepared in 80 mM HEPES buffer) was mixed with 400 ng of pBR322, 5 μM of $\text{Cu}(\text{phen})_2(\text{ClO}_4)_2$ (prepared in DMSO) and 1 μL of 20 mM Na-L-ascorbate. Samples were incubated at 37 °C for 30 min before being quenched with 6x loading dye (Fermentas), containing 10 mM Tris-HCl (pH 7.6), 0.03% bromophenol blue, 0.03% xylene cyanol, 60% glycerol and 60 mM EDTA, then loaded onto agarose gel (1%) containing 2.0 μL of GelRed™ (10,000X). Electrophoresis was completed at 80 V for 1.5 h using a wide mini-sub cell (BioRad) in 1XTAE buffer (Millipore).

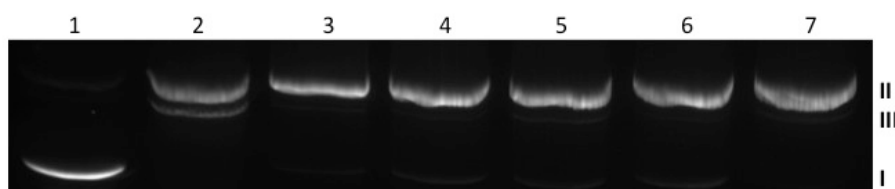


Figure III.33 Cleavage reactions using $\text{Cu}(\text{phen})_2(\text{ClO}_4)_2$ with 1 mM Na-L-ascorbate with phenol (5 – 100 μM) in the presence of 1 mM added reductant. Lane 1: pUC19 control; lane 2: **CuPhen**; lane 3: **CuPhen** + 5 μM phenol; lane 4: **CuPhen** + 10 μM phenol; lane 5: **CuPhen** + 20 μM phenol; lane 6: **CuPhen** + 40 μM phenol; lane 7: **CuPhen** + 100 μM phenol

III.5.6 Viscosity experiments

15 mL dsDNA (Deoxyribonucleic acid sodium salt from Salmon Testes, Sigma-Aldrich, D1626-1G) solution was prepared at 1×10^{-3} M in 80 mM HEPES buffer for each working sample. Stock solutions prepared in DMSO were added according to the gradual increasing $[\text{drug}]/[\text{DNA}]$ (r) ratios of 0.02, 0.04, 0.06, 0.08, 0.10, 0.12, 0.14, 0.16, 0.18 and 0.2. Viscosity values, η , (unit: cP) were directly obtained by running 0# spindle in working samples at 60 rpm via DV-II-Programmable Digital Viscometer equipped with Enhanced Brookfield UL Adapter at room temperature. Data were presented as η / η_0 versus $[\text{compound}]/[\text{DNA}]$ ratio, in which η_0 and η refers to viscosity of each DNA working sample in the absence and presence of complex.⁴

III.4.7 Electrochemistry

III.4.7.1 Experimental:

Cyclic Voltammetry experiments were performed on a Solartron 1825 potentiostat. 1mM concentrations of CuPhen and CuPDT were used in all experiments and the CV's were scanned initially in the cathodic direction. The working electrode was Glassy Carbon (2mm diameter), the reference was a non-aqueous Ag/Ag^+ ($E_{1/2} = 0.075 \text{ V}$ versus Fc/Fc^+), and the counter was platinum. 0.1 M TBAPF₆ in DMF was used as the supporting electrolyte.

III.4.7.2 Results:

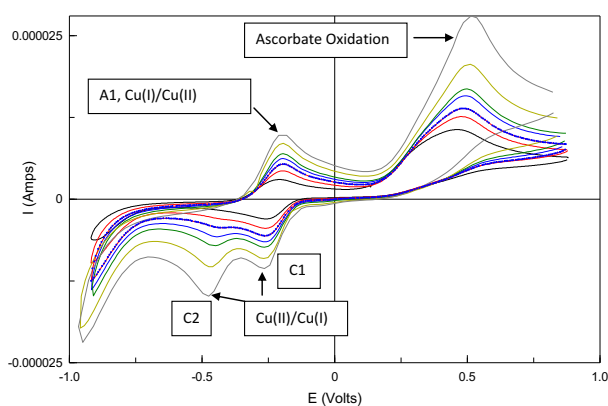


Figure III.34 Typical cyclic voltammograms detailing the redox behaviour of 1 mM **CuPhen** in the presence of 2 mM ascorbate, over a range of scan rates, in 0.1 M TBAPF₆/DMF. Glassy Carbon working electrode, platinum counter electrode, Ag^+/Ag non-aqueous reference electrode.

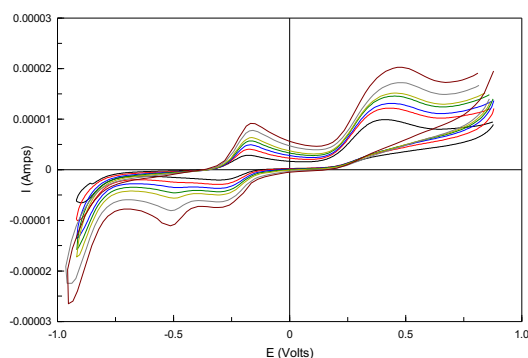


Figure III.35 Typical cyclic voltammograms detailing the redox behaviour of 1 mM **CuPDT** in the presence of 2 mM ascorbate, over a range of scan rates, in 0.1 M TBAPF₆/DMF. Glassy Carbon working electrode, platinum counter electrode, Ag^+/Ag non-aqueous reference electrode.

Table III.2 Summary of electrochemical parameters for **CuPhen** and **CuPDT** in the absence and presence of ascorbate. The redox behaviour of **CuPhen** is near reversible in the presence of ascorbate, $\Delta E_p = 0.065$ V. **CuPDT** remains quasi-reversible in the presence of ascorbate, $\Delta E_p = 0.119$ V.

Cu (I)/(II) redox couple	$E_{p,a}$	$E_{p,c}$	ΔE_p	2mM AA, $E_{p,a}$	E_{p,c_1}	E_{p,c_2}	ΔE_p
Cu(phen)₂(ClO₄)₂	-0.406	-0.514	0.108	-0.220	-0.285	-0.473	0.065
Cu(PDT)₂(ClO₄)₂	-0.329	-0.458	0.128	-0.175	-0.294	-0.492	0.119

III.4.7.3 Randles-Sevcik Analysis

III.4.7.3.1 Cu(phen)₂(ClO₄)₂:

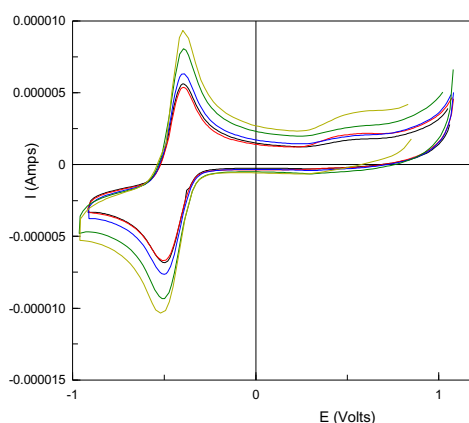


Figure III.36 Typical cyclic voltammograms detailing the redox behaviour of 1 mM **CuPhen** over a range of scan rates, in 0.1 M TBAPF₆/DMF. Glassy Carbon working electrode, platinum counter electrode, Ag⁺/Ag non-aqueous reference electrode.

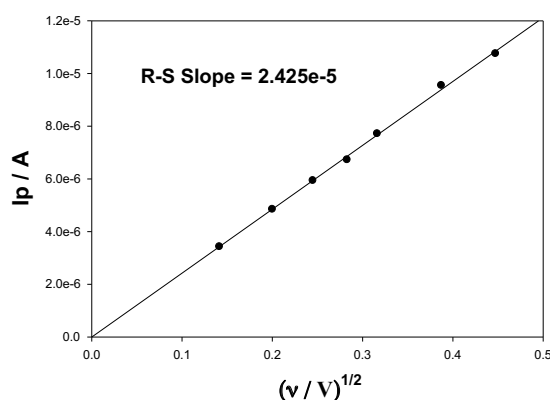


Figure III.37 Corresponding Randles-Sevcik Plot, 1 mM **CuPhen**, the peak currents exhibit a linear dependence with the square root of the scan rate. Thus the redox behaviour of **CuPhen** is under diffusion control.

III.4.7.3.2 CuPDT

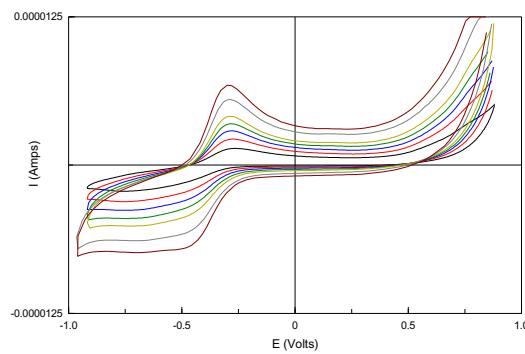


Figure III.38 Typical cyclic voltammograms detailing the redox behaviour of 1 mM **CuPDT** over a range of scan rates, in 0.1 M TBAPF₆/DMF. Glassy Carbon working electrode, platinum counter electrode, Ag⁺/Ag non-aqueous reference electrode.

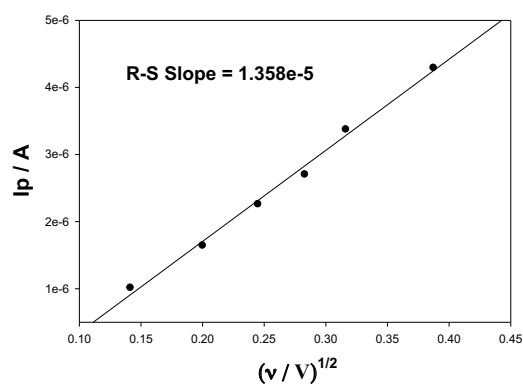


Figure III.39 Randles-Sevcik behaviour of **CuPDT**, indicating a diffusion controlled redox regime

References

1. A. Bencini, V. Lippolis, *Coord. Chem. Rev.* 2010, **254**, 2096-2180.
2. (a) V.W.W. Yam, C.C. Ko, N. Zhu, *J. Am. Chem. Soc.* 2004, **126**, 12734–12735; (b) R.A. Kopelman, S.M. Snyder, N.L. Frank, *J. Am. Chem. Soc.* 2003, **125**, 13684–13685.
3. G. Roelfs, B.L. Feringa, *Angew. Chem., Int. Ed.* 2005, **44**, 3230–3232.
4. (a) G. Accorsi, A. Listorti, K. Yoosaf, N. Armaroli, *Chem. Soc. Rev.*, 2009, **38**, 1690–1700; (b) A. Lavie-Cambot, M. Cantuel, Y. Leydet, G. Jonusauskas, D. Bassani, N. McClenaghan, *Coord. Chem. Rev.*, 2008, **252**, 2572–2584; (c) D. Scaltrito, D. Thompson, J. O’Callaghan, G. Meyer, *Coord. Chem. Rev.*, 2000, **208**, 243–266; (d) P.H. Kwan, M. J. MacLachlan, T.M. Swager, *J. Am. Chem. Soc.* 2004, **126**, 8638–8639; (e) G.R. Pabst, O.C. Pfüller, J. Sauer, *Tet. Lett.* 1998, **39**, 8825–8828.
5. (a) M. McCann, A.L.S. Santos, B.A. da Silva, M.T.V. Romanos, A.S. Pyrrho, M. Devereux, K. Kavanagh, I. Fichtner, A. Kellett, *Tox. Res.* 2012, **1**, 47-54 and references therein; (b) M. McCann, A. Kellett, K. Kavanagh, M. Devereux, A.L.S. Santos, *Curr. Med. Chem.* 2012, **19**, 2703-2714, and references therein; (c) A. Shulman, F.P. Dwyer, *Chelating Agents and Metal Chelates*, Chapter 9, Edited by F.P. Dwyer, D.P. Mellor, Academic Press, New York and London, 1964.
6. (a) K.E. Erkkila, D.T. Odom, J.K. Barton, *Chem. Rev.* 1999, **99**, 2777–2796; (b) A.M. Thomas, M. Nethaji, A.R. Chakravarty, *J. Inorg. Biochem.* 2004, **98**, 1087–1094; (c) C. Chen, L. Milne, R. Landgraf, D. Perrin, D. Sigman, *ChemBioChem*, 2001, **2**, 735–740; (d) H. Niyazi, J.P. Hall, K. O’Sullivan, G. Winter, T. Sorenson, J.M. Kelly, C.J. Cardin, *Nature Chemistry*, 2012, **4**, 621–628; (e) H. Song, J.T. Kaiser, J.K. Barton, *Nature Chemistry*, 2012, **4**, 621–628; (f) T.K. Goswami, S. Gadadhar, A.A. Karande, A.R. Chakravarty, *Polyhedron*, 2012, in press, <http://dx.doi.org/10.1016/j.poly.2012.06.018>
7. (a) K. Gislason, S.T. Sigurdsson, *Eur. J. Org. Chem.* **2010**, 4713–4718; (b) J. Muller, *Eur. J. Inorg. Chem.* **2008**, 3749–3763.
8. Y. Cheng, X. Han, H. Ouyanga, Y. Rao, *Chem. Commun.* 2012, **48**, 2906–2908.
9. J.E. Dickeson, L.A. Summers, A. Lindsay, *Aust. J. Chem.* 1970, **23**, 1023–1027.

10. B. Krishnakumar, M. Swaminathan, *J. Organomet. Chem.* 2010, **695**, 2572-2577.
11. V.W-W. Yam, K.K-W. Lo, K-K. Cheung, R.Y-C. Kong, *J. Chem. Soc., Chem. Commun.*, 1995, (11), 1191-1193.
12. F. da Silva Miranda, A.M.Signori, J. Vicente, B. de Souza, J.P.Priebe, B.Szpoganicz, N.SanchesGonçalves, A.Neves, *Tetrahedron*, 2008 **64** 5410–5415.
13. J. Bolger, A. Gourdon, E. Ishow, J.-P. Launay, *J. Chem. Soc., Chem. Commun.* 1995, (17), 1799-1800.
14. G.R. Pabst, O.C. Pfüller, J. Sauer, *Tet. Lett.* **1998**, 39, 8825-8828.
15. J.A.A.W.Elmens, R.de Gelder, A. Rowan, R.J.M. Nolte, *J. Chem. Soc., Chem. Commun.* **1998**, (15), 1553-1554.
16. B. Coyle, M. McCann, V. McKee, M. Devereux, *ARKIVOC*, 2003, **7(VII)** 59-66.
17. M. Lourak, R. Vanderesse, A. Vicherat, J. Jamal-Eddinea, M. Marraud, *Tet.Lett.* 2000, 41 8773–8776.
18. G.-J.Xu, Y.-Y.Kou, L. Feng, S.-P.Yan, D.-Z.Liao, Z.-H. Jiang, P. Cheng, *Appl. Organometal. Chem.* 2006, **20**, 351–356.
19. M. McCann, B. Coyle, S. McKay, P. McCormack, K. Kavanagh, M. Devereux, V. McKee, P. Kinsella, R. O'Connor, M. Clynes, *BioMetals*, 17, 2004, 635-654.
20. G. Murphy, C. Murphy, B. Murphy, B. Hathaway, *J. Chem. Soc., Dalton Trans.* 1997, 2653-2660.
21. A.Kellett, O. Howe, M. O'Connor, M. McCann, B.S. Creaven, S.McClean, A. Foltyn-Arfa, A. Casey, M. Devereux, *Free Rad. Biol. Med.* 2012, **53**, 564-576.
22. D.S. Sigman, D.R. Graham, V. D'Aurora, A.M. Stern, *J. Biol. Chem.* 1979, **254**, 12269-12272.

CHAPTER IV

Regulating Bioactivity of Cu^{2+} Bis-1,10-Phenanthroline Artificial Metallonucleases with Sterically Functionalised Pendant Carboxylates

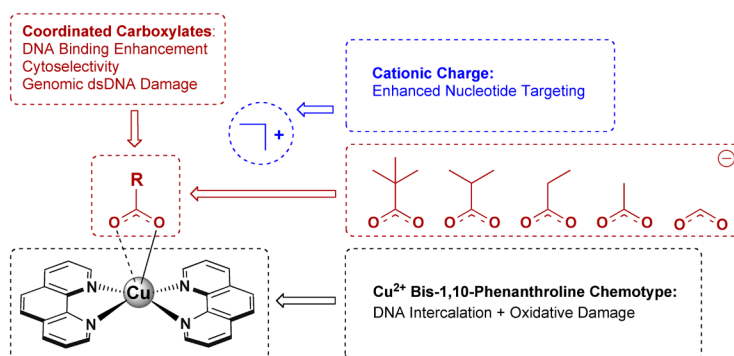
This work was published in the *Journal Of Medicinal Chemistry*, 2013, **56**, 21, pp8599-8615

Prisecaru A., McKee V., Howe O., Rochford G., McCann M, Colleran J., Barron N., Pour M., Gathergood N. and Kellett A.

My contribution to this paper is: Manuscript 1st author, synthesis and characterization of the complexes. DNA cleavage, binding and viscosity analyses, UV-vis stability studies and the quantification of H_2O_2 catalysis using Amplex Red

IV.1 Abstract

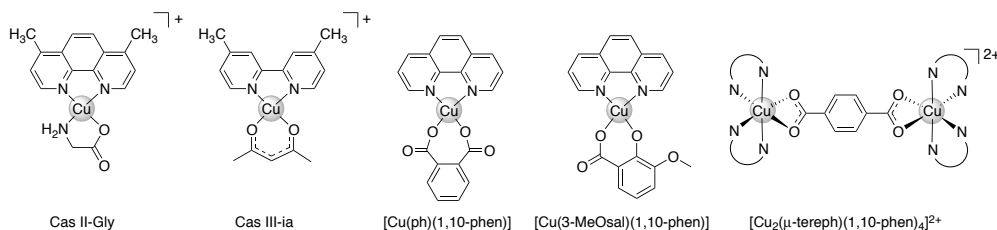
The synthetic chemical nuclease, $[\text{Cu}(1,10\text{-phenanthroline})_2]^{2+}$, has stimulated research within metallonuclease development and in the area of cytotoxic metallodrug design. Our analysis reveals, however, that this agent is “promiscuous” as it binds both dsDNA and protein biomolecules, without specificity, and induces general toxicity to a diversity of cell lineages. Here, we describe the synthesis and characterisation of small-molecule metallonucleases containing the redox-active cation; $[\text{Cu}(\text{RCOO})(1,10\text{-phen})_2]^+$, where 1,10-phen = 1,10-phenanthroline and $\text{R} = -\text{H}$, $-\text{CH}_3$, $-\text{C}_2\text{H}_5$, $-\text{CH}(\text{CH}_3)_2$ and $-\text{C}(\text{CH}_3)_3$. The presence of coordinated carboxylate groups in the complex cation function to enhance dsDNA recognition, reduce serum albumin binding and offer control of toxicity toward human cancer cells, gram positive and negative bacteria and fungal pathogens. The induction of genomic dsDNA breaks (DSBs) were identified in ovarian adenocarcinoma cells using immunodetection of $\gamma\text{-H2AX}$. Formate, acetate and pivalate functionalised complexes induced DSBs in a higher percentage of cells compared with $[\text{Cu}(1,10\text{-phen})_2]^{2+}$ which supports the importance of inner-sphere modification toward enhancing targeted biological application.



IV.2 Introduction

Small copper-phenanthroline molecules with DNA and RNA recognition properties represent important chemotypes capable of abrogating nucleic acid sequences through metal-driven oxidative cleavage.^{1,2} The chemical nuclease, $[\text{Cu}(1,10\text{-phen})_2]^{2+}$, is a well studied reagent which randomly cleaves nucleic acids in the presence of molecular oxygen (or hydrogen peroxide) upon reduction to Cu^+ .³⁻⁷ This agent oxidises duplex DNA (dsDNA) without specificity, predominately at the minor groove with C-H bonds at C1', C4', and C5' being the main targets of abstraction.⁸ Arising from this application, the attachment, or tethering, of 1,10-phen to DNA targeting agents, proteins and single-stranded nucleic acid vectors have successfully delivered sequence-specific scission upon incubation with Cu^{2+} ions in a reducing chemical environment.⁹⁻¹⁴ Furthermore, this complex may also have application as a chemical protease with the oxidative degradation of peptide bonds having already been reported.^{15,16} While the intracellular metal-chelating ligand, 1,10-phen, is known to elicit excellent *in vitro* antifungal,^{17,18} antibacterial¹⁹ and anticancer activities²⁰ alone, or as part of a metal complex,²¹⁻²⁴ recent interest has focused on the modification of this ligand to afford phenazine-type structures of extended π -symmetry for use within metal DNA-binding probes,^{25,26} some with selective chemotherapeutic utility.²⁷ The therapeutic potential of Cu^{2+} 1,10-phenanthroline-based complexes continues to be actively explored and the inclusion of inner-sphere, oxygen-donor ligands, has recently produced a series of complexes with significant biological potential.²⁸⁻³⁵ For example, the complex $[\text{Cu}(\text{glycinate})(4,7\text{-dimethyl-1,10-phenanthroline})(\text{H}_2\text{O})](\text{NO}_3)$ (Cas II-gly, Scheme IV.1) from the "Casiopeina" series³⁶ was found to have excellent *in vivo* cytotoxicity toward glioma C6 implanted mice with the mechanism being attributed to induction of both caspase-dependent and -independent apoptosis.³⁷ Cas II-gly also induced nuclear fragmentation through a process linked with the intracellular generation of reactive oxygen species (ROS). Another variant of the "Casiopeina" series, $[\text{Cu}(\text{acetylacetonato})(4,4'\text{-dimethyl-2,2'-bipyridine})](\text{NO}_3)$ (Cas III-ia, Scheme IV.1), was also found to exert antineoplastic effects on glioma C6.³⁸ In this particular study the authors showed that mitogen-activated protein kinase, JNK, initiated autophagic and apoptotic pathways through sustained ROS intracellular

generation by Cas III-ia. Yet further examples of *N,N'*-*O,O'* chelated Cu^{2+} complexes of this therapeutic class include the two reagents, $[\text{Cu}(o\text{-phthalate})(1,10\text{-phen})].2(\text{H}_2\text{O})^{39}$ and $[\text{Cu}(3\text{-methoxysalicylate})(1,10\text{-phen})]^{40}$ (Scheme IV.1), which were developed recently by this group. The *o*-phthalate complex was found to generate high levels of intracellular ROS, bind dsDNA and induce genomic dsDNA breaks (DSBs) within ovarian cancer cells (SK-OV-3) that were identified by $\gamma\text{-H2AX}$ immunofluorescence. Furthermore, the methoxysalicylate complex was found to be a potent superoxide dismutase mimetic (SODm), but did not exhibit catalase nor COX-1 / COX-2 mimetic properties. The proposed net effect here is the generation of an intracellular microenvironment rich in hydrogen peroxide (H_2O_2) that is not further detoxified (to O_2 or H_2O). Contaminant ROS-mediated apoptosis was suspected to follow thereafter with the complex displaying promising potential toward a range of epithelial malignancies. The final example of the therapeutic potential of this class arises from the activity of the dinuclear cytotoxin, $[\text{Cu}_2(\mu\text{-terephthalate})(1,10\text{-phen})_4]^{2+}$ (Scheme IV.1).^{41,42} This agent, again, is a potent ROS generator that displays *in vitro* cytotoxicity toward epithelial malignancies and also has the capacity to induce oxidative degradation on duplex DNA without exogenous reductant.



Scheme IV.1 Molecular structures of cytotoxic Cu^{2+} complexes incorporating *N,N'*-*O,O'* or *N,N'*-*O,N''* chelators.

Given the recent focus on Cu^{2+} based cytotoxic agents,^{43,44} in particular those containing coordinated carboxylate or carbonyl ligands,^{28,29} the current work seeks to identify, from a structure-activity perspective, the role that coordinated carboxylates have on modulating the biological profile of $[\text{Cu}(1,10\text{-phen})_2]^{n+}$ based complexes. Thus, in this study we have prepared the cationic series, $[\text{Cu}(\text{RCOO})(1,10\text{-phen})_2]^+$ (where $\text{R} = -\text{H}$, $-\text{CH}_3$, $-\text{C}_2\text{H}_5$, $-\text{CH}(\text{CH}_3)_2$ and $-\text{C}(\text{CH}_3)_3$), in order to identify the effect that primary, sterically functionalized,

carboxylates have on modulating; (i.) serum albumin binding, (ii.) dsDNA binding, (iii.) superhelical and linearised plasmid dsDNA damage and (iv.) broad spectrum cytotoxicity toward human cells and pathogenic bacteria and fungi. Furthermore, (v.) interactions with hydrogen peroxide by Fenton chemistry, which are believed to be fundamental to the induction of ROS-mediated DNA damage,⁴⁵ along with (vi.) the detection of intracellular DSBs on genomic DNA within human ovarian cancer cells (SK-OV-3) were examined by γ -H2AX antibody immunofluorescence using both confocal microscopy and flow cytometry.

IV.3 Results And Discussion

IV.3.1 Synthesis and characterisation

Complexes were prepared by firstly isolating the Cu^{2+} bis-1,10-phen complex, $[\text{Cu}(1,10\text{-phen})_2](\text{NO}_3)_2$ (**Cu-Phen**) via the treatment of copper nitrate with two molar equivalents of 1,10-phen in aqueous-ethanol solvent. Treatment of **Cu-Phen** with excess sodium salt of the carboxylic acid (RCOO^-Na^+ , $\text{R} = -\text{H}$, $-\text{CH}_3$, $-\text{C}_2\text{H}_5$, $-\text{CH}(\text{CH}_3)_2$ and $-\text{C}(\text{CH}_3)_3$) yielded deep blue methanolic solutions from which the agents crystallized upon slow evaporation (Fig. IV.1 and section IV.6.1). Each complex contains the molecular cation, $[\text{Cu}(\text{RCOO})(1,10\text{-phen})_2]^+$, where the coordination cation is charge balanced by an anionic nitrate (NO_3^-), with the exceptions of **Cu-Pro-Phen** where the counterion is carbonate (presumably obtained from atmospheric CO_2 during crystallization), and **Cu-Piv-Phen**, for which the charge is balanced by an uncoordinated pivalate anion. Both **Cu-Pro-Phen** and **Cu-Piv-Phen** crystallise with two independent cations in the asymmetric unit (Appendix A.B.2). Each complex crystallises with a number of water solvate molecules in the lattice and **Cu-Piv-Phen** also contains a molecule of pivalic acid. Each cation has irregular geometry, perhaps best described as approximately square pyramidal, with N_3O basal plane, one of the phenanthroline nitrogen donors axial, and a weak interaction with the second carboxylate oxygen. Comparison of the coordination geometry (Appendix Table A.B.26) shows that in each cation there is one long Cu-N(phen) bond (range 2.17 – 2.22 Å) and the remaining three are significantly shorter (1.98 – 2.08 Å). The angles between the planes of the two phenanthroline units ranges from 62.03(7)°

to 88.5(1)°. In each complex the cations are π -stacked into chains and there is an extensive hydrogen bonded network involving the anions, the solvate water molecules and, in most cases, the coordinated carboxylate. The exception is **Cu-Piv-Phen**, in which the cation is not included in the hydrogen bonding. Further details on each structure are given in the supplementary data. High-resolution ESI mass spectra of all complexes (section 3.6.2. and Appendix A.B.3) revealed parent m/z peaks of the bis-phen cation, $[\text{Cu}(\text{RCOO})(1,10\text{-phen})_2]^+$ ($[\text{M}]^+$), with the base peak in each spectra corresponding to the equivalent mono-phen, cationic species, $[\text{Cu}(\text{RCOO})(1,10\text{-phen})]^+$. IR spectroscopy (Appendix A.B.1) also confirmed each compound to contain vibrational peaks characteristic of coordinated aromatic imines and carboxylate ligands.⁴⁶

The electronic spectra of the carboxylate complexes are characteristic of the **Cu-Phen** spectrum (Fig. IV.2), with the presence of coordinated carboxylate groups conferring modest additional absorption intensity (ϵ) to the λ_{d-d} band. Furthermore, the electronic spectra of the phenanthroline complexes are distinctive compared to the simple Cu^{2+} nitrate salt, $\text{Cu}(\text{NO}_3)_2$, and metal-free 1,10-phen. The redox behavior of the complexes was investigated, using cyclic voltammetry, in the presence and absence of exogenous reductant (Na-L-ascorbate) (Table IV.1). In the absence of reductant, none of the complexes display reversibility and the presence of coordinated carboxylates results in larger $\text{Cu}^{2+}/\text{Cu}^+$ redox couple separation ($\Delta E_p \geq 113$ mV) when compared with **Cu-Phen** ($\Delta E_p = 75$ mV). Addition of 2 mM ascorbate results in a significant anodic shift in the $\text{Cu}^{2+}/\text{Cu}^+$ redox couple of all complexes, indicative of a more facile electron transfer regime. While **Cu-Phen** and **Cu-Pro-Phen** complexes tend toward reversibility in the presence of ascorbate ($\Delta E_p = 69$ and 66 mV, respectively), the remaining carboxylate complexes remain quasi-reversible with ΔE_p values of ≥ 98 mV. Electrochemical and electronic absorption properties of all complexes were investigated over a prolonged periods of time in order to examine their solution stability (section IV.6.4. and IV.6.5.). Negligible changes in redox behaviour and absorption maxima and intensity were observed for all samples and there was no evidence that complex breakdown to $[\text{Cu}(1,10\text{-phen})]^2+$ or $[\text{Cu}(1,10\text{-phen})_2]^2+$ had occurred.

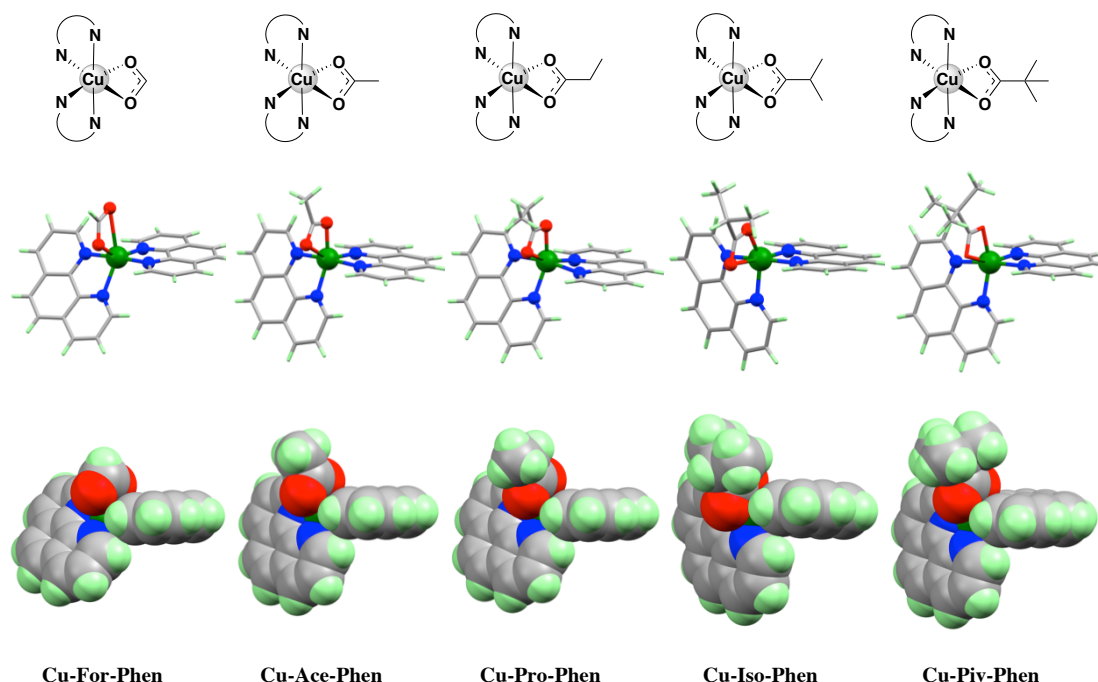


Figure IV.40 Molecular structures of the $[\text{Cu}(\text{RCOO})(1,10\text{-phen})_2]^+$ cations (top), single X-ray crystal structures of the complexes (centre), and perspective space-filled views of the five cations (bottom).

Table IV.1 Electrochemical parameters (V) for complexes in the absence and presence of added reductant (2 mM Na-L-ascorbate). Analysis conducted in 10% v/v DMF.

Complex	$E_{\text{Pa}}^{[a]}$	$E_{\text{Pc}}^{[a]}$	$\Delta E_{\text{p}}^{[a]}$	$E_{\text{Pa}}^{[b]}$	$E_{\text{Pc}}^{[b]}$	$\Delta E_{\text{p}}^{[b]}$
Cu-Phen	-0.041	-0.116	0.075	-0.019	-0.088	0.069
Cu-For-Phen	-0.036	-0.149	0.113	0.290	0.180	0.110
Cu-Ace-Phen	-0.314	-0.121	0.193	0.275	0.171	0.104
Cu-Pro-Phen	-0.143	-0.328	0.185	0.244	0.178	0.066
Cu-Iso-Phen	-0.194	-0.359	0.165	0.278	0.180	0.098
Cu-Piv-Phen	-0.146	-0.411	0.265	0.303	0.186	0.117

[a] complex without exogenous agent (V) [b] complex with added Na-L-ascorbate (V)

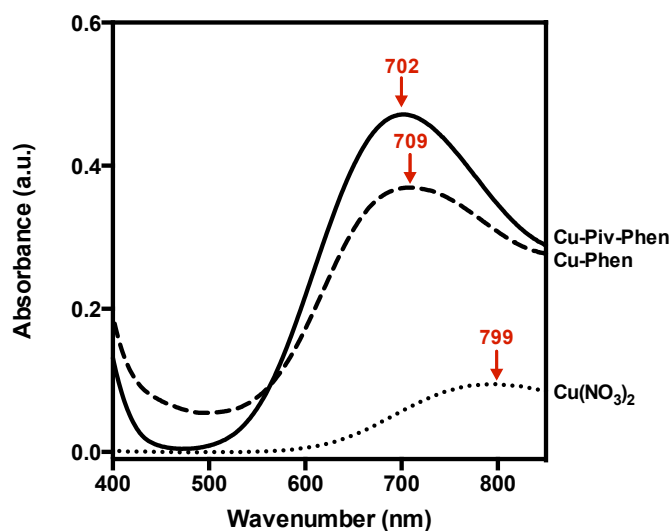


Figure IV.41 Electronic spectra of selected metal complexes recorded in 100% methanol at 5 mM complex or metal salt concentrations with λ_{d-d} maxima indicated; $\text{Cu}(\text{NO}_3)_2$ (····), **Cu-Phen** (---) and **Cu-Piv-Phen** (—).

IV.3.2 Binding affinity toward bovine serum albumin and calf thymus DNA

Tryptophan fluorescence quenching of bovine serum albumin (BSA, 0.015 mM) was examined at 37°C using a 295 nm excitation and 350 nm emission wavelength with measurements being recorded 5 min post exposure to the tested agent ([Q], 1 - 50 μM). Simple Cu^{2+} ions, from $\text{Cu}(\text{NO}_3)_2$, and the bis-phen complexes all display upward-curving, non-linear Stern-Volmer, fluorescence quenching (Fig. IV.3). Data could be suitably modeled using a quenching ‘Sphere-of-Action’ plot (Fig. IV.3 and Table IV.2) that accounts for immediate quenching of the fluorophore by the presence of a quencher molecule within a sphere of volume (V).⁴⁷ Cu^{2+} ions display the highest affinity for BSA with K_{SV} (Stern-Volmer quenching constant for the accessible fraction) and K_{A} (binding constant) being $1.02 \times 10^5 \text{ M}^{-1}$ and $4.23 \times 10^4 \text{ M}^{-1}$, respectively. The K_{A} values and r (radius of sphere) for the complexes decrease in accordance with steric bulk of the coordinated carboxylates with the **Cu-Piv-Phen** complex displaying the lowest affinity of all toward BSA and being nearly an order of magnitude lower than free Cu^{2+} ions. Metal-free 1,10-phen displays linear Stern-Volmer quenching (Fig. VI.3) with quenching coefficient of $2.01 \times 10^4 \text{ M}^{-1}$ along with K_{A} of $2.54 \times 10^4 \text{ M}^{-1}$. Analysis also revealed the average number of occupied tryptophan sites (from a maximum of 2) within BSA by these compounds; Cu^{2+}

ions interact with 1.48 TRP residues with the carboxylate complexes occupying between 1.20 - 1.38 residues ($n = 1.20$ for **Cu-Piv-Phen**).

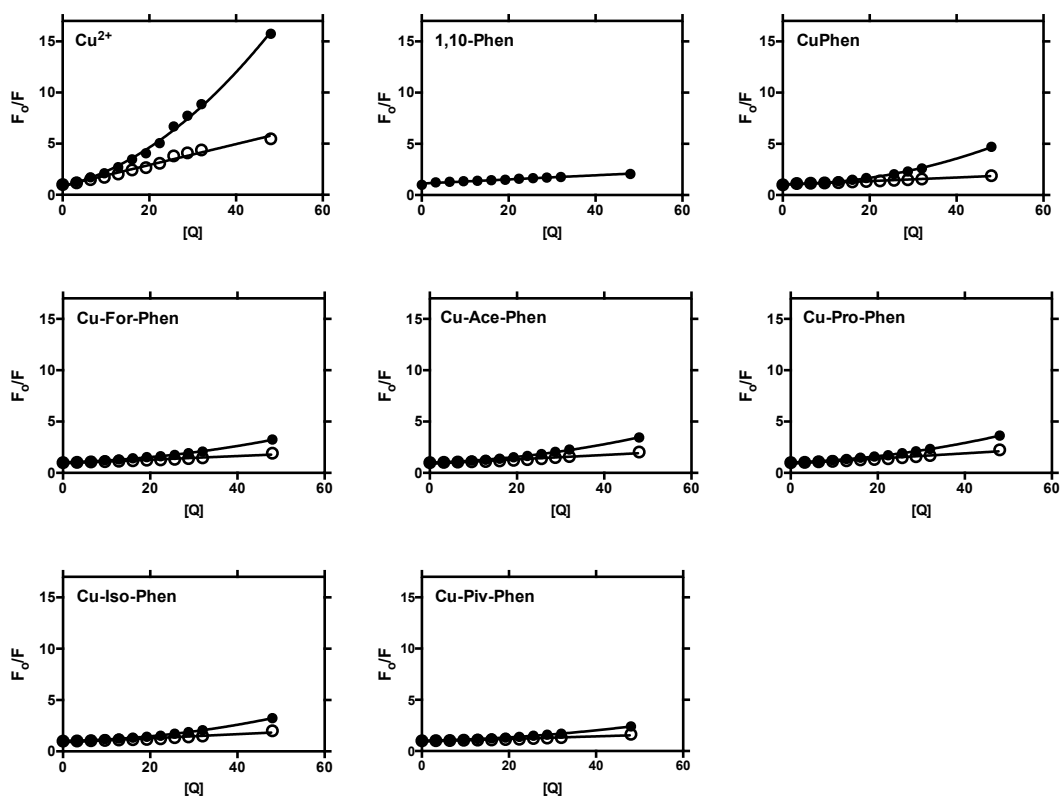


Figure IV.42 BSA tryptophan fluorescence quenching for Cu^{2+} ions, 1,10-phen along with the carboxylate complexes. Cu^{2+} complexes display non-linear quenching (solid circles) and are modeled using a quenching ‘Sphere-of-Action’ (open circles) with data points being displayed as an average of triplicate measurement.

Table IV.2 BSA tryptophan fluorescence quenching by Cu²⁺ ions, 1,10-phen and complexes.

Compound	$K_{SV} \times 10^4 \text{ M}^{-1}$	$V \times 10^4 \text{ M}^{-1}$	$r \text{ (Å)}$	n	$K_A \times 10^4 \text{ M}^{-1}$	R^2
Cu²⁺	10.22	2.50	206	1.48	4.23	0.99
1,10-Phen	2.01	-	-	0.79	2.54	0.99
CuPhen	1.75	2.20	215	1.15	2.83	0.97
Cu-For-Phen	1.77	1.10	164	1.26	1.26	0.99
Cu-Ace-Phen	2.53	1.10	164	1.31	1.13	0.98
Cu-Pro-Phen	2.52	1.00	158	1.26	1.32	0.99
Cu-Iso-Phen	1.99	1.00	158	1.28	1.04	0.99
Cu-Piv-Phen	1.22	0.90	153	1.20	0.93	0.98

n = number of occupied binding sites; K_A = binding constant; K_{SV} = Stern-Volmer quenching of accessible fraction; R^2 = goodness of fit; V = sphere of action volume; r = radius of sphere (Å); Cu²⁺ = Cu(NO₃)₂;

CuPhen = [Cu(1,10-phen)₂](ClO₄)₂;

Sphere-of-action:

$$\frac{V}{N'} = \frac{4}{3}\pi r^3$$

Sphere-of-action plot:

$$\frac{F}{F_0} = (1 + K_D[Q])\exp([Q]V\frac{N}{1000})$$

N' = Avogadro's number / 1000

Complex binding to dsDNA was studied using competitive ethidium bromide (Et⁺) fluorescence displacement on ctDNA (calf-thymus, ultra-high purity) with further quenching analysis of Hoechst 33258 (groove binder) and Et⁺ (intercalator) revealing binding mode data. For these assays high-throughput, 96-well plate methods were conducted using assays we recently reported.⁴⁸ The competition assay utilizes an optimized mixture of ctDNA (10 μM in DNAP) and EtBr (12.6 μM) which was incubated for 1 h with added quencher ([drug]) in a total volume of 100 μL (Fig. IV.4) while a mixture of ctDNA (25 μM in DNAP) and either Hoechst 33258 or EtBr (5 μM) was incubated with added drug in the quenching study (Fig. IV.5). Measurements were conducted using excitation and emission filters of 530 and 590 nm for Et⁺ and 360 and 460 nm for Hoechst. The quenching by Cu²⁺ ions and 1,10-phen did not reach 50% up to 300 μM and thus these agents had weak apparent DNA binding constants (K_{app} , Table IV.3A). Coordination of Cu²⁺ to bis-1,10-phen in the **Cu-Phen** complex induces a marked enhancement in DNA binding ($K_{app} = 6.67 \times 10^5$)⁴⁸ with the agent displacing bound ethidium to higher degree than Hoechst (Table IV.3B). The K_{app} values for the carboxylate complexes are significantly enhanced, by at least 10-fold, relative to **Cu-Phen** and increase with steric bulk of the ancillary ligand. **Cu-Piv-Phen** displays the highest DNA affinity (8.26×10^6), greater even than the established groove-binding agents netropsin and pentamidine under these conditions (pH = 7.2). Quenching analysis (Figure IV.5, Table IV.3B) reveals all complexes displace DNA-bound Et⁺ with higher specificity than Hoechst,

however, Q values between Et^+ and Hoechst are relatively small compared with netropsin and pentamidine that have high specificity for the minor groove.⁴⁹ Thus, while the presence of coordinated carboxylates function to significantly enhance quenching relative to **Cu-Phen**, it appears the binding region of these small molecules is unselective. Viscosity measurements, on salmon testes dsDNA (1 mM in DNAP), were conducted under identical buffered conditions as the fluorescence quenching and displacement assays (Fig. IV.6 and Table IV.3C). Results for the minor groove binding agent, pentamidine, and intercalating agent, ethidium bromide, displayed expected behavior with a decrease and significant increase in viscosity being observed, respectively. Furthermore, the partial intercalating agent Cu^{2+} mono-1,10-phenanthroline, $[\text{Cu}(1,10\text{-phen})]^{2+}$, exhibited hydrodynamic behavior between these two standard reagents. **Cu-Phen**, and all of the carboxylate complexes strongly exhibited intercalative profiles and there was a notable overlap between viscosity measurements and ethidium quenching (Table IV.4B and IV.3C) with complexes of enhanced viscosity displaying higher quenching of bound ethidium. Overall, the acetate, propanoate and pivalate complexes appear to deliver a greater degree of intercalative penetration compared with **Cu-Phen**.

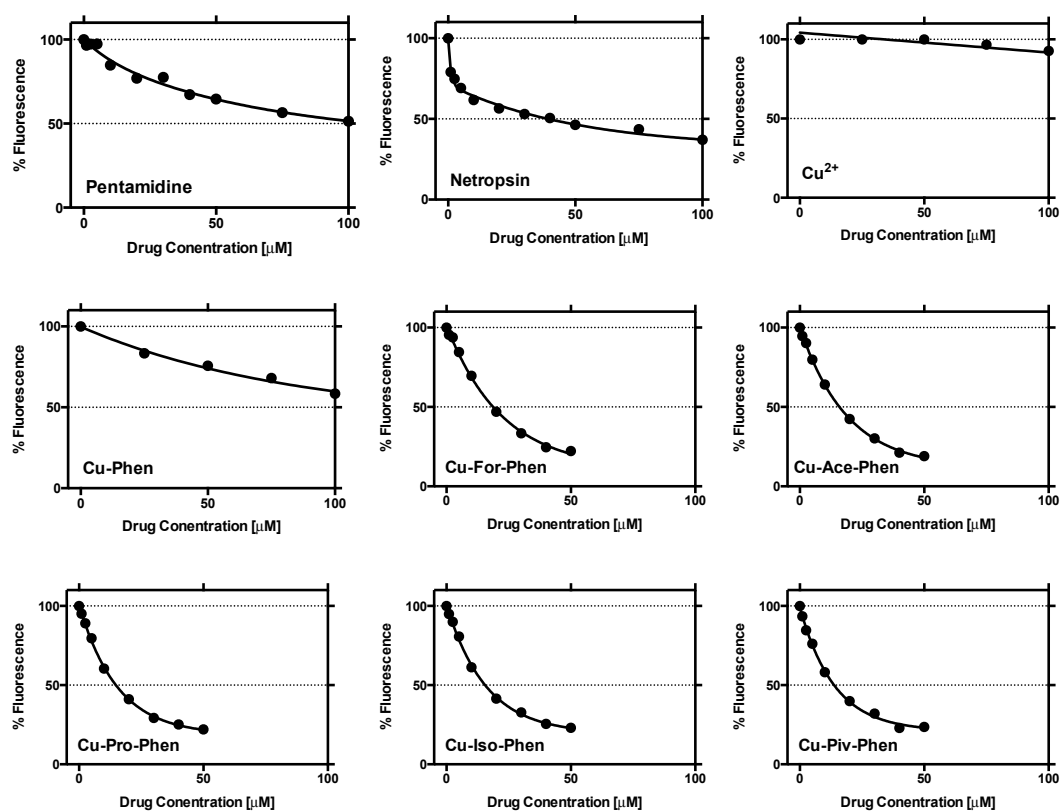


Figure IV.43 Competitive fluorescence quenching of ethidium bromide (12.6 μM) bound to ctDNA (10 μM in DNAP) by DNA binding drugs, Cu^{2+} and metal complexes. Data points displayed as an average of triplicate measurement.

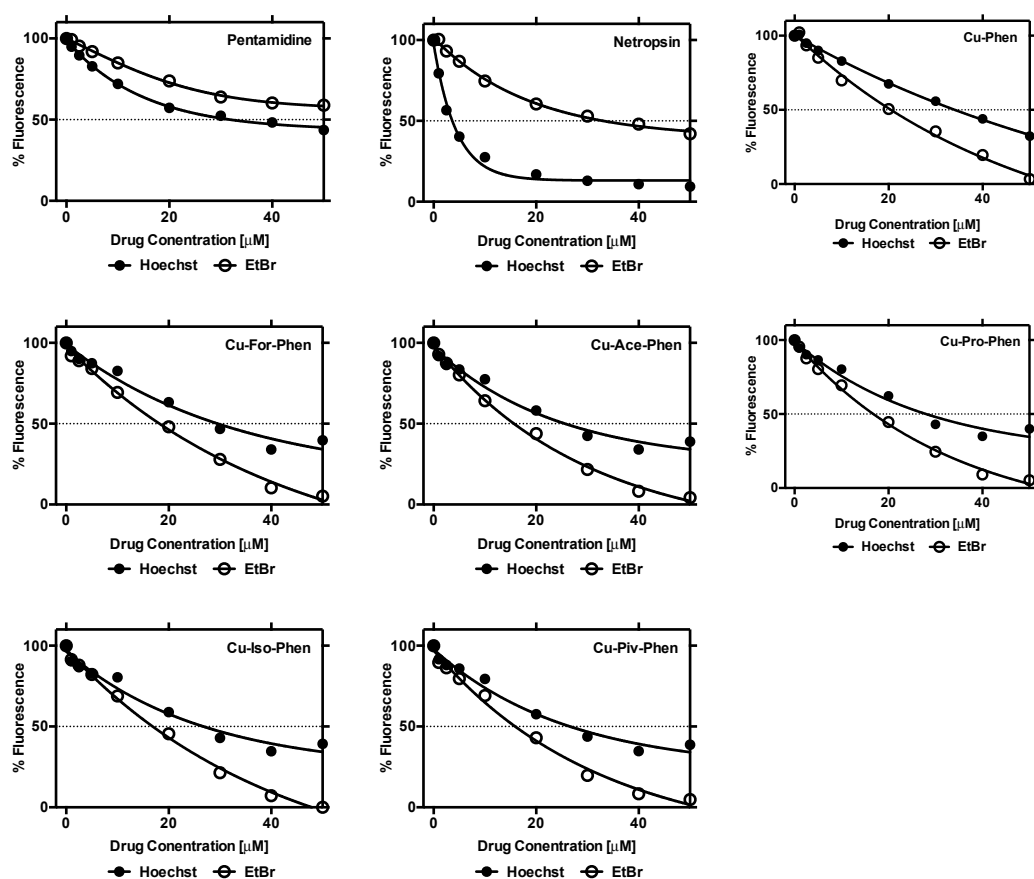


Figure IV.44 Fluorescence quenching of bound intercalator (ethidium) or minor groove binder (Hoechst 33258) to ctDNA by minor groove binding drugs, pentamidine and netropsin along and metal complexes. Data points are displayed as an average of triplicate measurement.

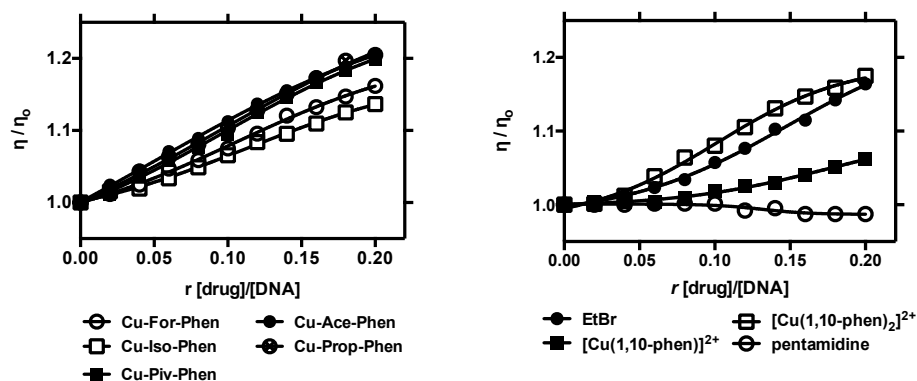


Figure IV.45 Viscosity data from the complexes, standard DNA binding agents and the partial intercalator $[\text{Cu}(1,10\text{-phen})]^{2+}$.

Table IV.3 A. Apparent ctDNA binding constants (K_{app}) determined using competitive ethidium bromide competitive quenching, **B.** fluorescence quenching (Q) values obtained against ctDNA bound with Hoechst 33258 (groove binder) or ethidium bromide (intercalator), and **C.** relative viscosity at $r = 0.20$ using dsDNA from salmon testes.

Compound	A.		B.		C.
	C_{50}^* (μM)	K_{app}^{**} (M^{-1})	Q^{***} Hoechst 33258 (μM)	Q^{***} Ethidium Bromide (μM)	η/η_0^\dagger
Cu^{2+}	>300	N/A	-	-	-
1,10-Phen	>300	N/A	-	-	-
Cu-Phen ⁴⁸	179.21	6.67×10^5	34.96	20.38	1.174
Cu-For-Phen	18.66	6.41×10^6	28.05	19.10	1.161
Cu-Ace-Phen	16.49	7.20×10^6	25.2	16.97	1.205
Cu-Pro-Phen	15.39	7.77×10^6	26.38	16.97	1.204
Cu-Iso-Phen	15.70	7.62×10^6	25.57	18.70	1.136
Cu-Piv-Phen	14.48	8.26×10^6	25.5	17.33	1.198
Netropsin ⁴⁸	39.99	4.77×10^6	3.50	35.98	1.007
Pentamidine ⁴⁸	109.41	1.09×10^6	35.86	>150	0.987

* C_{50} = concentration required to reduce fluorescence by 50%; $\text{Cu}^{2+} = \text{Cu}(\text{OAc})_2$;

CuPhen = $[\text{Cu}(1,10\text{-phen}_2)](\text{ClO}_4)_2$; ** $K_{app} = K_e \times 12.6/C_{50}$

where $K_e = 9.5 \times 10^6 \text{ M (bp)}^{-1}$; N/A = not applicable;

*** Q = displacement of 50% initial fluorescence from DNA-bound dye.

† relative viscosity at $r = 0.20$.

IV.3.3 *In vitro* cytotoxicity

To examine the broad-spectrum chemotherapeutic properties within this class, a range of cytotoxicity experiments were conducted with human cancer cells of the prostate (PC3), ovaries (SK-OV-3) and non-cancerous prostate (immortalised PNT1A) (Fig. IV.7 and Table IV.4). A range of gram positive (SA, *Staphylococcus aureus*; MRSA; methicillin resistant *Staphylococcus aureus*; SE, *Staphylococcus epidermidis*; EF, *Enterococcus sp.*) and gram negative (EC, *Escherichia coli*; KP, *Klebsiella pneumonia*; KP-E, *Klebsiella pneumonia*; PA, *Pseudomonas aeruginosa*) bacteria were also examined (Fig. IV.8 and Table IV.5) along with an extensive range of pathogenic fungi (CA1, *Candida albicans* ATCC 44859; CA2, *Candida albicans* ATCC 90028; CA3, *Candida parapsilosis* ATCC 22019; CK1, *Candida krusei* ATCC 6258, and clinical yeast isolates CK2, *Candida krusei* E28; CT, *Candida tropicalis* 156; CG, *Candida glabrata* 20/I; CL, *Candida lusitanae* 2446/I; TA, *Trichosporon asahii* 1188, along with filamentous fungi AF, *Aspergillus fumigatus* 231; AC, *Absidia corymbifera* 272; TM, *Trichophyton mentagrophytes* 445) (Fig. IV.9 and Table IV.6).

The chemotherapeutic drug cisplatin and 1,10-phen displayed no activity, up to 200 μM , over 24 h when tested in human cell lines, however, both agents were

active over 96 h with IC_{50} values ranging 1.0 - 4.5 μ M (cisplatin) and 2.4 – 4.7 μ M (1,10-phen). **CuPhen** displayed higher 24 h activity within PC3 than at 96 h (1.1 μ M versus 15.2 μ M) while its 96 h IC_{50} in PNT1A and SK-OV-3 were 1.8 μ M and 0.6 μ M, respectively. The presence of carboxylate groups were found to significantly modulate the 24 h cytotoxicity within PC3 and PNT1A with bulkier ligands markedly enhancing the IC_{50} response across the series (**Cu-Piv-Phen**; PC3 = 3.2 μ M, PNT1A = 14.5 μ M). The Cu^{2+} complexes were unanimously more active, at both 24 and 96 h, within platinum-resistant ovarian cancer cells (SK-OV-3) when compared with PC3 and PNT1A cells.

The antibacterial values (MIC_{95}) of the compounds were examined at 24 and 48 h and against a wide range of microbes. 1,10-phen displayed low or no activity among the gram positive and negative bacteria, with the exception of *Enterococcus* where an MIC_{95} of 62.5 μ M was recorded. The most active species against all bacterial strains was **Cu-Iso-Phen** with MIC_{95} values ranging 15.60 – 31.25 μ M (except on *P. aeruginosa*). Remarkably, the least active agent was the next complex in the series, **Cu-Piv-Phen**, which was significantly less cytotoxic than all other complexes with MIC_{95} ranging between 62.5 – 1000 μ M.

In contrast to its antibacterial properties, the antifungal activity of metal-free 1,10-phenanthroline surpassed all of the tested metal complexes and ranged consistently between 7.81 – 15.61 μ M across both filamentous and non-filamentous lineages. This result is in broad agreement with previous findings of this group and others.¹⁸ Indeed, the activity of this chelator is attributed to the sequestering of essential intracellular trace metals (e.g. Zn^{2+}), which seriously impedes the survival of fungal pathogens. **Cu-Phen** was also found to be consistently cytotoxic across this complete fungal panel (MIC_{80} range: 7.81 – 31.25 μ M) while **Cu-Pro-Phen** was remarkably less toxic to all isolates (MIC_{80} = 250 μ M). The overall trend of the antifungal activities appears to be somewhat Gaussian in shape; activity decreases going from 1,10-phen to **Cu-Pro-Phen** before an increase in the antimycotic effects of the bulkier carboxylate complexes, **Cu-Iso-Phen** and **Cu-Piv-Phen**, becomes evident.

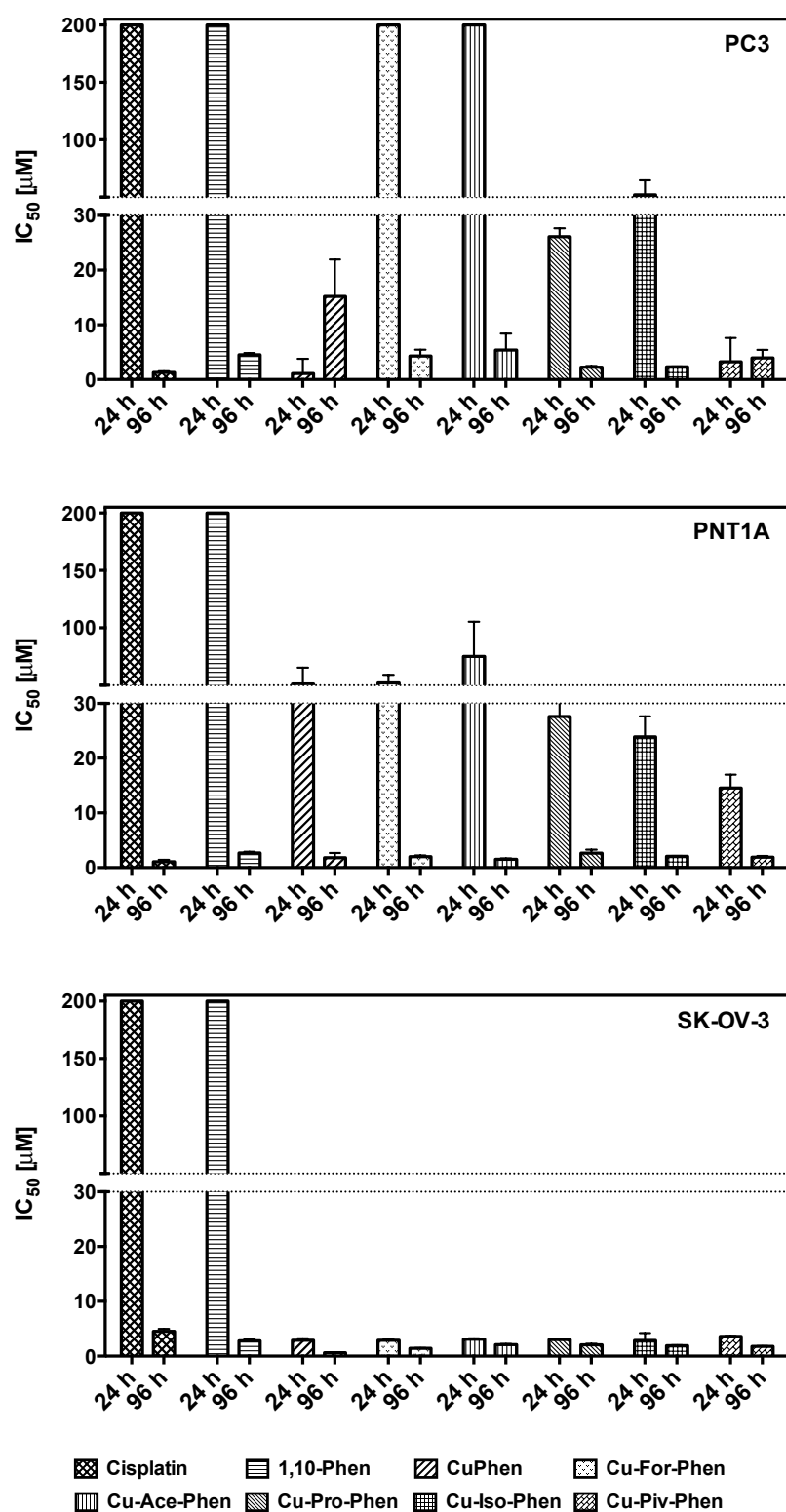


Figure IV.46 IC_{50} data (at the 95% confidence interval) of metal complexes, 1,10-phen and cisplatin toward human cancer cells of the prostate (PC3), ovaries (SK-OV-3), non-cancerous prostate (PNT1A) post 24 h and 96 h exposure.

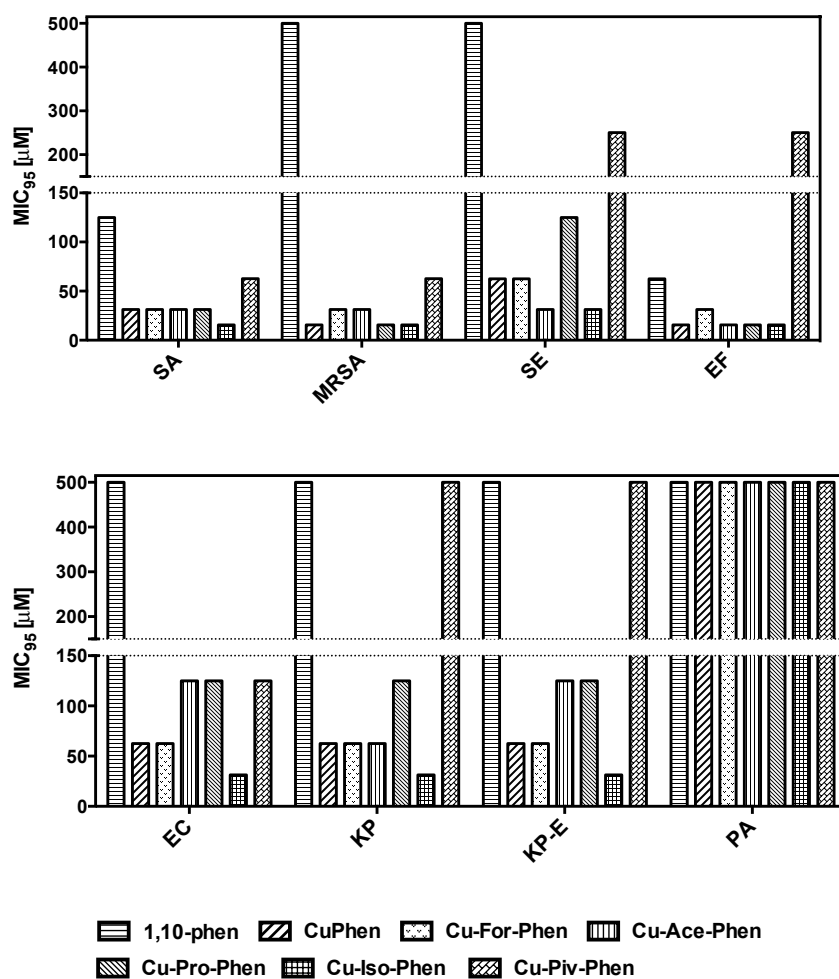


Figure IV.47 MIC₉₅ data of metal complexes and 1,10-phen toward a range of gram positive and negative bacteria post 24 h or 48 h exposure (note: both 24 h and 48 h activities were identical). SA, *Staphylococcus aureus*; MRSA, methicillin resistant *Staphylococcus aureus*; SE, *Staphylococcus epidermidis*; EF, *Enterococcus* sp.; EC, *Escherichia coli*; KP, *Klebsiella pneumonia*; KP-E, *Klebsiella pneumonia*; PA, *Pseudomonas aeruginosa*.

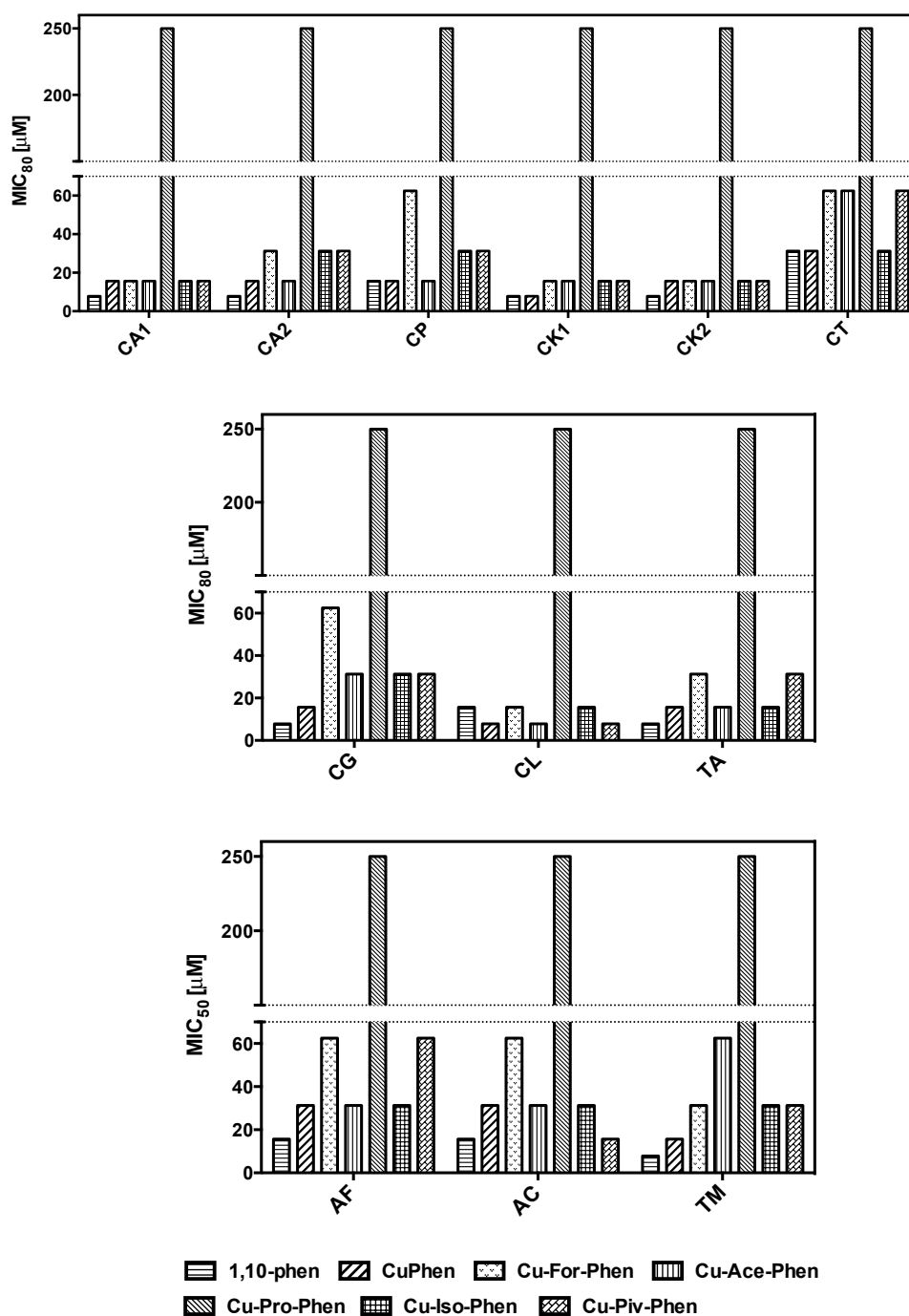


Figure IV.48 MIC data of metal complexes and 1,10-phen toward a range of pathogenic fungi post 24 h or 48 h exposure to non-filamentous fungi and post 72 h or 120 h exposure to filamentous fungi (note: both 24 h / 48 h and 72 h / 120 h activities were identical). CA1, *Candida albicans* ATCC 44859; CA2, *Candida albicans* ATCC 90028; CA3, *Candida parapsilosis* ATCC 22019; CK1, *Candida krusei* ATCC 6258, clinical yeast isolates CK2, *Candida krusei* E28; CT, *Candida tropicalis* 156; CG, *Candida glabrata* 20/I; CL, *Candida lusitanae* 2446/I; TA, *Trichosporon asahii* 1188, and filamentous fungi AF, *Aspergillus fumigatus* 231; AC, *Absidia corymbifera* 272; TM, *Trichophyton mentagrophytes* 445.

Table IV.4 *In vitro* cytotoxicity data for complexes, Cu²⁺ ions, 1,10-phen and cisplatin toward human derived cancer and non-cancers cells.

Compound	IC ₅₀ (μM)					
	PC3		PNT1A		SKOV3	
	24 h	96 h	24 h	96 h	24 h	96 h
Cu ²⁺	>200	>200	>200	>200	>200	>200
Cisplatin	>200	1.30±0.23	>200	1.07±0.37	121.00±0.37	4.53±0.43
1,10-Phen	>200	4.52±0.32	>200	2.67±0.23	>200	2.79±0.37
CuPhen	1.10±2.68	15.20±6.74	51.14±14.13	1.82±0.86	2.91±0.33	0.61±0.00
Cu-For-Phen	>200	4.32±1.14	52.01±7.02	1.98±0.23	2.88±0.14	1.41±0.07
Cu-Ace-Phen	>200	5.41±3.01	75.02±30.29	1.51±0.18	3.04±0.19	2.05±0.14
Cu-Pro-Phen	26.09±1.56	2.25±0.22	27.60±11.37	2.62±0.66	3.02±0.10	2.07±0.19
Cu-Iso-Phen	52.00±12.70	2.31±0.08	23.89±3.74	2.05±0.07	2.86±1.36	1.91±0.09
Cu-Piv-Phen	3.26±4.34	3.96±1.45	14.56±2.44	1.90±0.21	3.59±0.10	1.78±0.05

Cu²⁺ = CuCl₂; CuPhen = [Cu(1,10-phen)₂](NO₃)₂

Table IV.5 *In vitro* cytotoxicity data for complexes, Cu²⁺ ions and 1,10-phen toward gram positive and negative bacteria.

Compound	MIC ₉₅ (μM)							
	Gram positive				Gram negative			
	SA	MRSA	SE	EF	EC	KP	KPE	PA
	*24 h / 48 h							
Cu ²⁺	2000	2000	2000	2000	2000	2000	2000	>2000
1,10-Phen	125	500	1000	62.5	2000	1000	1000	2000
CuPhen	31.25	15.62	62.5	15.62	62.5	62.5	62.5	>1000
Cu-For-Phen	31.25	31.25	62.5	31.25	62.5	62.5	62.5	>1000
Cu-Ace-Phen	31.25	31.25	31.25	15.62	125	62.5	62.5	>1000
Cu-Pro-Phen	31.25	15.62	125	15.62	125	125	125	>1000
Cu-Iso-Phen	15.62	15.62	31.25	15.62	31.25	31.25	31.25	1000
Cu-Piv-Phen	62.5	62.5	250	250	125	500	1000	>1000

Cu²⁺ = CuCl₂; CuPhen = [Cu(1,10-phen)₂](NO₃)₂; *24 h and 48 h MIC₉₅ activities were identical in each test; MIC₉₅ values for all complexes against PA were 2000

Table IV.6 *In vitro* cytotoxicity data for complexes, Cu²⁺ ions and 1,10-phen toward filamentous and non-filamentous pathogenic fungi.

Compound	MIC ₈₀ (μM)						MIC ₅₀ (μM)					
	Non-filamentous*						Filamentous**					
	CA1	CA2	CA3	CK1	CK2	CT	CG	CL	TA	AF	AC	TM
	24 h / 48 h											
Cu ²⁺	2000	2000	2000	2000	2000	2000	2000	2000	2000	2000	2000	2000
1,10-Phen	7.81	7.81	15.62	7.81	7.81	31.25	7.81	15.62	7.81	15.62	15.62	7.81
CuPhen	15.62	15.62	15.62	7.81	15.62	31.25	15.62	7.81	15.62	31.25	31.25	15.62
Cu-For-Phen	15.62	31.25	62.50	15.62	15.62	62.50	62.50	15.62	31.25	62.50	62.50	31.25
Cu-Ace-Phen	15.62	15.62	15.62	15.62	15.62	62.50	31.25	7.81	15.62	31.25	31.25	62.50
Cu-Pro-Phen	250	250	250	250	250	250	250	250	250	250	250	250
Cu-Iso-Phen	15.62	31.25	31.25	15.62	15.62	31.25	31.25	15.62	15.62	31.25	31.25	31.25
Cu-Piv-Phen	15.62	31.25	31.25	15.62	15.62	62.50	31.25	7.81	31.25	62.50	15.62	31.25

Cu²⁺ = CuCl₂; CuPhen = [Cu(1,10-phen)₂](NO₃)₂; *24 h and 48 h MIC₈₀ values were identical in each test; **72 h and 120 h MIC₅₀ values were identical in each test

IV.3.4 Artificial metallonuclease activity

The artificial metallonuclease activity of the complexes was studied using both supercoiled (SC) and linearized dsDNA. None of the complexes cleaved superhelical plasmid DNA (pBR322; Roche (Cat. 10481238001) or NEB (Cat. N3033L)) when incubated for up to 10 hours. SC pBR322 was degraded, however, in the presence of exogenous reductant (Na-L-ascorbate) or oxidant (H_2O_2) (Fig. IV.10 A and B). In these experiments 400 ng of SC DNA was incubated with 2.5 – 20.0 μM of tested complex, along with 1 mM of exogenous substance, for 30 min before being quenched and examined using agarose gel electrophoresis. Simple Cu^{2+} ions had no effect on the plasmid under these conditions (data not shown). With added reductant, **Cu-Phen** was the most efficient cleavage agent; almost complete conversion from SC (Form I) to nicked (Form II, open circular, OC) form at 5 μM was observed with linear conformation (Form III) being generated at 10 and 20 μM . Furthermore, the presence of 20 μM of **Cu-Phen** was found to completely deplete DNA as evidenced by laddering of the FIII band. The carboxylate complexes also induce significant degradation of SC DNA with added reductant at 10 and 20 μM with nuclease activity at lower concentrations not being evident. Propionate, isobutyrate and pivalate complexes can be described as the more active within the functionalised series owing to the amount of Form I DNA remaining after 10 μM of exposure in addition to the relative amount of Form III at 20 μM (Fig. IV.10 A). **Cu-Phen** was again the most active species in the presence of exogenous oxidant (Fig. IV.10 B) although it was obvious that reductant is more influential, overall, in the cleavage reactions. The propionate, isobutyrate and pivalate complexes were again the most active carboxylate-containing nucleases with exogenous H_2O_2 as evidenced by the amount of Form I remaining at the highest exposure level (20 μM). Linearized pBR322, generated using the endonuclease EcoRI then purified using anion exchange column chromatography (Qiagen, section IV.6.3 for protocol), was subsequently examined as a substrate for artificial metallonuclease activity. Interestingly, it was found that this conformation of DNA was more susceptible to degradation by Cu^{2+} bis-phen complexes (5 μM) (Fig. IV.10 C). In order to study the mechanism of DNA degradation on linearised DNA a series of trapping species were added to the reactions (Fig. IV.10 D – G). The trapping of hydrogen peroxide generated by

the addition of 1000 units of catalase enzyme (Fig IV.10 D) and the cuprous (Cu^+) species through the introduction of 100 μM of neocuproine (Fig IV.10 G) were found to almost completely inhibit the cleavage of linearised dsDNA. Furthermore, it appears the cleavage mechanism is also dependent, somewhat, on the production of superoxide ($\text{O}_2^{\cdot-}$) and the hydroxyl radical ($\cdot\text{OH}$) as the addition of bovine superoxide dismutase (1000 units) and the hydroxyl radical scavenger, DMSO (10% v/v) were found to hinder the cleavage reactions somewhat (Fig IV.10 E and F).

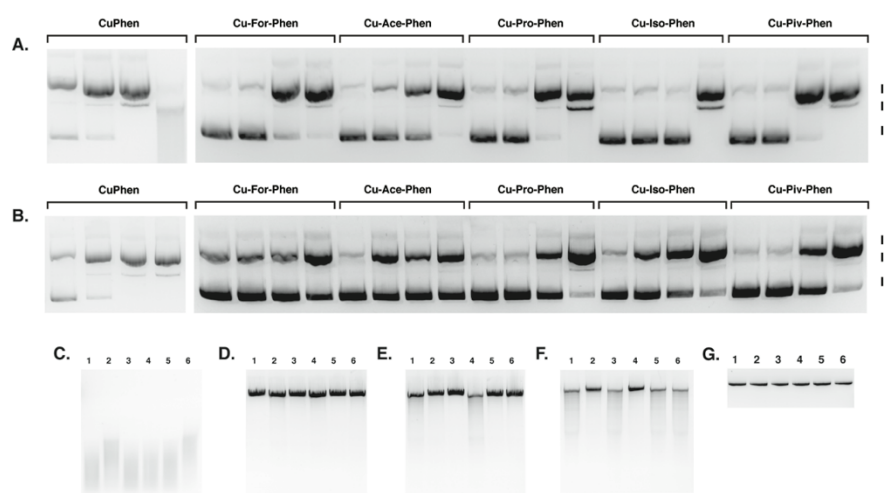


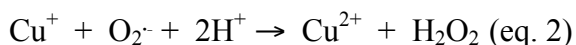
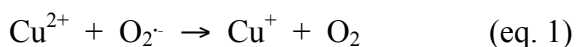
Figure IV.49 Degradation of superhelical pBR322 with Cu^{2+} complexes, using 2.5, 5.0, 10.0 and 20.0 μM of tested agent (from left to right), in the presence of **A.** 1 mM Na-L-ascorbate and **B.** 1 mM H_2O_2 . Reactions were carried out using 400 ng of pBR322 plasmid DNA for 30 min at 37 °C in 80 mM HEPES at pH 7.2 with 25 mM NaCl before being quenched and analysed using agarose gel electrophoresis. Degradation of linearized pBR322 (by EcoRI) in **C.** with 5 μM of 1. **CuPhen**, 2. **Cu-For-Phen**, 3. **Cu-Ace-Phen**, 4. **Cu-Pro-Phen**, 5. **Cu-Iso-Phen** and 6. **Cu-Piv-Phen**; **D.** + 1000 Units of Catalase; **E.** + 1000 Units of SOD; **F.** + 10% v/v DMSO, and; **G.** + 100 μM neocuproine.

IV.3.5 Interactions with H_2O_2

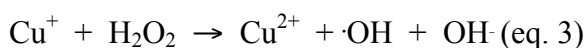
The importance of hydrogen peroxide in the cleavage mechanism of dsDNA (Fig. IV.8D) is believed to arise from superoxide dismutase mimetic (SODm) activity (eq. 1 and 2) which is followed thereafter by the Fenton reaction (eq. 3). Thus, H_2O_2 is both generated and transformed to the hydroxyl radical ($\cdot\text{OH}$), which is capable of C–H deoxyribose bond activation, by $\text{Cu}^+/\text{Cu}^{2+}$ catalysis at

the DNA interface.¹ Furthermore, this group and others have published on the excellent SOD mimetic properties of Cu²⁺ bis-phenanthroline complexes.^{40,50}

SOD:



Fenton:



The interactions of all complexes with 5 μM of hydrogen peroxide (H_2O_2) was followed using the Amplex Red assay (Invitrogen). In this assay the concentration of peroxide was detected fluorometrically, in the presence of horseradish peroxidase, using 530 nm excitation and 590 nm emission (Fig. IV.11 A). All complexes had no effect on H_2O_2 in the absence of exogenous reductant (Na-L-ascorbate) (data not shown). However, in the presence of 100 μM of Na-L-ascorbate, peroxide degradation was identified kinetically over a 2 h window (Fig. IV.11 B). The most active complex, **CuPhen**, reduced the H_2O_2 concentration by almost 50% at ~19 min while the bulkier carboxylate derivatives (**Cu-Pro-Phen**, **Cu-Iso-Phen** and **Cu-Piv-Phen**) induced 50% degradation between 40 – 45 min with the remaining two reagents, **Cu-For-Phen** and **Cu-Ace-Phen**, ablating 50% of H_2O_2 fluorescence at ~53 and ~63 min respectively. It is significant to note the strong correlation between the artificial metallonuclease activity (Fig. IV.11 A and B) and Fenton-type breakdown of H_2O_2 in this overall series.

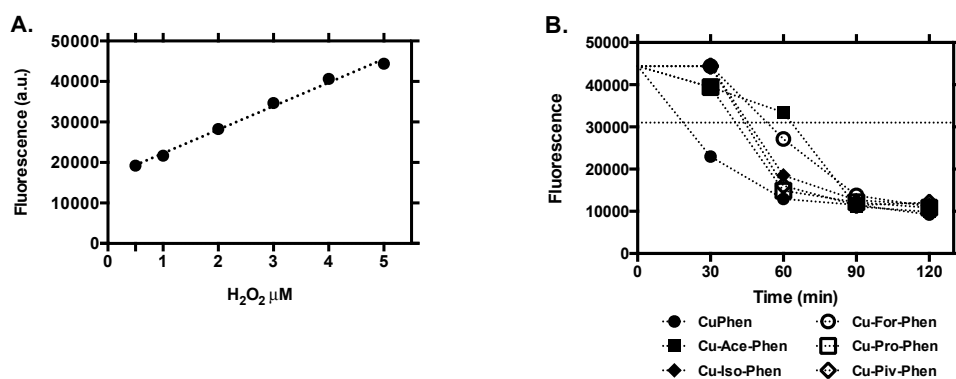


Figure IV.50 A. Standard fluorescence response curve from H₂O₂ detected using the Amplex Red assay (Invitrogen) using 530 nm excitation and 590 nm emission; B. Fenton breakdown of H₂O₂ (5 μM) over a period of 120 min in the presence of Cu²⁺ complexes (5 μM in EtOH) and 100 μM of Na-*L*-ascorbate.

IV.3.6 Induction of dsDNA breaks in SK-OV-3 cells

Double strand DNA breaks (DSBs) were identified using immunodetection of γ -H2AX foci in SK-OV-3 cells exposed for 24 h to an IC₂₅ dose of cisplatin and the carboxylate-derivatised complexes and were compared to a non-drug treated control. It should be noted that while the IC₂₅ for the Cu²⁺ complexes against SK-OV-3 are all quite similar (0.78 – 1.78 μM), a much higher concentration of cisplatin (25.65 μM) was required to induce the IC₂₅ response in this cell line. After double-strand break induction, formation of γ -H2AX foci due to phosphorylation at Ser-139 of histone H2AX represents an early event of DNA damage response to DSBs.⁵¹ These foci represent DSBs in a 1:1 manner and thus can be used as an excellent biomarker for the repair process to DNA damage.⁵² The detection and visualization of γ -H2AX by flow cytometry allow the assessment of DNA damage, related DNA damage proteins and DNA repair. γ -H2AX therefore has application in detecting genomic damage caused by cytotoxic chemical agents, especially in the context of cancer treatment and therapy.⁵³ γ -H2AX foci were visualised by confocal microscopy (Fig. IV.12) with nuclei being shown in red (propidium iodide (PI) staining, 543 nm excitation) and DSBs being shown in green (primary antibody, anti-phospho-histone H2A.X, 488 nm excitation). Foci could clearly be visualised in the cells treated with cisplatin and the complexes when compared to the untreated control. Interstrand crosslinking (ICL) agents, such as cisplatin, are known to stimulate the DNA repair pathway that initiates dual incisions on either side of one arm of

the crosslink, releasing the covalent linkage between the two DNA strands.⁵⁴ ROS active metallo-drugs with DNA binding properties have also been purported to inducing DSBs due to free radical DNA oxidation.³⁹ All Cu²⁺ complexes examined in this series displayed foci due to DSBs that could be visualised by confocal microscopy (Fig. IV.12). In order to quantify DSBs through γ -H2AX fluorescence, flow cytometry analysis was employed (Fig. IV.13). Mean intensity fluorescence (MIF) analysis of γ -H2AX positive nuclei showed **CuPhen** as producing the highest intensity foci, however, these foci were present only within a relatively low proportion of cells (~11%). Of the carboxylate complexes examined, the formate, acetate and pivalate complexes (**Cu-For-Phen**, **Cu-Ace-Phen** and **Cu-Piv-Phen**), displayed both high MIF values and were present in a significant proportion of cells (46%, 24% and 17% respectively). The least active agent, overall, was **Cu-Pro-Phen** while cisplatin displayed both high MIF and percentage positive γ -H2AX cells. It is highly significant, however, that the Cu²⁺ 1,10-phen complexes were examined at a far lower, >25 times lower in some instances, than this clinical therapeutic.

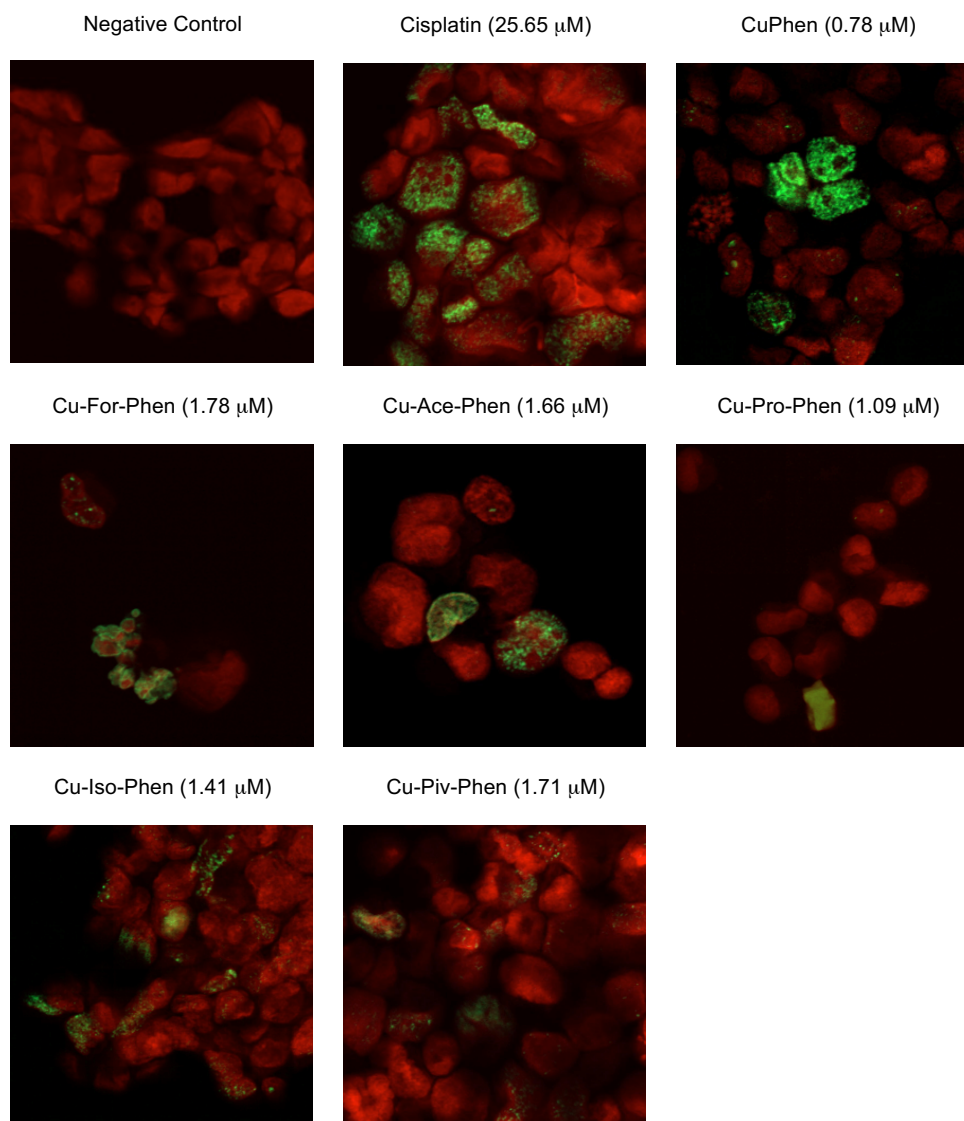


Figure IV.51 Confocal microscopy images of γ -H2AX foci (green) within propidium iodide stained SK-OV-3 nuclei (red) after 24 h of drug treatment at the IC₂₅ level (indicated in μ M).

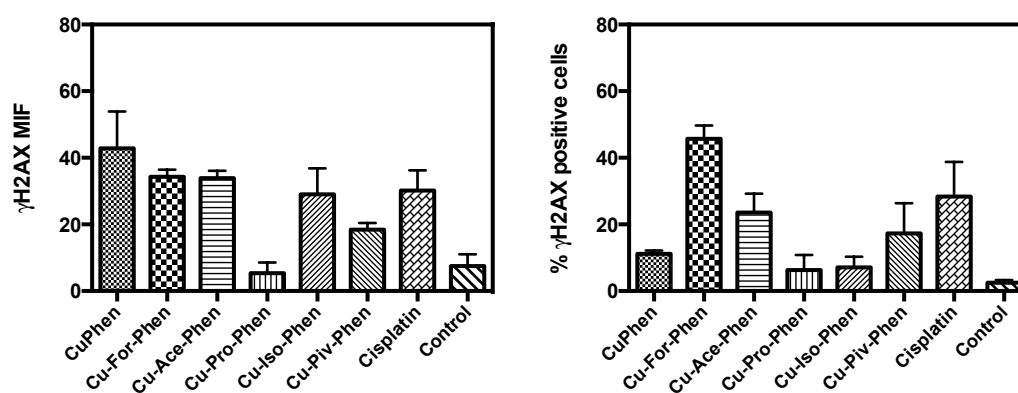


Figure IV.52 Mean intensity fluorescence \pm SD, in arbitrary units, of γ -H2AX fluorescence in SK-OV-3 cells (left) and percentage of overall γ -H2AX positive SK-OV-3 cells (\pm SD) (right).

IV.4 Conclusion

The coordination of sterically functionalised carboxylate groups to the cation, $[\text{Cu}(1,10\text{-phenanthroline})_2]^{2+}$, enhances dsDNA binding by at least 10-fold, and the activity increases with steric bulk of the ancillary ligand with the pivalate complex, **Cu-Piv-Phen**, displaying the highest binding constant ($K_{\text{app}} = 8.26 \times 10^6 \text{ M}^{-1} (\text{bp})$). Conversely, the bovine serum albumin (BSA) binding constant decreases with steric bulk and thus, **Cu-Piv-Phen** displayed the lowest affinity ($K_A = 0.94 \times 10^4 \text{ M}^{-1}$) to this protein.

The presence of carboxylate groups were found to enhance cytotoxicity within human prostate cancer cells (PC3) and immortalised, non-cancerous prostate epithelial cells (PNT1A) over 24 hours, with the bulkier ligands markedly enhancing the IC_{50} response (e.g. **Cu-Piv-Phen**, PC3, $\text{IC}_{50} = 3.26 \text{ }\mu\text{M}$). All carboxylate complexes, however, were equal in their efficacy (IC_{50} 0.61 – 3.59 μM) over both 24 and 96 h periods against human ovarian cancer cells (SK-OV-3). The antibacterial and antifungal properties of the complexes were examined against a wide range of pathogenic microbes and **Cu-Iso-Phen** was found to be highly active against both gram positive and negative strains (MIC_{95} 15.62 – 31.25 μM), while **Cu-Iso-Phen** was also active against both filamentous and non-filamentous fungi (MIC_{80} , filamentous, 15.62 – 31.25 μM ; MIC_{50} , non-filamentous = 31.25 μM). Significantly, cytoselectivity was identified in this series with **Cu-Piv-Phen** being remarkably less cytotoxic than all others toward both gram positive and negative bacteria (MIC_{95} 62.5 – 1000 μM) while **Cu-Pro-Phen** had significantly lower selectivity against all fungal strains ($\text{MIC}_{80/50} = 250 \text{ }\mu\text{M}$). The addition of carboxylate groups to the **Cu-Phen** reagent did not enhance DNA cleavage activity, with **Cu-Phen** being the most active of all complexes tested in the presence exogenous reductant and oxidant. However, **Cu-Prop-Phen**, **Cu-Iso-Phen** and **Cu-Piv-Phen** can be described as the most active within the functionalised series. This trend was also seen in their Fenton-type interaction with hydrogen peroxide using the Amplex Red assay, with **Cu-Phen** being the most active, followed thereafter by **Cu-Pro-Phen**, **Cu-Iso-Phen** and **Cu-Piv-Phen**. Detection of double-strand breaks (DSBs) on genomic DNA within ovarian cancer cells (SK-OV-3), identified using immunodetection of γ -

H2AX foci, revealed that the simple formate and acetate complexes, **Cu-For-Phen** and **Cu-Ace-Phen**, along with **Cu-Piv-Phen**, could induce high intensity foci and were, unlike **Cu-Phen**, present in a significant proportion of cells, ~46%, ~24% and ~17% respectively.

Our analysis on $[\text{Cu}(\text{1,10-phen})_2]^{2+}$ (**Cu-Phen**) reveals this complex as having both moderate protein (bovine serum albumin, BSA) binding and DNA intercalating (calf thymus dsDNA) properties. **Cu-Phen** can also be classified as a non-selective cytotoxin of human cancer cells, gram positive and negative bacteria and pathogenic fungi. Furthermore, while this species is an excellent *in vitro* artificial metallonuclease, its induction of double strand DNA breaks (DSBs) in SK-OV-3 cells occur in a relatively low proportion of cells (~11%) only. Thus, **Cu-Phen** can be considered a “promiscuous” agent and most likely targets multiple cellular processes, via free-radical oxidative stress. The coordination of sterically functionalised carboxylates to this cation, however, results in series of compounds with enhanced DNA recognition, reduced albumin binding with improved cytoselectivity between human cancer cells, bacterial and fungal cells. Overall, the importance of inner-sphere modification by carboxylate ligands to the targeted biological application (genomic DNA damage) in this class of compound is evident as formate, acetate and pivalate complexes induce DSBs in a higher percentage of SK-OV-3 cells compared to the parent **Cu-Phen** complex. With this in mind, we are exploiting the possibility of generating engineered metallonucleases *via* functional modification to the organic group of the carboxylate anion. The synthetic methodology we have reported here could be a very effective approach and, in principle, would involve two synthetic steps. Firstly, a sequence-targeting protein or nucleic acid (T) is selected and attached via the organic group of the carboxylate ligand, T-RCOOH. Secondly, the sodium salt of this functionalised carboxylate, T-RCOO⁻Na⁺, is bound to the $[\text{Cu}(\text{1,10-phen})_2]^{2+}$ cation to form the engineered artificial metallonuclease, $[\text{T-RCOO-Cu}(\text{1,10-phen})_2]^+$.

IV.5 Experimental

Chemicals and deoxyribonucleic acid sodium salt from salmon testes were purchased from Sigma Aldrich (Ireland) and used without further purification. Ultra Pure ctDNA was supplied from Invitrogen (Cat.15633-019), supercoiled plasmid DNA (pBR322) was supplied by Roche Diagnostics Ltd. (UK) (Cat. 10481238001) or NEB (Cat. N3033L). Solid-state IR were recorded on a KBr matrix using a Nicolet FT-IR 5DXB FT-IR. Elemental analytical data for all complexes were recorded by the Microanalytical Laboratory, University College Dublin, Ireland and correspond to >95% purity. Electronic spectra were recorded at 25 °C in HPLC grade methanol using an Agilent Cary 100 spectrophotometer. Electrospray ionisation mass spectra were recorded on a Thermo Fisher Exactive Orbitrap mass spectrometer coupled to an Advion TriVersa Nanomate injection system. Note: although **Cu-Pro-Phen** and **Cu-Piv-Phen** crystallise with two independent cations in the asymmetric unit, both complexes were examined as monomeric cations in all biological tests conducted.

IV.5.1 Synthesis

[Cu(1,10-Phen)₂](NO₃)₂ (Cu-Phen) was obtained as a green solid by refluxing copper(II) nitrate hemi(pentahydrate) (0.51 g, 2.1 mmol) and 1,10 phenanthroline monohydrate (0.85 g, 4.2 mmol) in ethanol for 2 hours at 90 °C. On cooling to room temperature the product was filtrated, washed with a minimum amount of cold ethanol and then air-dried. Yield: 0.90 g (77 %). Anal. Calc. for C₂₄H₁₆CuN₆O₆: Percent calcd. C, 52.60; H, 2.92; N, 15.34, Percent found: C, 54.58; H, 2.98; N, 15.83 IR (KBr): 3415, 1513, 1386, 1363, 1297, 1034, 845, 718 cm⁻¹, UV-vis (methanol): λ_{d-d} = 709 nm, ε_{max} = 65.86 mol⁻¹ dm³ cm⁻¹.

[Cu(R-COO)(1,10-Phen)₂]⁺ general procedure: samples were obtained as blue crystals upon treating an aqueous solution of the sodium carboxylate salt with a methanolic solution of **Cu-Phen** (0.51g, 0.93 mmol) (1:1) in an methanol/aqueous (2:1 v/v) solution under stirring at room temperature for 15 min. The resulting clear, dark blue solutions were allowed to stand at room temperature and after slow evaporation blue prismatic crystals formed within 10 days. **Cu-For-Phen**, **[Cu(For)(1,10-Phen)₂](NO₃)·6H₂O**, empirical formula:

$C_{25}H_{29}CuN_5O_{11}$, 0.48 g (81 %); IR(KBr): 3436, 1611, 1584, 1514, 1424, 1383, 1348, 851, 723 cm^{-1} , UV-vis (methanol): $\lambda_{d-d} = 693$ nm, $\epsilon_{max} = 70.75$ $mol^{-1} dm^3 cm^{-1}$, solubility: MeOH, DMF, DMSO, H₂O (partially), ESI-MS: 468.06 $m/z = [M]^+$, 287.99 $m/z = [M - 1,10\text{-phenanthroline}]^+$. **Cu-Ace-Phen**, **[Cu(Ace)(1,10-Phen)₂](NO₃)₂·2H₂O**, empirical formula: $C_{26}H_{23}CuN_5O_7$, Yield: 0.49 g (91 %); IR(KBr): 3346, 1576, 1570, 1514, 1427, 1364, 846, 722, 675 cm^{-1} , UV-vis (methanol): $\lambda_{d-d} = 691$ nm, $\epsilon_{max} = 84.29$ $mol^{-1} dm^3 cm^{-1}$, solubility: MeOH, EtOH, DMF, DMSO (partially), ESI-MS: 482.08 $m/z = [M]^+$, 302.01 $m/z = [M - 1,10\text{-phenanthroline}]^+$. **Cu-Pro-Phen**, **[Cu(Pro)(1,10-Phen)]₂·½(CO₃)·4½H₂O**, empirical formula: $C_{27.50}H_{30}CuN_4O_8$ Yield: 0.41 g (72 %); IR(KBr): 3362, 1576, 1559, 1516, 1395, 1382, 849, 729 cm^{-1} , UV-vis (methanol): $\lambda_{d-d} = 696$ nm, $\epsilon_{max} = 79.40$ $mol^{-1} dm^3 cm^{-1}$, solubility: MeOH, EtOH, DMSO, DMF and CHCl₃ (partially), ESI-MS: 496.09 $m/z = [M]^+$, 316.03 $m/z = [M - 1,10\text{-phenanthroline}]^+$. **Cu-Iso-Phen**, **[Cu(Iso)(1,10-Phen)₂]₂·2(NO₃)·4H₂O**, empirical formula: $C_{28}H_{27}CuN_5O_7$ Yield: 0.37 g (65 %); IR(KBr): 3366, 1568, 1552, 1512, 1401, 1376, 1367, 851, 723 cm^{-1} , UV-vis (methanol): $\lambda_{d-d} = 698$ nm, $\epsilon_{max} = 79.65$ $mol^{-1} dm^3 cm^{-1}$, solubility: MeOH, DMF, CHCl₃, DMSO, ESI-MS: 510.11 $m/z = [M]^+$, 330.04 $m/z = [M - 1,10\text{-phenanthroline}]^+$. **Cu-Piv-Phen**, **[Cu(Piv)(1,10-Phen)₂]₂(piv)₂·(Hpiv)·9H₂O**, empirical formula: $C_{36.50}H_{48}CuN_4O_{9.50}$ Yield: 0.56 g (79 %); IR(KBr): 1545, 1516, 1478, 1369, 1363, 1229, 1103, 850, 721 cm^{-1} , UV-vis (methanol): $\lambda_{d-d} = 701$ nm, $\epsilon_{max} = 93.67$ $mol^{-1} dm^3 cm^{-1}$, solubility: MeOH, DMSO, ESI-MS: 522.23 $m/z = [M - 2H]^+$, 344.06 $m/z = [M - 1,10\text{-phenanthroline}]^+$.

IV.5.2 Electrochemistry

Cyclic Voltammetry experiments were performed on a Solartron 1825 potentiostat and data analysed using CorrView software. The concentrations of $[Cu(RCOO)(1,10\text{-phenanthroline})_2]^+$ complexes and Na-L-ascorbate were 1 mM and 2 mM (1:2 ratio), respectively, in all experiments and the CVs were scanned initially in the cathodic direction. The working electrode was Glassy Carbon (2 mm diameter), the reference electrode was a non-aqueous Ag⁺/Ag ($E_{1/2} = 0.075$ V versus Fc/Fc⁺), and the counter electrode was platinum. The supporting electrolyte was 0.1 M TBAPF₆ in 10% v/v DMF. Electrodes were polished using 0.05 micron aluminium oxide paste on microcloth (both Buehler) and sonicated

for ten minutes in ethanol prior to analysis. All quoted potentials were obtained at a scan rate of 100 mV s⁻¹.

IV.5.3 X-Ray Crystallography

Data were collected at 150(2)K on a Bruker Apex II CCD diffractometer using MoK α radiation (λ = 0.71073Å) (Table IV.7 and Appendix A.B.2). The structures were solved by direct methods and refined on F² using all the reflections with SHELXL or SHELXL2012.⁵⁵ Unless otherwise stated, all the non-hydrogen atoms were refined using anisotropic atomic displacement parameters and hydrogen atoms were inserted at calculated positions using a riding model. In **Cu-Ace-Phen** the coordinated nitrate anion is disordered over two positions and was refined with 85:15 occupancy of the sites. In **Cu-Pro-Phen** one of the phen groups is disordered and was modelled with 50:50 occupancy over two sites and the asymmetric unit contains two full-occupancy water molecules and four refined as 50% occupancy. The hydrogen atoms of the water molecules were not located and have not been included in the refinement. **Cu-Piv-Phen** was refined as a 2-component merohedral twin (twin matrix -1 0 0 0 1 0 0 1 -1 and BASF 0.21).

Table IV.7 Crystallographic data for the five carboxylate complexes generated

Identification code	Cu-For-Phen	Cu-Ace-Phen	Cu-Pro-Phen	Cu-Iso-Phen	Cu-Piv-Phen
Formula	[Cu(phen) ₂ (HCOO)] (NO ₃)·6H ₂ O	[Cu(phen) ₂ (OAc)] (NO ₃)·2H ₂ O	[Cu(phen) ₂ (pro)]· ½(CO ₃)·4½H ₂ O	[Cu(phen) ₂ (isobut)] ₂ · 2(NO ₃)·4H ₂ O	[Cu(phen) ₂ (piv)] ₂ (piv) ₂ · (Hpiv)·9H ₂ O
Empirical formula	C ₂₅ H ₂₉ CuN ₅ O ₁₁	C ₂₆ H ₂₃ Cu N ₅ O ₇	C _{27.50} H ₃₀ CuN ₄ O ₈	C ₂₈ H ₂₇ CuN ₅ O ₇	C _{36.50} H ₄₈ CuN ₄ O _{9.50}
Formula weight	639.07	581.03	608.09	609.09	758.33
Crystal system	Monoclinic	Triclinic	Monoclinic	Orthorhombic	Triclinic
Space group	P2 ₁ /n	P $\bar{1}$	C 2/c	P2 ₁ 2 ₁ 2 ₁	P $\bar{1}$
Unit cell a (Å)	14.8372(12)	8.5126(4)	31.873(5)	14.9422(10)	16.091(2)
b (Å)	12.4670(10)	10.3864(5)	12.4716(19)	17.0635(12)	17.367(2)
c (Å)	15.5706(12)	14.6033(6)	14.264(2)	21.2699(14)	17.454(2)
(°)	90	83.2710(10)	90	90	60.321(2)
(°)	109.0920(10)	82.9980(10)	93.879(2)	90	66.311(2)
(°)	90	76.2690(10)	90	90	89.747(2)
Volume (Å ³)	2721.8(4)	1239.68(10)	5656.9(15)	5423.1(6)	3762.8(9)
Z	4	2	8	8	4
Density calc. (Mg/m ³)	1.560	1.557	1.428	1.492	1.339
Absorption coeff (mm ⁻¹)	0.873	0.939	0.828	0.862	0.640
F(000)	1324	598	2528	2520	1600
Crystal description	blue plate	blue block	blue block	blue lath	blue plate
Reflections collected	22925	17094	23362	55103	29693
Independent refl [R _{int}]	5353 [0.0463]	6174 [0.0260]	5815 [0.0593]	13446 [0.0708]	13193 [0.0560]
Data / restraints / param	5353 / 18 / 415	6174 / 12 / 381	5815 / 984 / 527	13446 / 12 / 763	13193 / 27 / 974
Goodness-of-fit on F ²	1.068	1.054	1.050	1.004	1.046
R indices R1, wR2 [I>2σ(I)]	0.0463, 0.1232	0.0309, 0.0779	0.0943, 0.2839	0.0422, 0.0847	0.0643, 0.1663
R indices R1, wR2 (all data)	0.0659, 0.1361	0.0380, 0.0812	0.1419, 0.3299	0.0771, 0.0973	0.0960, 0.1891
Absolute structure param	n/a	n/a	n/a	-0.022(9)	n/a
Diff. peak and hole (e.Å ⁻³)	1.310 and -0.872	0.398 and -0.321	1.873 and -0.885	0.383 and -0.580	0.564 and -0.680

IV.5.4 Bovine Serum Albumin Binding

To a quartz cuvette containing 15 μ M of Bovine Serum Albumin (A7030, Sigma) in HEPES buffer (10 mM, pH = 7.2) and NaCl (25 mM), an aliquot of complex, ligand or metal salt was added and the resulting solution was incubated at 37°C for 5 min. Triplicate experiments were conducted, across a drug concentration range of 1–50 μ M, on an LS55 PerkinElmer Fluorescence Spectrometer using an excitation wavelength of 295 nm using a slit width of 7 nm. An emission wavelength of 350 nm was used for the quenching analysis of BSA.

IV.5.5 DNA Binding⁴⁸

IV.5.5.1 Competitive ethidium displacement. See section III.4.4.1

IV.5.5.2 DNA–ethidium fluorescence quenching. See section III.4.4.2

IV.5.5.2 Viscosity. See section III.5.6

IV.5.6 *In Vitro* Cytotoxicity with Human-Derived Cancer Cell Lines

The human ovarian cancer cell line SK-OV-3 (ATCC[®] HTB-77[™]), the human prostate cancer cell line PC-3 (ATCC[®] CRL-1435[™]) (ATCC, Manassas, VA, USA), the and the normal prostate epithelial cell PNT1A immortalised with SV40 (Sigma-Aldrich) were all grown in RPMI1640 (Sigma) supplemented with 2 mM L-glutamine and 10% fetal bovine serum (FBS) in T75 flasks (Nunc) in a 37 °C in a humidified atmosphere with 5% CO₂. Cells were maintained by splitting 70-80% confluent cultures with 0.25% trypsin/EDTA solution and seeding at high densities (2-4 x 10,000 cells/cm²). All drugs were tested on all cell lines using the 3-(4,5- dimethylthiazol-2-yl)-2,5-diphenyltetrazolium bromide (MTT) assay. The cells were trypsinised as described previously to obtain a cell suspension of each of the adherent cell lines. The cells were then counted on a coulter counter (Beckman Coulter) so that appropriate cell numbers could be plated in 96-well plates (Nunc) for the required timepoints of 24 h (2,500 cells) or 96 h (1,250 cells) exposures of cells to each compound. Each IC₅₀ value represents the mean of three independent experiments (\pm standard error).

IV.5.6.1 MTT assay This method is based on the reduction of the tetrazolium salt MTT into a crystalline blue formazan product by the cellular oxidoreductases of viable cells.⁵⁷ The resultant formazan crystal formation is proportional to the number of viable cells. Cells were seeded in 96-well plates and incubated at 37 °C in 5% CO₂ for 24 h to ensure attachment and growth of all cells. Cells were treated with a 4-log range of concentration of the test compounds, in triplicate, from 0.1 to 500 mM or with a solvent control (0.5% DMSO) in complete medium for 24 or 96 hr exposure times by incubation. The cells were then incubated with 20 µl of MTT (5 mg/ml) in 0.1 M phosphate-buffered saline (PBS), pH = 7.4, at 37 °C in a humid atmosphere with 5% CO₂ for 4 h. The medium was then gently aspirated from test cultures and 100 µl of DMSO was added to each well. The plates were then shaken for 2 min and the absorbance was read at 550 nm in a Varioscan plate reader. The IC₅₀ value was defined as the concentration of test compound required to reduce the absorbance of the MTT–formazan crystals by 50%, indicating 50% cell deactivation.

IV.5.7 Antibacterial Activity⁵⁸

In vitro antibacterial activities of the compounds were evaluated on a panel of three ATCC strains (*Staphylococcus aureus* ATCC 6538, *Escherichia coli* ATCC 8739, *Pseudomonas aeruginosa* ATCC 9027) and five clinical isolates (*Staphylococcus aureus* MRSA HK5996/08, *Staphylococcus epidermidis* HK6966/08, *Enterococcus* sp. HK14365/08, *Klebsiella pneumoniae* HK11750/08, *Klebsiella pneumoniae* ESBL HK14368/08) from the collection of fungal strains deposited at the Department of Biological and Medical Sciences, Faculty of Pharmacy, Charles University, Hradec Králové, Czech Republic. The above-mentioned ATCC strains also served as the quality control strains. All the isolates were maintained on Mueller-Hinton agar prior to being tested. Dimethyl sulfoxide (100%) served as a diluent for all compounds; the final concentration did not exceed 2%. Mueller-Hinton agar (MH, HiMedia, Čadersky-Envitek, Czech Republic) buffered to pH 7.4 (±0.2) was used as the test medium. The wells of the microdilution tray contained 200 µL of the Mueller-Hinton medium with 2-fold serial dilutions of the compounds (1000 to 0.244 µmol/L) and 10 µL of inoculum suspension. Inoculum in MH medium was prepared to give a final concentration of 0.5 McFarland scale (1.5×10^8 cfu.mL⁻¹). The trays were

incubated at 37 °C and MICs were read visually after 24 h and 48 h. The MICs were defined as 95% inhibition of the control growth. MICs were determined twice and in duplicate. The deviations from the usually obtained values were no higher than the nearest concentration value up and down the dilution scale.

IV.5.8. Antifungal Activity^{59,60}

In vitro antifungal activities of the compounds were evaluated on a panel of four ATCC strains (*Candida albicans* ATCC 44859, *Candida albicans* ATCC 90028, *Candida parapsilosis* ATCC 22019, *Candida krusei* ATCC 6258) and eight clinical yeast isolates (*Candida krusei* E28, *Candida tropicalis* 156, *Candida glabrata* 20/I, *Candida lusitaniae* 2446/I, *Trichosporon asahii* 1188) and filamentous fungi (*Aspergillus fumigatus* 231, *Absidia corymbifera* 272, *Trichophyton mentagrophytes* 445) from the collection of fungal strains deposited at the Department of Biological and Medical Sciences, Faculty of Pharmacy, Charles University, Hradec Králové, Czech Republic. Three ATCC strains were used as the quality control strains. All of the isolates were maintained on Sabouraud dextrose agar prior to being tested. Minimum inhibitory concentrations (MICs) were determined by modified CLSI standard of microdilution format of the M27-A3 and M38-A2 documents.^{59,60} Dimethyl sulfoxide (100 %) served as a diluent for all compounds; the final concentration did not exceed 2%. RPMI 1640 (Sevapharma, Prague) medium supplemented with L-glutamine and buffered with 0.165 M morpholinepropanesulfonic acid (Serva) to pH 7.0 by 10 M NaOH was used as the test medium. The wells of the microdilution tray contained 200 µL of the RPMI 1640 medium with 2- fold serial dilutions of the compounds (1000 to 0.244 µmol/L for the new compounds) and 10 µL of inoculum suspension. Fungal inoculum in RPMI 1640 was prepared to give a final concentration of $5 \times 10^3 \pm 0.2$ cfu.mL⁻¹. The trays were incubated at 35 °C and MICs were read visually after 24 h and 48 h. The MIC values for the dermatophytic strain (*T. mentagrophytes*) were determined after 72 h and 120 h. The MICs were defined as 80% inhibition (IC₈₀) of the control growth for yeasts and as 50% inhibition (IC₅₀) of the control growth for filamentous fungi. MICs were determined twice and in duplicate. The deviations from the usually obtained values were no higher than the nearest concentration value up and down the dilution scale.

IV.5.9 DNA Cleavage Studies

IV.5.9.1 Nuclease activity using plasmid pBR322 Reactions were carried out according to the literature procedure.³ Briefly, in a total volume of 20 μ L using 80 mM HEPES buffer (Fisher) at pH 7.2 with 25 mM NaCl, an aliquot of the stock complex (prepared in DMF) was mixed with 400 ng of supercoiled pBR322 (Roche) and/or 400 ng of linearised pBR322 (see ESI for procedure) and 1 μ L of 20 mM Na-L-ascorbate and/or H₂O₂ where appropriate. Samples were incubated at 37 °C before being quenched with 6x loading dye (Fermentas), containing 10 mM Tris-HCl (pH 7.6), 0.03% bromophenol blue, 0.03% xylene cyanol, 60% glycerol and 60 mM EDTA, then loaded onto agarose gel (1%) containing 2.0 μ L of GelRedTM (10,000X). Electrophoresis was completed at 80 V for 1.5 h using a wide mini-sub cell (BioRad) in 1xTAE buffer (Millipore).

IV.5.10 Quantitation of Hydrogen Peroxide with Amplex Red

A 5 mL stock solution of 100 μ M Amplex Red containing 10 mM Amplex Red reagent and 10 U/ml horseradish Peroxidase (HRP) was prepared in 1x buffer as per Amplex Red hydrogen peroxide/peroxidase assay kit (Invitrogen, A22188). A standard fluorescence response curve from H₂O₂ was obtained by adding a series of aliquots (0.5 – 5 μ M) H₂O₂ to 50 μ L Amplex Red stock solution and the volume was adjusted to 100 μ L with 1x buffer in each well. An aliquot containing 5 μ M of tested compounds, 5 μ M H₂O₂ and 100 μ M Na-L-Ascorbate (where appropriate) previously incubated for 30-120 min were added to 50 μ L Amplex Red solution and the volume was adjusted to 100 μ L using 1x buffer. The fluorescence intensity of the reaction mixture was measured with a Bio-Tek synergy HT multi-mode microplate reader equipped with filter set for excitation and emission at 530 nm and 590 nm.⁶¹

IV.5.11 Detection of double-strand DNA breaks (DSBs) within SK-OV-3 Cancer cells

The ability of the complexes, metal-free 1,10-phenanthroline and cisplatin to induce DSBs within SK-OV-3 cells was determined using immunodetection of γ H2AX foci. DSBs were visualized via confocal microscopy using an LSM 510 META laser scanning microscope equipped with an argon laser (488 nm) and HeNe laser (543 nm) and quantified via flow cytometry using a CyFlow Space

Flow cytometer equipped with a blue diode pumped solid-state laser (488 nm). SK-OV-3 cells were exposed to an IC₂₅ dose of tested compound over 24 h and were then incubated for 2 h with the primary antibody (anti-phosphohistone H2A.X (Ser139), clone JBW301, mouse; Millipore) and thereafter with the fluorescein isothiocyanate (FITC)-labeled secondary antibody (Alexa Fluor 488 goat anti-mouse immunoglobulin G; Invitrogen) for 1 h in darkness. For visualization of the nucleus, cells were stained with the fluorescent DNA intercalator propidium iodide (PI). After exposure, the drug-treated and control cells were divided equally, with 50% being used for confocal analysis and 50% for flow cytometry. Flow analysis was conducted in triplicate for three independent experiments. Full experimental details are similar to those recently reported by Schmitz and colleagues.⁶²

IV.6 Methods

IV.6.1 Crystallography

IV.6.1.1 Computing details Data collection: Bruker *APEX2*, for cell refinement: Bruker *SAINT*; data reduction: Bruker *SAINT*; program(s) used to solve structure: *SHELXS97* (Sheldrick, 2008). Program(s) used to refine structure: *SHELXL97* (Sheldrick, 2008) for **Cu-for-phen**, **Cu-ace-phen**, **Cu-iso-phen**; *SHELXL2012* (Sheldrick, 2012) for **Cu-pro-phen**, **Cu-piv-phen**. For all compounds, molecular graphics: Bruker *SHELXTL*; software used to prepare material for publication: Bruker *SHELXTL*.

IV.6.1.2 Solution and Refinement Data were collected at 150(2)K on a Bruker Apex II CCD diffractometer using MoK α radiation ($\lambda = 0.71073\text{\AA}$). The structures were solved by direct methods and refined on F^2 using all the reflections.⁶³ The weighted R-factor wR and goodness of fit S are based on F^2 , conventional R-factors R are based on F, with F set to zero for negative F^2 . The threshold expression of $F^2 > 2\sigma(F^2)$ is used only for calculating R-factors(gt) etc. and is not relevant to the choice of reflections for refinement. R-factors based on F^2 are statistically about twice as large as those based on F, and R-factors based on ALL data will be even larger. Unless otherwise stated, all the non-hydrogen atoms were refined using anisotropic atomic displacement parameters and hydrogen atoms were inserted at calculated positions using a riding model.

IV.6.1.3 Geometry All esds (except the esd in the dihedral angle between two l.s. planes) are estimated using the full covariance matrix. The cell esds are taken into account individually in the estimation of esds in distances, angles and torsion angles; correlations between esds in cell parameters are only used when they are defined by crystal symmetry. An approximate (isotropic) treatment of cell esds is used for estimating esds involving l.s. planes.

IV.6.2 Electrospray ionisation mass spectra (ESI-MS)

Samples were prepared in 100% methanol prior to electrospray ionisation mass spectra analysis recorded on a Thermo Fisher ExactiveOrbitrap mass spectrometer coupled to an AdvionTriVersaNanomate injection system.

IV.6.3 Linearisation of pBR322

In a total volume of 20 μL using 5 μL of 1 $\mu\text{g}/\mu\text{L}$ supercoiled pBR322 (NEB), 5 μL of 10 x HEPES, 2.5 μL of 20,000 U/mL EcoRV (NEB) or 2.5 μL of 20,000 U/mL HindIII (NEB), 5 μL of NeBuffer 3 or 5 μL of NeBuffer 2 (NEB), 1 μL BSA (NEB) (where appropriate) and nuclease free H_2O were added to bring up volume to 20 μL . This mixture was allowed to incubate at 37 $^{\circ}\text{C}$ for 2.5 h. 1 μL of the mixture was loaded onto agarose gel and run at 70 V for 30 min to confirm linearization. Linear DNA from the mixture was then cleaned up from the enzymatic reactions, using QIAquick Purification Protocol (QIAGEN) as per manual instructions. The linear DNA obtained was quantified using the NanoDrop, ND-1000 Spectrophotometer.

IV.6.4 Electrochemical Stability of Complexes

The electrochemical stability of the Cu complexes was investigated over a period of 13 hours. Voltammograms were performed on 1 mM solutions of Cu complex every 4 hours to monitor any changes in redox behaviour. Deviation from the complex redox profiles, performed in freshly prepared samples, would indicate complex instability. Negligible changes in the solution phase electrochemistry was observed for all complexes - the electrochemical stability of Cu-For-Phen over the 13 hour time period is displayed in Fig. IV.14(a) to illustrate this point. Further evidence that the complexes remain structurally intact is shown in Fig. IV.14(b), where the redox profile of $[\text{Cu}(1,10\text{phenanthroline})]^{2+}(\text{NO}_3^-)_2$ is compared to that of $[\text{Cu}(\text{bis-}1,10\text{ phenanthroline})]^{2+}(\text{NO}_3^-)_2$. The Cu mono-phen

complex exhibits poor reversibility, with ill-defined redox peaks and corresponding low currents. In addition, on continuous potential cycling of a GC electrode in the Cu mono-phen solution, some copper deposition onto the GC surface is observed. In contrast, the electrochemical activity of the Cu bis-phen complex is very well defined and exhibits near reversible ($\Delta E_p = 69$ mV) redox behaviour at this scan rate.

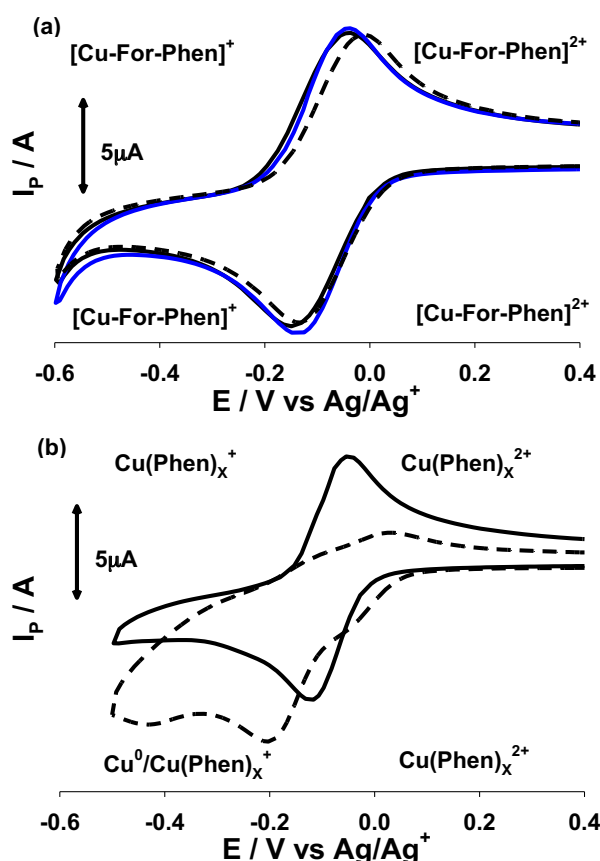


Figure IV.53 Typical cyclic voltammogram traces, recorded at a scan rate of 100 mV s^{-1} , for (a) 1 mM solution of Cu-For-Phen, after 1 hour (solid black trace), 4 hours (solid blue trace), and 13 hours (dashed trace); (b) 1 mM solutions of Cu(bis-phen), (solid trace), and Cu(mono-phen), (dashed trace). Experimental conditions; glassy carbon working electrode, platinum counter electrode, non-aqueous Ag / Ag^+ reference electrode, 0.1M TBAPF₆ in 10% v/v DMF.

IV.6.5 UV-vis stability studies

The UV-vis spectrophotometric stability of all Cu^{2+} complexes were investigated over a period of 10 days and were compared with $[\text{Cu}(1,10\text{-phen})]^{2+}$ and $[\text{Cu}(1,10\text{-phen})_2]^{2+}$ complexes. Scans were performed, at 5 mM in 80 mM HEPES with 3.5 % v/v methanol, every 24 h between 400 and 900 nm.

Negligible changes to the absorption maxima and intensity were observed for all complexes and are presented in Fig. IV.15*i*. Further evidence that the complexes remain structurally intact, is illustrated in Fig. IV.15*ii*., where the absorption spectra of $[\text{Cu}(1,10\text{-phen})]^{2+}$ (mono-phen) is shown along with $[\text{Cu}(1,10\text{-phen})_2]^{2+}$ (bis-phen). The absorption maximum ($\lambda_{\text{d-d}}$) of the mono-phen complex was found to be 644 nm, whereas the absorption maximum of bis-phen was 697 nm.

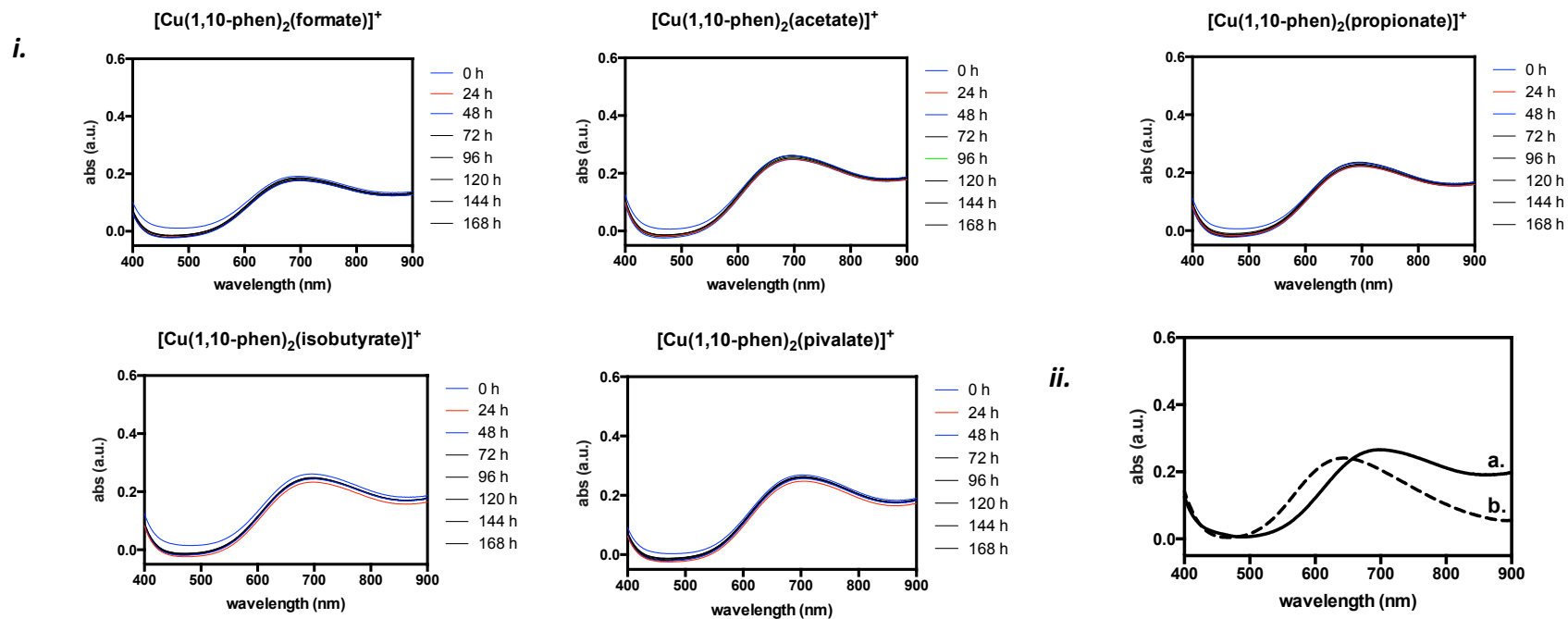


Figure IV.54 Absorption spectra of *i.* 5 mM $[\text{Cu}(1,10\text{-phen})(\text{R-COO})]^{2+}$ in 80 mM HEPES with 3.5% v/v methanol between 0- 168 h, recorded every 24 h, *ii.* Absorption spectra of 5 mM Cu-bis-phen (*a.*) and Cu-mono-phen (*b.*) in 80 mM HEPES.

References

1. Pitie, M.; Pratviel, G. Activation of DNA carbon-hydrogen bonds by metal complexes. *Chem. Rev.* **2010**, 110, 1018-59.
2. Meunier, B. *DNA and RNA Cleavers and Chemotherapy of Cancer and Viral Diseases*. Kluwer Academic Publishers: London, 1995; Vol. 479.
3. Sigman, D. S.; Graham, D. R.; D'Aurora, V.; Stern, A. M. Oxygen-dependent cleavage of DNA by the 1,10-phenanthroline . cuprous complex. Inhibition of Escherichia coli DNA polymerase I. *J. Biol. Chem.* **1979**, 254, 12269-72.
4. Marshall, L. E.; Graham, D. R.; Reich, K. A.; Sigman, D. S. Cleavage of Mmmmethodsdeoxyribonucleic acid by the 1,10-phenanthroline-cuprous complex. Hydrogen peroxide requirement and primary and secondary structure specificity. *Biochem.* **1981**, 20, 244-250.
5. Thederahn, T. B.; Kuwabara, M. D.; Larsen, T. A.; Sigman, D. S. Nuclease activity of 1,10-phenanthroline-copper: kinetic mechanism. *J. Am. Chem. Soc.* **1989**, 111, 4941-4946.
6. Sigman, D. S. Chemical nucleases. *Biochem.* **1990**, 29, 9097-105.
7. Sigman, D. S.; Mazumder, A.; Perrin, D. M. Chemical Nucleases. *Chem. Rev.* **1993**, 93, 2295-2316.
8. Pratviel, G.; Bernadou, J.; Meunier, B. Carbon—Hydrogen Bonds of DNA Sugar Units as Targets for Chemical Nucleases and Drugs. *Angew. Chem. Int. Ed. Engl.* **1995**, 34, 746-769.
9. Sigman, D. S.; Bruice, T. W.; Mazumder, A.; Sutton, C. L. Targeted Chemical Nucleases. *Acc. Chem. Res.* **1993**, 26, 98-104.
10. Bruice, T. W.; Wise, J. G.; Rosser, D. S. E.; Sigman, D. S. Conversion of .lambda. phage Cro into an operator-specific nuclease. *J. Am. Chem. Soc.* **1991**, 113, 5446-5447.
11. Pitie, M.; Meunier, B. Preparation of a spermine conjugate of the bis-phenanthroline ligand Clip-Phen and evaluation of the corresponding copper complex. *Bioconjug. Chem.* **1998**, 9, 604-11.
12. Pitie, M.; Burrows, C. J.; Meunier, B. Mechanisms of DNA cleavage by copper complexes of 3-clip-phen and of its conjugate with a distamycin analogue. *Nucleic Acids Res.* **2000**, 28, 4856-64.

13. Hoog, P.; Boldron, C.; Gamez, P.; Slidregt-Bol, K.; Roland, I.; Pitie, M.; Kiss, R.; Meunier, B.; Reedijk, J. New approach for the preparation of efficient DNA cleaving agents: ditopic copper-platinum complexes based on 3-Clip-Phen and cisplatin. *J. Med. Chem.* **2007**, 50, 3148-52.
14. Bales, B. C.; Pitie, M.; Meunier, B.; Greenberg, M. M. A minor groove binding copper-phenanthroline conjugate produces direct strand breaks via beta-elimination of 2-deoxyribonolactone. *J. Am. Chem. Soc.* **2002**, 124, 9062-3.
15. Lembach, K. J.; Dobkin, M. B.; Louie, R. E. *Virus Inactivation in Plasma Products: Inactivation of Viruses with 1,10-Phenanthroline*. S Karger Pub: 1989.
16. Kito, M.; Takenaka, Y.; Urade, R. The 1,10-phenanthroline micelles-copper(I) complex catalyzes protein degradation. *FEBS Lett.* **1995**, 362, 39-42.
17. Blank, F. In vitro fungistatic action of phenanthrolines against pathogenic fungi. *Nat.* **1951**, 168, 516-7.
18. McCann, M.; Kellett, A.; Kavanagh, K.; Devereux, M.; Santos, A. L. Deciphering the Antimicrobial Activity of Phenanthroline Chelators. *Curr. Med. Chem.* **2012**, 19, 2703-14.
19. Macleod, R. A. The toxicity of o-phenanthroline for lactic acid bacteria. *J. Biol. Chem.* **1952**, 197, 751-61.
20. McCann, M.; Devereux, M.; Santos, A. L. S.; Hilger, R. A.; Silva, B. A.; Romanos, M. T. V.; Pyrrho, A. S.; Kavanagh, K.; Fichtner, I.; Kellett, A. In vitro and in vivo studies of the biological activities of 1,10-phenanthroline, 1,10-phenanthroline-5,6-dione and copper(II) and silver(I) perchlorate complexes of 1,10-phenanthroline-5,6-dione. *Tox. Res.* **2012**, 1, 47-54.
21. Heffeter, P.; Jakupec, M. A.; Korner, W.; Wild, S.; von Keyserlingk, N. G.; Elbling, L.; Zorbas, H.; Korynevskaya, A.; Knasmüller, S.; Sutterluty, H.; Micksche, M.; Keppler, B. K.; Berger, W. Anticancer activity of the lanthanum compound [tris(1,10-phenanthroline)lanthanum(III)]trithiocyanate (KP772; FFC24). *Biochem. Pharmacol.* **2006**, 71, 426-40.
22. Narla, R. K.; Dong, Y.; D'Cruz, O. J.; Navara, C.; Uckun, F. M. Bis(4,7-dimethyl-1,10-phenanthroline) sulfatooxovanadium(IV) as a novel apoptosis-inducing anticancer agent. *Clin. Cancer Res.* **2000**, 6, 1546-56.
23. Coyle, B.; Kavanagh, K.; McCann, M.; Devereux, M.; Geraghty, M. Mode of anti-fungal activity of 1,10-phenanthroline and its Cu(II), Mn(II) and Ag(I) complexes. *Biometals* **2003**, 16, 321-9.

24. Randford, A. D.; Sadler, P. J. Cytotoxicity and antiviral activity of transition-metal salicylato complexes and crystal structure of Bis(diisopropylsalicylato)(1,10-phenanthroline)copper(II). *Dalton Trans.* **1993**, 3393-3399.
25. Niyazi, H.; Hall, J. P.; O'Sullivan, K.; Winter, G.; Sorensen, T.; Kelly, J. M.; Cardin, C. J. Crystal structures of Lambda-[Ru(phen)₂dppz]²⁺ with oligonucleotides containing TA/TA and AT/AT steps show two intercalation modes. *Nat. Chem.* **2012**, 4, 621-628.
26. Song, H.; Kaiser, J. T.; Barton, J. K. Crystal structure of Delta-[Ru(bpy)₂dppz]²⁺ bound to mismatched DNA reveals side-by-side metalloinsertion and intercalation. *Nat. Chem.* **2012**, 4, 615-620.
27. Komor, A. C.; Schneider, C. J.; Weidmann, A. G.; Barton, J. K. Cell-Selective Biological Activity of Rhodium Metalloinsertors Correlates with Subcellular Localization (vol 134, pg 19223, 2012). *J. Amer. Chem. Soc.* **2013**, 135, 2863-2863.
28. Tardito, S.; Marchio, L. Copper compounds in anticancer strategies. *Curr. Med. Chem.* **2009**, 16, 1325-48.
29. Ruiz-Azuara, L.; Bravo-Gomez, M. E. Copper compounds in cancer chemotherapy. *Curr. Med. Chem.* **2010**, 17, 3606-15.
30. Anbu, S.; Kandaswamy, M.; Kamalraj, S.; Muthumarry, J.; Varghese, B. Phosphatase-like activity, DNA binding, DNA hydrolysis, anticancer and lactate dehydrogenase inhibition activity promoting by a new bis-phenanthroline dicopper(II) complex. *Dalton Trans.* **2011**, 40, 7310-8.
31. Silva, P. P.; Guerra, W.; Silveira, J. N.; Ferreira, A. M. D.; Bortolotto, T.; Fischer, F. L.; Terenzi, H.; Neves, A.; Pereira-Maia, E. C. Two New Ternary Complexes of Copper(II) with Tetracycline or Doxycycline and 1,10-Phenanthroline and Their Potential as Antitumoral: Cytotoxicity and DNA Cleavage. *Inorg. Chem.* **2011**, 50, 6414-6424.
32. Ramakrishnan, S.; Shakthipriya, D.; Suresh, E.; Periasamy, V. S.; Akbarsha, M. A.; Palaniandavar, M. Ternary Dinuclear Copper(II) Complexes of a Hydroxybenzamide Ligand with Diimine Coligands: the 5,6-dmp Ligand Enhances DNA Binding and Cleavage and Induces Apoptosis. *Inorg. Chem.* **2011**, 50, 6458-6471.

33. Rajendiran, V.; Karthik, R.; Palaniandavar, M.; Stoeckli-Evans, H.; Periasamy, V. S.; Akbarsha, M. A.; Srinag, B. S.; Krishnamurthy, H. Mixed-ligand Copper(II)-phenolate complexes: Effect of coligand on enhanced DNA and protein binding, DNA cleavage, and anticancer activity. *Inorganic Chemistry* **2007**, 46, 8208-8221.
34. Zhang, S. C.; Zhu, Y. G.; Tu, C.; Wei, H. Y.; Yang, Z.; Lin, L. P.; Ding, J.; Zhang, J. F.; Guo, Z. J. A novel cytotoxic ternary copper(II) complex of 1,10-phenanthroline and L-threonine with DNA nuclease activity. *J. Inorg. Biochem.* **2004**, 98, 2099-2106.
35. Terenzi, A.; Tomasello, L.; Spinello, A.; Bruno, G.; Giordano, C.; Barone, G. (Dipyrido[3,2-a:2',3'-c]phenazine)(glycinato)copper(II) perchlorate: a novel DNA-intercalator with anti-proliferative activity against thyroid cancer cell lines. *J. Inorg. Biochem.* **2012**, 117, 103-10.
36. Alemon-Medina, R.; Brena-Valle, M.; Munoz-Sanchez, J. L.; Gracia-Mora, M. I.; Ruiz-Azuara, L. Induction of oxidative damage by copper-based antineoplastic drugs (Casiopeinas). *Cancer Chemother. Pharmacol.* **2007**, 60, 219-28.
37. Trejo-Solis, C.; Palencia, G.; Zuniga, S.; Rodriguez-Ropon, A.; Osorio-Rico, L.; Luvia, S. T.; Gracia-Mora, I.; Marquez-Rosado, L.; Sanchez, A.; Moreno-Garcia, M. E.; Cruz, A.; Bravo-Gomez, M. E.; Ruiz-Ramirez, L.; Rodriguez-Enriquez, S.; Sotelo, J. Cas IIgly induces apoptosis in glioma C6 cells in vitro and in vivo through caspase-dependent and caspase-independent mechanisms. *Neoplasia* **2005**, 7, 563-74.
38. Trejo-Solis, C.; Jimenez-Farfan, D.; Rodriguez-Enriquez, S.; Fernandez-Valverde, F.; Cruz-Salgado, A.; Ruiz-Azuara, L.; Sotelo, J. Copper compound induces autophagy and apoptosis of glioma cells by reactive oxygen species and JNK activation. *BMC Cancer* **2012**, 12, 156.
39. Kellett, A.; Howe, O.; O'Connor, M.; McCann, M.; Creaven, B. S.; McClean, S.; Foltyn-Arfa Kia, A.; Casey, A.; Devereux, M. Radical-induced DNA damage by cytotoxic square-planar copper(II) complexes incorporating o-phthalate and 1,10-phenanthroline or 2,2'-dipyridyl. *Free Radic. Biol. Med.* **2012**, 53, 564-76.
40. O'Connor, M.; Kellett, A.; McCann, M.; Rosair, G.; McNamara, M.; Howe, O.; Creaven, B. S.; McClean, S.; Kia, A. F.; O'Shea, D.; Devereux, M.

Copper(II) complexes of salicylic acid combining superoxide dismutase mimetic properties with DNA binding and cleaving capabilities display promising chemotherapeutic potential with fast acting in vitro cytotoxicity against cisplatin sensitive and resistant cancer cell lines. *J. Med. Chem.* **2012**, 55, 1957-68.

41. Kellett, A.; O'Connor, M.; McCann, M.; McNamara, M.; Lynch, P.; Rosair, G.; McKee, V.; Creaven, B.; Walsh, M.; McClean, S.; Foltyn, A.; O'Shea, D.; Howe, O.; Devereux, M. Bis-phenanthroline copper(II) phthalate complexes are potent in vitro antitumour agents with 'self-activating' metallo-nuclease and DNA binding properties. *Dalton Trans.* **2011**, 40, 1024-7.

42. Prisecaru, A.; Devereux, M.; Barron, N.; McCann, M.; Colleran, J.; Casey, A.; McKee, V.; Kellett, A. Potent oxidative DNA cleavage by the di-copper cytotoxin: $[\text{Cu}_2(\mu\text{-terephthalate})(1,10\text{-phen})_4]^{2+}$. *Chem. Comm.* **2012**, 48, 6906-8.

43. Cater, M. A.; Pearson, H. B.; Wolyniec, K.; Klaver, P.; Bilandzic, M.; Paterson, B. M.; Bush, A. I.; Humbert, P. O.; La Fontaine, S.; Donnelly, P. S.; Haupt, Y. Increasing Intracellular Bioavailable Copper Selectively Targets Prostate Cancer Cells. *ACS Chem. Biol.* **2013**.

44. Palanimuthu, D.; Shinde, S. V.; Somasundaram, K.; Samuelson, A. G. In vitro and in vivo anticancer activity of copper bis(thiosemicarbazone) complexes. *J. Med. Chem.* **2013**, 56, 722-34.

45. Gutteridge, J. M.; Halliwell, B. The role of the superoxide and hydroxyl radicals in the degradation of DNA and deoxyribose induced by a copper-phenanthroline complex. *Biochem. Pharmacol.* **1982**, 31, 2801-5.

46. Nakamoto, K. *Infrared and Raman Spectra of Inorganic and Coordination Compounds*. 5th ed.; John Wiley and Sons: 1997; Vol. B.

47. Lakowicz, J. R. Quenching of Fluorescence. In *Principles of Fluorescence Spectroscopy*, Springer: 2006; pp 278-327.

48. McCann, M.; McGinley, J.; Ni, K.; O'Connor, M.; Kavanagh, K.; McKee, V.; Colleran, J.; Devereux, M.; Gathergood, N.; Barron, N.; Prisecaru, A.; Kellett, A. A new phenanthroline-oxazine ligand: synthesis, coordination chemistry and atypical DNA binding interaction. *Chem. Comm.* **2013**, 49, 2341-3.

49. Jenkins, T. C. Optical Absorbance and Fluorescence Techniques for Measuring DNA-Drug Interactions. In *Methods in Molecular Biology*, Vol. 90:

Drug-DNA Interaction Protocols, Fox, K. R., Ed. Humana Press: New Jersey, 1997.

50. Goldstein, S.; Michel, C.; Bors, W.; Saran, M.; Czapski, G. A critical reevaluation of some assay methods for superoxide dismutase activity. *Free Radic. Biol. Med.* **1988**, 4, 295-303.

51. Kuo, L. J.; Yang, L. X. Gamma-H2AX - a novel biomarker for DNA double-strand breaks. *In Vivo* **2008**, 22, 305-9.

52. Paull, T. T.; Rogakou, E. P.; Yamazaki, V.; Kirchgessner, C. U.; Gellert, M.; Bonner, W. M. A critical role for histone H2AX in recruitment of repair factors to nuclear foci after DNA damage. *Curr. Biol.* **2000**, 10, 886-95.

53. Bonner, W. M.; Redon, C. E.; Dickey, J. S.; Nakamura, A. J.; Sedelnikova, O. A.; Solier, S.; Pommier, Y. GammaH2AX and cancer. *Nat. Rev. Cancer* **2008**, 8, 957-67.

54. Clingen, P. H.; Wu, J. Y.; Miller, J.; Mistry, N.; Chin, F.; Wynne, P.; Prise, K. M.; Hartley, J. A. Histone H2AX phosphorylation as a molecular pharmacological marker for DNA interstrand crosslink cancer chemotherapy. *Biochem. Pharmacol.* **2008**, 76, 19-27.

55. Sheldrick, G. M. A short history of SHELX. *Acta Cryst.* **2008**, A64, 112-122.

56. Liu, Y. C.; Chen, Z. F.; Liu, L. M.; Peng, Y.; Hong, X.; Yang, B.; Liu, H. G.; Liang, H.; Orvig, C. Divalent later transition metal complexes of the traditional chinese medicine (TCM) liriodenine: coordination chemistry, cytotoxicity and DNA binding studies. *Dalton Trans.* **2009**, 10813-23.

57. Mosmann, T. Rapid colorimetric assay for cellular growth and survival: application to proliferation and cytotoxicity assays. *J. Immunol. Methods* **1983**, 65, 55-63.

58. *Methods for Dilution Antimicrobial Susceptibility Tests for Bacteria that Grow Aerobically. Approved Standard – Seventh Edition, Document M07-A.* Clinical Laboratory Standards Institute: Wayne, PA, 2006.

59. *Reference Method for Broth Dilution Antifungal Susceptibility Testing of Yeasts. Approved standard. Document M27-A3.* Clinical Laboratory Standard Institute: Wayne, PA, 2008.

60. *Reference Method for Broth Dilution Antifungal Susceptibility Testing of Filamentous Fungi. Approved standard. Document M38-A2.* . Clinical Laboratory Standard Institute: Wayne, PA, 2008.
61. Rhee, S. G.; Chang, T. S.; Jeong, W.; Kang, D. Methods for detection and measurement of hydrogen peroxide inside and outside of cells. *Mol. Cells* **2010**, 29, 539-49.
62. Brzozowska, K.; Pinkawa, M.; Eble, M. J.; Muller, W. U.; Wojcik, A.; Kriehuber, R.; Schmitz, S. In vivo versus in vitro individual radiosensitivity analysed in healthy donors and in prostate cancer patients with and without severe side effects after radiotherapy. *Int. J. Radiat. Biol.* **2012**, 88, 405-13.
63. G.M. Sheldrick, *ActaCryst.* 2008, A64, 112-122

Chapter V

Copper Phenanthrene Oxidative Chemical Nucleases

This paper was published in *Inorganic Chemistry*, 2014, **53**, 10, pp5392-5404

Prisecaru A., Molphy Z., Slator C., Barron, N., McCann M., Colleran J., Chandran D., Gathergood N. and Kellett A.

My contribution to this paper is: Manuscript 1st author with Zara Molphy, chemical nuclease activity using the “on chip” microfluidic analysis and the comparison study of different DNA plasmids cleavage activity. Contributed with DNA quenching and T_M of poly[d(G-C)₂] and poly[d(A-T)₂] synthetic nucleotides.

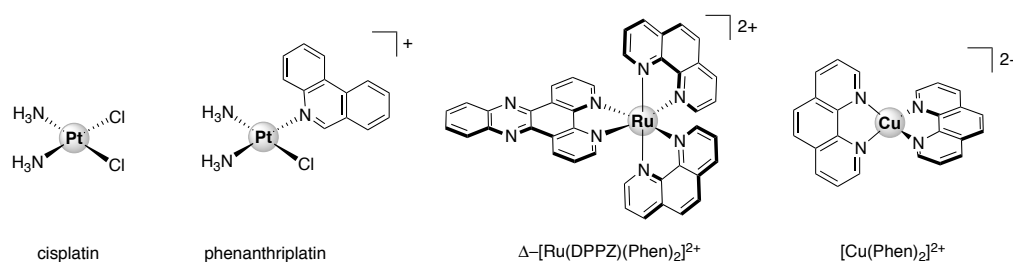
V.1. Abstract

Here we report the synthesis and isolation of a series of bis-chelate Cu^{2+} phenanthroline–phenazine cationic complexes of $[\text{Cu}(\text{DPQ})(\text{Phen})]^{2+}$, $[\text{Cu}(\text{DPPZ})(\text{Phen})]^{2+}$ and $[\text{Cu}(\text{DPPN})(\text{Phen})]^{2+}$ (where DPQ = dipyridoquinoxaline, DPPZ = dipyridophenazine and DPPN = benzo[*i*]dipyridophenazine). These compounds have enhanced DNA recognition relative to the well studied chemical nuclease, $[\text{Cu}(\text{Phen})_2]^{2+}$ (bis-Phen), with calf thymus DNA binding constants of DPQ and DPPZ agents ($\sim 10^7 \text{ M}(\text{bp})^{-1}$) being the highest currently known for Cu^{2+} phenanthrene compounds. Complex DNA binding follows $\text{DPQ} \approx \text{DPPZ} > \text{DPPN} > \text{bis-Phen}$ with fluorescence quenching and thermal melting experiments on poly[d(A-T)₂] and poly[d(G-C)₂] supporting intercalation at both the minor and major groove. Phenazine complexes, however, show enhanced targeting and oxidative cleavage on CpG rich DNA, and have comparable *in vitro* cytotoxicity toward the cisplatin resistant ovarian cancer line SKOV3, as the clinical oxidative DNA damaging drug, doxorubicin (adriamycin). In this study we also describe how a novel “on chip” method devised for the Bioanalyser 2100 was employed to quantify dsDNA damage, with high precision, by the complex series on pUC19 DNA (49% A-T, 51% G-C). Both DPQ and bis-Phen complexes are highly efficient oxidizers of pUC19, with DPQ being the most active of the overall series. It is apparent therefore, that oxidative chemical nuclease activity on homogenous canonical DNA is not entirely dependent on dynamic nucleotide binding affinity or intercalation and this observation is corroborated through catalytic interactions with the superoxide anion radical and Fenton breakdown of hydrogen peroxide.

V.2. Introduction

The advent of coordinating phenanthrene-based intercalators to transition metal cations has unveiled a new frontier for DNA-targeted metallodrug development.¹ While the application of *cis*-diamminedichloroplatinum(II) (cisplatin) continues to be a cornerstone of modern cancer chemotherapy,² the functionalisation of this agent with intercalating ligands³ and the construction of non-platinum metallo-intercalators with bis- and tris-phenanthrene chelated symmetry,⁴ has revealed unique but structurally interrelated chemotypes of promising biological utility.

Significant examples of these cationic agents (see Scheme V.1) include; *cis*-[Pt(NH₃)₂(phenanthridine)Cl]⁺ (phenanthriplatin)⁵ which exhibits a unique spectrum of activity within the National Cancer Institute 60-cell tumoral panel and enhanced cellular uptake relative to cisplatin; Δ-[Ru(DPPZ)(Phen)₂]²⁺ which has excellent DNA recognition properties and is widely known as a ‘light switch’ complex due to photoluminescence nucleotide binding enhancement,⁶ and; [Cu(Phen)₂]²⁺ which is an effective chemical nuclease that induces DNA degradation through free radical oxidation of deoxyribose.⁷⁻⁹ Thus, by varying both the metal centre and coordinated phenanthrene base, unique interactions on DNA and within human-derived cancer cells can be achieved.



Scheme V.1 Molecular structures of cytotoxic platinum(II) complexes cisplatin and phenanthriplatin, the ruthenium(II) DNA light switch complex, Δ-[Ru(DPPZ)(Phen)₂]²⁺, and the copper(II) chemical nuclease, [Cu(Phen)₂]²⁺.

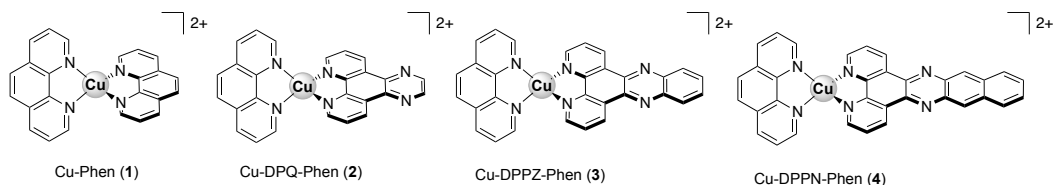
The chemical nuclease [Cu(Phen)₂]²⁺ is capable of abstracting hydrogen (·H) from the pentose ring of DNA in the presence of both exogenous reductant (Cu²⁺ → Cu⁺) and oxidant (O₂ or H₂O₂), under a quasi-reversible electrochemical process,^{7,8} and has served as an important template for cytotoxic metallodrug design.¹⁰ The mechanism of abstraction is sequential and is dependent on both Cu⁺ and hydrogen peroxide (H₂O₂).¹¹ Furthermore, the production of H₂O₂ in the reaction is believed to result from superoxide dismutase (SOD) mimetic activity,¹² post electron-transfer from Cu⁺ to O₂. [Cu(Phen)₂]²⁺ oxidises DNA without specificity, predominately at the minor groove and in an effort to improve this lack of specificity, chimeric [Cu(Phen)₂]²⁺ molecules have been generated using target-specific, DNA-recognition vectors of single-stranded DNA^{13,14} and also with the adenine-thymine (A-T) specific minor groove binder, distamycin.^{15,16}

In this study we report the synthesis and isolation of a series of bis-chelate Cu²⁺ phenanthroline–phenazine cationic complexes of [Cu(DPQ)(Phen)]²⁺, [Cu(DPPZ)(Phen)]²⁺ and [Cu(DPPN)(Phen)]²⁺ (where DPQ = dipyrido[3,2-*f*:2',3'-*h*]quinoxaline, DPPZ = dipyrido[3,2-*a*:2',3'-*c*]phenazine and DPPN = benzo[*i*]dipyrido[3,2-*a*:2',3'-*c*]phenazine). Since designer metal-chelating phenazine ligands have shown outstanding potential within Ru²⁺ DNA-selective binding probes,¹⁷⁻²⁰ a question remains unanswered regarding their biological activity within Cu²⁺ complexes towards, (*i.*) nucleotide equilibrium binding affinity, base-specific targeting and intercalation, (*ii.*) oxidative chemical nuclease activity, (*iii.*) redox behaviour including interactions with superoxide and hydrogen peroxide, and (*iv.*) cytotoxicity toward platinum resistant human-derived cancer cells. Our aim here was to investigate how systematic extension of the ligated phenazine ligand influences DNA recognition and oxidative degradation, and how this study can ultimately supply basic information toward the design of enhanced artificial chemical nucleases of biological utility. In order to identify and compare the DNA degradation profiles in this family of structurally related compounds, we proposed the development of a capillary electrophoresis, microfluidic chip, assay for the Bioanalyzer 2100 (Agilent Technologies) which is capable of high resolution sizing and quantitation of dsDNA fragments based on normalisation to internal markers and a standard DNA ladder.²¹⁻²³

V.3. Results

V.3.1 Preparation of the complexes The quinoxaline and phenazine ligands (DPQ, DPPZ and DPPN), were generated through Schiff-base condensation reactions of 1,10-phenanthroline-5,6-dione with either ethylenediamine, *o*-phenylenediamine or 2,3-diaminonaphthalene, with some modification to previously reported methods.²⁴⁻²⁶ The bis-phenanthroline complex, [Cu(Phen)₂](NO₃)₂ (**Cu-Phen, 1**), was prepared by aqueous-ethanol reflux of 1,10-phenanthroline with copper(II) nitrate (2:1).²⁷ The complexes, [Cu(DPQ)(Phen)](NO₃)₂ (**Cu-DPQ-Phen, 2**), [Cu(DPPZ)(Phen)](NO₃)₂ (**Cu-DPPZ-Phen, 3**) and [Cu(DPPN)(Phen)](NO₃)₂ (**Cu-DPPN-Phen, 4**) (Scheme V.2) were generated by firstly isolating the mono-phenanthroline complex,

[Cu(Phen)](NO₃)₂, and subsequently treating this with one equivalent of the corresponding phenazine ligand.



Scheme V.2 Molecular structures of the Cu²⁺ coordination complexes **1-4**.

V.3.2 Binding affinity to calf thymus and salmon testes DNA The DNA binding affinity of the complex series was determined using calf-thymus DNA (ctDNA, Ultra-Pure, Invitrogen) and salmon testes double stranded DNA (Sigma) by ethidium bromide and Hoechst 33258 fluorescence quenching and competition studies²⁸ and also through viscosity analysis (Figure V.1 and Table V.1). The presence of phenazine ligands in the complex cation function to significantly enhance ctDNA binding affinity with K_{app} (apparent DNA binding constant) values for **Cu-DPQ-Phen** and **Cu-DPPZ-Phen** reagents being at the order of $\sim 3 \times 10^7 \text{ M(bp)}^{-1}$ and of similar magnitude as the intercalating polypeptide antibiotic, actinomycin D. The DPPN-containing complex, although binding by an order of magnitude over **Cu-Phen**, was the lowest ctDNA binding phenazine complex at $\sim 6 \times 10^6 \text{ M(bp)}^{-1}$. Fluorescence quenching (Q) of limited bound Hoechst 33258 (minor groove binder) and ethidium bromide (intercalator) bound ctDNA were examined to identify potential binding specificity. Unlike the classical intercalator, actinomycin D, and minor groove binding agent, netropsin, the complex series did not display a large degree of discrimination for the quenching either of the selected fluorophores. The quenching effects of the DPQ and DPPZ complexes are stronger, overall, than **Cu-Phen**, however, this trend is reversed as the phenazine agents displace bound Hoechst with slightly more efficiency than ethidium bromide compared with **Cu-Phen**. Viscosity analysis on salmon testes dsDNA fibres revealed **Cu-DPQ-Phen** as having a significant intercalating (hydrodynamic) binding effect, followed thereafter by **Cu-DPPZ-Phen**, **Cu-Phen** and finally **Cu-DPPN-Phen**. In nearly all experiments conducted, the Cu²⁺ complexes exhibited distinctive behaviour compared to the simple [Co(NH₃)₆]³⁺ complex which is known only to have electrostatic binding

affinity to the surface of DNA. Indeed this effect was confirmed by our analysis of its inability to displace intercalated ethidium, enhanced ability to displace minor groove, surface bound, Hoechst 33258, and an overall decrease in relative viscosity.

Table V.2 Fluorescence quenching (Q) of limited ethidium bromide (5 μM) bound poly[d(G-C)₂] and poly[d(A-T)₂] (25 μM) by standard agents netropsin, actinomycin D and Cu²⁺ complexes.

Compound	Q (μM) poly[d(A-T) ₂]	Q (μM) poly[d(G-C) ₂]
Netropsin	4.08	>>200
Actinomycin D	>>200	5.47
Cu-Phen	13.34	7.96
Cu-DPQ-Phen	8.34	3.97
Cu-DPPZ-Phen	11.60	10.12
Cu-DPPN-Phen	96.56	44.18

Table V.3 Influence of standard agents (netropsin, actinomycin D) and copper phenazine complexes on the thermal denaturation of poly[d(G-C)₂] and poly[d(A-T)₂] alternating co-polymers.

Compound	ΔT_M (°C) poly[d(A-T) ₂]	ΔT_M (°C) poly[d(G-C) ₂]
Netropsin	12.32 \pm 0.79	2.83 \pm 0.38
Actinomycin D	-0.32 \pm 0.29	12.10 \pm 0.95
Cu-Phen	-0.02 \pm 0.29	6.64 \pm 1.58
Cu-DPQ-Phen	0.60 \pm 0.18	11.39 \pm 1.10
Cu-DPPZ-Phen	0.50 \pm 0.10	10.44 \pm 1.10
Cu-DPPN-Phen	-0.39 \pm 0.21	2.10 \pm 1.03

ΔT_M = difference in thermal melting (T_M) of drug treated nucleotide at $r = 0.1$ compared with drug untreated nucleotide

V.3.5 Chemical nuclease activity. The oxidative chemical nuclease activity of the complex series was identified using a novel ‘on chip’ method devised for the Agilent 2100 Bioanalyzer which is outlined in Figure V.3. The DNA 7500 microfluidic chip was employed as it can detect and quantify linear dsDNA fragments sized between 100–7500 bp by capillary electrophoresis. Superhelical plasmid DNA (pUC19, 2686 bp) was generated by *E. coli* and subsequently linearised by the type II endonuclease, *HindIII*, which has one recognition sequence on this vector. Linear pUC19 (400 ng) was then purified on an anion exchange column (Qiagen) and incubated with 500 nM of complex, under standard atmospheric conditions, in the presence of 1 mM reductant (sodium-L-ascorbate). At successive time periods, between 1-30 min, aliquots were removed from each reaction and quenched with 100 μM of both neocuproine (2,9-dimethyl-1,10-phenanthroline) and EDTA (ethylenediamine-tetraacetic acid).

Complex-treated and untreated linear DNA samples (1 μ L) were then loaded onto the Agilent DNA 7500 microfluidic chip. Further, sample wells were also loaded with standard DNA markers sized at 50 and 10380 bp which are evident in each electrogram. Untreated pUC19 produced a single, high-resolution, peak located at \sim 2870 bp (Figure V.4 [A], time = 0) which was within the experimental error margin for nucleotide sizing accuracy (\pm 10% CV). Degradation of pUC19 by each complex was followed by a reduction in peak area and peak height intensity and was accompanied by asymmetric tailing; indicative of smaller fragments being sheared off through chemical nuclease activity. Typical electrograms generated are shown in Figure V.4 [A] which details the untreated control DNA (time = 0) and each copper complex kinetically exposed to pUC19 at specific time points indicated. Further, typical electropherograms generated by each complex are shown in Figure V.4 [D] which detail the standard DNA ladder (L), untreated control pUC19 (lane 1) and complex treated DNA between either 1-15 min (for **Cu-Phen** and **Cu-DPQ-Phen** complexes) or 1-30 min (for **Cu-DPPZ-Phen** and **Cu-DPPN-Phen** complexes) (lanes 2-12). In our preliminary experiments we discovered that bis-phen and DPQ complexes were much more efficient in degrading pUC19, hence, our analysis on the Bioanalyzer was conducted on a shorter timeframe for both these agents. Quantification of pUC19 damage was achieved (Figure V.4, centre) using peak height reduction and peak area reduction analysis from triplicate electrograms and comparisons of cleavage efficiency were made based on the time taken to degrade 50% (D_{50}) of pUC19 with 100% being taken as the normalised intensity of triplicate untreated pUC19 DNA. Both **Cu-Phen** and **Cu-DPQ-Phen** are remarkably efficient in degrading dsDNA and are similar, in terms of both their D_{50} values and overall profile. Analysis by pUC19 peak height reduction shows that both agents similarly reduce intensity, by 50%, after \sim 2 min, however, **Cu-Phen** has a marked enhancement over **DPQ-Phen** between 4.0-7.5 min on comparison of peak area degradation. Nonetheless, the DPQ agent totally degrades the plasmid by 7.5 min under both analyses whereas it is \sim 10 min before this is achieved by **Cu-Phen**. The DPPZ and DPPN reagents are less efficient in their chemical nuclease activity with **Cu-DPPZ-Phen** displaying rapid degradation between 5 and 12.5 min (D_{50} \sim 7.5 min by peak height) while **Cu-DPPN-Phen** delivers a somewhat linear profile over the complete timeframe

(D_{50} ~12.5 min by peak height). Further evidence the DPPZ agent is a more efficient chemical nuclease compared with **Cu-DPPN-Phen** can be gleaned from peak area analysis. DPPZ completely digests the plasmid by ~20 min while at the end of our analysis (30 min) a small concentration of nucleotide remained within the DPPN treated sample.

V.3.6 Interactions with superhelical pUC19. The interaction of purified superhelical pUC19 (generated using *E. coli* as described above) with the complex series was studied under similar conditions (500 nM [complex] with 1 mM reductant) (Figure V.5) using standard agarose gel electrophoresis. All complexes induced complete degradation of the superhelix with the exception of **Cu-DPPN-Phen**, where evidence of nicked (Form I) and linear (Form II) tertiary conformations remained after 30 min. The importance of Cu^+ and hydrogen peroxide in the cleavage mechanism were demonstrated by the complete inhibition of nuclease activity upon addition of 1000 U of bovine liver catalase (Figure V.5b) and 100 μM of neocuproine (Figure V.5c). Further trapping studies revealed that bovine superoxide dismutase (1000 U, Figure V.5d) could strongly inhibit **Cu-DPPN-Phen** from plasmid digestion and this complex, along with **Cu-DPPZ-Phen**, were also impeded by the hydroxyl radical scavenger, DMSO (10 % v/v, Figure V.5e).

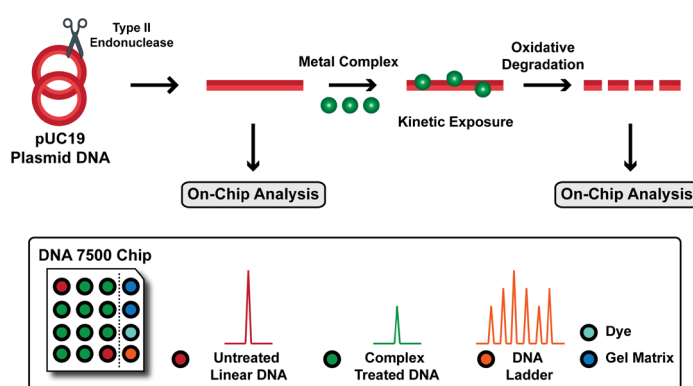


Figure V.57 'On-Chip' protocol for examining artificial metallonuclease activity using the Bioanalyzer 2100.

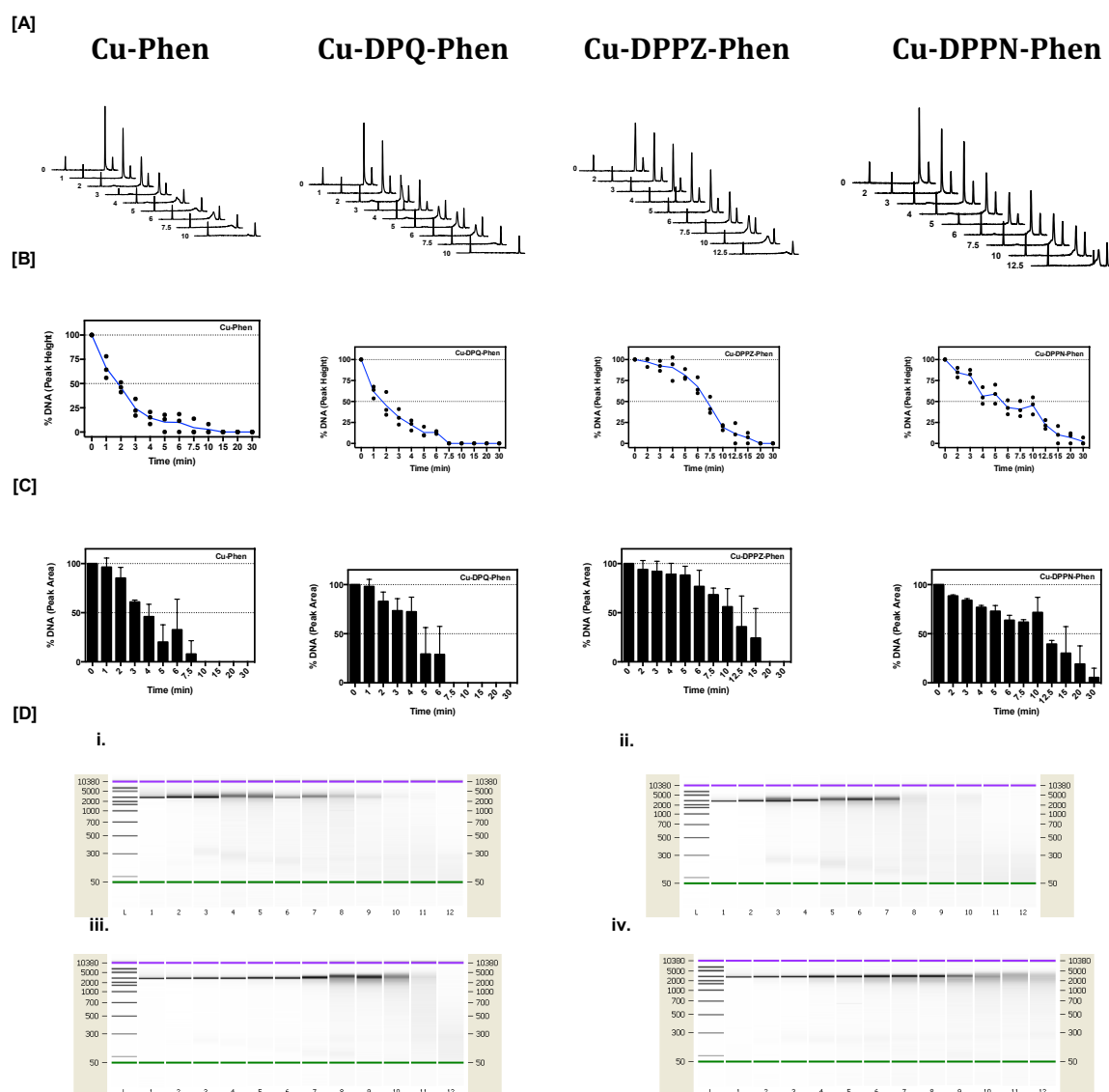


Figure V.58 [A] Electrograms of linearized pUC19 (400 ng) exposed to metal complex (500 nM) between 0 – 12.5 min on the Bioanalyzer 2100 with DNA 7500 microfluidic chips, [B] %DNA degradation (from peak height analysis of triplicate experiments, error bars \pm S.D.) of pUC19 exposed to Cu^{2+} complexes between 0-30 min, [C] %DNA degradation (from peak area analysis of triplicate experiments, error bars \pm S.D.) of pUC19 exposed to Cu^{2+} complexes between 0-30 min, and, [D] typical electropherograms generated by the Bioanalyzer 2100, L = ladder, lane 1 = pUC19 control, lanes 2-12 = pUC19 + complex exposed between 1-15 min for bis-phen (i.) and DPQ (ii.) samples and between 1-30 min for DPPZ (iii.) and DPPN (iv.) samples.

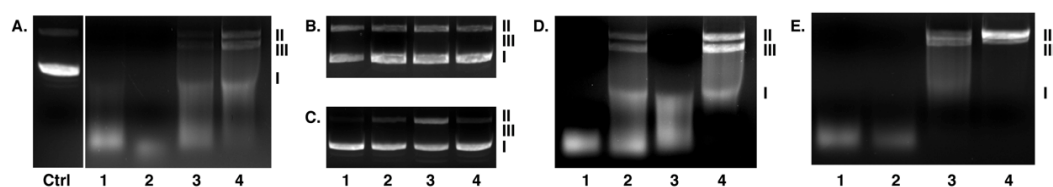


Figure V.59 Agarose gel electrophoresis of purified (EDTA free) supercoiled pUC19 (400 ng) with 1 mM Na-L-ascorbate incubated for 30 min with 500 nM of metal complexes (A), and in the presence of 1000 units of bovine liver catalase (B), 100 μ M neocuproine (C), 1000 units of bovine SOD (D) and 10% v/v DMSO (E). Ctrl = pUC19 complex untreated control, Lanes 1-4 = 500 nM **Cu-Phen**, **Cu-DPQ-Phen**, **Cu-DPPZ-Phen** and **Cu-DPPN-Phen**, respectively.

V.3.7 Comparison study of pUC19 and pBC4 cleavage efficacy In order to determine the chemical nuclease on DNA of different guanine-cytosine (G-C) composition, commercially available pUC19 (2686 bp, 51% G-C, NEB, N3033L), and pBC4 (10673 bp, 59% G-C, donated by NEB) were analysed using gel electrophoresis in the presence of 1 mM of added reductant (Na-L-ascorbate). It should be noted that both plasmids are supplied in EDTA buffered solution and so chemical nuclease activity was examined at higher complex concentration. Further, the pBC4 plasmid is *recA*⁺ and so does not have dimer deficiency usually associated with commercially available strains used for plasmid production. As a consequence, pBC4 migrates as two bands: the plasmid monomer followed by the dimer, and so this plasmid is not suitable to identify conversion between superhelical (Form I) to nicked (Form II) or linear (Form III) conformations due to the overlapping nature of the dimer and FII or FIII bands. This plasmid, however, can be exploited for artificial metallonuclease activity in its linearised form and we employed the type II endonuclease, *AgeI*, to generate FIII of the plasmid. For comparison purposes, pUC19 was also required in a linearised form and this was completed using the type II endonuclease, *ScaI*. Both pBC4 and pUC19 (400 ng) were then exposed, over 30 min, to between 2.5 – 10.0 μ M of the complex series, in the presence of 1 mM exogenous ascorbate, with each reaction containing the same amount of EDTA (40.0 μ M) (Figure V.6). The chemical nuclease activity of **Cu-DPQ-Phen** and **Cu-DPPZ-Phen** were found to be independent of %G-C content with the DPQ complex being the most effective cleaving agent, overall, inducing complete digestion of both pUC19 and pBC4 upon 5 μ M exposure. **Cu-DPPN-Phen** was found to have a

remarkably low effect on pUC19 oxidation but was more reactive toward pBC4. In contrast to the observed activities of the phenazine reagents, **Cu-Phen** was selectively reactive toward the plasmid of lower %G-C content, and this was evidenced through complete disappearance of pUC19 at a 5 μ M, while the majority of pBC4 remained unaffected under identical conditions.

The final aspect of this study involved the characterisation of nuclease activity on commercial (EDTA buffered) supercoiled pUC19 plasmid. In this experiment a fixed concentration of metal complex (10 μ M) was exposed to 400 ng of superhelical DNA over 30 min in the presence of 1 mM added reductant (Figure V.7) and reactions all contained a final concentration of EDTA of 56 μ M. Surprisingly, **Cu-Phen** was found to only partially nick (FI \rightarrow FII) pUC19 while **Cu-DPPN-Phen** had little or no oxidative affect. **Cu-DPQ-Phen** and **Cu-DPPZ-Phen**, however, facilitated complete conversion to the nicked form (FII) of pUC19 and this observation supports the enhanced stability of these chemical nucleases within a competing, EDTA chelated, environment.

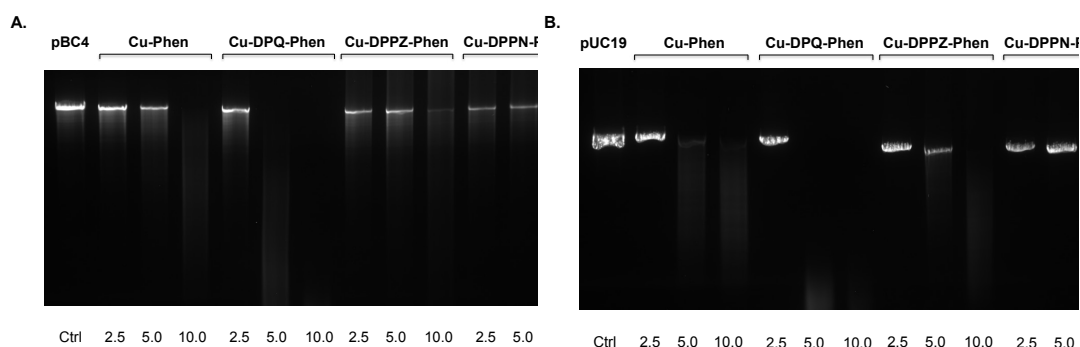


Figure V.60 Degradation of 400 ng of linearised plasmid pBC4 (A.) and pUC19 (B.) DNA with 2.5, 5.0, and 10.0 μ M of tested metal complex in the presence of 1 mM of added reductant for 30 min at 37 $^{\circ}$ C; A. pBC4 (59% G-C); B. pUC19 (51% G-C).

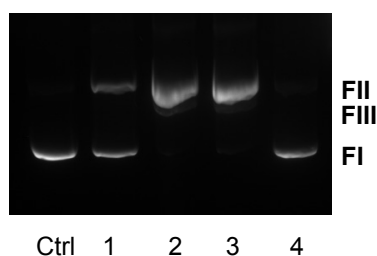


Figure V.61 DNA cleavage reactions with 10 μ M of **Cu-Phen**, **Cu-DPQ-Phen**, **Cu-DPPZ-Phen**, and **Cu-DPPN-Phen** (lanes 1 – 4, respectively) with 400 ng of commercial (EDTA buffered) superhelical pUC19. Reactions were carried out with 1 mM of added Na-L-ascorbate over 30 min at 37 $^{\circ}$ C.

V.3.8 *In vitro* cytotoxicity toward SKOV3 cancer cells.

Flow cytometric analysis using Guava ViaCount reagent was used to examine the cytotoxic properties of the complex series and the clinical antitumor agent, doxorubicin, on human SKOV3 ovarian cancer cells. This cell line was selected as it possesses both a mutant *p53* gene and is intrinsically resistant to cisplatin.^{29,30} The ViaCount reagent determines viability of a cell population based upon differential membrane permeability of two fluorescent DNA intercalators which classify live and dead cell ratios. SKOV3 cells were incubated with drug concentrations ranging 100 – 0.10 μM over 24 h (Figure V.8). Cytotoxicity data used to calculate the IC_{50} values (at the 95% confidence interval) were derived from sigmoidal, non-linear regression curves (Fig. V.11). The IC_{50} complex trend follows **Cu-DPPZ-Phen** > **Cu-DPQ-Phen** > **Cu-Phen** > **Cu-DPPN-Phen**, with all compounds exhibiting significant 24 h *in vitro* cytotoxicity values of 0.59, 1.34, 1.40 and 3.55 μM , respectively. The most active complex, **Cu-DPPZ-Phen**, is comparable to that of the clinically used chemotherapeutic drug doxorubicin, with both agents exhibiting potent inhibitory values in the nano-molar region. Indeed, doxorubicin (adriamycin) was specifically selected for this study due to its clinical DNA damaging properties related to intercalation and topoisomerase II inhibition.³¹⁻³³

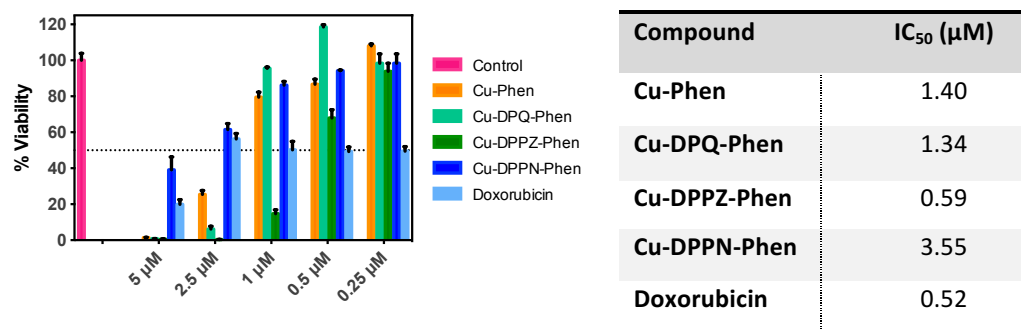
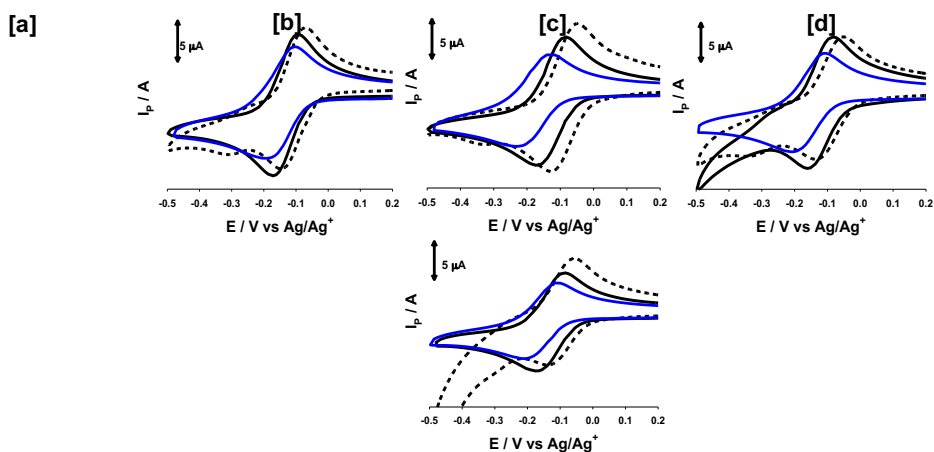


Figure V.62 Dose response inhibition and IC_{50} values (at the 95% confidence interval) of Cu^{2+} complexes and the clinical agent, doxorubicin, within SKOV3 human cancer cells over 24 h of drug exposure.

V.3.9 Electrochemistry and redox interactions with the superoxide radical anion and hydrogen peroxide The electrochemical behaviour of each complex was investigated in the absence and presence of an excess of Na-L-ascorbate and hydrogen peroxide (Figure V.9). All complexes exhibit well-defined, quasi-

reversible redox profiles, with added oxidant or reductant having little effect on the reversibility of electron transfer reactions for each complex. Added reductant does shift the redox potentials anodically, while added oxidant shifts the complex redox potentials to more cathodic values. It is interesting to note that added reductant does increase the concentration of Cu(I) species in solution; this is reflected in the observed enhancement of complex oxidation peak currents. Conversely, on addition of peroxide, the expected increase in reduction peak currents for each complex, corresponding to a solution phase increase in Cu(II) species, is not observed. Thus, a kinetic constraint exists in the electrochemical regeneration of Cu(I) in the presence of oxidant, and may be indicative of the presence of copper-hydroperoxo species being generated in solution. The superoxide dismutase mimetic (SODm) properties of the group were investigated using the NBT (nitro-blue-tetrazolium) assay where a xanthine / xanthine oxidase system served as the source of superoxide radical anion ($O_2^{\bullet-}$).³⁴ All complexes displayed similar, concentration-dependent, SODm activity (Figure V.10b) and have notable catalytic rates with K_{cat} values ranging between $9.80 \times 10^6 \text{ M}^{-1} \text{ s}^{-1}$ (**Cu-DPPZ-Phen**) and $7.64 \times 10^6 \text{ M}^{-1} \text{ s}^{-1}$ (**Cu-DPPN-Phen**). Complexes were then examined for their Fenton-like activity using the Amplex Red hydrogen peroxide assay (Invitrogen). None of the compounds were found to degrade H_2O_2 (5 μM) in the absence of reductant (results not shown), however, in the presence of Na-L-ascorbate (100 μM) all four chemical nucleases displayed one-phase exponential decay of peroxide (Figure V.10a and Table V.4). The rate of degradation, overall, is kinetically sluggish with the rate constants for **Cu-Phen** and **Cu-DPQ-Phen** being 3.22 and 3.54 s^{-1} , respectively, and being over two times that of **Cu-DPPZ-Phen** (1.56 s^{-1}) and **Cu-DPPN-Phen** (1.26 s^{-1}) complexes. It is significant to note the overlap between Fenton behaviour and chemical nuclease activity with the most efficient reagents, $[\text{Cu}(\text{DPQ})(\text{Phen})]^{2+}$ and $[\text{Cu}(\text{Phen})_2]^{2+}$, ablating H_2O_2 fluorescence at twice the rate of the DPPZ and DPPN complexes. Furthermore, given the series significant SODm activity and redox electrochemical profiles, it seems the rate-limiting factor in the chemical nuclease activity is, predominately, due to the subsequent metallo-hydroperoxo reaction.



Entry	Complex	[i]			[ii]			[iii]		
		E_{Pa}	E_{Pc}	ΔE_p	E_{Pa}	E_{Pc}	E_{Pa}	E_{Pa}	E_{Pc}	ΔE_p
[a]	1	-0.096	-0.171	0.075	0.074	-0.137	0.069	-0.104	0.190	0.086
[b]	2	-0.081	-0.175	0.094	-0.51	-0.129	0.78	-0.124	-0.211	0.087
[c]	3	0.082	-0.162	0.080	-0.057	-0.131	0.074	-0.105	-0.211	0.06
[d]	4	-0.100	-0.181	0.081	-0.060	-0.144	0.084	-0.100	-0.190	0.90

Figure V.63 Cyclic voltammograms describing the redox behavior of 1 mM of complex, at a scan rate of 100 mV s^{-1} , (solid black trace), and in the presence of 2 mM Na-L-ascorbate (dashed black trace), and 2 mM H_2O_2 (solid blue trace), [a] **Cu-Phen**, [b] **Cu-DPQ-Phen**, [c] **Cu-DPPZ-Phen** and, [d] **Cu-DPPN-Phen**, and, electrochemical parameters (V) for complexes, and in the presence of added Na-L-ascorbate, and H_2O_2 (bottom). Analysis conducted in 10% v/v DMF; [i] complex without exogenous treatment (V) [ii] complex with added Na-L-ascorbate (V) [iii] complex with added H_2O_2 (V).

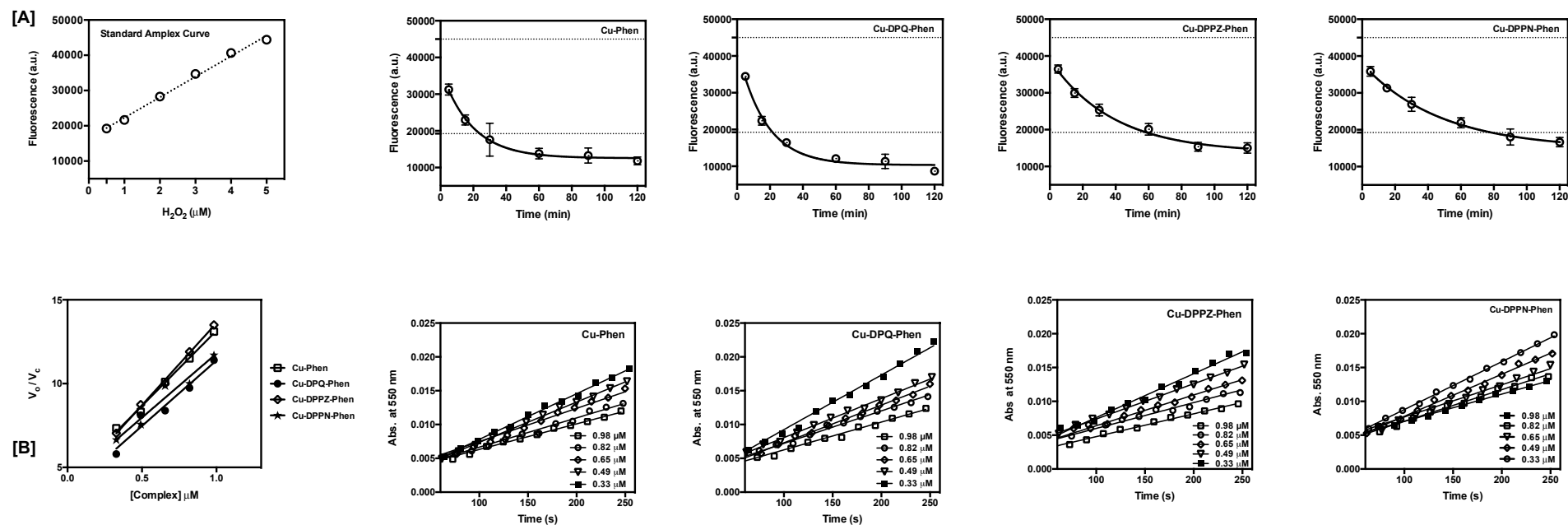
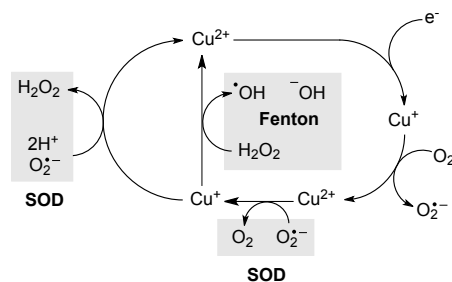


Figure V.64 [A] Fenton-like degradation of hydrogen peroxide (5 μM) in the presence of 5 μM of metal complex and 100 μM Na-L-ascorbate determined using the Amplex Red hydrogen peroxide assay kit (Invitrogen) (replicate experiments conducted on four separate occasions), a calibration curve is also shown which details the linear ($r^2 > 0.99$) fluorescent response achieved from hydrogen peroxide detection in the assay, [B] superoxide dismutase mimetic (SODm) activity determined by the xanthine/xanthine-oxidase system, metal complexes were examined between 0.98 – 0.33 μM at 25 $^{\circ}C$ under constant enzymatic production of superoxide ($\sim 1 \mu M / min$) using the detector molecule, nitrobluetetrazolium chloride and this data was plotted as a function of V_0/V_c (catalytic rate in the absence / presence of catalyst) as a function of [complex] to yield the catalytic rate K_{cat} in units, $M^{-1} s^{-1}$.

Table V.4 Kinetic properties of the complex series under Fenton-like and SODm conditions and catalytic cycle of Cu⁺/Cu²⁺ ions with molecular oxygen, superoxide and hydrogen peroxide.

Compound	H ₂ O ₂ (Fenton)	SODm
	K (s ⁻¹) [a]	K_{cat} (M ⁻¹ s ⁻¹) [b]
Cu-Phen	3.22	8.97 × 10 ⁶
Cu-DPQ-Phen	3.54	7.82 × 10 ⁶
Cu-DPPZ-Phen	1.56	9.80 × 10 ⁶
Cu-DPPN-Phen	1.26	7.64 × 10 ⁶

[a] Fenton degradation of 5 μM hydrogen peroxide in the presence of 5 μM complex and 100 μM Na-L-ascorbate. [b] Superoxide dismutase mimetic (SODm) activity determined by the xanthine/xanthine-oxidase system.



V.4 Discussion

The incorporation of designer phenazine ligands in the “bis-phen”, [Cu(Phen)₂]²⁺, chemical nuclease model pronounces DNA recognition and intercalation with significant enhancement to the dynamic binding constant for dipyrido[3,2-*f*:2',3'-*h*]quinoxaline (DPQ) and dipyrido[3,2-*a*:2',3'-*c*]phenazine (DPPZ) containing complexes; [Cu(DPQ)(Phen)]²⁺ and [Cu(DPPZ)(Phen)]²⁺. To our knowledge these binding constants ($K_{app} \sim 3 \times 10^7$ M(bp)⁻¹) are the highest reported to date for any existing copper(II) phenanthrene complex and surpass the [Cu(Phen)₂]²⁺ cation by ~60 fold. Additionally, these values compare favourably with the binding constants of actinomycin D, identified in this study as 2.92×10^7 M(bp)⁻¹, and rhodium(III) complexes *rac*-[Rh(phi)(phen)₂]³⁺ and *rac*-[Rh(phi)₂(bipy)]³⁺ ($K_b \approx 10^6 - 10^7$ M⁻¹)³⁵ (where phi = 9,10-phenanthrene-quinone-diimine and bpy = 2,2'-bipyridine) but do not match the ctDNA binding affinity of ruthenium(II) DPPZ complexes, Δ-[Ru(DPPZ)(Phen)₂]²⁺ or Λ-[Ru(DPPZ)(Phen)₂]²⁺ ($K_{eff} \approx 10^8$ M⁻¹).⁶ Indeed, the lowest binding constant among the three phenazine complexes generated ($K_{app} \sim 6 \times 10^6$ M(bp)⁻¹), observed for the [Cu(DPPN)(Phen)]²⁺ complex, is on par with many high affinity copper(II) binding constants in the literature.³⁶ Interestingly, copper(II) DPQ and DPPZ compounds have shown only mediocre DNA binding constants ($K_b = 10^4 - 10^3$ M⁻¹) when complexed with amino acid chelators *L*-leucine, *L*-tryptophan and

L-tyrosine which, surprising, have far lower binding constants than the amino acid complex $[\text{Cu}(\text{glycine})(\text{DPPZ})]^+$ ($K_b \sim 10^6 \text{ M}^{-1}$) along with $[\text{Cu}(\text{L-arginine})(\text{DPQ})]^+$ and $[\text{Cu}(\text{L-arginine})(\text{DPPZ})]$ ($K_b \sim 10^5 \text{ M}^{-1}$ and $K_{\text{app}} \sim 10^6 \text{ M}^{-1}$).³⁷⁻⁴¹ Enhanced binding constants ($K_{\text{app}} \approx 5 \times 10^6 \text{ M}^{-1}$) were observed, however, for binuclear complexes, $[\{\text{Cu}(\text{DPQ})(\text{DMF})\}_2(\mu\text{-OH})_2]^{2+}$ and $[\{\text{Cu}(\text{DPPZ})(\text{DMF})\}_2(\mu\text{-OH})_2]^{2+}$, which feature two phenazine ligands spanning opposite directions along the hydroxide bridged Cu-Cu axis.⁴² Thus, in addition to the influence of an extended phenazine π -framework, our results suggest a prominent role for the ancillary chelated phenanthroline in nucleotide binding affinity. These ligands are presumably involved in secondary interactions with DNA bases or at the surface of the minor groove and may function to optimise complex binding geometry.^{17,18,43}

The complex series have distinctive nucleotide binding specificity compared with netropsin and actinomycin D. Their ability to similarly quench Hoechst 33258 and ethidium bromide bound ctDNA flurogenic dyes, along with their broadly analogous displacement of limited bound ethidium to poly[d(G-C)₂] and poly[d(A-T)₂], departs substantially from the observed binding specificity of these classical minor groove binding or intercalating agents. Thermal melting analysis, however, reveals that both DPQ and DPPZ complexes extensively stabilize poly[d(G-C)₂] denaturation, comparable to actinomycin D, and that the overall complex series have a large degree of similarity with this intercalator given their negligible stabilization on poly[d(A-T)₂]. Taken together, it appears likely that the complexes intercalate DNA at both the minor and major groove, and this interaction is appreciably enhanced by the presence of coordinated phenazine ligands, in particular DPQ and DPPZ.

We have reported a novel “on chip” microfluidic method for the Agilent Bioanalyzer 2100 for examining, with high precision, chemical nuclease activity. In our view, this technique offers advantages over existing methodologies (e.g. band densitometry) in the quantitation of dsDNA damage and undoubtedly has application in quantifying the activity of cytotoxic DNA damaging drugs, in particular those from families of structurally related agents. Further, this technique is suited for detecting sequence-specific metallodrug DNA interactions

as in our laboratory we have observed the effects of introducing a second endonuclease (*SalI*) with single site-recognition specificity on this sequence. The analysis methods we have employed on the Bioanalyzer 2100 to detect DNA degradation involve both peak height and peak area intensity reduction. Our motivation for applying both techniques stems from the observation that the Cu^{2+} complexes induced random damage, and thus asymmetric peak tailing on the pUC19 fragments (due to shearing chemical nuclease effects) were evident in each electrogram. This factor had an influence on peak area intensity and so we found that peak height analysis was suitable to employ as a tandem method to enhance the overall accuracy of the technique. Our work revealed the $[\text{Cu}(\text{DPQ})(\text{Phen})]^{2+}$ complex as the most active chemical nuclease within this series, however, the degradation kinetics of this reagent are closely followed by $[\text{Cu}(\text{Phen})_2]^{2+}$. The interaction of the phenazine complexes with pBC4 (59% G-C) and pUC19 (51% G-C) plasmid DNA, however, reveal significant differences compared with the $[\text{Cu}(\text{Phen})_2]^{2+}$ cation in terms of chemical nuclease efficacy. $[\text{Cu}(\text{Phen})_2]^{2+}$ had enhanced activity toward the lower G-C containing plasmid (pUC19) while each of the phenazine complexes maintained, or enhanced, their activity toward the higher G-C content plasmid (pBC4). This data suggests Cu^{2+} phenazine compounds may have targeting properties toward CpG (cytosine-phosphate-guanine) islands which are found in the promoter regions of many mammalian genes.^{44,45} Thus, it is of significant future importance to examine the DNA targeting properties of these phenazine complexes within cisplatin resistant cancer cell models such as SKOV3. While these complexes, in particular **Cu-DPPZ-Phen**, display interesting *in vitro* chemotherapeutic potential compared with doxorubicin on SKOV3, their targeted DNA damaging effects have yet to be identified. Indeed, we have recently reported that although **Cu-Phen** has significant cytotoxic properties toward SKOV3, this agent non-selectively induces DNA damage and can be classified as a “promiscuous” cytotoxin.²⁷

All complexes in this study have excellent superoxide dismutase mimetic activities (K_{cat} $7.6 - 9.8 \times 10^6 \text{ M}^{-1} \text{ s}^{-1}$) but are slow, kinetically, within the Fenton reaction ($\text{Cu}^+ + \text{H}_2\text{O}_2 \rightarrow \text{Cu}^{2+} + \cdot\text{OH} + \text{OH}^-$). Significantly, however, Fenton breakdown follows linearized pUC19 chemical nuclease efficiency in the overall series (**Cu-DPQ-Phen** > **Cu-Phen** >> **Cu-DPPZ-Phen** > **Cu-DPPN-Phen**) with

DPQ and the bis-phen complex consuming peroxide at twice the rate constant of DPPZ and DPPN reagents.

In summary, we have shown that phenazine functionalized Cu^{2+} phenanthroline complexes offer a clear enhancement toward DNA binding affinity relative to the well studied $[\text{Cu}(\text{Phen})_2]^{2+}$ cation and possess the highest ctDNA binding affinities currently known for Cu^{2+} phenanthrene complexes. We have reported new on-chip methodology for determining dsDNA degradation and it is our opinion that both this technique and these Cu^{2+} phenazine reagents will have an important future role to play in the development of site-directed, gene-silencing, artificial metallonucleases for use as targeted chemotherapeutics for human disease.

V.5 Materials And Methods

V.5.1 Preparation of ligands and metal complexes. Chemicals and reagents of analytical grade for the preparation of organic ligands and metal complexes were purchased from Sigma-Aldrich (Ireland) and used without further purification.

V.5.1.1 Preparation of 1,10-phenanthroline-5, 6-dione (phendio). Phendio was prepared according to the literature method reported by Dickeson and Summers with slight modification.²⁴ 1,10-phenanthroline (4.00 g, 22.19 mmol) and potassium bromide (4.00 g, 33.6 mmol) were thoroughly mixed and slowly added to an ice-cold mixture of H_2SO_4 (40 mL) and HNO_3 (20 mL). The solution was refluxed for 3 hours at 100 °C, then cooled to room temperature, poured onto crushed ice (~400 mL) and neutralised with an aqueous NaOH solution (80.0 g per 400 mL) to a pH between 4-5, yielding a yellow solution. The solution was extracted by CHCl_3 (in 8×100 mL portions). The organic phase was combined and dried with anhydrous magnesium sulphate then filtered before being evaporated to dryness, whereupon a bright yellow solid (4.03 g) was obtained. The product could be further purified by recrystallisation from HPLC grade methanol but was sufficiently pure to use in subsequent reactions. Yield: 4.03 g (86 %). ^1H NMR (400 MHz, CDCl_3): 9.05 (dd, $J = 4.6, 1.8$ Hz, 2H), 8.44 (dd, $J = 7.9, 1.8$ Hz, 2H), 7.52 (dd, $J = 7.9, 4.6$ Hz, 2H). IR (ATR, cm^{-1}): 3348, 3061,

1678, 1559, 1458, 1412, 1290, 1204, 1114, 1009, 924, 806, 734. Solubility: DMF, EtOH, DMSO (partially), Mp: 258-260 °C.

V.5.1.2 Preparation of dipyrido[3,2-*f*:2',3'-*h*]quinoxaline (DPQ). DPQ was prepared according to the literature method reported by Hambley *et al.* with some modification.²⁶ To a solution of phendio (0.510 g, 2.44 mmol) in water (35 mL) was added ethylenediamine (0.70 mL, 7.50 mmol) and the resultant suspension was refluxed for 12 hours at 60 °C. The resulting product was washed with water (10 mL) and minimum volume of diethyl ether. Yield: 0.372 g (66 %). ¹H NMR (400 MHz, CDCl₃): 9.47 (dd, *J* = 8.2, 1.8 Hz, 2H), 9.24 (dd, *J* = 4.3, 1.8 Hz, 2H), 9.19 (s, 2H), 7.96 (dd, *J* = 8.2, 4.3 Hz, 2H). IR (ATR, cm⁻¹): 2990, 1570, 1472, 1466, 1206, 1073, 1077, 825, 803, 739. Solubility: DMF, EtOH, DMSO (partially). Mp: 330-335 °C.

V.5.1.3 Preparation of dipyrido[3,2-*a*:2',3'-*c*]phenazine (DPPZ). DPPZ was prepared according to literature with slight changes made to the method.²⁴ A methanolic solution (20 mL) of 1,2-phenylenediamine dihydrochloride (0.640 g, 3.53 mmol) was refluxed until it was dissolved. A warm ethanolic solution of phendio (0.500 g, 2.38 mmol) was prepared (20 mL), added over the methanolic solution and refluxed with constant stirring for 3 hours. The resulting solution was vacuum filtered and recrystallised from EtOH producing metallic-like orange filaments. Yield: 0.521 g (78 %). ¹H NMR (400 MHz, CDCl₃): 9.58 (dd, *J* = 8.1, 1.7 Hz, 2H), 9.20 (dd, *J* = 4.5, 1.7 Hz, 2H), 8.29 (dd, *J* = 6.5, 3.4 Hz, 2H), 7.86 (dd, *J* = 6.5, 3.4 Hz, 2H), 7.73 (dd, *J* = 8.1, 4.5 Hz, 2H). IR (ATR, cm⁻¹): 3040, 1615, 1570, 1486, 1412, 1336, 1077, 1072, 808, 739. Solubility: DMF, EtOH, DMSO (partially). Mp: 248-253 °C.

V.5.1.4 Preparation of benzo[*i*]dipyrido[3,2-*a*:2',3'-*c*]phenazine (DPPN). DPPN was prepared according to literature with slight changes made to the method.²⁵ To a solution of phendio (0.300 g, 1.422 mmol), in EtOH (45 mL) was added 2,3-diaminonaphthalene (0.339 g, 2.136 mmol) and the resulting suspension was refluxed for 3 hours, during which time an orange precipitate formed. The precipitate was vacuum filtered, washed with cold ethanol and allowed to dry. Yield: 0.443 g (93 %). ¹H NMR (400 MHz, CDCl₃): 9.49 (dd, *J* = 8.1, 1.8 Hz, 2H), 9.16 (dd, *J* = 4.4, 1.8 Hz, 2H), 8.80 (s, 2H), 8.09 (dd, *J* = 6.5,

3.1 Hz, 2H), 7.68 (dd, J = 8.1, 4.4 Hz, 2H), 7.53 (dd, J = 6.5, 3.1 Hz, 2H). IR (ATR, cm^{-1}): 3362, 1628, 1583, 1565, 1409, 1360, 1274, 1128, 1070, 1033, 892, 871, 850, 817. Solubility: DMF (partially). Mp: 283-285 °C.

V.5.1.5 Preparation of $[\text{Cu}(\text{Phen})](\text{NO}_3)_2$. To a solution of copper(II) nitrate hemipentahydrate (1 g, 4.3 mmol), in EtOH (75 ml) was added Phen (0.78 g, 4.3 mmol) and the resulting suspension was refluxed for 2 hours. The solution was left to stand for 12 hours, then vacuum filtered and washed with a minimum volume of cold EtOH. Yield: 1.43 g (90 %). Anal. Calc. for $\text{C}_{12}\text{H}_8\text{CuN}_4\text{O}_6$: C, 39.19; H, 2.19; N, 15.23. %Found: C, 39.65; H, 2.06; N, 14.92. IR (ATR, cm^{-1}): 3068, 1583, 1451, 1426, 1270, 1151, 1110, 1011, 972, 847, 807, 739, 719. Solubility: DMF, EtOH.

V.5.1.6 Preparation of $[\text{Cu}(\text{Phen})_2](\text{NO}_3)_2$ (Cu-Phen). This complex was prepared according to the method reported by Prisecaru *et al.*²⁷

V.5.1.7 General procedure for preparing $[\text{Cu}(\text{N,N}')(\text{phen})](\text{NO}_3)_2$ complexes (where N,N' = DPPZ, DPPN and DPQ). To a solution of $[\text{Cu}(\text{phen})(\text{NO}_3)_2]$ (0.1 g, 0.27 mmol) in EtOH (30 mL) was added 0.27 mmol of either DPQ (0.063 g), DPPZ (0.076 g) or DPPN (0.090 g) and the resulting suspension was stirred for 12 hours at 50 °C. The solution was vacuum filtered and washed with a minimum volume of cold EtOH. **$[\text{Cu}(\text{DPQ})(\text{phen})](\text{NO}_3)_2 \cdot 0.5\text{H}_2\text{O}$ (Cu-DPQ-Phen).** Yield: 0.1207 g (73 %). Anal. Calc. for $\text{C}_{26}\text{H}_{17}\text{CuN}_8\text{O}_{6.5}$: C, 51.28; H, 2.81; N, 18.40. %Found: C, 51.15; H, 2.29; N, 18.68. IR (ATR, cm^{-1}): 3034, 1581, 1472, 1360, 1288, 1210, 1081, 818, 718. Solubility: DMF, DMSO (partially). **$[\text{Cu}(\text{DPPZ})(\text{phen})](\text{NO}_3)_2$ (Cu-DPPZ-Phen).** Yield: 0.0709 g (41 %). Anal. Calc. for $\text{C}_{30}\text{H}_{18}\text{CuN}_8\text{O}_6$: C, 55.43; H, 2.79; N, 17.24. %Found: C, 56.38; H, 2.88; N, 17.83. IR (ATR, cm^{-1}): 3023, 1578, 1451, 1376, 1292, 1076, 819, 718, 729. Solubility: DMF, DMSO (partially). **$[\text{Cu}(\text{DPPN})(\text{phen})](\text{NO}_3)_2 \cdot 2\text{H}_2\text{O}$ (Cu-DPPN-Phen).** Yield: 0.1341 g (67 %). Anal. Calc. for $\text{C}_{34}\text{H}_{24}\text{CuN}_8\text{O}_8$: C, 55.47; H, 3.29; N, 15.22. %Found: C, 55.42; H, 2.76; N, 15.38. IR (ATR, cm^{-1}): 3020, 1578, 1518, 1375, 1358, 1290, 1046, 868, 719. Solubility: DMF, DMSO (partially).

V.5.2 DNA binding studies.

The fluorescence quenching assay, the competitive ethidium bromide displacement assay and viscosity measurements were all conducted according to the method reported by Kellett *et al.*²⁸ (see section III.4.4)

V.5.2.1 Fluorescence quenching for poly[d(A-T)₂] and poly[d(G-C)₂].

Solutions of double stranded alternating co-polymers, poly[d(A-T)•d(A-T)] (Sigma PO883, $\epsilon_{260} = 13,100 \text{ M (bp)}^{-1} \text{ cm}^{-1}$) and poly[d(G-C)•d(G-C)] (Sigma P9389, $\epsilon_{260} = 16,800 \text{ M(bp)}^{-1} \text{ cm}^{-1}$) were prepared in nuclease free water and quantified on a Cary 100 UV-vis spectrophotometer. A working solution of 50 μM poly[d(A-T)₂] (or poly[d(G-C)₂]) along with 10 μM ethidium bromide (EtBr) in HEPES buffer (80 mM, pH = 7.2) and NaCl (40 mM) was prepared. Stock solutions of metal complexes, metal salts and groove binding drugs were prepared at ~4 mM in DMF and further diluted with 80 mM in HEPES buffer. 50 μL of the poly[d(A-T)₂] (or poly[d(G-C)₂]) EtBr working solution were placed in each well of a 96 well microplate with the exception of the blanks which contained 95 μL of 80 mM HEPES and 5 μM of EtBr. Serial aliquots of the tested compound were added to the working solutions and the volume adjusted to 100 μL in each well such that the final concentration of nucleotide and EtBr were 25 μM and 5 μM respectively. The plate was then allowed to incubate at room temperature for 5 min before being analysed using a Bio-Tek synergy HT multi-mode microplate reader with excitation and emission wavelengths being set to 530 and 590 nm for EtBr detection. Concentrations of the tested compounds were optimized such that fluorescence was 30-40% of the initial control at their highest reading. Each drug concentration was measured in duplicate. From a plot of fluorescence versus added drug concentration, the Q value is given by the concentration required to effect 50% removal of the initial fluorescence of the bound dye.

V.5.3 Thermal melting experiments. Analysis was carried out on an Agilent Cary 100 dual beam spectrophotometer equipped with a 6x6 Peltier multicell system with temperature controller. For poly[d(G-C)₂]; In a final volume of 1 mL using Starna black-walled quartz cuvettes with tight-fitting seals, 2 mM of NaOAc buffer (pH = 5.0), 1 mM NaCl and poly[d(G-C)₂] (Sigma, P9389) were

added to give a final absorbance of between 0.18 – 0.20 absorbance units at 260 nm ($\epsilon_{\text{max}} = 8,400 \text{ M}^{-1} \text{ cm}^{-1}$). For poly[d(A-T)₂]; in a final volume of 1 mL using Starna black-walled quartz cuvettes with tight-fitting seals, 50 mM NaOAc buffer (pH = 5.0), 250 mM NaCl and poly[d(A-T)₂] (Sigma, PO883) were added to give a final absorbance of between 0.18 – 0.20 absorbance units at 260 nm ($\epsilon_{\text{max}} = 6,600 \text{ M}^{-1} \text{ cm}^{-1}$). Stock solutions of metal complexes, netropsin and actinomycin D, prepared beforehand in DMF, were dissolved in 80 mM HEPES (pH 7.2). An aliquot of test reagent was then added to each cuvette such that an *r* value of 0.1 was achieved ($r = [\text{compound}]/[\text{nucleotide}]$). The test reagent and respective alternating co-polymer were then incubated for 10 minutes at 20 °C prior to commencing the temperature ramp. Thermal melting measurements were recorded at 260 nm at 0.25 s intervals. Temperature was ramped at 3 °C / min over then range 20.0 – 97.0 °C. The spectral bandwidth (SBW) was set to 1. Temperature was calibrated, for each measurement, using a temperature probe placed in an identical black-walled cuvette containing equivalent buffer and NaCl. Samples were run in triplicate and the melting temperature, *T_M* (°C), was calculated using the built-in derivative method on the instrument.

V.5.4 Artificial metallonuclease activity

V.5.4.1 Generation of pUC19 DNA. The vector pUC19 was generated following the transformation of *E. coli* using an LB ampicillin resistant media protocol and extracted using a maxi-prep kit protocol (NucleoBond Xtra Midi Plus, EF-Macherey-Nagel) and then quantified using the NanoDrop (ND-1000 Spectrophotometer).

V.5.4.2 Gel electrophoresis experiments on pUC19 DNA. Reactions were carried out according to the literature procedure by Kellett *et al.*⁴⁶ (see section III.4.5.1) Trapping experiments with 100 µM neocuprione (Sigma, N1501), 10% v/v of DMSO, and 1000 units of bovine SOD enzyme (Sigma, S7571) and 1000 units of catalase enzyme from bovine liver (Sigma, C1345) were also examined using this procedure.

V.5.4.3 Linearization of supercoiled pUC19. In a total volume of 20 µL using 5 µg of supercoiled pUC19, 5 µL of 10x HEPES buffer, 2.5 µL of 20,000 U/mL

HindIII (NEB), 5 μ L of NeBuffer 2 (NEB), 1 μ L BSA (NEB) and nuclease free water were added. This mixture was allowed to incubate at 37 °C for 2.5 h after which 1 μ L of this mixture was loaded onto an agarose gel to confirm linearization. Linear DNA from the mixture was then purified from the enzymatic reaction, using a QIAquick Purification column (QIAGEN). Linearised DNA was quantified using the NanoDrop (ND-1000 Spectrophotometer).

V.5.4.4 Microfluidic chip analysis of DNA degradation on the Agilent Bioanalyzer 2100. In a total volume of 20 μ L using 80 mM HEPES buffer (Fisher) at pH 7.2 with 25 mM NaCl, 500 nM of the complex was mixed with 400 ng of linear pUC19 and 1 mM Na-L Ascorbate. Samples were incubated at 37 °C for between 1-30 min and quenched with both neocuproine (100 μ M) and EDTA (100 μ M) before being loaded onto a DNA 7500 microfluidic chip as per the manufacturers protocol.²³ Data was then collected using Agilent 2100 Bioanalyzer. Electrograms generated by the Bioanalyzer 2100 for all complexes are available in the supporting material.

V.5.4.5 Chemical nuclease of linearized pUC19. In a total volume of 20 μ L using 400 ng of supercoiled pUC19 (2686 bp), 1 μ L *SaII* (20,000 U/mL, NEB, cleaving the plasmid at one site located at 429 bp), 2 μ L 10x HEPES buffer, 2 μ L NEBuffer 3.1, and nuclease free water were added. The reaction mixture was allowed to incubate at 37 °C for 1.5 h, after which the endonuclease was heat inactivated at 65 °C for 20 min. After cooling, an aliquot of the stock complex and 1 mM Na-L ascorbate were added to the reaction mixture and the final concentration of EDTA was adjusted (where appropriate) to ensure a final concentration 56.0 μ M before incubation at 37 °C for 30 min was completed. The reaction was then quenched with 6x loading dye (Fermentas) and DNA fragments were subjected to gel electrophoresis (prepared and stained as previously described).

V.5.4.6 Chemical nuclease of linearized pBC4. In a total volume of 20 μ L using 400 ng of supercoiled pBC4 (10,673 bp), 1 μ L *AgeI* (20,000 U/mL, NEB, cleaving the plasmid at one site located at 5037 bp), 2 μ L 10x HEPES buffer, 2 μ L NEBuffer 1, 0.2 μ L BSA and nuclease free water were added. Reaction

mixture was allowed to incubate at 37 °C for 1.5 h, after which the endonuclease was heat inactivated at 65 °C for 20 min. After cooling, an aliquot of the stock complex and 1 mM Na-L ascorbate were added to the reaction mixture and the final concentration of EDTA was adjusted (where appropriate) to ensure a final concentration 40.0 μ M before incubation at 37 °C for 30 min was completed. The reaction was then quenched with 6x loading dye (Fermentas) and DNA fragments were subjected to gel electrophoresis (prepared and stained as previously described).

V.5.5 Cell culture experiments SKOV-3 cells were grown in RPMI 1640 supplemented with 10% fetal calf serum (FCS) at 37 °C in a humidified atmosphere with 5% CO₂. Compound viability was tested using Guava Viacount reagent following 24 h exposure. Positive control, doxorubicin, was purchased from Sigma Aldrich as a European Pharmacopoeia reference standard. DMSO stocks for the complexes **Cu-Phen**, **Cu-DPQ-Phen**, **Cu-DPPZ-Phen**, **Cu-DPPN-Phen** and doxorubicin were prepared in 1 mL ranging from 11-34 mM.

V.5.5.1 ViaCount Assay SKOV3 cells were seeded at an initial density of 4 x 10⁴ cell/mL in 96-well plates and incubated overnight prior to drug addition. DMSO stocks of the complexes and controls diluted in RPMI 1640 containing 10% FCS, to give following final concentrations in 200 μ L wells: 5.0, 2.5, 1.0, 0.5 and 0.25 μ M. A DMSO control of the highest incubation concentration was also included. Cells were incubated for 24 h at 37°C in a humidified atmosphere with 5% CO₂. After 24 h exposure, spent media was removed and cells were washed once with 200 μ L PBS and detached using 50 μ L 1X trypsin subsequent addition of 50 μ L media. Cells were transferred to 96-well round bottom plates with 100 μ L Millipore's ViaCount reagent incubated at room temperature in the dark for 10 min. Viability data was collected on Guava EasyCyte HT flow cytometer using Guava Viacount software.

V.5.6 Electrochemistry Electrochemical measurements were performed on a Solartron 1825 potentiostat and data were analysed using *CorrView* software. Electrochemistry was performed in 1 mM solutions of each complex, made up in 0.1 M TBAPF₆ in 10% v/v DMF, as the supporting electrolyte. Concentrations of added reductant and oxidant were 2 mM to ensure an excess was present in

solution (ratio 1:2, complex:reductant/oxidant). Electrochemical cell set-up: Glassy Carbon working electrode (2 mm diameter), platinum wire counter electrode, non-aqueous Ag/Ag⁺ reference electrode ($E_{1/2} = 0.075$ V versus Fc/Fc⁺). Glassy carbon electrodes were polished using alumina oxide powder (0.05 micron) on a microcloth (Buehler). Cyclic voltammetric data presented were obtained after steady-state was attained, at a scan rate of 100 mV s⁻¹, with scans initiating in the cathodic direction.

V.5.7 Superoxide dismutase mimetic activity. The SOD mimetic activities of the complexes were determined using a nitroblue tetrazolium (NBT) assay,³⁴ in which the xanthine/xanthine oxidase system serves as the source of superoxide radicals. The quantitative reduction of NBT to blue formazan by O₂^{•-} was followed spectrophotometrically using a thermostatically controlled Agilent Cary 100 dual-beam spectrophotometer at 550 nm at 25 °C. Reagents were obtained from Sigma–Aldrich and the assays were run in a total volume of 3 mL. Tabulated results were derived from linear regression analyses and are reported as V_o / V_c (rate in the absence of catalyst / rate in the presence) versus catalyst concentration which yielded the catalytic rate ($K_{cat} \text{ M}^{-1} \text{ s}^{-1}$).

V.5.8 H₂O₂ breakdown assay. A 5 mL stock solution of 100 μM Amplex Red containing 10 mM Amplex Red reagent and 10 U/ml horseradish Peroxidase (HRP) was prepared in 1x buffer as per Amplex Red hydrogen Peroxide/Peroxidase assay kit instruction (Invitrogen – Cat. A22188). A standard fluorescence response curve from H₂O₂ was obtained by adding a series of aliquots (0.5 – 5 μM) H₂O₂ the Amplex Red stock solution and the volume was adjusted to 100 μL with 1x buffer in each sample well. An aliquot containing 5 μM of tested compounds, 5 μM H₂O₂ and 100 μM Na-L-Ascorbate that were previously incubated between 0 – 120 min were added to 50 μL Amplex Red solution and again the volume was adjusted to 100 μL using 1x buffer. The fluorescence intensity of the reaction mixture was measured with a Bio-Tek synergy HT multi-mode microplate reader equipped with excitation and emission filters at 530 nm and 590 nm.⁴⁷

V.5.9 Optimization of thermal melting on poly[d(A-T)₂] and poly[d(G-C)₂]

V.5.9.1 Overview. In order to examine the stabilization effects on poly[d(G-C)₂] and poly[d(A-T)₂], a series of optimisation experiments were conducted to identify the most suitable pH and ionic buffer strength required (ESI). Previous reports on drug binding effects to G-C polynucleotides, where strands are bound through three hydrogen bonds at each base pair, could not be identified owing to polymer stabilization beyond the limit of detection (>110 °C). In our experiments, suitable conditions for the melting of poly[d(G-C)₂] ($T_M = 80.74$ °C) were found at pH 5.0 in 2.0 mM sodium acetate buffer containing 1.0 mM NaCl. In order to maintain similar experimental conditions for the thermal melting on poly[d(A-T)₂], where strands are bound through two hydrogen bonds between each base pair only, pH 5.0 sodium acetate buffered (50 mM) solutions containing 250 mM of NaCl were employed for the thermal melting of this polynucleotide ($T_M = 69.32$ °C).

V.5.9.2 Poly[d(G-C)₂]. It was necessary to carry out experimental optimisation before commencing thermal melting analysis as it was noted in literature previously published, the T_M for poly(dG-dC)•poly(dC-dG) could not be determined as it was beyond the level of detection, in some cases >110 °C.^{48,49} Thermal melting analysis was initially investigated in potassium phosphate buffer at pH 7.2 with varying NaCl concentrations of 0.1 mM, 1 mM and 2 mM generating T_M values of 90.60 °C, 89.57 °C and 91.52 °C for the untreated polymer, respectively. It was therefore necessary to identify conditions where the T_M of poly[d(G-C)₂] would be lower prior to the addition of any stabilizing test compound. Varying concentrations (2.0 – 5.0 mM) of sodium acetate buffer (NaOAc) at pH 5.0 were then investigated in the presence and absence of added NaCl (Table 5). 2.0 mM NaOAc buffer with 1.0 mM of added NaCl gave a favourable T_M value of 80.74 °C which was used in all thermal denaturation studies.

Table V.5 Thermal melting analysis of poly[d(G-C)₂] under alternating buffer, pH and ionic strength.

Buffer	Buffer (mM)	Added NaCl (mM)	T _M (°C)
Phosphate (pH 7)	50	0.1	90.60
	50	1.0	89.57
	50	2.0	91.52
NaOAc (pH 5)	2.0	0.0	73.02
	2.0	1.0	80.74
	2.5	0.0	89.02
	5.0	0.0	86.02

References

- (1) Liu, H.-K.; Sadler, P. J. *Acc. Chem. Res.* **2011**, *44*, 349.
- (2) Jamieson, E. R.; Lippard, S. J. *Chem. Rev.* **1999**, *99*, 2467.
- (3) Lippard, S.; Bond, P.; WU, K.; Bauer, W. *Science* **1976**, *194*, 726.
- (4) Zeglis, B. M.; Pierre, V. C.; Barton, J. K. *Chem. Commun.* **2007**, 4565.
- (5) Park, G. Y.; Wilson, J. J.; Song, Y.; Lippard, S. J. *Proc. Natl. Acad. Sci. U.S.A.* **2012**, *109*, 11987.
- (6) Hiort, C.; Lincoln, P.; Norden, B. *J. Am. Chem. Soc.* **1993**, *115*, 3448.
- (7) Sigman, D. S.; Graham, D. R.; D'Aurora, V.; Stern, A. M. *J. Biol. Chem.* **1979**, *254*, 12269.
- (8) Sigman, D. S.; Mazumder, A.; Perrin, D. M. *Chem. Rev.* **1993**, *93*, 2295.
- (9) Chen, C.-h. B.; Milne, L.; Landgraf, R.; Perrin, D. M.; Sigman, D. S. *ChemBioChem.* **2001**, *2*, 735.
- (10) Santini, C.; Pellei, M.; Gandin, V.; Porchia, M.; Tisato, F.; Marzano, C. *Chem. Rev.* **2013**.
- (11) Gutteridge, J. M. C.; Halliwell, B. *Biochem. Pharm.* **1982**, *31*, 2801.
- (12) Goldstein, S.; Michel, C.; Bors, W.; Saran, M.; Czapski, G. *Free Rad. Biol. Med.* **1988**, *4*, 295.
- (13) Sigman, D. S.; Bruice, T. W.; Mazumder, A.; Sutton, C. L. *Acc. Chem. Res.* **1993**, *26*, 98.
- (14) Chen, C. H.; Sigman, D. S. *Proc. Natl. Acad. Sci. U.S.A.* **1986**, *83*, 7147.
- (15) Bales, B. C.; Kodama, T.; Weledji, Y. N.; Pitié, M.; Meunier, B.; Greenberg, M. M. *Nucleic Acids Res.* **2005**, *33*, 5371.
- (16) Pitié, M.; Burrows, C. J.; Meunier, B. *Nucleic Acids Res.* **2000**, *28*, 4856.
- (17) Niyazi, H.; Hall, J. P.; O'Sullivan, K.; Winter, G.; Sorensen, T.; Kelly, J. M.; Cardin, C. J. *Nat. Chem.* **2012**, *4*, 621.
- (18) Song, H.; Kaiser, J. T.; Barton, J. K. *Nat. Chem.* **2012**, *4*, 615.
- (19) Holmlin, R. E.; Dandliker, P. J.; Barton, J. K. *Angew. Chem. Inter. Ed. Engl.* **1997**, *36*, 2714.
- (20) Hall, J. P.; Cook, D.; Morte, S. R.; McIntyre, P.; Buchner, K.; Beer, H.; Cardin, D. J.; Brazier, J. A.; Winter, G.; Kelly, J. M.; Cardin, C. J. *J. Am. Chem. Soc.* **2013**, *135*, 12652.
- (21) Wang, J. *Nucleic Acids Res.* **2000**, *28*, 3011.
- (22) <http://www.agilent.com/>.

- (23) <http://www.genomics.agilent.com/en/Bioanalyzer-DNA-RNA-Kits/DNA-Analysis-Kits/?cid=AG-PT-105&tabId=AG-PR-1040>.
- (24) Dickeson, J.; Summers, L. *Aust. J. Chem.* **1970**, *23*, 1023.
- (25) Yam, V. W.-W.; Lo, K. K.-W.; Cheung, K.-K.; Kong, R. Y.-C. *Chem. Commun.* **1995**, 1191.
- (26) Collins, J. G.; Sleeman, A. D.; Aldrich-Wright, J. R.; Greguric, I.; Hambley, T. W. *Inorg. Chem.* **1998**, *37*, 3133.
- (27) Prisecaru, A.; McKee, V.; Howe, O.; Rochford, G.; McCann, M.; Colleran, J.; Pour, M.; Barron, N.; Gathergood, N.; Kellett, A. *J. Med. Chem.* **2013**, *56*, 8599.
- (28) McCann, M.; McGinley, J.; Ni, K.; O'Connor, M.; Kavanagh, K.; McKee, V.; Colleran, J.; Devereux, M.; Gathergood, N.; Barron, N.; Prisecaru, A.; Kellett, A. *Chem. Commun.* **2013**, *49*, 2341.
- (29) O'Connor, P. M.; Jackman, J.; Bae, I.; Myers, T. G.; Fan, S.; Mutoh, M.; Scudiero, D. A.; Monks, A.; Sausville, E. A.; Weinstein, J. N.; Friend, S.; Fornace, A. J., Jr.; Kohn, K. W. *Cancer Res.* **1997**, *57*, 4285.
- (30) O'Neill, C. F.; Koberle, B.; Masters, J. R. W.; Kelland, L. R. *Br. J. Cancer.* **1999**, *81*, 1294.
- (31) Momparler, R. L.; Karon, M.; Siegel, S. E.; Avila, F. *Cancer Res.* **1976**, *36*, 2891.
- (32) Capranico, G.; Kohn, K. W.; Pommier, Y. *Nucleic Acids Res.* **1990**, *18*, 6611.
- (33) Pang, B.; Qiao, X.; Janssen, L.; Velds, A.; Groothuis, T.; Kerkhoven, R.; Nieuwland, M.; Ovaa, H.; Rottenberg, S.; van Tellingen, O.; Janssen, J.; Huijgens, P.; Zwart, W.; Neefjes, J. *Nat. Commun.* **2013**, *4*, 1908.
- (34) Goldstein, S.; Czapski, G. *Free Radicals: A Practical Approach*; IRL Press at Oxford University Press: New York, 1996.
- (35) Arkin, M. R.; Stemp, E. D. A.; Turro, C.; Turro, N. J.; Barton, J. K. *J. Am. Chem. Soc.* **1996**, *118*, 2267.
- (36) Liu, Z.-C.; Wang, B.-D.; Yang, Z.-Y.; Li, Y.; Qin, D.-D.; Li, T.-R. *Eur. J. Med. Chem.* **2009**, *44*, 4477.
- (37) Chen, J.; Ren, X.; Le, X.; Feng, X. *Chin. J. Chem.* **2010**, *28*, 2179.
- (38) Le, X. Y.; Gu, Q.; Song, Z. J.; Zhuang, C. X.; Feng, X. L. *J. Coord. Chem.* **2007**, *60*, 1359.

- (39) Rao, R.; Patra, A. K.; Chetana, P. R. *Polyhedron* **2008**, *27*, 1343.
- (40) Terenzi, A.; Tomasello, L.; Spinello, A.; Bruno, G.; Giordano, C.; Barone, G. *J. Inorg. Biochem.* **2012**, *117*, 103.
- (41) Patra, A. K.; Bhowmick, T.; Roy, S.; Ramakumar, S.; Chakravarty, A. R. *Inorg. Chem.* **2009**, *48*, 2932.
- (42) Thomas, A. M.; Nethaji, M.; Chakravarty, A. R. *J. Inorg. Biochem.* **2004**, *98*, 1087.
- (43) Liu, J.-G.; Zhang, Q.-L.; Shi, X.-F.; Ji, L.-N. *Inorganic Chemistry* **2001**, *40*, 5045.
- (44) Jaenisch, R.; Bird, A. *Nat. Genet.* **2003**, *33*, 245.
- (45) Spruijt, Cornelia G.; Gnerlich, F.; Smits, Arne H.; Pfaffeneder, T.; Jansen, Pascal W. T. C.; Bauer, C.; Münzel, M.; Wagner, M.; Müller, M.; Khan, F.; Eberl, H. C.; Mensinga, A.; Brinkman, Arie B.; Lephikov, K.; Müller, U.; Walter, J.; Boelens, R.; van Ingen, H.; Leonhardt, H.; Carell, T.; Vermeulen, M. *Cell* **2013**, *152*, 1146.
- (46) Prisecaru, A.; Devereux, M.; Barron, N.; McCann, M.; Collieran, J.; Casey, A.; McKee, V.; Kellett, A. *Chem. Commun.* **2012**, *48*, 6906.
- (47) Rhee, S.; Chang, T.-S.; Jeong, W.; Kang, D. *Mol. Cells* **2010**, *29*, 539.
- (48) García, B.; Leal, J. M.; Ruiz, R.; Biver, T.; Secco, F.; Venturini, M. *J. Phys. Chem. B* **2010**, *114*, 8555.
- (49) Saha, I.; Hossain, M.; Suresh Kumar, G. *J. Phys. Chem. B* **2010**, *114*, 15278.
- (50) Wilson, D.; Tanious, F. A.; Fernandez-Saiz, M.; Rigl, C. T. Evaluation of Drug-Nucleic Acid Interactions by Thermal Melting Curves. In *Methods in Molecular Biology, Vol. 90: Drug-DNA Interaction Protocols*, Fox, K. R., Ed. Humana Press: New Jersey, **1997**; pp. 219–240.
- (51) Doktycz, M. J. Nucleic Acids: Thermal Stability and Denaturation. In *eLS*; John Wiley & Sons, Ltd, **2001**.

Chapter VI

The phosphate clamp: sequence selective nucleic acid binding profiles and conformational induction of endonuclease inhibition by cationic Triplatin complexes

This paper was published in *Nucleic Acids Research*, 2014, **42**, 22, pp13474-13487

Prisecaru A., Molphy Z., Kipping R.G., Peterson E.J., Qu Y., Kellett A., and Farrell N.P.

My contribution to this paper is: Manuscript 1st author, DNA binding on different types of DNA and tRNA, nuclease inhibition using the “on chip” microfluidic analysis.

VI. 1 Abstract

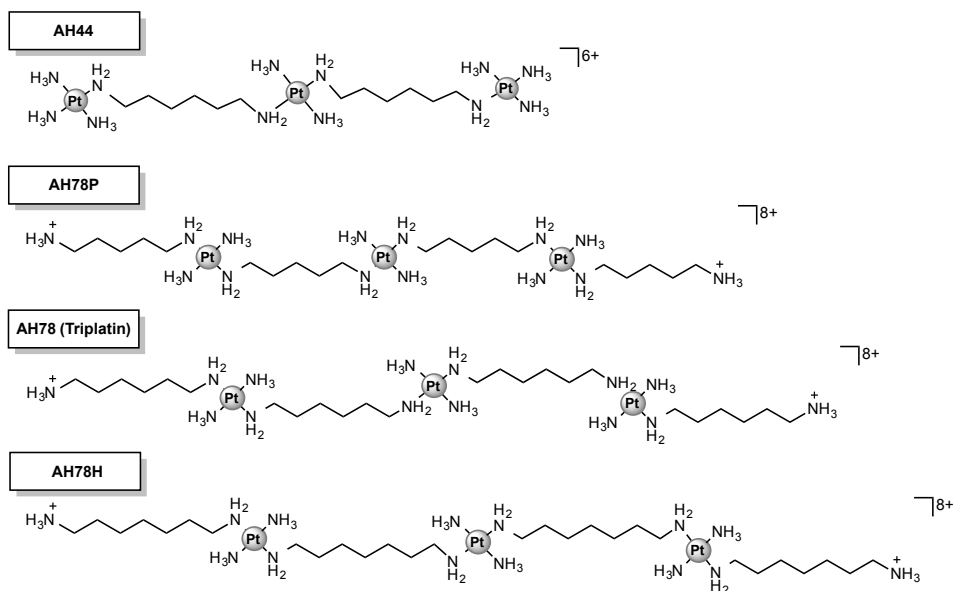
The substitution-inert polynuclear platinum(II) complex (PPC) series, [$\{trans\text{-Pt}(\text{NH}_3)_2(\text{NH}_2(\text{CH}_2)_n\text{NH}_3)\}_2\text{-}\mu\text{-(}trans\text{-Pt}(\text{NH}_3)_2(\text{NH}_2(\text{CH}_2)_n\text{NH}_2)_2\}\text{] (NO}_3)_8$, where $n = 5$ (AH78P), 6 (AH78 TriplatinNC) and 7 (AH78H), are potent non-covalent DNA binding agents where nucleic acid recognition is achieved through use of the “phosphate” clamp where the square-planar tetra-am(m)ine Pt(II) coordination units all form bidentate N-O-N complexes through hydrogen bonding with phosphate oxygens. The modular nature of PPC-DNA interactions results in high affinity for calf thymus DNA ($K_{\text{app}} \sim 5 \times 10^7 \text{ M}^{-1}$). The phosphate clamp-DNA interactions result in condensation of superhelical and B-DNA, displacement of intercalated ethidium bromide, and facilitate cooperative binding of Hoechst 33258 at the minor groove. The effect of linker chain length on DNA conformational changes was examined and the pentane-bridged complex, AH78P, was optimal for condensing DNA with results in the nanomolar region. Analysis of binding affinity and conformational changes for sequence-specific oligonucleotides by ITC, dialysis, ICP-MS, CD and 2D- ^1H NMR experiments indicate that two limiting modes of phosphate clamp binding can be distinguished through their conformational changes and strongly suggest that DNA condensation is driven by minor-groove spanning. Triplatin-DNA binding prevents endonuclease activity by type II restriction enzymes *Bam*HI, *Eco*RI and *Sal*I and inhibition was confirmed through the development of an on-chip microfluidic protocol.

VI.2 Introduction

The X-ray crystal structure of the Dickerson-Drew Dodecamer, (DDD, [d(CGCGAATTCGCG)]₂) with the non-covalently binding trinuclear platinum compound TriplatinNC (AH78), Scheme VI.1, described a new mode of ligand-DNA recognition distinct from the conventional modes of intercalation and groove binding (NDB entry 2DYW) (1). Hydrogen bonding with phosphate oxygens results in either backbone tracking or groove spanning through formation of “phosphate clamps” where the square-planar tetra-am(m)ine Pt(II) coordination units all form bidentate N-O-N complexes with phosphate oxygen

OP atoms, Figure VI.1. The generality of the motif has been confirmed by a second crystal and molecular structure with TriplatinNC-A (AH44) – that is with $L = \text{NH}_3$ (6+) instead of $-\text{NH}_2(\text{CH}_2)_6\text{NH}_3^+$ (8+), See Scheme VI.1 (2). In both cases, the conformation in the DDD-Phosphate Clamp complexes differs significantly from that of the native structure (NDB entry BDL084). The structural distortions caused are principally axial bending and axial path length shortening ratio, which are significantly greater than those of the control DDD. Helical parameters are perturbed and the minor groove width profile is modestly impacted. The axial bending is similar to that induced by the cisplatin intrastrand 1,2-GG adduct, (3), but achieved solely through H-bonding and electrostatic interactions. The phosphate clamp is analogous to that of the guanidino group of arginine which shows an analogous, but attenuated clamping ability in which two OP atoms form a clamp-like structure, the Arginine Fork (4, 5). The discovery of new molecular mechanisms by which small molecules modify DNA structure, reactivity and biological repair contributes significantly to potential drug development as DNA is a clinically important target (6, 7). The broad class of polynuclear platinum complexes (PPCs) may now be divided into those complexes capable of Pt-DNA covalent bond formation such as BBR3464, the only “non-classical” platinum drug to enter human clinical trials, and those “non-covalently binding” compounds depicted in Scheme VI.1 with inherently substitutionally-inert PtN_4 coordination spheres (8). Specifically, TriplatinNC has demonstrated interesting biological activity in its own right. The complex is cytotoxic at micromolar concentrations, similar to cisplatin, in a range of human tumor cell lines but is unaffected by serum degradation (9). The induction of apoptosis in tumor cells suggests that covalent Pt-DNA bond formation is not a prerequisite for antitumor activity for compounds with high DNA affinity, a further shift in the structure-activity paradigm of platinum antitumor agents. Simultaneous multi-element imaging using NanoSIMS (nano-scale secondary ion mass spectrometry), exploiting the novel combination of ^{195}Pt and ^{15}N in platinum-am(m)ine antitumor drugs, confirmed localization of TriplatinNC in the nucleolus of MCF7 cells (10), with implications for interaction with ribosomal DNA and/or RNA within the nucleolus.

The nature of the PPC chemotype means it is a discrete and modular DNA binding device with high potential as a drug-design scaffold. Within the non-covalently binding motif, possible systematic changes include dinuclear complexes such as $[\{\text{Pt}(\text{NH}_3)_3\}_2\text{-}\mu\text{-spermidine}]^{5+}$ and $[\{\text{Pt}(\text{NH}_3)_3\}_2\text{-}\mu\text{-spermine}]^{6+}$ connected *via* polyamine central linkers rather than the $\{\text{Pt}(\text{tetraamine})\}$ trinuclear unit, and the use of the 'dangling' amine versus NH_3 as ligand to add further overall charge diversity (8). Binding studies of AH44 to DNA polymers of varying base composition—or topology—revealed high affinity and limited discrimination in terms of binding constant and mode (11,12). Both TriplatinNC and AH44 are significantly more effective nucleic acid condensing agents compared to spermine (11,12). A further modification to affect DNA binding interactions is variation of alkanediamine chain length in the trinuclear structures of Scheme VI.1. In principle, modifying distances between phosphate clamp coordination units (12.46 Å from NDB entry 2DYW) could be used to maximize overlap with phosphate-phosphate distances of RNA and differing DNA conformations. In this contribution we describe the effects of TriplatinNC congeners, Scheme VI.1, on DNA binding affinity and inhibition of endonuclease enzyme recognition by various biophysical and molecular biological methods. Preliminary comparisons with tRNA affinity are made and in all cases the minor groove binding agents, netropsin and pentamidine, along with the cationic cobalt(III) complex, $[\text{Co}(\text{NH}_3)_6]^{3+}$, were examined to delineate new properties within this class of drug molecule. A general question in all of this work is: how do the solution binding properties reflect the crystallographically determined modes of groove spanning and backbone tracking as shown in Figure VI.1. This contribution demonstrates that the two distinctive limiting interaction modes may be distinguished by their formational dependence on tertiary DNA helical topology and G-C content and suggests that DNA condensation is driven by minor-groove recognition.



Scheme VI.1 Molecular structures of $[\{Pt(NH_3)_3\}_2-\mu-\{trans-Pt(NH_3)_2(NH_2(CH_2)_6NH_2)_2\}]^{6+}$ (AH44, TriplatinNC-A) and $[\{trans-Pt(NH_3)_2(NH_2(CH_2)_nNH_3)\}_2-\mu-(trans-Pt(NH_3)_2(NH_2(CH_2)_nNH_2)_2)]^{8+}$ cations where $n = 5$ (AH78P), 6 (AH78H, TriplatinNC) and 7 (AH78H).

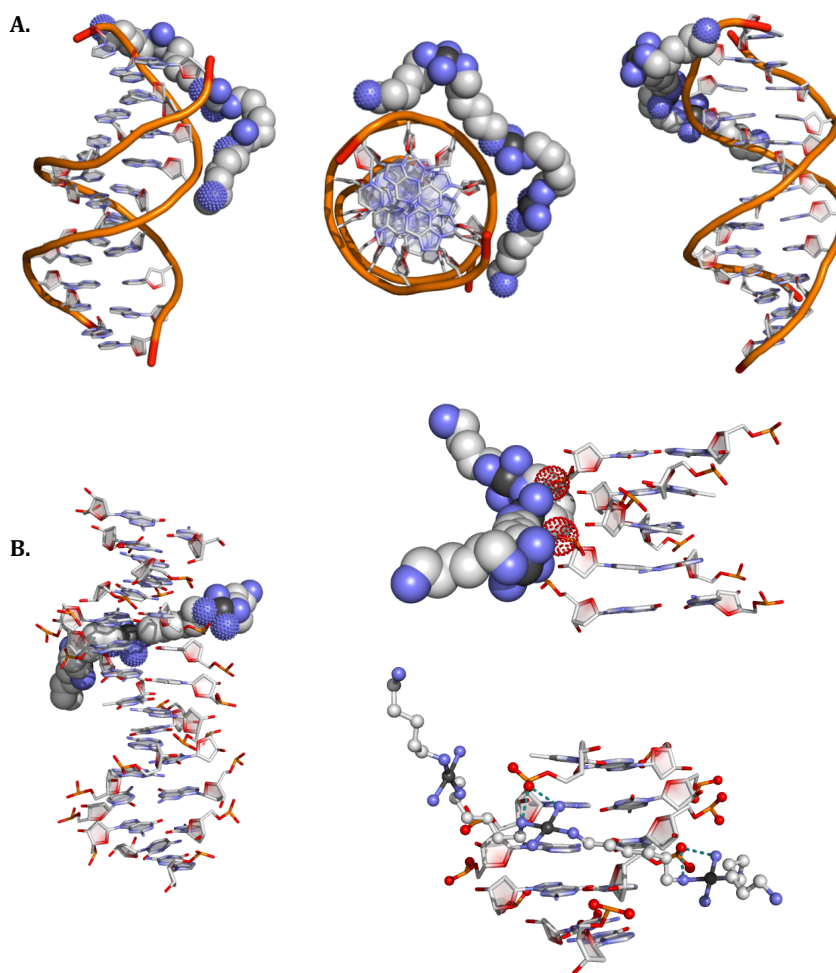


Figure VI.65 Perspective views of the double-stranded B-DNA Dickerson-Drew dodecamer bound to TriplatinNC via backbone tracking (**A**) and groove-spanning (**B**) modes (1, NDB entry 2DYW). DNA backbone (connecting P positions), orange; carbon, grey80; oxygen, red; nitrogen, slate (all in cartoon mode). Triplatin complex (space-filling mode) atoms coloured as DNA; platinum, grey30. Platinum(II) amine nitrogen atoms, and selected phosphate coordinated oxygen atoms, engaged in phosphate clamping shown with dotted surface. Figures generated by PyMOL Molecular Graphics System, Version 1.5.0.4 Schrödinger, LLC.

VI. 3 Materials and Methods

Chemicals and deoxyribonucleic acid sodium salt from salmon testes were purchased from Sigma Aldrich (Ireland) and used without further purification. Ultra Pure calf-thymus DNA (CT-DNA, Cat.15633-019) and transfer RNA (tRNA, AM7119) was supplied from Invitrogen, supercoiled plasmid DNA (pUC19, Cat. N3033L) and restriction endonucleases *Aat*II (R0117 S; 20,000 U/ml), *Bam*HI (R0136 S; 20,000 U/ml), *Eco*RI (R0101 S; 20,000 U/ml) and *Sal*I (R 0138 S; 20,000 U/ml) were supplied by NEB. Fluorescence measurements

were conducted using a Bio-Tek Synergy HT multi-mode microplate reader; viscosity was measured with DV-II Programmable Digital Viscometer equipped with Enhanced Brookfield UL Adapter; thermal melting analysis was carried out on an Agilent Cary 100 dual beam spectrophotometer equipped with a 6x6 Peltier system and microfluidic chip experiments were conducted on the Bioanalyzer 2100 platform using DNA 7500 chips supplied by Agilent Technologies Ireland.

VI.3.1. Preparation of Triplatin complexes [*trans*-Pt(NH₃)₂(NH₂(CH₂)_nNH₃)}₂-μ-*trans*-Pt(NH₃)₂(NH₂(CH₂)_nNH₂)₂] (NO₃)₈

The “non-covalent” compounds with varying chain lengths (*n* = 5,6,7) were synthesized by adapting published procedures (8,13). The complexes AH78P, AH78 (TriplatinNC) and AH78H were characterized by C,H,N, elemental analysis and ¹H and ¹⁹⁵Pt NMR Spectroscopy. Purity was confirmed by HPLC. For *n* = 5, ¹H NMR (δ(¹H), D₂O, ppm): 2.99 (t, 4H); 2.66 (t,12H); 1.66 (m, 16H); 1.38 (m,8H). δ(¹⁹⁵Pt NMR, D₂O, ppm): -2675. HPLC Purity 99.8%. For *n* = 6, ¹H NMR (δ(¹H), D₂O, ppm): 2.95 (t, 4H); 2.62 (t,12H); 1.60 (m, 16H); 1.38 (m,16H). δ(¹⁹⁵Pt NMR, D₂O, ppm): -2680. HPLC Purity 99.0%. For *n* = 7, ¹H NMR (δ(¹H), D₂O, ppm): 2.98 (t, 4H); 2.62 (t,12H); 1.62 (m, 16H); 1.32 (m,24H). δ(¹⁹⁵Pt NMR, D₂O, ppm): -2680. HPLC Purity 99.0%

VI.3.2. DNA binding experiments

VI.3.2.1. Competitive ethidium bromide displacement Experiments were conducted in a similar manner to the high-throughput method reported by Kellett *et al.* (14). Each drug concentration was measured in triplicate, on at least two separate occasions, and the apparent binding constants were calculated using $K_{app} = K_b \times 12.6/C_{50}$ where $K_b = 8.80 \times 10^6 \text{ M(bp)}^{-1}$ (K_{app} = apparent binding constant). (see section III.4.4.1)

VI.3.2.2. DNA binding kinetic studies A working solution of 20.0 μM of ctDNA along with 25.2 μM of EtBr in HEPES buffer (80 mM, pH = 7.2) and NaCl (40 mM) was prepared. 50 μL of DNA-EtBr working solution were placed in each well of a 96 well microplate with the exception of the controls, which

contained 100 μL of buffer. A 1.0 μM aliquot of test complex was then added to each well plate such that an r value of 0.1 was achieved ($r = [\text{complex}] / [\text{ctDNA}]$, $\epsilon_{\text{max}} = 12824 \text{ M}(\text{bp})^{-1} \text{ cm}^{-1}$ for ctDNA) and the volume was adjusted to 100 μL such that the final concentration of CT-DNA and EtBr were 10.0 μM and 12.6 μM , respectively. Fluorescence measurements were recorded using a Bio-Tek synergy HT multi-mode microplate reader with excitation and emission wavelengths being set to 530 and 590 nm. Kinetic studies were analysed over 1 h period at room temperature with measurements taken at 68-second intervals.

VI.3.2.3. DNA fluorescence quenching Experiments were conducted in a similar manner to the high-throughput method reported previously (14). (see section III.4.4.2)

VI.3.2.4. Viscosity studies (15). See section III.5.6 for experimental

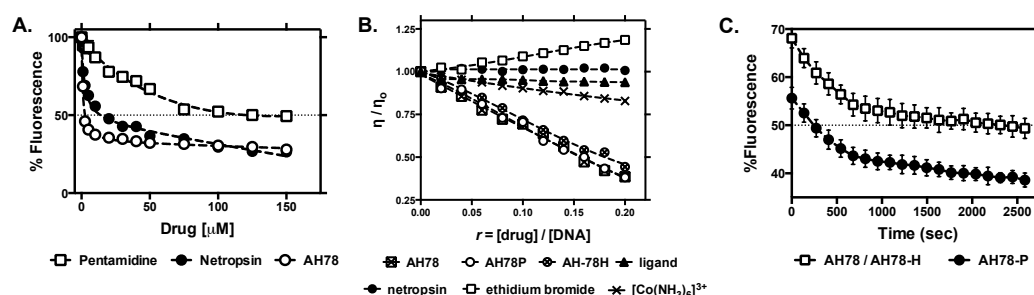


Figure VI.66 **A.** Competitive fluorescence binding of TriplatinNC (AH78), pentamidine, and netropsin to ethidium bromide (12.6 μM) saturated solutions of calf thymus DNA (10 μM) (data points generated from triplicate measurement, error bars \pm S.D.). **B.** Relative viscosity changes in salmon testes dsDNA (1 mM) upon treatment with tested agents. **C.** Kinetic competitive fluorescence binding of ethidium bromide (12.6 μM) bound calf thymus DNA(ctDNA) (10.0 μM) upon titration of Triplatin complex at $r = 0.10$ (data points generated from triplicate measurement, error bars \pm S.D., note that AH78 and AH78H produced identical, overlapping, quenching profiles).

VI.3.2.5 Viscosity analysis on sheared stDNA

A concentrated solution of dsDNA (deoxyribonucleic acid sodium salt from salmon testes fibres (stDNA), Sigma-Aldrich, D1626) was prepared by dissolving the fibres in 80 mM HEPES buffer. The solution was initially vortexed for ~ 20 min until all visible DNA fibres had dissolved and then, in order to shear the DNA, the solution passed rapidly through an 18-gauge needle

15 times before being sonicated for 90 min. A 15 mL stDNA solution was then prepared at 1×10^{-3} M in 80 mM HEPES buffer with viscosity being recorded as previously described.

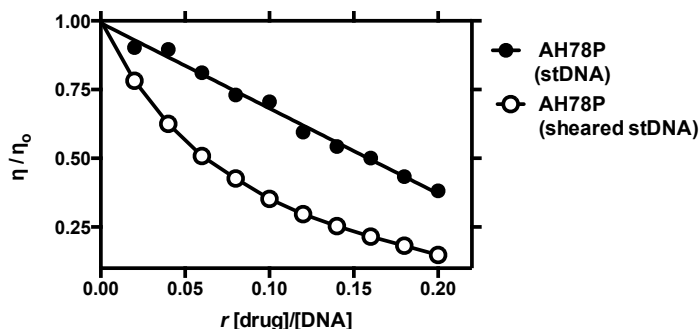


Figure VI.67 .Relative viscosity changes in salmon testes dsDNA (1 mM) upon treatment with AH78P using both sheared and non-sheared stDNA.

VI.3.2.6 ctDNA thermal melting analysis (16). In a final volume of 1 mL using black-walled quartz cuvettes (Starna) with tight-fitting seals, 50 mM potassium phosphate buffer (pH = 7.8), 2.0 mM NaCl and CT-DNA were added to give a final absorbance of 0.5 absorbance units at 260 nm. Stock solutions of platinum complexes were prepared in nuclease-free H₂O, minor-groove binders (netropsin and pentamidine), the cobalt(III) complex, [Co(NH₃)₆](NO₃)₃, and the intercalator EtBr, were prepared in 80 mM HEPES. A 3.75 μ M aliquot of test reagent was then added to each cuvette such that an r value of 0.05 was achieved ($r = [\text{compound}] / [\text{ctDNA}]$, $\epsilon_{\text{max}} = 6,600$). Thermal melting measurements were recorded at 260 nm at 0.5 s intervals over a temperature range of 20 – 97 °C. Temperature was calibrated for each measurement using a temperature probe placed in an identical black-walled cuvette containing 50 mM of phosphate buffer. The temperature was ramped at 3.5 °C / min with data being collected every 0.5 °C. The spectral bandwidth (SBW) was set to 1. Replicate samples were run in triplicate and the melting temperature, T_M (°C), was calculated using the built-in derivative method on the instrument.

VI.3.2.7 Thermal melting analysis on modified DNA The concentrations of nucleic acids (expressed as nucleotides) were determined spectrophotometrically using the extinction coefficients $\epsilon_{260} = 6000 \text{ M}^{-1} \text{ cm}^{-1}$ for calf thymus DNA, $\epsilon_{260} = 6225 \text{ M}^{-1} \text{ cm}^{-1}$ for *Clostridium perfringens* (Type XII, Sigma) (17), $\epsilon_{262} = 6650$

$\text{M}^{-1}\text{cm}^{-1}$ for poly[d(A-T)₂] (16) and $\epsilon_{260} = 6000 \text{ M}^{-1}\text{cm}^{-1}$ for poly(dA)-poly(dT) (18). The 100 μM polynucleotide DNA samples were incubated with TriplatinNC at a ratio $r = 0.05$ (r being the ratio of drug per nucleotide) in 10 mM NaClO₄ at 37 °C for 1 h. All samples were degassed prior to measurement. The absorbance at 260 nm was recorded while the temperature was increased from 20 to 95 °C at a rate of 0.5 °C/min.

VI.3.2.8 DNA association assay 100 μM CT-DNA, poly(dA-dT)₂ or poly(dG-dC)₂ were incubated with 5 μM TriplatinNC ($r = 0.05$) at 37°C protected from light for 1 h in 10 mM phosphate buffer and 50 mM NaCl at pH 7.4. Subsequently the samples were divided into two equal parts. One mixture was used as control and the other one was dialyzed against the same buffer for 24 h. The buffer solution was exchanged every 8 h. The modified DNA was digested with 500 μL HNO₃ concentrated and 500 μL water at 95 °C for 3 h. 1000 μL of water was added and the platinum content was determined by ICP-MS. The experiment was conducted thrice and the determined platinum concentrations were averaged.

VI.3.2.9 Comparative binding of mithramycin towards poly(dG-dC)₂ in the presence and absence of TriplatinNC Samples were prepared in buffer solutions containing 10 mM PO₄³⁻, 50 mM NaCl and 10 mM MgCl₂ (pH 7.4). The concentrations of mithramycin A ($\epsilon_{400} = 10000 \text{ M}^{-1} \text{cm}^{-1}$) and poly(dG-dC)₂ ($\epsilon_{254} = 8400 \text{ M}^{-1} \text{cm}^{-1}$) were determined spectrophotometrically. Poly(dG-dC)₂ was incubated with TriplatinNC at a ratio of 0.05 drug/nucleotide at 37°C for 1 h. Varying amounts of mithramycin A were added in the r range of 0.0 – 0.25 to modified and untreated DNA. The samples were kept for 24h at 37 °C in the dark. The final concentration of poly(dG-dC)₂ in the samples was 100 μM . Fluorescence spectra were recorded with a Cary Eclipse spectrofluorometer. To avoid photodegradation the fluorescence excitation wavelength was set to 470 nm. The absorbance of the samples at this wavelength was less than 0.05 with the inner filter effect therefore being neglected. Spectra were recorded in the range of 525 to 625 nm.

VI.3.2.10 Circular dichroism experiments The polynucleotides poly(dG-dC)₂ and poly(dA-dT)₂ were incubated with TriplatinNC at 37°C in the dark for 1h at variable r values ($r = [\text{initial number of molecules of platinum complex in solution}] / [\text{number of bases of DNA in solution}]$). CD spectra were recorded at room temperature using a Jasco J600 Spectropolarimeter and a 10 mm sub-micro cuvette. The buffer background was subtracted from the obtained spectra. Concentration of DNA was 50 μM bases in a phosphate buffer (10 mM phosphate, 50 mM NaCl, pH 7.0).

VI.3.2.11 ITC of polynuclear DNA titrated with TriplatinNC The polynucleotides poly(dG-dC)₂, poly[d(A-T)₂] and poly(dA)-poly(dT) as well as the TriplatinNC solutions each were prepared in 10 mM PO₄³⁻ and 50 mM NaCl buffer solution with pH 7.0. All samples were degassed immediately before use. The drug solution (250 μM) was titrated into the DNA mixture (300 μM) by making 25 injections of 11 μL each every 300 sec at a stirring rate of 310 rpm at 20 °C. The actual heats of binding were obtained after subtracting the heats of dilution for the injections of TriplatinNC into buffer. Origin 7.0 software was used to fit the corrected data and determine the thermodynamic parameters. The heat of the first injection was not included in the fitting process. Each experiment was performed in duplicate.

VI.3.2. NMR Analysis of TriplatinNC Modified DNA Oligomers

VI.3.2.1. NMR Spectroscopy The NMR spectra were recorded on a Bruker AVANCE III 600 MHz spectrometer (¹H, 600.1 MHz) fitted with a pulsed field gradient module and 5mm inverse quadruple resonance (QXI) probe. The ¹H NMR chemical shifts are internally referenced to TSP. The two-dimensional [¹H,¹H] COSY and NOESY spectra were acquired with water suppression using the excitation sculpting, TOCSY spectra were recorded with the watgate 3-9-19 pulse sequence.

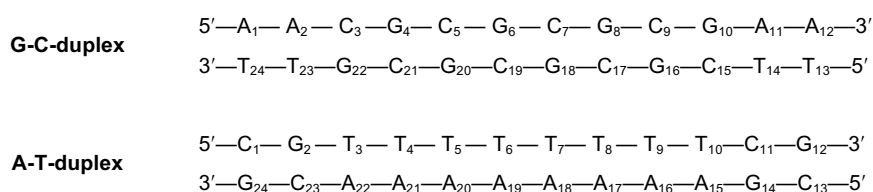


Figure VI.4 Sequences of double-stranded dodecamers examined for interactions with TriplatinNC by 2D NMR Spectroscopy

VI.3.2.2. NMR experimental and results All samples were prepared in 99.99% D₂O or 8% D₂O / 92% H₂O with 10 mM PO₄³⁻, 300 mM NaCl and adjusted to pD 6 or pH 6 with DNO₃/NaOD or HNO₃/NaOH. All two-dimensional [¹H, ¹H] NMR experiments were obtained with 1 mM oligomer and 1 mM oligomer with 1 mM TriplatinNC. The assignments of the resonances for the oligomers and in the presence of TriplatinNC were conducted in the standard manner as described in previous reports (19,20).

VI.3.3. Endonuclease enzyme inhibition

VI.3.3.1. Linearization of pUC19 Supercoiled plasmid pUC19 (2686 bp) was linearised by the *AatI* endonuclease according to the standard methods. Linear DNA was then purified from the enzymatic reaction using QIAquick PCR purification (QIAGEN) and quantified using the NanoDrop (ND-1000) spectrophotometer.

VI.3.3.2. Inhibition study In a typical binding experiment, 400 ng of linear pUC19 was mixed with a series of aliquots of platinum complexes prepared in nuclease-free H₂O (Ambion, AM9932) and the reaction mixture was incubated at 37 °C for 24 h. Subsequent digestions experiments were performed by incubating the drug treated and untreated primary digest of pUC19 with *Bam*HI, *Eco*RI or *Sal*I endonucleases. This reaction was carried out by adding 1 µL of restriction enzyme (20,000 U/mL), and 2.5 µL NEBuffer 3.1 (NEB) and/or 2.5 µL *Eco*RI buffer (where applicable) to the digestion reaction which was allowed to incubate at 37 °C for 2.5 h. Reactions were then subjected to electrophoresis (in 1.0% agarose, stained as previously described). Reactions of *Bam*HI and *Sal*I were then examined using the DNA 7500 microfluidic chip prepared as per the manufacturers protocol with data being collected on the Agilent Bioanalyzer 2100 platform

{<http://www.genomics.agilent.com/en/Bioanalyzer-TapeStation-/?pgid=AG-PG-1>}.

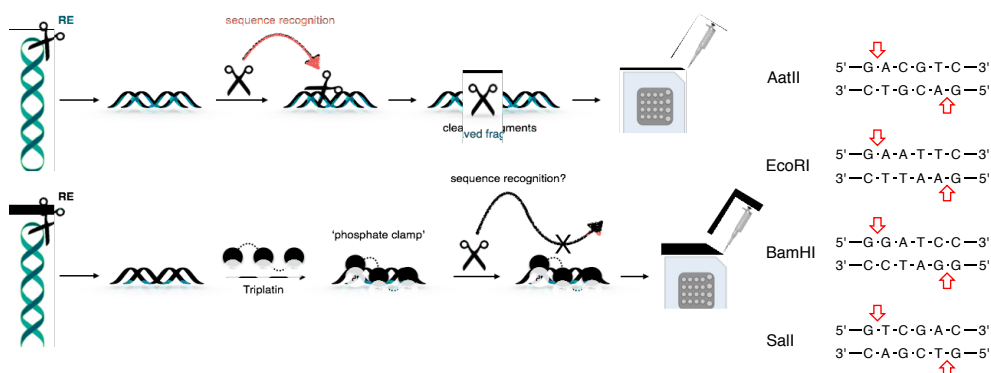


Figure VI.5 Experimental protocol designed for the Bioanalyzer 2100 to identify site-specific endonuclease inhibition by Triplatin complexes with *EcoRI*, *BamHI* and *Sall*.

VI.3.4. tRNA binding

VI.3.4.1 tRNA–ethidium fluorescence quenching A working solution of 160.0 μM transfer RNA (tRNA, Invitrogen AM7119, $\epsilon_{260} = 9250 \text{ M}^{-1} \text{ cm}^{-1}$ expressed as molarity of the phosphate group for tRNA (22) along with 25.2 μM EtBr in HEPES buffer (80 mM, pH = 7.2) and NaCl (40 mM) was prepared. Stock solutions of metal complexes and metal salt were prepared in nuclease-free H_2O (Ambion, AM9932). 50 μL of the tRNA-EtBr working solution were placed in each well of a 96 well microplate with the exception of the blanks, which contained 100 μL of buffer. Serial aliquots of the tested compound were added to the working solutions and the volume was adjusted to 100 μL in each well such that the final concentration of tRNA and EtBr were 80.0 μM and 12.6 μM , respectively. The plate was allowed to incubate at room temperature for 1 h before analysis using a Bio-Tek synergy HT multi-mode microplate reader with excitation and emission wavelengths being set to 530 and 590 nm, respectively. Each drug concentration was measured in triplicate, and the apparent binding constants were calculated using $K_{\text{app}} = K_{\text{b}} \times 12.6/C_{50}$ where $K_{\text{b}} = 6.78 \times 10^4 \text{ M}(\text{bp})^{-1}$ (K_{app} = apparent binding constant).

VI.3.4.2 tRNA thermal melting analysis In a final volume of 1 mL using Starna black-walled quartz cuvettes with tight-fitting seals, 50 mM potassium phosphate buffer (pH = 7.8), 1 M NaCl and tRNA were added to give a final absorbance of ~ 1.1 absorbance units at 260 nm. Stock solutions of metal complexes were prepared in nuclease-free H_2O . An aliquot of test reagent was then added to each

cuvette such that an r value of 0.1 was achieved ($r = [\text{compound}]/[\text{tRNA}]$, $\epsilon_{\text{max}} = 9250 \text{ M}^{-1}\text{cm}^{-1}$ expressed as molarity of phosphate group for tRNA). Thermal melting measurements were recorded at 260 nm at 0.5 s intervals over a temperature range of 20-90 °C. Temperature was calibrated for each measurement using a temperature probe placed in an identical black-walled cuvette containing 50 mM of phosphate buffer and 1M NaCl. The temperature was ramped at 4 °C / min with data being collected every 0.5 °C. The spectral bandwidth (SBW) was set to 1. Replicate samples were run in triplicate and the overall melting temperature, T_{M} (°C), was calculated using the built-in derivative method on an Agilent Cary 100 dual beam spectrophotometer equipped with a 6 x 6 multicell system.

VI.4. Results And Discussion

VI.4.1. Binding to calf thymus and salmon testes DNA

To identify DNA binding properties of this series, calf thymus DNA (ctDNA) and salmon testes DNA (stDNA) were examined through a variety of biophysical methods including ethidium bromide (EtBr) fluorescent competition studies, fluorescence quenching of limited bound EtBr (23) and Hoechst dye 33258 (24), thermal melting and viscosity analysis. In all tests conducted, the minor groove binding agents, netropsin and pentamidine, along with the cationic cobalt(III) complex, $[\text{Co}(\text{NH}_3)_6]^{3+}$, were examined as reference agents against which new properties of these phosphate clamping platinum(II) complexes could be identified.

Thermal melting on ctDNA (Table VI.1 and appendix A.C.2) revealed netropsin extensively stabilised the thermal denaturation ($\Delta T_{\text{M}} = +7.47 \pm 0.50$) (25) while pentamidine and $[\text{Co}(\text{NH}_3)_6]^{3+}$ yielded either no, or negligible, effects under our tested conditions. Triplatin complexes all stabilised ctDNA melting temperature to a similar degree as netropsin (e.g. $\Delta T_{\text{M}} = +8.20 \pm 0.26$ for AH78) and by analogy it is likely that this effect arises through the groove spanning-interaction where platinum(II) phosphate clamps form on opposing sides of the minor groove rather than backbone tracking along one single strand (1, 2). Indeed, the minor groove, which is A·T rich, is the first tract to melt within B-DNA (16) and

thus groove-spanning Triplatin interactions at A·T sequences are likely to confer thermal stabilisation on the nucleotide polymer.

Competitive fluorescence binding to EtBr-saturated ctDNA solutions were performed in triplicate using a high-throughput binding method (14) and results are shown in Figure VI.2A and Table VI.1. The intrinsic binding constant (K_b) of EtBr, was identified as $8.8 \times 10^6 \text{ M(bp)}^{-1}$ through direct spectrophotometry (appendix A.C.6) and the apparent DNA binding constants (K_{app}) for the tested compounds were calculated based on the K_b of EtBr and concentration required to displace 50 % of this bound fluorophore. The K_{app} values for netropsin and pentamidine were identified as 2.55×10^6 and $8.77 \times 10^5 \text{ M(bp)}^{-1}$, respectively, while the cobalt(III) complex and metal free diamine ligand, 1,6-hexanediamine, were unable to displace 50% of bound intercalator up to 300 μM . Triplatin complexes were highly efficient at displacing bound EtBr with all three having almost identical binding constants of $\sim 5 \times 10^7 \text{ M(bp)}^{-1}$. In order to identify their relative binding kinetics to DNA, each complex was examined under constant fluorescence measurement at 10% drug load ($r = [\text{complex}] / [\text{DNA}] = 0.10$), in the presence of saturated EtBr bound ctDNA (Figure VI.2C). Hexane- and heptanediamine-bridged complexes (AH78 and AH78H) were 50 % bound by ~ 34 min while for the pentanediamine complex a considerably faster interaction was evident at ~ 4.5 min.

In order to characterise condensation of DNA, viscosity experiments were conducted using stDNA fibres exposed to the Triplatin series at drug:DNA ratios (r) between 0.01 to 0.20 (Figure VI.2B and Table VI.1). As expected, EtBr exhibited classical intercalative binding with concentration-dependent relative viscosity enhancement (26) while the groove-binding agent, netropsin, had negligible influence only. The cobalt(III) cation, $[\text{Co}(\text{NH}_3)_6]^{3+}$, condensed DNA, in broad agreement with previous work by Kankia *et al.* (27). Triplatin complexes compact and precipitate DNA and this effect is pronounced with distinctive η/η_0 values for all three complexes. Indeed, viscosity by Triplatin molecules decreases in linear fashion with the overall trend almost dwarfing the relative viscosity changes of the standard tested agents. To mitigate the effects of long range coiling, which can significantly impact viscosity (28), high molecular

weight stDNA fibres were vigorously sheared (see section VI.3.2.5)(29) before being examined under identical conditions describe above. Long range coiling effects of non-sheared stDNA can be discounted as Triplatin had greater condensation effects on sheared stDNA (Figure VI.3). We postulate that shorter DNA fragments aggregate more efficiently due to enhanced intramolecular phosphate clamping interactions driven by greater accessibility to smaller nucleotide fragments.

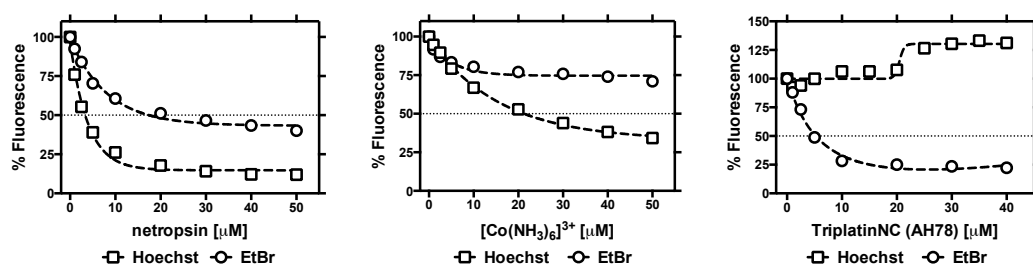


Figure VI.6 Normalised fluorescence quenching of limited ethidium bromide or Hoechst 33258 (5 μ M) bound dsDNA (ctDNA) (25 μ M) upon titration of minor groove binding agents, netropsin and pentamidine, $[\text{Co}(\text{NH}_3)_6]\text{Cl}_3$ and the TriplatinNC (data points presented as an average of triplicate measurement, error bars \pm S.D.).

Binding mode interactions were determined using fluorescence quenching of limited bound EtBr and Hoechst 33258 to ctDNA (Figure VI.15). The minor groove binding agents, netropsin and pentamidine, and the cationic cobalt(III) complex – which has surface binding properties on nucleic acids (30) – displaced the minor groove fluorogen Hoechst 33258 with greater specificity than intercalated EtBr. In contrast to these standards, the Triplatin series exhibited unique profiles. Firstly, the Triplatin series efficiently ablated EtBr fluorescence with quenching values (Q) of the order of ~ 5 μ M. Secondly, the complexes induce cooperative binding of Hoechst 33258 at the minor groove as evident through fluorescence enhancement by approximately 25% within each assay. The cooperative binding of Hoechst 33258 can be understood from the minor groove width opening caused by the phosphate clamps as structurally characterised in the Dickerson Drew Dodecamer (1,2,31). This interaction may conceivably facilitate selective binding by A·T targeting molecules such as Hoechst dye. The quenching of EtBr fluorescence, in contrast, may be connected to a

conformational change, or condensation effect, on the tertiary structure of DNA that disfavors intercalative penetration.

Table VI.1 DNA binding properties of test compounds.

Compound	C_{50} (μM) ^[a]	K_{app} (M^{-1}) ^[b]	Q Hoechst ^[c]	Q Ethidium ^[c]	η / η_0 ^[d]	ΔT_{M} ($^{\circ}\text{C}$) ^[e]
Netropsin	44.26	2.50×10^6	03.31	22.55	1.007	$+7.47 \pm 0.50$
Pentamidine	126.38	8.77×10^5	58.45	N/A	0.987	$+0.03 \pm 0.02$
[Co(NH₃)₆]Cl₃	>300	N/A	23.18	273.62	0.828	$+0.08 \pm 1.12$
AH78	1.96	5.65×10^7	N/A	4.88	0.385	$+6.98 \pm 0.02$
AH78H	1.97	5.62×10^7	N/A	5.42	0.381	$+8.20 \pm 0.26$
AH78P	2.14	5.18×10^7	N/A	5.07	0.443	$+6.74 \pm 0.64$

[a] C_{50} = concentration required to reduce fluorescence by 50% during competitive ethidium bromide displacement assay on ctDNA [b] $K_{\text{app}} = K_{\text{b}} \times 12.6/C_{50}$ where $K_{\text{b}} = 8.8 \times 10^6 \text{ M}(\text{bp})^{-1}$ [c] quenching of 50% initial fluorescence (μM) from limited DNA-bound dye [d] relative viscosity at $r = 0.20$ [e] ΔT_{M} = difference in thermal melting (T_{m}) ($^{\circ}\text{C}$) of drug treated CT-DNA at $r = 0.05$ compared with drug untreated CT-DNA.

VI.4.2 Base-specific nucleic acid interactions

The “classical” minor groove binders such as netropsin and Hoechst 33258 by definition show distinct binding preferences for A-T tracts. In the case of the platinum compounds studied here it is of fundamental interest to examine how the two canonical modes of binding elucidated by crystallography are reflected in base-specific interactions. The presence of specific A-T interactions for non-covalent polynuclear platinum complexes is indicated by protection of the minor groove toward alkylation and is also confirmed (specifically for AH44) through 2D NMR experiments on the self-complementary duplex d(GGTAATTACC)₂, which is a ‘high-affinity’ sequence for minor groove binders such as Hoechst 33258 and used extensively for solution and solid-state studies of ‘classical’ minor groove binders (19). Base-specific interactions were studied using predominantly TriplatinNC (AH78) given the similarities in behaviour on random-sequence DNA observed above. There is a clear correlation between A·T content and the stabilising effect of TriplatinNC (Figure VI.7). The difference in melting temperature increases with the amount of A·T base pairs from $\Delta T_M = +7.0$ °C for ctDNA to +22.6 °C for *Clostridium perfringens* DNA (73% A·T), and then finally to > +28 °C for pure A·T polynucleotides. To our knowledge such a high increase in melting temperature is unprecedented for a non-covalent DNA-binding small molecule at such low concentration ($r = 0.05$). It is noteworthy that the ΔT_M of TriplatinNC-modified homopolymeric and alternating copolymeric sequences are almost identical showing that stabilisation arises from the discrete binding of TriplatinNC, and is not influenced by the initial melting temperature of the untreated polynucleotide. The associated binding strength of TriplatinNC to three sets of polymers - poly[d(G-C)₂], poly[d(A-T)₂] and poly(dA)-poly(dT) - were then identified through ICP-MS and revealed that platinum content is reduced by approximately 50 % after dialysis on all DNA types but there is no apparent selectivity with base composition (Figure VI.7).

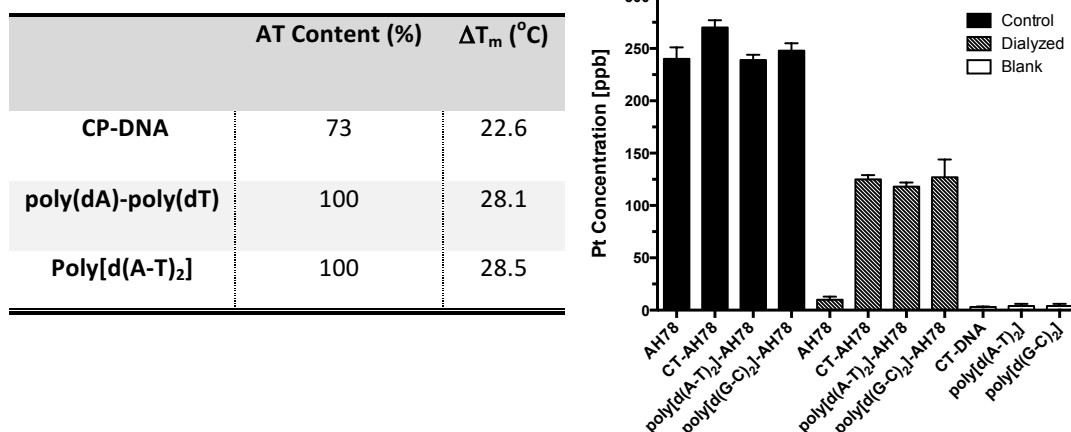


Figure VI.7 Thermal melting temperatures (at $r = 0.05$) of TriplatinNC on modified DNA (CP-DNA = *clostridium perfringens* DNA) (left) and platinum concentration (in ppb) determined using ICP-MS on various DNA types (100 μ M) upon treatment with TriplatinNC (5 μ M) (right).

VI.4.3 Fluorescence Inhibition Assay A selection of double stranded DNA polymers of varying G·C content—poly[d(G·C)₂] (100%), *Micrococcus lysodeikticus* DNA (ML-DNA; 72%), ctDNA (42%), and poly[d(A·T)₂] (0%)—were next examined under saturated EtBr competitive binding conditions (Figure VI.8 and Table VI.2) to characterise potential base-specific binding constants. The classical agents netropsin and actinomycin D exhibited predictable behaviour with the minor groove binder favouring A·T rich polymers while, conversely, the intercalator preferred G·C. Affinity values for netropsin and all trinuclear platinum compounds for the G·C and ML DNAs were similar to those found for ctDNA, See Tables VI.1 and Table VI.2. Unexpectedly, detectable binding constants (up to 500 μ M exposure) were not obtained for poly[d(A·T)₂] for TriplatinNC. The congeners were then examined and a detectable binding constant was observed only for AH78P ($K_{app} = 9 \times 10^5 \text{ M}(\text{bp})^{-1}$). This finding is in contrast to complex AH44 (Scheme VI.1) that displays some slight preference for A-T sequences when compared to nucleic acids of varying base composition (12). This evidence suggests that the DNA binding constants for the TriplatinNC class are dependent, and highly conserved, on polymers containing G·C content. But given the evidence of strong ΔT_m , questions now arise regarding the binding mode of this class toward conformationally distinct regions on DNA. Are there limited but high-affinity binding sites on A-T rich tracts, and are the distinctive binding modes—groove spanning and backbone tracking—linked to base-

specificity or tertiary helical topology, and if so, which of these modes are the drivers behind binding affinity and condensation? To probe these significant issues, further experiments on selected A·T and G·C polymers and oligonucleotides using circular dichroism, isothermal titration calorimetry, and 2D-NMR Spectroscopy were undertaken.

Table VI.2 Apparent DNA binding constants (K_{app}) of test compounds to dsDNA of varying A·T content.

	$K_{app} \text{ M(bp)}^{-1}$			
	poly[d(A·T) ₂]	ctDNA	ML-DNA	poly[d(G·C) ₂]
	(100% AT)	(58% AT)	(28% AT)	(0% AT)
Actinomycin D	N/A	2.92×10^7	3.03×10^7	5.25×10^7
Netropsin	5.75×10^7	2.50×10^6	N/A	N/A
AH78	N/A	5.65×10^7	2.78×10^7	3.18×10^7
AH78H	N/A	5.62×10^7	1.44×10^7	1.95×10^7
AH78P	9.03×10^5	5.18×10^7	1.36×10^7	3.58×10^7

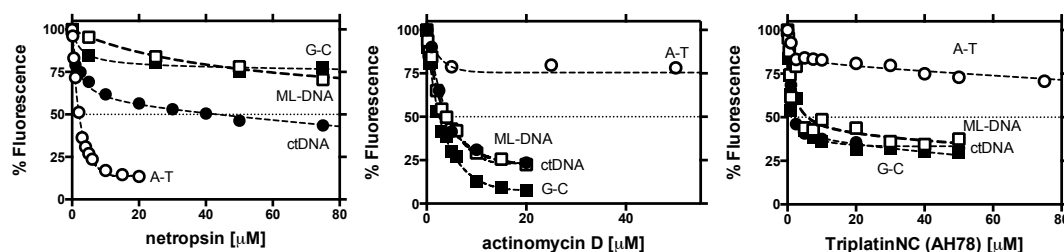


Figure VI.8 Competitive fluorescence binding of netropsin, actinomycin D, and TriplatinNC to ethidium bromide (12.6 μM) saturated solutions of calf thymus DNA, *Micrococcus lysodeikticus* DNA (ML-DNA), poly[d(A·T)₂], and poly[d(G·C)₂] polynucleotides (10 μM).

VI.4.4 Conformational Changes The changes in ellipticity of poly[d(A·T)₂] and poly[d(G·C)₂] with varying amounts of TriplatinNC are shown in Figures VI.9. The platinum compound significantly alters the secondary structure of poly[d(A·T)₂] with ellipticity of the band at 263.5 nm gradually diminishing upon complex treatment resulting in positive to negative shifts up to a drug loading ratio of 5% ($r = 0.05$). Furthermore, the appearance of a positive band around 290 nm at higher molar ratios – a wavelength where DNA normally does not absorb –

indicates the formation of ψ -DNA. On the other hand, almost no change in the secondary structure of the poly[d(G·C)₂] polymer is induced upon TriplatinNC binding. The only significant alteration in the spectrum occurs at high drug loading when DNA condensation leads to ψ -DNA arrangement and subsequently precipitation takes place. Negligible changes in the secondary structure of poly[d(G·C)₂] upon TriplatinNC binding were corroborated through competitive fluorescence binding analysis of mithramycin A; one of the few small molecules that binds to the minor groove of G-C rich sequences (32,33). Binding of mithramycin A is not affected by the presence of TriplatinNC as fluorescence intensities of the DNA-bound antibiotic increase in a linear fashion to exactly the same extent for the TriplatinNC modified poly[d(G·C)₂], as for the untreated polynucleotide (Figure VI.9C). Control experiments confirmed that TriplatinNC did not interfere with the intrinsic fluorescence of mithramycin A itself (results not shown). This result confirms that TriplatinNC does not span the minor groove of poly[d(G·C)₂] and therefore does not prevent the interaction of other molecules within this region of DNA. Taken together these results suggest that, although the association strength of TriplatinNC to A·T and G·C polynucleotides are indistinguishable, backbone tracking is the predominant binding mode for the G·C duplex. Minor groove spanning interactions by the trinuclear platinum complexes, however, are characteristic of polynucleotides with A·T content. For example, cooperative enhancement of the minor groove binding fluorophore Hoechst 33258 occurs for both ctDNA and, to a larger extent, poly[d(A·T)₂] (Figure VI.9D). Isothermal titration calorimetry (ITC) analysis lends further support toward the concept of selective groove spanning of A·T, rather than G·C, polynucleotides (Appendix A.C.4). Not only do the shapes of the isotherms differ appreciably but also the generated reaction heat is about 10 times lower for the G·C polynucleotide (Table VI.3). While a high signal-to-noise ratio of the poly[d(G·C)₂] isotherm made mathematical analysis unreasonable, analysis was possible for both poly[d(A·T)₂] and poly(dA)-poly(dT) isotherms (34,35). The curves of both A·T polynucleotides are very similar and show three reaction stages for binding, condensation and precipitation. Excluding the integrated heats of precipitation, isotherms were then fitted using a two-stage binding site model

that revealed a highly exothermic condensation phase for both A·T polynucleotides (36).

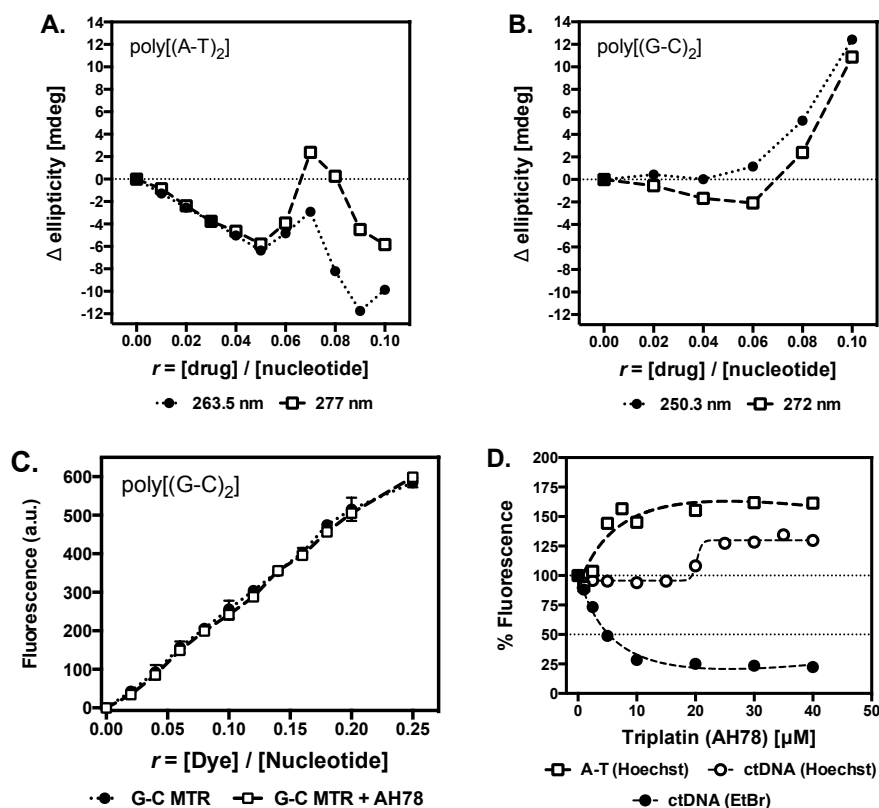


Figure VI.9 Changes in helical ellipticity of key absorbance bands upon treatment of poly[d(A-T)₂] (A) and poly[d(G-C)₂] (B) with TriplatinNC (AH78), the comparative binding of mithramycin A (MTR) to poly[d(G-C)₂] in the presence and absence of TriplatinNC (C), and quenching of limited bound Hoechst (5 μ M) or ethidium bromide (5 μ M) to ctDNA and poly[d(A-T)₂] (25 μ M) polynucleotides (D).

Table VI.3 Best fit parameters for the titration of poly[d(A-T)₂] and poly(dA)-poly(dT) with TriplatinNC

	N	K x 10 ⁷ [M ⁻¹]	ΔH [cal/mol]	ΔS [cal/mol*K]	ΔG [kcal/mol]
<i>Parameters for first binding step</i>					
CT-DNA	0.062 ±0.003	22.7 ±8.0	3438 ±32	49.8 ±0.8	-11.2 ±0.02
Poly[d(A-T) ₂]	0.041 ±0.003	42.9 ±13.3	7880 ±335	66.3 ±1.7	-11.5 ±0.20
poly(dA)-poly(dT)	0.026 ±0.002	125.5 ±63.5	9709 ±30	74.5 ±1.3	-12.1 ±0.30
<i>Parameters for second binding step</i>					
CT-DNA	0.070 ±0.001	0.483 ±0.151	402 ±128	31.8 ±0.5	-8.9 ±0.2
Poly[d(A-T) ₂]	0.050 ±0.002	0.85 ±0.33	-7101 ±232	7.3 ±0.1	-9.2 ±0.2
poly(dA)-poly(dT)	0.039 ±0.003	1.65 ±1.01	-3107 ±74	22.0 ±1.2	-9.5 ±0.4

VI.4.5 2D NMR Spectroscopy Finally, 2D NMR spectroscopy was used to examine the binding modes using both an A-T rich and a G-C rich duplex, section VI.3.2 and appendix A.C.5.

VI.4.6 TriplatinNC modified A-T-Duplex The changes in the proton resonances for the A-T-rich dodecamer (Figure VI.4) in the presence of TriplatinNC confirm that for both strands mainly the thymines and adenosines are affected by platinum drug binding, appendix A.C.5. A preference of binding towards one strand over the other is not observed. The changes in chemical shifts for T-NH and T-CH₃ result from structural changes of the dodecamer upon binding of TriplatinNC. In NOESY analysis there are many NOE contacts between the TriplatinNC and the non-exchangeable protons of the oligonucleotide. NOE cross peaks are observed with all A-H₂ protons as connections seem to be stronger for TpNC-L2/L5 than L3/L4, suggesting that TriplatinNC spans/binds in minor groove, and there are strong connectivities with A-H1' and T-H1', and somewhat weaker contacts with C-H1' (Figure VI.10). Cross-peaks with H2'/H2'' can not be conclusively identified due to overlapping peaks but strong NOE contacts with H3'/H4' and H5'/H5'' protons are present. These latter sugar connectivities in the proximity of the backbone phosphates point toward backbone binding. No cross-peaks with A-NH₂ or C-

NH₂ or T-CH₃ are visible indicating that major groove binding can be ruled out. Contacts to the imino protons of the nucleobases are also not detected. For the platinum compound, participation of the L1 protons is inconclusive since many H₂'' protons have a similar chemical shift. Connectivities for NH₃/NH₂ groups of TriplatinNC with the oligomer are not observed. It is noteworthy that the NOE contacts between A-H₂ protons and H₂'/H₂'' seem to be stronger in the presence of TriplatinNC. This could reflect the narrowing of the minor groove as a consequence of the binding of the platinum drug. In summary the results strongly suggest that TriplatinNC spans the minor groove.

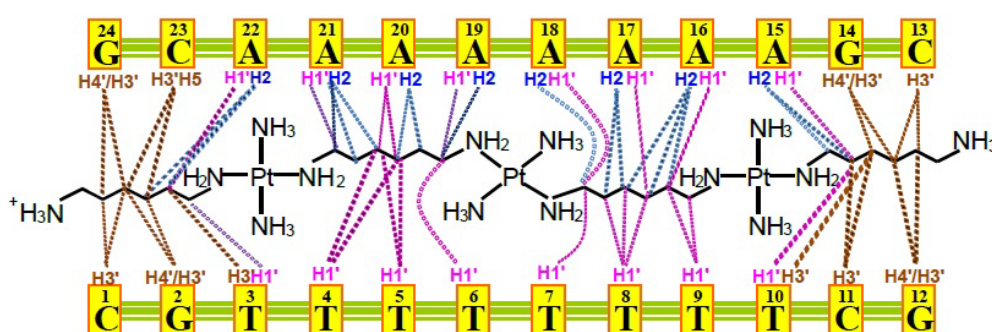


Figure VI.10 Summary of NOE contacts between TriplatinNC and the self-complementary A-T rich duplex.

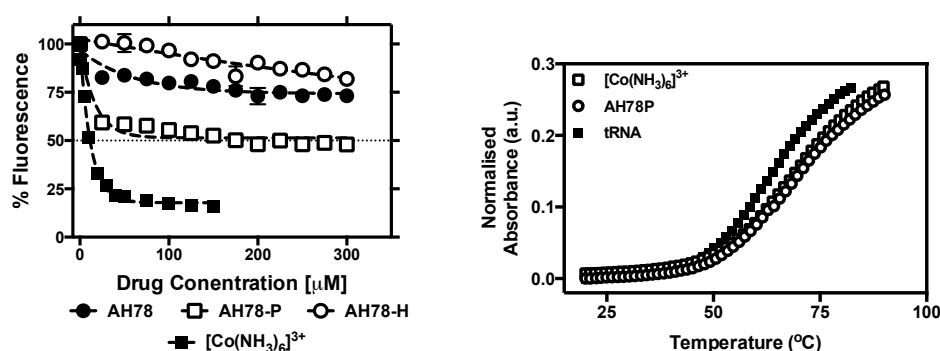
VI.4.7 Consequences for the TriplatinNC modified GC-duplex In contrast to the AT-duplex the changes in the GC-rich dodecamer upon binding of TriplatinNC are considerably smaller, with changes mainly occurring for the H1' chemical shifts. These shift variations arise most probably from induced structural changes since the spectra showed only few contacts in the minor groove. Weak cross-peaks are observed between TpNC-L3/L4 and G-H₈ and C-H₆ as well as G-H1' and C-H1'. The cross-peaks with H₂'/H₂'' sugar protons seem to be more pronounced but the strongest connectivities are observed in the H₃'/H₄'/H₅'/H₅'' region. The fact that no connections with G-NH₂ or C-NH₂ are detected implies that binding *via* major or minor groove spanning can be excluded. Connectivities between NH₂R/NH₃ protons of the platinum drug with the dodecamer can not be detected. Overall these results suggest that TriplatinNC binds predominantly in a backbone tracking manner towards GC-rich DNA.

In summary, elucidation of solution binding by TriplatinNC and congeners to DNA clearly display two modes consistent with backbone tracking and groove-spanning interactions. What is clear from these experiments, and is of particular significance toward our understanding of novel “non-covalent” platinum nucleic acid interactions, is that each mode is dependent on base specificity or local helical topological parameters. We suggest that backbone tracking is the predominant binding mode of TriplatinNC type complexes in duplexes containing G-C nucleobases. Conversely, groove-spanning interactions are localised to the minor groove and are specifically dependent of A-T content. Furthermore, the groove-spanning motif has far greater impact on tertiary nucleic acid structure and is the main driver of DNA condensation and cooperative interactions at the minor groove.

VI.4.8 Binding to yeast tRNA

To characterize Triplatin interactions with ribonucleic acid, and thus potentially differentiate binding activity with DNA, yeast transfer RNA (tRNA) was examined through fluorescence quenching experiments and thermal melting analysis. We initially characterised the intrinsic binding constant (K_b) of ethidium bromide to tRNA using direct spectrophotometry at 260 nm as $6.78 \times 10^4 \text{ M}^{-1}$ (Appendix A.C.6) which is in good agreement with Sakai *et al.* (37). A fixed concentration of EtBr (12.6 μM) was then titrated against increasing concentrations of tRNA in order to identify the fluorescence saturation binding point (80.0 μM). Further, we then defined the apparent binding constant of tested samples to tRNA (K_{app}) within this method as; $K_{app} = K_b \times 12.6/C_{50}$, where K_b is the intrinsic binding constant of EtBr to tRNA and C_{50} is the concentration (in μM) of tested agent required to displace 50% of the bound intercalated fluorophore (38, 39). Quenching experiments were then examined with Triplatin complexes and $[\text{Co}(\text{NH}_3)_6]\text{Cl}_3$ titrated against EtBr-saturated tRNA solutions (Figure VI.11). Somewhat unexpectedly, only the pentanediamine Triplatin complex (AH78P) displaced 50% of bound EtBr and we estimate the binding constant of this agent to the fluorescent EtBr binding region of tRNA as $4.80 \times 10^3 \text{ M}(\text{bp})^{-1}$, an order of magnitude below the $[\text{Co}(\text{NH}_3)_6]\text{Cl}_3$ complex ($7.95 \times 10^4 \text{ M}(\text{bp})^{-1}$). Indeed, electrostatic binding by $[\text{Co}(\text{NH}_3)_6]^{3+}$ to RNA has previously

been identified on ribozyme (P4-P5-P6 portion) tandem G-U base pairs in the major groove (40). Thermal denaturation was then identified (Figure VI.11B and Figure VI.11C) with AH78P once again being the only platinum(II) complex to appreciably stabilise tRNA. Overall, the ability of Triplatin complexes to displace fluorogenically bound EtBr and stabilise thermal denaturation of tRNA appears favoured by shorter linker chain length molecules. It is possible, however, that Triplatin molecules may bind tRNA at non-fluorescent EtBr binding sites (41) that have negligible influence on thermal denaturation. Atomic Force Microscopy experiments on tRNA adducted by AH78 do indeed show condensation of the ribonucleotide but the results are not inconsistent if there is a subset of Triplatin binding sites different to those of EtBr (12).



Compound	C_{50} (μM) [a]	K_{app} (M ⁻¹) [b]	ΔT_m (°C) [c]
EtBr	-	-	+2.14 ± 0.31
[Co(NH ₃) ₆]Cl ₃	10.74	7.95 x 10 ⁴	+1.10 ± 0.10
AH78	>300		+0.20 ± 0.56
AH78H	>300		+0.13 ± 0.63
AH78P	177.61	4.80 x 10 ³	+1.39 ± 0.60

[a] C_{50} = concentration required to reduce fluorescence by 50% during competitive EtBr displacement assay [b] $K_{app} = K_b \times 12.6/C_{50}$ where $K_b = 6.78 \times 10^4 \text{ M(bp)}^{-1}$ [c] ΔT_m = differential thermal melting (T_m) (°C) of drug treated tRNA at $r = 0.10$ compared with drug untreated tRNA.

Figure VI.11 A. Competitive fluorescence binding of platinum complexes (AH78, AH78P and AH78H) and the cobalt(III) complex, [Co(NH₃)₆]Cl₃, to EtBr (12.6 μM) saturated solutions of transfer RNA (tRNA) (80 μM) (data points presented as an average of triplicate measurement, error bars ± S.D.). **B.** Normalised thermal melting profiles of untreated tRNA (~130 μM in tRNAp) along with AH78P and [Co(NH₃)₆]³⁺ treated (13 μM) tRNA examined in 50 mM potassium phosphate buffer with 1 M NaCl. **C.** tRNA binding properties of test compounds.

VI.4.9 Interactions with superhelical pUC19 and endonuclease inhibition

It is axiomatic that strong ligand binding to nucleic acids will interfere with protein recognition and processing. The effects of complex interactions on superhelical pUC19 plasmid DNA (pDNA) migration and subsequently sequence recognition by type II restriction endonucleases were examined. Agarose gel electrophoresis of superhelical pUC19 showed that the pentanediamine complex, AH78P, begins to inhibit plasmid migration at 0.50 μM with complete condensation occurring thereafter, Figure VI.12A. Higher concentrations of the longer hexanediamine AH78 and heptanediamine AH78H were required to initiate condensation (3.0 μM) while the metal-free ligand yielded no effect. The behaviour by all Triplatin compounds here is entirely different to classical *cis*-platinum(II) and trinuclear BBR3464 type complexes. These agents covalently platinate superhelical pDNA and engage in concentration-dependent unwinding of the Form I superhelix (42,43,44).

To identify if Triplatin-bound DNA can prevent sequence recognition by type II restriction endonucleases, pUC19 was then linearised by the restriction enzyme *AatII* and subjected to a second endonuclease treatment of either *BamHI*, *EcoRI* or *SaII*, each of which also have one recognition sequence on pUC19 (Figure VI.12). The results of these control experiments are shown in Figure VI.12B where the linearised band of pUC19 at 2,686 bp disappears and two smaller fragments emerge between 2,188–2,221 bp and 465–498 bp corresponding to site-selective excision. With Triplatin experiments, complexes were pre-incubated for 24 h at 37 °C with linearised pUC19 at the range 1.0 – 10.0 μM for AH78 and AH78H, and between 0.25 – 1.00 μM for AH78P before the introduction of *BamHI*, *EcoRI* or *SaII*, (Figure VI.12 C–E). Triplatin complexes inhibit endonuclease excision in a concentration-dependent manner as characterised by the disappearance of pUC19 fragments at higher complex exposure. Inhibition is comparable between the hexanediamine and heptanediamine- bridged AH78 and AH78H, respectively, where concentrations of 2.5 μM initiate condensation with bands becoming fainter and then disappearing >5 μM . The pentanediamine-linked AH78P displays a similar concentration-dependent inhibitory trend with the exception that lower concentrations (0.50 μM) are required to inhibition excision, before complete condensation occurs thereafter (0.75 – 1.00 μM). It is notable that Triplatin

complexes do not preferentially inhibit cutting by any of these three site-specific endonucleases. Instead, the inhibitory properties are congruent, depending only on complex concentration and the linker chain length (AH78P \gg AH78 \approx AH78H).

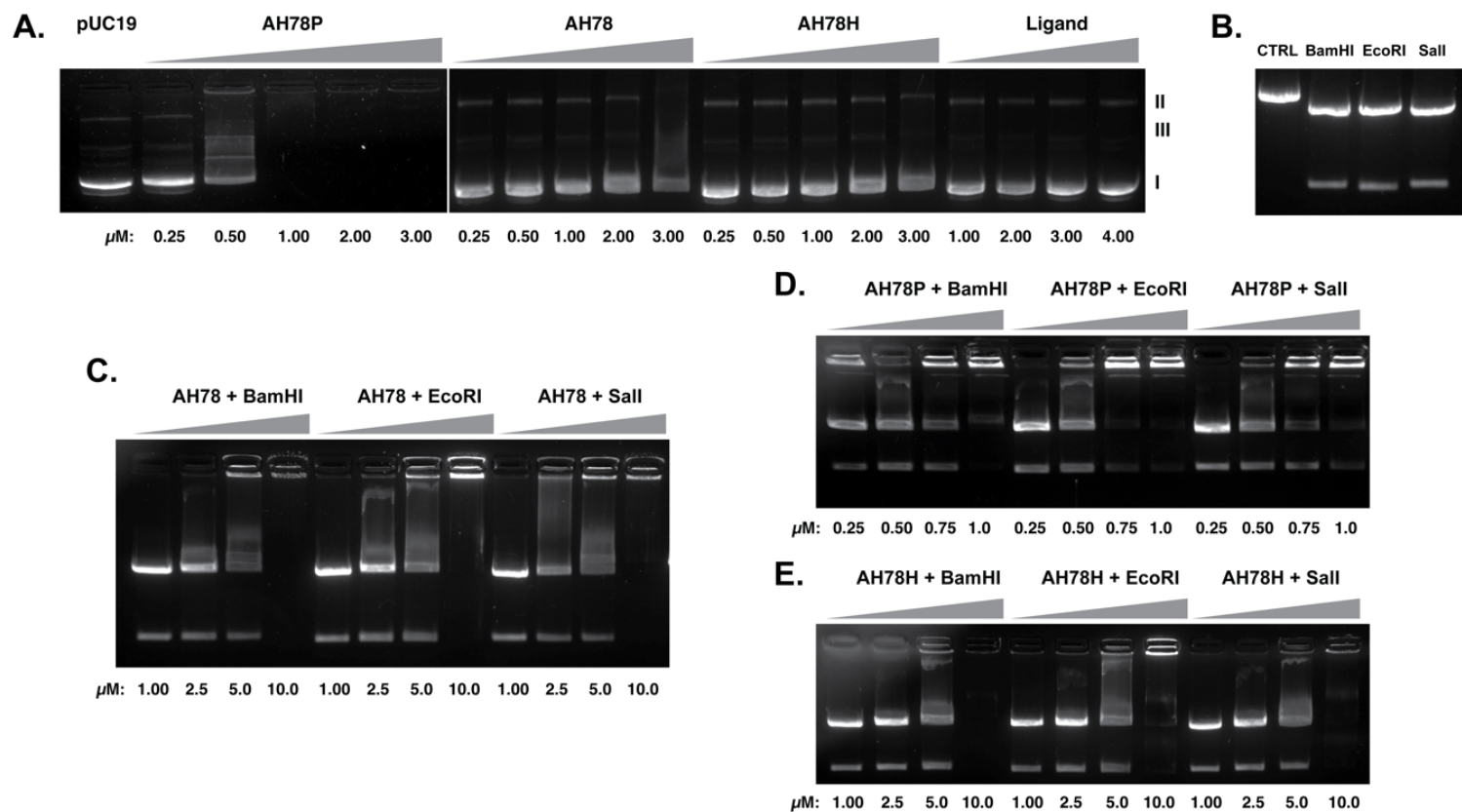


Figure VI.12 A. Influence of Triplatin complexes and the metal-free ligand on superhelical pUC19 (400 ng) migration examined under agarose gel electrophoresis. B. AatII linearized pUC19 (CTRL) after exposure to type II endonucleases. C. – E. Cleavage experiments on linearised pUC19, pre-incubated for 24 h with either; AH78 (1.0 – 10 μM), AH78P (0.25 – 1.0 μM) or AH78H (1.0 – 10 μM) by type II endonucleases *Bam*HI, *Eco*RI and *Sall*.

VI.4.10 On-chip identification of endonuclease inhibition

Although the condensation effects of DNA by Triplatin complexes have clearly been demonstrated through changes in viscosity and gel electrophoresis in this study and also through atomic force microscopy (AFM) analysis in recent work (11,12), a question remains regarding the exact nature of endonuclease inhibition by the Triplatin series – condensation effects rendering both bands undetectable by gel electrophoresis should be distinguished from endonuclease inhibition through ligand (Triplatin)-DNA binding. In order to provide answers to this question, an on-chip DNA microfluidic method was devised using the Bioanalyzer 2100 platform (Agilent Technologies) and is shown in Figure VI.5. The Bioanalyzer 2100 was selected due to its ability for high-resolution sizing and quantitation of dsDNA fragments through capillary electrophoresis (45,46) {<http://www.agilent.com>}. We employed DNA 7500 microfluidic chips, designed to identify dsDNA fragments sized between 100–7500 bp, for the detection of endonuclease excision on linearised pU19 (2,686 bp). Superhelical pUC19, initially linearised by the restriction enzyme *AatII* and purified using anion exchange chromatography, was then exposed to two restriction endonucleases, *BamHI* and *SalI*, in a similar manner as described above.

Electrograms from the microfluidic chip analysis of untreated and enzyme-treated pUC19 are shown in Figure VI.13A and Appendix A.C.1 In each electrogram, internal standard upper and lower DNA markers sized at 50 and 10380 bp are evident. Linear pUC19 produced a single high-resolution peak located at ~2870 bp which was clearly within the experimental error margin for nucleotide sizing accuracy ($\pm 10\%$ CV). Treatment by *BamHI* or *SalI* resulted in the disappearance of this band and the emergence of two smaller sequences located at ~500 bp, and ~2200 bp which correspond to the expected site-selective enzymatic restriction activity. Triplatin complexes were then incubated for 24 h with linearised pUC19 (400 ng) prior to the exposure to *BamHI* or *SalI*. Tests were conducted in a similar manner to the electrophoresis experiments described above with AH78 and AH78H complexes being examined across a higher range than AH78P (Figure VI.15B–E). Concentration dependent endonuclease inhibition was identified in each set of experiments conducted. Taking complex AH78 with *BamHI* treatment as an example (Figure VI.13B): at lower complex concentrations of 1.0 and 2.5 μM the restriction enzyme efficiently cuts pUC19

into two smaller fragments and the results here are almost identical to the control experiment in Figure VI.13A. At higher concentrations however, the native pUC19 band at ~2,870 bp begins to appear and this band intensifies at the maximum exposure level (10 μ M) as the *Bam*HI excision fragments at ~490 and ~2200 bp diminish. Thus, in the presence of Triplatin complex, the pUC19 vector is protected from site-selective endonuclease excision. The trend observed in Figure VI.12C–E is largely present in these experiments, however, 10 μ M of AH78H was unable to completely protect pUC19 from endonuclease excision by *Sal*I (Figure VI.12D). On comparison with the agarose gel of this same experiment (Figure VI.12E), no bands are evident for pUC19 or the excision fragments. This indicates that complex AH78H has condensed both the native, or protected, plasmid along with the excised fragments. Another significant observation is the ability of AH78P to block endonuclease activity at nano-molar concentration levels (<1.0 μ M) as evident in Figure VI.12C. The pentanediamine bridged triplatinum(II) complex, therefore, has excellent selectivity for condensation and endonuclease inhibition on this dsDNA particular sequence (51% GC and 49% AT content).

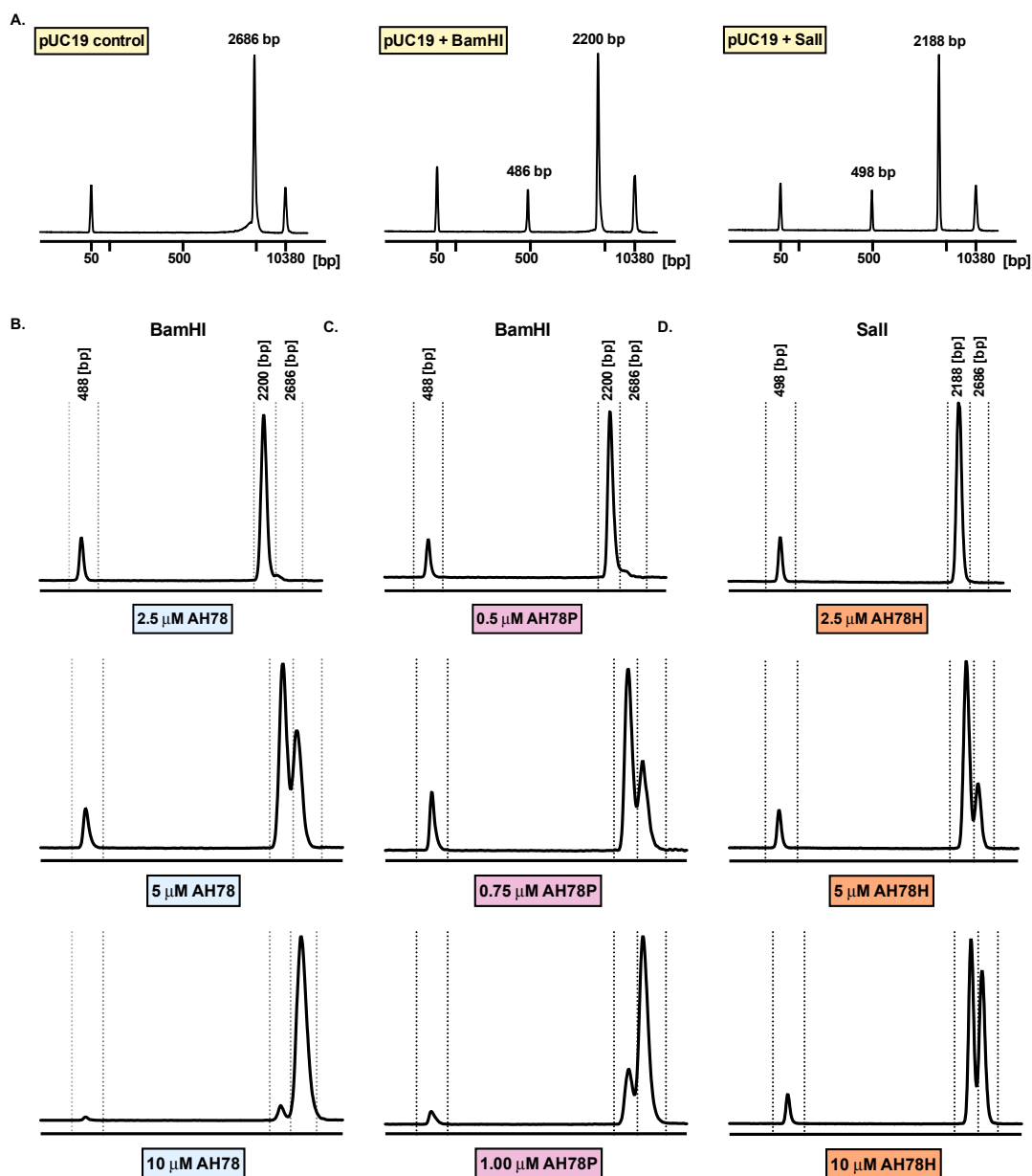


Figure VI.13 A. Electrograms generated using the Bioanalyzer 2100 of AatII linearised pUC19 plasmid DNA with treatment by endonucleases *Bam*HI and *Sal*I. Electrograms of linearised pUC19 pre-incubated for 24 h with either AH78, AH78P or AH78H, followed by exposure over 2.5 h to the type II restriction endonuclease *Bam*HI (B and C) or *Sal*I (D).

VI.5 Conclusions

The results here demonstrate the unique nucleic acid binding properties of 8+ charged “non-covalent” PtN₄ type complexes binding through the phosphate clamp motif previously characterised by ‘backbone tracking’ and ‘groove spanning’ (1, 2). The overall features from this and complementary studies, (11,12), confirm that the crystallographically observed structures exist in solution and are relevant in explaining the biological activity of this series. The phosphate clamp, through its groove spanning, has apparent similarities to classical minor groove binders (e.g. netropsin) – indicated by quenching of intercalated ethidium bromide and stabilisation of nucleic acid thermal denaturation, protection of the minor groove toward alkylation, (19), and the presence of many A-T minor groove contacts observed through 2D NMR experiments on self-complementary A-T rich duplexes (Figure VI.10 and Ref. 19). However, the phosphate clamp is distinguished by higher apparent binding constants to ctDNA and highly efficient condensation effects on both DNA and tRNA (11,12). The structural modifications of the phosphate clamp result in cooperative enhancement of minor groove binders such as netropsin and Hoechst 32258. The base-specific studies allow differentiation between the dynamic effects of backbone tracking and groove spanning - backbone tracking is the predominant binding mode of TriplatinNC type complexes in duplexes containing G-C nucleobases while, conversely, groove-spanning interactions are localised to the minor groove and are specifically dependent of A-T content. The latter has far greater impact on tertiary nucleic acid structure and the minor-groove residency of the platinum complex is the main driver of DNA condensation and cooperative interactions at the minor groove. The combined results further identify the phosphate clamp as a distinct mode of DNA binding, discrete from the canonical intercalator and minor groove binders. The modular nature of the polynuclear chemotype allows for systematic modification of the chemotype. Apparent binding constants on ctDNA are identical among the series ($K_{app} \sim 5 \times 10^7 \text{ M}^{-1}$) and are similar to recently reported non-terminally functionalised di- and tri-platinum(II): AH44 (Scheme VI.1), $[\{\text{Pt}(\text{NH}_3)_3\}_2\text{-}\mu\text{-spermidine}]^{5+}$ and $[\{\text{Pt}(\text{NH}_3)_3\}_2\text{-}\mu\text{-spermine}]^{6+}$ ($K_{app} \sim 3 \times 10^7 \text{ M}^{-1}$). However, more subtle effects may be identified and in this study the slightly shorter pentanediamine-linked compound shows a number of effects (rapid interaction in competitive fluorescence experiments, EtBr

displacement from tRNA, more efficient inhibition of pUC19 plasmid migration) suggesting the nucleic acid “fit” may be modulated by the choice of diamine linker in this complex class. The combined effects of high binding constants and condensation effects of Triplatin complexes, has significant consequences for inhibition of protein-DNA interactions. Type II restriction endonuclease inhibition on pUC19 was witnessed at G-G, G-A and G-T excision regions of *Bam*HI, *Eco*RI, and *Sal*I enzymes in the presence of Triplatin-bound DNA. These results were visualised using agarose gel electrophoresis and then confirmed through the development of an on-chip microfluidic protocol for the Bioanalyzer 2100. There is again, a distinct dependency on linker chain length with the pentanediamine complex inhibiting, or protecting, linearised pUC19 from digestion at the nanomolar exposure level while a ten-fold concentration increase ($\geq 5.0 \mu\text{M}$) by hexane- and heptane-bridged Triplatin cations were required to block restriction activity. In summary, the studies clearly display two modes of DNA binding consistent with backbone tracking and groove-spanning interactions where each mode is dependent on base specificity or local helical topological parameters.

References

1. Komeda, S., Moulaei, T., Woods, K.K., Chikuma, M., Farrell, N.P. and Williams, L.D. (2006) A third mode of DNA binding: Phosphate clamps by a polynuclear platinum complex. *J. Am. Chem. Soc.*, **128**, 16092–16103.
2. Komeda, S., Moulaei, T., Chikuma, M., Odani, A., Kipping, R., Farrell, N.P. and Williams, L.D. (2011) The phosphate clamp: a small and independent motif for nucleic acid backbone recognition. *Nucleic Acids Res.*, **39**, 325–336.
3. Takahara, P.M., Rosenzweig, A.C., Frederick, C.A. and Lippard, S.J. (1995) Crystal structure of double-stranded DNA containing the major adduct of the anticancer drug cisplatin. *Nature*, **377**, 649–652.
4. Klein, D.J., Schmeing, T.M., Moore, P.B. and Steitz, T.A. (2001) The kink-turn: a new RNA secondary structure motif. *EMBO J.*, **20**, 4214–4221.
5. Calnan, B.J., Tidor, B., Biancalana, S., Hudson, D. and Frankel, A.D. (1991) Arginine-mediated RNA recognition: the arginine fork. *Science*, **252**, 1167–1171.
6. Hurley, L.H. (2002) DNA and its associated processes as targets for cancer therapy. *Nat. Rev. Cancer*, **2**, 188–200.
7. Boer, D.R., Canals, A. and Coll, M. (2009) DNA-binding drugs caught in action: the latest 3D pictures of drug-DNA complexes. *Dalton Trans.*, 10.1039/B809873P.
8. Mangrum, J.B. and Farrell, N.P. (2010) Excursions in polynuclear platinum DNA binding. *Chem. Commun.*, **46**, 6640–6650.
9. Benedetti, B.T., Peterson, E.J., Kabolizadeh, P., Martínez, A., Kipping, R. and Farrell, N.P. (2011) Effects of noncovalent platinum drug-protein interactions on drug efficacy: use of fluorescent conjugates as probes for drug metabolism. *Mol. Pharm.*, **8**, 940–948.
10. Wedlock, L.E., Kilburn, M.R., Liu, R., Shaw, J.A., Berners-Price, S.J. and Farrell, N.P. (2013) NanoSIMS multi-element imaging reveals internalisation and nucleolar targeting for a highly-charged polynuclear platinum compound. *Chem. Commun.*, **49**, 6944–6946.
11. Malina, J., Farrell, N.P. and Brabec, V. (2014) DNA condensing effects and sequence selectivity of DNA binding of antitumor noncovalent polynuclear platinum complexes. *Inorg. Chem.*, **53**, 1662–1671.
12. Malina, J., Farrell, N.P. and Brabec, V. (2014) Noncovalent trinuclear platinum complexes efficiently condense/aggregate nucleic acids and inhibit enzymatic activity. *Angew. Chem.* In Press.
13. Harris, A.L., Yang, X., Hegmans, A., Povirk, L., Ryan, J.J., Kelland, L. and Farrell, N.P. (2005) Synthesis, characterization, and cytotoxicity of a novel

highly charged trinuclear platinum compound. Enhancement of cellular uptake with charge. *Inorg. Chem.*, **44**, 9598–9600.

14. McCann, M., McGinley, J., Ni, K., O'Connor, M., Kavanagh, K., McKee, V., Colleran, J., Devereux, M., Gathergood, N., Barron, N., et al. (2013) A new phenanthroline-oxazine ligand: synthesis, coordination chemistry and atypical DNA binding interaction. *Chem. Commun.*, **49**, 2341–2343.

15. Prisecaru, A., McKee, V., Howe, O., Rochford, G., McCann, M., Colleran, J., Pour, M., Barron, N., Gathergood, N. and Kellett, A. (2013) Regulating bioactivity of Cu²⁺ bis-1,10-phenanthroline artificial metallonucleases with sterically functionalized pendant carboxylates. *J. Med. Chem.*, **56**, 8599–8615.

16. David Wilson, W., Tanious, F., Fernandez-Saiz, M. and Ted Rigl, C. (1997) Evaluation of Drug-Nucleic Acid Interactions by Thermal Melting Curves. In *Methods in Molecular Biology*TM. Springer New York, New Jersey, Vol. 90, pp. 219–240.

17. Barceló, F., Ortiz-Lombardía, M. and Portugal, J. (2001) Heterogeneous DNA binding modes of berenil. *Biochim. Biophys. Acta*, **1519**, 175–184.

18. Remeta, D.P., Mudd, C.P., Berger, R.L. and Breslauer, K.J. (1993) Thermodynamic characterization of daunomycin-DNA interactions: comparison of complete binding profiles for a series of DNA host duplexes. *Biochemistry*, **32**, 5064–5073.

19. Qu, Y., Moniodis, J.J., Harris, A.L., Yang, X., Hegmans, A., Povirk, L.F., Berners-Price, S.J. and Farrell, N.P. (2012) Non-Covalent Polynuclear Platinum Compounds as Polyamine Analogs in *Polyamine Drug Discovery*, RSC Drug Discovery Series No. 17, 191–204.

20. Qu, Y., Scarsdale, N.J., Tran, M.-C. and Farrell, N. (2003) Cooperative effects in Long-range 1,4 DNA-DNA Interstrand Cross-links formed by Polynuclear Platinum Complexes. An Unexpected *syn*-Orientation of Adenine Bases Outside the Binding Sites. *J. Biol. Inorg. Chem.* **8**, 19-28.

21. Carter, M.T., Rodriguez, M. and Bard, A.J. (1989) Voltammetric studies of the interaction of metal chelates with DNA. 2. Tris-chelated complexes of cobalt (III) and iron (II) with 1, 10-phenanthroline and 2, 2'-bipyridine. *J. Am. Chem. Soc.*, **111**, 8901–8911.

22. Marty, R., N'soukpoé-Kossi, C.N., Charbonneau, D.M., Kreplak, L. and Tajmir-Riahi, H.-A. (2009) Structural characterization of cationic lipid-tRNA complexes. *Nucleic Acids Res.*, **37**, 5197–5207.

23. Wang, A.H.-J. (1992) Intercalative drug binding to DNA. *Curr. Opin. Struct. Biol.*, **2**, 361–368.

24. Bailly, C., Colson, P., Hénichart, J.-P. and Houssier, C. (1993) The different binding modes of Hoechst 33258 to DNA studied by electirc linear dichroism. *Nucleic Acids Res.*, **21**, 3705–3709.

25. Luck, G., Triebel, H., Waring, M. and Zimmer, C. (1974) Conformation

dependent binding of netropsin and distamycin to DNA and DNA model polymers. *Nucleic Acids Res.*, **1**, 503–530.

26. Luedtke, N.W., Hwang, J.S., Nava, E., Gut, D., Kol, M. and Tor, Y. (2003) The DNA and RNA specificity of eilatin Ru(II) complexes as compared to eilatin and ethidium bromide. *Nucleic Acids Res.*, **31**, 5732–5740.

27. Kankia, B.I., Buckin, V. and Bloomfield, V.A. (2001) Hexamminecobalt(III)-induced condensation of calf thymus DNA: circular dichroism and hydration measurements. *Nucleic Acids Res.*, **29**, 2795–2801.

28. Lerman, L.S., (1961) Structural considerations in the interaction of DNA and acridines, *J. Mol. Biol.*, **3**, 18–30.

29. Cohen, G., and Eisenberg, H., (1969) Viscosity and sedimentation study of sonicated DNA–proflavine complexes, *Biopolymers*, **8**, 45–55.

30. Cheatham, T.E. and Kollman, P.A. (1997) Insight into the stabilization of A-DNA by specific ion association: spontaneous B-DNA to A-DNA transitions observed in molecular dynamics simulations of d[ACCCGCGGGT]₂ in the presence of hexaamminecobalt(III). *Structure*, **5**, 1297–1311.

31. Harris, A., Qu, Y. and Farrell, N.P. (2005) Unique cooperative binding interaction observed between a minor groove binding Pt anti-tumor agent and Hoeschst Dye 33258. *Inorg. Chem.* **44**, 1196–1198.

32. Sastry, M.; Fiala, R. and Patel, D. J. (1995) *Journal of Molecular Biology*, **251**, 674.

33. Geierstanger, B. H. and Wemmer, D. E. (1995) *Annual Review of Biophysics and Biomolecular Structure*, **24**, 463.

34. Matulis, D., Rouzina, I. and Bloomfield, V.A. (2000) Thermodynamics of DNA binding and condensation: isothermal titration calorimetry and electrostatic mechanism. *J. Mol. Biol.*, **296**, 1053–1063.

35. Kim, W., Yamasaki, Y. and Kataoka, K. (2006) Development of a fitting model suitable for the isothermal titration calorimetric curve of DNA with cationic ligands. *J. Phys. Chem. B*, **110**, 10919–10925.

36. Wilson, R.W. and Bloomfield, V.A. (1979) Counter ion-induced condensation of deoxyribonucleic acid: a light-scattering study. *Biochemistry*, **18**, 2192–2196.

37. Sakai, T.T., Torget, R., Josephine, I., Freda, C.E. and Cohen, S.S. (1975) The binding of polyamines and of ethidium bromide to tRNA. *Nucleic Acids Res.*, **2**, 1005–1022.

38. Jones, C.R., Bolton, P.H. and Kearns, D.R. (1978) Ethidium bromide binding to transfer RNA: transfer RNA as a model system for studying drug-RNA interactions. *Biochemistry*, **17**, 601–607.

39. Olmsted, J. and Kearns, D.R. (1977) Mechanism of ethidium bromide fluorescence enhancement on binding to nucleic acids. *Biochemistry*, **16**, 3647–3654.
40. Kieft, J.S. and Tinoco, I. (1997) Solution structure of a metal-binding site in the major groove of RNA complexed with cobalt (III) hexammine. *Structure*, **5**, 713–721.
41. Liebman, M., Rubin, J. and Sundaralingam, M. (1977) Nonintercalative binding of ethidium bromide to nucleic acids: crystal structure of an ethidium-tRNA molecular complex. *Proc. Natl. Acad. Sci. U.S.A.*, **74**, 4821–4825.
42. Bellon, S.F., Coleman, J.H. and Lippard, S.J. (1991) DNA unwinding produced by site-specific intrastrand crosslinks of the antitumor drug cis-diamminedichloroplatinum(II). *Biochemistry*, **30**, 8026–8035.
43. Brabec, V., Kaspárková, J., Vrána, O., Nováková, O., Cox, J.W., Qu, Y. and Farrell, N. (1999) DNA modifications by a novel bifunctional trinuclear platinum phase I anticancer agent. *Biochemistry*, **38**, 6781–6790.
44. Ruhayel, R.A., Langner, J.S., Oke, M.-J., Berners-Price, S.J. and Zgani, I. (2012) Chimeric Platinum-Polyamines and DNA Binding. Kinetics of DNA Interstrand Cross-Link Formation by Dinuclear Platinum Complexes with Polyamine Linkers. *J. Am. Chem. Soc.*, **134**, 7135–7146.
45. Molphy, Z., Prisecaru, A., Slator, C., Barron, N., McCann, M., Colleran, J., Chandran, D., Gathergood, N. and Kellett, A. (2014) Copper phenanthrene oxidative chemical nucleases. *Inorg. Chem.*, **53**, 5392–5404.
46. Wang, J. (2000) From DNA biosensors to gene chips. *Nucleic Acids Res.*, **28**, 3011–3016.

Appendix A

A.A.1 X-ray crystallography of methyl 2-(4-hydroxyphenyl)-4a,12b-dihydro-2H-[1,4]oxazino[2,3-f][1,10]phenanthroline-3-carboxylate (PDT)

Table A.A.1 Crystal data and structure refinement for PDT·MeOH.

Empirical formula	C ₂₃ H ₁₉ N ₃ O ₅	
Formula weight	417.41	
Temperature	150(2) K	
Wavelength	0.71073 Å	
Crystal system	Monoclinic	
Space group	P2(1)/c	
Unit cell dimensions	a = 10.2862(8) Å	= 90°.
	b = 20.0798(16) Å	=
	90.1550(10)°.	
	c = 9.6427(8) Å	= 90°.
Volume	1991.6(3) Å ³	
Z	4	
Density (calculated)	1.392 Mg/m ³	
Absorption coefficient	0.100 mm ⁻¹	
F(000)	872	
Crystal size	0.43 x 0.35 x 0.14 mm ³	
Crystal description	colourless block	
Theta range for data collection	1.98 to 28.33°.	
Index ranges	-13<=h<=13, -26<=k<=26, -12<=l<=12	
Reflections collected	20407	
Independent reflections	4961 [R(int) = 0.0268]	
Completeness to theta = 26.00°	100.0 %	
Absorption correction	Semi-empirical from equivalents	
Max. and min. transmission	0.9861 and 0.9583	
Refinement method	Full-matrix least-squares on F ²	
Data / restraints / parameters	4961 / 0 / 287	
Goodness-of-fit on F ²	1.049	
Final R indices [I>2sigma(I)]	R1 = 0.0410, wR2 = 0.1061	
R indices (all data)	R1 = 0.0551, wR2 = 0.1150	
Largest diff. peak and hole	0.290 and -0.237 e.Å ⁻³	

Table A.A.2. Atomic coordinates ($\times 10^4$) and equivalent isotropic displacement parameters ($\text{\AA}^2 \times 10^3$). $U(\text{eq})$ is defined as one third of the trace of the orthogonalized U^{ij} tensor.

	x	y	z	$U(\text{eq})$
N(1)	7704(1)	3902(1)	10605(1)	32(1)
C(1)	8269(2)	4394(1)	9916(2)	36(1)
C(2)	9234(1)	4295(1)	8917(2)	32(1)
C(3)	9624(1)	3657(1)	8615(1)	26(1)
C(4)	9038(1)	3120(1)	9313(1)	23(1)
C(5)	9356(1)	2437(1)	9018(1)	22(1)
C(6)	8724(1)	1936(1)	9696(1)	23(1)
C(7)	7742(1)	2066(1)	10709(1)	24(1)
C(8)	7079(1)	1553(1)	11410(1)	29(1)
C(9)	6168(1)	1718(1)	12380(2)	36(1)
C(10)	5924(1)	2391(1)	12629(2)	37(1)
N(2)	6513(1)	2890(1)	11985(1)	32(1)
C(11)	7423(1)	2732(1)	11026(1)	25(1)
C(12)	8079(1)	3272(1)	10306(1)	24(1)
O(1)	8939(1)	1284(1)	9406(1)	27(1)
C(13)	10171(1)	1124(1)	8747(1)	24(1)
C(14)	11208(1)	962(1)	9798(1)	23(1)
C(15)	11547(1)	306(1)	10081(1)	27(1)
C(16)	12460(1)	150(1)	11089(2)	30(1)
C(17)	13079(1)	659(1)	11819(1)	28(1)
O(2)	13972(1)	544(1)	12825(1)	38(1)
C(18)	12775(1)	1319(1)	11510(1)	28(1)
C(19)	11847(1)	1466(1)	10523(1)	26(1)
C(20)	10598(1)	1688(1)	7821(1)	24(1)
C(21)	11529(1)	1477(1)	6712(1)	27(1)
O(3)	11614(1)	907(1)	6344(1)	42(1)
O(4)	12246(1)	1975(1)	6229(1)	37(1)
C(22)	13159(2)	1789(1)	5151(2)	49(1)
N(3)	10260(1)	2299(1)	7958(1)	23(1)
O(31)	14632(1)	-721(1)	12893(1)	41(1)
C(32)	15288(2)	-950(1)	11693(2)	54(1)

Table A.A.3. Bond lengths [\AA] and angles [$^\circ$].

N(1)-C(1)	1.3262(18)	C(11)-C(12)	1.4542(18)
N(1)-C(12)	1.3539(16)	O(1)-C(13)	1.4552(15)
C(1)-C(2)	1.399(2)	C(13)-C(14)	1.5053(18)
C(2)-C(3)	1.3730(18)	C(13)-C(20)	1.5089(17)
C(3)-C(4)	1.4072(17)	C(14)-C(15)	1.3893(17)
C(4)-C(12)	1.4096(17)	C(14)-C(19)	1.3945(17)
C(4)-C(5)	1.4405(17)	C(15)-C(16)	1.3856(19)
C(5)-C(6)	1.3647(17)	C(16)-C(17)	1.3942(19)
C(5)-N(3)	1.4101(16)	C(17)-O(2)	1.3534(16)
C(6)-O(1)	1.3580(15)	C(17)-C(18)	1.3933(18)
C(6)-C(7)	1.4318(18)	C(18)-C(19)	1.3778(19)
C(7)-C(8)	1.4087(17)	C(20)-N(3)	1.2817(16)
C(7)-C(11)	1.4098(18)	C(20)-C(21)	1.4989(18)
C(8)-C(9)	1.367(2)	C(21)-O(3)	1.2006(16)
C(9)-C(10)	1.395(2)	C(21)-O(4)	1.3284(16)
C(10)-N(2)	1.3254(18)	O(4)-C(22)	1.4509(17)
N(2)-C(11)	1.3556(17)	O(31)-C(32)	1.418(2)
C(1)-N(1)-C(12)	117.63(12)	N(2)-C(11)-C(7)	122.12(12)
N(1)-C(1)-C(2)	123.52(12)	N(2)-C(11)-C(12)	118.25(12)
C(3)-C(2)-C(1)	119.10(12)	C(7)-C(11)-C(12)	119.64(11)
C(2)-C(3)-C(4)	119.14(12)	N(1)-C(12)-C(4)	123.11(12)
C(3)-C(4)-C(12)	117.49(11)	N(1)-C(12)-C(11)	117.49(11)
C(3)-C(4)-C(5)	122.52(11)	C(4)-C(12)-C(11)	119.37(11)
C(12)-C(4)-C(5)	119.96(11)	C(6)-O(1)-C(13)	116.42(9)
C(6)-C(5)-N(3)	121.25(11)	O(1)-C(13)-C(14)	111.69(10)
C(6)-C(5)-C(4)	119.89(11)	O(1)-C(13)-C(20)	110.37(10)
N(3)-C(5)-C(4)	118.72(10)	C(14)-C(13)-C(20)	110.76(10)
O(1)-C(6)-C(5)	122.26(11)	C(15)-C(14)-C(19)	118.19(12)
O(1)-C(6)-C(7)	115.60(11)	C(15)-C(14)-C(13)	120.97(11)
C(5)-C(6)-C(7)	122.06(11)	C(19)-C(14)-C(13)	120.84(11)
C(8)-C(7)-C(11)	118.42(12)	C(16)-C(15)-C(14)	121.39(12)
C(8)-C(7)-C(6)	122.50(12)	C(15)-C(16)-C(17)	119.79(12)
C(11)-C(7)-C(6)	119.08(11)	O(2)-C(17)-C(18)	117.90(12)
C(9)-C(8)-C(7)	119.00(13)	O(2)-C(17)-C(16)	122.97(12)
C(8)-C(9)-C(10)	118.43(13)	C(18)-C(17)-C(16)	119.12(12)
N(2)-C(10)-C(9)	124.68(13)	C(19)-C(18)-C(17)	120.46(12)
C(10)-N(2)-C(11)	117.34(12)	C(18)-C(19)-C(14)	120.99(12)

N(3)-C(20)-C(21)	121.25(11)
N(3)-C(20)-C(13)	125.31(11)
C(21)-C(20)-C(13)	113.39(10)
O(3)-C(21)-O(4)	124.95(13)
O(3)-C(21)-C(20)	121.84(12)
O(4)-C(21)-C(20)	113.19(11)
C(21)-O(4)-C(22)	114.72(12)
C(20)-N(3)-C(5)	116.22(11)

Table A.A.4 Anisotropic displacement parameters ($\text{\AA}^2 \times 10^3$). The anisotropic displacement factor exponent takes the form: $-2 \pi^2 [h^2 a^{*2} U^{11} + \dots + 2 h k a^* b^* U^{12}]$

	U^{11}	U^{22}	U^{33}	U^{23}	U^{13}	U^{12}
N(1)	36(1)	25(1)	36(1)	-1(1)	8(1)	5(1)
C(1)	45(1)	20(1)	43(1)	-2(1)	8(1)	4(1)
C(2)	38(1)	21(1)	37(1)	3(1)	6(1)	-2(1)
C(3)	29(1)	22(1)	29(1)	2(1)	4(1)	0(1)
C(4)	23(1)	21(1)	24(1)	0(1)	-1(1)	0(1)
C(5)	22(1)	20(1)	23(1)	1(1)	1(1)	0(1)
C(6)	23(1)	19(1)	28(1)	1(1)	-2(1)	-1(1)
C(7)	21(1)	26(1)	26(1)	3(1)	-2(1)	-2(1)
C(8)	25(1)	30(1)	34(1)	6(1)	-2(1)	-5(1)
C(9)	26(1)	42(1)	38(1)	11(1)	3(1)	-8(1)
C(10)	27(1)	46(1)	38(1)	4(1)	10(1)	-2(1)
N(2)	27(1)	37(1)	33(1)	1(1)	7(1)	0(1)
C(11)	21(1)	29(1)	25(1)	2(1)	0(1)	1(1)
C(12)	25(1)	23(1)	26(1)	0(1)	1(1)	2(1)
O(1)	26(1)	18(1)	38(1)	1(1)	3(1)	-2(1)
C(13)	28(1)	17(1)	28(1)	-1(1)	3(1)	0(1)
C(14)	25(1)	19(1)	25(1)	1(1)	4(1)	-1(1)
C(15)	27(1)	18(1)	37(1)	0(1)	-1(1)	-3(1)
C(16)	29(1)	19(1)	42(1)	5(1)	-2(1)	-2(1)
C(17)	26(1)	28(1)	30(1)	5(1)	1(1)	-2(1)
O(2)	39(1)	32(1)	43(1)	7(1)	-13(1)	-3(1)
C(18)	32(1)	23(1)	29(1)	-3(1)	0(1)	-5(1)
C(19)	32(1)	18(1)	27(1)	0(1)	4(1)	-1(1)
C(20)	27(1)	21(1)	23(1)	0(1)	-1(1)	0(1)
C(21)	33(1)	24(1)	25(1)	1(1)	0(1)	5(1)
O(3)	55(1)	27(1)	44(1)	-11(1)	12(1)	2(1)
O(4)	47(1)	26(1)	39(1)	4(1)	20(1)	6(1)
C(22)	57(1)	49(1)	43(1)	5(1)	28(1)	13(1)
N(3)	26(1)	21(1)	24(1)	1(1)	1(1)	1(1)
O(31)	33(1)	37(1)	51(1)	16(1)	8(1)	-2(1)
C(32)	43(1)	64(1)	56(1)	9(1)	9(1)	2(1)

Table A.A.5 Hydrogen coordinates ($\times 10^4$) and isotropic displacement parameters ($\text{\AA}^2 \times 10^3$).

	x	y	z	U(eq)
H(1)	8005	4837	10110	43
H(2)	9615	4664	8454	39
H(3)	10281	3579	7943	32
H(8)	7262	1100	11211	35
H(9)	5712	1383	12874	43
H(10)	5290	2500	13307	44
H(13)	10035	721	8153	29
H(15)	11146	-44	9572	33
H(16)	12663	-302	11283	36
H(18)	13209	1670	11982	33
H(19)	11640	1918	10333	31
H(22A)	13648	2183	4856	74
H(22B)	12682	1605	4357	74
H(22C)	13762	1453	5512	74
H(32A)	15877	-602	11359	82
H(32B)	14651	-1056	10968	82
H(32C)	15789	-1350	11922	82
H(2O)	14135(16)	87(9)	12894(17)	40
H(31)	14065(18)	-1005(9)	13122(18)	40

Table A.A.6 Hydrogen bonds [\AA and $^\circ$].

D-H...A	d(D-H)	d(H...A)	d(D...A)	$\angle(\text{DHA})$
O(2)-H(2O)...O(31)	0.935(18)	1.700(18)	2.6295(15)	171.8(16)
O(31)-H(31)...N(1)#1	0.846(18)	2.205(18)	2.9090(16)	140.7(15)
O(31)-H(31)...N(2)#1	0.846(18)	2.299(18)	3.0297(17)	144.8(15)

Symmetry transformations used to generate equivalent atoms: #1 $-x+2, y-1/2, -z+5/2$
Least-squares planes (x,y,z in crystal coordinates) and deviations from them
(* indicates atom used to define plane)

$7.2066 (0.0018) x + 0.5999 (0.0046) y + 6.8562 (0.0017) z = 13.0561 (0.0018)$

* 0.0008 (0.0011) N1
* -0.0350 (0.0013) C1
* -0.0301 (0.0013) C2
* 0.0055 (0.0012) C3
* 0.0300 (0.0011) C4
* 0.0153 (0.0010) C5
* -0.0053 (0.0010) C6
* -0.0107 (0.0011) C7
* -0.0389 (0.0012) C8
* -0.0199 (0.0012) C9
* 0.0148 (0.0012) C10
* 0.0281 (0.0011) N2
* 0.0169 (0.0012) C11
* 0.0283 (0.0012) C12
3.1659 (0.0022) C1_\$2
3.2947 (0.0015) C3_\$2
3.2947 (0.0015) C3_\$2
3.3836 (0.0014) C4_\$2
3.4510 (0.0013) C5_\$2
3.2608 (0.0016) N1_\$2
3.4094 (0.0014) N2_\$2
3.4904 (0.0015) C6_\$2
3.4694 (0.0016) C7_\$2
3.3638 (0.0015) C12_\$2

Rms deviation of fitted atoms = 0.0231

equiv \$2 x, 0.5-y, 0.5+z

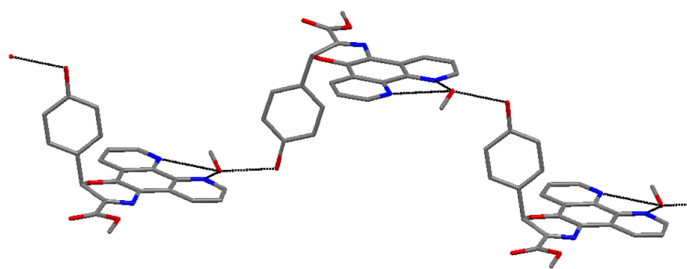


Fig. A.A.1 A view of **PDT·MeOH** showing the orthogonal nature of the phenol ring with respect to the oxazine ring and also the hydrogen bonding involving the phenol OH and methanol OH.

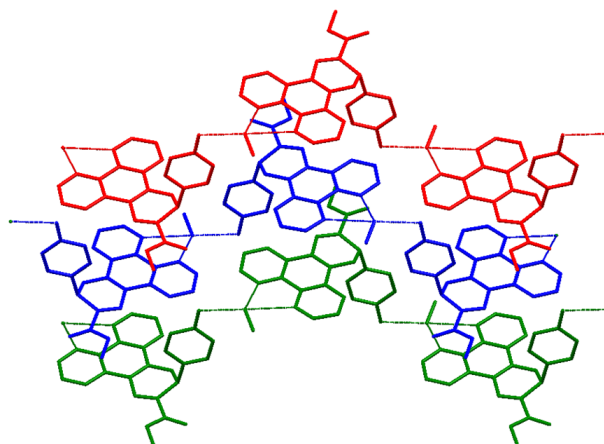


Fig. A.A.2 A view of **PDT·MeOH** showing that hydrogen bonding occurs only between the same layers of molecules.

Appendix B

A.B.1 Infrared spectroscopy of $[\text{Cu}(\text{R-COO})(1,10\text{-Phen})_2]^+$

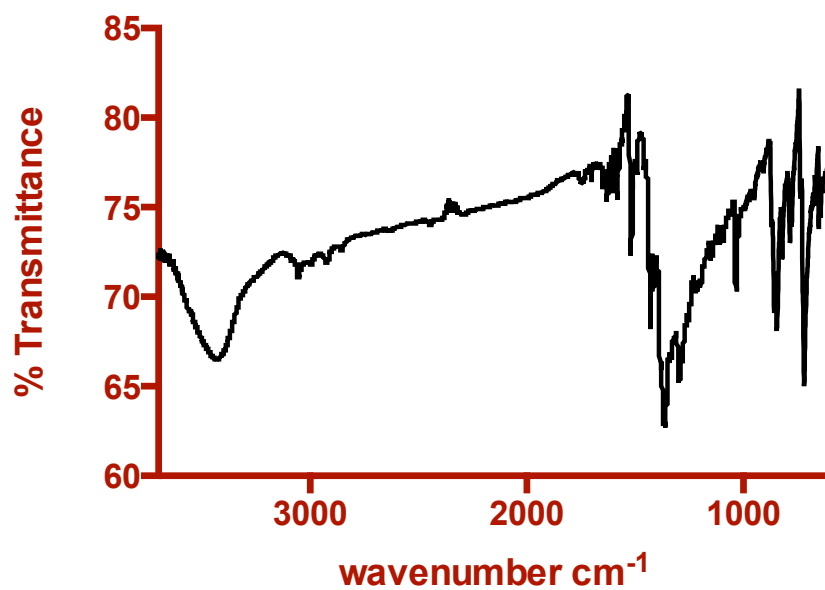


Figure A.B.1 IR spectra of $[\text{Cu}(1,10\text{-Phen})_2](\text{NO}_3)_2$, (Cu-Phen)

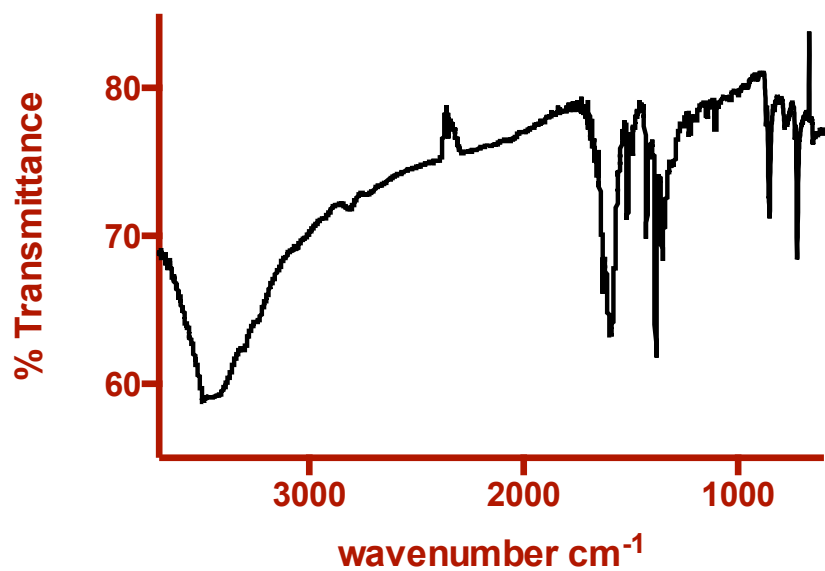


Figure A.B.2 IR spectra of $[\text{Cu}(\text{For})(1,10\text{-Phen})_2](\text{NO}_3) \cdot 6\text{H}_2\text{O}$, (Cu-For-Phen)

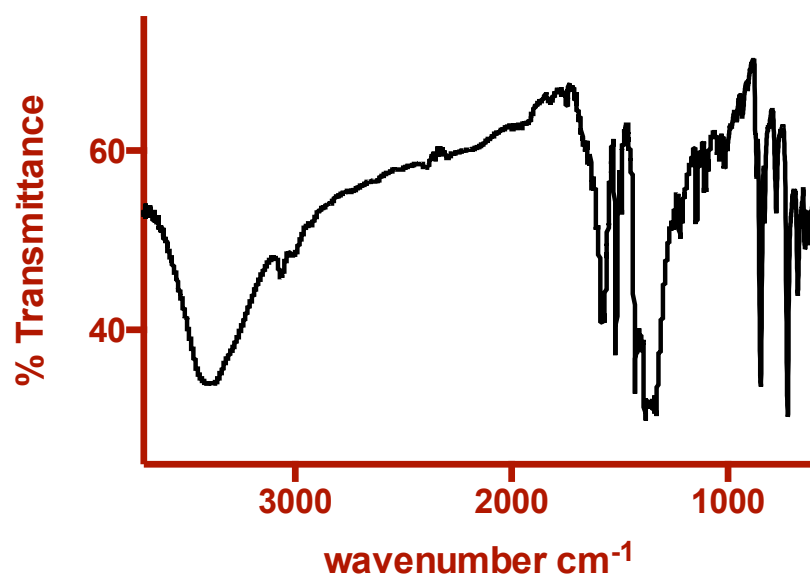


Figure A.B.3 IR spectra of $[\text{Cu}(\text{Ace})(1,10\text{-Phen})_2](\text{NO}_3) \cdot 2\text{H}_2\text{O}$, (Cu-Ace-Phen)

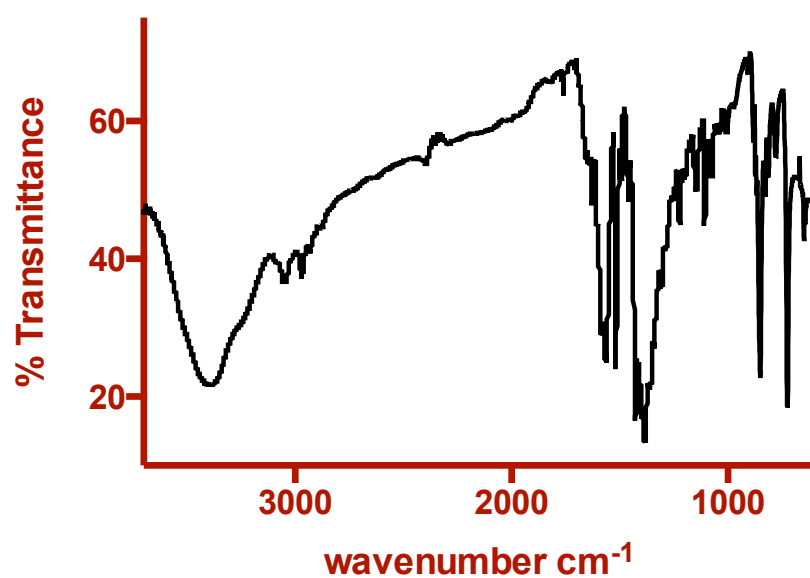


Figure A.B.4 IR spectra of $[\text{Cu}(\text{Pro})(1,10\text{-Phen})] \cdot \frac{1}{2}(\text{CO}_3) \cdot 4\frac{1}{2}\text{H}_2\text{O}$, (Cu-Pro-Phen)

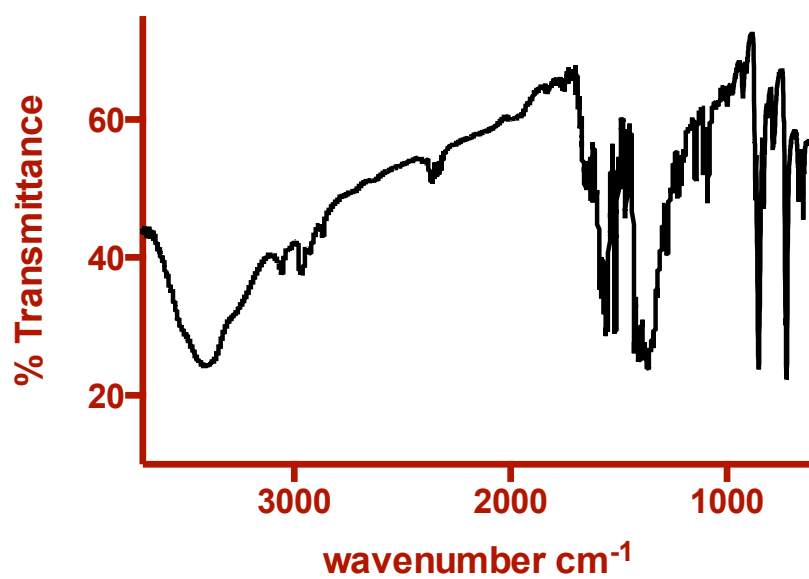


Figure A.B.5 IR spectra of $[\text{Cu}(\text{Iso})(1,10\text{-Phen})_2]_2 \cdot 2(\text{NO}_3) \cdot 4\text{H}_2\text{O}$, (Cu-Iso-Phen)

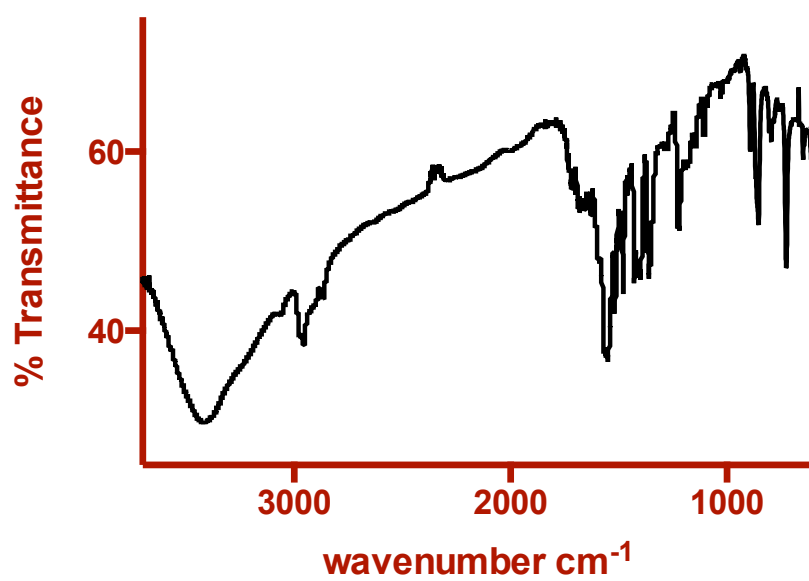


Figure A.B.6 IR spectra of $[\text{Cu}(\text{Piv})(1,10\text{-Phen})_2]_2(\text{piv})_2 \cdot (\text{Hpiv}) \cdot 9\text{H}_2\text{O}$, (Cu-Piv-Phen)

A.B.2 Crystallography

A.B.2.1 $[\text{Cu}(\text{For})(1,10\text{-Phen})_2](\text{NO}_3)_6 \cdot 6\text{H}_2\text{O}$, (Cu-For-Phen)

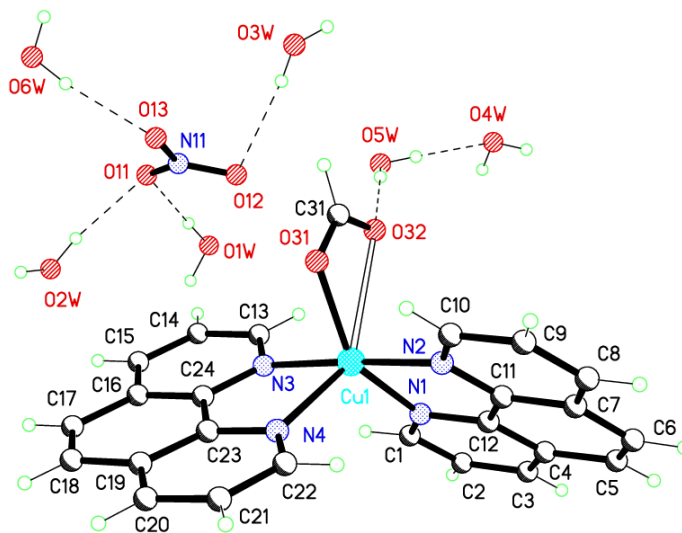


Figure A.B.7 Crystal structure of Cu-For-Phen

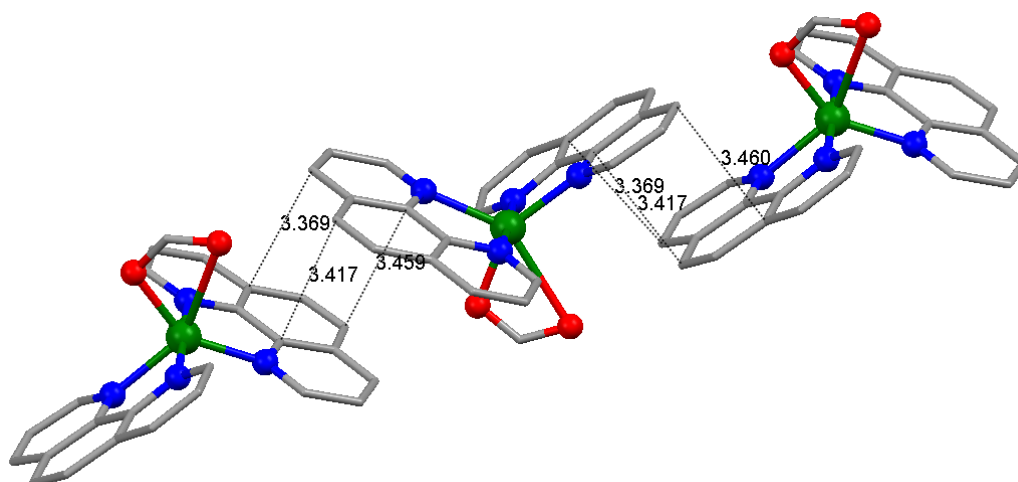


Figure A.B.9 π - π stacking linking the cations into zig-zag chains.

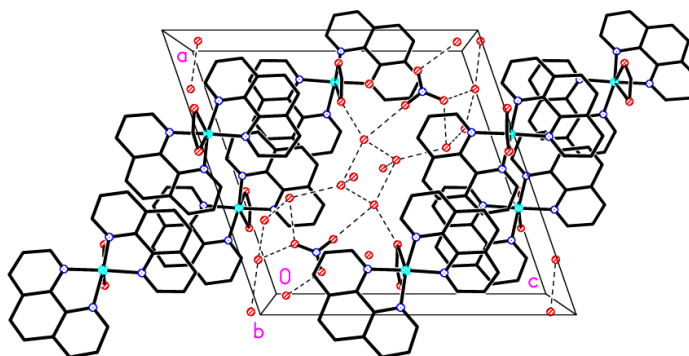


Figure A.B.10 The chains are linked by H-bonding involving the nitrate anions and water molecules.

Table A.B.1 Crystal data of Cu-For-Phen

$C_{25}H_{29}CuN_5O_{11}$	$F(000) = 1324$
$M_r = 639.07$	$D_x = 1.560 \text{ Mg m}^{-3}$
Monoclinic, $P2_1/n$	Mo $K\alpha$ radiation, $\lambda = 0.71073 \text{ \AA}$
$a = 14.8372 (12) \text{ \AA}$	Cell parameters from 4135 reflections
$b = 12.467 (1) \text{ \AA}$	$\theta = 2.3\text{--}25.0^\circ$
$c = 15.5706 (12) \text{ \AA}$	$\mu = 0.87 \text{ mm}^{-1}$
$\beta = 109.092 (1)^\circ$	$T = 150 \text{ K}$
$V = 2721.8 (4) \text{ \AA}^3$	Plate, blue
$Z = 4$	$0.49 \times 0.30 \times 0.05 \text{ mm}$

Table A.B.2 Data collection of Cu-For-Phen

Bruker APEX-II CCD diffractometer	5353 independent reflections
Radiation source: fine-focus sealed tube	3939 reflections with $I > 2\sigma(I)$
graphite	$R_{\text{int}} = 0.046$
ϕ and ω scans	$\theta_{\text{max}} = 26.0^\circ$, $\theta_{\text{min}} = 1.7^\circ$
Absorption correction: multi-scan <i>SADABS</i> v2008/1, Sheldrick, G.M., (2008)	$h = -18 \rightarrow 18$
$T_{\text{min}} = 0.674$, $T_{\text{max}} = 0.958$	$k = -15 \rightarrow 15$
22925 measured reflections	$l = -19 \rightarrow 19$

Table A.B.3 Refinement data of Cu-For-Phen

Refinement on F^2	Primary atom site location: structure-invariant direct methods
Least-squares matrix: full	Secondary atom site location: difference Fourier map
$R[F^2 > 2\sigma(F^2)] = 0.046$	Hydrogen site location: inferred from neighbouring sites
$wR(F^2) = 0.136$	H atoms treated by a mixture of independent and constrained refinement
$S = 1.07$	$w = 1/[\sigma^2(F_o^2) + (0.0678P)^2 + 2.7897P]$ where $P = (F_o^2 + 2F_c^2)/3$
5353 reflections	$(\Delta/\sigma)_{\max} = 0.001$
415 parameters	$\Delta\rho_{\max} = 1.31 \text{ e } \text{\AA}^{-3}$
18 restraints	$\Delta\rho_{\min} = -0.87 \text{ e } \text{\AA}^{-3}$

Table A.B.4 Geometric parameters (\AA , $^\circ$) of Cu-For-Phen

Cu1—N2	1.982 (3)	N3—C13	1.329 (4)
Cu1—N3	1.988 (3)	N3—C24	1.365 (4)
Cu1—O31	2.027 (2)	C13—C14	1.404 (5)
Cu1—N1	2.057 (3)	C14—C15	1.367 (5)
Cu1—N4	2.181 (3)	C15—C16	1.407 (5)
N1—C1	1.330 (4)	C16—C24	1.397 (4)
N1—C12	1.357 (4)	C16—C17	1.438 (5)
C1—C2	1.400 (5)	C17—C18	1.336 (5)
C2—C3	1.367 (5)	C18—C19	1.439 (5)
C3—C4	1.408 (5)	C19—C20	1.405 (5)
C4—C12	1.406 (4)	C19—C23	1.411 (4)
C4—C5	1.437 (5)	C20—C21	1.371 (5)
C5—C6	1.349 (5)	C21—C22	1.399 (5)
C6—C7	1.428 (5)	C22—N4	1.324 (4)
C7—C11	1.406 (4)	N4—C23	1.360 (4)
C7—C8	1.407 (5)	C23—C24	1.437 (4)
C8—C9	1.369 (5)	O31—C31	1.268 (4)
C9—C10	1.397 (5)	O32—C31	1.234 (4)
C10—N2	1.331 (4)	N11—O12	1.166 (5)
N2—C11	1.361 (4)	N11—O13	1.190 (4)
C11—C12	1.424 (4)	N11—O11	1.257 (4)

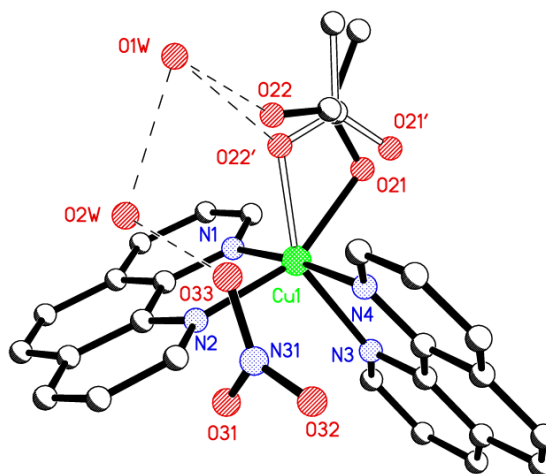
N2—Cu1—N3	176.80 (10)	N1—C12—C11	117.0 (3)
N2—Cu1—O31	91.58 (10)	C4—C12—C11	119.3 (3)
N3—Cu1—O31	89.71 (10)	C13—N3—C24	118.7 (3)
N2—Cu1—N1	81.78 (10)	C13—N3—Cu1	125.7 (2)
N3—Cu1—N1	98.73 (10)	C24—N3—Cu1	115.0 (2)
O31—Cu1—N1	146.33 (9)	N3—C13—C14	122.0 (3)
N2—Cu1—N4	96.51 (10)	C15—C14—C13	119.6 (3)
N3—Cu1—N4	80.46 (10)	C14—C15—C16	119.4 (3)
O31—Cu1—N4	95.07 (9)	C24—C16—C15	117.8 (3)
N1—Cu1—N4	118.41 (10)	C24—C16—C17	118.9 (3)
C1—N1—C12	117.9 (3)	C15—C16—C17	123.3 (3)
C1—N1—Cu1	131.0 (2)	C18—C17—C16	121.4 (3)
C12—N1—Cu1	111.04 (19)	C17—C18—C19	121.3 (3)
N1—C1—C2	122.3 (3)	C20—C19—C23	116.7 (3)
C3—C2—C1	119.9 (3)	C20—C19—C18	124.4 (3)
C2—C3—C4	119.6 (3)	C23—C19—C18	118.9 (3)
C12—C4—C3	116.6 (3)	C21—C20—C19	120.2 (3)
C12—C4—C5	118.7 (3)	C20—C21—C22	119.0 (3)
C3—C4—C5	124.6 (3)	N4—C22—C21	123.0 (3)
C6—C5—C4	121.3 (3)	C22—N4—C23	118.3 (3)
C5—C6—C7	121.4 (3)	C22—N4—Cu1	132.3 (2)
C11—C7—C8	117.2 (3)	C23—N4—Cu1	108.70 (19)
C11—C7—C6	118.1 (3)	N4—C23—C19	123.0 (3)
C8—C7—C6	124.7 (3)	N4—C23—C24	117.7 (3)
C9—C8—C7	119.7 (3)	C19—C23—C24	119.3 (3)
C8—C9—C10	119.7 (3)	N3—C24—C16	122.4 (3)
N2—C10—C9	122.0 (3)	N3—C24—C23	117.3 (3)
C10—N2—C11	118.8 (3)	C16—C24—C23	120.3 (3)
C10—N2—Cu1	127.4 (2)	C31—O31—Cu1	106.6 (2)
C11—N2—Cu1	113.8 (2)	O32—C31—O31	125.4 (3)
N2—C11—C7	122.5 (3)	O12—N11—O13	115.4 (5)
N2—C11—C12	116.3 (3)	O12—N11—O11	117.9 (4)
C7—C11—C12	121.1 (3)	O13—N11—O11	126.6 (4)
N1—C12—C4	123.7 (3)		

Table A.B.5 Hydrogen-bond geometry (Å, °) of Cu-For-Phen

$D-H\cdots A$	$D-H$	$H\cdots A$	$D\cdots A$	$D-H\cdots A$
$O1W-H1WA\cdots O3W^i$	0.85 (2)	2.03 (2)	2.870 (4)	167 (4)
$O1W-H1WB\cdots O11$	0.84 (2)	2.01 (2)	2.846 (4)	170 (5)
$O2W-H2WB\cdots O11$	0.84 (2)	1.97 (2)	2.798 (4)	171 (4)
$O2W-H2WA\cdots O6W^{ii}$	0.82 (2)	1.94 (2)	2.752 (4)	172 (4)
$O3W-H3WA\cdots O2W^{iii}$	0.82 (2)	1.99 (2)	2.782 (4)	162 (5)
$O3W-H3WB\cdots O13$	0.81 (2)	2.67 (3)	3.260 (7)	132 (4)
$O4W-H4WB\cdots O5W^{iv}$	0.80 (2)	2.04 (2)	2.837 (4)	170 (5)
$O4W-H4WA\cdots O1W^{iv}$	0.80 (2)	2.05 (3)	2.804 (4)	157 (5)
$O5W-H5WA\cdots O4W$	0.79 (2)	2.00 (2)	2.781 (4)	169 (5)
$O5W-H5WB\cdots O32$	0.81 (2)	1.98 (2)	2.777 (4)	168 (5)
$O6W-H6WB\cdots O4W^v$	0.82 (2)	1.96 (2)	2.765 (4)	168 (6)
$O6W-H6WA\cdots O13$	0.81 (2)	2.02 (2)	2.830 (6)	172 (5)

Symmetry codes: (i) $-x-1/2, y-1/2, -z+3/2$; (ii) $-x, -y+1, -z+2$; (iii) $-x-1/2, y+1/2, -z+3/2$; (iv) $-x-1, -y+1, -z+1$; (v) $x+1/2, -y+3/2, z+1/2$.

A.B.2.2 [Cu(Ace)(1,10-Phen)₂](NO₃)·2H₂O, (Cu-Ace-Phen)

**Figure A.B.11** Crystal structure of Cu-Ace-Phen

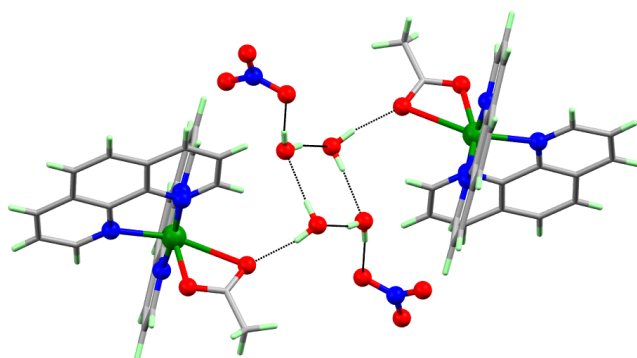


Figure A.B.12 The coordinated nitrate anion is disordered over two positions and was refined with 85:15 occupancy of the sites.

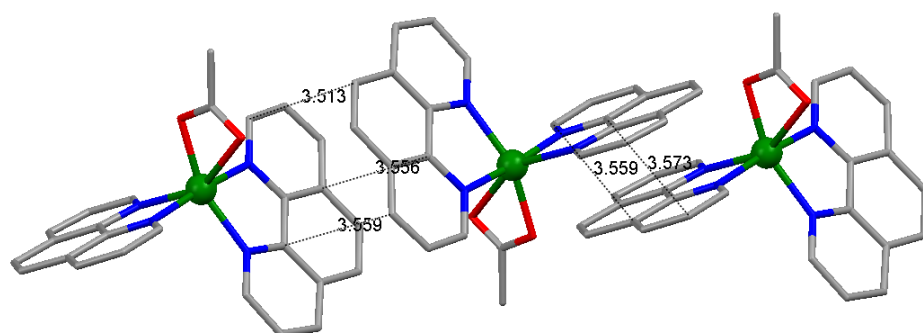


Figure A.B.13 The cations are linked into zig-zag chains by π - π stacking

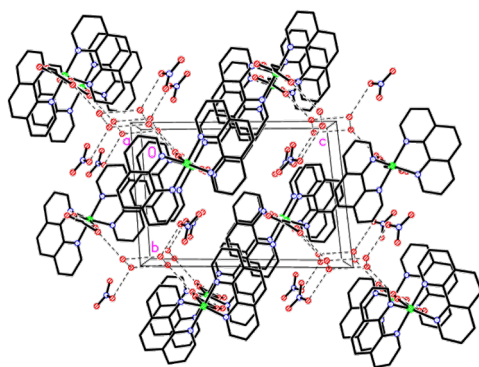


Figure A.B.14 The chains are linked by H-bonding involving the nitrate anions and water molecules.

Table A.B.6 Crystal data of Cu-Ace-Phen

$C_{26}H_{23}CuN_5O_7$	$Z = 2$
$M_r = 581.03$	$F(000) = 598$
Triclinic, $P\bar{1}$	$D_x = 1.557 \text{ Mg m}^{-3}$
$a = 8.5126 (4) \text{ \AA}$	Mo $K\alpha$ radiation, $\lambda = 0.71073 \text{ \AA}$
$b = 10.3864 (5) \text{ \AA}$	Cell parameters from 6002 reflections
$c = 14.6033 (6) \text{ \AA}$	$\theta = 2.4\text{--}28.2^\circ$
$\alpha = 83.271 (1)^\circ$	$\mu = 0.94 \text{ mm}^{-1}$
$\beta = 82.998 (1)^\circ$	$T = 150 \text{ K}$
$\gamma = 76.269 (1)^\circ$	Block, blue
$V = 1239.68 (10) \text{ \AA}^3$	$0.47 \times 0.24 \times 0.08 \text{ mm}$

Table A.B.7 Data collection of Cu-Ace-Phen

Bruker APEX-II CCD diffractometer	6174 independent reflections
Radiation source: fine-focus sealed tube	5328 reflections with $I > 2\sigma(I)$
graphite	$R_{\text{int}} = 0.026$
ϕ and ω scans	$\theta_{\text{max}} = 28.3^\circ$, $\theta_{\text{min}} = 2.0^\circ$
Absorption correction: multi-scan <i>SADABS</i> v2008/1, Sheldrick, G.M., (2008)	$h = -11 \rightarrow 11$
$T_{\text{min}} = 0.667$, $T_{\text{max}} = 0.929$	$k = -13 \rightarrow 13$
17094 measured reflections	$l = -19 \rightarrow 19$

Table A.B.8 Refinement of Cu-Ace-Phen

Refinement on F^2	Primary atom site location: structure-invariant direct methods
Least-squares matrix: full	Secondary atom site location: difference Fourier map
$R[F^2 > 2\sigma(F^2)] = 0.031$	Hydrogen site location: inferred from neighbouring sites
$wR(F^2) = 0.081$	H atoms treated by a mixture of independent and constrained refinement
$S = 1.05$	$w = 1/[\sigma^2(F_o^2) + (0.0368P)^2 + 0.5118P]$ where $P = (F_o^2 + 2F_c^2)/3$
6174 reflections	$(\Delta/\sigma)_{\text{max}} < 0.001$
381 parameters	$\Delta_{\text{max}} = 0.40 \text{ e \AA}^{-3}$
12 restraints	$\Delta_{\text{min}} = -0.32 \text{ e \AA}^{-3}$

Table A.B.9 Geometric parameters (Å, °) of Cu-Ace-Phen

Cu1—N1	1.9981 (14)	N3—C24	1.356 (2)
Cu1—O21	2.0076 (17)	C13—C14	1.400 (3)
Cu1—N4	2.0156 (14)	C14—C15	1.367 (3)
Cu1—O22'	2.019 (9)	C15—C16	1.407 (3)
Cu1—N2	2.0559 (14)	C16—C24	1.410 (2)
Cu1—N3	2.1815 (14)	C16—C17	1.438 (3)
Cu1—O22	2.589 (2)	C17—C18	1.354 (3)
Cu1—O21'	2.599 (10)	C18—C19	1.436 (3)
N1—C1	1.330 (2)	C19—C23	1.403 (2)
N1—C12	1.358 (2)	C19—C20	1.410 (3)
C1—C2	1.397 (3)	C20—C21	1.366 (3)
C2—C3	1.368 (3)	C21—C22	1.401 (2)
C3—C4	1.408 (3)	C22—N4	1.328 (2)
C4—C12	1.404 (2)	N4—C23	1.365 (2)
C4—C5	1.434 (3)	C23—C24	1.439 (2)
C5—C6	1.352 (3)	O21—C25	1.279 (5)
C6—C7	1.435 (3)	O22—C25	1.242 (6)
C7—C11	1.398 (2)	C25—C26	1.505 (4)
C7—C8	1.412 (3)	O21'—C25'	1.25 (2)
C8—C9	1.365 (3)	O22'—C25'	1.273 (18)
C9—C10	1.400 (3)	C25'—C26'	1.515 (16)
C10—N2	1.326 (2)	N31—O32	1.229 (2)
N2—C11	1.362 (2)	N31—O31	1.239 (2)
C11—C12	1.431 (2)	N31—O33	1.243 (2)
N3—C13	1.324 (2)		
N1—Cu1—O21	91.81 (6)	C11—N2—Cu1	111.44 (11)
N1—Cu1—N4	174.22 (6)	N2—C11—C7	123.42 (15)
O21—Cu1—N4	93.20 (6)	N2—C11—C12	116.58 (14)
N1—Cu1—O22'	92.2 (3)	C7—C11—C12	119.99 (15)
O21—Cu1—O22'	52.8 (3)	N1—C12—C4	122.92 (15)
N4—Cu1—O22'	93.1 (3)	N1—C12—C11	116.84 (14)
N1—Cu1—N2	81.76 (6)	C4—C12—C11	120.22 (15)
O21—Cu1—N2	156.96 (6)	C13—N3—C24	118.31 (15)
N4—Cu1—N2	94.68 (5)	C13—N3—Cu1	131.59 (12)
O22'—Cu1—N2	105.1 (3)	C24—N3—Cu1	110.09 (11)
N1—Cu1—N3	96.66 (5)	N3—C13—C14	122.66 (17)
O21—Cu1—N3	98.06 (6)	C15—C14—C13	119.53 (18)
N4—Cu1—N3	79.79 (5)	C14—C15—C16	119.52 (17)

O22'—Cu1—N3	149.8 (3)	C15—C16—C24	117.07 (16)
N2—Cu1—N3	104.63 (5)	C15—C16—C17	123.71 (17)
N1—Cu1—O22	94.57 (5)	C24—C16—C17	119.22 (17)
O21—Cu1—O22	55.67 (5)	C18—C17—C16	120.65 (17)
N4—Cu1—O22	90.63 (5)	C17—C18—C19	121.54 (17)
O22'—Cu1—O22	3.7 (3)	C23—C19—C20	117.30 (16)
N2—Cu1—O22	102.59 (5)	C23—C19—C18	118.92 (17)
N3—Cu1—O22	151.75 (5)	C20—C19—C18	123.78 (16)
N1—Cu1—O21'	94.7 (2)	C21—C20—C19	119.70 (16)
O21—Cu1—O21'	4.1 (2)	C20—C21—C22	119.55 (17)
N4—Cu1—O21'	90.2 (2)	N4—C22—C21	122.25 (17)
O22'—Cu1—O21'	55.7 (3)	C22—N4—C23	118.73 (15)
N2—Cu1—O21'	160.5 (2)	C22—N4—Cu1	126.16 (12)
N3—Cu1—O21'	94.8 (2)	C23—N4—Cu1	115.11 (11)
O22—Cu1—O21'	58.4 (2)	N4—C23—C19	122.47 (16)
C1—N1—C12	118.25 (15)	N4—C23—C24	117.57 (14)
C1—N1—Cu1	128.40 (12)	C19—C23—C24	119.97 (15)
C12—N1—Cu1	113.36 (11)	N3—C24—C16	122.90 (16)
N1—C1—C2	122.57 (17)	N3—C24—C23	117.39 (15)
C3—C2—C1	119.51 (17)	C16—C24—C23	119.68 (15)
C2—C3—C4	119.53 (16)	C25—O21—Cu1	103.9 (2)
C12—C4—C3	117.20 (16)	C25—O22—Cu1	77.9 (2)
C12—C4—C5	118.54 (16)	O22—C25—O21	122.1 (3)
C3—C4—C5	124.25 (16)	O22—C25—C26	121.0 (4)
C6—C5—C4	121.25 (17)	O21—C25—C26	116.8 (4)
C5—C6—C7	121.11 (17)	C25'—O21'—Cu1	77.0 (10)
C11—C7—C8	116.98 (16)	C25'—O22'—Cu1	103.0 (10)
C11—C7—C6	118.89 (16)	O21'—C25'—O22'	123.3 (16)
C8—C7—C6	124.11 (16)	O21'—C25'—C26'	119.2 (16)
C9—C8—C7	119.38 (16)	O22'—C25'—C26'	117.5 (17)
C8—C9—C10	119.77 (17)	O32—N31—O31	119.77 (17)
N2—C10—C9	122.53 (17)	O32—N31—O33	119.98 (18)
C10—N2—C11	117.91 (15)	O31—N31—O33	120.23 (17)
C10—N2—Cu1	130.65 (12)		

Table A.B.10 Hydrogen-bond geometry (Å, °) of Cu-Ace-Phen

$D-H\cdots A$	$D-H$	$H\cdots A$	$D\cdots A$	$D-H\cdots A$
$O1W-H1WA\cdots O22$	0.84 (2)	1.87 (2)	2.704 (2)	170 (3)
$O1W-H1WB\cdots O2W$	0.83 (2)	1.91 (2)	2.732 (2)	176 (3)
$O2W-H2WA\cdots O33$	0.81 (2)	2.05 (2)	2.853 (2)	169 (3)
$O2W-H2WB\cdots O1W^i$	0.78 (2)	1.99 (2)	2.748 (3)	164 (3)

Symmetry code: (i) $-x+1, -y, -z$.

A.B.2.3 [Cu(Pro)(1,10-Phen)] $\cdot\frac{1}{2}(\text{CO}_3)\cdot 4\frac{1}{2}\text{H}_2\text{O}$, (Cu-Pro-Phen)

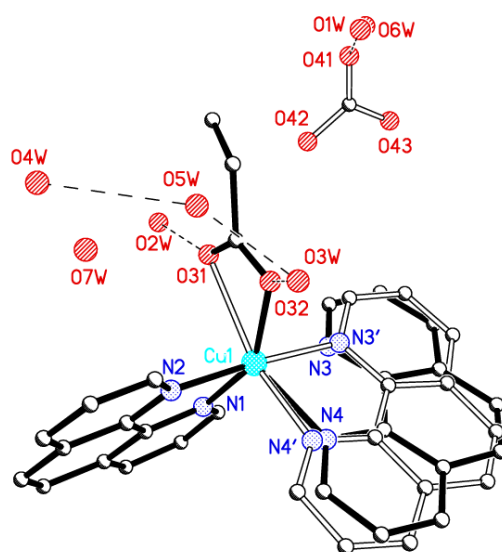


Figure A.B.15 Crystal structure of Cu-Pro-Phen

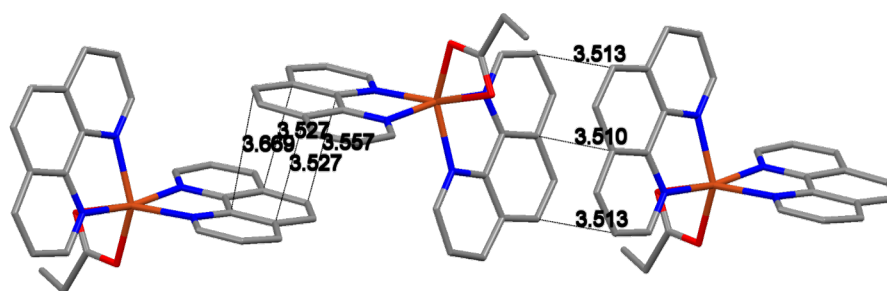


Figure A.B.16 One of the 1,10-phen groups is disordered and was modeled with 50:50 occupancy over two sites.

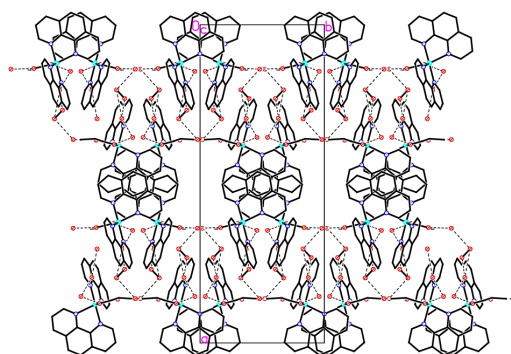


Figure A.B.17 The cations are π -stacked into chains and the chains are linked by H-bonding, which includes the counter ion. H-bond network resulting is also disordered; a reasonable set of interactions is shown in the final H-bond table (Table A.B.15).

Table A.B.11 Crystal data of Cu-Pro-Phen

$C_{27.50}H_{30}CuN_4O_8$	$F(000) = 2528$
$M_r = 608.09$	$D_x = 1.428 \text{ Mg m}^{-3}$
Monoclinic, $C2/c$	Mo $K\alpha$ radiation, $\lambda = 0.71073 \text{ \AA}$
$a = 31.873 (5) \text{ \AA}$	Cell parameters from 5053 reflections
$b = 12.4716 (19) \text{ \AA}$	$\theta = 2.2\text{--}25.0^\circ$
$c = 14.264 (2) \text{ \AA}$	$\mu = 0.83 \text{ mm}^{-1}$
$\beta = 93.879 (2)^\circ$	$T = 150 \text{ K}$
$V = 5656.9 (15) \text{ \AA}^3$	Block, blue
$Z = 8$	$0.40 \times 0.26 \times 0.26 \text{ mm}$

Table A.B.12 Data collection of Cu-Pro-Phen

Bruker APEX 2 CCD diffractometer	3442 reflections with $I > 2\sigma(I)$
ω rotation with narrow frames scans	$R_{\text{int}} = 0.059$
Absorption correction: multi-scan <i>SADABS</i> v2009/1, Sheldrick, G.M., (2009)	$\theta_{\text{max}} = 26.4^\circ$, $\theta_{\text{min}} = 1.8^\circ$
$T_{\text{min}} = 0.522$, $T_{\text{max}} = 0.745$	$h = -39 \rightarrow 39$
23362 measured reflections	$k = -15 \rightarrow 15$
5815 independent reflections	$l = -17 \rightarrow 17$

Table A.B.13 Refinement of Cu-Pro-Phen

Refinement on F^2	984 restraints
Least-squares matrix: full	Hydrogen site location: inferred from neighbouring sites
$R[F^2 > 2\sigma(F^2)] = 0.094$	H-atom parameters constrained
$wR(F^2) = 0.330$	$w = 1/[\sigma^2(F_o^2) + (0.1958P)^2 + 25.9775P]$ where $P = (F_o^2 + 2F_c^2)/3$
$S = 1.05$	$(\Delta/\sigma)_{\max} = 0.006$
5815 reflections	$\Delta_{\max} = 1.87 \text{ e } \text{\AA}^{-3}$
527 parameters	$\Delta_{\min} = -0.88 \text{ e } \text{\AA}^{-3}$

Table A.B.14 Geometric parameters (\AA , $^\circ$) of Cu-Pro-Phen

Cu1—O32	1.955 (8)	C21—C22	1.400 (15)
Cu1—N2	1.998 (5)	C22—N4	1.325 (13)
Cu1—N3'	2.008 (13)	N4—C23	1.344 (13)
Cu1—N3	2.035 (14)	C23—C24	1.442 (13)
Cu1—N4'	2.087 (13)	N3'—C13'	1.304 (13)
Cu1—N1	2.093 (6)	N3'—C24'	1.355 (13)
Cu1—N4	2.171 (14)	C13'—C14'	1.377 (13)
Cu1—C31	2.513 (9)	C14'—C15'	1.363 (15)
N1—C1	1.319 (8)	C15'—C16'	1.406 (15)
N1—C12	1.362 (7)	C16'—C24'	1.390 (12)
C1—C2	1.378 (10)	C16'—C17'	1.429 (15)
C2—C3	1.362 (10)	C17'—C18'	1.334 (16)
C3—C4	1.417 (10)	C18'—C19'	1.436 (14)
C4—C12	1.391 (9)	C19'—C20'	1.392 (15)
C4—C5	1.423 (10)	C19'—C23'	1.407 (12)
C5—C6	1.338 (10)	C20'—C21'	1.345 (15)
C6—C7	1.440 (9)	C21'—C22'	1.401 (14)
C7—C8	1.391 (9)	C22'—N4'	1.314 (13)
C7—C11	1.402 (8)	N4'—C23'	1.339 (12)
C8—C9	1.373 (10)	C23'—C24'	1.442 (13)
C9—C10	1.391 (9)	O31—C31	1.189 (11)
C10—N2	1.333 (8)	O32—C31	1.235 (9)
N2—C11	1.342 (8)	C31—C32	1.587 (13)
C11—C12	1.433 (8)	C32—C33	1.486 (11)
N3—C13	1.313 (13)	C40—O43 ⁱ	0.87 (2)
N3—C24	1.362 (13)	C40—O41	1.206 (15)
C13—C14	1.384 (14)	C40—O43	1.207 (14)
C14—C15	1.359 (16)	C40—O42	1.216 (16)

C15—C16	1.411 (15)	C40—C40 ⁱ	1.57 (3)
C16—C24	1.395 (13)	C40—O42 ⁱ	1.879 (19)
C16—C17	1.429 (15)	O42—O43 ⁱ	0.711 (16)
C17—C18	1.332 (17)	O42—C40 ⁱ	1.879 (19)
C18—C19	1.438 (16)	O43—O42 ⁱ	0.711 (16)
C19—C20	1.389 (15)	O43—C40 ⁱ	0.87 (2)
C19—C23	1.407 (12)	O43—O43 ⁱ	1.39 (3)
C20—C21	1.353 (16)		
O32—Cu1—N2	93.5 (3)	C22—N4—C23	117.7 (12)
O32—Cu1—N3'	86.3 (4)	C22—N4—Cu1	131.5 (10)
N2—Cu1—N3'	173.4 (4)	C23—N4—Cu1	110.6 (8)
O32—Cu1—N3	95.2 (4)	N4—C23—C19	122.8 (12)
N2—Cu1—N3	170.9 (4)	N4—C23—C24	117.8 (10)
O32—Cu1—N4'	105.8 (10)	C19—C23—C24	119.4 (11)
N2—Cu1—N4'	92.0 (4)	N3—C24—C16	123.1 (11)
N3'—Cu1—N4'	81.7 (5)	N3—C24—C23	116.5 (10)
O32—Cu1—N1	148.2 (3)	C16—C24—C23	120.2 (10)
N2—Cu1—N1	81.4 (2)	C13'—N3'—C24'	119.4 (12)
N3'—Cu1—N1	102.3 (4)	C13'—N3'—Cu1	127.4 (10)
N3—Cu1—N1	89.7 (4)	C24'—N3'—Cu1	113.1 (8)
N4'—Cu1—N1	105.7 (10)	N3'—C13'—C14'	122.4 (12)
O32—Cu1—N4	107.0 (10)	C15'—C14'—C13'	119.5 (12)
N2—Cu1—N4	101.1 (4)	C14'—C15'—C16'	119.5 (10)
N3—Cu1—N4	79.0 (5)	C24'—C16'—C15'	117.0 (10)
N1—Cu1—N4	104.7 (10)	C24'—C16'—C17'	118.8 (12)
O32—Cu1—C31	28.8 (3)	C15'—C16'—C17'	124.3 (11)
N2—Cu1—C31	92.3 (2)	C18'—C17'—C16'	121.2 (12)
N3'—Cu1—C31	90.7 (4)	C17'—C18'—C19'	121.4 (12)
N3—Cu1—C31	93.9 (4)	C20'—C19'—C23'	116.0 (11)
N4'—Cu1—C31	134.5 (10)	C20'—C19'—C18'	124.5 (11)
N1—Cu1—C31	119.7 (3)	C23'—C19'—C18'	119.5 (11)
N4—Cu1—C31	135.1 (10)	C21'—C20'—C19'	120.5 (12)
C1—N1—C12	118.4 (6)	C20'—C21'—C22'	119.1 (12)
C1—N1—Cu1	131.3 (5)	N4'—C22'—C21'	122.6 (12)
C12—N1—Cu1	110.4 (4)	C22'—N4'—C23'	117.8 (11)
N1—C1—C2	122.3 (7)	C22'—N4'—Cu1	131.7 (10)
C3—C2—C1	120.5 (7)	C23'—N4'—Cu1	110.5 (8)
C2—C3—C4	118.8 (7)	N4'—C23'—C19'	123.7 (11)
C12—C4—C3	116.9 (6)	N4'—C23'—C24'	118.0 (10)
C12—C4—C5	118.7 (6)	C19'—C23'—C24'	117.9 (10)

C3—C4—C5	124.4 (7)	N3'—C24'—C16'	122.1 (11)
C6—C5—C4	121.9 (7)	N3'—C24'—C23'	116.7 (10)
C5—C6—C7	121.0 (6)	C16'—C24'—C23'	121.2 (11)
C8—C7—C11	117.8 (6)	C31—O32—Cu1	101.6 (8)
C8—C7—C6	123.9 (6)	O31—C31—O32	122.9 (10)
C11—C7—C6	118.3 (6)	O31—C31—C32	119.8 (7)
C9—C8—C7	119.4 (6)	O32—C31—C32	117.2 (10)
C8—C9—C10	119.3 (7)	O31—C31—Cu1	73.4 (6)
N2—C10—C9	122.1 (7)	O32—C31—Cu1	49.6 (5)
C10—N2—C11	118.8 (5)	C32—C31—Cu1	166.7 (6)
C10—N2—Cu1	127.3 (5)	C33—C32—C31	110.9 (7)
C11—N2—Cu1	113.9 (4)	O43 ⁱ —C40—O41	152 (2)
N2—C11—C7	122.5 (6)	O43 ⁱ —C40—O43	82 (2)
N2—C11—C12	117.6 (5)	O41—C40—O43	124.5 (16)
C7—C11—C12	119.9 (6)	O43 ⁱ —C40—O42	35.1 (14)
N1—C12—C4	123.0 (6)	O41—C40—O42	120.5 (14)
N1—C12—C11	116.8 (6)	O43—C40—O42	114.9 (16)
C4—C12—C11	120.2 (6)	O43 ⁱ —C40—C40 ⁱ	49.6 (16)
C13—N3—C24	117.2 (12)	O41—C40—C40 ⁱ	154.7 (15)
C13—N3—Cu1	127.4 (10)	O43—C40—C40 ⁱ	33.1 (9)
C24—N3—Cu1	114.9 (9)	O42—C40—C40 ⁱ	83.7 (13)
N3—C13—C14	124.4 (13)	O43 ⁱ —C40—O42 ⁱ	88 (2)
C15—C14—C13	118.5 (13)	O41—C40—O42 ⁱ	119.7 (13)
C14—C15—C16	120.0 (12)	O43—C40—O42 ⁱ	8.8 (14)
C24—C16—C15	116.7 (11)	O42—C40—O42 ⁱ	118.5 (13)
C24—C16—C17	118.4 (12)	C40 ⁱ —C40—O42 ⁱ	40.0 (8)
C15—C16—C17	124.8 (12)	O43 ⁱ —O42—C40	44 (2)
C18—C17—C16	122.0 (13)	O43 ⁱ —O42—C40 ⁱ	15 (2)
C17—C18—C19	121.2 (13)	C40—O42—C40 ⁱ	56.2 (12)
C20—C19—C23	117.1 (12)	O42 ⁱ —O43—C40 ⁱ	100 (3)
C20—C19—C18	124.4 (12)	O42 ⁱ —O43—C40	156 (4)
C23—C19—C18	118.6 (12)	C40 ⁱ —O43—C40	97 (2)
C21—C20—C19	120.7 (12)	O42 ⁱ —O43—O43 ⁱ	152 (3)
C20—C21—C22	118.1 (13)	C40 ⁱ —O43—O43 ⁱ	59.4 (15)
N4—C22—C21	123.4 (14)	C40—O43—O43 ⁱ	38.2 (12)

Symmetry code: (i) $-x+1, y, -z+1/2$.

Table A.B.15 Hydrogen-bond geometry (Å, °) of Cu-Pro-Phen

$D-H\cdots A$		$D\cdots A$
$O1W\cdots O2W^i$		2.74(1)
$O1W\cdots O6W$		2.59(2)
$O1W\cdots O41$		2.98 (2)
$O2W\cdots O31$		2.64 (1)
$O2W\cdots O4W^{ii}$		2.80 (2)
$O3W\cdots O32$		2.77 (1)
$O3W\cdots O5W$		2.35 (3)
$O4W\cdots O5W$		2.90 (2)
$O6W\cdots O1W^{iii}$		2.79 (1)
$O6W\cdots O43^{iv}$		2.78(2)

Symmetry codes: (i) $x, 2-y, 1/2+z$; (ii) $1/2-x, 1/2+y, 1/2-z$; (iii) $1-x, 2-y, 1-z$; (iv) $1-x, y, 1/2-z$

A.B.2.4 $[\text{Cu}(\text{Iso})(1,10\text{-Phen})_2]_2 \cdot 2(\text{NO}_3) \cdot 4\text{H}_2\text{O}$, (Cu-Iso-Phen)

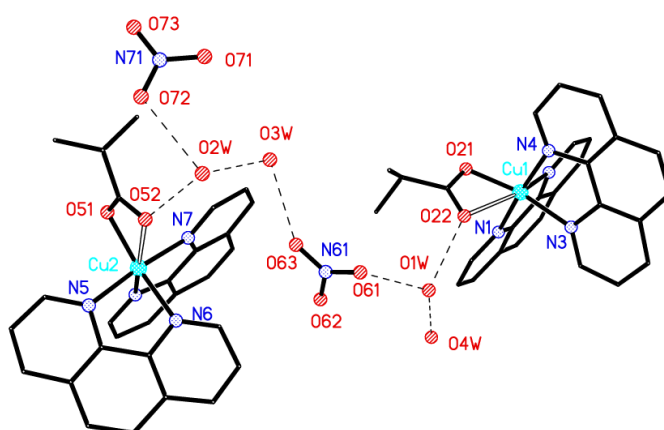


Figure A.B.18 Cu-Iso-Phen crystallises in the chiral space group $P2_12_12_1$ with two independent cations in the asymmetric unit. The carboxylate bonding is notably asymmetric.

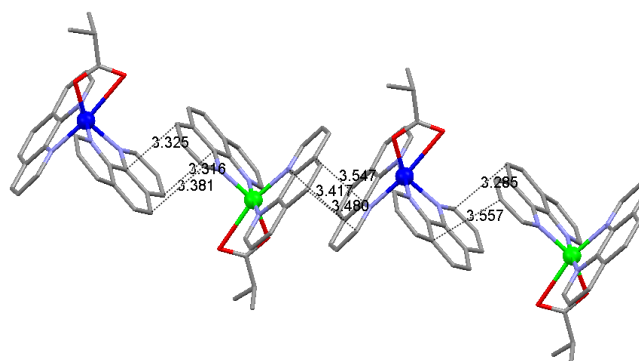


Figure A.B.19 The cations are π -stacked into zig-zag chains running parallel to the a axis.

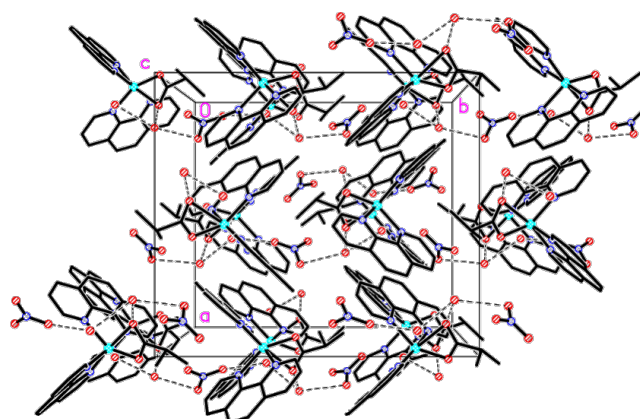


Figure A.B.20 The chains are linked together via H-bonding involving the water molecules and the nitrate anions.

Table A.B.16 Crystal data of Cu-Iso-Phen

$C_{28}H_{27}CuN_5O_7$	$D_x = 1.492 \text{ Mg m}^{-3}$
$M_r = 609.09$	Mo $K\alpha$ radiation, $\lambda = 0.71073 \text{ \AA}$
Orthorhombic, $P2_12_12_1$	Cell parameters from 7191 reflections
$a = 14.9422 (10) \text{ \AA}$	$\theta = 2.4\text{--}23.6^\circ$
$b = 17.0635 (12) \text{ \AA}$	$\mu = 0.86 \text{ mm}^{-1}$
$c = 21.2699 (14) \text{ \AA}$	$T = 150 \text{ K}$
$V = 5423.1 (6) \text{ \AA}^3$	Lath, blue
$Z = 8$	$0.51 \times 0.19 \times 0.06 \text{ mm}$
$F(000) = 2520$	

Table A.B.17 Data collection of Cu-Iso-Phen

Bruker APEX 2 CCD diffractometer	13446 independent reflections
Radiation source: fine-focus sealed tube	9498 reflections with $I > 2\sigma(I)$
graphite	$R_{\text{int}} = 0.071$
ω rotation with narrow frames scans	$\theta_{\text{max}} = 28.3^\circ$, $\theta_{\text{min}} = 1.8^\circ$
Absorption correction: multi-scan <i>SADABS</i> v2008/1, Sheldrick, G.M., (2008)	$h = -19 \rightarrow 19$
$T_{\text{min}} = 0.668$, $T_{\text{max}} = 0.950$	$k = -22 \rightarrow 22$
55103 measured reflections	$l = -27 \rightarrow 28$

Table A.B.18 Refinement data of Cu-Iso-Phen

Refinement on F^2	Secondary atom site location: difference Fourier map
Least-squares matrix: full	Hydrogen site location: inferred from neighbouring sites
$R[F^2 > 2\sigma(F^2)] = 0.042$	H atoms treated by a mixture of independent and constrained refinement
$wR(F^2) = 0.097$	$w = 1/[\sigma^2(F_o^2) + (0.0406P)^2]$ where $P = (F_o^2 + 2F_c^2)/3$
$S = 1.00$	$(\Delta/\sigma)_{\max} = 0.001$
13446 reflections	$\Delta_{\max} = 0.38 \text{ e } \text{\AA}^{-3}$
763 parameters	$\Delta_{\min} = -0.58 \text{ e } \text{\AA}^{-3}$
12 restraints	Absolute structure: Flack H D (1983), ActaCryst. A39, 876-881
Primary atom site location: structure-invariant direct methods	Flack parameter: -0.022 (9)

Table A.B.19 Geometric parameters (\AA , $^\circ$) of Cu-Iso-Phen

Cu1—O21	1.960 (2)	Cu2—N6	2.083 (2)
Cu1—N4	2.004 (3)	Cu2—N8	2.182 (3)
Cu1—N1	2.008 (3)	Cu2—O52	2.725 (2)
Cu1—N3	2.062 (3)	N5—C31	1.341 (4)
Cu1—N2	2.203 (3)	N5—C42	1.362 (4)
Cu1—O22	2.751 (2)	C31—C32	1.394 (5)
N1—C1	1.335 (4)	C32—C33	1.372 (5)
N1—C12	1.364 (4)	C33—C34	1.411 (5)
C1—C2	1.399 (5)	C34—C42	1.400 (4)
C2—C3	1.368 (5)	C34—C35	1.425 (4)
C3—C4	1.398 (5)	C35—C36	1.347 (5)
C4—C12	1.423 (5)	C36—C37	1.431 (5)
C4—C5	1.437 (5)	C37—C41	1.405 (4)
C5—C6	1.333 (5)	C37—C38	1.409 (5)
C6—C7	1.433 (5)	C38—C39	1.364 (5)
C7—C8	1.390 (5)	C39—C40	1.403 (4)
C7—C11	1.404 (5)	C40—N6	1.324 (4)
C8—C9	1.368 (5)	N6—C41	1.367 (4)
C9—C10	1.389 (5)	C41—C42	1.433 (4)
C10—N2	1.330 (4)	N7—C43	1.329 (4)
N2—C11	1.361 (4)	N7—C54	1.361 (4)
C11—C12	1.433 (5)	C43—C44	1.399 (4)
N3—C13	1.334 (4)	C44—C45	1.366 (5)
N3—C24	1.362 (4)	C45—C46	1.407 (5)

C13—C14	1.395 (4)	C46—C54	1.401 (4)
C14—C15	1.357 (5)	C46—C47	1.435 (5)
C15—C16	1.415 (5)	C47—C48	1.346 (5)
C16—C24	1.399 (4)	C48—C49	1.438 (5)
C16—C17	1.437 (5)	C49—C50	1.401 (5)
C17—C18	1.361 (5)	C49—C53	1.403 (4)
C18—C19	1.429 (5)	C50—C51	1.364 (5)
C19—C23	1.403 (4)	C51—C52	1.396 (5)
C19—C20	1.413 (5)	C52—N8	1.329 (4)
C20—C21	1.356 (5)	C53—N8	1.363 (4)
C21—C22	1.398 (5)	C53—C54	1.435 (4)
C22—N4	1.322 (4)	O51—C55	1.277 (4)
N4—C23	1.356 (4)	O52—C55	1.247 (4)
C23—C24	1.434 (4)	C55—C56	1.524 (4)
O21—C25	1.288 (4)	C56—C58	1.515 (5)
O22—C25	1.237 (4)	C56—C57	1.522 (5)
C25—C26	1.508 (4)	N61—O61	1.240 (4)
C26—C28	1.525 (5)	N61—O63	1.240 (4)
C26—C27	1.538 (5)	N61—O62	1.249 (4)
Cu2—O51	1.978 (2)	N71—O73	1.247 (4)
Cu2—N5	1.985 (3)	N71—O71	1.249 (4)
Cu2—N7	1.997 (3)	N71—O72	1.259 (4)
O21—Cu1—N4	92.41 (10)	O51—Cu2—N6	146.72 (9)
O21—Cu1—N1	92.67 (10)	N5—Cu2—N6	81.38 (10)
N4—Cu1—N1	174.03 (11)	N7—Cu2—N6	95.14 (10)
O21—Cu1—N3	152.68 (9)	O51—Cu2—N8	120.79 (9)
N4—Cu1—N3	81.56 (10)	N5—Cu2—N8	93.38 (10)
N1—Cu1—N3	95.30 (10)	N7—Cu2—N8	79.85 (11)
O21—Cu1—N2	115.14 (9)	N6—Cu2—N8	92.39 (9)
N4—Cu1—N2	95.84 (11)	O51—Cu2—O52	53.47 (8)
N1—Cu1—N2	79.15 (11)	N5—Cu2—O52	93.31 (9)
N3—Cu1—N2	92.04 (9)	N7—Cu2—O52	93.78 (9)
O21—Cu1—O22	53.05 (8)	N6—Cu2—O52	93.86 (8)
N4—Cu1—O22	92.54 (9)	N8—Cu2—O52	171.45 (8)
N1—Cu1—O22	93.02 (10)	C31—N5—C42	117.6 (3)
N3—Cu1—O22	100.38 (8)	C31—N5—Cu2	128.0 (2)
N2—Cu1—O22	165.93 (8)	C42—N5—Cu2	114.0 (2)
C1—N1—C12	118.4 (3)	N5—C31—C32	122.7 (3)
C1—N1—Cu1	125.8 (2)	C33—C32—C31	119.4 (3)
C12—N1—Cu1	115.9 (2)	C32—C33—C34	119.9 (3)

N1—C1—C2	122.1 (4)	C42—C34—C33	116.7 (3)
C3—C2—C1	120.3 (4)	C42—C34—C35	118.8 (3)
C2—C3—C4	119.4 (3)	C33—C34—C35	124.4 (3)
C3—C4—C12	117.5 (3)	C36—C35—C34	121.4 (3)
C3—C4—C5	124.5 (3)	C35—C36—C37	121.5 (3)
C12—C4—C5	118.0 (4)	C41—C37—C38	117.1 (3)
C6—C5—C4	121.5 (4)	C41—C37—C36	118.1 (3)
C5—C6—C7	122.2 (4)	C38—C37—C36	124.7 (3)
C8—C7—C11	117.4 (3)	C39—C38—C37	119.3 (3)
C8—C7—C6	124.4 (4)	C38—C39—C40	120.1 (3)
C11—C7—C6	118.2 (4)	N6—C40—C39	122.4 (3)
C9—C8—C7	119.8 (3)	C40—N6—C41	118.0 (3)
C8—C9—C10	119.5 (4)	C40—N6—Cu2	131.2 (2)
N2—C10—C9	122.8 (3)	C41—N6—Cu2	110.8 (2)
C10—N2—C11	117.8 (3)	N6—C41—C37	123.1 (3)
C10—N2—Cu1	132.0 (2)	N6—C41—C42	116.5 (3)
C11—N2—Cu1	110.0 (2)	C37—C41—C42	120.3 (3)
N2—C11—C7	122.8 (3)	N5—C42—C34	123.7 (3)
N2—C11—C12	116.9 (3)	N5—C42—C41	116.5 (3)
C7—C11—C12	120.3 (3)	C34—C42—C41	119.7 (3)
N1—C12—C4	122.3 (3)	C43—N7—C54	118.6 (3)
N1—C12—C11	117.9 (3)	C43—N7—Cu2	125.9 (2)
C4—C12—C11	119.8 (3)	C54—N7—Cu2	115.5 (2)
C13—N3—C24	117.7 (3)	N7—C43—C44	122.1 (3)
C13—N3—Cu1	130.9 (2)	C45—C44—C43	119.9 (3)
C24—N3—Cu1	111.4 (2)	C44—C45—C46	119.1 (3)
N3—C13—C14	122.2 (3)	C54—C46—C45	117.8 (3)
C15—C14—C13	120.5 (3)	C54—C46—C47	118.9 (3)
C14—C15—C16	119.2 (3)	C45—C46—C47	123.3 (3)
C24—C16—C15	116.9 (3)	C48—C47—C46	120.9 (3)
C24—C16—C17	119.4 (3)	C47—C48—C49	121.9 (3)
C15—C16—C17	123.7 (3)	C50—C49—C53	117.4 (3)
C18—C17—C16	120.2 (3)	C50—C49—C48	124.5 (3)
C17—C18—C19	121.5 (3)	C53—C49—C48	118.1 (3)
C23—C19—C20	116.9 (3)	C51—C50—C49	119.8 (3)
C23—C19—C18	119.0 (3)	C50—C51—C52	119.3 (3)
C20—C19—C18	124.0 (3)	N8—C52—C51	122.9 (3)
C21—C20—C19	119.3 (3)	N8—C53—C49	122.7 (3)
C20—C21—C22	119.9 (3)	N8—C53—C54	117.0 (3)
N4—C22—C21	122.4 (3)	C49—C53—C54	120.3 (3)
C22—N4—C23	118.3 (3)	N7—C54—C46	122.4 (3)

C22—N4—Cu1	128.7 (2)	N7—C54—C53	117.7 (3)
C23—N4—Cu1	113.1 (2)	C46—C54—C53	119.9 (3)
N4—C23—C19	123.0 (3)	C52—N8—C53	117.9 (3)
N4—C23—C24	117.1 (3)	C52—N8—Cu2	132.1 (2)
C19—C23—C24	119.8 (3)	C53—N8—Cu2	109.7 (2)
N3—C24—C16	123.6 (3)	C55—O51—Cu2	108.8 (2)
N3—C24—C23	116.3 (3)	C55—O52—Cu2	74.58 (18)
C16—C24—C23	120.0 (3)	O52—C55—O51	123.0 (3)
C25—O21—Cu1	109.78 (19)	O52—C55—C56	119.9 (3)
C25—O22—Cu1	73.91 (18)	O51—C55—C56	117.0 (3)
O22—C25—O21	123.0 (3)	C58—C56—C57	111.4 (3)
O22—C25—C26	121.5 (3)	C58—C56—C55	113.1 (3)
O21—C25—C26	115.4 (3)	C57—C56—C55	108.7 (3)
C25—C26—C28	112.1 (3)	O61—N61—O63	120.3 (3)
C25—C26—C27	108.2 (3)	O61—N61—O62	119.9 (3)
C28—C26—C27	110.9 (3)	O63—N61—O62	119.7 (3)
O51—Cu2—N5	93.22 (10)	O73—N71—O71	120.0 (3)
O51—Cu2—N7	93.41 (10)	O73—N71—O72	120.6 (3)
N5—Cu2—N7	172.30 (11)	O71—N71—O72	119.3 (3)

Table A.B.20 Hydrogen-bond geometry (Å, °) of Cu-Iso-Phen

<i>D</i> —H \cdots <i>A</i>	<i>D</i> —H	H \cdots <i>A</i>	<i>D</i> \cdots <i>A</i>	<i>D</i> —H \cdots <i>A</i>
O1 <i>W</i> —H1 <i>WA</i> \cdots O22	0.84 (2)	2.01 (2)	2.808 (4)	160 (4)
O1 <i>W</i> —H1 <i>WB</i> \cdots O61	0.84 (2)	2.06 (2)	2.889 (4)	170 (5)
O2 <i>W</i> —H2 <i>WA</i> \cdots O52	0.85 (2)	1.94 (2)	2.786 (3)	171 (4)
O2 <i>W</i> —H2 <i>WB</i> \cdots O72	0.84 (2)	2.05 (2)	2.872 (4)	166 (4)
O3 <i>W</i> —H3 <i>WA</i> \cdots O2 <i>W</i>	0.84 (2)	2.01 (2)	2.856 (5)	179 (6)
O3 <i>W</i> —H3 <i>WB</i> \cdots O63	0.83 (2)	2.10 (3)	2.889 (4)	158 (6)
O4 <i>W</i> —H4 <i>WA</i> \cdots O1 <i>W</i>	0.83 (2)	2.03 (2)	2.847 (5)	174 (6)
O4 <i>W</i> —H4 <i>WB</i> \cdots O73 ⁱ	0.82 (2)	2.16 (2)	2.972 (4)	169 (6)

Symmetry code: (i) *x*, *y*-1, *z*.

A.B.2.5 [Cu(Piv)(1,10-Phen)₂]₂(piv)₂·(Hpiv)·9H₂O, (Cu-Piv-Phen)

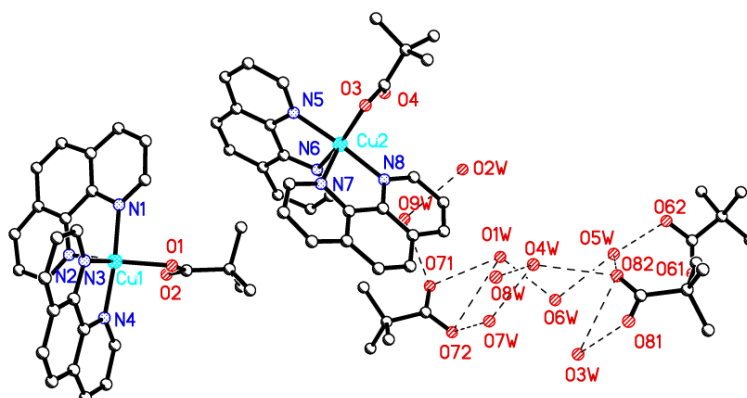


Figure A.B.21 The structure of Cu-Piv-Phen was refined as a 2-component merohedral twin (twin matrix -1 0 0 0 1 0 0 1 -1 and BASF 0.21).

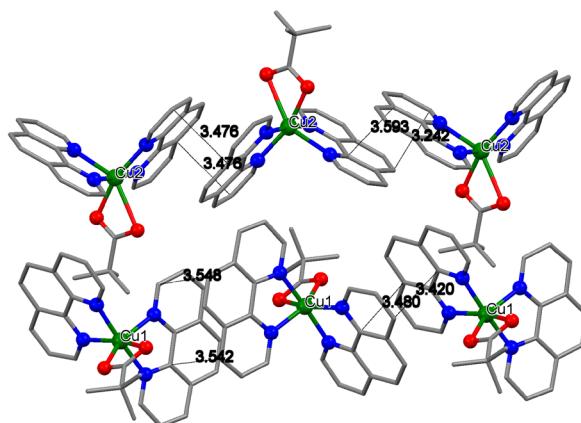


Figure A.B.22 The asymmetric unit contains two independent [Cu(phen)₂(piv)]⁺ cations, two pivalate anions and one pivalic acid molecule as well as nine solvate water molecules. The acidic proton of the pivalic acid molecule was located from a difference map.

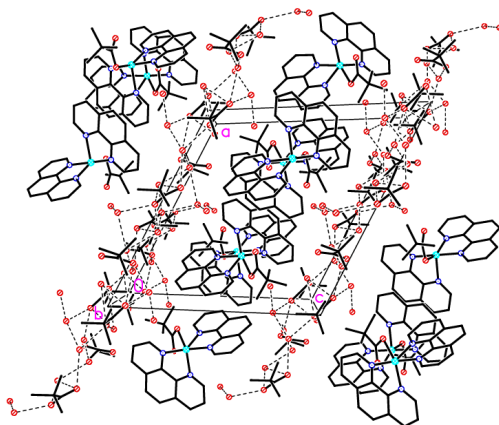


Figure A.B.23 The cations form two independent chains by π - π stacking, while the anions, pivalic acid and water molecules are linked by a H-bonding network.

Table A.B.21 Crystal data of Cu-Piv-Phen

$C_{36.50}H_{48}CuN_4O_{9.50}$	$Z = 4$
$M_r = 758.33$	$F(000) = 1600$
Triclinic, $P\bar{1}$	$D_x = 1.339 \text{ Mg m}^{-3}$
$a = 16.091 (2) \text{ \AA}$	Mo $K\alpha$ radiation, $\lambda = 0.71073 \text{ \AA}$
$b = 17.367 (2) \text{ \AA}$	Cell parameters from 4276 reflections
$c = 17.454 (2) \text{ \AA}$	$\theta = 2.4\text{--}21.4^\circ$
$\alpha = 60.321 (2)^\circ$	$\mu = 0.64 \text{ mm}^{-1}$
$\beta = 66.311 (2)^\circ$	$T = 150 \text{ K}$
$\gamma = 89.747 (2)^\circ$	Plate, blue
$V = 3762.8 (9) \text{ \AA}^3$	$0.28 \times 0.22 \times 0.09 \text{ mm}$

Table A.B.22 Data collection of Cu-Piv-Phen

Bruker APEX 2 CCD diffractometer	9396 reflections with $I > 2\sigma(I)$
Radiation source: fine-focus sealed tube	$R_{\text{int}} = 0.056$
ω rotation with narrow frames scans	$\theta_{\text{max}} = 25.0^\circ$, $\theta_{\text{min}} = 1.5^\circ$
Absorption correction: multi-scan <i>SADABS</i> v2009/1, Sheldrick, G.M., (2009)	$h = -19 \rightarrow 19$
$T_{\text{min}} = 0.607$, $T_{\text{max}} = 0.745$	$k = -20 \rightarrow 20$
29693 measured reflections	$l = -20 \rightarrow 20$
13193 independent reflections	

Table A.B.23 Refinement data of Cu-Piv-Phen

Refinement on F^2	27 restraints
Least-squares matrix: full	Hydrogen site location: mixed
$R[F^2 > 2\sigma(F^2)] = 0.064$	H atoms treated by a mixture of independent and constrained refinement
$wR(F^2) = 0.189$	$w = 1/[\sigma^2(F_o^2) + (0.1075P)^2 + 0.1184P]$ where $P = (F_o^2 + 2F_c^2)/3$
$S = 1.05$	$(\Delta/\sigma)_{\max} = 0.001$
13193 reflections	$\Delta\rho_{\max} = 0.56 \text{ e } \text{\AA}^{-3}$
974 parameters	$\Delta\rho_{\min} = -0.68 \text{ e } \text{\AA}^{-3}$

Table A.B.24 Geometric parameters (\AA , $^\circ$) of Cu-Piv-Phen

Cu1—N1	1.993 (5)	C33—C34	1.410 (9)
Cu1—N4	1.995 (5)	C34—C42	1.392 (8)
Cu1—O1	1.999 (4)	C34—C35	1.420 (8)
Cu1—N2	2.068 (5)	C35—C36	1.331 (10)
Cu1—N3	2.217 (5)	C36—C37	1.422 (9)
N1—C1	1.319 (8)	C37—C38	1.411 (9)
N1—C12	1.362 (7)	C37—C41	1.413 (8)
C1—C2	1.404 (9)	C38—C39	1.368 (9)
C2—C3	1.357 (10)	C39—C40	1.402 (9)
C3—C4	1.398 (9)	C40—N6	1.330 (7)
C4—C12	1.400 (8)	N6—C41	1.354 (7)
C4—C5	1.433 (9)	C41—C42	1.433 (8)
C5—C6	1.340 (10)	C43—N7	1.321 (7)
C6—C7	1.441 (9)	C43—C44	1.400 (8)
C7—C11	1.401 (8)	N7—C54	1.360 (7)
C7—C8	1.411 (9)	C44—C45	1.366 (9)
C8—C9	1.350 (10)	C45—C46	1.422 (9)
C9—C10	1.412 (9)	C46—C54	1.396 (8)
C10—N2	1.327 (8)	C46—C47	1.425 (9)
N2—C11	1.348 (7)	C47—C48	1.344 (10)
C11—C12	1.435 (8)	C48—C49	1.434 (9)
N3—C13	1.347 (8)	C49—C53	1.414 (8)
N3—C24	1.348 (7)	C49—C50	1.415 (9)
C13—C14	1.399 (9)	C50—C51	1.373 (9)
C14—C15	1.367 (9)	C51—C52	1.392 (8)
C15—C16	1.399 (9)	C52—N8	1.316 (7)

C16—C24	1.413 (8)	N8—C53	1.355 (7)
C16—C17	1.419 (8)	C53—C54	1.443 (8)
C17—C18	1.364 (9)	O3—C55	1.273 (7)
C18—C19	1.417 (8)	O4—C55	1.227 (7)
C19—C20	1.399 (8)	C55—C56	1.520 (8)
C19—C23	1.413 (8)	C56—C57	1.492 (10)
C20—C21	1.359 (8)	C56—C59	1.527 (9)
C21—C22	1.386 (8)	C56—C58	1.562 (10)
C22—N4	1.342 (8)	O61—C61	1.200 (8)
N4—C23	1.350 (7)	O62—C61	1.296 (8)
C23—C24	1.429 (8)	C61—C62	1.520 (10)
O1—C25	1.278 (7)	C62—C64	1.503 (11)
O2—C25	1.234 (7)	C62—C63	1.522 (11)
C25—C26	1.516 (8)	C62—C65	1.566 (10)
C26—C29	1.516 (10)	O71—C71	1.226 (8)
C26—C27	1.529 (9)	O72—C71	1.266 (8)
C26—C28	1.542 (9)	C71—C72	1.550 (9)
Cu2—N5	1.994 (5)	C72—C75	1.493 (10)
Cu2—N8	2.000 (5)	C72—C74	1.512 (9)
Cu2—O3	2.025 (5)	C72—C73	1.550 (10)
Cu2—N6	2.085 (5)	O81—C81	1.224 (8)
Cu2—N7	2.216 (5)	O82—C81	1.232 (8)
N5—C31	1.309 (7)	C81—C82	1.552 (9)
N5—C42	1.372 (7)	C82—C85	1.514 (9)
C31—C32	1.410 (8)	C82—C84	1.518 (9)
C32—C33	1.364 (9)	C82—C83	1.550 (9)
N1—Cu1—N4	174.27 (19)	C33—C32—C31	119.1 (6)
N1—Cu1—O1	92.10 (18)	C32—C33—C34	120.2 (6)
N4—Cu1—O1	93.57 (18)	C42—C34—C33	116.3 (5)
N1—Cu1—N2	81.53 (19)	C42—C34—C35	118.8 (6)
N4—Cu1—N2	93.75 (19)	C33—C34—C35	124.8 (6)
O1—Cu1—N2	152.75 (18)	C36—C35—C34	121.5 (6)
N1—Cu1—N3	99.04 (19)	C35—C36—C37	121.9 (6)
N4—Cu1—N3	78.76 (18)	C38—C37—C41	116.7 (6)
O1—Cu1—N3	104.28 (16)	C38—C37—C36	125.1 (6)
N2—Cu1—N3	102.88 (18)	C41—C37—C36	118.3 (6)
C1—N1—C12	117.6 (5)	C39—C38—C37	119.5 (6)
C1—N1—Cu1	128.4 (4)	C38—C39—C40	119.7 (6)
C12—N1—Cu1	114.0 (4)	N6—C40—C39	122.7 (6)
N1—C1—C2	122.9 (6)	C40—N6—C41	117.8 (5)

C3—C2—C1	119.4 (6)	C40—N6—Cu2	130.8 (4)
C2—C3—C4	119.5 (6)	C41—N6—Cu2	111.3 (4)
C3—C4—C12	117.5 (6)	N6—C41—C37	123.6 (5)
C3—C4—C5	124.9 (6)	N6—C41—C42	117.0 (5)
C12—C4—C5	117.7 (6)	C37—C41—C42	119.3 (5)
C6—C5—C4	122.5 (6)	N5—C42—C34	123.6 (5)
C5—C6—C7	120.2 (6)	N5—C42—C41	116.2 (5)
C11—C7—C8	116.6 (6)	C34—C42—C41	120.2 (5)
C11—C7—C6	119.6 (6)	N7—C43—C44	122.2 (6)
C8—C7—C6	123.8 (6)	C43—N7—C54	118.5 (5)
C9—C8—C7	119.6 (6)	C43—N7—Cu2	132.0 (4)
C8—C9—C10	120.3 (6)	C54—N7—Cu2	109.4 (3)
N2—C10—C9	121.2 (6)	C45—C44—C43	120.1 (6)
C10—N2—C11	118.7 (5)	C44—C45—C46	118.9 (6)
C10—N2—Cu1	130.1 (4)	C54—C46—C45	117.0 (6)
C11—N2—Cu1	111.1 (4)	C54—C46—C47	119.7 (6)
N2—C11—C7	123.5 (5)	C45—C46—C47	123.3 (6)
N2—C11—C12	117.6 (5)	C48—C47—C46	121.5 (6)
C7—C11—C12	118.9 (5)	C47—C48—C49	120.4 (6)
N1—C12—C4	123.0 (5)	C53—C49—C50	116.3 (6)
N1—C12—C11	115.8 (5)	C53—C49—C48	119.9 (6)
C4—C12—C11	121.1 (5)	C50—C49—C48	123.7 (6)
C13—N3—C24	118.0 (5)	C51—C50—C49	119.7 (6)
C13—N3—Cu1	132.5 (4)	C50—C51—C52	119.5 (6)
C24—N3—Cu1	109.4 (4)	N8—C52—C51	122.6 (6)
N3—C13—C14	121.9 (6)	C52—N8—C53	119.0 (5)
C15—C14—C13	119.9 (6)	C52—N8—Cu2	125.4 (4)
C14—C15—C16	119.9 (6)	C53—N8—Cu2	115.7 (4)
C15—C16—C24	116.8 (6)	N8—C53—C49	122.8 (5)
C15—C16—C17	123.5 (6)	N8—C53—C54	118.5 (5)
C24—C16—C17	119.6 (5)	C49—C53—C54	118.6 (5)
C18—C17—C16	121.1 (6)	N7—C54—C46	123.3 (5)
C17—C18—C19	120.9 (6)	N7—C54—C53	116.8 (5)
C20—C19—C23	118.1 (5)	C46—C54—C53	119.9 (5)
C20—C19—C18	122.7 (6)	C55—O3—Cu2	103.4 (4)
C23—C19—C18	119.1 (6)	O4—C55—O3	121.2 (6)
C21—C20—C19	119.2 (5)	O4—C55—C56	121.0 (6)
C20—C21—C22	119.8 (6)	O3—C55—C56	117.8 (6)
N4—C22—C21	122.9 (6)	C57—C56—C55	111.8 (6)
C22—N4—C23	117.9 (5)	C57—C56—C59	111.4 (6)
C22—N4—Cu1	125.5 (4)	C55—C56—C59	108.0 (5)

C23—N4—Cu1	116.6 (4)	C57—C56—C58	110.3 (7)
N4—C23—C19	122.1 (5)	C55—C56—C58	109.4 (5)
N4—C23—C24	117.6 (5)	C59—C56—C58	105.7 (6)
C19—C23—C24	120.2 (5)	O61—C61—O62	123.7 (6)
N3—C24—C16	123.5 (5)	O61—C61—C62	124.0 (7)
N3—C24—C23	117.5 (5)	O62—C61—C62	112.2 (6)
C16—C24—C23	118.9 (5)	C64—C62—C61	109.8 (6)
C25—O1—Cu1	103.8 (3)	C64—C62—C63	111.3 (8)
O2—C25—O1	122.1 (6)	C61—C62—C63	110.4 (6)
O2—C25—C26	120.4 (6)	C64—C62—C65	108.8 (7)
O1—C25—C26	117.5 (5)	C61—C62—C65	107.4 (7)
C29—C26—C25	110.2 (5)	C63—C62—C65	109.0 (6)
C29—C26—C27	110.0 (6)	O71—C71—O72	122.6 (6)
C25—C26—C27	107.0 (6)	O71—C71—C72	119.6 (6)
C29—C26—C28	109.4 (6)	O72—C71—C72	117.8 (6)
C25—C26—C28	111.1 (5)	C75—C72—C74	112.3 (6)
C27—C26—C28	109.2 (6)	C75—C72—C73	109.7 (6)
N5—Cu2—N8	174.88 (18)	C74—C72—C73	106.3 (6)
N5—Cu2—O3	92.17 (18)	C75—C72—C71	108.5 (6)
N8—Cu2—O3	92.93 (17)	C74—C72—C71	110.6 (5)
N5—Cu2—N6	81.13 (19)	C73—C72—C71	109.3 (6)
N8—Cu2—N6	94.08 (18)	O81—C81—O82	122.3 (6)
O3—Cu2—N6	162.73 (17)	O81—C81—C82	117.0 (6)
N5—Cu2—N7	99.54 (18)	O82—C81—C82	120.6 (6)
N8—Cu2—N7	79.61 (17)	C85—C82—C84	109.8 (6)
O3—Cu2—N7	94.91 (17)	C85—C82—C83	110.2 (5)
N6—Cu2—N7	101.87 (17)	C84—C82—C83	109.5 (5)
C31—N5—C42	118.2 (5)	C85—C82—C81	107.2 (5)
C31—N5—Cu2	127.8 (4)	C84—C82—C81	109.7 (5)
C42—N5—Cu2	114.0 (4)	C83—C82—C81	110.6 (5)
N5—C31—C32	122.6 (6)		

Table A.B.25 Hydrogen-bond geometry (Å, °) of Cu-Piv-Phen

<i>D</i> —H··· <i>A</i>	<i>D</i> —H	H··· <i>A</i>	<i>D</i> ··· <i>A</i>	<i>D</i> —H··· <i>A</i>
O62—H62···O5 <i>W</i>	0.84	1.73	2.553 (7)	164
O1 <i>W</i> —H1 <i>WA</i> ···O71 ⁱ	0.84 (2)	1.94 (2)	2.773 (7)	176 (8)
O1 <i>W</i> —H1 <i>WB</i> ···O71	0.83 (2)	2.14 (3)	2.964 (7)	170 (7)
O1 <i>W</i> —H1 <i>WB</i> ···O72	0.83 (2)	2.61 (5)	3.268 (7)	137 (7)
O2 <i>W</i> —H2 <i>WB</i> ···O9 <i>W</i>	0.82 (2)	2.04 (2)	2.862 (7)	173 (7)
O2 <i>W</i> —H2 <i>WA</i> ···O72 ⁱ	0.84 (2)	2.13 (4)	2.927 (7)	158 (8)

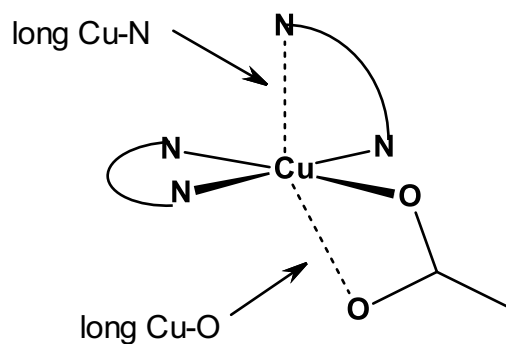
O3 <i>W</i> —H3 <i>WA</i> ···O81	0.85 (2)	2.40 (2)	3.238 (8)	174 (7)
O3 <i>W</i> —H3 <i>WA</i> ···O82	0.85 (2)	2.57 (7)	3.166 (9)	129 (7)
O3 <i>W</i> —H3 <i>WB</i> ···O81 ⁱⁱ	0.84 (2)	2.34 (9)	2.767 (7)	112 (7)
O4 <i>W</i> —H4 <i>WA</i> ···O7 <i>W</i>	0.85 (2)	2.27 (5)	2.920 (7)	134 (6)
O4 <i>W</i> —H4 <i>WB</i> ···O82	0.86 (2)	2.05 (4)	2.857 (7)	155 (7)
O5 <i>W</i> —H5 <i>WA</i> ···O82	0.82 (2)	1.95 (4)	2.682 (8)	149 (8)
O5 <i>W</i> —H5 <i>WB</i> ···O6 <i>W</i>	0.82 (2)	2.14 (6)	2.775 (8)	134 (7)
O6 <i>W</i> —H6 <i>WA</i> ···O1 <i>W</i>	0.85 (2)	1.86 (2)	2.708 (7)	176 (7)
O6 <i>W</i> —H6 <i>WB</i> ···O5 <i>W</i>	0.85 (2)	2.42 (9)	2.775 (8)	106 (7)
O7 <i>W</i> —H7 <i>WA</i> ···O72	0.85 (2)	2.02 (3)	2.856 (8)	167 (9)
O7 <i>W</i> —H7 <i>WB</i> ···O81 ⁱⁱ	0.84 (2)	1.95 (4)	2.742 (7)	157 (8)
O8 <i>W</i> —H8 <i>WA</i> ···O3 <i>W</i> ⁱⁱ	0.83 (2)	2.21 (4)	3.015 (8)	163 (8)
O8 <i>W</i> —H8 <i>WB</i> ···O4 <i>W</i>	0.85 (2)	1.99 (4)	2.809 (8)	161 (10)
O9 <i>W</i> —H9 <i>WA</i> ···O71	0.84 (2)	1.97 (3)	2.769 (6)	160 (7)
O9 <i>W</i> —H9 <i>WB</i> ···O6 <i>W</i> ⁱ	0.85 (2)	2.07 (4)	2.864 (7)	155 (8)

Symmetry codes: (i) $-x+1, -y, -z+2$; (ii) $-x+2, -y, -z+2$.

Table A.B.26 Comparison Geometric Data

Complex	Angle between N-Cu-N planes (°)	Short Cu-O (Å)	Long Cu-O (Å)	Long Cu-N(Å)	Shorter Cu-N(Å)
Cu-For-Phen [Cu(phen)₂(HCOO)](NO₃)·6H₂O	62.03(7)	2.027(2)	2.731(2)	2.181(3)	1.982(3) 1.988(3) 2.057(3)
Cu-Ace-Phen [Cu(phen)₂(OAc)](NO₃)·2H₂O	75.62(4)	2.008(2)* 2.019(9)*	2.589(2)* 2.599(10)*	2.1815(14)	1.9981(14) 2.0156(14) 2.0559(14)
Cu-Pro-Phen [Cu(phen)₂(pro)]·½(CO₃)·2H₂O	75.0(9)* 74.5(9)*	1.955(8)	2.513(9)	2.171(14)*	1.998(5) 2.035(14)* 2.093(6)
Cu-Iso-Phen [Cu(phen)₂(isobut)]₂·2(NO₃)·4H₂O	88.5(1) 87.9(1)	1.960(2) 1.978(2)	2.751(2) 2.725(2)	2.203(3) 2.182(3)	2.004(3) 1.985(3) 2.008(3) 1.997(3) 2.0062(3) 2.083(2)
Cu-Piv-Phen [Cu(phen)₂(piv)]₂(piv)₂·(Hpiv)·9H₂O	77.4(2) 78.5(2)	1.999(4) 2.025(5)	2.576(5) 2.551(5)	2.217(5) 2.216(5)	1.993(5) 1.994(5) 1.995(5) 2.000(5) 2.068(5) 2.085(5)

* Affected by disorder



A.B.3 Electrospray ionisation mass spectra (ESI-MS)

2011_1115#52-71 RT: 0.77-1.03 AV: 20 NL: 2.63E8
T: FTMS (1,1) + p NSI Full ms [100.00-2000.00]

Cu-For-Phen

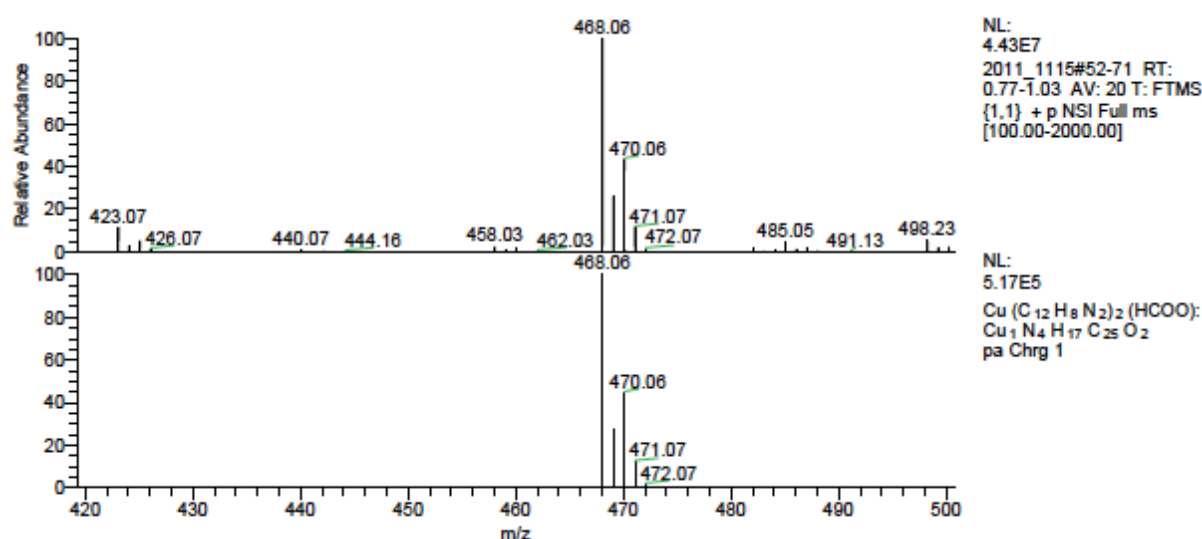
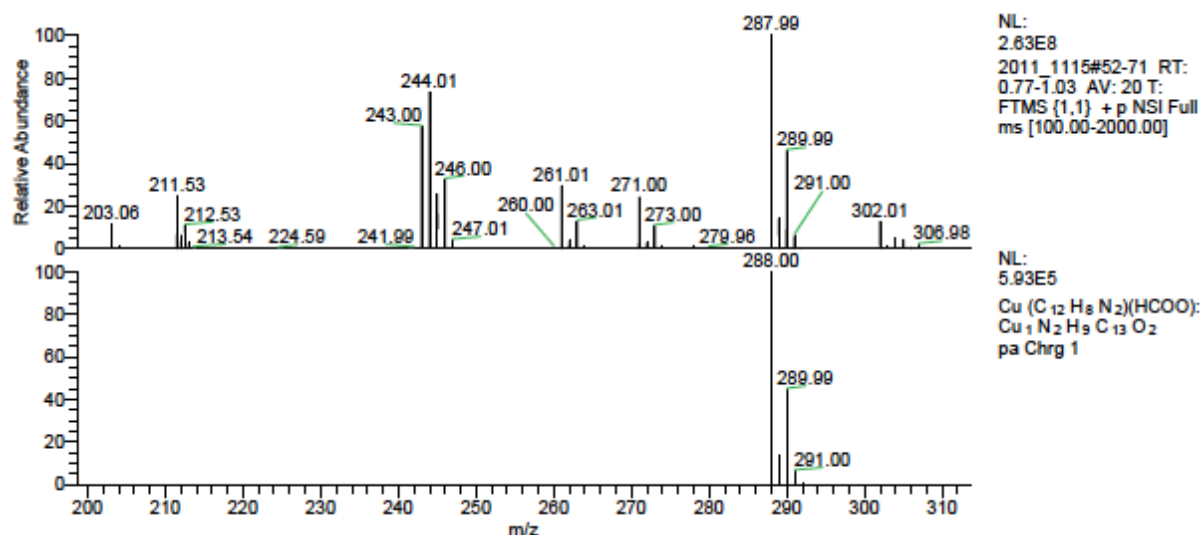
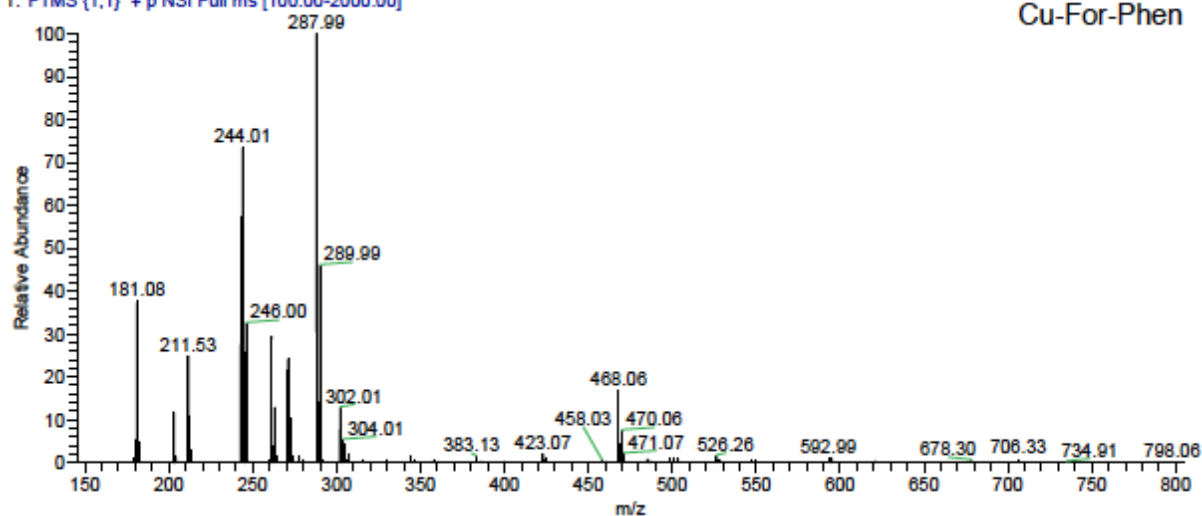


Figure A.B.24 Mass spec. of Cu-For-Phen

2011_1114-reun#2-73 RT: 0.03-0.98 AV: 72 NL: 6.64E8
T: FTMS (1,1) + p NSI Full ms [100.00-2000.00]

Cu-Ace-Phen

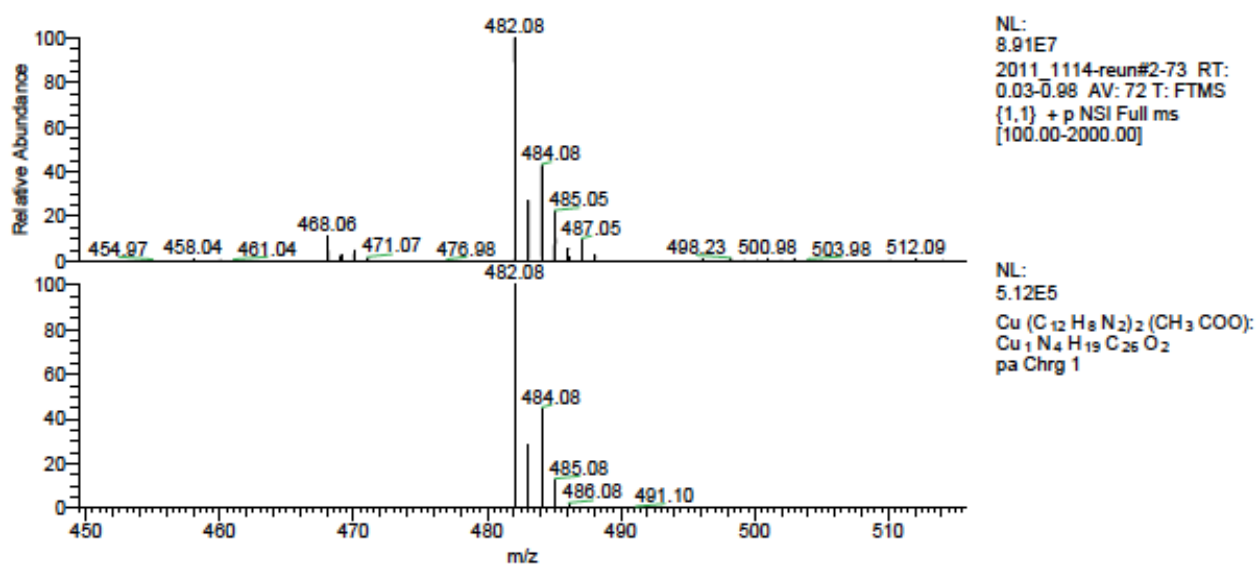
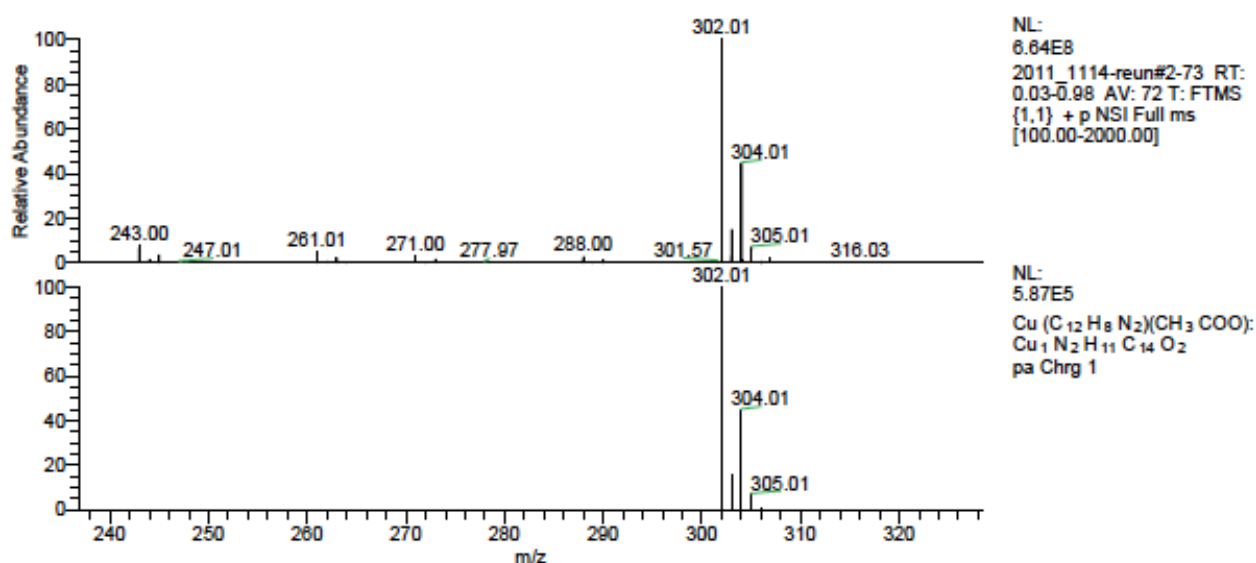
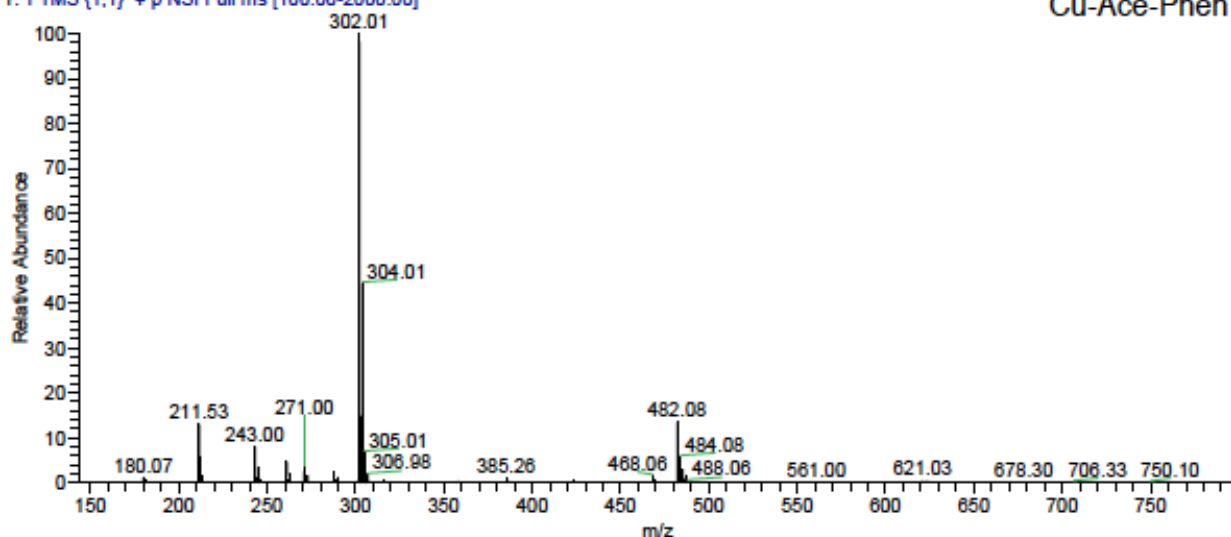


Figure A.B.25 Mass spec. of Cu-Ace-Phen

2011_1116#2-76 RT: 0.02-1.01 AV: 75 NL: 6.34E8
T: FTMS (1,1) + p NSI Full ms [100.00-2000.00]

Cu-Pro-Phen

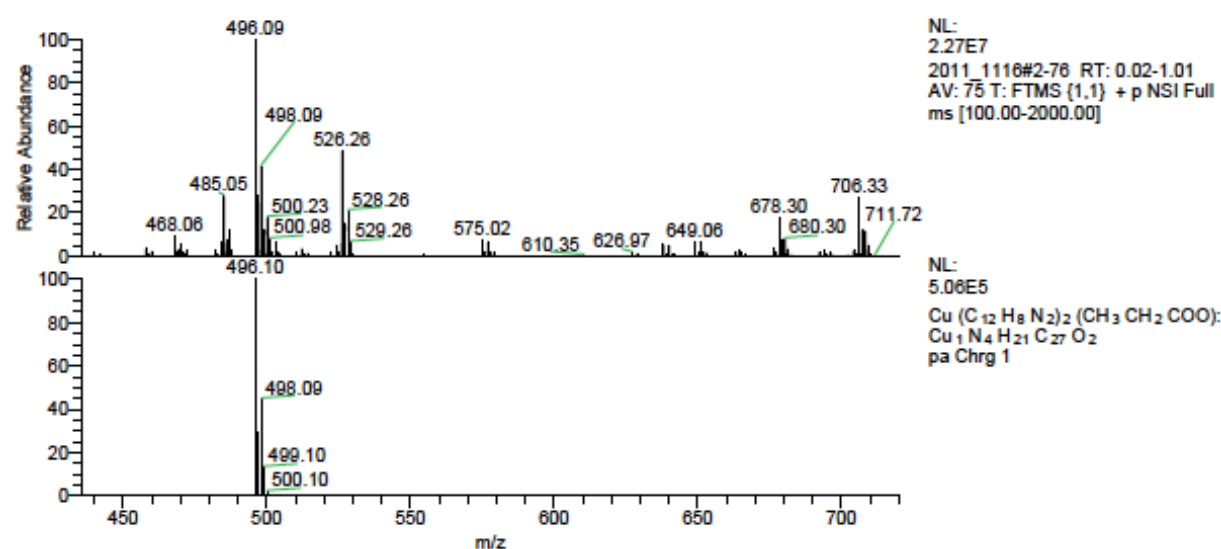
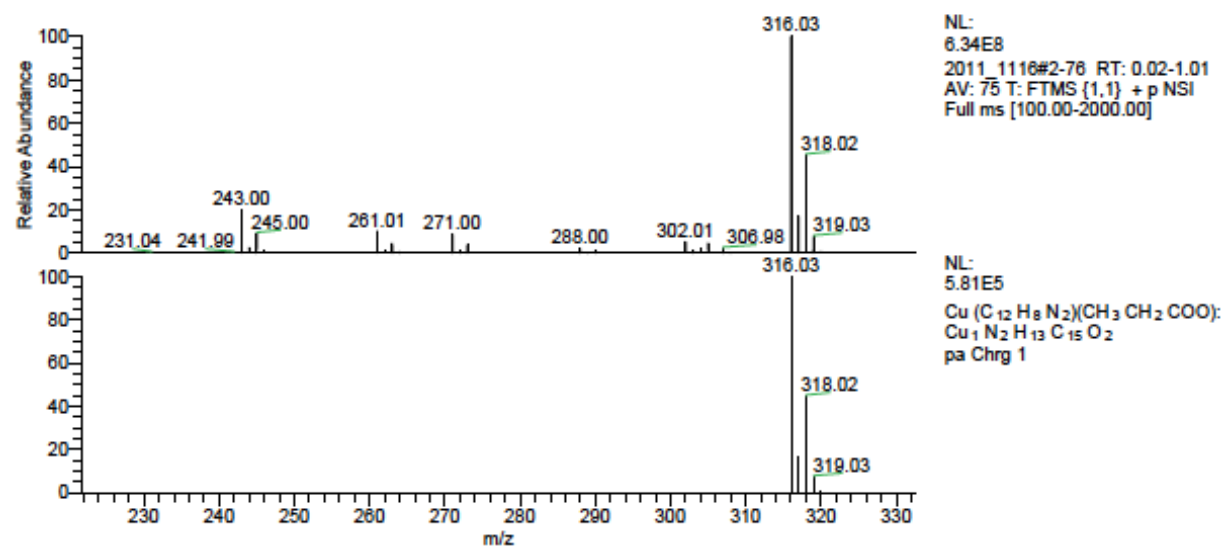
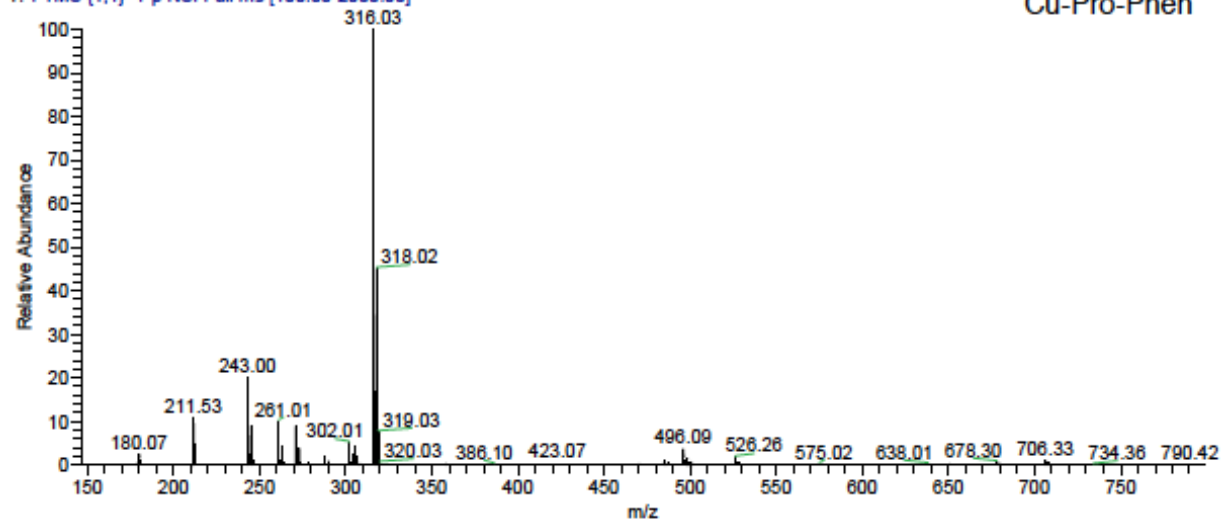


Figure A.B.26 Mass spec. of Cu-Pro-Phen

2011_1113#3-75 RT: 0.03-1.00 AV: 73 NL: 6.38E8
T: FTMS (1,1) + p NSI Full ms [100.00-2000.00]

Cu-Iso-Phen

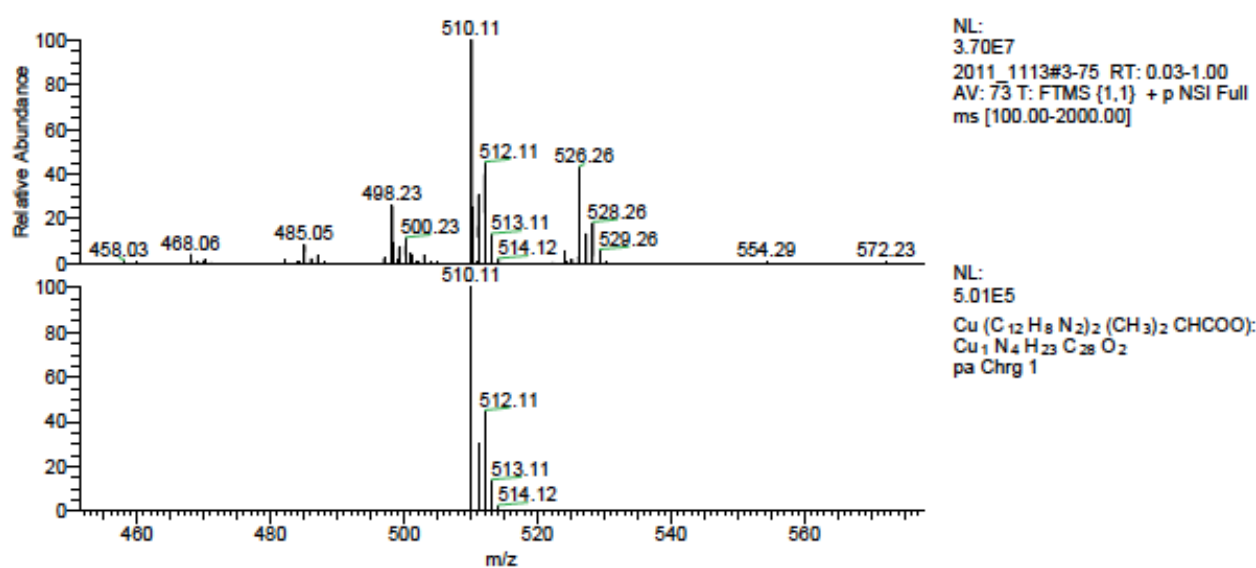
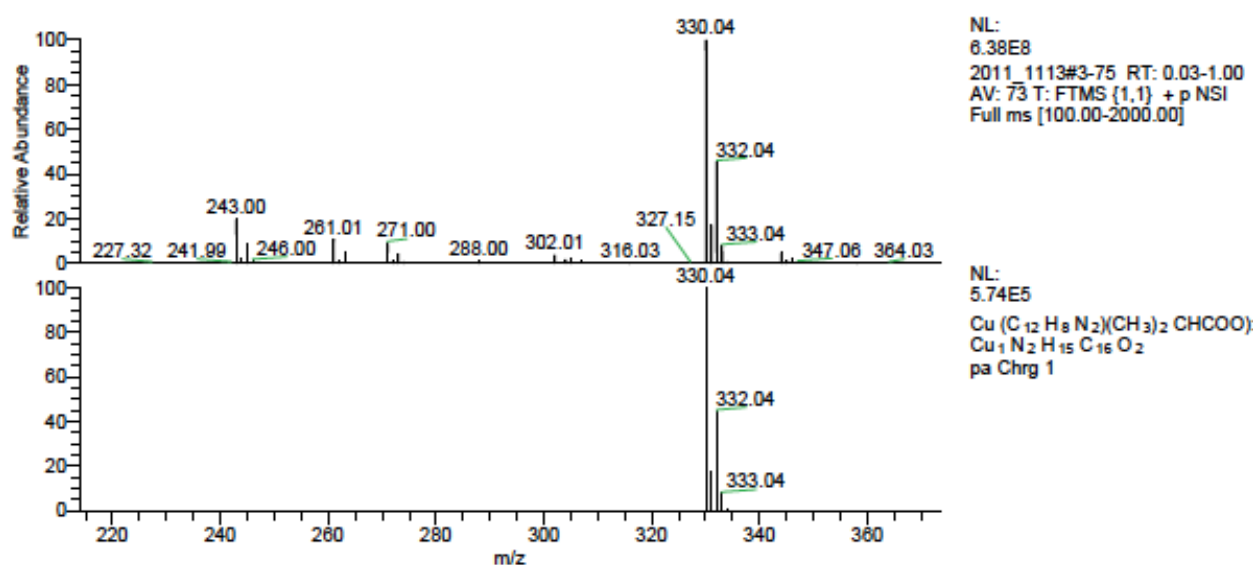
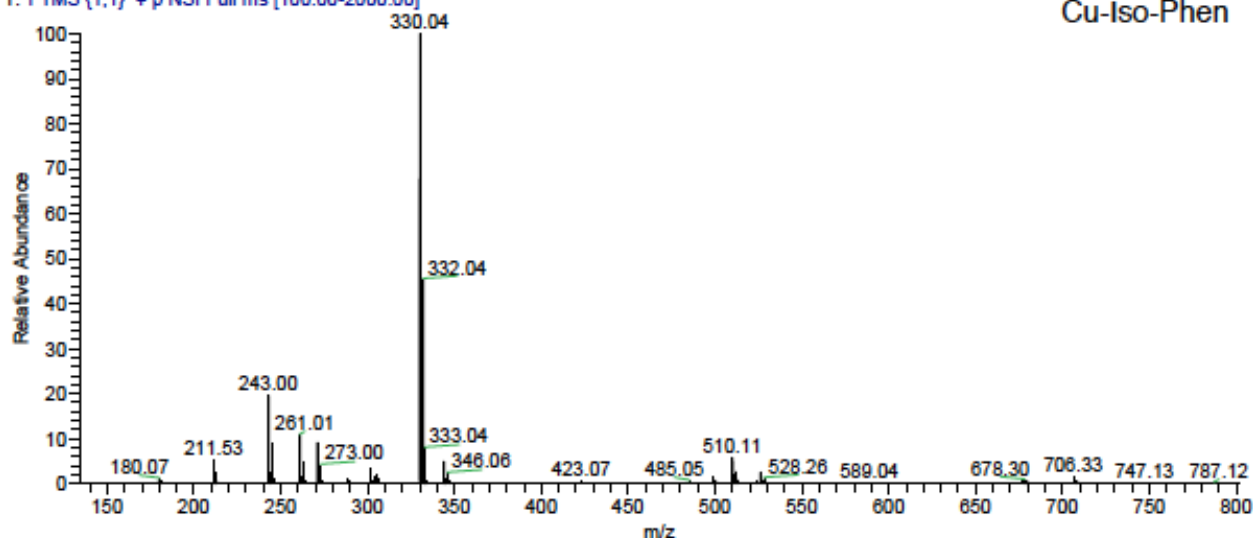


Figure A.B.27 Mass spec. of Cu-Iso-Phen

2013_0229#4-75 RT: 0.04-1.00 AV: 72 NL: 1.70E8
T: FTMS (1,1) + p NSI Full ms [100.00-2000.00]

Cu-Piv-Phen

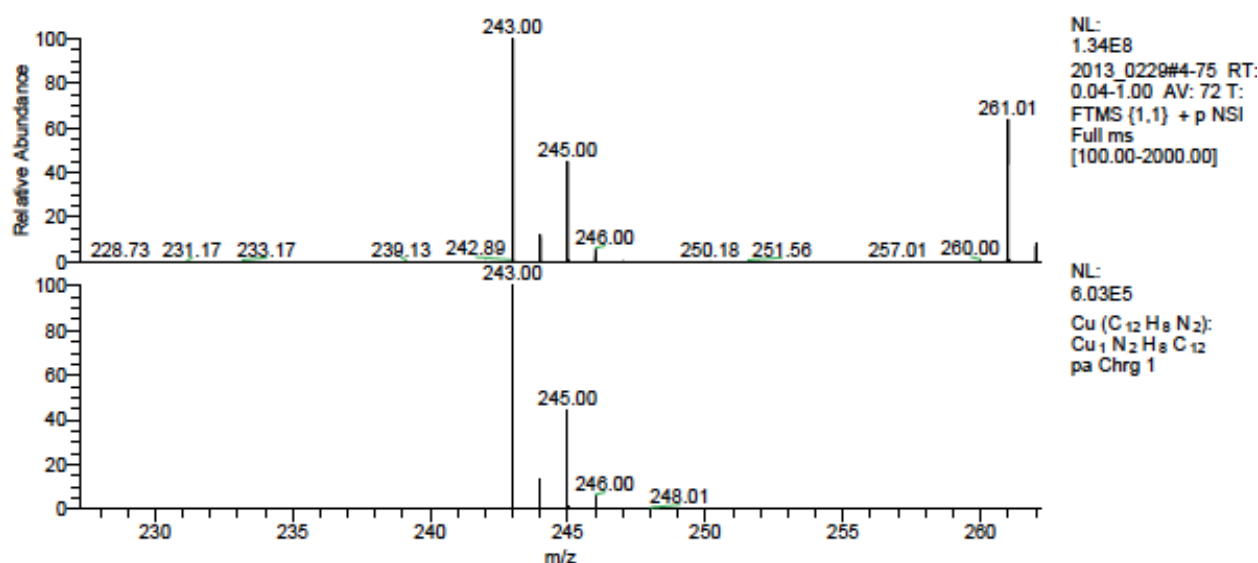
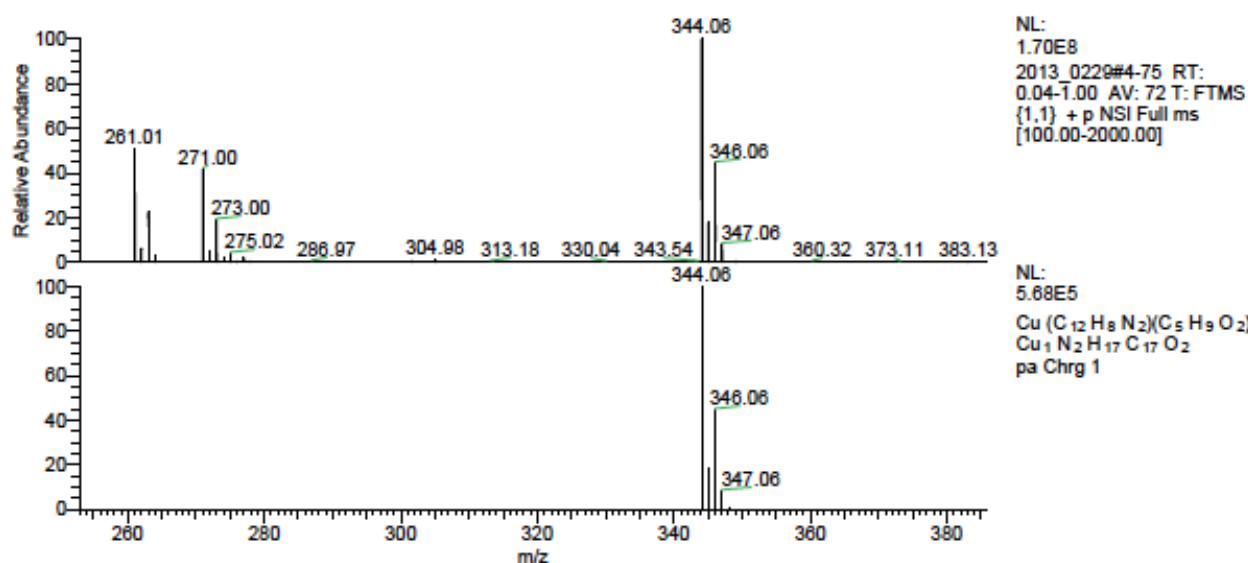
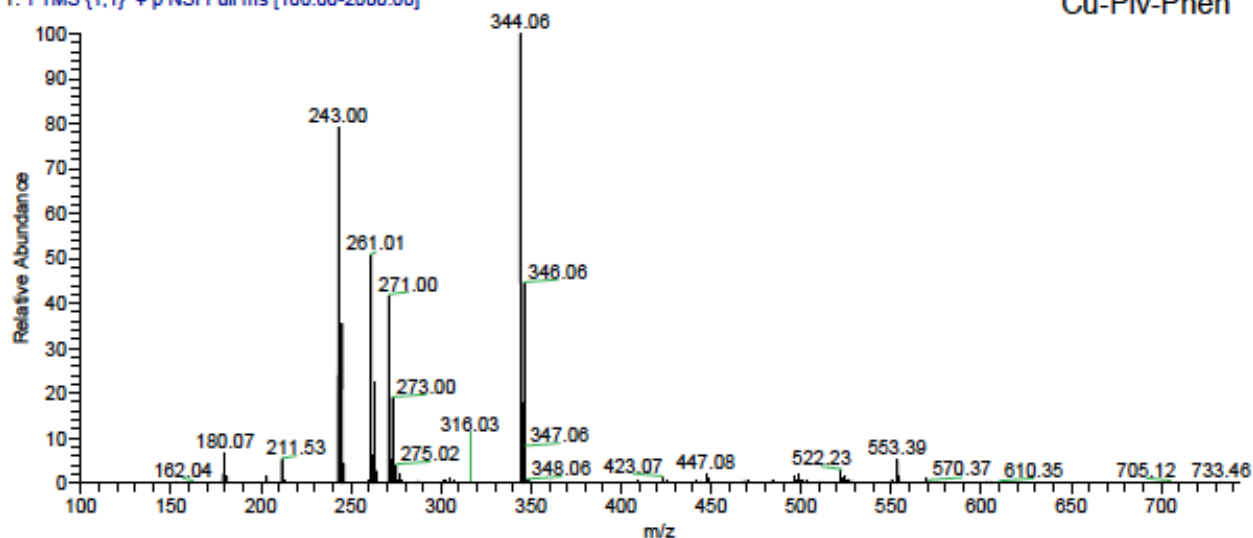


Figure A.B.28 Mass spec. of Cu-Piv-Phen

Appendix C

A.C.1 Electrogram data generated by the Bioanalyzer 2100

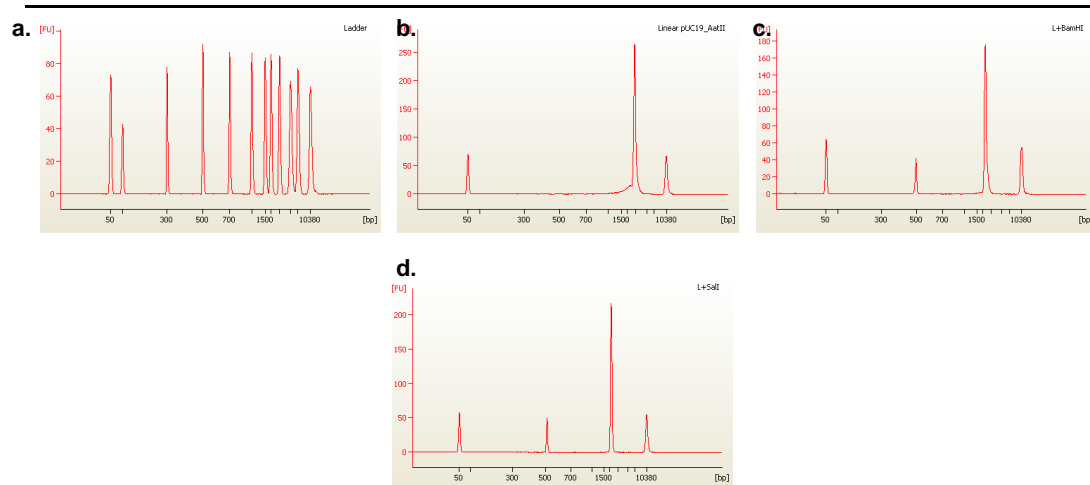


Figure A.C.1 Control bioanalyzer electrograms of (a.) a standard DNA ladder, (b.) linearised pUC19 plasmid DNA, and linearised pUC19 after treatment with type II restriction endonucleases: (c.) *Bam*HI and (d.) *Sal*I.

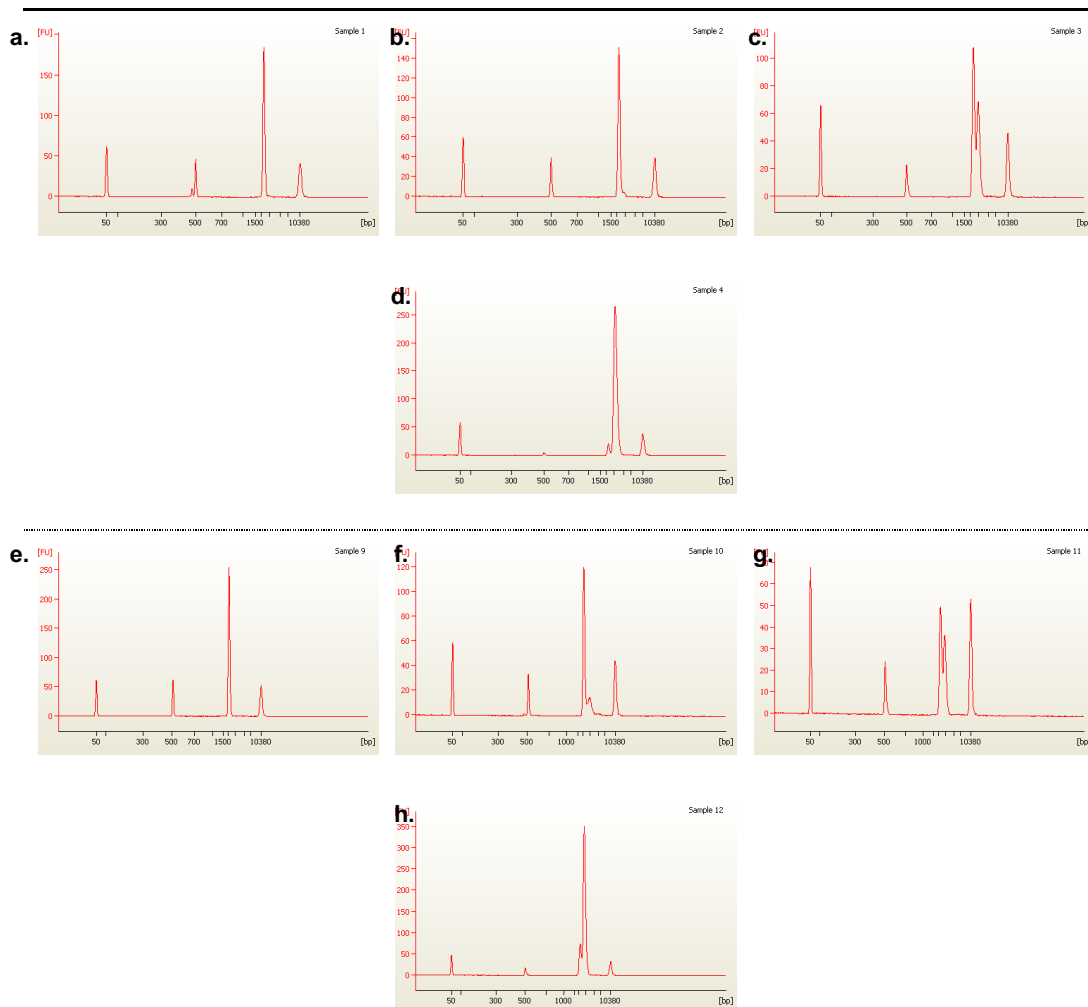


Figure A.C.2 Bioanalyzer electrograms of linearised pUC19 pre-incubated for 24 h with AH78 followed by exposure (4 h) to the type II restriction endonuclease *Bam*HI or *Sal*I. (a.) 1.0 μ M AH78 + *Bam*HI, (b.) 2.5 μ M AH78 + *Bam*HI, (c.) 5.0 μ M AH78 + *Bam*HI, (d.) 10.0 μ M AH78 + *Bam*HI, (e.) 1.0 μ M AH78 + *Sal*I, (f.) 2.5 μ M AH78 + *Sal*I, (g.) 5.0 μ M AH78 + *Sal*I, and (h.) 10.0 μ M AH78 + *Sal*I.

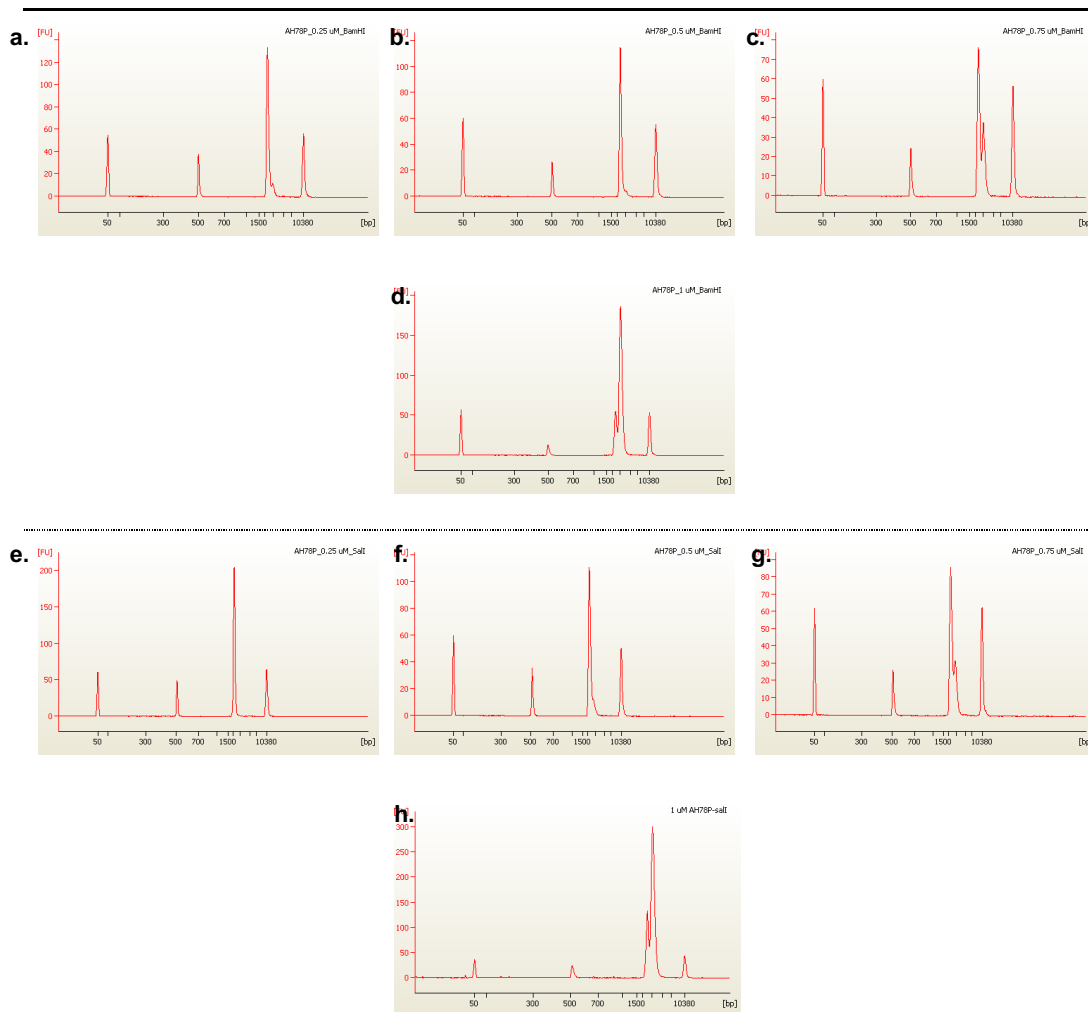


Figure A.C.3 Bioanalyzer electrograms of linearised pUC19 pre-incubated for 24 h with AH78P followed by exposure (4 h) to the type II restriction endonuclease *Bam*HI or *Sal*I. (a.) 0.25 μ M AH78 + *Bam*HI, (b.) 0.50 μ M AH78 + *Bam*HI, (c.) 0.75 μ M AH78 + *Bam*HI, (d.) 1.00 μ M AH78 + *Bam*HI, (e.) 0.25 μ M AH78 + *Sal*I, (f.) 0.50 μ M AH78 + *Sal*I, (g.) 0.75 μ M AH78 + *Sal*I, and (h.) 1.00 μ M AH78 + *Sal*I.

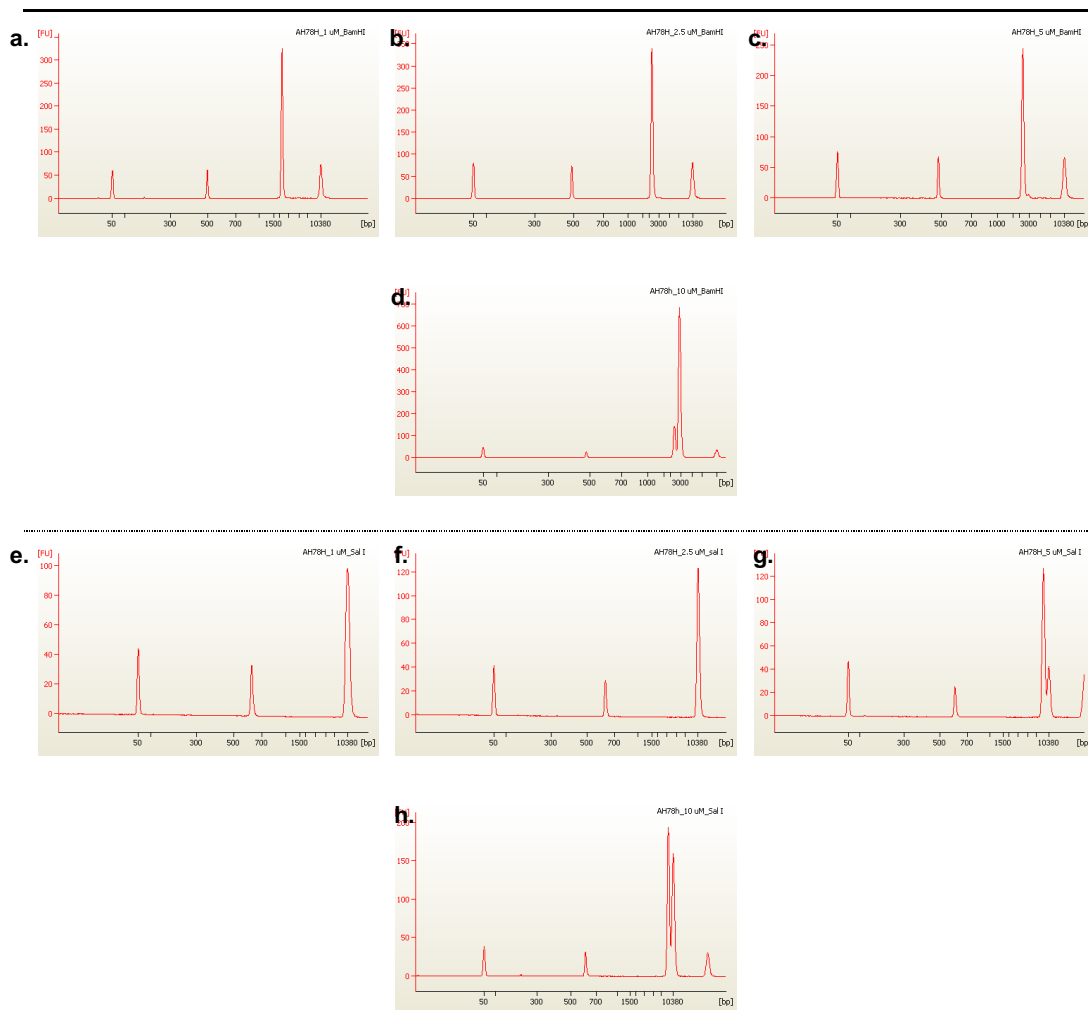


Figure A.C.4 Bioanalyzer electrograms of linearised pUC19 pre-incubated for 24 h with AH78H followed by exposure (4 h) to the type II restriction endonuclease *Bam*HI or *Sal*I. (a.) 1.0 μ M AH78 + *Bam*HI, (b.) 2.5 μ M AH78 + *Bam*HI, (c.) 5.0 μ M AH78 + *Bam*HI, (d.) 10.0 μ M AH78 + *Bam*HI, (e.) 1.0 μ M AH78 + *Sal*I, (f.) 2.5 μ M AH78 + *Sal*I, (g.) 5.0 μ M AH78 + *Sal*I, and (h.) 10.0 μ M AH78 + *Sal*I.

A.C.2 ctDNA thermal melting analysis

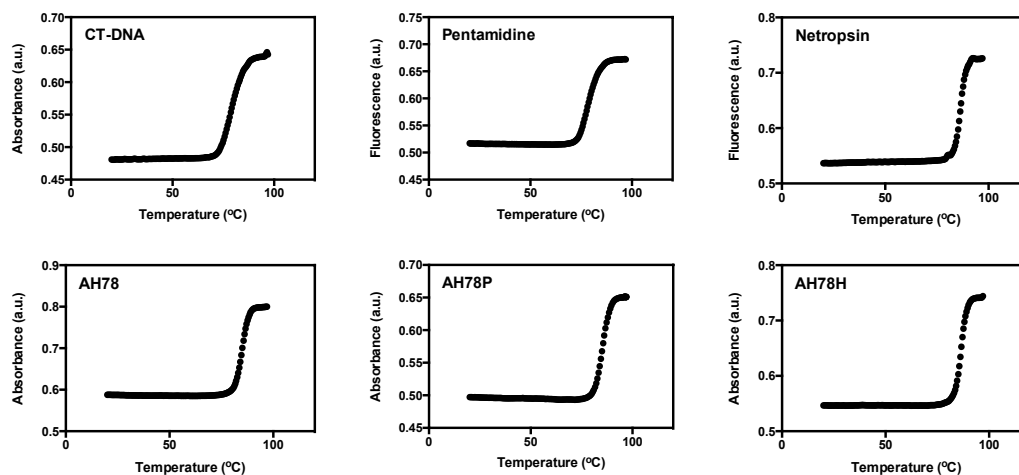


Figure A.C.5 Typical thermal melting profiles of untreated CT-DNA (75 μM in DNAP) and drug treated (+3.75 μM of tested complex or organic drug) in 50 mM potassium phosphate buffer with 2 mM NaCl, [Drug]/[DNA] drug loading was at $r = 0.05$.

A.C.3 Circular dichroism experiments

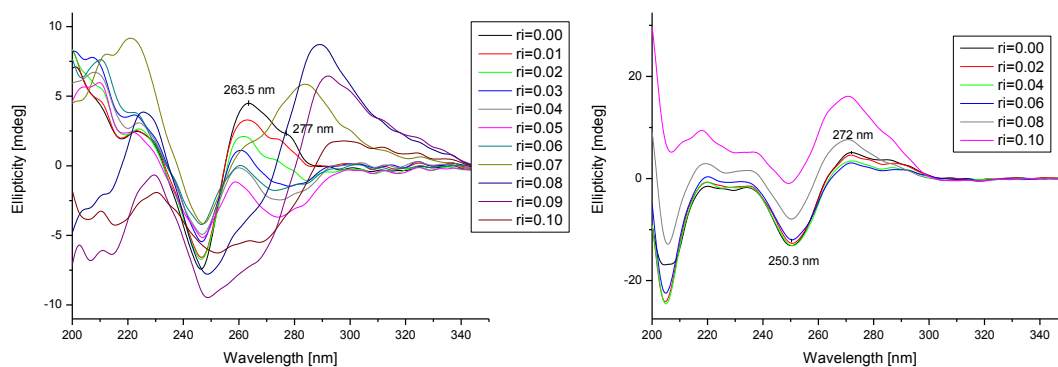


Figure A.C.6 CD spectra of poly(dA-dT)₂ (left) and poly(dG-dC)₂ (right) treated with various amounts of TpNC

A.C.4 ITC of polynuclear DNA titrated with TriplatinNC

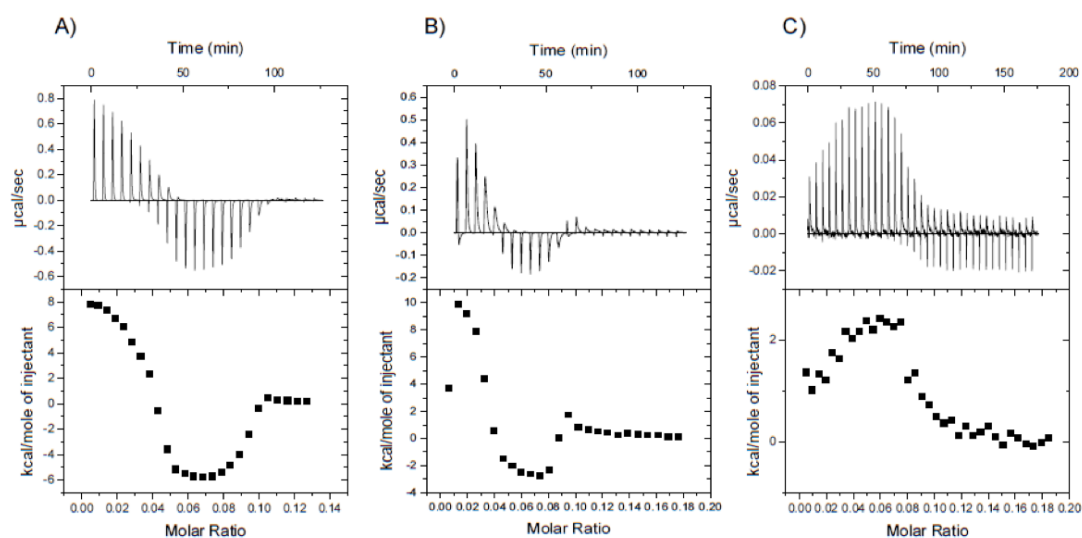


Figure A.C.7 Isotherms of the reaction of TriplatinNC poly(dA-dT)₂ (A), poly(dA)-poly(dT) (B), and poly(dG-dC)₂ (C); the top panels show the heat of each injection, bottom panels represent the integrated heat signals versus molar ratio.

A.C.5 NMR Analysis of TriplatinNC Modified DNA Oligomers

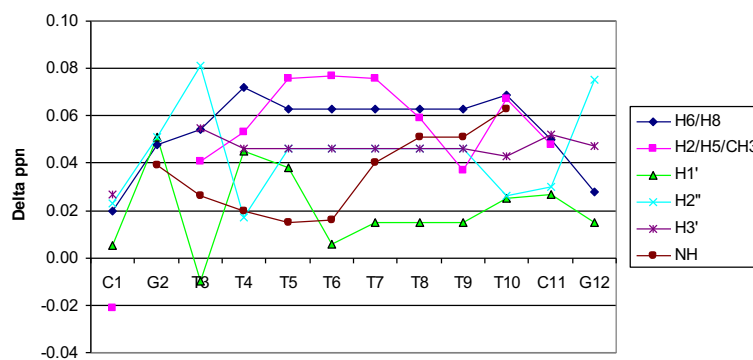


Figure A.C.8 A: Change in chemical shifts for nucleotides of the T-rich strand ($\delta_{(\text{oligomer}+\text{AH78})} - \delta_{\text{oligomer}}$)

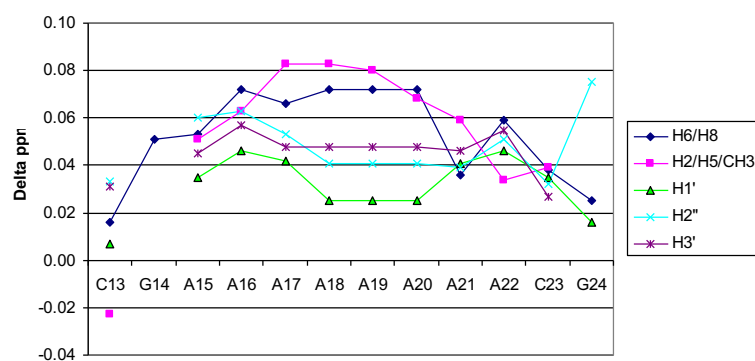


Figure A.C.8 B: Change in chemical shifts for nucleotides of the A-rich strand ($\delta_{(\text{oligomer}+\text{AH78})} - \delta_{\text{oligomer}}$)

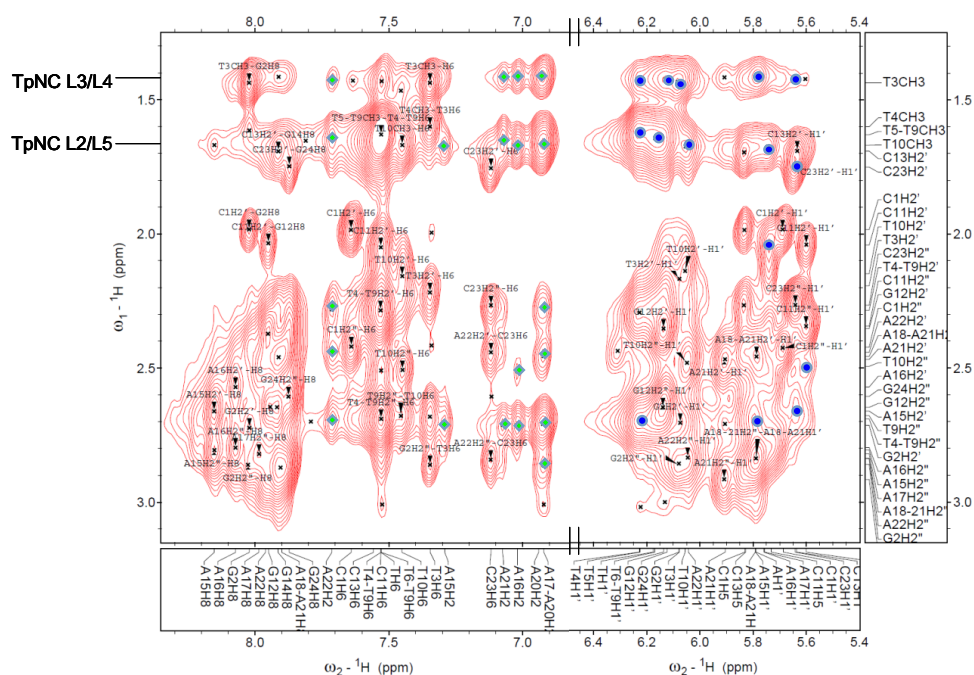
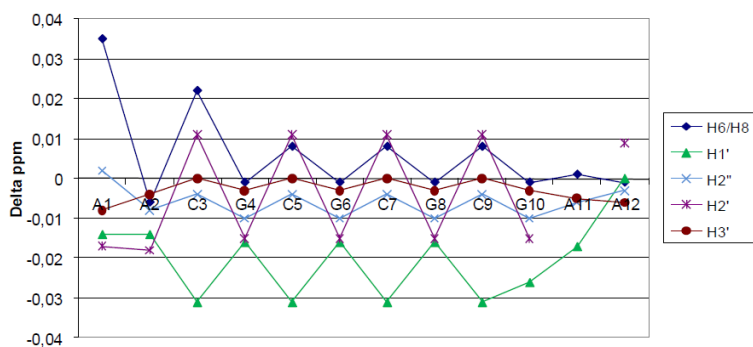


Figure A.C.9 The interaction of AT-rich dodecamer and TriplatinNC, NOE contacts of TriplatinNC (TpNC) with A-H2 (green) and H1' (blue) protons



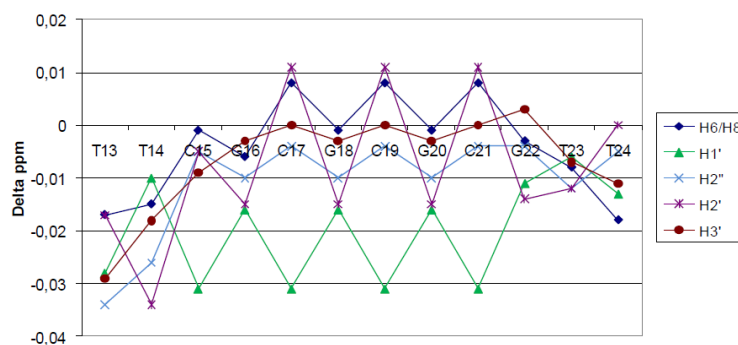


Figure A.C.10 Change in chemical shifts for GC-rich nucleotides ($\delta(\text{oligomer}+\text{AH78}) - \delta(\text{oligomer})$), Top: 1-12 strand 1 and Bottom: 13-24 strand 2.

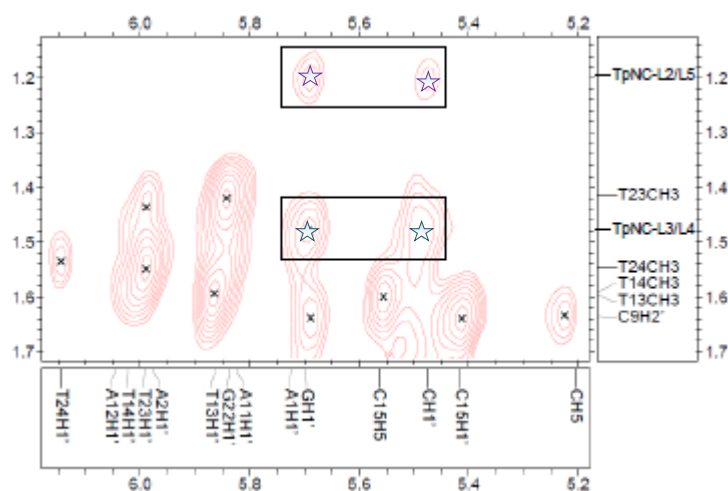


Figure A.C.11 The interaction of GC-rich dodecamer and TriplatinNC, NOE contacts of H1' of the GC with TriplatinNC-L2/L5 (purple ☆) and TriplatinNC-L3/L4 (blue ☆) protons.

A.C.6 Binding affinity of ethidium bromide to ctDNA and tRNA

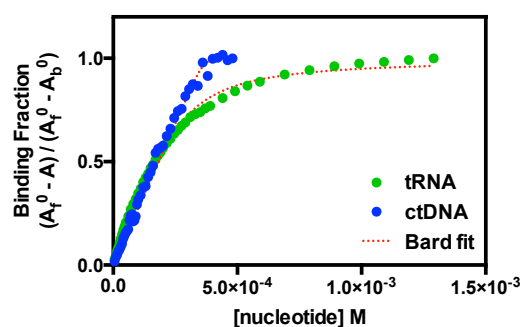


Figure A.C.12 Fraction of ethidium bromide (EtBr, 100 μM) bound to either tRNA or ctDNA determined by direct spectrophotometry at 480 nm (EtBr) and fitted with nonlinear regression using the Bard equation. A_f^0 = abs. of free EtBr, A = abs. of EtBr after each aliquot of titrated nucleotide, A_b^0 = abs. of fully bound EtBr.

$$\frac{(A_f^0 - A)}{(A_f^0 - A_b^0)} = \frac{b - (b^2 - \frac{2K_b^2 C_t [\text{DNA}]}{n})^{\frac{1}{2}}}{2K_b C_t} \quad [1]$$

$$b = 1 + K_b C_t + \frac{K_b [\text{DNA}]}{2n} \quad [2]$$

Table A.C.1 Binding affinity of ethidium bromide (100 μM) to ctDNA ($\epsilon = 12,824$) and tRNA ($\epsilon = 9,250$) determined by direct spectrophotometry at 480 nm using the Bard equation [1] and [2].

Nucleotide	$K_b \text{ M(bp)}^{-1}$	n	r^2
ctDNA	8.80×10^6	1.82	>0.99
tRNA	6.78×10^4	1.35	>0.99

K_b = intrinsic binding constant, n = number of binding sites, r^2 = goodness of fit (Bard equation)

A.C.8 tRNA thermal melting analysis

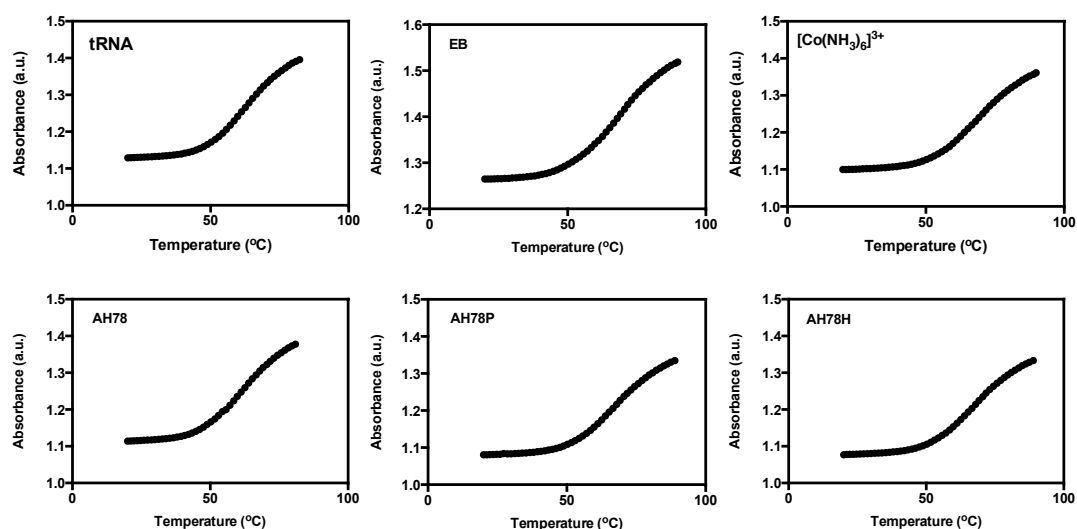


Figure A.C.13 Typical thermal melting profiles of untreated tRNA ($\sim 130 \mu\text{M}$ in tRNAp) and drug treated ($+13 \mu\text{M}$ of tested complex or organic drug) in 50 mM potassium phosphate buffer with 1 M NaCl; [Drug]/[DNA] drug loading was at $r = 0.10$.

Appendix D

“Metal-Based Antimicrobial Protease Inhibitors”

This work was published in *Current Medicinal Chemistry*, 2013, **20**, 25, pp3134-3151.

Kellett A., Prisecaru A., Slator C., Molphy Z., McCann M.

My contribution to this review paper is: manuscript author, literature review of section “Parasitic Protease Inhibitors”

A.D.1 Abstract

Limitations associated with the production cost, metabolic instability, side-effects, resistance and poor pharmacokinetics of organic protease inhibitors (PIs), which form an essential component of the front line HAART treatment for HIV, have fuelled efforts into finding novel, transition metal-based alternatives. Some of the attractive features of metal-based therapeutics include synthetic simplicity, solubility control, redox capability, expansion of coordination number and topography matching of the complex to the protein's active site. Building asymmetry into the complex, which may offer better discrimination between host and rogue cell, can readily be achieved through coordination of chiral ligands to the metal centre. Although the scope of this review has been limited to metal-based agents that have been reported to bind/inhibit HIV-1 and parasitic proteases, some desirables, such as high activity, low dosage, minimal toxicity, cross-inhibition, unique binding modes and selectivity, have already been delivered. The variability of the d-block metals, coupled with the availability of designer organic ligands, augers well for the future development of clinical metallo-drugs for deployment against protease-associated, fatal diseases.

A.D.2 Introduction

In this review we describe the current state-of-art in metallo-drug design for antimicrobial protease inhibition (PI). Rather than attempting an exhaustive list of protease-active metal-based agents, we discuss a selection of compounds active against the viral protease, HIV-1P, along with tropical parasitic proteases of malaria, trypanosomiasis and leishmaniasis. While attempts have been made to include every class of these biologically active compounds, it is possible that existing metallo-antimicrobial agents, with yet unidentified mechanism, target protease (PR) enzymes. Thus, our prerequisite for including each complex was that an inhibitory effect against either microbial or viral PR was registered. In many instances, an associated microbial inhibitory study accompanied PI, from which it was possible to elucidate structure-activity-relationships.

The interaction of metallo-drugs with protein targets has recently gained significant traction in the literature. In-depth reviews entitled "Targeting proteins with metal complexes",[1] "Metal-based antitumour drugs in the post-

genomic era: what comes next?”,[2] “Gold compounds as therapeutic agents for human diseases”[3] and “Metal compounds as enzyme inhibitors”[4] describe important protein molecular targets outside that of genomic DNA, which for decades captured almost total focus arising from the clinical advancement of Pt(II) chemotherapeutics. In this context, the development of metallo-drugs associated with abrogation of PR, is now of significant appeal in the treatment of infectious viral and parasitic human disease. Significantly, numerous shortcomings with efficacy, production cost, emerging resistance, poor pharmacokinetics and a limited number of viable lead compounds are now complicating many of the current treatment regimes used against HIV, malaria, trypanosomiasis and leishmaniasis. In each of these maladies, some of which are among the world's leading infectious killers and impose a devastating health burden throughout developing countries, PR is known to play an integral role in the disease pathology.[5-7] For example, HIV-1 protease contains an aspartic-active residue that is essential in the replication lifecycle of new, infectious viral particles[8]; Falcipain-2, a cysteine protease, plays a vital role in the malarial life cycle by degrading hemoglobin at the early trophozoite stage,[9] and; the cysteine protease, cruzain, is known to play a crucial biological role in cell remodeling during transformation of the insect epimastigote stage of *Trypanosoma cruzi* to the infectious metacyclic stage.[10] Additionally, *Escherichia coli* protease, FtsH, has interesting characteristics as it is the only membrane-bound ATP-dependent protease, and it is the only PR that is essential for *E. coli* cell growth and viability.[11] A review of serine, cysteine, aspartyl and metalloproteases mechanisms has recently been published by Fass and Bibi *et al.*[12]

The field of bioinorganic chemistry is actively being explored in order to discover therapeutically diverse, nonpeptidic, PIs.[13] Significantly, a variety of molecular symmetries can be produced and controlled through the use of selected metal ions which give rise to square-planar, tetrahedral and polyhedral structures. Additionally, coordinated ligands can be held in specific orientations to match the active binding site of the protease enzyme. Other properties of these compounds, such as ionic radius, redox potential, acidity and solubility, can be controlled through the use of selected metal ions and counterions, giving rise to potentially bioavailable, minimally toxic and site-specific PIs.

A.D.3 HIV-1 Protease Inhibitors

A.D.3.1 Introduction

The human immunodeficiency virus (HIV) is a retrovirus belonging to the family, *retroviridae*. HIV is the precursor to the debilitating, progressive and eventually fatal disease, acquired immunodeficiency syndrome (AIDS).[8] HIV-1 protease is an aspartic protease that is essential in the replication lifecycle of new, infectious viral particles. HIV-1 protease is a homodimer protein,[6] containing two identical subunits composed of 99 amino acids with the active site lying between these subunits and containing a highly conserved sequence (Asp25-Thr26-Gly27) (Figure A.D.1).[8, 14] These conserved triads contain the catalytically active aspartate residues,[8] responsible for peptide cleavage of polyproteins at specific sites, mediated by water molecules.[14] The aspartates are located in a hydrophobic pocket, enclosed by six amino acids; Pro-81, Val-82 and Ile-84 at the base of the active site, with Ile-47, Gly-48 and Ile-54 located on two flexible molecular flaps that encase the polyprotein substrate when bound to the active site.[6] PR plays a crucial role in the viral replication cycle as it is essential for the processing of polyproteins previously transcribed from *gag* and *pol* genes of the viral genome.[15] The polyproteins are cleaved by protease to generate the mature proteins and enzymes[16] essential for the proteolytic maturation and generation of infectious viral particles. The inhibition or mutation of the protease active site can lead to the development of morphologically immature and non-infectious viral particles, which are incapable of infecting host immune cells.[8] Indeed, the absence of this functional protease (e.g. through mutation at Asp25) has previously been shown to produce immature and non-infectious particles.[17, 18] Protease inhibitors can act as polyprotein mimics that are recognised and cleaved by the enzyme, rendering it inactive.[19]

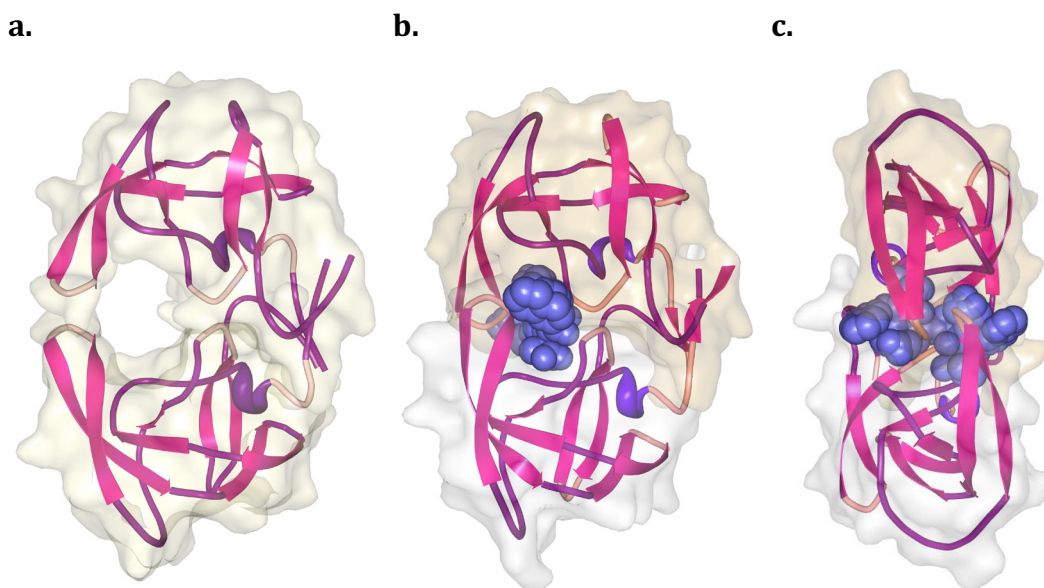


Figure A.D.68 Top-down views of HIV-1 protease, **a.** unbound (PDB 1HHP) and, **b.** bound to the organic antiviral agent saquinavir (PDB 1HXB). A rear view of saquinavir bound in the active site is shown in **c.**

Currently, there are ten organic-based, FDA approved protease inhibitors (PIs).[20] These compounds, which act via competitive enzyme inhibition (Figure VII.1 b and c), are employed in conjugation with nucleoside reverse transcriptase inhibitors (NRTIs) for the treatment of HIV. However, various limitations in their therapeutic application are known to exist owing to; multistep synthetic production costs, adverse side-effects, poor pharmacokinetics and emerging resistant strains of the HIV virus. [21] Organic PIs are also known to be metabolically unstable, have low oral bioavailability and have low tolerance levels when administered in conjugation with other pharmaceuticals.[22] Resistance due to amino acid substitution in the active site or distant sites[23] results in alterations in the active, site-specific structure changing both the number and nature of contact points between the inhibitor and the binding domain and thus perturbing the overall binding affinity of the inhibitor.[24-26] Metal-based therapeutics represent attractive PIs owing to their relative ease of synthesis, three-dimensional variability, charge and unique binding affinity compared to organic PIs. In this section, we discuss the development of metallacarborane, polyoxometalate, gold and copper compounds which have been designed to inhibit the HIV-1 protease enzyme.

A.D.3.2 Metallacarboranes

Carboranes are a class of inorganic, polyhedral boron clusters that contain at least one carbon atom bound into an electron-delocalised cage skeleton.[27] Metallacarboranes contain carbon, boron, hydrogen along with metal atoms present in, or associated with, the cage framework (Figure A.D.2). Carboranes were initially used as high-boron content molecules for boron neutron capture therapy (BNCT) but have now expanded into areas of drug discovery and molecular imaging, such as radio-immunodetection and radioimmunotherapy.[28] These molecules have had a significant impact on environmental chemistry, organic synthesis, medicine and materials science.[27] Metallacarboranes have become a subject of growing interest due to properties such as the cage rigidity and its relative rotary motion, hydrophobicity and chemical and thermal stability.[29] The stability of these compounds originates from the delocalized bonding within their triangular boron facets over the complete cage structure, giving rise to three-dimensional aromaticity.[30] Metallacarboranes are known to vary in size from 4 to 14 vertices in a single polyhedral framework, the majority of which contain C_2B_3 , C_2B_4 or C_2B_9 (Figure A.D.1 g. – j.) ligands capable of functioning as 6-electron donors to a metal centre.[29] Larger, multicage systems can be formed from the linkage or fusion of two or more of these subunits. The metal centre can be replaced by a wide number of transition metals, thus changing the total charge of the compound. The shape and charge of metallacarboranes, therefore, can be adapted to a specific biological function such as inhibition of the HIV-1 protease enzyme.

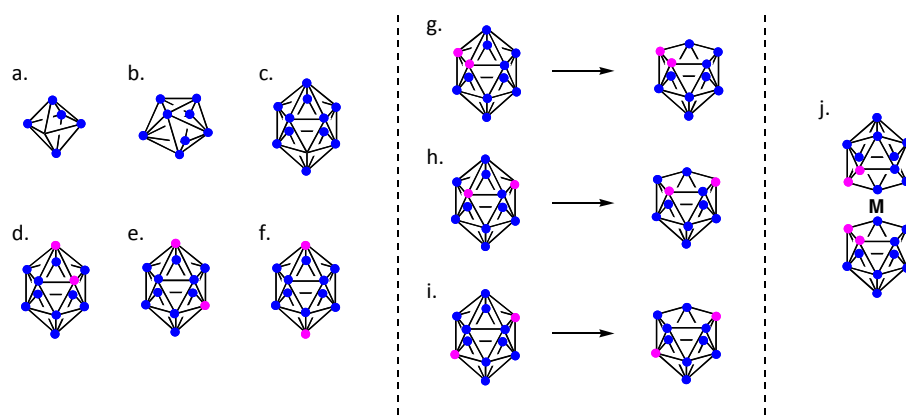


Figure A.D.69 Molecular structures of octahedral (a.), dodecahedral (b.) and icosahedral (c.) borane cages; *ortho*-, *meta*- and *para*-icosahedral carboranes are represented in structures d. to f. respectively; formation of *nido*-carboranes results through modification of *o*-, *m*- and *p*-cages in g. to i., respectively; metallocarboranes such as the *commo*-metallabisdicarbollide (j.) are generated from metal coordinated *nido*-clusters. (• = boron; • = carbon)

In 2005, Cígler, Konvalinka *et al.* reported that a range of anionic, icosahedral metallocarboranes (*commo*-cobaltabisdicarbollide type) and substituted derivatives thereof, possessed potent inhibitory activity against HIV-1 protease (Table A.D.1, **1-6**).^[31] The agents exhibited impressive inhibitory constants with the most active agent (**6**) reporting a K_i (inhibition constant) value of 2.2 nM and an EC_{50} of 0.25 μ M. These agents showed no toxicity in tissue culture and were selective toward protease. The compounds showed only weak inhibition toward human cathepsin D and pepsin and no activity against trypsin, papain and amylase. In a subsequent study by the same group these agents were also shown to be specific, competitive inhibitors of drug-resistant HIV proteases.^[32] These cobaltacarboranes demonstrated nanomolar K_i values toward the wild-type HIV-1 protease, and, although their activity was not as efficient as the clinical agents tested, they showed a low relative loss of activity against a range of mutated PRs, some of which had been amplified from HIV-1 positive patients who were heavily pre-treated with various PIs. In this study a “vitality” model was introduced as a measure of the relative capability of a mutated enzyme to cleave its substrate in the presence of an inhibitor. Interestingly, specific mutations in the PR were found to dramatically increase (50- to 1000-fold) the vitality for saquinavir, indinavir and nelfinavir, while the metallocarboranes did not suffer the same fate. The crystal structure of the wild-type enzyme in complex with cobalt bis(1,2-dicarbollide) (**1**) revealed a unique

binding mode of metallocarboranes in the HIV PR active site (Figure A.D.3).[31]
The molecules bind asymmetrically into two hydrophobic pockets that are formed by the side chains of residues Pro81, Ile84 and Val82 residues and covered by the flap residues, Ile47, Gly48 and Ile54.

Table A.D.1 Structures and activities of metallacarborane HIV-1 protease inhibitors. (• = boron; • = carbon; • = cobalt)

Entry	Structure	EC ₅₀ (μM)
1		6
2		20
3		6
4		13
5		3
6		0.25

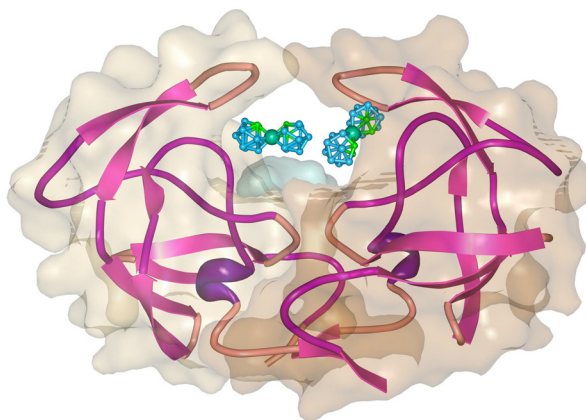
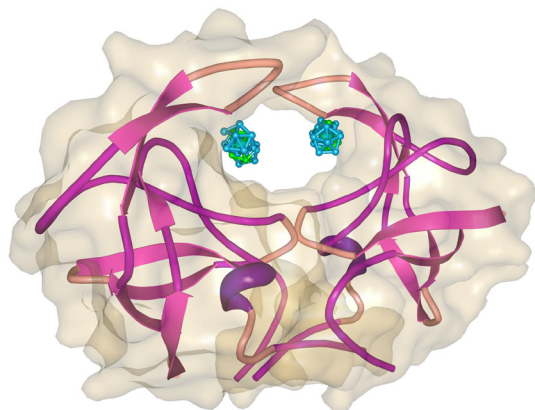


Figure A.D.70 HIV-1 protease ligated by two cobaltabis(1,2-dicarbollide) molecules (PDB 1ZTZ).

As a consequence of the enhanced activity exhibited by the dual cage compounds **5** and **6**, an expanded study of PR inhibition was undertaken using modified dual cage, metallocarbollide clusters linked with *N*-substituted dioxane groups.[30] Substituents were altered in the linker region, differing in functionality, bulkiness and charge, and their *in vitro* inhibitory effects were observed using HIV-1 PR (Table A.D.2). The dual cage cobalt bis(dicarbollide) compounds, **7** to **20**, showed impressive IC₅₀ values in the nanomolar range, while compound **20** had a significantly lower PI value of 8.5 μ M. Interestingly, in this study, compounds **17** and **18**, which contain three borane cages, displayed the highest PI activity and although compound **19** had lower comparable inhibitory activity, its K_i constant was 20 times greater than the parent compound **7**.

The X-ray crystal structure of the dual cage compound **7** with the HIV-1 PR enzyme revealed some differences in its binding mode when compared to the single cage cobaltabis(1,2-dicarbollide) molecule (**1**).[30] In both crystal structures, the cobalt bis(1,2-dicarbollide) cluster occupies a hydrophobic pocket whose base is formed by enzyme residues. However, whereas asymmetrical binding of the two individual bis(1,2-dicarbollide) clusters occurs for clusters **1** (Figure A.D.4, b.), the dual cage cluster compound **7** occupy their binding sites symmetrically (Figure A.D.4, a.).

a.



b.

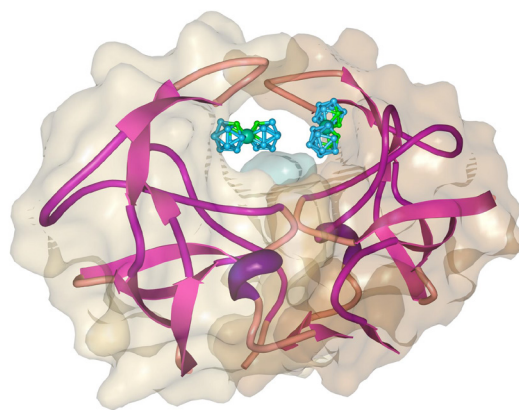
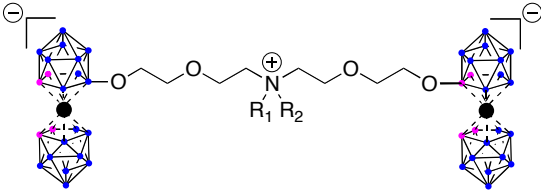
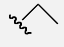
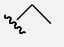
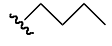
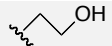
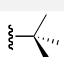
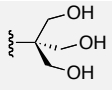
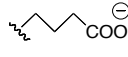
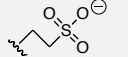
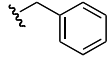
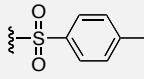
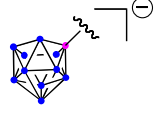
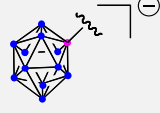
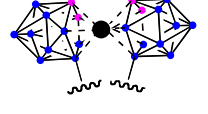
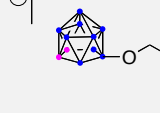



Figure A.D.71 Perspective views of **a.** the dual cage metallocarbollide compound **7**, bound to HIV-1 PR (PDB 3I8W) and, **b.** two individual cobaltabis(1,2-dicarbollide) molecules from compound **1** bound to HIV-1 PR (PDB 1ZTZ).

Table A.D.2 Structures and activities of dual cage metallacarborane HIV-1 protease inhibitors.

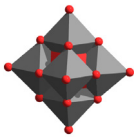
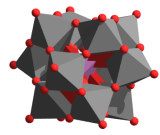
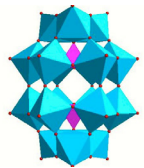
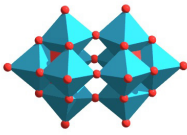
(• = boron; • = carbon; • = cobalt)

General formula:				
				
Entry	Substituent groups R^1	R^2	IC_{50} (nM)	
7	H	H	140	
8			160	
9		H	100	
10		H	140	
11		H	130	
12		H	190	
13		H	110	
14		H	110	
15		H	140	
16		none	70	
17		H	50	
18		H	58	
19		H	250	
20			8500	

A.D.3.3 Polyoxometalates

Polyoxometalates (POMs) are early transition metal oxygen clusters, held together by metal-to-oxygen bonds.[33] POMs have been extensively studied due to their antibacterial, anticancer and antiviral activities,[33-35] along with electrocatalytic[36] and, more recently, nanotechnology applications.[37] The five types of d^0 transition metal ions that form POMs are; V^V , Nb^V , Ta^V , Mo^{VI} and W^{VI} , with the last two forming the largest number of complexes.[38] The principle structural unit in POMs is composed of MO_6 octahedra and they are further sub-categorised into isopoly- and heteropoly-compounds, the former containing only metal and oxygen atoms, with the latter having one or more heteroatoms at defined sites. Hetero-polyoxometalates can incorporate approximately 78% of the elements of the Periodic Table in their structural framework and with the heteroatom being either surface accessible or inaccessible.[39] POMs are arranged into families (Table A.D.3) based on their geometric structure, for example, Lindqvist (hexametalate), Keggin, Wells-Dawson and Decatungstate, with further tri-vacant and double structural derivatives being found within these classes. POMs can be extensively synthetically-modified in composition, size, shape, charge density, redox activity and acidity.[21] The solubility of POMs can also be easily altered, rendering the compounds soluble in virtually all media via counterion choice. Another advantage of POMs is their inexpensive synthesis compared to multi-step organic peptide-mimics.[40] For these reasons, POMs are extensively studied as they represent ideal pharmacophores capable of high efficacy combined with low toxicity. POMs, which are often considered structurally analogous to the fullerenes,[41] represent lead compounds as HIV-1 inhibitors and have been shown to possess potent *in vitro* antiviral properties.

Table A.D.3 Selected polyoxometalate families, formulae and structures.

Family	Molecular Formula	Structure
Lindqvist	$[\text{W}_6\text{O}_{19}]^{x-}$	
Keggin	$[\text{XW}_{12}\text{O}_{40}]^{x-}$	
Wells-Dawson	$[\text{X}_2\text{W}_{18}\text{O}_{62}]^{x-}$	
Decatungstate	$[\text{W}_{10}\text{O}_{32}]^{4-}$	

One of the most prominently studied POMs is the cryptate HPA-23, $(\text{NH}_4)_{17}\text{Na}(\text{NaSb}_9\text{W}_{21}\text{O}_{86})$. [42] The agent dominated much of the early POM antiviral research [43-45] with spectroscopy studies revealing that, despite the anion's high charge density, it was capable of crossing cell membranes and remaining intact for interactions with biological substrates. [46] The antiviral activity of HPA-23 within AIDS patients was observed by Rozenbaum *et al.* [47] and the agent was introduced into clinical trials in France and the US in the 1980s. However, testing was subsequently abandoned due to the adverse, dosed-related toxicity of the drug. [48] A comprehensive review of the antiviral properties of HPA-23, along with an extensive range of POMs, has been conducted by Hill and co-workers. [33]

A study conducted by Inouye *et al.* in 1992 identified that POMs possessing the Keggin and Wells-Dawson type structures possessed enhanced antiviral activity. [49] Hill and co-workers subsequently examined the protease activity of a group of high molecular weight (*ca.* 4500 g mol⁻¹), niobium-containing polyoxometalates based on the Wells-Dawson structural family (Table A.D.4, **21-24**). [21] Significantly, these agents were found to selectively inhibit HIV-1 protease with IC₅₀ values below 2.0 μM (Table A.D.4) and had no effects against pepsin when tested at a concentration of 100 μM. Significantly, these Nb-POMs

demonstrated potent anti-HIV-1 activity while being minimally toxic to peripheral blood mononuclear cells (PBMC). Molecular modelling experiments revealed that the α_2 -isomer, $[\text{P}_2\text{W}_{17}\text{NbO}_{62}]^{7-}$ (**24**), does not occupy the active protease site but forms oxygen-to-hydrogen bonds at amino acids, Lys45, Lys43 and Lys55 located in the hinge region behind the hair-pin flaps of the HIV protease (Figure A.D.5) with two POMs binding per protease homo-dimer. This work thus identified a new, selective mode of inhibition, potentially rendering these agents less sensitive to amino acid substitution mutations occurring within the active protease site.

Table A.D.4 HIV-1 protease inhibition, antiviral and cytotoxicity data for a range of Nb-POMs.

Entry	POM	IC ₅₀ (μM)	Anti-HIV-1 Activity	Cytotoxicity
		(HIV-1P)	PBMC EC ₅₀ (μM)	PBMC IC ₅₀ (μM)
21	K ₇ [α_1 -P ₂ W ₁₇ (NbO ₂)O ₆₁]	2.0	0.78	66
22	K ₇ [α_2 -P ₂ W ₁₇ (NbO ₂)O ₆₁]	1.2	0.81	74
23	K ₇ [α_1 -P ₂ W ₁₇ NbO ₆₂]	1.5	0.83	>100
24	K ₇ [α_2 -P ₂ W ₁₇ NbO ₆₂]	1.8	0.17	50

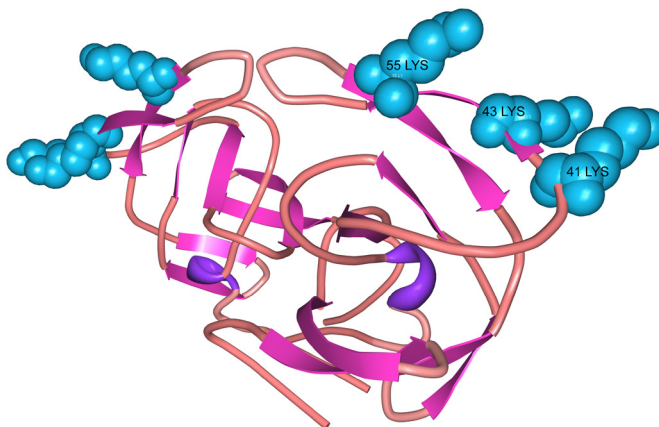


Figure A.D.72 Crystal structure of a synthetic HIV-1 protease (PDB 3HVP) with lysine residues 55, 43 and 41 shown (spacefill, coloured teal) along the hinge region behind the hair-pin flaps.

In a recent, preliminary study by Patzke *et al.* an extensive range of POMs were examined for their ability to inhibit a mutant HIV-1 protease (Q7K) and were compared to Keggin- and Dawson-type POMs containing functionalised organic side chains.[40] In these experiments, where assay buffer composition was varied, it was generally found that POMs containing the Dawson-type

architecture were more effective in their protease inhibition. Additionally, butyl-functionalised Sn-POMs were found to exert the strongest inhibitory effect among the DMSO-soluble agents regardless of the POM framework. Other potentially significant results were observed for propionic acid derivatised POM molecules.

A.D.3.3 Gold Complexes

In the late 19th century, Robert Koch discovered the bacteriostatic properties of gold cyanide against the tubercle *bacillus*.^[50] This discovery resulted in the development of gold complexes such as aurothioglucose, sodium aurothiomalate and auranofin (Figure A.D.6) for the treatment of rheumatoid arthritis. Of the many gold thiolates originally approved for use for the treatment of rheumatoid arthritis, gold sodium thiomalate and gold thioglucose remain in use within the US, while sodium bis(thiosulfato)gold-(I) and sodium thiopropanolsulfonate-*S*-gold(I) are in clinical use in Europe.^[51] These compounds can also be employed in the treatment of bronchial asthma and investigations are currently underway for the use of both gold(I) and gold(III) complexes for the treatment of cancer, malaria and Chagas disease.^[52]

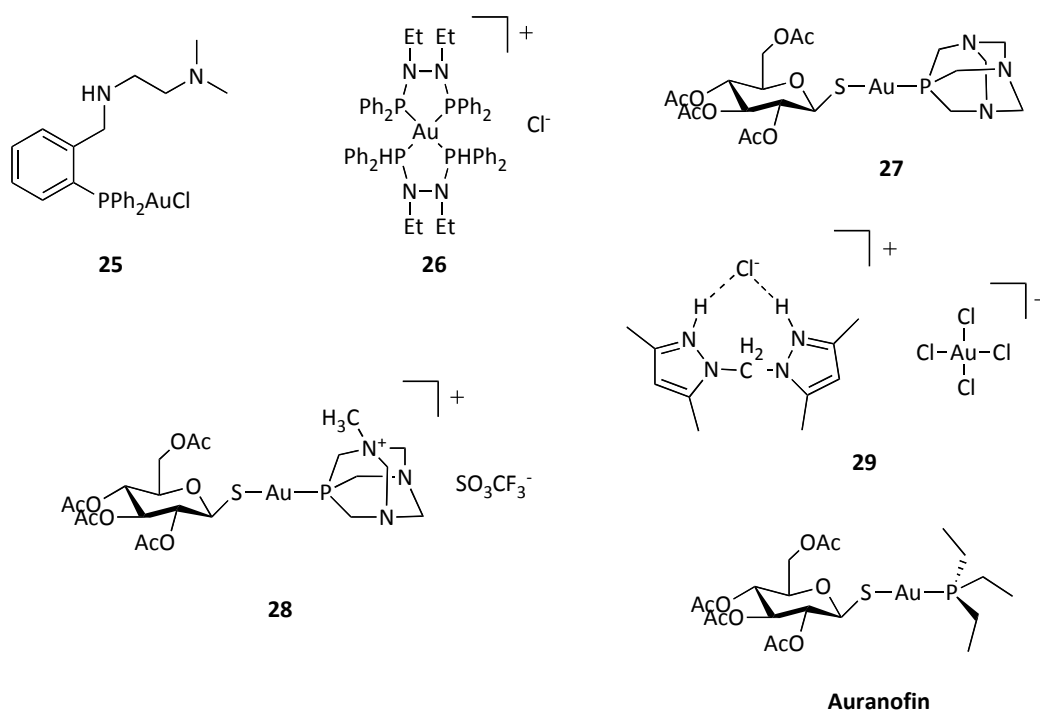


Figure A.D.73 Molecular structures of the HIV-1 PR active Au(I) phosphine complexes, **25** to **29**, the Au(III) tetrachloride anion in complex **5** and auranofin.

The anti-HIV activity of gold compounds have not been as thoroughly investigated in comparison to their anti-arthritic and antitumour properties. Although auranofin was the first documented metal phosphine complex to be used to treat rheumatoid arthritis,[3] observations made from the clinical data of a HIV patient receiving auranofin for psoriatic arthritis, spurred interest in chrysotherapy as a potential treatment of the viral disease, AIDS. It is interesting to note that, despite this patient refusing to accept antiviral HIV drugs, a significant increase in the CD4+ lymphocyte count was observed even though AIDS is associated with an irreversible decline in this cell type.[53] As chrysotherapy was known to produce $[\text{Au}(\text{CN})_2]^-$ metabolites, one theory linked the possible inhibitory effect of this complex to metallo-ligand exchange reactions, with gold binding to sulfhydryl groups in the active site of reverse transcriptase (RT), thus leading to a remission in the overall AIDS status of the patient.[54] These findings have prompted further studies of gold compounds as potentially novel anti-HIV therapeutics.

Gold possesses two common oxidation states within biological environments, Au(I) ($[\text{Xe}]4f^{14}5d^{10}$) and Au(III) ($[\text{Xe}]4f^{14}5d^8$). Au(I) compounds are thermodynamically more stable than gold(III) and have considerably lower toxicity levels associated with their usage. Thus, the majority of gold compounds reported to have anti-HIV activity are those in the +1 oxidation state. Furthermore, Au(III) complexes are generally considered to be strong oxidizing agents which can be easily reduced to gold(I), and are therefore targets for naturally occurring biological reductants (e.g. glutathione). A recent study by Meyer *et al.* examined eleven Au(I) phosphine compounds, to determine their inhibitory effect on HIV RT and PR inhibition. Four of the complexes tested (Figure A.D.6, **25** to **28**) were found to inhibit HIV-1 PR ($\geq 50\%$) at $100\ \mu\text{M}$, while cross-inhibition for both HIV-1 RT and PR was noted for complex **25**. [54] In comparison, many of this tested group exhibited EC_{50} values of $25\ \mu\text{M}$ when examined against HIV reverse transcriptase (RT), with none being significantly cytotoxic toward peripheral blood mononuclear cells (PBMC).

There are fewer examples in the literature of Au(III) HIV-1 PR inhibitor complexes, although the Au(III) tetrachloride anion, in the bis-pyrazole complex (tetrachloro-(bis-(3,5-dimethylpyrazolyl)methane)gold(III) chloride), has

recently shown inhibition at 100 μ M (Figure A.D.6, **29**).[55] In this study, the simple salt, $\text{H}[\text{AuCl}_4]\cdot\text{H}_2\text{O}$, was a less effective HIV-1P inhibitor at this same concentration. Complex **29** also exhibited RT activity at 5 μ M, suggesting that it may be more applicable toward RT inhibition rather than PR. The anti-HIV properties of gold complexes has recently been reviewed and a detailed discussion of potentially new HIV RT-active compounds can be found therein.[56]

A.D.3.4 Copper Complexes

The HIV-1P inhibitory effects of an extensive range metal ions was reported in 1991 by Karlström and Levine.[57] Using an extensive range of metal cations these researchers demonstrated that Cu(II) and Hg(II) ions possessed potent inhibitory effects on wild-type HIV-1 protease (Table A.D.5). Through a series of elegant experiments, they demonstrated that cysteine residues in the wild-type protease were required for Cu(II) ion to directly inhibit the enzyme. Thus, a synthetic protease containing no cysteine residues was found to function normally in the presence of added cupric ions. Further analysis revealed that the inhibition was independent of O_2 and that catalytic function could not be restored through the addition of the metal ion sequestering agent, EDTA, to the reaction. Binding analysis studies revealed that approximately two cupric ions were required per stoichiometric unit of PR and that the non-cysteine containing, synthetic, HIV-PR could be inhibited by cupric ions only in the presence of the reducing agent, dithiothreitol (DTT).

Table A.D.5 Effect of metal cations on wild-type protease activity.[57]

Metal ion	Activity
(25 μM)	% Control
Al ³⁺	94
Ca ²⁺	100
Co ²⁺	92
Cr ³⁺	96
Cu²⁺	<2
Fe ²⁺	94
Fe ³⁺	93
Hg²⁺	<2
K ⁺	92
Mg ²⁺	91
Mn ²⁺	95
Ni ²⁺	94
Pb ²⁺	92
Zn ²⁺	99

Given that the activity of the non-cysteine protease could be repressed by Cu(II) ions in the presence of the chelating reducing agent, DTT, a subsequent study by Davis, Levine *et al.* tested this hypothesis by using the Cu(I) chelate, bathocuprione disulfonic acid (BCDS-Cu⁺) (Figure A.D.7, **30**).[58] While BCDS-Cu⁺ complex was not quite as active at inhibiting the wild-type HIV-1P (IC₅₀ = 4 μ M) compared to free Cu(I) ions (IC₅₀ = 1 μ M), it was equally as effective against the synthetic PR (IC₅₀ = 4 μ M) which lacks the cysteine groups essential for cuprous (and cupric) ion inhibition. Interestingly, the study also revealed that neocuprione-Cu⁺ (Figure A.D.7, **31**) did not inhibit wild-type PR and had only a limited inhibitory effect on the synthetic PR up to a tested maximum concentration of 25 μ M.

The HIV-1 protease activity of a family of boronated porphyrins was reported by DeCamp, Craik *et al.* and among the agents tested was the Cu(II) metalloporphyrin complex (Figure A.D.7, **32**).[59] This complex displayed significant HIV-1P inhibition (0.975 μ M) although its activity was much lower than that of the metal-free porphyrin (IC₅₀ = 0.185 μ M). The Cu(II) complex did, however, display lower lethality toward COS A6 cells (LD₅₀ = 80 μ M) compared to the parent porphyrin (LD₅₀ = 25 μ M). Further analysis of the metal-free

porphyrin revealed that it was highly specific toward HIV-1P and HIV-2P, with considerably lower inhibitory effects toward renin, cathepsin D and pepsin proteases.

The de novo design of the Cu(II) complex, bis-(2-pyridylcarbonyl)-amido copper(II) nitrate (Figure A.D.7, **33**), as a protease inhibitor was reported after docking studies revealed the complex fitted the active protease site.[60] The agent was found to competitively inhibit HIV-1P ($K_i = 480 \pm 120 \mu\text{M}$) and was non-active in the presence of added EDTA. A more efficient copper(II) HIV-1P inhibitor (Figure A.D.7, **34**) was later reported which inhibited the wild-type HIV-1P at $1.1 \mu\text{M}$. [61, 62] This agent also demonstrated >20% inhibition toward the synthetic, non-cysteine protease in the concentration range 1.7 to $2.0 \mu\text{M}$. In contrast, complexes **35** and **36** (Figure VII.7) did not inhibit the synthetic protease enzyme and exhibited an identical inhibitory profile and value to that of the 'free' Cu(II) ion. Thus, it appeared likely these complexes readily dissociate their Cu(II) ions in solution.

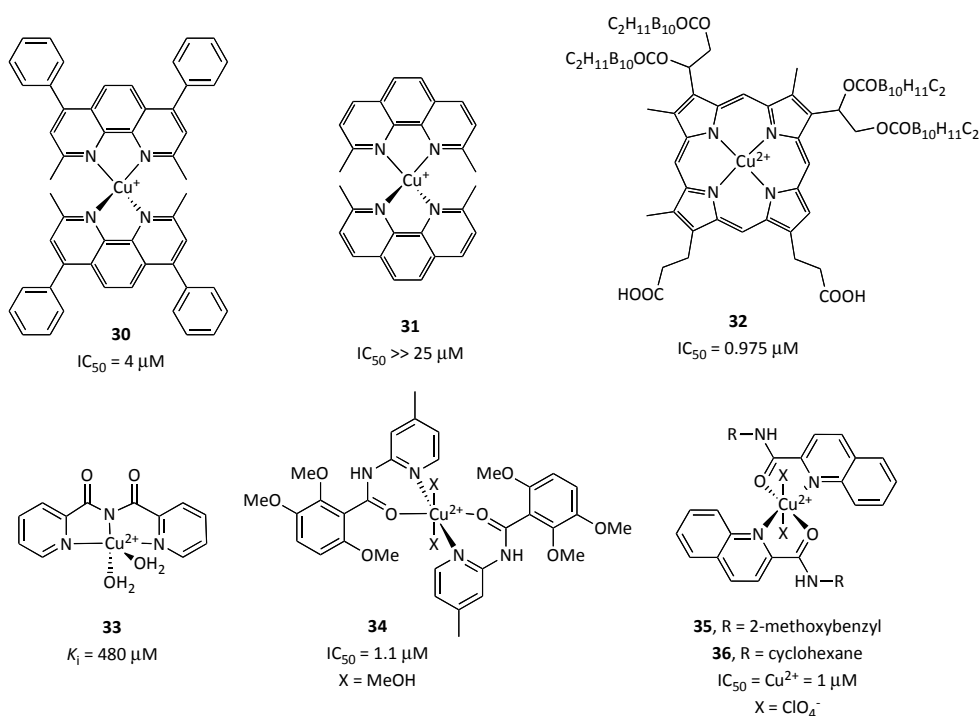


Figure A.D.74 Molecular structures and HIV-1P inhibitory properties of a range of copper(I) and copper(II) complexes.

A.D.4 Parasitic Protease Inhibitors

A.D.4.1 Introduction

Proteolytic enzymes are known to perform essential metabolic and regulatory roles within parasitic microorganisms.[5, 63] Serine-, cysteine-, and metallo-proteases are found in many of these pathogens where they perform critical functions in colonisation and evasion of the host immune defence, acquisition of nutrients for growth and proliferation, and in damaging tissue during infection.[64, 65] Important parasite proteases include cathepsin B and cathepsin L-like (family C1) and also calpain-like (family C2).[63] Cysteine proteases, which contain a thiol functional group within their active site, constitute a family of emerging parasitic targets that are divided into two main groups often referred to as clans CA and CD.[66] The proteolytic activity of these cysteine proteases arises from the presence of both Cys- and His- residues in the active site, with the crucial step in the catalytic process being the formation of a reactive imidazolium- thiolate ion pair ($\text{His-Im}^+ / \text{Cys-S}^-$).[67]

Infection by *Plasmodium falciparum*, the most virulent human malaria pathogen,[68-72] is now estimated to be responsible for between 500,000 and 1,000,000 deaths annually.[68] Falcipain-2 (Fp2) belongs to the papain family of cysteine proteases and plays an important role in the malarial life cycle.[9, 73] Inhibition of Fp2 by either protein-based inhibitors, such as cystatin[74] (Figure A.D.8 a.) or small organic molecules, such as epoxysuccinate (E64) [72] (Figure A.D.8 b.) have revealed protease as a prime target for the development of effective anti-malarial agents.[75] Indeed, while the E64 inhibitor is an example is a non-specific inhibitor of cysteine proteases, it is a useful template for medicinal chemists looking to design specific inhibitors. Treatment of malaria and *Trypanosoma cruzi* infections with cysteine protease inhibitors have been demonstrated in mice and several other parasitic organisms with homologous proteases may now be potential targets.[76-78] Cysteine protease inhibitors have also been shown to reduce worm size and egg number in *Schistosoma mansoni*, confirming the importance of this class of protease to the parasite.[63] Furthermore, the enzymes have been found to play an integral role in parasitic life cycles of *Plasmodia*, *Trypanosoma* and *Leishmania* with functions in nutrition, host invasion, protein processing, and evasion of the host immune response.[79, 80]

Significant efforts have been made in the design and therapeutic application of metal-based chemotherapeutic agents directed against tropical diseases such as malaria, trypanosomiasis and leishmaniasis.[3, 66, 81] Metal complexes of the antimalarial quinolone-based drug chloroquine[82] (**CQ**) (Figure A.D.9), such as the ruthenium(II) complex, $\{[\text{RuCl}_2(\text{CQ})]\}_2$ (**RuQ**),[83] the ferrocene-functionalised compound, ferrochloroquine (**FQ**)[84] and the Au(I) complex, $[\text{Au}(\text{PPh}_3)(\text{CQ})]\text{PF}_6$,[85] have shown superior drug properties, both in terms of parasite growth inhibition and activity toward CQ-resistant strains, compared to the parent organic drug. Indeed **FQ** is currently one of the most advanced antimalarial candidate drugs being clinically trialled by Sanofi-Aventis.[86, 87] Reasons for the enhanced mode of action displayed by **FQ** remain unknown although a recent study by Christophe Biot *et al.* demonstrated the ferrochloroquine bioprobe, ruthenoquine, accumulated in the digestive vacuole of the parasite which is the same target organelle as the organic antimalarial drug, **CQ**. [88] For over half a century, the chemotherapeutic drugs of choice for the treatment of leishmaniasis have been the antimony(V) stibonic acid-derived complexes, sodium stibogluconate (Pentostam®) and meglumine antimoniate (Glucantime®).[81, 89, 90] In order to achieve clinical effectiveness, these compounds must be aged prior to administration and this process appears to give rise to a multitude of uncharacterized daughter compounds. Possible structures for some forms of these clinical antileishmanial Sb(V) compounds are shown in Figure VII.9. Their mode of inhibitory action also remains largely unknown although it is thought that various proteins, particularly those containing thiol groups, become inhibited by the agents which are also known to cause severe side effects in patients.

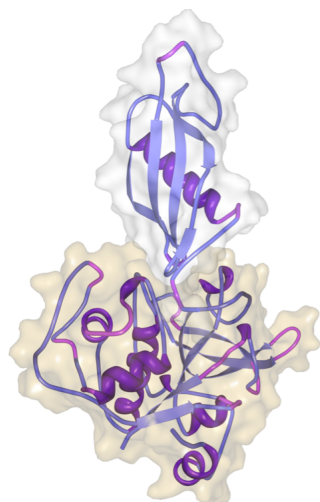
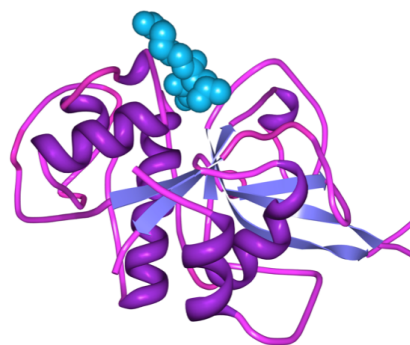
a.**b.**

Figure A.D.75 Crystal structures of, **a.** *Plasmodium falciparum* cysteine protease, Falcipain-2 (coloured cream) bound to a cystatin inhibitor (coloured white) (PDB 1YVB),[74] and **b.** of Falcipain-2 with the small molecule cysteine protease inhibitor, epoxysuccinate E64 (coloured teal) (PDB 3BPF).[72]

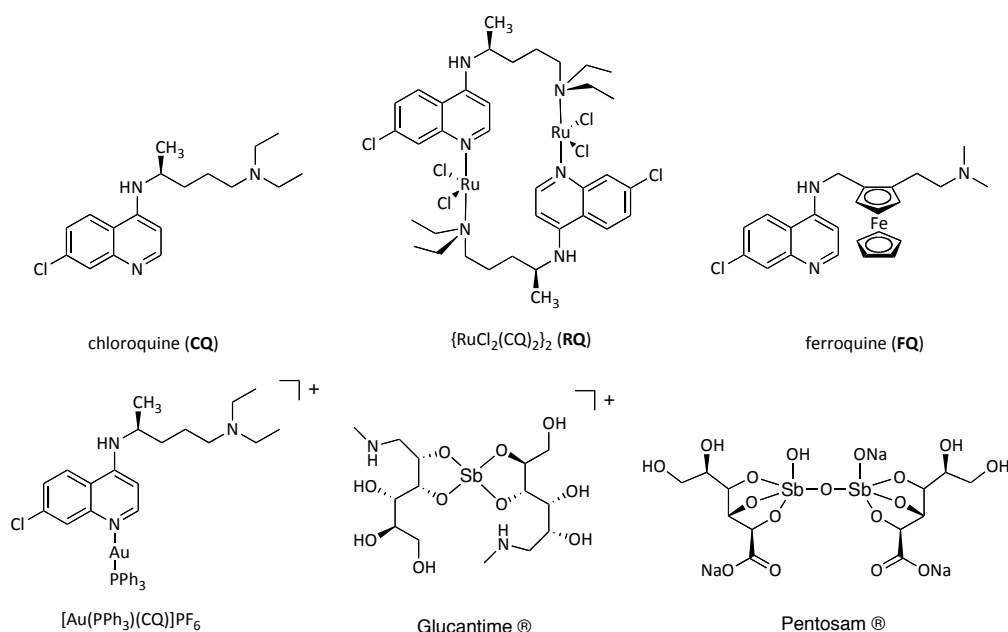


Figure A.D.76 Molecular structures for the antimalarial drugs chloroquine (CQ), $\{[\text{RuCl}_2(\text{CQ})_2]\}_2$ (RQ), ferroquine (FQ), $[\text{Au}(\text{PPh}_3)(\text{CQ})]\text{PF}_6$ and the antileishmaniasis Sb(V) complexes, Glucantime® and Pentosam®.

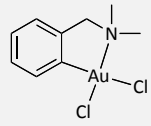
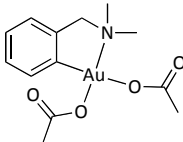
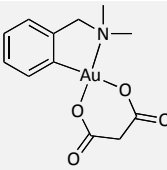
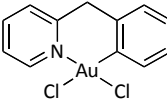
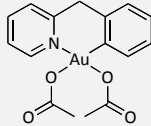
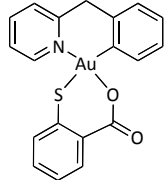
Given the wide platform of metal-based compounds either in clinical use or under investigation for the treatment of tropical diseases, coupled with the essentially of protease enzymes for parasite survival, there has been significant

interest in the design of metallodrugs as effective agents toward protease inhibition.

A.D 4.2 Gold(I) and gold(III) complexes

Recently, Fricker *et al.* reported the activity of gold(III) cyclometallated complexes as cathepsin cysteine protease inhibitors.[7, 79] The group previously observed, through NMR studies, that the antitumour candidate complexes **37-39** (Table A.D.6) had a preference for binding S-donor ligands and thus decided to examine the activity of compounds **37-42** as possible inhibitors of cathepsin B. All six complexes were significantly active against the protease with the mercapto-benzoate bis-chelate complex, **42**, being the most efficient. Further analysis of complex **41** using cysteine parasite proteases, Cruzain (*T. cruzi*) and cpB (*L. major*), revealed broadly similar inhibitory activity (IC_{50} Cruzain = 0.7 μ M; cpB = 1.7 μ M) as cathepsin B. Complex **41** was also examined, *in vivo*, for its ability to increase the life cycle duration of *T. cruzi* infected macrophage cells, therefore measuring its effectiveness at preventing exogenous cell death and subsequent release of infectious parasites. However, at a concentration of 10 μ M, the complex did not extend the life cycle of infected macrophage cells beyond that observed for the control (5 days).

Table A.D.6 Molecular structures and cathepsin B inhibitory effects of cycetometallated Au(III) complexes.[79]

Compound	Molecular Structure	IC ₅₀ value (μM)
37		1.36 ± 0.04
38		0.60 ± 0.04
39		0.61 ± 0.01
40		0.85 ± 0.21
41		1.29 ± 0.09
42		0.18 ± 0.03

The antimalarial activity of a selection of gold(I) complexes, **43-47** (Table A.D.7), along with the known Au(I) and Pt(II) therapeutics, auranofin and cisplatin, were assessed by Micale, Messori *et al.*[91] It was found that these structurally diverse chelator complexes induced pronounced but reversible inhibition of Fp2 with K_i values falling within the micromolar range. The gold compounds were subsequently tested for their ability to inhibit *P. falciparum* growth *in vitro* with activity also being observed in the micromolar range. Further analysis failed to establish any direct correlation between enzyme inhibition and reduction of *P. falciparum* growth suggesting that Fp2 inhibition, ascribed to the Au(I) complex binding to the cysteine active site, may represent just one of multiple mechanisms through which the complexes retard parasitic growth. Interestingly, in this study auranofin showed nearly complete inhibition

of *P. falciparum* growth ($IC_{50} = 0.142 \mu M$) with cisplatin being only moderately active by comparison ($IC_{50} = 27.40 \mu M$).

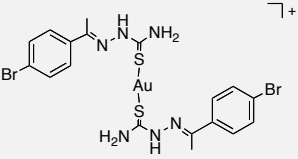
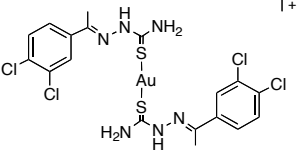
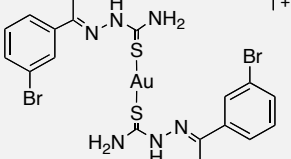
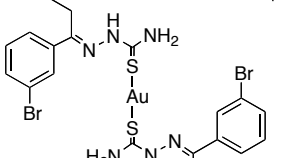
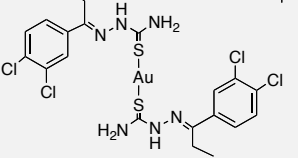
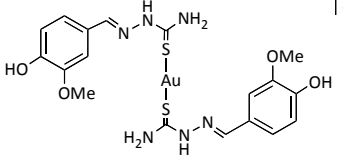
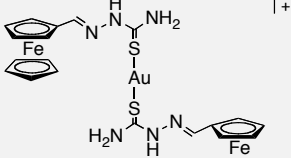
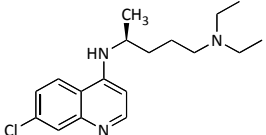
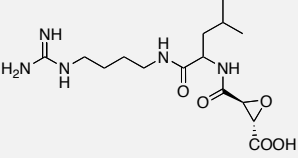
Table A.D.7 Inhibition of Fp2 and antiplasmodial activity of gold(I) and gold(III) complexes.[91]

Compound	Molecular Structure	Fp2 inhibition K_i (μM)	IC_{50} <i>P. falciparum</i> (μM)
43		11 ± 2.0	1.33 ± 0.27
43		1.8 ± 0.2	4.51 ± 0.44
44		1.4 ± 0.2	5.11 ± 0.46
45		1.5 ± 0.2	2.30 ± 1.00
46		Not detected	5.16 ± 0.14
47		2.0 ± 0.3	4.82 ± 0.26
Auranofin		Not detected	0.142 ± 0.00
Cisplatin		Not detected	27.40 ± 2.00

The Chibale group utilized a different structural approach in the development of gold(I) complexes as potential antimalarial drugs.[69] Through the use of coordinated thiosemicarbazone ligands (TSCs), which had received considerable attention due to their inhibition of the *T. cruzi* protease enzyme cruzain,[92] the group rationally generated a series of Au(I) complexes. The hypothesis here was

that coordination of gold(I), itself having an affinity toward thiolated proteins, to the TSC ligand would result in an enhanced Fp2 inhibitory and antiplasmodial agent. A series of seven linear Au(I) complexes were generated (**48-54**, Table A.D.8), with complex **54** being further functionalised with ferrocene. These complexes were examined along with the clinical antimalarial drug **CQ** and known Fp2 inhibitor **E64** for their Fp2 enzyme inhibitory and **CQ**-sensitive and resistant antiplasmodial properties. With the exception of the methoxy-phenol complex (**53**), all tested complexes displayed low micromolar inhibition toward the **CQ**-resistant strain with favourable results to inhibitor **E64**. Complexes **48-52** were also considerably active toward the **CQ**-sensitive strain while, interestingly, the ferrocene containing agent, **54**, was 14-times less active when compared with the W2 strain. The organic drug **CQ** was clearly the most active antiplasmodial agent with IC_{50} values being 0.095 and 0.017 μM for the resistant (W2) and sensitive (D10) strains, respectively. The Fp2 inhibitory responses from the seven TSC Au(I) complexes produced a variety of K_i responses. The most active agents were the dichlorobenzene agent, **49**, and the ferrocene-derived complex, **54**, which gave inhibitory responses at 0.87 and 8.89 μM , respectively. Overall, no correlation between Fp2 inhibition and antiplasmodial activity was identified which again raises the question of falcipain-2 protease being the primary target for these compounds.

Table A.D.8 FP-2 inhibition and antiplasmodial activity of gold(I) TSC complexes.[69]

Compound	Cationic Complex /Organic Structure	Fp2 inhibition	IC ₅₀ <i>P. falciparum</i> CQ-sensitive (D10)	IC ₅₀ <i>P. falciparum</i> CQ-resistant (W2)
μM				
48		59.4	2.02	3.55
49		0.87	6.92	2.74
50		93.9	6.26	2.80
51		46.5	3.84	2.81
52		63.6	4.76	3.06
53		Not detected	>10	>20
54		8.89	>20	1.28
CQ		Not detected	0.017	0.095
E64		0.034	ND	3.00

A.D 4.3 Palladium(II) and Oxorhenium(V) complexes

As part of the Fricker group's study into the development of cyclometallated complexes (**37-42**, Table A.D.6), a series of palladium(II) and oxorhenium(V) complexes (Figure A.D.10) were also examined for their ability to inhibit the protease, cathepsin B.[7] Of the bidentate Pd(II) aminomethyl-phenyl complexes developed (**55** to **57**), the pyridine complex, **55**, displayed the greatest inhibitory activity ($IC_{50} = 1.52 \mu M$). Tridentate Pd(II) complexes of bis-thiomethyl-phenyl ligands (**58-60**) were also significantly active with further improvement in cathepsin B inhibition being noted for complex **59** ($IC_{50} = 0.40 \mu M$). The protease inhibitory properties for '3+1' oxorhenium complexes (**61-66**) also yielded a series of interesting results within this study. The ReO(V) complexes incorporating bis-mercaptomethyl-pyridine tridentate ligands (**61-63**) displayed a variety of activities with an impressive IC_{50} value being observed for the pyridinethionato complex (**63**) ($IC_{50} = 0.12 \mu M$). The most active compound in the series was **64**, which incorporated the bis-ethanethiolato-thiol tridentate ligand. This agent displayed excellent, low nano-molar inhibition of cathepsin B ($IC_{50} = 0.0088 \mu M$).

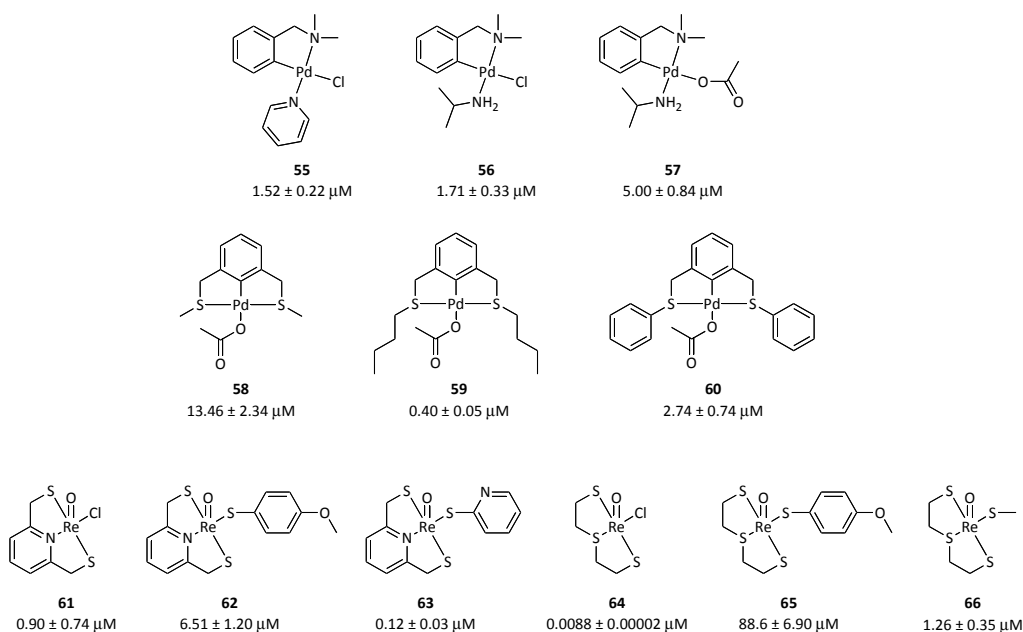


Figure A.D.77 Molecular structures and cathepsin B inhibitory properties of a range of gold(I) and oxo-rhenium(V) complexes.

A comparative analysis of complexes **59**, **62**, **63**, **64** and **66**, using a panel of cysteine parasite proteases, Cruzain (*T. cruzi*) and cpB (*L. major*), along with the serine protease, chymotrypsin, was conducted (Table A.D.9). The oxorhenium(V) complexes, **63** and **64**, were the most active agents, overall, against all proteases. It is also interesting to note that complex **64** appears to be highly specific toward cathepsin B and is approximately 4.5 and 23 times less effective toward cruzain and cpB, respectively. *In vivo* analysis of the five complexes for their ability to increase the life cycle duration of *T. cruzi* infected macrophage cells (normally 5 days) was conducted at both 10 and 1 μM concentrations. The Pd(II) complex **59** induced toxicity toward the macrophage cells at 10 μM , however, at 1 μM it prevented infected macrophage cell death for the duration of the experiment (42 days). Other results of note from this particular experiment were the extension to the life cycle, to day 32, induced by 10 μM of the ReO(V) complexes **62** and **66**. The final aspect of this study involved the growth inhibition of *Leishmania* promastigoties, the extracellular form of the parasite's life cycle, with the Pd(II) complex, **59**, being the only active species.

Table A.D.9 Comparative IC₅₀ inhibitory values for selected complexes against parasite cysteine proteases and chymotrypsin.

Compound	Cat B	Cruzain	<i>L. major</i> cpB	Chymotrypsin
μM				
59	0.40	0.07	2.1	>25
62	6.51	0.35	1.0	>25
63	0.12	0.015	0.07	Not detected
64	0.0088	0.04	0.2	>25
66	1.26	5.0	>10	>25

The chiral dinuclear cyclopalladated complex [$\{\text{Pd}(\text{C}^2\text{N-S-dmpa})\text{Cl}\}_2(\mu\text{-dppf})$] ($\text{C}^2\text{N-S-dmpa}$ = *N,N*-dimethyl-1-phenethylamine and dppf = bis-(diphenylphosphine)-ferrocene) (**67**, Figure A.D.11), was reported by Caires *et al.* in 2005 as an effective antitumoural agent capable of reducing solid tumour mass *in vivo*.^[93] The compound displayed significant inhibitory properties toward the cysteine proteases; papain (IC₅₀ = 1.3 μM), cathepsin B (IC₅₀ = 4.5 μM) and cathepsin L (IC₅₀ = 1.6 μM). This palladacycle was also found to bind free cathepsin B as well as to the enzyme-substrate complex with dissociation constants of $K_{\text{H}} = 12 \mu\text{M}$ and $K_{\text{a}} = 12 \mu\text{M}$, respectively. Although, in this case, complex **67** was not examined as an antiparasitic protease inhibitor, this study along with others,^[94] stimulated further research into this class of compound for treating against parasitic diseases. Matsuo *et al.* subsequently investigated the *in vivo* antitumoural agent **68** (Figure A.D.11),^[95] as a possible therapeutic against *T. cruzi*, the causative agent of Chagas disease.^[96] These researchers found the dinuclear compound to; inhibit trypomastigote cell invasion, decrease intracellular amastigote proliferation, and to be effective *in vivo*, at very low doses, as a trypanocidal drug. Significantly, the agent was found to be approximately 340-fold more cytotoxic to parasites than mammalian cells and was more effective than benznidazole, one of the only clinical drugs available to treat Chagas disease. More recently, the mononuclear palladacycle complex, **69**, which also contains the chiral $\text{C}^2\text{N-S-dmpa}$ ligand, was reported by Paladi, Barbiéri *et al.* as an effective *in vitro* and *in vivo* agent against *Leishmania amazonensis*.^[80] Zymography assays, conducted along with the epoxysuccinate protease inhibitor **E64** (Figure A.D.8 b.), revealed that **69** completely inhibited the cysteine protease activity of *L. amazonensis* amastigotes. The complex

displayed excellent *in vitro* inhibitory activity against the parasite ($IC_{50} = 2.13$ nM), a result that compared favourably with the therapeutic agent, amphotericin B ($IC_{50} = 15.58$ nM). Treatment of *L. amazonensis*-infected macrophages with either complex **69** or the Sb(V) therapeutic, Glucantime® (Figure A.D.9), showed the complex to be vastly more effective agent ($IC_{50} = 128.55$ nM). *In vivo* treatment of mice infected with *L. amazonensis* with 320 µg/kg/QOD of **69** for 1 month resulted in significantly smaller foot lesions in comparison to the untreated control and also compared favourably to a Glucantime® treated control. Furthermore, complex **69** and Glucantime® were found to reduce the *in vivo* parasite load by 97% and 99%, respectively.

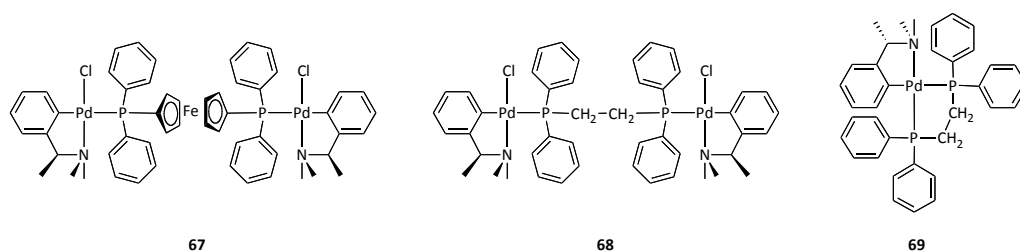


Figure A.D.78 Molecular structures of dinuclear (**67** and **68**) mononuclear (**69**) cyctometallated Pd(II) phosphine complexes.

A.D.5. Conclusion

With respect to the HIV-1 protease enzyme, a number of relatively non-toxic cobaltacarboranes have delivered EC_{50} values in the low nanomolar range and were selective towards the homodimer protein. In some instances, X-ray crystallographic analysis revealed unique binding modes of single- and dual-cage cobaltacarbollide clusters in the active site of the HIV wild-type enzyme. Polyoxometallates, which have demonstrated potent *in vitro* antiviral properties, represent exciting lead compounds as HIV-1 inhibitors. The high charge density anions can traverse cell membranes and remain intact for interactions with biological substrates. Molecular modelling studies conducted on a heterometallic polyoxotungstate identified a new, selective mode of inhibition based on hydrogen-bonding to specific amino acids on the periphery of the enzyme's active site, a feature which suggests that the complex might be less sensitive to amino acid substitution mutations within the protease. Gold(I) phosphine complexes appear to be only moderately active against HIV-1 PR but,

importantly, there is evidence of cross-inhibition for both HIV-1 RT and HIV-1 PR. A structurally diverse range of copper(II) complexes, and also 'free' copper(II) ions, display potent inhibitory effects and the activity of the latter species appears intimately linked to the presence of cysteine residues in the protease. Significant inroads have also been made in targeting the proteolytic enzymes of parasitic microorganisms, particularly those associated with malaria, trypanosomiasis and leishmaniasis. Ruthenium(II), iron(II) and gold(I) complexes incorporating the antimalarial quinolone-based drug, chloroquine, have activities exceeding that of metal-free chloroquine. The anti-arthritis, gold(I) prescription drug, auranofin, shows almost complete inhibition of *Plasmodium falciparum* growth at low micromolar concentrations. Additionally, a variety of gold(I) and gold(III) complexes are also active against prominent, thiolated proteins in *Trypanosoma cruzi*. Palladium(II) and oxorhenium(V) complexes constructed from tridentate ligands provide both activity and selectivity across a range of cysteine parasite proteases whilst being relatively silent against chymotrypsin. Furthermore, low micromolar concentrations of a palladium(II) complex can provide a lifeline to *T. cruzi*-infected macrophage cells. Dinuclear palladium(II) complexes, configured with a diphosphine and a chiral amine ligand, impress against cysteine proteases, discriminate positively between parasite and mammalian cells, and offer a better prognosis for the treatment of Chagas disease compared to the clinical drug, benznidazole. Leishmaniasis, in a mouse model, also responds well to treatment with an asymmetric, cyclopalladated complex, as evidenced by shrinkage of foot lesions and a dramatic reduction in parasite load.

To progress the rational design of even more effective, metal-based, protease inhibitors it is essential that we address the shortages of both computer modelling studies and the X-ray crystallographic data available on metal-complex-protease interactions. Furthermore, an important example from literature we wish to highlight is the rational design of oxorhenium complexes by Baird *et al.*[97] where it has been proposed that ligand modification can give enzyme selectivity and an inhibition mechanism has been proposed based on experimental data. Our final comment on the design of effective bioinorganic protease inhibitors is that it is crucial for researchers to examine, and report, the effects of uncoordinated metal ions and metal-free ligands on PR before describing inhibitory properties

on the corresponding complexes. The inhibitory evidence from Cu^{2+} , Hg^{2+} and Au^{3+} ions alone demonstrate that PR activity may not arise from a discrete complex being present in the reaction and therefore, it should not be taken for granted that simple metal ions and free ligands have negligible effects on PR.

References

- [1] Meggers, E., Targeting proteins with metal complexes. *Chem Commun (Camb)*, **2009**, (9), 1001-1010.
- [2] Sava, G.; Bergamo, A.; Dyson, P.J., Metal-based antitumour drugs in the post-genomic era: what comes next? *Dalton Trans.*, **2011**, 40, (36), 9069-9075.
- [3] Berners-Price, S.J.; Filipovska, A., Gold compounds as therapeutic agents for human diseases. *Metallomics*, **2011**, 3, (9), 863-873.
- [4] Gasser, G.; Metzler-Nolte, N. *Metal Compounds as Enzyme Inhibitors*. Wiley-VCH, **2011**.
- [5] Rosenthal, P.J., Cysteine proteases of malaria parasites. *Int J Parasitol*, **2004**, 34, (13-14), 1489-1499.
- [6] Li, D.; Liu, M.S.; Ji, B.; Hwang, K.C.; Huang, Y., Identifying the Molecular Mechanics and Binding Dynamics Characteristics of Potent Inhibitors to HIV-1 Protease. *Chem Biol Drug Des*, **2012**, 80, (3), 440-454.
- [7] Fricker, S.P., Cysteine proteases as targets for metal-based drugs. *Metallomics*, **2010**, 2, (6), 366-377.
- [8] Molla, A.; Granneman, G.R.; Sun, E.; Kempf, D.J., Recent developments in HIV protease inhibitor therapy. *Antiviral Res*, **1998**, 39, (1), 1-23.
- [9] Pandey, K.C.; Wang, S.X.; Sijwali, P.S.; Lau, A.L.; McKerrow, J.H.; Rosenthal, P.J., The Plasmodium falciparum cysteine protease falcipain-2 captures its substrate, hemoglobin, via a unique motif. *Proc Natl Acad Sci U S A*, **2005**, 102, (26), 9138-9143.
- [10] Doyle, P.S.; Zhou, Y.M.; Hsieh, I.; Greenbaum, D.C.; McKerrow, J.H.; Engel, J.C., The Trypanosoma cruzi protease cruzain mediates immune evasion. *PLoS Pathog*, **2011**, 7, (9), e1002139.
- [11] Krzywda, S.; Brzozowski, A.M.; Verma, C.; Karata, K.; Ogura, T.; Wilkinson, A.J., The crystal structure of the AAA domain of the ATP-dependent protease FtsH of Escherichia coli at 1.5 Å resolution. *Structure*, **2002**, 10, (8), 1073-1083.
- [12] Erez, E.; Fass, D.; Bibi, E., How intramembrane proteases bury hydrolytic reactions in the membrane. *Nature*, **2009**, 459, (7245), 371-378.
- [13] Pokorna, J.; Machala, L.; Rezacova, P.; Konvalinka, J., Current and Novel Inhibitors of HIV Protease. *Viruses*, **2009**, 1, (3), 1209-1239.

- [14] Issa, F.; Kassiou, M.; Rendina, L.M., Boron in drug discovery: carboranes as unique pharmacophores in biologically active compounds. *Chem Rev*, **2011**, *111*, (9), 5701-5722.
- [15] West, M.L.; Fairlie, D.P., Targeting HIV-1 protease: a test of drug-design methodologies. *Trends Pharmacol Sci*, **1995**, *16*, (2), 67-75.
- [16] Wlodawer, A.; Miller, M.; Jaskolski, M.; Sathyanarayana, B.K.; Baldwin, E.; Weber, I.T.; Selk, L.M.; Clawson, L.; Schneider, J.; Kent, S.B., Conserved folding in retroviral proteases: crystal structure of a synthetic HIV-1 protease. *Science*, **1989**, *245*, (4918), 616-621.
- [17] Ashorn, P.; McQuade, T.J.; Thaisrivongs, S.; Tomasselli, A.G.; Tarpley, W.G.; Moss, B., An inhibitor of the protease blocks maturation of human and simian immunodeficiency viruses and spread of infection. *Proc Natl Acad Sci U S A*, **1990**, *87*, (19), 7472-7476.
- [18] Lambert, D.M.; Petteway, S.R., Jr.; McDanal, C.E.; Hart, T.K.; Leary, J.J.; Dreyer, G.B.; Meek, T.D.; Bugelski, P.J.; Bolognesi, D.P.; Metcalf, B.W.; et al., Human immunodeficiency virus type 1 protease inhibitors irreversibly block infectivity of purified virions from chronically infected cells. *Antimicrob Agents Chemother*, **1992**, *36*, (5), 982-988.
- [19] Clavel, F.; Hance, A.J., HIV drug resistance. *N Engl J Med*, **2004**, *350*, (10), 1023-1035.
- [20] Santos, A.F.; Soares, M.A., HIV Genetic Diversity and Drug Resistance. *Viruses*, **2010**, *2*, (2), 503-531.
- [21] Judd, D.A.; Nettles, J.H.; Nevins, N.; Snyder, J.P.; Liotta, D.C.; Tang, J.; Ermolieff, J.; Schinazi, R.F.; Hill, C.L., Polyoxometalate HIV-1 protease inhibitors. A new mode of protease inhibition. *J Am Chem Soc*, **2001**, *123*, (5), 886-897.
- [22] Kempf, D.J.; Codacovi, L.; Wang, X.C.; Kohlbrenner, W.E.; Wideburg, N.E.; Saldivar, A.; Vasavanonda, S.; Marsh, K.C.; Bryant, P.; Sham, H.L.; et al., Symmetry-based inhibitors of HIV protease. Structure-activity studies of acylated 2,4-diamino-1,5-diphenyl-3-hydroxypentane and 2,5-diamino-1,6-diphenylhexane-3,4-diol. *J Med Chem*, **1993**, *36*, (3), 320-330.
- [23] Molla, A.; Korneyeva, M.; Gao, Q.; Vasavanonda, S.; Schipper, P.J.; Mo, H.M.; Markowitz, M.; Chernyavskiy, T.; Niu, P.; Lyons, N.; Hsu, A.; Granneman, G.R.; Ho, D.D.; Boucher, C.A.; Leonard, J.M.; Norbeck, D.W.;

Kempf, D.J., Ordered accumulation of mutations in HIV protease confers resistance to ritonavir. *Nat Med*, **1996**, 2, (7), 760-766.

[24] Chen, Z.; Li, Y.; Schock, H.B.; Hall, D.; Chen, E.; Kuo, L.C., Three-dimensional structure of a mutant HIV-1 protease displaying cross-resistance to all protease inhibitors in clinical trials. *J Biol Chem*, **1995**, 270, (37), 21433-21436.

[25] Ridky, T.W.; Kikonyogo, A.; Leis, J.; Gulnik, S.; Copeland, T.; Erickson, J.; Wlodawer, A.; Kurinov, I.; Harrison, R.W.; Weber, I.T., Drug-resistant HIV-1 proteases identify enzyme residues important for substrate selection and catalytic rate. *Biochemistry*, **1998**, 37, (39), 13835-13845.

[26] Hong, L.; Zhang, X.C.; Hartsuck, J.A.; Tang, J., Crystal structure of an in vivo HIV-1 protease mutant in complex with saquinavir: insights into the mechanisms of drug resistance. *Protein Sci*, **2000**, 9, (10), 1898-1904.

[27] Grimes, R.N., Metallocarboranes in the new millennium. *Coord. Chem. Rev.*, **2000**, 200, 773-811.

[28] Armstrong, A.F.; Valliant, J.F., The bioinorganic and medicinal chemistry of carboranes: from new drug discovery to molecular imaging and therapy. *Dalton Trans*, **2007**, (38), 4240-4251.

[29] Farras, P.; Juarez-Perez, E.J.; Lepsik, M.; Luque, R.; Nunez, R.; Teixidor, F., Metallocarboranes and their interactions: theoretical insights and their applicability. *Chem Soc Rev*, **2012**, 41, (9), 3445-3463.

[30] Rezacova, P.; Pokorna, J.; Brynda, J.; Kozisek, M.; Cigler, P.; Lepsik, M.; Fanfrlik, J.; Rezac, J.; Grantz Saskova, K.; Sieglöva, I.; Plesek, J.; Sicha, V.; Gruner, B.; Oberwinkler, H.; Sedlacek, J.; Krausslich, H.G.; Hobza, P.; Kral, V.; Konvalinka, J., Design of HIV protease inhibitors based on inorganic polyhedral metallocarboranes. *J Med Chem*, **2009**, 52, (22), 7132-7141.

[31] Cigler, P.; Kozisek, M.; Rezacova, P.; Brynda, J.; Otwinowski, Z.; Pokorna, J.; Plesek, J.; Gruner, B.; Doleckova-Maresova, L.; Masa, M.; Sedlacek, J.; Bodem, J.; Krausslich, H.G.; Kral, V.; Konvalinka, J., From nonpeptide toward noncarbon protease inhibitors: metallocarboranes as specific and potent inhibitors of HIV protease. *Proc Natl Acad Sci U S A*, **2005**, 102, (43), 15394-15399.

[32] Kozisek, M.; Cigler, P.; Lepsik, M.; Fanfrlik, J.; Rezacova, P.; Brynda, J.; Pokorna, J.; Plesek, J.; Gruner, B.; Grantz Saskova, K.; Vaclavikova, J.; Kral, V.;

- Konvalinka, J., Inorganic polyhedral metallacarborane inhibitors of HIV protease: a new approach to overcoming antiviral resistance. *J Med Chem*, **2008**, *51*, (15), 4839-4843.
- [33] Rhule, J.T.; Hill, C.L.; Judd, D.A.; Schinazi, R.F., Polyoxometalates in Medicine. *Chem Rev*, **1998**, *98*, (1), 327-358.
- [34] Hasenknopf, B., Polyoxometalates: introduction to a class of inorganic compounds and their biomedical applications. *Front Biosci*, **2005**, *10*, 275-287.
- [35] Gerth, H.U.; Rompel, A.; Krebs, B.; Boos, J.; Lanvers-Kaminsky, C., Cytotoxic effects of novel polyoxotungstates and a platinum compound on human cancer cell lines. *Anticancer Drugs*, **2005**, *16*, (1), 101-106.
- [36] Kogerler, P.; Tsukerblat, B.; Muller, A., Structure-related frustrated magnetism of nanosized polyoxometalates: aesthetics and properties in harmony. *Dalton Trans*, **2010**, (1), 21-36.
- [37] Long, D.L.; Burkholder, E.; Cronin, L., Polyoxometalate clusters, nanostructures and materials: from self assembly to designer materials and devices. *Chem Soc Rev*, **2007**, *36*, (1), 105-121.
- [38] Hill, C.L.; Weeks, M.S.; Schinazi, R.F., Anti-HIV-1 activity, toxicity, and stability studies of representative structural families of polyoxometalates. *J Med Chem*, **1990**, *33*, (10), 2767-2772.
- [39] Hill, C.L., Introduction: Polyoxometalates-Multicomponent Molecular Vehicles To Probe Fundamental Issues and Practical Problems. *Chem Rev*, **1998**, *98*, (1), 1-2.
- [40] Flutsch, A.; Schroeder, T.; Grutter, M.G.; Patzke, G.R., HIV-1 protease inhibition potential of functionalized polyoxometalates. *Bioorg Med Chem Lett*, **2011**, *21*, (4), 1162-1166.
- [41] Sijbesma, R.; Srdanov, G.; Wudl, F.; Castoro, J.A.; Wilkins, C.; Friedman, S.H.; DeCamp, D.L.; Kenyon, G.L., Synthesis of a fullerene derivative for the inhibition of HIV enzymes. *J. Am. Chem. Soc.*, **1993**, *115*, (15), 6510-6512.
- [42] Fischer, J.; Ricard, L.; Weiss, R., The structure of the heteropolytungstate (NH₄)₁₇Na NaW₂₁Sb₉O₈₆·14H₂O. An inorganic crypate. *J Am Chem Soc*, **1976**, *98*, (10), 3050-3052.

- [43] Ablashi, D.V.; Twardzik, D.R.; Easton, J.M.; Armstrong, G.R.; Luetzeler, J.; Jasmin, C.; Chermann, J.C., Effects of 5-tungsto-2-antimoniate in oncogenic DNA and RNA virus-cell systems. *Eur J Cancer*, **1977**, *13*, (7), 713-720.
- [44] Chermann, J.C.; Sinoussi, F.C.; Jasmin, C., Inhibition of RNA-dependent DNA polymerase of murine oncornaviruses by ammonium-5-tungsto-2-antimoniate. *Biochem Biophys Res Commun*, **1975**, *65*, (4), 1229-1236.
- [45] Herve, M.; Sinoussi-Barre, F.; Chermann, J.C.; Herve, G.; Jasmin, C., Correlation between structure of polyoxotungstates and their inhibitory activity on polymerases. *Biochem Biophys Res Commun*, **1983**, *116*, (1), 222-229.
- [46] Cholewa, M.; Legge, G.J.; Weigold, H.; Holan, G.; Birch, C.J., The use of a scanning proton microprobe to observe anti-HIV drugs within cells. *Life Sci*, **1994**, *54*, (21), 1607-1612.
- [47] Rozenbaum, W.; Dormont, D.; Spire, B.; Vilmer, E.; Gentilini, M.; Griscelli, C.; Montagnier, L.; Barre-Sinoussi, F.; Chermann, J.C., Antimoniotungstate (HPA 23) treatment of three patients with AIDS and one with prodrome. *Lancet*, **1985**, *1*, (8426), 450-451.
- [48] Moskovitz, B.L., Clinical trial of tolerance of HPA-23 in patients with acquired immune deficiency syndrome. *Antimicrob Agents Chemother*, **1988**, *32*, (9), 1300-1303.
- [49] Inouye, Y.; Tokutake, Y.; Kuniyama, J.; Yoshida, T.; Yamase, T.; Nakata, A.; Nakamura, S., Suppressive effect of polyoxometalates on the cytopathogenicity of human immunodeficiency virus type 1 (HIV-1) in vitro and their inhibitory activity against HIV-1 reverse transcriptase. *Chem Pharm Bull (Tokyo)*, **1992**, *40*, (3), 805-807.
- [50] Benedek, T.G., The history of gold therapy for tuberculosis. *J Hist Med Allied Sci*, **2004**, *59*, (1), 50-89.
- [51] Shaw, I.C., Gold-based therapeutic agents. *Chem Rev*, **1999**, *99*, (9), 2589-2600.
- [52] Dabrowiak, J.C. *Metals in Medicine*. Wiley: New York, **2009**.
- [53] Shapiro, D.L.; Masci, J.R., Treatment of HIV associated psoriatic arthritis with oral gold. *J Rheumatol*, **1996**, *23*, (10), 1818-1820.
- [54] Fonteh, P.; Meyer, D., Novel gold(I) phosphine compounds inhibit HIV-1 enzymes. *Metallomics*, **2009**, *1*, (5), 427-433.

- [55] Fonteh, P.N.; Keter, F.K.; Meyer, D.; Guzei, I.A.; Darkwa, J., Tetra-chloro-(bis-(3,5-dimethylpyrazolyl)methane)gold(III) chloride: An HIV-1 reverse transcriptase and protease inhibitor. *J Inorg Biochem*, **2009**, *103*, (2), 190-194.
- [56] Fonteh, P.N.; Keter, F.K.; Meyer, D., HIV therapeutic possibilities of gold compounds. *Biometals*, **2010**, *23*, (2), 185-196.
- [57] Karlstrom, A.R.; Levine, R.L., Copper inhibits the protease from human immunodeficiency virus 1 by both cysteine-dependent and cysteine-independent mechanisms. *Proc Natl Acad Sci U S A*, **1991**, *88*, (13), 5552-5556.
- [58] Davis, D.A.; Branca, A.A.; Pallenberg, A.J.; Marschner, T.M.; Patt, L.M.; Chatlynne, L.G.; Humphrey, R.W.; Yarchoan, R.; Levine, R.L., Inhibition of the human immunodeficiency virus-1 protease and human immunodeficiency virus-1 replication by bathocuproine disulfonic acid CuI⁺. *Arch Biochem Biophys*, **1995**, *322*, (1), 127-134.
- [59] DeCamp, D.L.; Babe, L.M.; Salto, R.; Lucich, J.L.; Koo, M.S.; Kahl, S.B.; Craik, C.S., Specific inhibition of HIV-1 protease by boronated porphyrins. *J Med Chem*, **1992**, *35*, (18), 3426-3428.
- [60] Lebon, F.; Rosny, E.d.; Reboud-Ravaux, M.I.; Durant, F.o., De novo drug design of a new copper chelate molecule acting as HIV-1 protease inhibitor. *European Journal of Medicinal Chemistry*, **1998**, *33*, (9), 733-737.
- [61] Lebon, F.; Boggetto, N.; Ledecq, M.; Durant, F.; Benatallah, Z.; Sicsic, S.; Lapouyade, R.; Kahn, O.; Mouithys-Mickalad, A.; Deby-Dupont, G.; Reboud-Ravaux, M., Metal-organic compounds: a new approach for drug discovery. N1-(4-methyl-2-pyridyl)-2,3,6-trimethoxybenzamide copper(II) complex as an inhibitor of human immunodeficiency virus 1 protease. *Biochem Pharmacol*, **2002**, *63*, (10), 1863-1873.
- [62] Lebon, F.; Ledecq, M.; Dieu, M.; Demazy, C.; Remacle, J.; Lapouyade, R.; Kahn, O.; Durant, F., Synthesis and structural analysis of the copper(II) complexes of N2-(2-pyridylmethyl)-2-pyridinecarboxamide. *J Inorg Biochem*, **2001**, *86*, (2-3), 547-554.
- [63] Sajid, M.; McKerrow, J.H., Cysteine proteases of parasitic organisms. *Mol Biochem Parasitol*, **2002**, *120*, (1), 1-21.
- [64] Chapman, H.A.; Riese, R.J.; Shi, G.P., Emerging roles for cysteine proteases in human biology. *Annu Rev Physiol*, **1997**, *59*, 63-88.

- [65] Supuran, C.T.; Scozzafava, A.; Clare, B.W., Bacterial protease inhibitors. *Med Res Rev*, **2002**, 22, (4), 329-372.
- [66] Navarro, M.; Gabbiani, C.; Messori, L.; Gambino, D., Metal-based drugs for malaria, trypanosomiasis and leishmaniasis: recent achievements and perspectives. *Drug Discov Today*, **2010**, 15, (23-24), 1070-1078.
- [67] Abbenante, G.; Fairlie, D.P., Protease inhibitors in the clinic. *Med Chem*, **2005**, 1, (1), 71-104.
- [68] Rosenthal, P.J.; Wollish, W.S.; Palmer, J.T.; Rasnick, D., Antimalarial effects of peptide inhibitors of a Plasmodium falciparum cysteine proteinase. *J Clin Invest*, **1991**, 88, (5), 1467-1472.
- [69] Khanye, S.D.; Smith, G.S.; Lategan, C.; Smith, P.J.; Gut, J.; Rosenthal, P.J.; Chibale, K., Synthesis and in vitro evaluation of gold(I) thiosemicarbazone complexes for antimalarial activity. *J Inorg Biochem*, **2010**, 104, (10), 1079-1083.
- [70] Cortes, A.; Mellombo, M.; Mueller, I.; Benet, A.; Reeder, J.C.; Anders, R.F., Geographical structure of diversity and differences between symptomatic and asymptomatic infections for Plasmodium falciparum vaccine candidate AMA1. *Infect Immun*, **2003**, 71, (3), 1416-1426.
- [71] Anderson, T.J.; Haubold, B.; Williams, J.T.; Estrada-Franco, J.G.; Richardson, L.; Mollinedo, R.; Bockarie, M.; Mokili, J.; Mharakurwa, S.; French, N.; Whitworth, J.; Velez, I.D.; Brockman, A.H.; Nosten, F.; Ferreira, M.U.; Day, K.P., Microsatellite markers reveal a spectrum of population structures in the malaria parasite Plasmodium falciparum. *Mol Biol Evol*, **2000**, 17, (10), 1467-1482.
- [72] Kerr, I.D.; Lee, J.H.; Pandey, K.C.; Harrison, A.; Sajid, M.; Rosenthal, P.J.; Brinen, L.S., Structures of falcipain-2 and falcipain-3 bound to small molecule inhibitors: implications for substrate specificity. *J Med Chem*, **2009**, 52, (3), 852-857.
- [73] Pandey, K.C.; Dixit, R., Structure-function of falcipains: malarial cysteine proteases. *J Trop Med*, **2012**, 2012, 345195.
- [74] Wang, S.X.; Pandey, K.C.; Somoza, J.R.; Sijwali, P.S.; Kortemme, T.; Brinen, L.S.; Fletterick, R.J.; Rosenthal, P.J.; McKerrow, J.H., Structural basis for unique mechanisms of folding and hemoglobin binding by a malarial protease. *Proc Natl Acad Sci U S A*, **2006**, 103, (31), 11503-11508.

- [75] Hogg, T.; Nagarajan, K.; Herzberg, S.; Chen, L.; Shen, X.; Jiang, H.; Wecke, M.; Blohmke, C.; Hilgenfeld, R.; Schmidt, C.L., Structural and functional characterization of Falcipain-2, a hemoglobinase from the malarial parasite *Plasmodium falciparum*. *J Biol Chem*, **2006**, *281*, (35), 25425-25437.
- [76] McKerrow, J.H., Development of cysteine protease inhibitors as chemotherapy for parasitic diseases: insights on safety, target validation, and mechanism of action. *Int J Parasitol*, **1999**, *29*, (6), 833-837.
- [77] Rosenthal, P.J.; Lee, G.K.; Smith, R.E., Inhibition of a *Plasmodium vinckei* cysteine proteinase cures murine malaria. *J Clin Invest*, **1993**, *91*, (3), 1052-1056.
- [78] Engel, J.C.; Doyle, P.S.; Hsieh, I.; McKerrow, J.H., Cysteine protease inhibitors cure an experimental *Trypanosoma cruzi* infection. *J Exp Med*, **1998**, *188*, (4), 725-734.
- [79] Fricker, S.P.; Mosi, R.M.; Cameron, B.R.; Baird, I.; Zhu, Y.; Anastassov, V.; Cox, J.; Doyle, P.S.; Hansell, E.; Lau, G.; Langille, J.; Olsen, M.; Qin, L.; Skerlj, R.; Wong, R.S.; Santucci, Z.; McKerrow, J.H., Metal compounds for the treatment of parasitic diseases. *J Inorg Biochem*, **2008**, *102*, (10), 1839-1845.
- [80] Paladi, C.d.S.; Pimentel, I.A.S.; Katz, S.; Cunha, R.L.O.R.; Judice, W.A.d.S.; Caires, A.C.F.; Barbi/Veri, C.L.c., In Vitro and In Vivo Activity of a Palladacycle Complex on *Leishmania (Leishmania) amazonensis*. *PLoS Negl Trop Dis*, **2012**, *6*, (5), e1626.
- [81] Sanchez-Delgado, R.A.; Anzellotti, A.; Suarez, L. *Metal Complexes as Chemotherapeutic Agents Against Tropical Diseases, Malaria, Trypanosomiasis, and Leishmaniasis*. Marcel Dekker, **2004**.
- [82] Newton, P.; White, N., Malaria: new developments in treatment and prevention. *Annu Rev Med*, **1999**, *50*, 179-192.
- [83] Sanchez-Delgado, R.A.; Navarro, M.; Perez, H.; Urbina, J.A., Toward a novel metal-based chemotherapy against tropical diseases. 2. Synthesis and antimalarial activity in vitro and in vivo of new ruthenium- and rhodium-chloroquine complexes. *J Med Chem*, **1996**, *39*, (5), 1095-1099.
- [84] Biot, C.; Glorian, G.; Maciejewski, L.A.; Brocard, J.S., Synthesis and antimalarial activity in vitro and in vivo of a new ferrocene-chloroquine analogue. *J Med Chem*, **1997**, *40*, (23), 3715-3718.

- [85] Navarro, M.; Perez, H.; Sanchez-Delgado, R.A., Toward a novel metal-based chemotherapy against tropical diseases. 3. Synthesis and antimalarial activity in vitro and in vivo of the new gold-chloroquine complex [Au(PPh₃)(CQ)]PF₆. *J Med Chem*, **1997**, *40*, (12), 1937-1939.
- [86] <http://clinicaltrials.gov/ct2/show/NCT00563914?term=ferroquin&rank=2>
- [87] <http://clinicaltrials.gov/ct2/show/NCT00988507>
- [88] Biot, C.; Dubar, F.; Khalife, J.; Slomianny, C., Opening up the advantages of the ruthenocenic bioprobes of ferroquine: distribution and localization in Plasmodium falciparum-infected erythrocytes. *Metallomics*, **2012**, *4*, (8), 780-783.
- [89] Berman, J.D.; Grogil, M., Leishmania mexicana: chemistry and biochemistry of sodium stibogluconate (Pentostam). *Exp Parasitol*, **1988**, *67*, (1), 96-103.
- [90] Mesa-Valle, C.M.; Moraleda-Lindez, V.; Craciunescu, D.; Alonso, M.P.; Osuna, A., In vitro action of new organometallic compounds against Trypanosomatidae protozoa. *Arzneimittelforschung*, **1993**, *43*, (9), 1010-1013.
- [91] Micale, N.; Cinellu, M.A.; Maiore, L.; Sannella, A.R.; Severini, C.; Schirmeister, T.; Gabbiani, C.; Messori, L., Selected gold compounds cause pronounced inhibition of Falcipain 2 and effectively block P. falciparum growth in vitro. *J Inorg Biochem*, **2011**, *105*, (12), 1576-1579.
- [92] Du, X.; Guo, C.; Hansell, E.; Doyle, P.S.; Caffrey, C.R.; Holler, T.P.; McKerrow, J.H.; Cohen, F.E., Synthesis and structure-activity relationship study of potent trypanocidal thio semicarbazone inhibitors of the trypanosomal cysteine protease cruzain. *J Med Chem*, **2002**, *45*, (13), 2695-2707.
- [93] Bincoletto, C.; Tersariol, I.L.; Oliveira, C.R.; Dreher, S.; Fausto, D.M.; Soufen, M.A.; Nascimento, F.D.; Caires, A.C., Chiral cyclopalladated complexes derived from N,N-dimethyl-1-phenethylamine with bridging bis(diphenylphosphine)ferrocene ligand as inhibitors of the cathepsin B activity and as antitumoral agents. *Bioorg Med Chem*, **2005**, *13*, (8), 3047-3055.
- [94] Mesa-Valle, C.M.; Moraleda, V.; Lazuen, J.; Craciunescu, D.; Osuna, A., Action of new organometallic complexes against Leishmania donovani. *J Antimicrob Chemother*, **1997**, *40*, (1), 47-57.
- [95] Rodrigues, E.G.; Silva, L.S.; Fausto, D.M.; Hayashi, M.S.; Dreher, S.; Santos, E.L.; Pesquero, J.B.; Travassos, L.R.; Caires, A.C., Cyclopalladated

compounds as chemotherapeutic agents: antitumor activity against a murine melanoma cell line. *Int J Cancer*, **2003**, *107*, (3), 498-504.

[96] Matsuo, A.L.; Silva, L.S.; Torrecilhas, A.C.; Pascoalino, B.S.; Ramos, T.C.; Rodrigues, E.G.; Schenkman, S.; Caires, A.C.; Travassos, L.R., In vitro and in vivo trypanocidal effects of the cyclopalladated compound 7a, a drug candidate for treatment of Chagas' disease. *Antimicrob Agents Chemother*, **2010**, *54*, (8), 3318-3325.

[97] Mosi, R.; Baird, I.R.; Cox, J.; Anastassov, V.; Cameron, B.; Skerlj, R.T.; Fricker, S.P., Rhenium inhibitors of cathepsin B (ReO(SYS)X (where Y = S, py; X = Cl, Br, SPhOMe-p)): Synthesis and mechanism of inhibition. *J Med Chem*, **2006**, *49*, (17), 5262-5272